A0203

Current status of NEDO project on durability and reliability of SOFC cell-stacks

Teruhisa Horita
National Institute of Advanced Industrial Science and Technology (AIST)
Umezono 1-1-1, Tsukuba, 305-8568 Ibaraki/Japan

Contact authors: www.EFCF.com/ContactRequest

Abstract

The Japanese national R&D project on SOFC durability and reliability has been conducting by the New Energy Development Organization (NEDO) for more than 10 years. The current project focused on the elucidation of the degradation mechanism for the rapid evaluation method of a lifetime of 10 years (90,000 hours). Until 2017, we have completed the evaluation methods for the lifetime of stacks by the elucidation of the degradation mechanisms. From 2018 to 2019, the project was extended for focusing on the improvement of the efficiency of SOFC cell-stacks. The target of the project is the following: (1) to make a concept for high efficient SOFC cell-stack over 65%LHV and (2) to make a concept of toughness on cell-stacks with load cycling. This paper reports recent achievements on the concepts for high efficiency and load cycling of stacks in 2018-2019. Some cell-stacks showed relatively high stability against high fuel utilization over Uf=80%: the degradation rate was about 0.3-2.0 %/kh, which is the same level of normal condition. The post analyses were examined at the samples with high Uf operation. In the stacks operated at high Uf, Ni oxidation and microstructure change were observed at Ni-YSZ anode. The feasibility study on high efficiency and load cycling of stacks suggested the possibility and limitation of stacks that operated at high efficient modes.

https://doi.org/10.5281/zenodo.4518679

Introduction

The Japanese national R&D project on SOFC durability and reliability has been conducting by the New Energy Development Organization (NEDO) for more than 10 years [1-3]. A recent project is “Technology Development for Promotion of Practical Application of Solid Oxide Fuel Cells (FY 2013- 2019)”, in which much efforts were focused on the elucidation of degradation mechanism and the development of evaluation method of the lifetime of cell-stacks (Fig.1). During the first term of the project (2013-2017), the rapid evaluation methods of durability were developed to evaluate the lifetime with 10 years (90,000 hours) [4]. The Central Research Institute for Electric Power Industries (CRIEPI) developed the current interruption methods for the evaluation of resistance arising from the stacks with electrode polarization and ohmic resistances. Several universities and research institutes proposed the advanced evaluation methods for degradation of cell-stacks, such as impurity concentration at the electrode/electrolyte interfaces (AIST), 3D-reconstruction and microstructure change evaluation methods with FIB-SEM/STEM (Kyoto Univ., Univ. Tokyo, and Kyushu University), stress and mechanical strength evaluation under operation condition (Tohoku Univ.), and simulation methods of electrode-cell-stack performances (Kyoto Univ., Univ. Tokyo, Tohoku Univ., and AIST). From 2018, according to the Japanese Basic Hydrogen Plan for promoting the higher efficiency and wider application of fuel cells by the Japanese government [5, 6], we started the feasibility study of SOFC stacks durability with high-efficient and load cycling modes [7,8]. In this paper, the progress of the project is reported especially on the feasibility of stack durability at high efficiency (LHV 65% concept) and load cycling in 2018-2019.

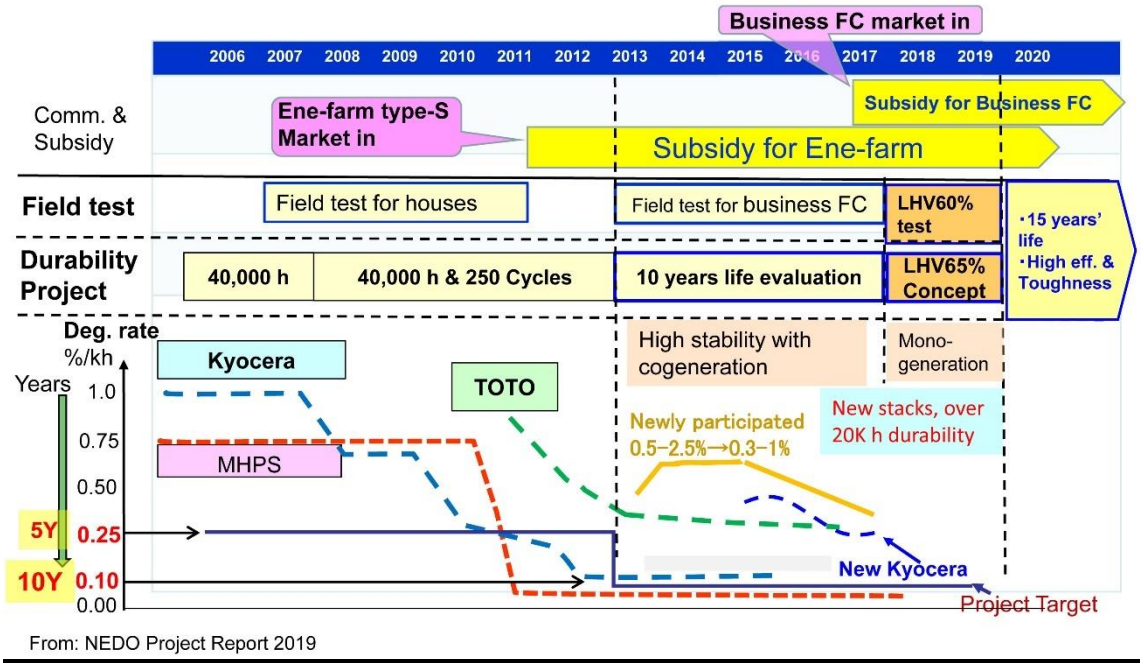

Figure 1 History of national project on SOFC durability and improvement of degradation rates.

Project structure and member

Figure 2 shows a structure of the recent project for the development of the concept with high-efficient/toughness cell-stacks. The project is composed of four research sub-projects: 1) Stack durability evaluation, 2) Clarification of degradation mechanism, 3) Evaluation methods development, and 4) Integration and Summary. The sub-project is correlated with each other for promoting the R&D and to accomplish the target. On the left-hand side, several cell-stack developers (KYOCERA Corporation Ltd., NGK-Insulators Co., Ltd., MORIMURA SOFC TECHOLOGY Co., LTD, and DENSO CORPORATION) supplied their stacks to the CRIEPI for the evaluation of degradation in the long-term operation at high fuel utilization over 80% and load cycling. Other topics were conducted by a collaboration with some companies and universities/ research institutes. On the right-hand side, the degradation mechanism was investigated at the academic consortium (universities and research institute) by using their superior analytical techniques.

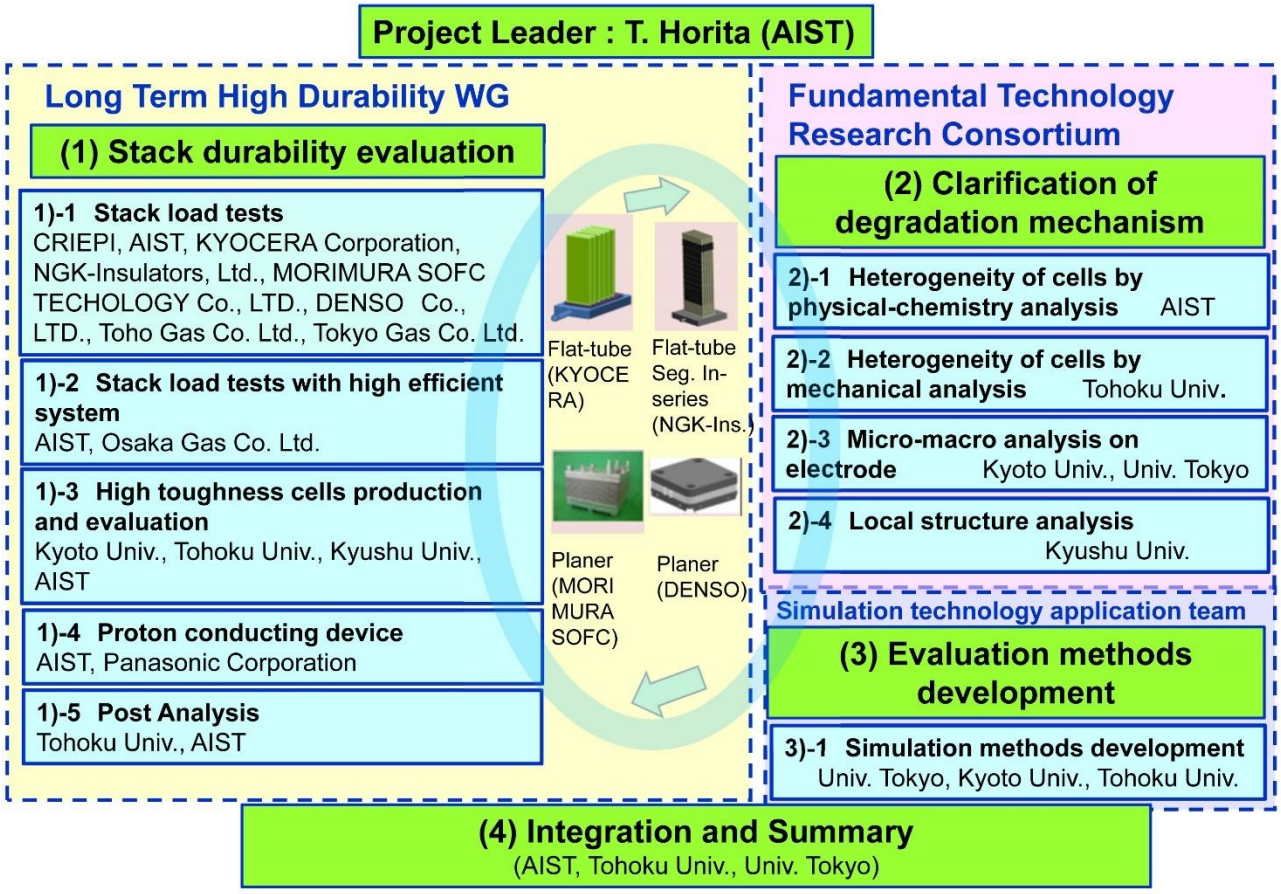

Figure 2 Schematic diagram of the project structure of "Fundamental study for Rapid Evaluation Method of SOFC Durability (2018-2019)."

(MORIMURA SOFC TECHNOLOGY CO., LTD: inherited Planer SOFC business from NGK sparkplug from 2019)

https://doi.org/10.5281/zenodo.4518679

Stack durability test under high efficiency

The long-term operation tests with relatively high fuel utilization have been conducted for four practical stacks. Table 1 summarizes the degradation rates and degradation factors of stacks over ten thousand hours' operation measured by CRIEPI. The degradation rates of flat-tube (KYOCERA Corporation), segment in-series (NGK Insulators), planer (MORIMURA SOFC TECHOLOGY Co., LTD), and planer (DENSO Corporation) are examined between the high (Uf=80 and 85%) and normal (Uf~70%) fuel utilizations. The degradation rates at high fuel utilization are similar values between high and normal, indicating high stability under high fuel utilization examined. The main degradation factor of these stacks is an increase of resistance at the ohmic and the polarization of cathode, which is the same increase trends under the normal fuel utilization conditions. With increasing fuel utilization up to 85%, the stack degradation gradually increased in the flat tubular stacks, while the degradation rates of segment in-series and planer show the same level with Uf=80%. Even high fuel utilization at Uf=85%, the degradation factors were the same with Uf=80%, which indicates a similar degradation mechanism occurred in the stacks. The degradation rates were also examined at several kinds of load cycling (power output fluctuation). The precise experimental results will be given in another paper elsewhere. The degradation by load cycling is relatively small with almost no difference in the degradation rates with the normal steady-state operation. The experimental results suggest that the possibility of high efficiency operation of the present cell-stacks, although microstructures of cells can be damaged at the nano-micrometer level of Ni-YSZ anode and cathode.

Table 1. Degradation rates and factors of several stacks under high fuel utilization (measured by CRIEPI) (Report from NEDO Project (2020).

Fuel utilization, Uf		**Flat tubular** (KYOCERA Co.)	**Segment in-series** (NGK Insulators)	**Planer** (MORIMURA SOFC TECH.)	**Planer** (DENSO Co.)
Uf=80%	Test of duration	11,348 h	12,100 h	18,815 h	5,477 h
	Degradation rate	0.34%/kh	0.46%/kh	0.31%/kh	2.85%/kh
	Main deg. factors	IR-loss, Cathode	IR-loss	IR-loss, Cathode	Cathode
Uf~70% reference	Deg.rate	0.33%/kh	0.49%/kh	0.34%/kh	~2.0%/kh
Uf=85%	Test of duration	6,899 h	7,760 h	9,030 h	No data
	Degradation rate	-0.51%/1kh	-0.52%/1kh	0.38%/1kh	No data
	Main deg. factors	IR-loss, Cathode	IR-loss	IR-loss, Cathode	No data

https://doi.org/10.5281/zenodo.4518679

Post Analysis of cell-stacks operated at high fuel utilization

The post analyses of cell-stacks after the high fuel utilization/load cycling tests were examined by the academic institutes (Universities and AIST). In this report, part of the obtained results is presented at Ni-YSZ anode of the flat-tube and planer stacks. Figure 3 shows an example of microstructures of Ni-YSZ anode/support (distribution of Ni by SEM/EDS) operated after load cycling under normal (Uf~70%) and high (Uf=80%) fuel utilization. The images are taken at the upper cells (outlet of fuel gases), where much amounts of water vapor exist in the fuel gases (left and middle), with reference at the bottom (left). As shown in Fig.3, no obvious Ni growth was observed at anode and support, suggesting the stability of microstructures in Ni-YSZ under load cycling. Even though the amount of water vapors, the microstructure is kept as the original in the observed areas. This indicates the stability of Ni-YSZ anode under high humidity conditions.

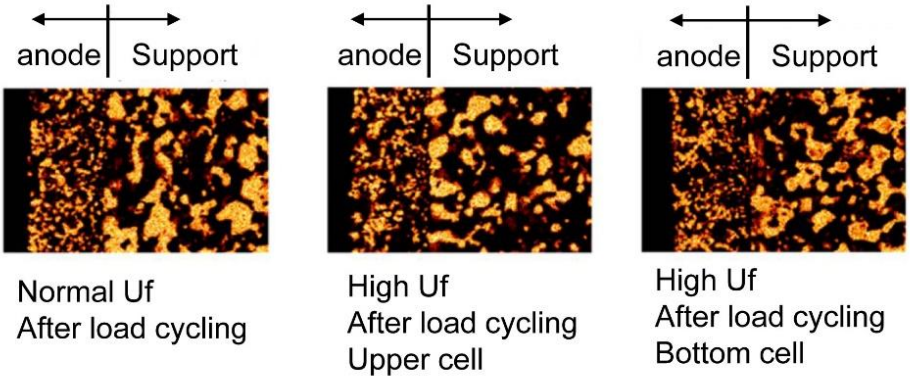

Figure 3 Microstructures of Ni at the Ni-YSZ anode and support: SEM/EDS mapping of Ni (data obtained by AIST, from NEDO project report (2020).

In the planer type cell-stacks (MORIMURA SOFC TECHNOLOGY Co., LTD.), there is a decrease of TPB length after the operation. Figure 4 shows the volume-specific TPB length of Ni-YSZ anode after the long-term operation of planer cells at the inlet and outlet of fuel gases. The TPB length decreased close to the anode/electrolyte interfaces at the outlet side of the cell, suggesting a significant loss of Ni close to the anode/electrolyte interfaces. Further microstructure analysis suggested that the loss of Ni particles in Ni-YSZ anode by the formation of $Ni(OH)_2$ and NiO due to high water vapor pressures and polarization. This indicates the significant movements of Ni by the diffusion or evaporation in the planer cells: the lower activity of Ni-YSZ anode at the outlet of fuel gases (higher water vapor pressure areas). Therefore, it is very important to evaluate the active areas working as anode under high water vapor pressures for high efficient modes.

https://doi.org/10.5281/zenodo.4518679

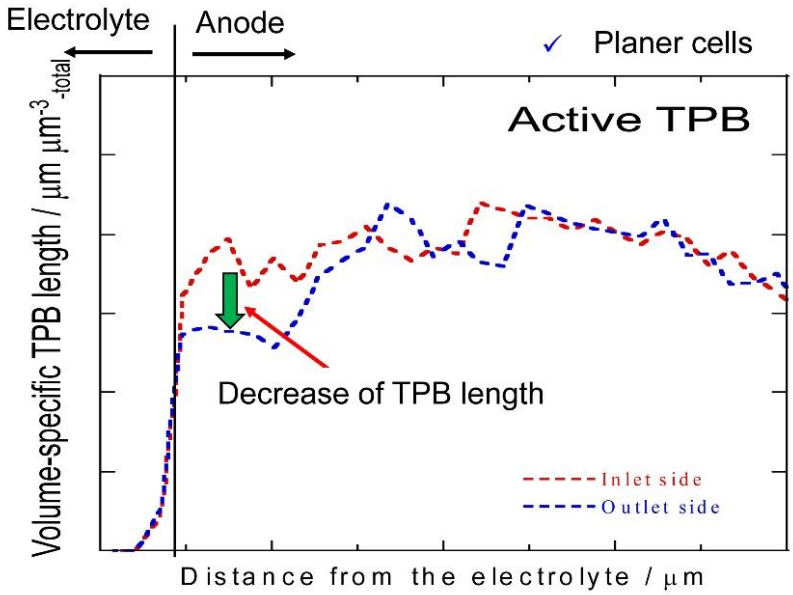

Figure 4 Length of TPB close to the anode/electrolyte interfaces by the 3D reconstruction methods (data obtained by Kyoto University, from NEDO project report (2020)).

Summary

The recent SOFC national project of Japan was introduced: NEDO project, “Technology Development for Promoting SOFC Commercialization/ Fundamental study for Rapid Evaluation Method of SOFC Durability (2018-2019)”. In the term of 2018-2019, the target of the project is (1) making a concept for high-efficient SOFC cell-stacks over 65%LHV and (2) making a concept for toughness on cell-stacks with load cycling. Rapid evaluation methods were applied to the samples after the high-efficient operation. The project was successful in making the concept for high efficiency and toughness of SOFC cell-stacks. The cell-stack showed relatively high stability against high fuel utilization (over 80%) and power output changes. By the post-analysis of cell-stacks after high fuel utilization and load cycling, there can be the formation of NiO due to the high water vapor pressures at the outlet of fuel gases in the planer cell-sack. Therefore, we need an optimization of fuel flows in the planer type for the high efficient mode operation. Further investigation is needed to improve the performance of cell-stacks.

Acknowledgments

The preset report was financially supported by the NEDO project “Technology Development for Promoting SOFC Commercialization/ Fundamental study for Rapid Evaluation Method of SOFC Durability (2018-2019)”. The author also thanks the working members from the following companies, universities, and research institutes: KYOCERA Corporation, MORIMURA SOFC TECHNOLOGY Co. LTD., NGK- Insulators Co, Ltd., DENSO Corporation, Osaka Gas Corporation Ltd., Tokyo Gas Corporation Ltd., Toho Gas Corporation Ltd., Central Research Institute for Electric Power Companies, National Institute of Advanced Industrial Science and Technology, Tohoku University, The University of Tokyo, Kyoto University, and Kyushu University.

References

1. H. Nirasawa, ECS Transactions, Vol.78 (1) 33-40 (2017).
2. H. Yokokawa, 26th Symposium on Solid Oxide Fuel Cells in Japan, 101A (2017).
3. H. Yokokawa, 27th Symposium on Solid Oxide Fuel Cells in Japan, 101A (2018).
4. H. Yokokawa et al., *Fuel Cells*, Vol.17, No.4, 473-497 (2017).
5. Japanese Basic Hydrogen Strategy (December 2017) https://www.meti.go.jp/english/press/2017/1226_003.html
6. Japanese Hydrogen and Fuel Cells Strategic Plan (March 2019) https://www.meti.go.jp/shingikai/energy_environment/suiso_nenryo/016.html
7. T. Horita, 28th Symposium on Solid Oxide Fuel Cells in Japan, 201A (2019).
8. T. Horita, ECS Transactions, Vol.91, (1) 247-253 (2019).

Keywords: EFCF 2020, SOx
Session A02: P2: Keynotes by FCH JU - EU Programs, US, Japan, China

https://doi.org/10.5281/zenodo.4518679

A0204

Solid Oxide Cells Development in China

Minfang Han, Zewei Lyu
(1) State Key Laboratory of Power Systems, Department of Energy and Power Engineering, Tsinghua University, 100084 Beijing/P.R. China
(2) Beijing Key Laboratory of CO_2 Utilization and Reduction Technology, Department of Energy and Power Engineering, Tsinghua University, 100084 Beijing/P.R. China
Contact authors: www.EFCF.com/ContactRequest

Abstract

Both Solid oxide fuel cell (SOFC) and Solid oxide electrolysis cell (SOEC) develop very quickly in the world recently. This work details the growth and evolution of SOFC technology from fundamental science to engineering in China. Supported by the Chinese National 973 Program of MOST (Ministry of Science and Technology of China) from 2011 to 2016, fundamental research was carried out to clear the scientific issues in SOFC area, including the construction of the cell structure and its electrochemical behavior, the coupled mechanisms of multi-physics and multi-scale in SOFC, as well as the energy management and analysis of overall system. Currently, the degradation mechanism of SOFC and durability enhancement, supported by National Key R&D Program of China from 2019 to 2023, is engaging in China. Meanwhile, the SOFC industry chain *from powder to power* has been constructed to solve the engineering issues, including materials preparation, cell manufacture, stack assembly and system integration. The first SOFC production line with the scale of 200,000 cells per year has been put into service in Xuzhou City, Jiangsu Province since August, 2019. Based on the scale-up of the cells and stacks, a coal-based fuel cell integrated demonstration system has been designed and built in Shanxi Province. Another highlighted national project in China is the *Coal Gasification Power System with Near Zero CO_2 Emission*, which is also supported by National Key R&D Program of China from 2017 to 2021. All these works will lay a foundation for practical application of SOFC technology in China, providing contributions to the future clean and high efficiency power plants using coal and other fuels. Meanwhile, SOEC related research has also lasted for years in China, which is mainly supported by local governments. From 2019, a SOEC demonstration project has been implemented by Tsinghua Team together with CHN ENERGY Investment Group Co. LTD, supported by Beijing Science and Technology Commission.

https://doi.org/10.5281/zenodo.4518715

1. Introduction

China's coal based natural resources determine the energy consumption structure dominated by coal in the short term. At present, thermal power accounts for more than 60% of total power generation in China, while the world average is about 38% [1]. Therefore, carbon emissions and pollution from coal utilization have attracted the greatest attention of all institutions, as the Chinese government has promised to achieve carbon neutrality by 2060 [2]. On the one hand, China has carried out a thorough technical transformation of coal-fired power plants, realizing the clean upgrading of the whole process [3,4]. On the other hand, renewable energy and hydrogen related technologies have also been strongly supported and demonstrated in recent years [1].
Solid oxide fuel cells (SOFCs) have attracted more and more attention due to their high electrical efficiency and fuel flexibility. The basic research on SOFC in Chinese academic institutions began around 2000, mainly supported by the National Natural Science Foundation of China (NSFC). Since 2011, the Ministry of science and technology of China (MOST) has supported comprehensive fundamental research, technology development and engineering demonstration of SOFCs through National Program on Key Basic Research Project (973 Program), National High-tech R&D Program of China (863 Program) and on-going National Key R&D Program of China. Besides, with the rapid development of renewable power in recent years, high temperature solid oxide electrolysis cells (SOECs) and reversible solid oxide cells (RSOCs) have also attracted the interest of large enterprises and local governments in China.

2. Fundamental Research

From 2012 to 2016, with the support of the 973 Program of MOST, more than ten research institutes, universities and companies cooperated to carry out comprehensive fundamental research, mainly to solve the scientific problems and practical applications of high-efficiency, reliable and low-cost SOFCs using carbon-based fuels, as shown in Figure 1.

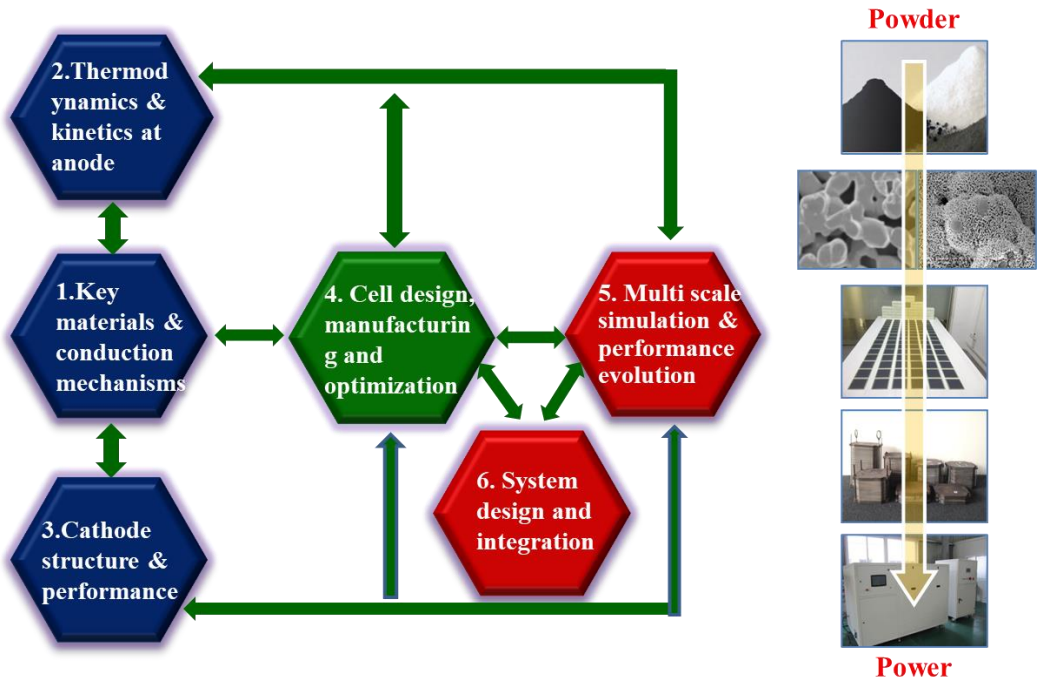

Figure 1. Project *Fundamental Research on Carbon-Based Fuel SOFC Systems* (2012-2016) supported by CHN 973 Program

https://doi.org/10.5281/zenodo.4518715

3. Technology Research and Development

Since 2018, with the support of the National Key R&D Program of China, two projects for single cell and stack lifetime extension have been launched. By studying the attenuation mechanism of single cells and key components in the stack, the degradation rate of short stack (W_e=500 W) will be reduced to less than 0.5%/1000 hrs. The expected lifetime of the mass-produced kilowatt stack will be more than 10,000 hours.

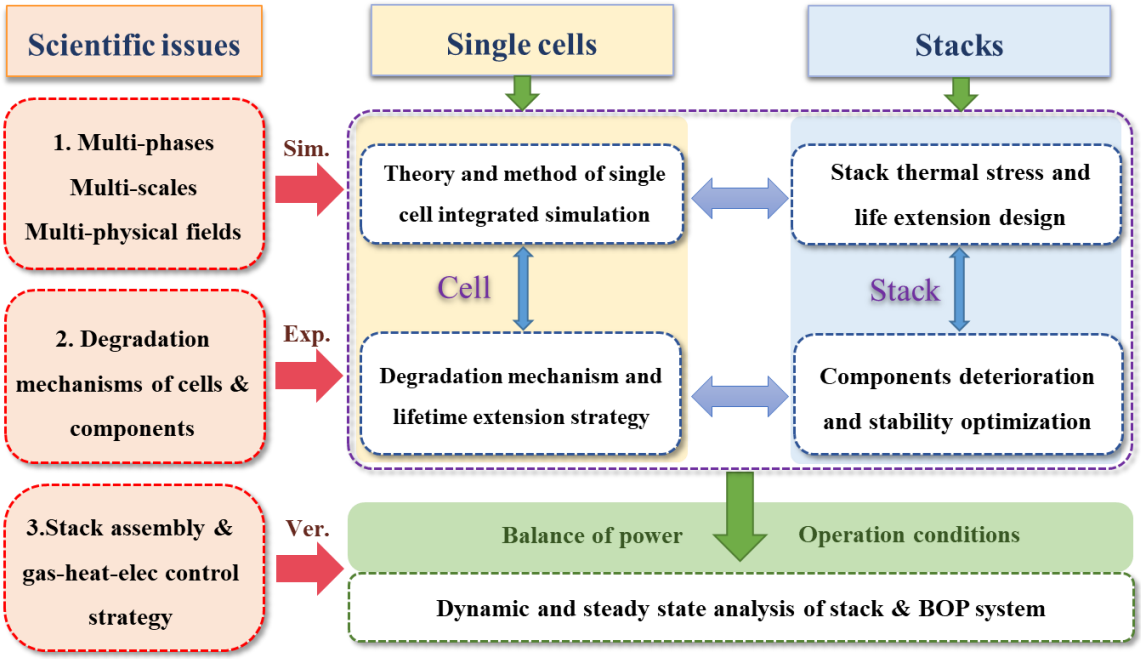

Figure 2. Project *Degradation Mechanism and Long Life Strategy of High Efficiency SOFCs* (2018-2023) supported by National Key R&D Program of China

Another highlighted project is the research on clean and efficient utilization of coal based on advanced coal gasification and purification technologies, high temperature fuel cells (MCFC and SOFC), and CO_2 capture and utilization, which is also supported by the National Key R&D Program of China. Based on this project, the first MW_{th} integrated coal gasification and fuel cell (IGFC) demonstration system with near zero CO_2 emission will be built, with electrical efficiency more than 50% and CO_2 capture rate more than 90%.

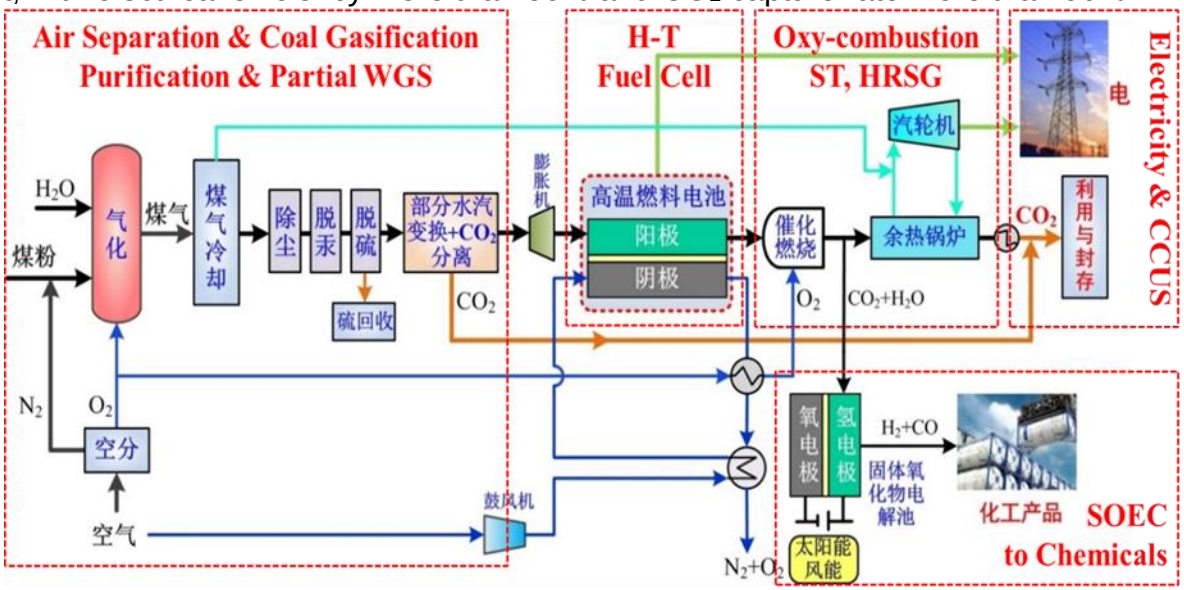

Figure 3. Project *Coal Gasification Power System with Near Zero CO_2 Emission* (2017-2021) supported by National Key R&D Program of China

https://doi.org/10.5281/zenodo.4518715

Regarded as the best choice for the utilization of excess renewable power, SOEC-related technology research and development have also been carried out with the support of local governments in China in recent years. From 2019, a demonstration project of 1 kW SOEC system has been implemented by Tsinghua Team together with CHN ENERGY Investment Group Co.,Ltd., which is supported by Beijing Science and Technology Commission. Under the background of current energy structure reform, SOEC technology can be combined with redundant thermal power or renewable power generation to produce H_2 and other sustainable fuels, which is an indispensable link in the future new energy network.

4. Industrial Development and Demonstration

The application prospect of SOFCs in the fields of distributed power generation and power system of vehicles has attracted the attention of some local governments and enterprises, which has accelerated the industrialization of SOFCs in China. The first SOFC mass production line with the scale of 200,000 single cells per year constructed by Xuzhou Huaqing Jingkun Energy Co.,Ltd. has been put into service since August, 2019. Another company, Chaozhou Three Circle Co.,Ltd., also has the mass production capacity of SOFC electrolyte, single cells and stacks. At the system level, a coal-based fuel cell integrated demonstration system has been designed and built in Shanxi Province in 2018. The maximum output power of the system is 15 kW, and the longest continuous operation time is nearly 1000 hours when using coal derived gas fuel.

Figure 4. Coal-based SOFC demonstration system in Jincheng, Shanxi province, China.

Besides, Weichai Power Co., Ltd. and Ceres Power jointly developed a stack with 30 kW output power, which will further be applied in commercial vehicles. At present, Weichai and Ceres plan to develop 10 bus systems and complete the verification in 2020.

https://doi.org/10.5281/zenodo.4518715

References

[1] BP Energy Outlook 2019 Edition
[2] China calls for global green revolution in the post-COVID era (https://news.cgtn.com/news/2020-09-22/Xi-Jinping-China-aims-to-achieve-carbon-neutrality-by-2060-TZX22EfJiE/index.html)
[3] Everything You Think You Know About Coal in China Is Wrong (https://www.americanprogress.org/issues/green/reports/2017/05/15/432141/everything-think-know-coal-china-wrong)
[4] Shiyan Chang, Jiankun Zhuo, Shuo Meng, Shiyue Qin, Qiang Yao, Clean Coal Technologies in China: Current Status and Future Perspectives, Engineering, Volume 2, Issue 4, 2016, Pages 447-459, https://doi.org/10.1016/J.ENG.2016.04.015.

Keywords: EFCF 2020, SOx
Session A02: P2: Keynotes by FCH JU - EU Programs, US, Japan, China

A0301

Status of Stack & System Development at Sunfire

Christian Walter, Konstantin Schwarze, Matthias Boltze, Kai Herbrig, Alexander Surrey
Sunfire GmbH
Gasanstaltstr. 2, 01237 Dresden/Germany

Contact authors: www.EFCF.com/ContactRequest

Abstract

Sunfire develops and produces high-temperature fuel cell (SOFC), electrolyzer (SOEC) and co-electrolysis (Co-SOEC) systems. SOFCs convert fuels and gases into electricity and heat for various applications. SOECs and Co-SOECs convert water and/or CO2 with preferably renewable electricity into hydrogen or syngas. With these technologies, Sunfire addresses a multitude of challenges in our energy system.
To be able to satisfy the needs of those varying products, Sunfire's SOC technology is continuously being improved on stack as well as on system integration level to achieve the optimal balance between high reliability, low manufacturing costs and high electrical efficiency.
In this publication, an update of the results of our long-term stack tests will be presented (new tests with our present stack design as well as updates of our long runners).
This will be followed by showing the next steps of the scale-up and automation of our production volumes.
Finally, an update of the status of our SOFC products for residential CHP (Sunfire-Home) and offgrid power (Sunfire-Remote) and SOEC (Sunfire-Hylink) as well as Co-SOEC (Sunfire-Synlink) applications will be given. Here the status of ongoing projects and next steps will be discussed.

https://doi.org/10.5281/zenodo.4518729

Introduction

Sunfire develops and produces high-temperature fuel cell (SOFC) and electrolyzer (SOEC) systems. SOFCs convert fuels and gases into electricity and heat and SOECs convert water and/or CO2 with preferably renewable electricity into hydrogen or syngas. With these technologies, Sunfire addresses a multitude of challenges in our energy systems.

The company was founded in 2010 by a team of experienced entrepreneurs and engineers. Sunfire has ~150 employees and is backed by Paul Wurth, Neste, idinvest Partners, Inven Capital and Total Energy Ventures as well as private investors.

Sunfire started with the production of stacks and small systems mainly for residential CHP (Sunfire-Home) and off-grid power applications (Sunfire-Remote) with outputs of less than 1 kW per unit. SOEC development started in 2012. Stacks, stack modules and systems have been successfully tested at ambient and pressurized conditions. [1] In 2014 first rSOC stack tests were performed, followed by a complete system development in cooperation with Boeing and during the GrInHy project. [2,3]

By expanding the product portfolio to hydrogen and syngas production (Sunfire-Hylink, Sunfire-Synlink), larger modules up to 150 kW SOEC power input have been developed. These modules are also implemented in the megawatt scale SOEC systems that will be operated starting 2020 in the framework of GrInHy2.0 and MultiPLHY and are the basis for all future large pilot plants.

To be able to satisfy the needs of those varying products, Sunfire's SOC technology is continuously being improved to achieve the optimal balance between high reliability, low manufacturing costs and high electrical efficiency.

In this publication, results of our recent stack development will be shown followed by an update on the scale-up of our production volumes as well as a short update on the status of our various products.

1. Stack Development

Sunfire's stack design is based on a planar, parallel-flow design with an open cathode which is optimized to achieve an ideal tradeoff between cost, performance, and degradation. It is an electrolyte supported (ESC) design with Crofer 22 APU as metal cassette, a Ni/GDC hydrogen electrode, a 3YSZ electrolyte and an LSCF oxygen electrode. It is developed to run in SOFC as well as in SOEC and Co-SOEC mode and is robust to thermal as well as redox cycles. In the following chapters, updates on the degradation results and improvements will be shown.

Long term test in SOFC mode.

Sunfire is continuously long-term testing its stacks in SOFC and SOEC mode. In Figure 1 the evolution of the ASR of a SMK-B230-type stack, which is tested alongside with another stack in a double stack test (each stack with 30 cells), operated for 23kh in SOFC mode is shown. The ASR is corrected to the fuel conversion polarization and temperature fluctuations. The BOL-ASR is ~650 mΩ cm²/kh and the linear degradation rate is ~17 mΩ cm²/kh in the first half and ~11 mΩ cm²/kh in the second half of the stack test.

https://doi.org/10.5281/zenodo.4518729

This suggests a decreasing degradation rate over time that also is accordance with known ageing mechanisms and verifies the general feasibility of Sunfires stack design over long operating times.

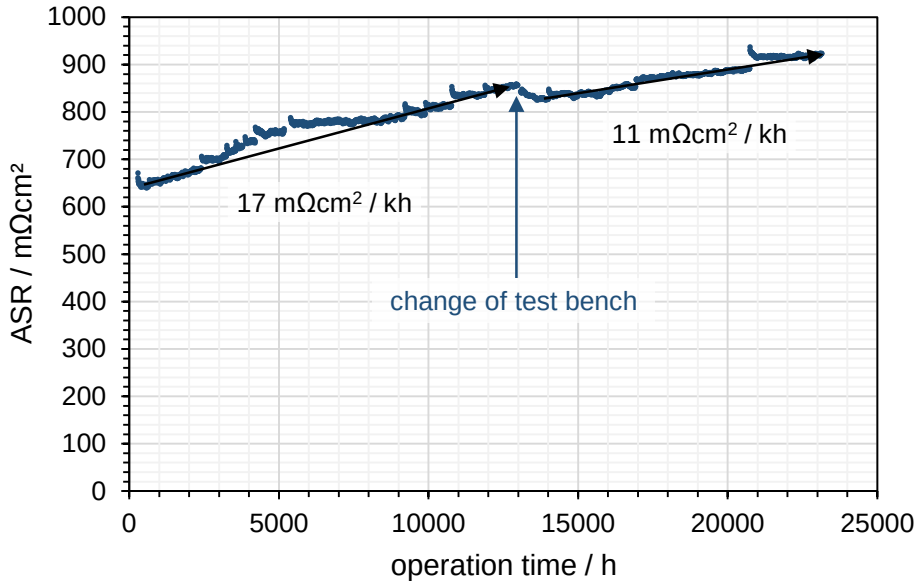

Figure 1. ASR evolution of a 30 cell stack during SOFC operation at 0.226 A/cm² with H2 as fuel.

Even though a lot of test bench failures with associated thermal cycles happened during this test, as can be seen by the little spikes in the ASR in Figure 1, no signs of cell breakages or other anomalies are present. The test is ongoing.

Degradation/long term tests in SOEC mode.

The ASR and degradation during SOEC operation for the recently approved SMK-B240-design [7] with a 30-cell stack operated at Sunfire is displayed in Figure 2.

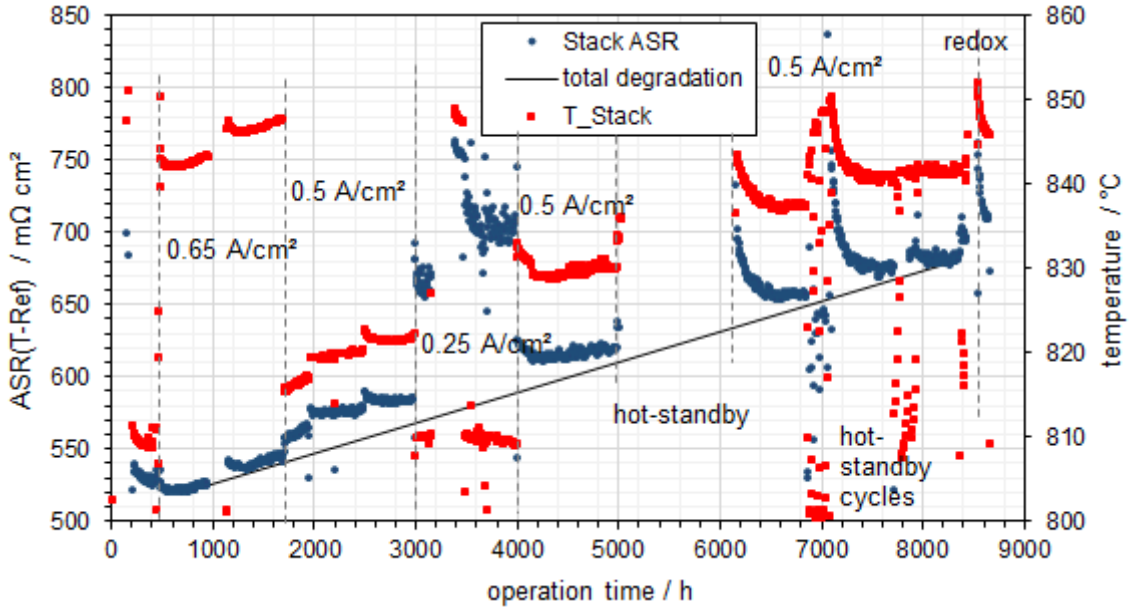

Figure 2. ASR evolution of 30 cell stack during SOEC operation at current densities varying from -0.25 to -0.65 A/cm². The linear degradation is 21 mΩ cm²/kh.

https://doi.org/10.5281/zenodo.4518729

As in the previous chapter, the ASR is corrected to the fuel conversion polarization. Furthermore, the stack ASR is temperature corrected to be able to see the material degradation itself. Because if the temperature correction is omitted, the resulting ASR-degradation is virtually zero because the existing material degradation is blurred by the ASR decrease due to the increasing operation temperature in the SOEC thermoneutral mode.

The initial ASR is ~525 mΩ cm² and thus lower than the values reported for the SOFC-mode (~650 mΩ cm²) due to thermoneutral operation that leads to a uniform temperature profile instead of the steep temperature profile that is observed in SOFC mode.

The calculated total ASR-degradation is ~21 mΩ cm²/kh for the complete test which included endothermal, slightly exothermic and mainly thermoneutral operation phases as well as various cycles (thermal, hot-standby and redox). The degradation of purely stationary operation was observed to be as low as 10 mΩ cm²/kh (e.g. from 4500 to 5000 h). The post-test-analysis revealed a small, however, relevant silicon contamination of the H2 electrodes which is believed to be a major cause of the SOEC operation. If this contamination can be eliminated, lower degradations comparable to the SOFC degradation reported in the previous chapter or to the degradation of cell tests [6] or for SOFC modes of the SMK-B240 design [7] are to be expected.

Degradation/long term tests in Co-SOEC mode

A 30 cell stack operated in Co-SOEC mode is presented in Figure 3 showing the evolution of the stack ASR and the stack temperature. The current density is 0.59 A/cm² with a conversation rate of 70% and a gas composition of $H_2O/CO_2/H_2/CO$=60/30/7/3 aiming at a H_2/CO ratio of approx. 2 in the produced syngas. The mean linear degradation amounts to 22 mΩ cm²/kh as indicated by the dashed line in Figure 3 which is similar to SOEC operation with steam. (At 1800 h the stationary operation was interrupted by a thermal cycle due to an increase in the SiO2 contamination which was reduced for the subsequent operation leading to a jump in ASR which was ignored for the calculation of stationary degradation values) In the post-test-analysis no damages or issues related to the Co-SOEC such as carbon deposition have been observed after the stationary operation. Again, small amounts of Si were found in the H_2 electrode leading to an increased degradation rate as also described in the previous chapter.

All the results shown in this chapter verify that, if silica contaminants can be avoided, the Sunfire cell and stack design can be operated in SOFC, SOEC, as well as CO-SOEC with low degradation rates and without any issues. Therefore, it is a solid foundation for Sunfire-Home and -Remote as well as Sunfire-Hylink and -Synlink systems.

https://doi.org/10.5281/zenodo.4518729

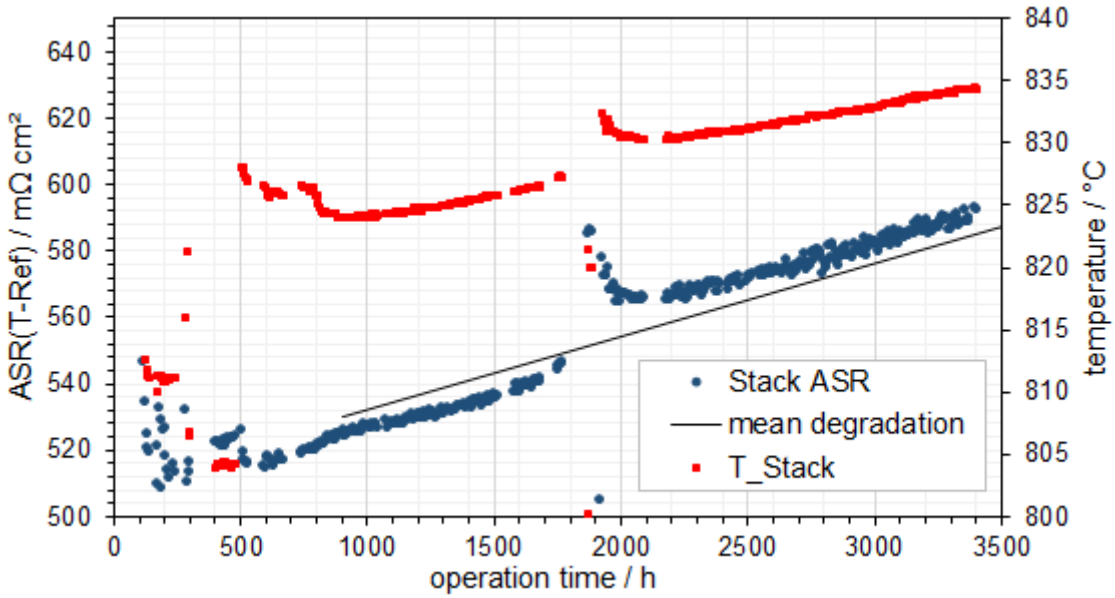

Figure 3. ASR evolution of a 30 cell stack during Co-SOEC operation with a mean degradation of 22 mΩ cm²/kh.

2. Industrial Scale-Up

To be able to fully industrialize our technology, the costs of the stacks need to be decreased further. This can either be done by changing the materials used within the stack or by implementing fully automated processes and scaling up the stack production. Sunfire is continuously working on both of those means. In this chapter, we will show 2 newly designed devices to increase production capacity and decrease the costs of the production step.

Automated MCF-WPS coater

To enhance the capacity and reduce the costs of our spray coating process an automated WPS-coater has been developed and produced. It has a cycle time of 10s per interconnect to be able to achieve approx. 60 MW SOEC output capacity per year and can be integrated in a fully automated production line if needed. Furthermore, it decreases the working time per stack by approx. 90 minutes and thus the costs significantly.
The device has already been tested preliminarily and will be put into full operation until end of October. (c.f. Figure 4)

https://doi.org/10.5281/zenodo.4518729

Figure 4. Automated MCF-WPS coating device

Automated Stacking device

In addition to the coater also an automated stacking device is currently under development. There, one stack shall be produced in a cycle time of less than 10 minutes. Also the stacking device can later be integrated into a fully automated production line and reduces the stacking time by approx. 130 minutes. Additionally, scrap rates will be decreased because manual stacking errors can be avoided.
The device is currently being designed and shall be put into operation in mid-2021.

3. Update on Product Development

Sunfire Home

After the takeover of new enerday GmbH by Sunfire GmbH in autumn 2018 our site in Neubrandenburg Germany, operates under the name Sunfire Fuel Cells GmbH. It is now advancing a joint platform technology for micro-CHP devices for residential buildings and off-grid power supplies.

With Sunfire-Home, Sunfire Fuel Cells is introducing an add-on micro-CHP solution for supplying electricity and heat to single-family homes with natural gas as fuel as well as with LPG for homes, that are not connected to public gas grid and offer an attractive option to replace boilers based on heating oil with a more environmentally friendly, efficient and innovative system.

The ***Home 750*** offers a rated electrical output of 750 W and a thermal output of 1,300 W. In addition to reducing emissions, the advantages of Sunfire-Home include high efficiency, fully automatic operation with remote access and simple integration with modern building technology such as a peak load boiler and a hot water storage tank.

https://doi.org/10.5281/zenodo.4518729

As part of the PACE market launch program, funded by the Fuel Cells and Hydrogen Joint Undertaking (FCH JU) with Horizon 2020, the first 500 devices will be placed on the market.

At Sunfire Fuel Cells the series production for Sunfire Home with a capacity of 500 units per year was started. The first units are shipped to costumers and are in operation (Figure 6)

Figure 5. Small scale series production at Sunfire Fuel Cells and first installed customer systems in operation

Sunfire Remote

Looking at Sunfire-Remote, Sunfire Fuel Cells promotes a compact SOFC-system for self-sufficient and off-grid power supply from pipeline gas and Propane. The units can be integrated in trailers or enclosures as well as in hybrid systems with batteries and photovoltaic panels. Typical applications include the power supply of measuring and control equipment for oil and gas pipelines, air traffic signal lighting of wind farms in the construction phase and the mobile power supply for security systems and telecommunications stations.

https://doi.org/10.5281/zenodo.4518729

Figure 6. Sunfire-Remote unit used as power supply for wind farms in the construction phase

The Sunfire-Remote ***R400*** units are battery chargers primarily and provide continuous power for a wide range of applications with an average power consumption up to 400 W. Load changes and peaks, also in the kilowatt range, can be covered by batteries that has to be selected according the needed capacities and specific requirements. Based on Sunfire's SOFC-technology the systems are perfectly suited for reliable, durable and independent off-grid power supply. Fueled by LPG/Propane or natural gas, they reach electrical efficiencies of up to 35 %. Due to the lack of combustion, they provide clean power with minimal noise.

Based on the ***Home750*** platform, Sunfire will introduce a larger off-grid system in 2020, called ***R900***, with up to 900 W DC power per unit.

Sunfire Hylink/Synlink

Today, Sunfire is the leading provider of HTE systems worldwide, quickly moving into the multi-megawatt market for industrial applications. By focusing on the utilization of industrial off-heat to maximize overall electrical efficiency, the operational cost for continuous hydrogen production can be kept at a minimum. With an electric consumption of ≤ 3.7 kWh/Nm3H2 approximately 30 % more product can be produced with the same electricity input compared to legacy technologies such as PEM and alkaline electrolysis. Sunfire units are therefore specifically suited for brown-field industrial applications, as demonstrated at the steel plant of Salzgitter, where a 730 kWAC HTE system is currently being installed within the GrInHy2.0 project, after successfully operating a 150 kWel,AC rSOC system since 2017. For more detailed information on the Sunfire SOEC product and the scale-up plan, please refer to [5].

https://doi.org/10.5281/zenodo.4518729

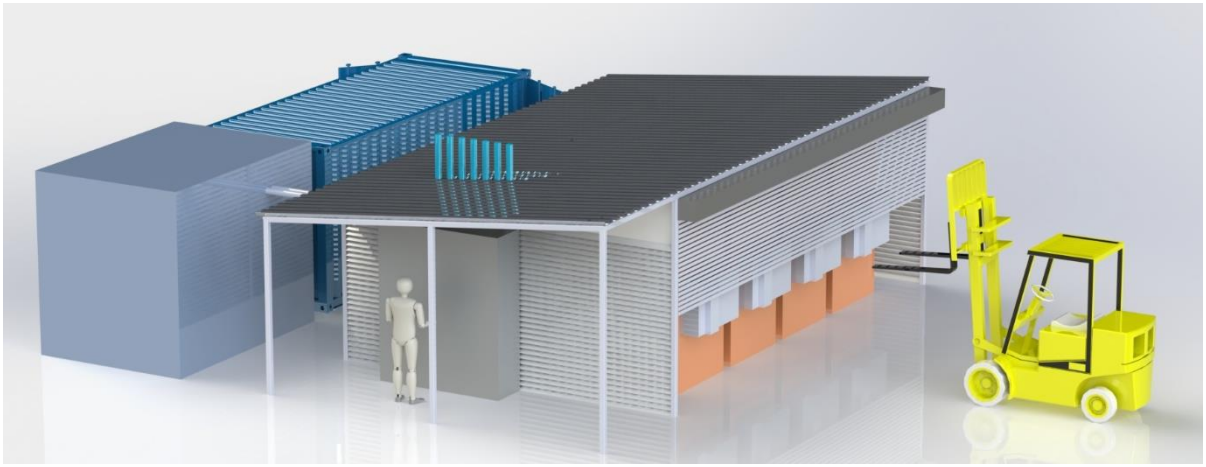

Figure 7. 1 MW HTE plant with power electronics container (blue) and dry cooler (grey) comprising 4 Generatioin 2 Sunfire-HyLink or Sunfire-SynLink Modules.

In addition to pure hydrogen electrolysis (SOEC or Sunfire-HyLink), Sunfire is also developing the Co-SOEC (Sunfire-SynLink) providing renewable syngas, a mixture of H2 and CO, for chemical applications and so-called Power-to-Liquid processes. The operation has been successfully demonstrated within the Kopernikus PtX project. Now the scale-up to industrial scale is next with the development of a Generation 2 HTE Module (Figure 7). The new module contains 60 stacks in a single housing and will be able to operate both in hydrogen electrolysis and co-electrolysis mode. This development strategy will ensure rapid scale-up of both product lines at once. The Generation 2 Module will provide a net production rate of more than 75 Nm^3/h hydrogen or syngas at a nominal power of approx. 300 kWAC at drastically cut manufacturing costs. It will enable HTE systems to reach a capacity of several MW and to be competitive on the electrolysis market. A first demonstration of the Gen2 will be a 2.5 MW Sunfire-HyLink plant at the Neste refinery in Rotterdam (Netherlands) within the EU funded MultiPLHY project [5].
A first Synlink pilot plant will be demonstrated on large scale by Sunfire's daughter company Norsk e-Fuel in Heroya (Norway) starting with 20 MW SynLink capacity to produce 10 million liters synthetic fuel per year in 2023

4. Summary and Outlook

Sunfire reaches low degradation values over several thousand hours (as shown in this contribution for at least 23kh in SOFC; 9kh in SOEC and 3.5kh in CO-SOEC) with its stack design. The industrial scale up of the production line up to 60MW a year is ongoing by continuously introducing automated devices leading to further decreased stack costs.

Sunfire's products are also continuously being improved. Sunfire Fuel Cells has scaled up its production capacity to 500 Sunfire-Home systems a year and already shipped the first units to customers in Germany. Furthermore, the 400 W Sunfire-Remote is available while the larger 900W unit will be introduced in 2020.

Within the project GrInHy2.0, Sunfire will install the first long-term demonstration units of an SOEC-system (Sunfire-Hylink) on megawatt scale at an iron and steel plant (GrInHy 2.0) and a refinery (MultiPHLY). In addition to that, Sunfire has also already shown that renewable syngas can be produced with its technology and will install a 20 MW SynLink / PtL plant in Heroya (Norway) in 2023.

https://doi.org/10.5281/zenodo.4518729

Acknowledgments

The authors gratefully acknowledge the financial support by the Federal Ministry for Economic Affairs and Energy of Germany in the project KOSOS (project number: 03ETB005A).

This project has received funding from the Fuel Cells and Hydrogen 2 Joint Undertaking (JU) under grant agreement No 826323. The JU receives support from the European Union's Horizon 2020 research and innovation programme and Denmark, France, Austria, Belgium, Sweden, Germany, Italy.

This project has received funding from the Fuel Cells and Hydrogen 2 Joint Undertaking under grant agreement No 700300. This Joint Undertaking receives support from the European Union's Horizon 2020 research and innovation program and Hydrogen Europe and N.ERGHY.

This project has received funding from the Fuel Cells and Hydrogen 2 Joint Undertaking (JU) under Grant Agreement No 826350. This Joint Undertaking receives support from the European Union's Horizon 2020 Research and Innovation program, Hydrogen Europe and Hydrogen Europe Research.

References

[1] O. Posdziech, K. Schwarze, J. Brabandt, Efficient hydrogen production for industry and electricity storage via high-temperature electrolysis, Intern. J. of Hydrogen Energy, Volume 44 issue 25, pages 19089-19101 2019.

[2] J. Mermelstein and O. Posdziech, Fuel Cells, Development and Demonstration of a Novel Reversible SOFC System for Utility and Micro Grid Energy Storage, Volume 17, issue 4, pages 562-570, 2017.

[3] K. Schwarze, O. Posdziech, J. Mermelstein, S. Kroop, Operational Results of an 150/30 kW RSOC System in an Industrial Environment, Fuel Cells, Volume 19, issue 4, Pages 374-380, 2019

[4] C. Geipel, K. Herbrig, F. Mittmann, M. Pötschke, L. Reichel, T. Strohbach, A. Surrey, C. Walter, Stack Development and Industrial Scale-Up, EFCF 13; A0303, (2018)

[5] O. Posdziech, T. Geißler, K. Schwarze, R. Blumentritt, System Development and Demonstration of Large-Scale High-Temperature Electrolysis, ECS Transactions SOFC-XVI, 2019

[6] J. Schefold et. al., 80,000 current on/off cycles in a one year long steam electrolysis test with a solid oxide cell, Intern. J. of Hydrogen Energy, Volume 45, issue 8, pages 5143-5154, 2020

[7] C. Geipel et. al., Stack Development and Industrial Scale-Up, ECS Transactions SOFC-XVI, 2019

Keywords: EFCF 2020, SOx
Session A03: Technology status at industry and major groups I

https://doi.org/10.5281/zenodo.4518729

A0302

Commercialization of the Steel Cell® technology: Latest Update

Robert Leah, Adam Bone, Per Hjalmarsson, Ahmet Selcuk, Mike Lankin, Mahfujur Rahman, Andy Clare, Gavin Reade, Florence Felix, Jeffrey De Vero, Xin Wang, Subhasish Mukerjee, Mark Selby
Ceres Power Ltd.
Viking House, Foundry Lane, RH13 5PX Horsham/UK

Contact authors: www.EFCF.com/ContactRequest

Abstract

Ceres continues to acquire commercial partners for its low-temperature metal supported SOFC technology (the 'Steel Cell®') based predominantly around the use of ceria. This unique design architecture allows for a robust, low cost, subsidy free fuel cell product, whilst retaining the advantages of fuel flexibility, high efficiency and low degradation.
Over the last year, several significant technological and commercial developments have taken place. The latest version 5 iteration of the core SteelCell® technology has completed verification and has been released to customers. This technology iteration offers higher power, the ability to operate at higher fuel utilization/efficiency and state-of-the-art performance degradation rates, whilst retaining the outstanding robustness to thermal cycling, vibration and REDOX cycling characteristic of SteelCell technology.
Major commercial developments include the commercial launch of a 4.2kW$_e$ light commercial CHP system with Miura in Japan, and ongoing strategic collaboration agreements with both Robert Bosch in Germany, primarily for manufacturing, and Weichai Power in China, for on-vehicle applications. In addition, a new collaboration and license agreement has been signed with Doosan in South Korea to jointly develop 5-20kW$_e$ low-carbon power generation systems.
Ceres now has active commercial programs at 1kW$_e$, 5kW$_e$, 10kW$_e$ and 10's of kW$_e$ and for that reason Ceres has developed an innovative 5kW$_e$ class stack design which can be used in an array to achieve higher power outputs. Development programs are ongoing with OEM's with global reach based in Japan, North America and Europe.
To meet the rapidly increasing demand for cells for customer programs, Ceres has invested in a larger manufacturing site near Redhill, UK capable of manufacturing >2MW/y initially with space for significant expansion. Despite the considerable challenges caused by the coronavirus pandemic, production has been rapidly ramped up at the new Redhill site during 2020 with investment released for further expansion of production capacity in the UK. Significantly, our first manufacturing licensee has successfully commenced pilot production in Bamberg, Germany, under ISO9001.
Product Development of a 1kW µCHP Hydrogen-only System Reference Design has demonstrated a 40% system level cost reduction compared to NG systems at 1kW scale at equivalent efficiency.
A further development has been the evaluation of SteelCell® technology for steam electrolysis applications, promising initial results of which are reported in this paper.

https://doi.org/10.5281/zenodo.4518770

Introduction

Ceres Power's unique low temperature metal-supported SteelCell® technology has now been successfully commercialized at a small scale, with a 4.2kW$_e$ system manufactured by Miura and using Ceres stacks and system architecture being commercially available and deployed to multiple sites in Japan. This unique design architecture allows for a robust, low cost, subsidy free fuel cell product, whilst retaining the advantages of fuel flexibility, high efficiency and low degradation. Ongoing relationships with strategic partners aim towards a much larger-scale commercial deployment of the technology into multiple applications.

The current V5 generation of SteelCell® technology has been available for use by customers for over two years, and has been incorporated into multiple customer products. Operation of V5 technology at high efficiency and very low performance degradation has been demonstrated for >27kh with multiple tests ongoing. As described elsewhere in these proceedings, degradation mechanisms in SteelCell technology are well understood, with the ability to make through-life performance predictions using a combination of extensive experimental testing and mathematical modelling.

To meet demand for cells and stacks from commercial programs, Ceres has established a dedicated manufacturing site in Redhill, UK approximately 20km from the company HQ Horsham. This is now operational for the production of cells and 5kW$_e$ stacks for both internal development and customer projects despite the challenges posed by the 2020 pandemic, and is designed to have an ultimate production capacity of >10MW/y.

Ceres currently has seen significant progress in four major strategic partners, in the public domain:

- Robert Bosch in Germany has a manufacturing license for the manufacture of both V5 cells and 5kW$_e$-stacks, and has set up a plant in Germany for initial low-volume production, mirroring Ceres' plant in the UK. The stacks are used in Bosch's 10kW$_e$ power generation system, designed to operate on both natural gas and hydrogen, a number of which are currently in operation.
- Weichai Power in China is developing a 30kW$_e$ range extender for light commercial EVs fueled on compressed natural gas using Ceres 5kW$_e$ stacks, and Ceres engineering expertise in the design of the system and control electronics. A prototype SOFC-powered bus has been demonstrated, the first time an SOFC stack has ever been used in this series hybrid configuration in a commercial road vehicle. Development of a production-ready version of the range-extender system is ongoing.
- Doosan in South Korea signed a joint development agreement with Ceres Power in 2019 for the development of 5-20kW$_e$ power systems for commercial applications. Doosan has very ambitions targets for the deployment of fuel cell technology in Korea, with 15GW$_e$ targeted by 2040.
- Miura in Japan has licensed Ceres' system design for use in natural-gas fueled CHP systems in commercial buildings, using Ceres-manufactured stacks and a licensed system architecture. These 4.2kW$_e$ systems are now commercially available on a limited basis and have been deployed successfully in Japan since October 2019. Miura is establishing a specialist maintenance team to support a wider deployment in the Japanese market.

https://doi.org/10.5281/zenodo.4518770

In addition to these commercial developments, Ceres has further strategically importantly joint product development programs with Honda in Japan, Cummins in the USA and several other confidential relationships with major global OEMs.

As Ceres is increasing evaluating the use of SteelCell technology for as part of the hydrogen economy. A project is underway to evaluate the use of SteelCell technology for steam electrolysis as described in the next section. This represents an additional and growing commercialization opportunity. In addition, a 1kW$_e$-class µCHP system has been demonstrated fueled by pure hydrogen, with a very simple low-cost system configuration.

The hydrogen fueled µCHP system was based on Ceres' well-established natural-gas fueled 'SteelGen' compact µCHP demonstrator. Without the requirement for the relatively complex fuel processing system in the NG-fueled system, it was estimated the overall system cost could be reduced by ~40%. On initial testing >50% net AC electrical efficiency has been demonstrated operating on hydrogen, with opportunities to increase this to 53% or greater with better optimization of components.

1.Application of SteelCell® Technology to Hydrogen Production by Steam Electrolysis

There has been increasing interest in recent years on the application of SOC technology for electrolysis for the production of hydrogen from renewable electricity. This has been identified as an additional commercial opportunity for Ceres, not least as the potential partners interested in electrolysis are different from the partners interested in power generation. Until very recently the performance of Ceres cells/stacks in electrolysis mode has not been evaluated in detail. In principle, the use of SteelCell technology for electrolysis should retain the advantages which have already seen it chosen as the preferred SOC technology for power generation by multiple global OEMs, in particular

- Robustness to thermal cycling and unplanned system shut-downs.
- Low cost cells and stacks, and reduced system and system integration costs due to the low operating temperature.
- Retention of the thermodynamic advantages of steam electrolysis relative to low temperature water electrolysis in terms of lower specific electrical energy demand, provided a source of waste/renewable heat for steam generation is available

An additional thermodynamic advantage of SteelCell technology is the low (by SOC standards) operating temperature. This means integration of electrolyzers with external sources of waste heat to provide some of the energy for reaction (where the stack is being operated at below the thermoneutral voltage) is feasible for a wider range of processes, as a lower grade of waste heat is required.

Techno-economic analysis shows that the levelized cost of electrolytic hydrogen (LCOH) is dominated by energy cost for all technologies. Therefore, if Green Hydrogen does indeed become a $2.5Tn industry as predicted by the Hydrogen Council [1], SOEC will have a significant advantage on LCOH for two reasons –

1. SOEC is substantially more efficient than low temperature approaches and, uniquely,
2. has the ability to utilize waste industrial heat. This is particularly relevant in the synthesis of more complex energy vectors like ammonia and e-Hydrocarbons which all present thermal integration opportunities.

https://doi.org/10.5281/zenodo.4518770

Early stage analysis indicates that both #1 and #2 are true for CERES SteelCell based SOEC technology. If this is true, we believe SteelCell will be compelling in this space for similar reasons to its success in Power Generation. These attributes offers a significant advantage as most techno-economic modelling for hard-to-abate industrial sectors (ammonia synthesis, steel, concrete, synthetic hydrocarbon fuels etc.), forecasts electrical efficiency as the key driver in achieving the lowest levelized cost of hydrogen. Such models suggest an advantage for CERES LT-SOEC technology which can run at optimum operating points well below the thermo-neutral voltage whilst utilising much more abundant, lower grade heat.

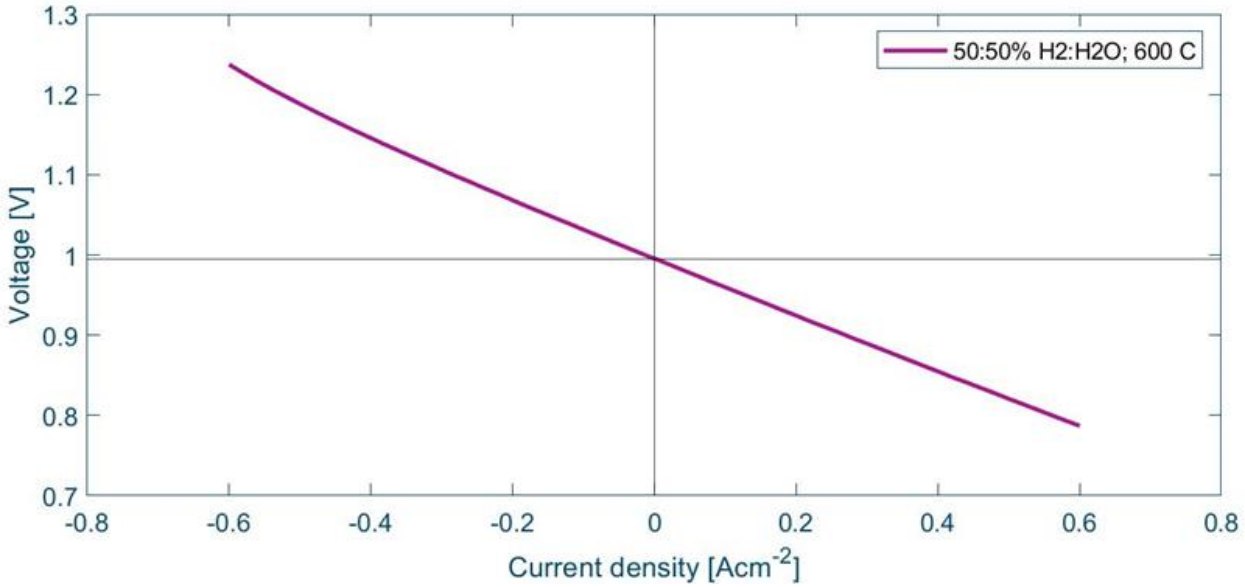

Figure 1: Reversible IV curve measured on a 1cm^2 button cell on a 50:50 H_2/H_2O mixture at 600°C

Figure 1 shows the IV curve from a button-cell test of a SteelCell operated reversibly between -600mAcm^{-2} and 600mAcm^{-2}. Note that Ceres makes button cells from sections cut from full-size cells, and therefore the intrinsic electrochemical performance has been validated to be fully representative. The IV curve is essentially fully reversible apart from some slight deviation from linearity at <-500mAcm^{-2} which indicates fuel-side mass transport is slightly more limiting in electrolysis mode but only at current densities significantly beyond those identified as commercially relevant.

A full stack validation programme is now underway. The results show that the area specific resistance (ASR) of repeating stack units is similar in SOEC mode compared to SOFC and that ASR is relatively independent on current density within the operating space explored so far. This is in line with observations for SteelCell stacks tested in SOFC mode.

Faradaic efficiency has been determined by measuring hydrogen output using a gas flow meter as well as measuring water condensate flows downstream a condensation/separation heat exchanger. The results showed that Faradaic efficiency of SteelCell stacks is 98±0.7%. This indicates that parasitic losses due to the electronic conductivity of the CGO electrolyte are adequately suppressed and have a negligible effect on electrolysis efficiency.

https://doi.org/10.5281/zenodo.4518770

A number of stacks are undergoing degradation testing at a range of commercially relevant current densities. These tests support evaluation of both microstructural evolution and degradation measurement. The ASR degradation rates for durability stacks, averaged over their respective test periods, are all in the range of 15-25±5 mcΩcm^{2}kh^{-1}. This is in line with what is typically measured in fuel cell mode during the first few thousand hours. No clear correlation with respect to current density has been observed. The degradation rates appear to decelerate with time, a trend that is typically observed when operating SteelCell stacks in fuel cells mode due to parabolic increases in ohmic resistance, as reported elsewhere in these proceedings.

Post-test analysis using scanning electron microscopy has found no evidence of either nickel migration away from the cathode/electrolyte interface or anode delamination, both of which are widely reported as major SOEC degradation mechanisms in literature.

Therefore, the conclusion so far is that no new, SOEC specific, steady state degradation mechanism appears to present itself within the first several thousands of hours testing. Understanding of degradation is built upon extensive testing and validation of SteelCell technology in SOFC mode, which gives greater confidence in the ability to extrapolate the results of relatively short-duration SOEC tests.

Considerably more extensive testing is required at larger scales, and possible optimisation of the cell and stack design for electrolysis (current evaluation has been performed on unmodified SOFC stacks), but the initial results shown here have demonstrated proof-of-concept for the use of SteelCell technology for electrolysis.

2. Long-term Testing of Technology Validation Stacks

Figure 2 shows the population of technology validation stacks where testing started at or before the time V5 SteelCell technology was released, meaning the longest running stacks have now been operating continuously for more than 3 years. These stacks are operating under long-term steady-state durability testing to establish lifetime and the long-term performance degradation rate. All the stacks previously reported [2] are still operating with no in-service failures in the last year. The tests have all been undertaken on the 1kW$_e$ platform, on a mixture of 150W-class stacks run with heavy instrumentation in a laboratory environment, 1kW$_e$-class stacks operating in stack test stands and 1kW$_e$-class stacks operating in full natural gas fueled micro-CHP systems. Some of the longer running 1kW$_e$ stacks have run in both stack test stands and micro-CHP systems which explains the jumps in operating voltage, primarily due to changes in the thermal environment between the two platforms (for example the bottom of the stack tends to be hotter in a micro-CHP system than in a test stand due to heat transfer from other BOP components). An important point to note is that there is little difference in performance or degradation between the different testing environments, demonstrating that the laboratory tests are representative of real world operation. Data also exist for long-term testing of 5kW$_e$ stacks but this is a newer stack platform so the test durations are shorter, and most 5kW$_e$ stacks are being tested under customer programs and are thus confidential.

The stacks shown in Figure 2 are all operating at a current density of 133 mAcm^{-2} at 75% fuel utilization and 51% internal steam methane reforming, at a nominal temperature of 610°C. At the time of writing the longest running test has been running since March 2017 and has accumulated 27kh under load. All stacks are achieving long-term degradation rates of 0.2%/kh or less, which is state-of-the-art for SOFC technology. Many of the long

running stacks are showing degradation rates approaching ~0.1%/kh as they demonstrate burn-in behavior typical of many SOFC stacks before the degradation rates stabilize. The burn-in period before stacks approach a linear degradation rate for the SteelCell is around 8-10kh.

Several external factors affect the stack degradation rate, so these data should be considered a representative of a “Well engineered” system.

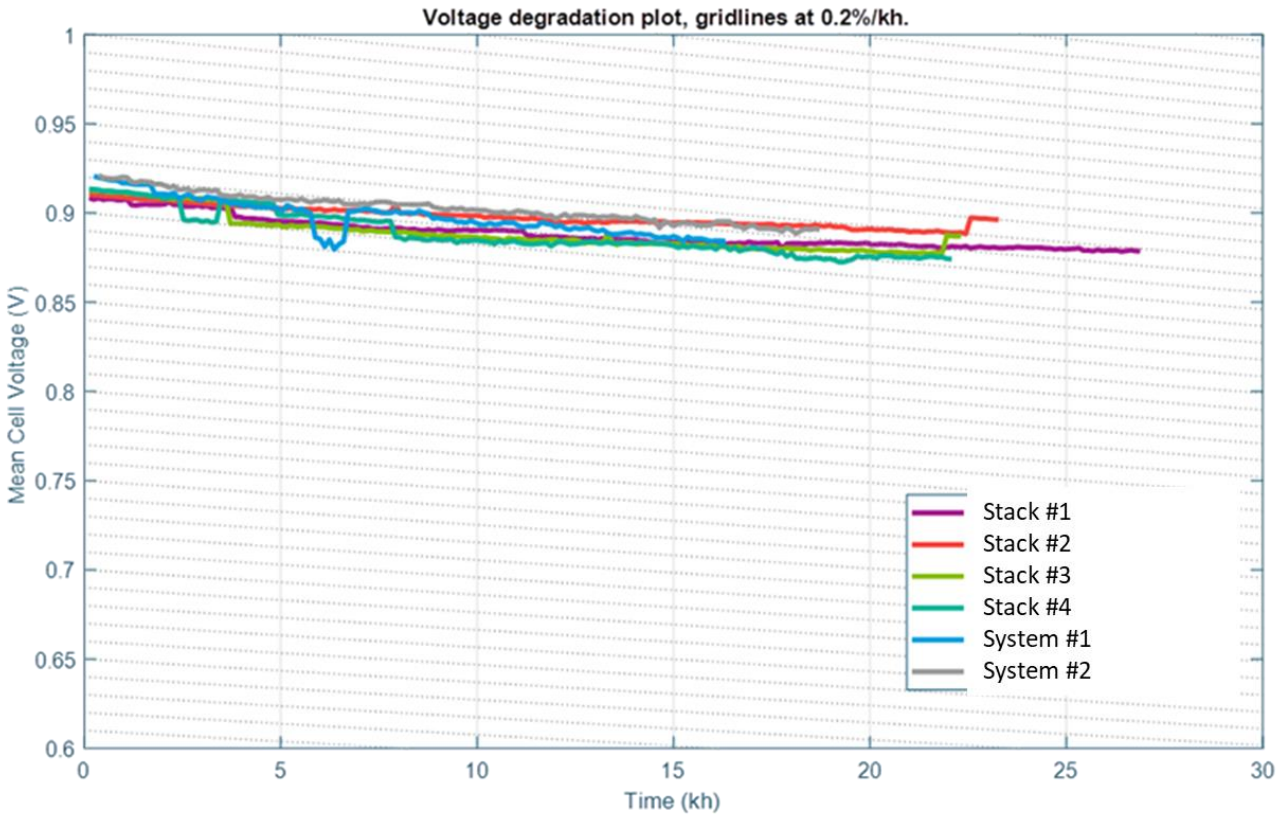

Figure 2. Mean cell voltage as a function of time for version 5 technology validation stacks under galvanostatic operation. Grid lines represent 0.2% degradation/kh.

Technology validation stacks have also been used to evaluate extending the operating window of the technology to significantly higher power densities.

.

https://doi.org/10.5281/zenodo.4518770

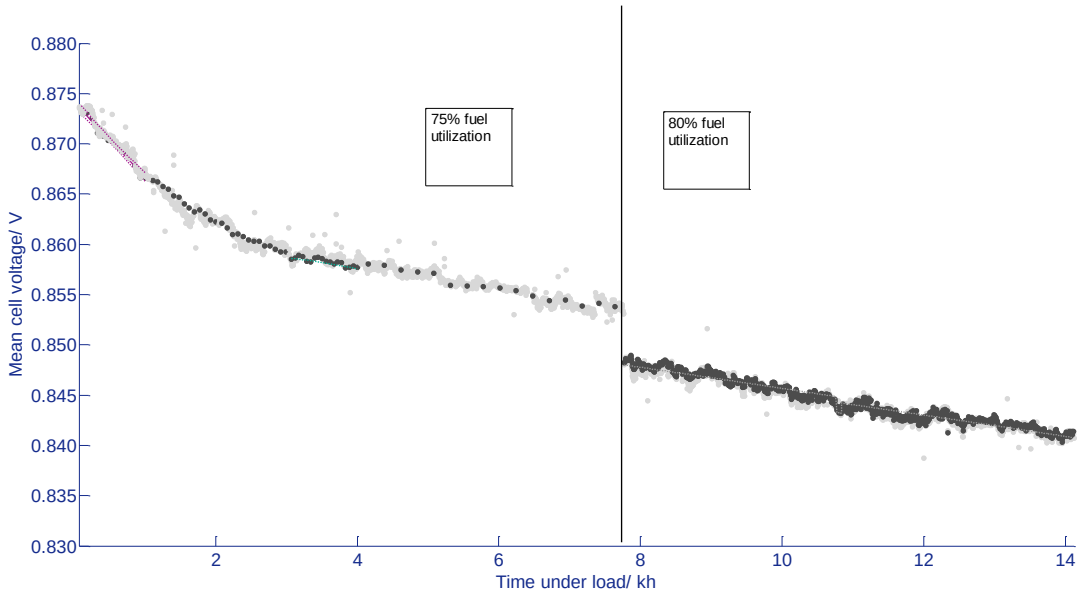

Figure 3. Mean cell voltage as a function of time for V5 technology validation stack operating at 255mAcm^{-2} at 75 and 80% fuel utilization.

Figure 3 shows the results from one nominally 150W-class stack operating at a slightly higher temperature (625°C) as part of a study into the effect of temperature on performance and degradation, and 255mAcm^{-2}, meaning the stack is generating ~300W. The stack was operated on simulated reformate at 75% fuel utilization (51% internal methane reforming) for the first 8kh, and then the fuel utilization was increased to 80% without affecting the voltage degradation rate (currently averaging -0.12%/kh). The stack has operated for 14.1kh and is still operating at the time of writing.

This shows the potential for operating SteelCell stacks at higher current densities in future, allowing a significant further reduction in the already highly competitive stack cost, without compromising efficiency as the lower stack operating voltage can be compensated for by operating at higher fuel utilization.

1. Conclusions

Ceres has now successfully commercialized its unique SteelCell® technology with Miura in Japan, with a commercially-available 4.2kW$_e$ CHP system, commenced manufacturing under license in Germany and achieved a world first in the application of SOFC to commercial vehicles in China and opened new areas to exploit its technology through electrolysis. Along side these engineering successes, Ceres has established multimillion pound strategic collaboration with Robert Bosch, Weichai Power and Doosan to deploy Ceres technology at scale in their products, along with ongoing relationships with multiple other customers.

In a world-first, SteelCell stacks have been successfully deployed as the prime-mover for an electric bus by Weichai Power in China, the first time SOFC technology has ever been used for this application, reflecting the exceptional robustness of the metal-supported technology to mechanical shock and thermal cycling.

Ceres has started evaluating the application of SteelCell technology to steam electrolysis, which has demonstrated that the cells are essentially reversible, and that there are no SOEC-specific degradation mechanisms which have been identified to date. In addition,

technoeconomic analysis has shown that SteelCell stacks operating at relatively low voltages, well below the thermoneutral potential, have the potential to offer an exceptionally low normalized cost of hydrogen, as the low stack operating temperature facilitates integration with a wide range of waste/renewable heat sources by comparison with more conventional SOC technology.

The latest version 5 release of SteelCell technology continues to display very low performance degradation rates, exceptional thermal cycle tolerance and very high efficiency. This technology has been integrated into both $1kW_e$ and $5kW_e$ stack platforms for multiple applications from $1kW_e$ to 10s of kW_e. This world class technology continues to improve and mature and attract more and more customers for commercialization in multiple markets globally.

With these successes, Ceres validates the commercial value of its collaborative business model through the ability to scale SOFC deployment, with all the attendant benefits, significantly faster than through traditionally vertically integrated Product Development approaches. This has been achieved by rigorous R&D and Engineering. Ceres has a core corporate value of “Creative Collaboration” and continues to seek new partners to broaden the deployment of this important technology class.

References

[1] http://bit.ly/HydrogenScalingUp

[2] R.T. Leah, P. A. Bone, A, Selcuk, M. Rahman, A. Clare, M. Lankin, F. Felix, S. Mukerjee and M.A. Selby, Latest Results and Commercialization of the Ceres Power SteelCell® Technology Platform, ECS Trans., 91(1), 51-61, (2019).

Keywords: EFCF 2020, SOx
Session A03: Technology status at industry and major groups I

https://doi.org/10.5281/zenodo.4518770

A0303

Status of HEXIS' SOFC Module Development

Andreas Mai, Jan Gustav Grolig, Venkatesh Sarda, Michael Dold, Alexander Schuler
Hexis AG
Zum Park 5, CH-8404 Winterthur

Contact authors: www.EFCF.com/ContactRequest

Abstract

HEXIS develops and manufactures SOFC-based micro-CHP units for houses and small companies. The current generation of the HEXIS SOFC unit "Leonardo", which has been developed in the past few years, is being tested both, in field and in the lab. Additionally, the development of the next generation system ("da Vinci") is also ongoing and the first 10 prototypes have been manufactured and are being tested.
Since the 1st of June 2020, Hexis has become part of mPower GmbH, based in Dresden, Germany, and whose parent company, h2e Power Systems Private Limited, is an Indian high-tech company based in Pune, India.
This paper will report the latest results of short-stack tests and of module and system tests based on the current system generations combined with historical data of the earlier Galileo systems. These include tests running for more than 52,000 h. Moreover, results of the "da Vinci" modules, reaching electrical efficiencies of 50 % AC, net and total efficiencies of 95 % (LHV) will be shown.
Long-term and cyclic testing of systems in lab tests as well as results on robustness and performance in the field will be discussed. Degradation rates as low as approx. 0.35 % / kh, i.e. 13 mΩ cm² / kh could be shown on the short-stack level for over 52,000 h. These stacks were analyzed with electrochemical impedance spectroscopy (EIS) at regular intervals, which could provide valuable insights in understanding fundamental degradation mechanisms for long term operation of SOFC stacks.
As of date, the field tests with the "Vitovalor SA-2" systems, which are based on the Leonardo SOFC unit have been running for approx. 10,000 h, with a lifetime prognosis of approx. 40,000 h.

https://doi.org/10.5281/zenodo.4518797

Introduction

HEXIS is developing and manufacturing SOFC-based micro-CHP units for houses and small companies. For the past few years, we have been developing the new generation (Leonardo) of the HEXIS SOFC units, which are now running in field and lab tests. Additionally, the development of the next system (da Vinci) generation was kicked off and first results on prototype level were achieved.

Since the 1st of June 2020, Hexis has become part of mPower GmbH, based in Dresden, Germany, whose parent company h2e Power Systems Private Limited, is an Indian high-tech company based in Pune, India. A corresponding purchase agreement was signed and consummated between mPower and Viessmann. The agreements also include the future cooperation of Hexis with the previous owner for the supply of SOFC fuel cell units. As Viessmann had announced, the family-owned company is focusing on the system integration of fuel cell modules into its own energy systems.

The Galileo 1000 N system was available on the market between 2013 & 2018. 105 Galileo systems are still in operation and provide important information on durability of components and SOFC stacks.

1. Approach: Concept of the HEXIS SOFC systems

While the technical market readiness could be demonstrated with the previous Galileo system back in 2013, it was clear that manufacturing costs must be significantly decreased, and that component availability will become an issue for some parts of the Galileo. Therefore, the development of a next-generation HEXIS-µCHP-system (internal name Leonardo) was started a few years ago. The aim was to significantly cut down manufacturing and component costs. The SOFC stack itself remained largely unchanged, so that most of the experience gained in the last years with the Galileo systems could be transferred to the new system. Also, catalytic partial oxidation (CPOx) was retained to reform natural gas.

The Leonardo unit (see Figure 1), like the Galileo, is made to fit in single-family homes and small multi-family homes. It has an electrical power output of approx. 1.5 kW_{el}, an electrical efficiency of 40 % (AC, net, LHV) and a total efficiency of 95 % (LHV).

As one path to market, the units will be mainly sold to HVAC OEMs to integrate it in their heating system portfolio. One of the first OEM that will integrate the SOFC unit as part of its Fuel Cells System Vitovalor SA-2 is Viessmann, HEXIS's former parent company.

Figure 1: HEXIS' new generation SOFC-unit "Leonardo" integrated into a Viessmann Vitovalor SA-2.

https://doi.org/10.5281/zenodo.4518797

2. Results

Short Stack long-term testing

In order to enable reliable prediction of long-term system performance, the generation of fuel cells employed in the Leonardo systems were tested extensively early-on in the development process. In 2014, two short stacks were started on steady-state conditions and under CPOx reformed natural gas. These tests have been monitored in regular intervals by I-V curves and electrochemical impedance spectroscopy. Long term data from these measurements is shown in Figures 2 and 3.

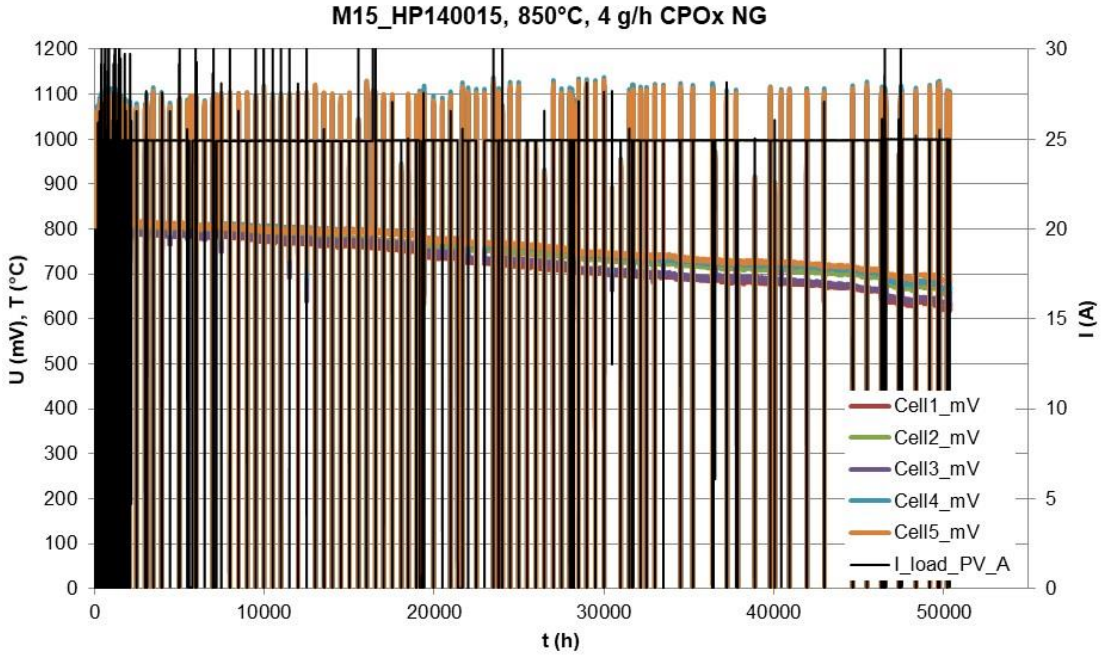

Figure 2: Long-term test data of a 5-cell short-stack operated with 4 g/h CPOx-reformed natural gas per cell (i.e. 51 W, LHV) for more than 52,000 h at 850°C. Combined Test: 50 Redox-cycles + 10 Thermo-Redox-cycles + steady-state operation. Average voltage degradation (2000 – 50,000 h): 2.9 mV/ kh, i.e. 0.35 % per 1,000 h. The test had to be stopped due to a failure of the test station.

https://doi.org/10.5281/zenodo.4518797

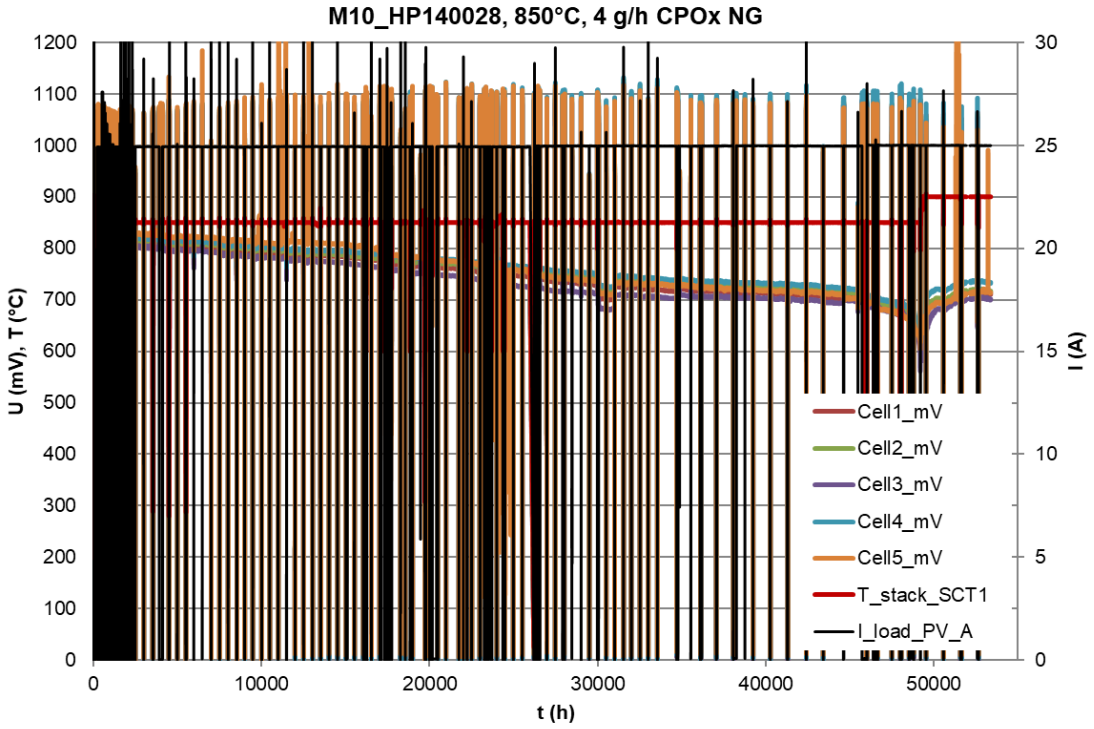

Figure 3: Long-term test data of a second 5-cell short-stack operated with 4 g/h CPOx-reformed natural gas per cell (i.e. 51 W, LHV) for more than 49,000 h at 850°C. Combined Test: 50 Redox-cycles + 10 Thermo-Redox-cycles + steady-state operation. Average voltage degradation (2400 – 45,000 h): 2.5 mV/ kh, i.e. 0.3 % per 1,000 h. At approx. 49,000 hours, a test station failure occurred, the test stand could be repaired, and the test continued, although the voltages started decreasing earlier (i.e. @ 47,000 h), they were able to recover after repair (not shown).

Figure 2 shows results of a long-term test on short-stack level that has been shown (in its "younger" state) many times before [1, 2]. The test was a combined test including cycles and long-term operation: first 50 redox cycles, then 10 thermo-redox-cycles till < 300 °C followed by steady-state operation. Later, a few additional thermo-redox-cycles were conducted, part of them planned, to investigate the cycling-sensitivity of "aged" stacks, part of them occurred unintentionally because of lab and test-rig failures. The observed voltage degradation rate is 0.35 % per 1000 h (i.e. 2.6 mV per 1000 h) based on the steady-state operation. As shown earlier [2], this voltage degradation corresponds to an ASR-degradation of approx. 13 mΩ cm² / kh and approx. 75 % of that degradation is stems from ohmic resistances.
Until the beginning of 2020, the stack had survived all the intended and unintended test conditions. The stack performance then dramatically decreased (i.e. loss of voltage during loading), and during dismounting the stack it became clear, that the reformer module was significantly deformed resulting in a huge leakage in the gas path and as a result in the loss of stack performance.

Figure 3 displays similar data for the "younger" brother, which was started slightly later than the one mentioned above. The test conditions and behaviour are quite similar, voltage degradation was slightly lower (i.e. 2.5 mV per 1000 h). Also, this stack showed a decreasing voltage in the beginning of 2020, in this case due to a failure of the de-sulphuration unit caused by a local sulphur peak in the natural gas supply. Following the replacement of the de-sulphuration unit and a short operation at higher temperatures (900 °C), cell voltages stabilized and recovered to almost old values. After a "recover" period the test station is now operating at old conditions again (i.e. 850 °C) and results so far seem to be promising.

https://doi.org/10.5281/zenodo.4518797

Due to the test station failure of the first short-stack, it was possible to investigate the oxide scale growth of the CFY interconnects. As reported earlier, oxide scale growth under the conditions present in the Hexis stack appeared to be more severe on the anode side of the interconnect, while the cathode side of the interconnect showed only thin oxide scales. This observation falls in line with past reports and is due to the imminent chromium evaporation process present at high oxygen partial pressures [3].

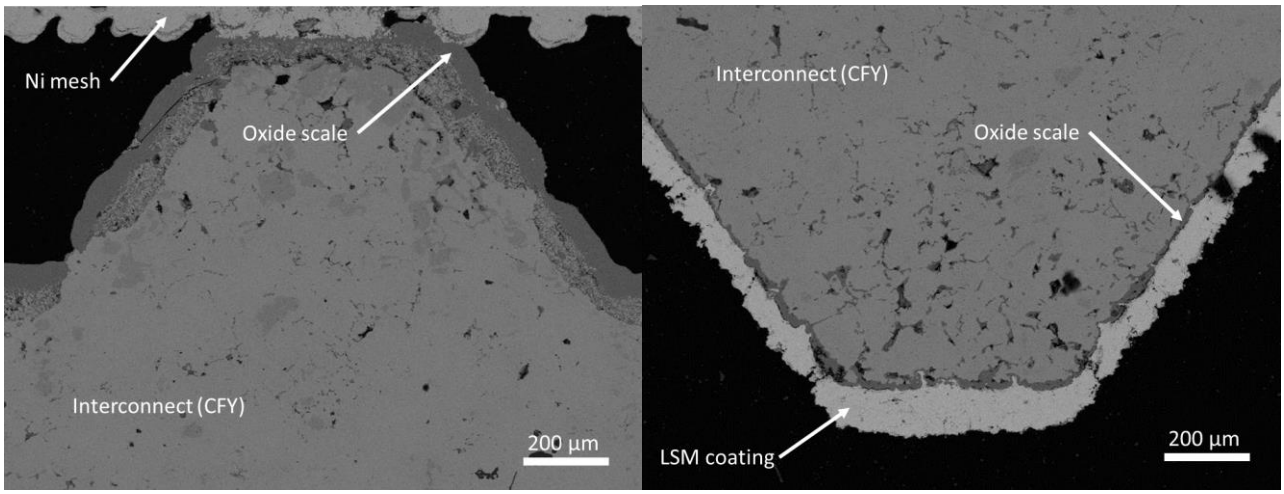

Figure 4: Cross-sections of an interconnect with anode side (left) and cathode side (right) contact ribs. The interconnect belonged to the short-stack discussed in Figure 2 and had been exposed to operating temperature of 850 °C for more than 52,000 h.

System Long-term Testing

The development of the new fuel cell unit *Leonardo* is in finalisation. Figure 5 shows results from field testing with 3 systems installed at end-customer-sites. All systems deliver around 1650 W_{el} DC, matching well to the targeted 1505 W_{el} (AC, net). To achieve this, gas inputs are set to 3800 - 3900 W depending on gas-quality, installation conditions and measurement accuracy, corresponding to 38 – 40 % electrical efficiency (LHV, AC, net).

Over 13,500 h, the gas input at maximum modulation point increases slightly to keep the electrical output constant despite the inherent stack degradation. The inherent degradation is in the same range as for the short-stacks and the former Galileo stacks, so that lifetimes of more than 40,000 h are also expected for the new units.

The larger variations in gas input and the corresponding electrical output modulations are due to heat demand variations at the installation sites, so that the heat-demand-driven system is modulating down when less heat is needed in the houses. At the minimum operating point, heat output is around 650 $W_{thermal}$, which fits well to the heat demand for warm water generation at the installation sites, displaying that an all-year-round operation is suitable, as long as a normal warm water demand is there. At the minimum operating point, electrical power output is still at approx. 400 W, fitting well to the baseload electrical consumption of the households.

https://doi.org/10.5281/zenodo.4518797

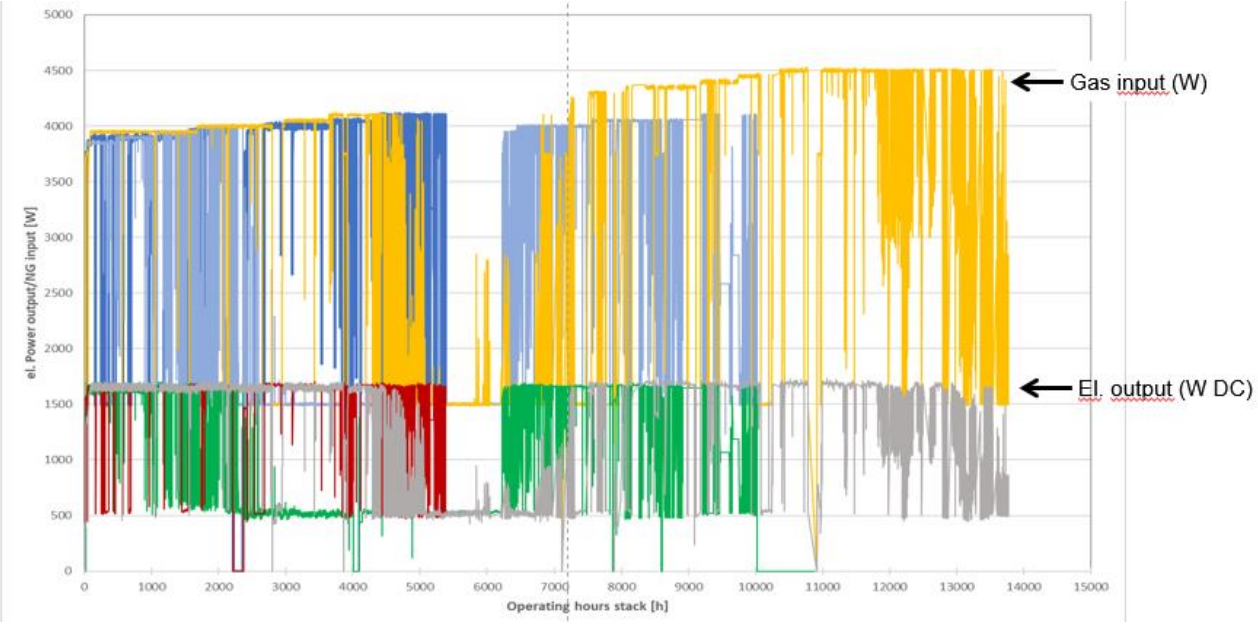

Figure 5: Electrical power output and gas input vs. operation time of a field test system from the current generation. The variations in gas input are due to heat demand variations in the installation sites, while the gas input at maximum power output is slightly increased to keep the electrical power output constant. Operating temperature approx. 830°C.

Demonstrator System with Steam-reforming

For the future, it is planned to equip systems with an in-built steam reformer to achieve higher electrical efficiencies. A demonstrator has been setup based on the Leonardo fuel cell module and modified to a new reformer design. For this, the number of cells per stack were reduced from 60 to 50. The nominal fuel input was reduced to 2500 W (LHV, natural gas). Figure 6 shows the stack performance and the I-V curve. The demonstrator system reached a maximum DC-efficiency of 58.9% at 1470 W electrical power output (DC), corresponding to an AC, net efficiency above 50 %. It achieved similar total efficiencies of more than 94 %, like the CPOx systems (at 30°C circuit return temperature) and was operated in a self-sustaining mode regarding process-water (i.e. the water needed for steam-reforming was condensed from the exhaust gases) at circuit return temperatures up to 45°C. This demonstrator has now been operating for 10,000 hours.

https://doi.org/10.5281/zenodo.4518797

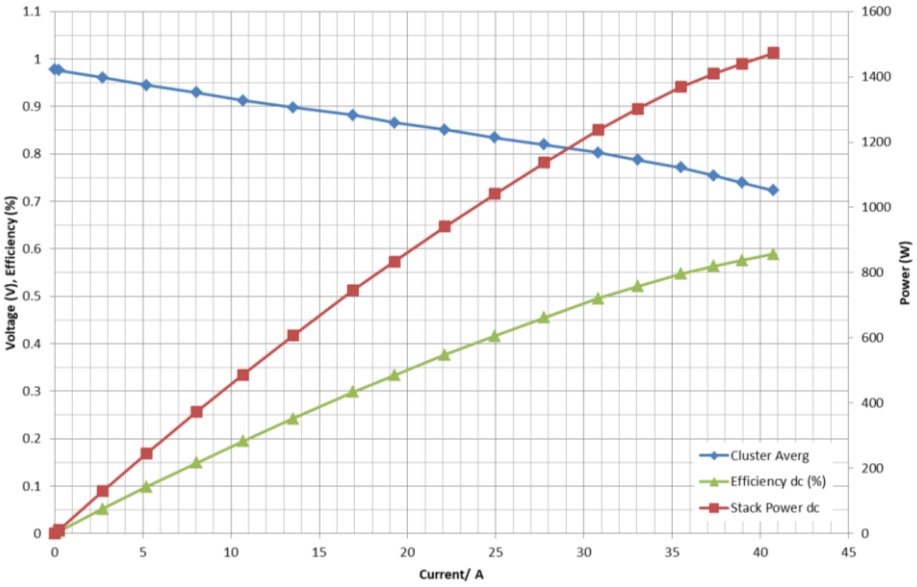

Figure 6: Voltage, el. power output and electrical efficiency of the “da Vinci” demonstrator system operated on 2500 W Natural Gas. Peak electrical efficiency: 58.9 % DC. Operating Temperature 850°C.

Conclusions and Outlook

HEXIS has developed its next generation SOFC-based µ-CHP unit, with the final version now running in field-tests. A demonstrator system shows electrical efficiencies of more than 50 % AC net, which will form the basis for the next generation of systems.

With its new parent companies, mpower and h2e, HEXIS will not only become the supplier of SOFC units to its former parent company Viessmann, but will also be open to supply its fuel cell units to other OEMs. Moreover, together with h2e and mpower, it is intended to expand the Hexis product portfolio to other applications e.g. in agriculture and/or for power supply of distant rural areas. Additionally, the product portfolio of HEXIS, mPower and h2e will also include other SOC applications like electrolysis and P2X applications in the future.

Acknowledgements

HEXIS was supported for the work presented by the German Federal Ministry of Transport and digital Infrastructure within the “National Hydrogen and Fuel Cell Technology Innovation Programme” in the two projects Leonardo (project Nr. 03BH105) and Leonardo II (project Nr. 03BH214A). The work on the steam reforming concept is supported by the Swiss Federal Office of Energy (SFOE) within the project “da Vinci”.

References

[1] Andreas Mai, Jan Gustav Grolig, Michael Dold, Felix Vandercruysse, Roland Denzler, Bernhard Schindler, Alexander Schuler, 13th European SOFC Forum, Lucerne, A0301, 2018

[2] Andreas Mai, Jan Gustav Grolig, Michael Dold, Felix Vandercruysse, Roland Denzler, Bernhard Schindler, Alexander Schuler, ECS Transactions, 91(1), 63-70, 2019

[3] Jan Gustav Grolig, Gino Longo, Andreas Mai, ECS Transactions, 91(1), 2181-2188, 2019

Keywords: EFCF 2020, SOx
Session A03: Technology status at industry and major groups I

https://doi.org/10.5281/zenodo.4518797

A0304

Progress of SOC development at Elcogen

Matti Noponen (1), Pauli Torri (1), Jukka Göös (1), Jouni Puranen (1), Sergii Pylypko (2), Marek Roostar (2), Enn Õunpuu (2)
(1) Elcogen, Niittyvillankuja 4, 01510 Vantaa/Finland
(2) Elcogen, Valukoja 23, 11415 Tallinn/Estonia

Contact authors: www.EFCF.com/ContactRequest

Abstract

Elcogen is one of the leading European manufacturers of solid oxide cell (SOC) technology. Elcogen products are unique combination of best in class performance and low-cost product structure. The unit cell and stack products are designed for low temperature operation enabling major cost reductions in the system level. Elcogen's operations are located in the Nordic-Baltic technology cluster of Finland and Estonia. This article summarizes the recent activities and development trends of Elcogen.

https://doi.org/10.5281/zenodo.4518827

Introduction

Elcogen is currently focused in ramping up its unit cell and stack production with the increased customer requests. The short-term goal is to set-up of a demonstration manufacturing plant for the unit cells and stacks with annual capacity of 50 MW. To facilitate the goals, Elcogen has signed EUR 12 million loan facility with The European Investment Bank (EIB). The loan is the first in the Baltic countries to get support under the InnovFin – EU-finance for innovators programme, which is financed from the EU's Horizon 2020 research and innovation programme. Specifically, the financing falls under InnovFin's Energy Demonstration Projects (EDP) facility.

Elcogen is continuously developing its products for higher performance, longer lifetime, lower costs, increased quality and expanded applications. This article summarizes Elcogen's latest test results of its commercial E3000 stack conducted to study the performance, long-term stability, thermocycle durability and manufacturing quality.

Elcogen stacks are built around company's internally manufactured unit cells. The unit cells are anode supported with cell structure combining anode contact layer (NiO, 2 μm), anode support layer (NiO/YSZ, 400 μm), anode functional layer (NiO/YSZ, 10 μm), electrolyte (YSZ, 3 μm), barrier layer (GDC, 2 μm), and cathode (LSC, 20 μm). The interconnect plates are manufactured from ferritic sheet metal and coated with MCO. The stack design for commercial application is called elcoStack® E3000 and the stack design for technology evaluation purposes elcoStack® E350. The difference between the design variants is the air supply means, i.e. elcoStack® E350 has fully manifolded air side structure as elcoStack® E3000 utilizes open air design. Figure 1 depicts elcoStack® E350 and elcoStack® E3000. The flow distribution and electrical contacting structures for both design variants are identical and thus the results obtained with both designs are directly comparable to each other. elcoStack® E350 design is easily integrable to most solid oxide fuel cell test stands and elcoStack® E3000 is optimized for large systems utilizing multiple stacks.

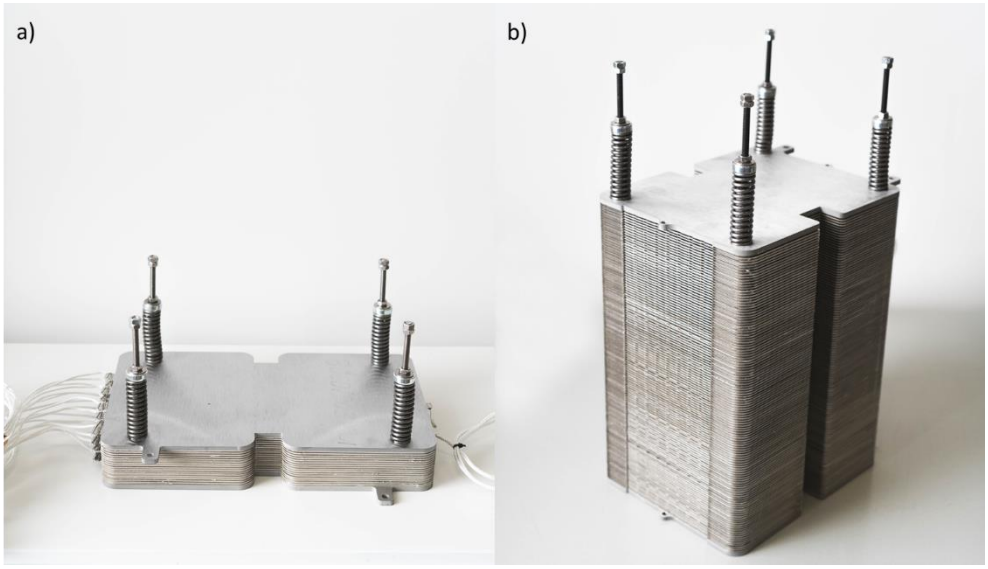

Figure 1. a) elcoStack® E350 with 15 unit layers, fully manifolded air structure, all unit layers equipped with voltage measurement cables and in-stack thermocouple. b) elcoStack® E3000 with 119 unit layers and open air structure.

https://doi.org/10.5281/zenodo.4518827

1. Performance and manufacturing quality

The main stack product for Elcogen is elcoStack® E3000. This is optimized for large SOFC systems utilizing multiple stacks. An example of such system is developed in EU's Horizon 2020 research and innovation program under Grant Agreement No 671403. Elcogen manufactures stacks to the system and Convion Ltd. is responsible for the system design and manufacturing.

In order to enable successful fuel cell systems, the stack quality has to be constant. Thus, Elcogen is monitoring the performance of every produced stack with quality assurance tests with as high detail level as is still practical without increasing the manufacturing costs. Elcogen's standard quality assurance protocol includes current-voltage characteristics test and effective fuel utilization dependency test. Quality assurance measurements are conducted according to IEC 62282-7-2. Stack temperature is recorded with two thermocouples, the first located at the inlet edge of the active cell area and the second one located at the outlet edge of the active cell area.

The current-voltage characteristics test is conducted with 1/1 ratio of H_2/N_2 with constant flow rate of 122 l_N/min. Cathode side is fed with air at constant flow rate of 327 l_N/min. Inlet temperature for the air is 590 °C and for the fuel 585 °C. Current is increased with 1 A/min sweep rate from 0A to 30A. The stack power is calculated as a product of the measured current and voltage.

The effective fuel utilization dependency test is conducted at constant current of 20 A. The test is conducted at partial load in order to highlight possible differences in the fuel utilization dependency between the stacks. Fuel is 1/1 ratio of H_2/N_2, and the fuel flow rate is decreased stepwise 54.6 – 50.3 – 46.7 – 45.0 – 43.7 – 42.3 – 40.8 l_N/min. Stabilization time at each flow rate level is 2 min. Cathode side is fed with air at constant flow rate of 327 l_N/min. Inlet temperature for the air is 590 °C and for the fuel 585 °C.

The current-voltage characteristics test results are depicted in Fig. 2. The average stack voltage at open circuit condition of elcoStack® E3000 is 141.8 V with standard deviation of 0.8 V. The mean unit layer voltage is 1.191 V and the deviation per unit layer is 0.007 V. The average stack voltage at nominal current, 30A, of elcoStack® E3000 is 105.0 V with standard deviation of 0.6 V. The mean unit layer voltage is 0.883 V and the deviation per unit layer is 0.005 V. The average stack temperature determined as the average between the stack inlet temperature (605 °C) and stack outlet temperature (667 °C) at the nominal current is measured to be 636 °C. Stack power at 30A is 3151 W with standard deviation of 23 W. The deviation per unit layer is 0.2 W as a single layer produces 26.5 W.

The effective fuel utilization dependency test results are depicted in Fig. 3. The average stack voltage of elcoStack® E3000 at 60% fuel utilization is 108.2 V with standard deviation of 0.3 V. The average stack voltage of elcoStack® E3000 at 80% fuel utilization is 104.5 V with standard deviation of 0.3 V. The deviation per unit layer is constant 0.003 V at these fuel utilization levels.

https://doi.org/10.5281/zenodo.4518827

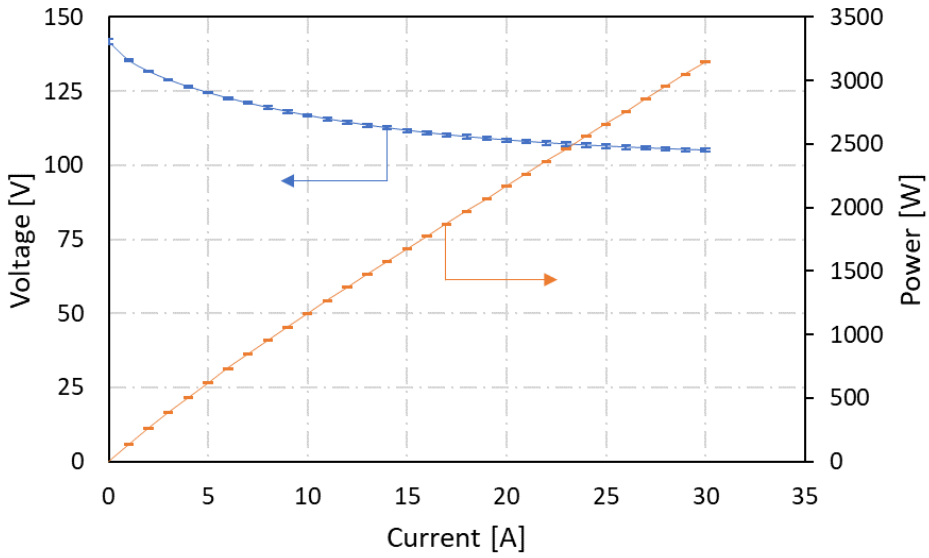

Figure 2. Current-voltage characteristics of elcoStack® E3000 measured with hydrogen. Error bars are calculated as standard deviations of the measured stacks.

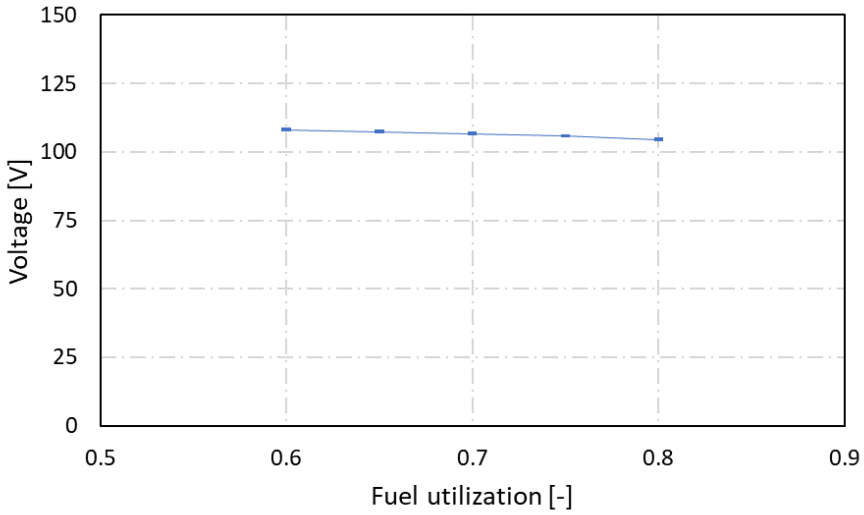

Figure 3. Effective fuel utilization dependency of elcoStack® E3000. Error bars are calculated as standard deviations of the measured stacks.

The current-voltage characteristics test with natural gas is conducted with 1/2.2 ratio of NG/H_2O with constant flow rate of 33 l_N/min. The gas composition is typical Finnish pipeline grade natural gas with lower heating value of 802.3 kJ/mol ([CH_4] = 98%, [C_2H_6] = 0.8%, [C_3H_8] = 0.2 %, [C_4H_{10}] = 0.02%, [N_2] = 0.9 %, [CO_2] = 0.1%). The odorant in natural gas, THT, is cleaned with a room temperature sorbent. Test is conducted at VTT Technical Research Centre of Finland Ltd. Natural gas is mixed with steam feed prior the reformer reactor. The gas composition fed to the stack is standardized in the test by controlling the outlet temperature of the steam reforming reactor to 590 °C. The resulting composition for the stack inlet is [CH_4] = 7%, [H_2O] = 26%, [CO] = 7%, [H_2] = 52%, [CO_2] = 8%. Cathode side is fed with air at constant flow rate of 327 l_N/min. Inlet temperature for the air and fuel is 590 °C. Current is increased with 1A/min sweep rate from 0A to 30A. The stack power is calculated as a product of the measured current and voltage.

https://doi.org/10.5281/zenodo.4518827

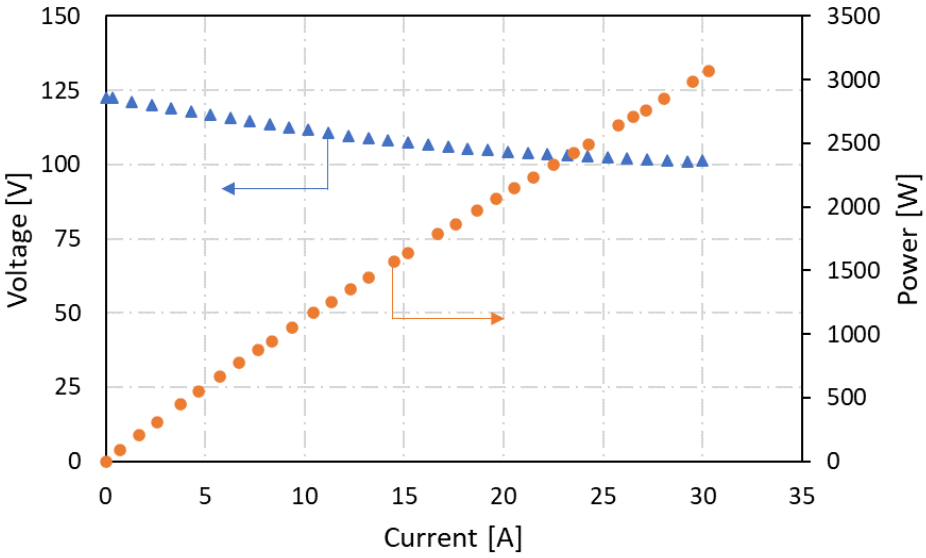

Figure 3. elcoStack® E3000 performance measured with natural gas.

2. Long-Term Stability

The long-term stability of elcoStack® is studied with steam reformed natural gas. The long-term stability experiment is conducted with standard elcoStack® material system and with two type stack configurations, E3000 and E350, see Fig. 1. Difference between the two stacks is the number of unit layers and the air side flow configuration. – E350 contains 15 and E3000 119 unit layers. E350 has closed air manifold structure and E3000 has an open-air structure as shown in Fig. 1.

Both stack tests are conducted at VTT Technical Research Centre of Finland Ltd. Testing conditions for the stacks are set to equal in terms of temperatures, current, fuel composition and flow rates per unit layers. Natural gas is mixed with steam feed prior the reformer reactor. The steam-to-natural gas ratio is 2.2. The gas composition fed to the stack is standardized in the test by controlling the outlet temperature of the steam reforming reactor to 590 °C. The resulting composition for the stack inlet is [CH_4] = 7%, [H_2O] = 26%, [CO] = 7%, [H_2] = 52%, [CO_2] = 8%. Fuel utilization in the test is 60% simulating conditions of a system equipped with anode exhaust gas recycle unit. The fuel cell cathode is fed with preheated air. The oxygen utilization is 22%. Both the air and fuel are heated to 590 °C for the stack inlet. The current at the nominal operation conditions is 30 A.

Figure 4 depicts the average unit layer voltage as a function of operation time for E3000 stack and the average unit layer voltage for unit layers 8 – 11 as a function of operation time for E350 stack. Layers 8 – 11 from E350 test are selected for this analysis due to their similar temperature profile nature compared to E3000 stack, i.e. end cell effects are then excluded from the analysis. The E350 has been operated at constant steam reforming conditions for 18700 hours and the test is still continued (August, 2020). The voltage decay over the whole operation time has been 0.4 %/1000h and the ASR decay 15 mΩ.cm^2/1000h. The voltage decay is determined as the slope divided by the intercept of linear regression of the mean unit layer voltage measured at the nominal conditions. The ASR decay is determined as the slope of linear regression of the mean unit layer voltage

https://doi.org/10.5281/zenodo.4518827

measured at the nominal conditions divided by the current density (0.25 A.cm^{-2}). The test period involves one load cycle at 5600 hours in which the current was switch off from 30 A to 0A instantly and full thermocycles due to scheduled laboratory maintenance at 7600 and 8600 hours. None of these interruptions caused any measurable degradation to the stack voltage. elcoStack® E3000 has been operated since June 2020 with natural gas achieving 1400 loading hours. The initial performance and degradation levels are comparable to the E350 test as can be seen from Fig 4 and the test is continued.

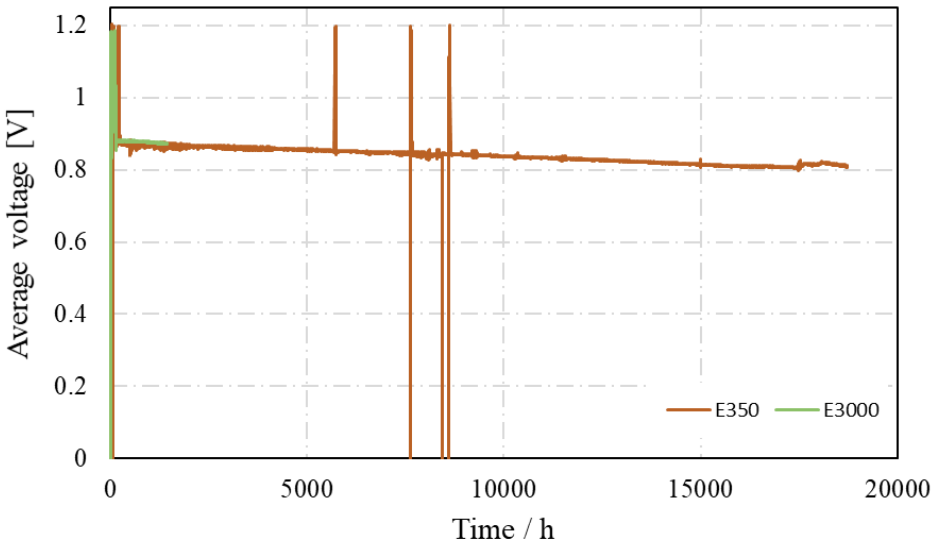

Figure 4. elcoStack® average voltage in long-term test.

3. Robustness in thermocycles

elcoStack® E3000 robustness in thermocycles is studied with conventional heat cycle process in which reducing gas is continuously supplied to the anode side and air to the cathode side, see Fig. 5. One cycle consists of a heating period from 50 °C to 600 °C at rate of 120 °C/h, testing period and a cooling period from 600 °C to 50 °C. During heating and testing periods, fuel side is fed with 1/1 mixture of H_2/N_2 at 122 l_N/min flow rate expect effective fuel utilization test in which ratio is kept constant but flow rate is decreased. During cooling phase, fuel side is fed with 5/95 mixture of H_2/N_2 at 106 l_N/min flow rate. Air side is fed with constant flow rate of 327 l_N/min. Testing phase includes current-voltage characteristics test and effective fuel utilization test, and these both are conducted with a similar process already explained previously. Stack is equipped with unit layer voltage measurement cables.

https://doi.org/10.5281/zenodo.4518827

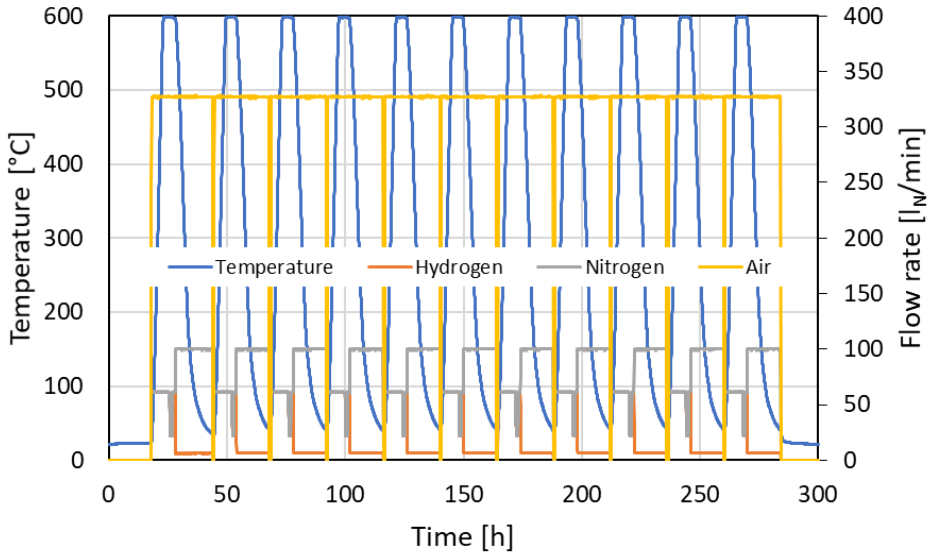

Figure 5. Temperature and gas flow rates in thermocycling testing.

Thermocycling test is conducted all together 11 times for the stack. Figure 6 depicts the stack voltage (diamonds) during the current-voltage characterization test at 0 A (OCV) and 30 A (NOC). The area around the diamonds indicate the difference between the maximum unit layer voltage and the minimum unit layer voltage. It is observed that no decay in stack voltage could be observed during the cycling test but actually the performance of the stack was improving. E.g. stack voltage after stack conditioning process was 138.8 V at OCV and 105.7 V at NOC, after 5 cycles was 141.6 V (OCV) and 107.0 V (NOC) and after 10 cycles 142.0 V (OCV) and 107.5 V (NOC). At respective cycles, the difference between the maximum and minimum unit layer voltages was 26 mV (OCV, cycle 0), 35 mV (OCV, cycle 5), 35 (OCV, cycle 10), and 47 mV (NOC, cycle 0), 50 mV (NOC, cycle 5), 47 mV (NOC, cycle 10).

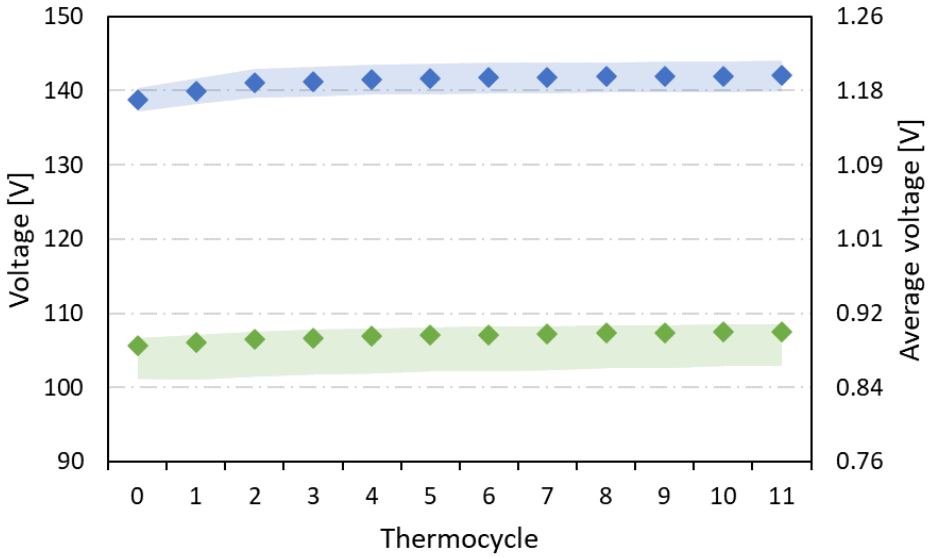

Figure 6. elcoStack® E3000 voltage in thermocycles. A diamond is stack voltage and average unit layer voltage, area is defined as the difference between the maximum and minimum unit layer voltage. Blue color indicates OCV values and green color NOC values.

https://doi.org/10.5281/zenodo.4518827

4. Summary

Elcogen is continuously developing its unit cell and stack products to be more efficient, robust and affordable for different applications. Elcogen products are unique as their operation temperature is 600 °C still being able of utilizing standard industrial materials and manufacturing methods allowing major cost reductions for the technology. This work summarizes some of the latest test results of Elcogen stack products highlighting the robustness, constant quality and long-term stability of elcoStack® E3000 products.

Acknowledgments

This work has received funding from the Fuel Cells and Hydrogen Joint Undertaking under Grant Agreement No 671403 and 735160. This Joint Undertaking receives support from the EU's Horizon 2020 research and innovation program and Hydrogen Europe. VTT Technical Research Centre of Finland Ltd is acknowledged for conducting the tests with natural gas.

Keywords: EFCF 2020, SOx
Session A03: Technology status at industry and major groups I

https://doi.org/10.5281/zenodo.4518827

A0305

Power-to-X activities at Haldor Topsoe: our approach for electrification of the chemicals industry

Rainer Küngas, Peter Blennow, Thomas Heiredal-Clausen, Tobias Holt Nørby, Jeppe Rass-Hansen, John Bøgild Hansen, Poul Georg Moses
Haldor Topsoe A/S, Haldor Topsøes Allé 1
DK-2800 Kgs. Lyngby/Denmark

Contact authors: www.EFCF.com/ContactRequest

Abstract

Haldor Topsoe considers electrolysis and solid oxide electrolysis cells (SOEC) in particular an enabling technology for the electrification of the chemical industry. Here, we present status updates on our various stepping stone projects, CO_2 electrolysis for CO production and H_2O electrolysis for biogas upgrading, as well as the demonstration project for the electrification of ammonia production.

Compared to other electrolysis technologies, SOEC allows for the conversion of CO_2 into useful chemicals at very high efficiencies and at a faradaic yield of 100%. Haldor Topsoe is commercializing the CO_2 electrolysis technology as eCOs™: a platform for on-site on-demand CO generation from CO_2 feedstock for customers requiring a reliable and safe feed of carbon monoxide at a scale of up to thousands of Nm^3 CO/h.

The use of SOEC for the production of H_2 is also interesting, not merely due to the inherently high conversion efficiencies that can be achieved, but also due to system-level synergies found in integrating the endothermal electrolysis process with an exothermal chemical synthesis process. The pilot plant for upgrading CO_2 in biogas into pipeline quality synthetic natural gas (SNG), located at Foulum, Denmark, provides an example of such integration.

Haldor Topsoe is a market leader in providing technological solutions and catalysts for the production of ammonia. Since 2000, Topsoe has commissioned >60 ammonia plants across the world with an accumulated capacity of almost 100 000 metric tonnes of NH_3 per day. It is Haldor Topsoe's ambition to become a technology provider for future fully electrified ammonia plants. A novel process is being developed where the nitrogen for the ammonia synthesis is provided by burning air between the SOEC stacks and utilizing steam generated in the Haber-Bosch loop as feedstock. This results in very efficient plant (71 % LHV efficiency) and eliminates investment in an air separation unit.

https://doi.org/10.5281/zenodo.4518845

Introduction

Carbon dioxide emissions from industrial sources account for approximately 20% of global energy-related CO_2 emissions (production of cement – 7%, iron and steel – 6%, chemicals – 5%, aluminium – 1%) [1]. Along with heavy transport and aviation, industry is a relatively challenging sector to decarbonize, but efforts to electrify industrial processes and to replace fossil fuels with climate-friendly alternatives (e.g. hydrogen, carbon monoxide or syngas produced via electrolysis) are intensifying. In the European Union, these efforts are supported by a strong political will [2].

Electrolysis is an enabling technology for de-coupling the production of industrial chemicals from the use of fossil fuels and therefore plays a central role in various Power-to-X scenarios. Here, X can be hydrogen, carbon monoxide, syngas, methanol, ammonia or any other chemical or fuel [3]. When electrolyzers are powered by renewable electricity, then the CO_2 emissions associated with the production of X will be minimal and may even be negative.

Currently, the majority of water electrolysis systems used for Power-to-X applications are based on alkaline electrolyzers [4]. However, while alkaline electrolysis is a mature technology, the conversion efficiency of alkaline cells remains low: electric power consumption on stack level is typically higher than 4.6 kWh/Nm^3 H_2 [4]. In large-scale Power-to-X plants, the levelized cost of product is to a large extent determined by the price of electricity and the electric power consumption of the electrolysis units [5]. Alternative electrolysis technologies, and SOEC in particular, are attractive due to the higher conversion efficiencies. For example, H_2 production at 3.1 kWh/Nm^3 H_2 on stack level has recently been demonstrated using SOECs [6]).

Here, we provide status updates on our various stepping stone projects towards large-scale Power-to-X projects: i) CO_2 electrolysis for CO production, ii) H_2O electrolysis for biogas upgrading, and iii) electrification of ammonia production.

1. CO_2 electrolysis for CO production

Haldor Topsoe is offering world's first commercial CO_2 electrolysis system based on SOEC technology [7]. The system, called the eCOs™ Plant, combines CO_2 electrolysis and gas purification in one unit and is capable of producing 96 Nm^3 high-purity carbon monoxide gas per hour. An eCOs™ Plant is a stand-alone unit with power, CO_2, and product gas connections (Fig. 1) that allows the customer to produce carbon monoxide on-site and on-demand from carbon dioxide feedstock. The eCOs™ technology can be used to produce CO a scale of up to thousands of Nm^3 CO/h.

On-site CO generation using the eCOs™ technology has several important advantages compared to common alternatives, such as CO supply by tube-trailers or gas cylinders. First, CO is produced on-site from unhazardous CO_2 feedstock, which is safe to store and handle. Secondly, CO can be produced on-demand only when needed, reducing or eliminating the need for storing large amounts of CO on-site. This significantly reduces the safety risks associated with handling and transportation of carbon monoxide. Thirdly, there is no inertia in the system, as CO production can be stopped instantaneously by cutting off the supply of power to the SOEC unit. An eCOs™ plant provides the customers with intimate control over their CO production, ensures security of supply, and drastically reduces costs for storage, rentals and connections. Finally, the unit is capable of supplying highly pure CO gas at an economically attractive price.

https://doi.org/10.5281/zenodo.4518845

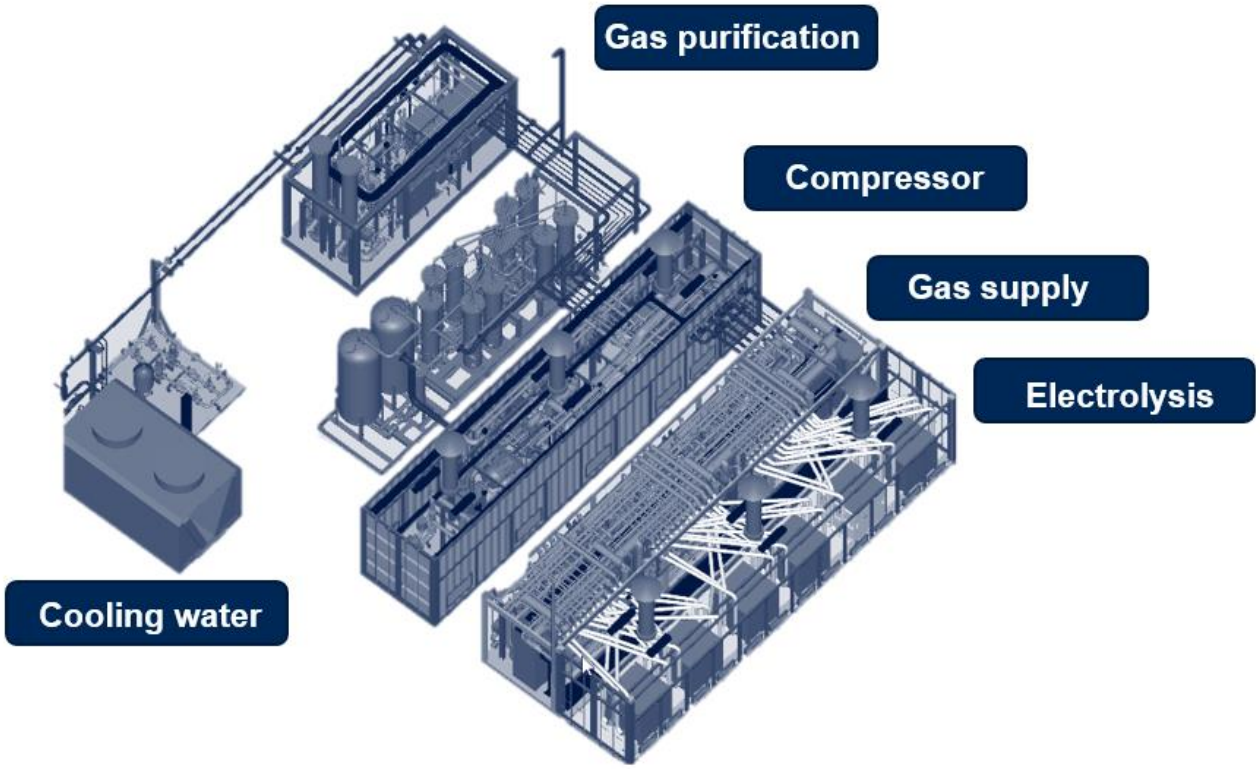

Figure 1. An eCOs^{TM} Plant capable of producing 96 Nm^3 CO/h. The plant is built up of six modules: electrolysis unit, gas supply unit, compressor unit, gas purification unit, cooling water unit, and control unit (the control unit is not shown).

Two eCOs^{TM} plants are scheduled to be commissioned in Ohio, USA, later this year. The 96 Nm^3 CO/h plant will have a modular design, and will consist of an electrolysis unit, a gas supply unit, a compressor unit, a gas purification unit, a cooling water unit, and a control unit (Fig. 1). Electrolysis, compressor, gas supply and control units will be housed in standard 40-foot containers for easier shipping and installation. The electrolysis unit will include 6 coreboxes, each with 8 TSP-1 stacks. These 96 Nm^3 CO/h plants will be the first commercial (subsidy-free) SOEC plants in the world.

TSP-1 stacks can successfully be operated in dry CO_2 electrolysis for extended periods of time. Fig. 2 shows the results of a system test with a TSP stack in a corebox operated at 750°C and at a current of -70 A, which corresponds to a production rate of 2.2 Nm^3 CO/h. The stack has been operated for almost 14 000 hours, during which it has produced more than 30 000 Nm^3 (35.5 tonnes) of CO. Despite being subjected to 21 thermal cycles, the degradation rate for the stack remained low: the average cell voltage increased at a rate of 7.9 mV kh^{-1}, when calculated over the entire test period, and 9.2 mV kh^{-1}, when calculated over the last 4 000 hours. On average, the stack consumed 3.44 kWh electric power for producing 1 Nm^3 CO.

Faradaic efficiency (FE) is a metric that is often used to describe the selectivity of electrochemical processes. In the context of CO_2 electrolysis for CO production, FE is defined as the fraction of total electrolysis current that is used towards reducing CO_2 to CO [8]. Obtaining FE efficiencies close to unity is non-trivial in low-temperature (aqueous) CO_2 electrolysis systems, where the CO_2 reduction reaction competes with the hydrogen evolution reaction and with other side-reactions, such as the production of hydrocarbons or oxygenates [8,9]. In SOEC systems operating in dry CO_2 electrolysis, FE values of 100% are relatively easy to obtain due to the fact that no water species is present in the feed gas. The FE values recorded during the 14 000-hour stack test are plotted in Fig. 3. Faradaic efficiency, determined using gas chromatography measurements on product gas,

https://doi.org/10.5281/zenodo.4518845

remained between 99% and 100% throughout the test (there were issues with the calibration of the gas chromatograph during the first part of the test). The uncertainty of the FE estimates is expected to be around +/- 1%, i.e. the slight differences in FE values observed in Fig. 3 are likely due to the measurement uncertainty and not fluctuations in stack FE.

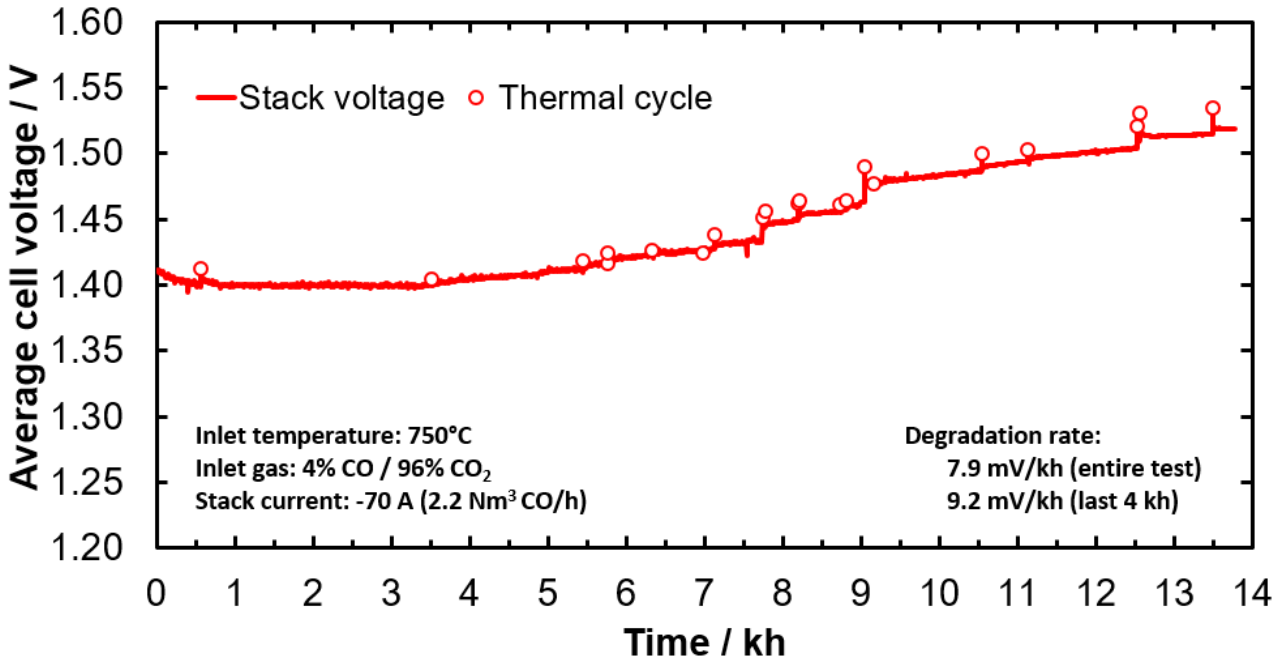

Figure 2. A system test of a TSP-1 stack in dry CO_2 electrolysis. The SOEC current was fixed at -70 A and the inlet temperature at 750°C. The stack was subjected to 21 thermal cycles (indicated by white circles) and several load cycles.

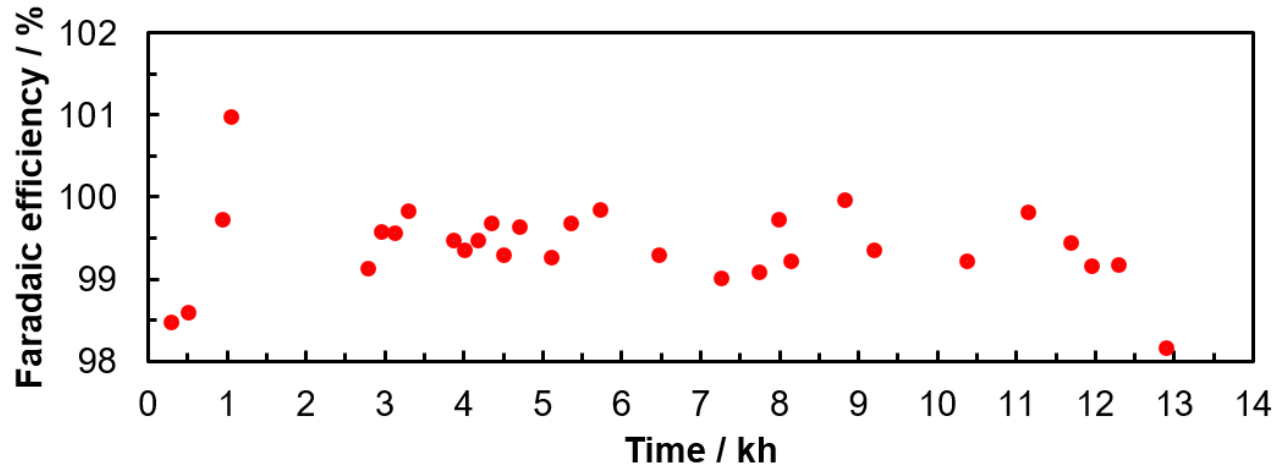

Figure 3. Faradaic efficiency towards CO production in the system test shown in Fig. 2, verified using gas chromatography measurements of the product gas. The gas chromatograph calibration was off during the first four measurements.

https://doi.org/10.5281/zenodo.4518845

2. H_2O electrolysis for biogas upgrading

Biogas produced by anaerobic digestion consists typically of methane and carbon dioxide in a volumetric ratio of approximately 6:4, as well as several thousand parts per million of various sulfur compounds (mainly H_2S) [5,6]. One way to upgrade the value of biogas is to mix it with hydrogen produced via steam electrolysis in a methanation reactor to produce synthetic natural gas (SNG). SOEC technology offers unique benefits in connection with biogas upgrading, because the heat released by the exothermal methanation step can be used to generate steam for high-temperature electrolysis, thus avoiding evaporation of water by electricity. Coupled with the favorable thermodynamics and kinetics at elevated temperatures, this increases the overall efficiency from electric power to additional methane product significantly.

In “El-upgraded biogas”, a project funded by the Danish Energy Agency (EUDP), a 10 Nm^3/h SNG demonstration plant based on SOEC, biogas desulphurization and catalytic methanation was designed, built and operated for more than 2100 hours. Very high energy conversion efficiency (H_2 production at 3.07 - 3.09 kWh/Nm^3), rapid load-following capability, and better than pipeline-quality SNG production was demonstrated [6].

A follow-up project “El-upgraded biogas II”, also funded by EUDP, aims to bring the technology readiness level from TRL 6 to TRL 8. The goal is to operate the demonstration plant for at least 4000 hours including transient operation to adapt to the anticipated future electricity market. During the 4000 hours the hydrogen production should be 16 Nm^3/h (corresponding to 10 Nm^3/h upgraded biogas starting with a raw gas with 40 % CO_2) with stack temperatures not exceeding 780 °C. Additionally, a more cost-effective sulfur removal unit using enriched air from SOEC will be introduced [10], preventive maintenance on balance-of-plant components will be carried out, and a steam clean-up step will be incorporated. The project partners include Haldor Topsoe and Aalborg University.

3. Electrification of NH_3 production

Ammonia (NH_3) is a commodity chemical with a global production capacity of around 180 million tonnes per year [11]. Ammonia is mainly used as a fertilizer but is also being seriously considered as a potential carbon-free fuel for the maritime industry. In order to replace 30% of the current marine fuel consumption with NH_3, an additional 150 million tonnes of ammonia would need to be produced [12]. Today, ammonia is almost exclusively generated from a feed gas of hydrogen and nitrogen, obtained via steam reforming of natural gas (Fig. 4A). Aided by better catalysts, improved process integration and the economies of scale, the average energy consumption of ammonia plants has been decreasing steadily over the past decades from over 60 GJ/tonne NH_3 in 1955 to 36.6 GJ/tonne NH_3 in 2008 The best-in-class NH_3 plants operate at ~28 GJ/tonne NH_3 [13]. Improved energy efficiency can be directly translated into a decrease in greenhouse gas emissions (on a tonne per tonne basis). However, even if it were possible to produce ammonia at the thermodynamic limit of 20 GJ/tonne NH_3, the resulting CO_2 emissions would still be substantial, making traditional pathways of ammonia production incompatible with future fossil- and CO_2-free energy scenarios.

Previously, ammonia plants using hydrogen produced by alkaline electrolyzers were common (Fig. 4B), and recently, in the light of increased concerns about CO_2 emissions and constantly decreasing renewable electricity prices, this technology is again gaining interest [14]. If the electricity required for running the electrolyzers and the air separation unit (ASUs) originates from renewable energy sources, then NH_3 can be produced with a low carbon footprint. However, the energy intensity of alkaline electrolyzers is high (> 4.6

kWh / kg H_2), which means that the energy consumption of such plants (>36 GJ/tonne NH_3 [11]) will be higher than for modern conventional plants.

If alkaline electrolyzers were replaced with SOECs as shown in Fig. 4C, the efficiency of the NH_3 plant could be increased considerably. Assuming the electrolysis cells are operated at the thermoneutral voltage of 1.29 V, the energy consumption of such electrified NH_3 plants would be around 26-27 GJ/tonne NH_3 [11]. However, an ASU is still required, which is very expensive and not easy to down-scale to smaller plant sizes (for distributed generation).

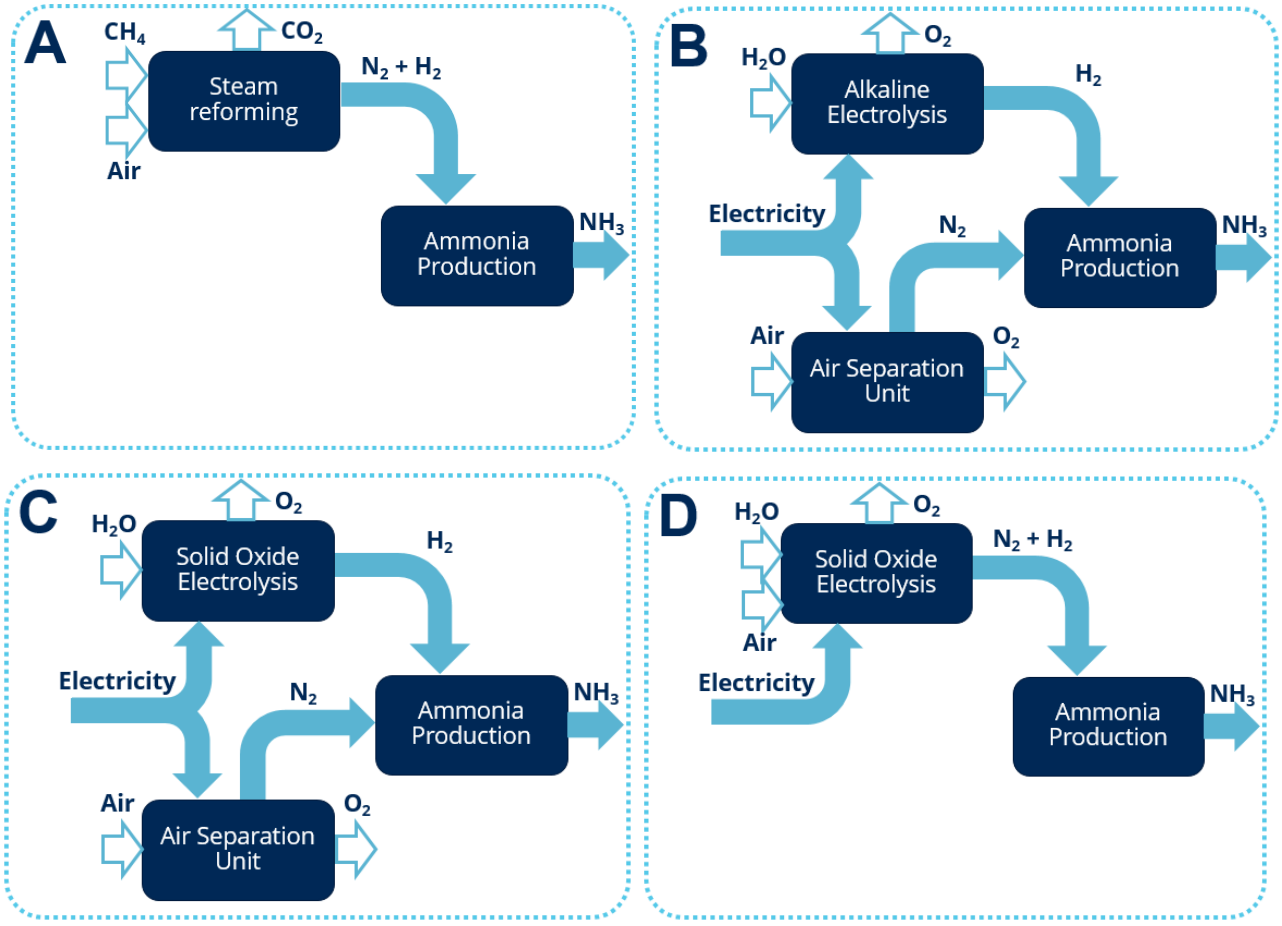

Figure 4. High-level block diagrams of different methods for producing ammonia: (A) conventional approach: steam reforming of natural gas, with air added to the secondary reformer, (B) combination of alkaline electrolysis and cryogenic air separation, (C) combination of SOEC and cryogenic air separation, and (D) a new method where SOEC provides both H_2 and N_2. In (D), SOEC acts simultaneously as an air separation unit and an electrolysis unit. Note that part of the heat required to convert water into steam can be provided by heat from the Haber-Bosch reactor.

Haldor Topsoe has developed a new process for ammonia synthesis gas generation that utilizes the unique capabilities of SOEC acting as an oxygen separation membrane, thereby obviating the need for an ASU (Fig. 4D) [11,15]. In such a plant, multiple steam electrolysis units would be connected in series, with catalytic burners located between consecutive stacks. Feed gas for the Haber-Bosch reaction (H_2 : N_2 = 3:1) would be generated on the fuel-side of the SOEC by combusting some of the electrolytic H_2 with air, which is added to the gas stream in the catalytic burners between stacks [11,15]. A 50 kW electrified ammonia plant based on the design shown in Fig. 4D will be demonstrated in

the project "SOC4NH3", funded by the Danish Energy Agency. The project partners include Haldor Topsoe (coordinator, technology and stack supplier), Aarhus University (host for the demonstration plant), DTU Energy (cell and stack tests). Additionally, transmission system operator Energinet, wind turbine manufacturer Vestas, and energy companies Ørsted and Equinor are to supply knowhow for techno- and socio-economic evaluations. The project will also include cell- and stack-level testing of NH_3 as fuel for SOFC.

Haldor Topsoe has been selected as the technology and catalyst provider for the ammonia synthesis section of the world's largest green ammonia plant, to be commissioned in 2025 [14]. The 5 billion USD project, owned by Air Products, NEOM and ACWA Power, will use 4 GW of renewable power to generate 650 t of H_2 per day, converting it to 1.2 million t of NH_3 per year [14]. The project will boast the world's largest ammonia loop. The produced ammonia will be distributed globally and cracked back to carbon-free H_2 for use at hydrogen refueling stations (Fig. 5). The project is an important milestone in Haldor Topsoe's NH_3 electrification roadmap [6]. While this plant will be based on alkaline electrolyzers, we envision that green NH_3 plants based on SOEC technology will be built in the future.

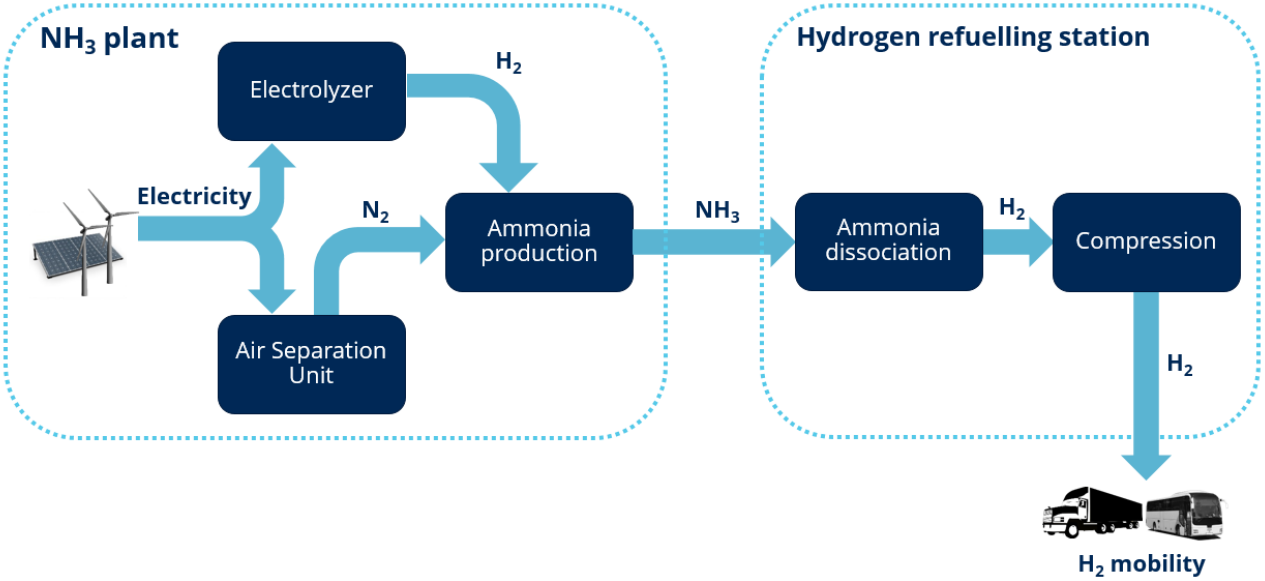

Figure 5. A high-level block diagram of the NH_3 plant powered by 4 GW of renewables, along with the proposed use of NH_3 for green mobility. Adapted from [14].

Conclusions

Haldor Topsoe is commercializing SOEC technology for CO production (eCOs^{TM}), with two electrolysis plants (each with a capacity of 96 Nm^3/h CO) scheduled for commissioning later this year. The plants will be the first subsidy-free SOEC plants in the world.

The proprietary TSP-1 stack design is suitable for long-term operation in dry CO_2 electrolysis. System tests have demonstrated stack lifetimes of almost 14 000 h (corresponding to ~30 000 Nm^3 (35.5 tonnes) of CO produced per stack), as well as robustness towards thermal and load cycles. The degradation rate for the stack was 7.9 mV kh^{-1} per cell, the average power consumption was 3.44 kWh/Nm^3 CO, and the Faradaic efficiency remained between 99-100% throughout the test. Based on these performance metrics, SOEC is by far the most efficient and mature technology for electrochemical CO_2 reduction.

https://doi.org/10.5281/zenodo.4518845

Haldor Topsoe's activities in H_2O electrolysis include continued development of an SOEC demonstration unit for biogas upgrading, aimed at lifting the TRL of the technology from 6 to 8. A new concept for producing feed gas for ammonia synthesis using SOECs, and without the need for cryogenic air separation units, will be demonstrated in a recently awarded project by the Danish Energy Agency.

Haldor Topsoe has been selected as the technology and catalyst provider for the ammonia synthesis section of the world's largest green ammonia plant, to be commissioned in 2025. The project is an important milestone in Topsoe's NH_3 electrification roadmap, and it is envisioned that green NH_3 plants based on SOEC technology will be built in the future.

Acknowledgements

Parts of this work have been financially supported by the Danish Energy Agency (EUDP) through projects EUDP 64017-05164 "El-upgraded biogas II", and EUDP 64017-0011 "EP2Gas – Efficient P2G combining SOEC and biomass gasification", EUDP 64018-0546 "SOC4NH3" as well as by Innovation Fund Denmark (IFD) through project 9067-00036B "REFORGE".

References

[1] IRENA, Hydrogen from Renewable Power: Technology Outlook for the Energy Transition (2018).
[2] Fuel Cells and Hydrogen Joint Undertaking, Hydrogen Roadmap Europe (2019).
[3] Energinet.dk, PTX in Denmark before 2030 (2019).
[4] G. Reitel, Power-to-Gas, in "*Fuel Cells: Data, Facts, and Figures*", 1st Ed. Editors: D. Stolten, R. C. Samsun, N. Garland, Wiley-VCH (2016).
[5] J. B. Hansen, *Faraday Discuss*., **182**, 9 (2015).
[6] R. Küngas, P. Blennow, T. Heiredal-Clausen, T. Holt Nørby, J. Rass-Hansen, J. B. Hansen, P. G. Moses, *ECS Trans.*, **91**(1), 215 (2019).
[7] Haldor Topsoe, "DeLille Oxygen Co. leases two eCOs™ units for cost-competitive onsite CO production", press release (2019), https://blog.topsoe.com/delille-oxygen-co.-leases-two-ecos-units-for-cost-competitive-onsite-co-production
[8] H.-R. Jhong, S. Ma, and P. J. A. Kenis, *Curr. Opinion Chem. Eng*., **2**, 191 (2013).
[9] C. Delacourt, P. L. Ridgway, J. B. Kerr, and J. Newman, *J. Electrochem. Soc*., **155**, B42 (2008).
[10] C. Dannesbroe, J. B. Hansen, I. Johannsen, *Biomass Conv. Bioref*., doi:10.1007/s13399-019-00570-7.
[11] J. B. Hansen, P. V. Hendriksen, *ECS. Trans.,* **91**(1), 2455 (2019).
[12] Alfa Laval, Hafnia, Haldor Topsoe, Vestas, Siemens Gamesa: Ammonfuel report (2020).
[13] International Fertilizer Industry Association: Energy efficiency and CO_2 emissions in ammonia production (2009).
[14] Air Products, "Air Products, ACWA Power and NEOM Sign Agreement for $5 Billion Production Facility in NEOM Powered by Renewable Energy for Production and Export of Green Hydrogen to Global Markets", press release (2020), http://www.airproducts.com/Company/news-center/2020/07/0707-air-products-agreement-for-green-ammonia-production-facility-for-export-to-hydrogen-market.aspx
[15] J. B. Hansen, A method for generating synthesis gas for ammonia production, WO19072608 A1.

Keywords: EFCF 2020, SOx
Session A03: Technology status at industry and major groups I

A0307

Evaluating the market attractiveness for Fuel Cell micro-Cogeneration units by applying a Multi- Criteria Evaluation (MCE)

Marco Kunz*, Tanaka Mbavarira, Benjamin Bowler, Christoph Imboden
Lucerne University of Applied Sciences and Arts (HSLU)
21 Technikumstrasse, CH-6048 Horw/Lucerne

Contact authors: www.EFCF.com/ContactRequest

Abstract

A market attractiveness analysis was conducted on the participation of residential fuel cell micro combined heat and power plants (FC-mCHPs) in the European grid service markets as part of the FCH-JU funded "Pathway to a Competitive European Fuel Cell micro-Cogeneration Market" (PACE) project. The aim of the analysis was to identify the most promising countries for FC-mCHP participation in grid services markets. As a number of factors of varying importance were considered in the selection process a Multi- Criteria Evaluation (MCE) approach was applied to compare alternatives and formalise a decision. In the given context, the MCE method was used to rank alternative countries based on a set of evaluation criteria that define a country's attractiveness. Criteria were identified and then weighted based on the conducted literature research and the results of the analytical hierarchical process applied during expert interviews with FC-mCHP manufacturers respectively. This resulted in a weighted definition of market attractiveness made up of factors relating to the economic value (comprising of spark spread, self-consumption policy and market potential) and market potential (comprising of potential market size, heat demand, future policy changes, and existing installed base). **Error! Reference source not found.**. For each country an overall country score was then determined. Scores were further enhanced by considering potential grid services revenues, as well as the regulations relating to market access for domestic flexibility and a high-level consideration of potential grid services revenues. The results of the MCE indicate that besides Germany, which was already proposed as a candidate by the PACE project, Belgium, the United Kingdom, Ireland and Italy currently have the highest market attractiveness for FC-mCHP's in Europe.

https://doi.org/10.5281/zenodo.4518860

Introduction

In this paper the methodology applied in the evaluation of market attractiveness for FC-mCHP is described in detail. An analysis of the market attractiveness of residential fuel cell micro combined heat and power plants (FC-mCHPs) was conducted as part of WP 4 in the H2020 project Pathway to Competitive FC mCHP Market (PACE). Germany, as the furthest developed FC-mCHP market within the EU, was excluded from the analysis as it was already chosen for a more in-depth analysis.

By starting off with a scan of the EU-28 plus Norway and Switzerland, the countries of interest were narrowed down with the assistance of PACE members in order to identify two promising countries for further analysis. The overarching criteria used for narrowing the country selection are country-specific mCHP market conditions which were rated based on attractiveness from the view point of PACE members, and pre-defined electrical power and grid service market criteria.

A multi-criteria evaluation (MCE[1]) was conducted with experts to analyse the market attractiveness of a country. An MCE is a structured approach to formalise a decision and to compare alternatives. In the given context, it was used to rank alternative countries based on a set of evaluation criteria defining their attractiveness (multi-attribute decision-making) [1]. In section 1, the methodology applied for the MCE is explained in more detail, section 2 summarizes the results of the conducted MCE and section 3 summarizes the findings.

1. Scientific Approach

The MCE was conducted following four steps. In Step 1, criteria relevant to the evaluation were defined based on literature research. In Step 2, the consortium members of the PACE project were asked to select countries from the EU-28 member states plus Switzerland and Norway that they deemed as having an attractive market, based on their professional experience and market knowledge. The selected countries were then analysed according to pre-defined criteria and assigned a numerical rating. The experts went on to assist in the weighting of the criteria using the Analytical Hierarchy Process (AHP)[2], allowing the results of the country criteria grading to be aggregated and the data to be analysed [2]. The country scores were evaluated in Step 3. Based on the data analysis, a ranking of the most promising countries was created. As a final step, the results were then validated within the consortium. Each of the steps are explained in more detail within this section.

[1] MCE is concerned with the allocation of scores to suit a specific objective on the basis of a variety of criteria that the selected countries should possess.

[2] AHP is a method used for pairwise comparison of elements or criteria, which are structured in defined hierarchy resulting in weights for the criteria and checking the consistency of the evaluation [11].

https://doi.org/10.5281/zenodo.4518860

Step 1: Criteria Definition

Relevant criteria for the evaluation of the market attractiveness were identified and chosen based on literature research. The criteria were defined to be mutually exclusive with no correlations or dependencies, to ensure balanced grading, and to differentiate national markets. Figure 1 shows the factor tree used for the MCE. The first level comprises the criteria *Economic Value Added* (EVA) and *Market Potential for FC* mCHP.

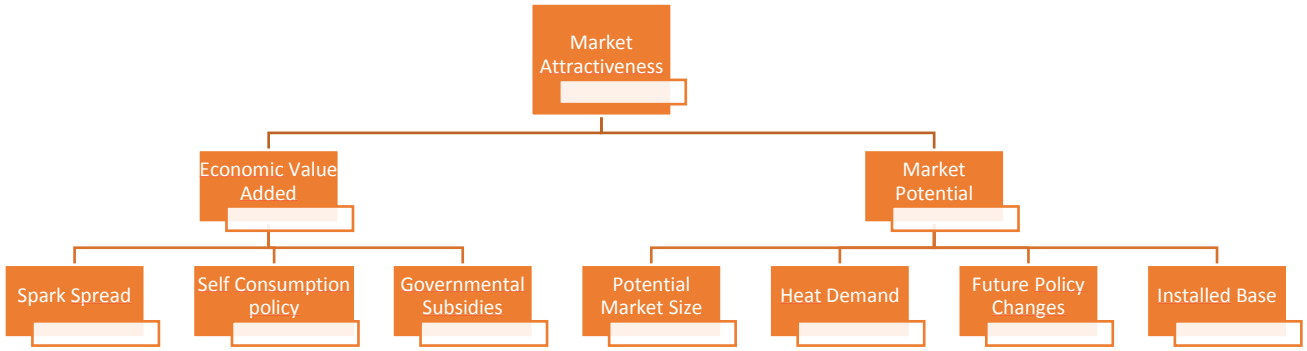

Figure 1: Hierarchical tree of criteria considered for MCE to evaluate market attractiveness

On the second level, the sub-criteria for the EVA, which reflects the attractiveness for installing a mCHP for homeowners, is assessed based on the *Spark Spread* (difference between gas and electricity prices), existing *Self-Consumption Policies* and *Government Subsidies*.

Spark Spread

The spark spread is defined as the economic value added from producing one unit of electricity, by considering the costs for the primary fuel (natural gas) and the efficiency of the mCHP. Hence, low natural gas prices or high electricity prices are in favour of a higher spark spread. The larger the spark spread between the gas and electricity prices, the higher is the attractiveness of the technology [3] due to the added value of the produced electricity. Therefore, countries with a large spark spread add more economic value and are ranked higher.

Self-Consumption Policy

Favourable self-consumption policies improve the business case by using the electricity on site instead of feeding it back into the grid at a lower tariff. Attractive self-consumption policies improve the business case for fuel cell micro-cogeneration.

Gouvernmental Subsidies

Government support programs, such as investment support, feed-in tariffs or tax incentives allow for a decrease in investment or increase in revenue during the operation period, which leads to a higher EVA. As stated in [4] the cost of a fuel cell is much higher than traditional heating technologies and therefore requires support schemes to establish itself in the market. Therefore, countries with governmental subsidies are considered more attractive and are ranked higher.

https://doi.org/10.5281/zenodo.4518860

Market Potential, as the other main criteria, is comprised of the sub-criteria *potential market size*, *heat demand*, *future policy changes* and the *installed base*, which are explained in more detail below.

Potential Market Size

An indicator for the potential market size is the market share of gas heating systems or the number of households which are connected to the gas grid. As stated in [5] future boiler market expectations are a good indicator for the potential market size for Fuel cell micro-Cogeneration.

Heat Demand

The characteristics of a typical building or climate conditions have an influence on the heat demand [6]. Those two factors have a significant influence on the annual load duration curve and hence the utilisation of the CHP unit. A higher heat demand is seen to lead to a higher attractiveness for FC mCHP.

Future Policy Changes

Policy changes can be favourable or unfavourable. Examples of a policy change in favor of CHP would be the implementation of governmental subsidy schemes or better access to aggregators to participate in the grid service market. Examples for future policy changes that disadvantage CHP are stricter CO2 laws. Policies can have a significant impact on technology, especially one such as FC-mCHP that couples the electric and gas sector and is thus subject to both policy frameworks.

Installed base

This criterion considers the number of installations from previous and ongoing projects such as ene.field and PACE, as well as installations of conventional mCHPs. The installed base gives an indication of existing supply chains and the willingness for people to buy the technology. The higher the installed base the more attractive a country is considered.

Step 2: Expert Analysis for Country scoring and criteria weighting

One-on-one interviews with the manufacturers participating in PACE were carried out, where the participants evaluated each criterion individually, giving an overall assessment of a country's mCHP market attractiveness. Each interviewee was allowed to select a maximum of four countries which they considered to have the most attractive markets. A balanced scale[3], ranging from "far below average" to "far above average" was applied to evaluate the country scoring with respect to each criterion, resulting in a numerical grading from 0 to 7. A 0 is assigned where no data is available, 1 is assigned when the grading is "far below average", and 7 is applied where the grading is "far above average" [7].

Then the relevance of each criterion was then assessed in a pairwise comparison, as shown in Table 1. In this instance, the criterion A (*EVA)* has been rated "more relevant" than criterion B (*Market Potential),* resulting in the intensity value 5.

[3] A rating scale that employs an equal number of favourable and unfavourable alternatives.

Table 1: Comparison of relevance example for EVA and Market Potential criteria

Criteria A	A dominates	A much more relevant	A more relevant	A slightly more relevant	A and B equally relevant	B slightly more relevant	B more relevant	B much more relevant	B dominates	Criteria B
EVA			X							Market potential
Intensity value	9	7	5	3	1	3	5	7	9	Intensity value

Such a comparison was made for each criterion against every other criterion of the same group, also by applying a balanced scale, to transfer the ratings into *intensity* values, as seen in Table 2. The intensity values represent the relative importance of one criterion over another [8]. A weighting value is calculated considering an aggregation of each expert's intensity value.

Table 2: Meaning of intensity values used for pairwise comparison adapted from [2]

Intensity of importance	Definition	Explanation
1	Equal importance	Two elements contribute equally to the objective
3	Moderate importance	Experience and judgment slightly favour one element over another
5	Strong Importance	Experience and judgment strongly favour one element over another
7	Very strong importance	One element is favoured very strongly over another, it dominance is demonstrated in practice
9	Extreme importance	The evidence favouring one element over another is of the highest possible order of affirmation
2,4,6,8	Intermediate values	When comprise is needed

A consistency ratio (CR) was used to check how aligned the respondents' answers were, where the linear fit method of calculating consistency as proposed by [9] was applied (see Equation 1).

$$CR = \frac{\lambda_{max} - n}{2.7699 * n - 4.3513 - n} < 0.1 \qquad \begin{matrix} \lambda_{max} & = \text{Consistency index} \\ \text{n} & = \text{Number of criteria} \end{matrix} \qquad (1)$$

Where the maximum right eigenvalue of each studied matrix is used as a consistency index and n is the number of criteria which are compared. The CR measures how consistent the judgments have been relative to large samples of purely random judgments. If the CR is in excess of 0.1, the judgments are untrustworthy because they are deemed too random [10].

Step 3: Aggregation of the weighted scores

For each country, the scores for the criteria were multiplied by the criteria weighting and summed up, resulting in an overall country score (see equation 2). Based on this score a raking of the countries could be created.

$$Country\ score = \sum w_i * x_i \qquad \begin{matrix} w_i & = \text{Weighting factors} \\ x_i & = \text{Criteria scores for country} \end{matrix} \qquad (2)$$

Step 4: Validation of the results

The *criteria* weighting and the selection of countries were both reviewed and accepted by the PACE team and advisory board.

2. Results

Based on the approach described in Section 1, this section presents the outcome of the country selection process based on inputs from manufacturers. Figure 2 illustrates the aggregated weights of each criterion according to the manufacturers in a factor tree.

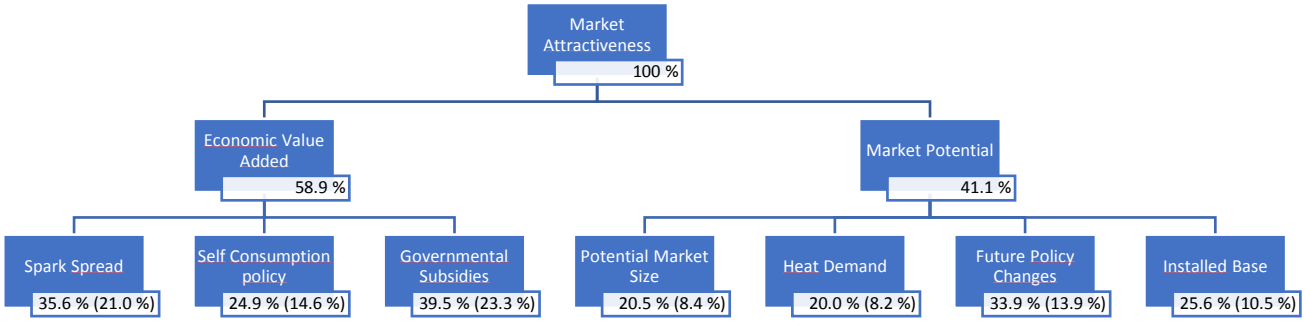

Figure 2 MCE Factor Tree including criteria weights.

From this, the following can be understood:

- The current *economic value added* that the technology yields has more relevance or holds more weight when compared to *future market potential*
- The existence of *governmental subsidies* is the single factor of greatest concern to the manufacturers when looking to enter a market, followed closely by the *spark spread*[4]
- *Potential market size, heat demand* and *installed base* are seen to play a minor role in comparison to other factors.

Based on these weights, the final scores for the countries were evaluated resulting in Belgium, Italy, Ireland and the United Kingdom as the top four countries, followed by the Czech Republic, the Netherlands, France and Spain. Figure 3 illustrates the individual scores for each criterion as well as the final overall score for each of the four countries based on the manufacturers' market knowledge. Important to note is that it was made explicit by the manufacturers that their knowledge of European markets is limited to Central and Western Europe. As such, countries outside these regions were discarded. This reduced the number of countries considered by approximately half.

From the results, it can be seen that Belgium mainly profited from its favourable spark spread, a large installed base and promising future policy changes. For Ireland, the high heat demand, a large potential market size as well as favourable future policy perspectives were the main drivers for its high result. Italy has a large potential market size with a well-established gas grid, as well as self-consumption policies in place. The United Kingdom mainly profited from its installed base, the high heat demand as well as a large potential market size.

[4] Difference between the wholesale market price of electricity and its cost of production using natural gas.

Figure 3: Spider diagrams of final four selected countries

The aim of this paper was to demonstrate a structured method to evaluating a countries market attractiveness. A multi-criteria evaluation method in combination with structured interviews was used to quantify the importance of each criterion and finally rank the countries.

The AHP process and pairwise comparison indicated that governmental subsidies, spark spread and favourable future policies are the key criteria in defining a country's market attractiveness.

As a result of the MCE Belgium, the United Kingdom, Ireland and Italy were evaluated as the countries with the highest market attractiveness for FC-mCHP within Europe.

https://doi.org/10.5281/zenodo.4518860

References

[1] J. Malczewski, GIS and Multicriteria Decision Analysis. John Wiley & Sons, 1999.
[2] R. W. Saaty, “The analytic hierarchy process-what it is and how it is used,” Math. Model., vol. 9, no. 3–5, pp. 161–176, 1987.
[3] A. D. Smith, N. Fumo, and P. J. Mago, “Spark spread - A screening parameter for combined heating and power systems,” Appl. Energy, 2011.
[4] H. Ammermann, P. Hoff, M. Atanasiu, J. Ayllor, M. Kaufmann, and O. Tisler, Advancing Europe’s energy systems: Stationary fuel cells in distributed generation. 2015.
[5] Energy Matters, “Micro-CHP potential analysis,” 2014.
[6] R. Beith, Small and micro combined heat and power (CHP) Systems: Advanced design, performance, materials and applications. 2011.
[7] H. H. Friedman and E. M. Friedman, “A Comparison of Six Overall Evaluation Rating Scales,” SSRN Electron. J., 2014.
[8] G. H. Tzeng and J. J. Huang, Multiple attribute decision making: Methods and applications. 2011.
[9] J. A. Alonso and M. T. Lamata, “Consistency in the analytic hierarchy process: A new approach,” Int. J. Uncertainty, Fuzziness Knowlege-Based Syst., vol. 14, no. 4, pp. 445–459, 2006.
[10] G. Coyle, “A Possible Method for Assessing The Relative Values of Alternative System Dynamics Models,” 20th Int. Conf. Syst. Dyn. Soc., no. 2001, pp. 1–14, 2002.
[11] P. CABAŁA, “Using the Analytic Hierarchy Process in Evaluating Decision Alternatives,” Oper. Res. Decis., vol. 20, no. 1, pp. 5–23, 2010.

Keywords: EFCF 2020, SOx
Session A03: Technology status at industry and major groups I

https://doi.org/10.5281/zenodo.4518860

A0503

Reversible SOC System Development and Testing: Status at AVL and Outlook

David Reichholf, Franz Koberg, Richard Schauperl, Martin Hauth
AVL List GmbH
Hans-List-Platz 1, 8020 Graz/Austria

Contact authors: www.EFCF.com/ContactRequest

Abstract

A reversible solid oxide cell system layout has been developed and tested as a proof-of-concept (PoC) system. The focus was to reach a simplified system layout in terms of the number of balance of plant (BoP) components, while enabling a high flexibility of the system and an efficient heat management including internal water evaporation. The 4.5/1.5kW ($P_{EC,el}/P_{FC,el}$) PoC system included the core functionalities, such as the main components for heat management and instrumentation. The PoC system was validated on a testbench, which provided media and electricity supply, as well as the automation system. The operation was carried out 100 hours without stack module and 500 hours with stack module primarily in manual operation. Various operating points in fuel cell (FC), as well as in electrolysis (EC) mode were tested, hot idle concepts investigated and switchover routines from FC to EC and vice versa elaborated. The PoC system showed very good operability in terms of flexible heat management in full-, as well as in part load operation and manual switch-over times lower than 15 minutes.
Based on this platform a fully functional rSOC carrier with a reasonable power range and automation is being developed, which will be integrated in a “real-world” simulation environment to show applicability of the technology in the context of renewable energy systems (RES).

https://doi.org/10.5281/zenodo.4550481

Introduction

Besides the potential to reach highest energy conversion efficiencies, solid oxide fuel cells are a technology with the capability to be operated in fuel cell mode to produce electricity by using gaseous fuel, as well as to produce gaseous fuel by using electricity. Thereby not only hydrogen or water, but also carbonaceous feedstocks can be utilized and converted. For both operation modes the same set of cells can be used. Therefore, reversible solid oxide cell (rSOC) systems have great potential to serve in future energy systems as a cost efficient energy conversion solution. To enable the reverse operation of solid oxide cells in real world applications, appropriate systems have to be developed. This, on the other hand, constitutes a challenge, due to the high temperatures and the different characteristics of the two operation modes.

Within the project “Aurora”, which was successfully completed by the end of 2019, AVL developed a rSOC system process design. The focus was set on flexible heat management with integrated steam generation and overall process simplicity, while aiming for as high efficiencies as possible. The novel process concept was realized in the form of a proof-of-concept (PoC) system, which was tested on a test bench at the premises of AVL. The tests approved the potential of the process design and revealed also potential for improvements. Based on this developments and gained know-how, a fully-functional rSOC system is currently under development in a follow-up project, called “Fully integrated reversible solid oxide cell system” – “FIRST”.

1. Scientific Approach

Within the Aurora project, a rSOC system concept at a scale of 33kW/100kW (P_{el_SOFC}/P_{el_SOEC}) was targeted. Based on 0-D process simulations and in an iterative process a novel system flowsheet was developed.
Thereby the focus laid on:

- System efficiency in fuel cell and electrolyzer operation mode
- Heat management
- Internal steam generation
- Controllability
- Minimization of balance-of-plant (BoP) components
- Availability of BoP components

A major challenge in the development of rSOC systems are the very different characteristics of the operation modes. In fuel cell operation mode high amounts of heat are produced via highly exothermal reactions inside the stack. This heat needs to be removed from the stack, which is mainly done via air supply on the air-side of the stack resulting in a significant air-flow. In electrolysis mode, endothermal reactions occur at the stack and hence leading to a much lower required air flow. Thus, besides completely different fuel feed compositions, also the air flow differ significantly between the two operation modes. These characteristics need to be considered and lead to a trade-off in the system design.

The final resulting system concept was scaled down to a stack power rating of 1.5kW/4.5kW (P_{el_SOFC}/P_{el_SOEC}) and reduced to a PoC system, which contained the key functionalities of the novel layout, such as the core heat management components and its control functions. However anode gas recirculation was not considered in the PoC setup. Other required functionalities, such as power supply, automation system and software, gas

https://doi.org/10.5281/zenodo.4550481

supply and safety instrumentations were planned to be covered by a testbed. Hardware specifications were derived from the process simulations of the PoC system. Controlling strategies and error handlings were developed accordingly.

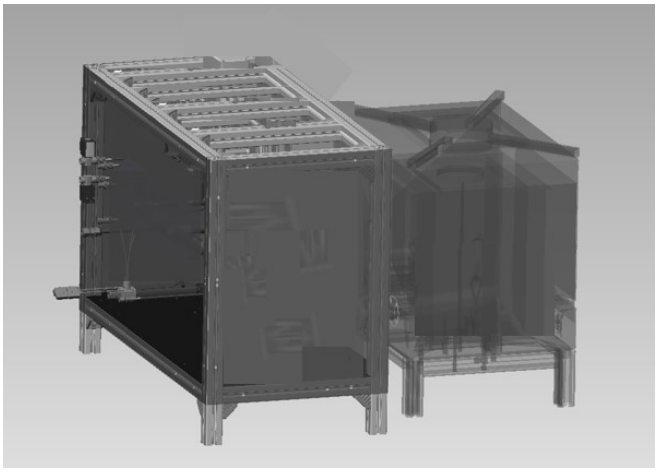

Figure 1: PoC Design

Based on the specifications and supplier feedback, the PoC system was designed mechanically with two different BoP settings, the components were procured, the system set up and prepared for testing. The final mechanical 3D design is shown in Figure 1. The PoC system used a stand-alone stack module, therefore, the BoP components were integrated as another stand-alone unit by itself. The focus was here to cover all main functionalities, but not to reach a high level of an integrated design.

2. Proof-of-Concept Testing

Setup on Testbed

Figure 2 shows the PoC installation on the testbed. On the right hand side, the BoP unit is connected to the gas supply of the test bed. On the left hand side the stack module is connected to the BoP unit likewise. The feed gases are pre-conditioned in the BoP unit before entering the stack module. The stack outlet gases are then post-conditioned in the BoP unit before leaving the system into the exhaust system of the test bed. Electrically, all actuators and sensors/measurement devices were connected to the respective interfaces of the test bed. Automation system, error handlings and visualization were also covered by the test bed.

https://doi.org/10.5281/zenodo.4550481

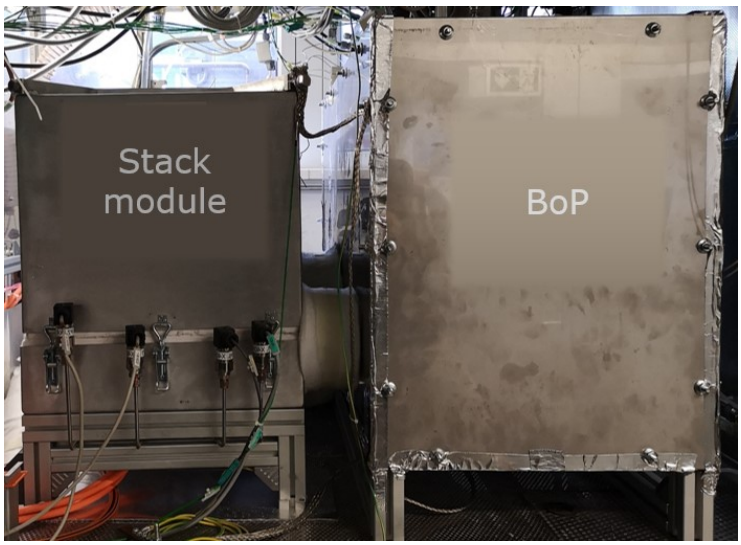

Figure 2: rSOC PoC Setup on Testbed

Testing Plan

The overall test plan included several testing phases, as shown in Figure 3. After the PoC system commissioning on the testbed, a pre-phase testing was done where the BoP unit was tested without stack module. This testing phase aimed for the validation of key functionalities of the BoP unit. Thereby the BoP unit was heated up and cooled down several times with the aim to reach certain stable temperature levels at the stack inlets. This heat up - cool down cycle tests lasted for about 100 hours. After the feasibility was proven and the milestone reached, the stack module was added to the setting. The tests including the stack module were conducted with two different BoP variants. Setup 1 was tested around 100h, decommissioned and adapted. Setup 2 was tested around 400h. Both settings were operated 24/7 mostly in manual operation by an operator.

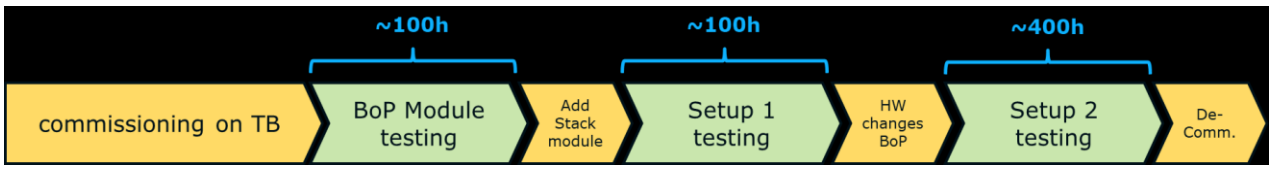

Figure 3: Overview testing scheme

The BoP setup 2 showed a much better controllability than setup 1 due to improved components. The PoC system was tested with various settings in fuel cell mode, electrolysis mode and in different hot-idle states. However, the main focus laid on the switchover routines from fuel cell into electrolysis mode and vice versa, to prove the viability of the whole system concept.

https://doi.org/10.5281/zenodo.4550481

3. Results

Simulation Results

A main outcome of the process simulations was the efficiency potential of the rSOC platform as developed. In steam electrolysis operation theoretically efficiencies up to 79% ($P_{el,DC}$ – LHV) could be achieved. In fuel cell operation, based on hydrogen fuel and depending on the actual stack technology, efficiencies between 50 -60% (LHV – $P_{el,DC}$) could be feasible.

Experimental/Testing Results

As described before, the feasibility of heating up the system according to the key functionalities constituted a milestone within the validation process. Figure 4 shows the temperature evolution over time of the stack inlet and outlet temperatures while heating the PoC system up to full load operation conditions in fuel cell mode. Since the focus of the heat up was not the timing, but reliability, the temperature ramp was thereby kept low of around 0.5 K/min. Besides the pre-phase testing without stack module, the system heat up was executed one time for each setup.

Steady state fuel cell operation in full load resulted in an overall electrical system efficiency of ~55% (LHV - $P_{el,DC}$) by using a hydrogen-nitrogen mixture as fuel and ~52% (LHV - $P_{el,DC}$) by using a hydrogen-steam mixture as fuel. Hereby parasitic loads such as for the gas supply, which were covered by the test bed, are not considered.
Due to safety restrictions on the available test bed it was not possible to operate the PoC system in full electrolysis load. This lead to heat management issues and cool down of the system to a certain level when operating the system in part load, caused by the “loose” design integration.

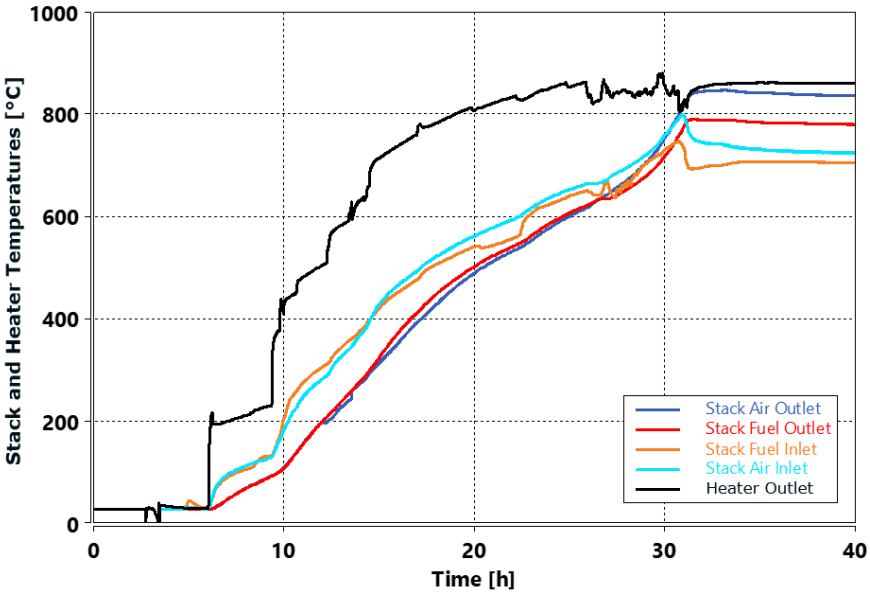

Figure 4: System heat-up temperature evolution

However, stable part load operation was feasible and switchover routines were elaborated at lower temperatures. Figures 5 a.-d. show two switchover routines. Figure 5 a. shows the total current supply and draw at the switchover from electrolysis mode to fuel cell mode and in Figure 5 b. the related average cell voltage is shown. The analogue charts are

shown for the switchover from fuel cell mode to electrolysis mode in Figure 5 c.-d.. Although the PoC system was operated in a manual manner, which means that the test bed operator had to change all settings manually, switchover times lower than 15 minutes could be reached in both directions. However, certain limitations existed. As shown in Figure 5 a. and b. the current ramp up in fuel cell mode was restricted by the low voltage, because the part load operation in electrolysis mode lead to a cool down of the stack. Lower stack temperatures increase ohmic losses and thereby decrease the cell voltage, which limits the current that can be drawn. An increase of the stack power required a heat up, which took time. It is key to keep in both operation modes the same stack temperature levels to enable fast switching and ramp up to full load operation.
The main challenge in the switchover routine from fuel cell mode to steam electrolysis mode is the ramp up of the steam supply. It constitutes a limitation, if less steam is supplied to the stack than the amount which is required for full load operation.

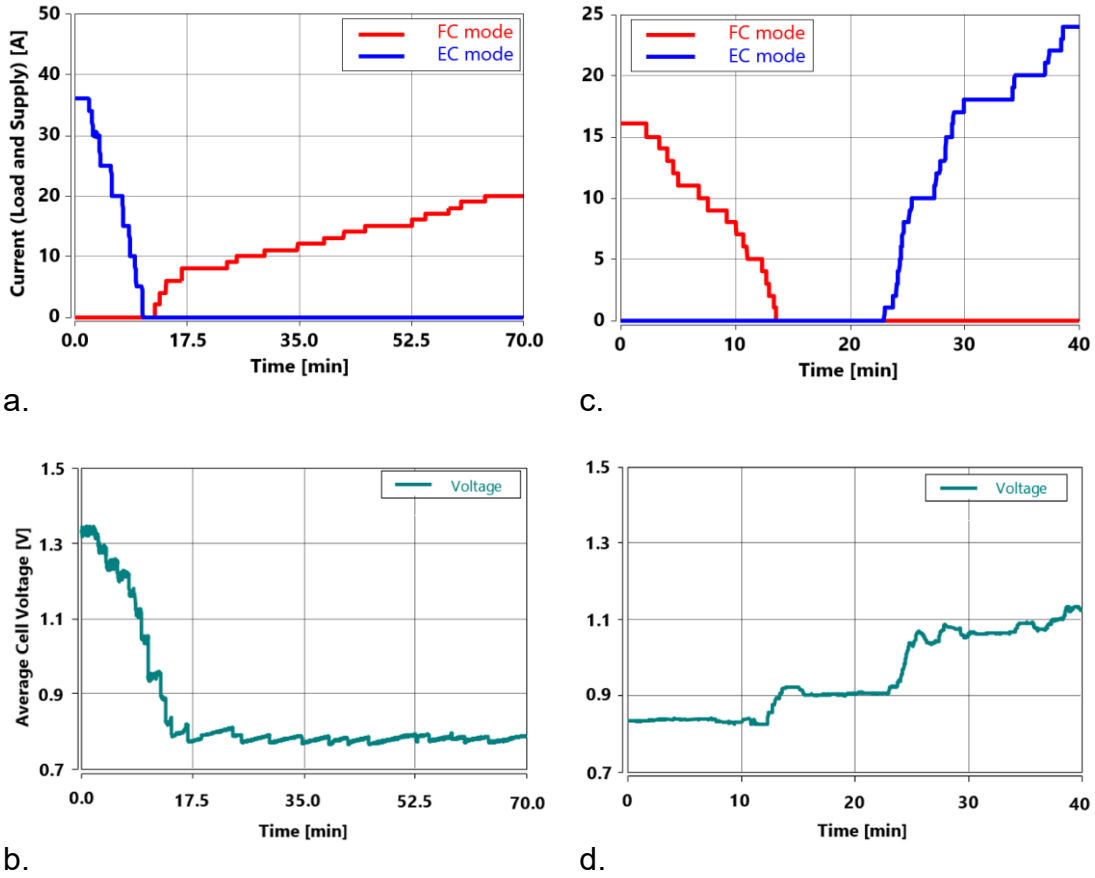

Figure 5 a-d.: Manual switch-over modulations

All in all, the key functionality of the system concept was validated, the main targets were met and potential improvements were identified.

https://doi.org/10.5281/zenodo.4550481

Outlook

Based on the results of the “Aurora” project, a follow-up system development is currently in work within the project “FIRST”, where a fully functional system is being developed.

The targets of the project are:
- setup of a fully automated rSOC system with internal steam generation
- integration into a building which contains a RES-PV installation
- implementation of predictive controlling algorithms
- fast operation mode switching times < 5 minutes
- highest efficiencies up to 60% in fuel cell mode with hydrogen fuel
- highest efficiencies up to 75% in steam electrolysis mode

To reach the goals, the rSOC system requires a well-executed mechanical design to minimize heat losses throughout the system and a mature automation system with appropriate controlling strategies. It will be set up and integrated into a “real-world” renewable energy system (RES) environment, where long term tests ~7000h are planned. The fully functional system will have a scale of 5kW/15kW ($P_{FC,el}$/$P_{EC,el}$) and should prove the applicability of the technology in the context of renewable energy systems. A key challenge is thereby the intermittency of electricity production by renewable energy sources and how rSOC systems can be integrated in the best way.

Acknowledgement

This research and development work received funding by the Austrian funding agency (FFG) within the projects Aurora (FFG#850459) and FIRST (FFG #871700).

Keywords: EFCF2020, SOx
Session A05: Technology status at industry and major groups II

https://doi.org/10.5281/zenodo.4550481

A0504

Solid Oxide Cell Technology for Space Applications

Brandon Buergler
ESTEC, Keplerlaan 1, 2200 AG Noordwijk, The Netherlands

Contact authors: www.EFCF.com/ContactRequest

Abstract

The solid oxide cell (SOC) technology offers many possibilities for space applications, such as power generation, energy storage, oxygen and hydrogen pumping or purification and electrolysis. The European Space Agency (ESA) is very interested and active in developing this technology for future space missions.
One of the most promising applications appears to be an energy storage system for application on Mars based on a reversible solid oxide fuel cell. The advantage of this system would be that it could allow for in situ resource utilisation (ISRU) of the CO_2 atmosphere of Mars. Thus, the reactant would not have to be taken from Earth, which reduces drastically the launch mass of a potential mission. Energy is stored in the form of CO and O_2 coming from the preceding electrolysis of CO_2. When electric energy is needed, these two reactants are electrochemically recombined.
Another potential application for the SOC technology is the electrolysis of water coming from local resources on the moon for provision of breathable O_2 for astronauts and H_2 as rocket fuel.
This paper aims at giving an insight of the possible applications in space, the benefits and challenges, and which developments have been, are currently and will be carried out by ESA and its partners.

https://doi.org/10.5281/zenodo.4550525

Introduction

In the past, fuel cell technology has been successfully applied in American manned spaceflight programmes like Gemini (early proton exchange membrane (PEM)), Apollo (alkaline) and the Space Shuttle (alkaline). These were all primary fuel cell technologies and could not be recharged. To generate electric power, H_2 and O_2 were consumed by a fuel cell. The product water could be consumed by the astronauts.
At ESA, fuel cells were previously considered for application predominantly in very high power telecom spacecraft [1]. In this application, the reactants have to be kept in a closed loop. The product water is collected and electrolysed when electric power is available. The H_2 and O_2 are stored and consumed by a fuel cell whenever electric power is needed. This kind of fuel cell system is referred to as a regenerative fuel cell system (RFCS). RFCS have a potential for high specific energy as compared to secondary batteries. However, the achievable specific energy greatly depends on the size of the system and increases with the amount of energy stored as can be seen in Figure 1. For Li-Ion batteries the specific energy does not change with system size.
In Figure 1, the achievable specific energy is compared for Li-Ion (150 Wh/kg), primary fuel cell system (FCS) and RFCS. Regenerative fuel cell systems (RFCS) could outperform batteries in terms of specific energy for large amounts of stored energy (Technical Note 2 of [2]). However, the increased energy density comes at a price: Compared to Li-Ion batteries, for which the roundtrip energy-efficiency of charge/discharge is above 90%, for RFCS it can be expected that it will be much lower in the range of 50%, which has implications on the system design especially on the sizing of solar generators commonly used for space missions.

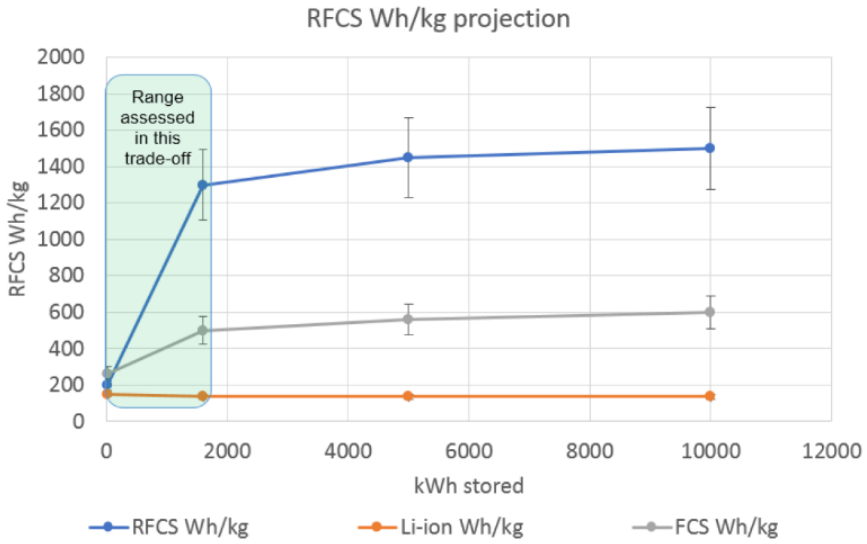

Figure 1 Evolution of energy density with stored amount of energy [2]

Several ESA-initiated activities have been completed in the domain [3-6], all of which were based on PEM technology. The concept of RFCS was successfully demonstrated with the required lifetime [7, 8]. Achieving the required specific energy, the thermal aspects and the reliability of the envisaged RFCS are considered to be key technical hurdles [6]. Nevertheless, in the ESA ARTES program the development of an RFCS for large telecom satellites is continued [9]. The developed systems can be easily adapted to the promising concept of high altitude pseudo satellites (HAPS). In HAPS the availability of very high specific energy density (>350 Wh/kg) technology is mission enabling. HAPS keep their position at around 20 km altitude requiring a rather high power. During the day they rely on power supplied by solar generators and at night by power coming from an energy storage

system based on batteries or RFCS. The technologies developed for telecom satellites or HAPS (Figure 2) can also be applied for lunar exploration, e.g. for the lunar night survival without radioisotope technologies. During the lunar night, which is extremely cold (~90 K) and lasts around 14 days, spacecraft or probes need to have sufficient power and energy to maintain an acceptable temperature in sensitive elements.

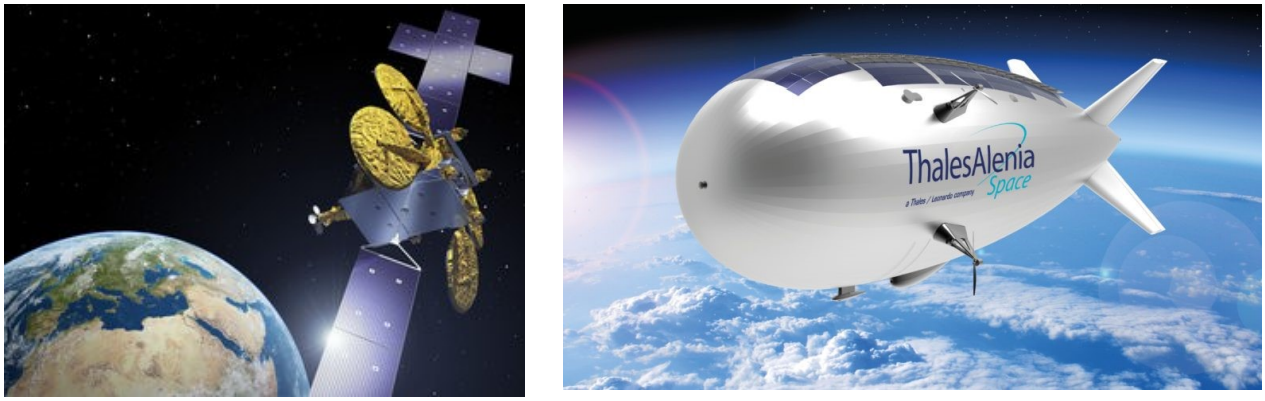

Figure 2 Neosat (left) an example of high power telecom satellite. HAPS (right)

There are different potential applications for fuel cells in space including primary fuel cells, electrolyser systems and regenerative fuel cell systems.

1. High power telecom spacecraft
2. Large telecommunication satellites and HAPS
3. Lunar night survival
4. For Mars robotic and human exploration with SOC technology using CO_2 as local resource
5. Missions to Neptune/Uranus using liquid CH_4/O_2 primary fuel cell for power provision from Jupiter distance onwards. Within the distance Earth to Jupiter, solar power can be used.
6. On Lunar or Martian manned stations
7. “Water propulsion”: Generation of H_2/O_2 rocket fuel coming from electrolysis of H_2O
8. Oxygen provision for manned missions using local H_2O resources on the Moon and on Mars
9. Functional power on launchers
10. Biomass-based fuel cell for manned space exploration

At the present time, HAPS and lunar night survival are seen to be the most promising applications. HAPS developments may currently not be funded by any ESA program, but since developments for high power telecom spacecraft are ongoing, the developed technologies can easily be applied for HAPS by the industrial partner.
Concerning human exploration to the Moon and to Mars, there is a lot of momentum with the recent American push to return to the Moon. In the Global Exploration Roadmap [10], published by a consortium of international space agencies, the next steps of a human settlement on the moon and a further step to be taken towards Mars are described. Fuel cell technologies are highly advantageous, if not mission enabling, for some of the envisaged missions. European fuel cell technologies should be at the forefront so that they can be applied in potential missions in the coming decade.

Because of the higher technology readiness level (TRL), the baseline technology for RFCS for telecom satellites, lunar night survival and water propulsion was mostly based on the PEM technology, but it could also be based on SOC.

https://doi.org/10.5281/zenodo.4550525

For energy storage on Mars, SOC energy storage systems are very promising because they allow to utilise the CO_2 in the Martian atmosphere. Consequently, the reactant would not have to be brought from Earth. Maximising the specific energy (in terms of Wh/kg), reliability and thermal aspects are the main drivers for space fuel cell systems.

Current solid oxide fuel cell and electrolyser technologies are at relatively low TRL in Europe for space applications. There are several significant technical barriers that need to be overcome in order to apply fuel cells in future space missions:

1. The resilience of fuel cells stacks to the mechanical environment during launch
2. The stack mass for terrestrial stationary applications is much too high for space applications (up to 0.1 kW/kg versus 1 kW/kg needed for space). Stack design to reach mass targets is challenging
3. System complexity, reliability, and redundancy approach
4. System integration and balancing of plant optimisation
5. Thermal management in space
6. Operation in zero gravity (spin in of terrestrial applications).
7. Development of gas storage tanks
8. Development of space grade components (like valves, pressure regulators, pumps)
9. Operation with pure oxygen instead of air

Mars applications

Energy storage

The Martian atmosphere offers up to 15 mbar of CO_2, which can be utilised an SOC based energy storage system for long duration energy provision. Energy can be stored in the form of CO and O_2 coming from the preceding electrolysis of CO_2. As compared to PEM, for which CO_2 is a catalyst poison, SOC can utilise the CO_2 as reactant. When electric energy is needed, these two reactants are electrochemically recombined. These systems have been studied already in ESA led activities [11-13] and the results have been published in the proceedings of the European Space Power Conference [14-16].

Such provisions are very relevant to the exploration of Mars. In particular to operations on its surface during nighttime, but also during periods of reduced sunlight availability e.g. during dust storms that can last for weeks if not months. The envisaged energy storage system comprises a CO_2 compressor (pumping system), an SOC stack/electrolyser (the unit that does both electrolysis and electric power generation), thermal control and gas bladders for the storage of CO, O_2, and CO_2. The stored energy capability of the system can be selected independently from the stack power (unlike with with batteries) by the size of the CO and O_2 bladders. In [13], a first designing and testing of a breadboard model based on reversible Solid Oxide Fuel Cells were performed. At the end of the test campaign, some issues were found with uncontrolled carbon formation, which did not allow for long duration operation. The main problem was identified to be insufficient temperature in certain regions of the stack. This favoured the formation of carbon by the Boudouard reaction and catalyzed by the nickel-electrode. To avoid this situation, ESA partners have developed carbon-tolerant perovskitic-type oxide materials $La_{0.75}Sr_{0.25}Cr_{0.9}Fe_{0.1}O_{3-\delta}$ (LSCrF), which are Ni-free and therefore do not contribute to carbon formation [17]. The avoidance of carbon formation is one of the major challenges for this technology. Another challenge will be the operation on pure oxygen instead of air.

In a currently running ESA activity [18], the performance of a redesigned breadboard system taking into account the lessons learned from the previous one shall be demonstrated without carbon formation. In a follow-on activity the development to an engineering model is planned. The target in this activity for the complete system is to build a breadboard at TRL 5.

Oxygen production from CO_2

Any manned exploration surface mission will rely on the availability of breathable oxygen for the crew. As already discussed, the SOC technology is well suited to convert CO_2 to CO and O_2. It is about to be utilised for the first time on Mars for oxygen production demonstration. On NASA's Mars 2020 *Perseverance* rover, an in-situ resource utilisation (ISRU) experiment (named *Moxie*), is embarked to demonstrate the feasibility of O_2 production from the Martian CO_2 [19]. The rover is currently on the way and is expected to land in February 2021.

Oxygen production from H_2O

On Mars, the presence of H_2O was confirmed [20, 21]. In higher latitudes even very pure water ice can be found. On the more accessible latitudes close to the equator ice containing soil may be available. The predominant water resource is present as hydrated minerals.
Further to this, on Martian missions there is a possibility to manufacture H_2/O_2 from water that is created in-situ by the carbo-thermal reduction of regolith by methane [22].
Another important point in the context of providing oxygen to manned surface missions is that the gas-mixture used in the crew cabin is lost through leakage and through air-lock operation. The oxygen can be replenished using the electrolysis of water coming from ISRU. However, the inert nitrogen, used to dilute the oxygen to a similar concentration as on Earth is lost and there is no easy way of providing this essential gas to the life support system. In [23] this point is addressed. The Martian atmosphere contains around 2.7% of N_2 and 1.6% of Ar, which could be used to create breathable air. This is a very important issue.

Chemicals production from H_2O and CO_2

SOC technology is also particularly suitable for producing syngas when CO_2 and H_2O are co-electrolysed. On Mars CO_2 is available independent of the location and water can be found in certain places, in which a co-electrolysis plant for production of chemicals could be feasible. Syngas can be converted using different catalysts to products which are of use for future space missions (e.g. methanol, methane or synthetic diesel).

Lunar applications

Energy Storage

For future missions to the lunar surface a capability for lunar night survival will be needed. One example of such a mission is the European Large Logistic Lander (EL3), of which an impression is shown in Figure 3. EL3 will have the capability to bring food, water, air and equipment to the surface, in support of crewed exploration projects such as NASA's Artemis programme. It is foreseen that EL3 will require the capability to survive on the surface through the lunar night. The most high-performing and reliable way to achieve this would be to rely on radioisotope technologies, e.g. radioisotope heating units (RHU) or radioisotope thermoelectric generators (RTG). As an alternative to these technologies, RFCS are currently being developed in an ESA-led R&D activity [2]. The development is based on PEM technology because of the higher TRL, but in principle SOC technology could also be

used for this application. RFCS become even more attractive when the emitted thermal power can be utilised in addition to the electrical output.

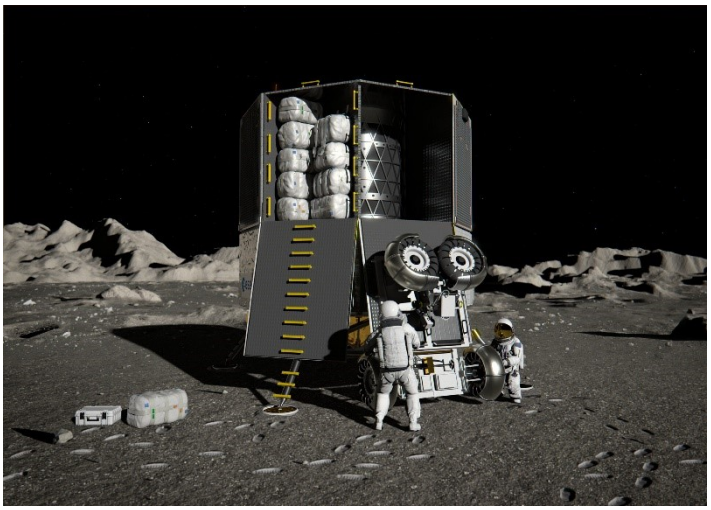

Figure 3 European Large Logistic Lander unloading cargo

Oxygen production from H_2O

It has been confirmed in the past years that H_2O is present at the lunar poles but it is not yet fully clear in which configuration this water is available [24, 25]. There are many unknowns concerning this point but it can be assumed that pre-processed water taken from this water ice bearing consolidated regolith could be fed to an electrolyser system based on SOC technology. As for Martian missions, also on the Moon there is a possibility to manufacture H_2/O_2 from water that is created in-situ by the carbo-thermal reduction of regolith by methane [22].

The solid oxide electrolyser cell (SOEC) technology offers many advantages compared to PEM such as higher efficiency, faster electrode kinetics due to the high operating temperature and higher tolerance for impurities. Because of several advantages the SOEC technology has over PEM, an activity based on SOC was launched for assessing a system that can convert in-situ H_2O on the Lunar or Martian surface to H_2 and O_2 [26]. SOEC technology was also chosen for assessment in order to avoid duplicating the parallel ongoing research on PEM. The objectives of the activity are to specify, design, build and test a breadboard of a high-pressure electrolyser based on the SOEC technology, which is capable of creating hydrogen and oxygen from ISRU water in the Lunar and Martian environment. The aim is to demonstrate the feasibility of high pressure SOE technology (up to 10 bars) for exploration surface missions.

A concept of the HP-SOE system is shown in Figure 4. The ISRU material is injected into the system, is pre-processed to extract the water. The processing itself is not part of the bread boarding. The dried material from which the water is extracted is released and is no longer useful (except the stored heat). Then this water is converted to gaseous water in a steamer and subsequently enters the SOE stack. At the anode the water is converted to H_2 and O^{2-} ions. The latter migrate through the SOEC material to the cathode side. The released electrons are conducted via the external electric circuit to the cathode side. At the cathode side the two O^{2-} ions are recombined with electrons to form O_2.

$$Anode: \quad H_2O \leftrightarrow O^{2-} + H_2 + 2e^-$$
$$Cathode: \quad O^{2-} + 2e^- \leftrightarrow \frac{1}{2} O_2$$

The formed H_2 and O_2 are collected in gas storage tanks. The unreacted water in the H_2 gas stream has to be separated and fed again to the electrolyser stack. The stack is equipped with an electric heater to reach the operating temperature of the SOEC electrolyte material (> 500° C). In order to reach a high system efficiency, the thermal management system (dotted line) is of utmost importance. Further components will be needed for the breadboard of this activity, which are not shown in Figure 4, e.g. gas valves, pressure regulators, safety valves, flow meters and pressure gauges.
This system will only be able to supply O_2. On the moon there is no access to an "inert" gas to allow for mixing of air and it seems likely that N_2 will have to be brought from Earth.

Electrochemical pumping

The possibility to conduct oxygen ions through a solid state material at elevated temperatures can be seen as a gift from nature. ESA is currently looking into the possibilities for electrochemical pumping of O_2, which can be used for pumping without moving parts as for example in mechanical pumps. Pumps need regular maintenance and are prone to failure, which is why for space missions the use of pumps is generally minimised. With electrochemical pumps gaseous oxygen can be compressed to higher pressure level by the use of electrical energy. Furthermore, the O_2 purity is expected to be higher when electrochemical systems are used.

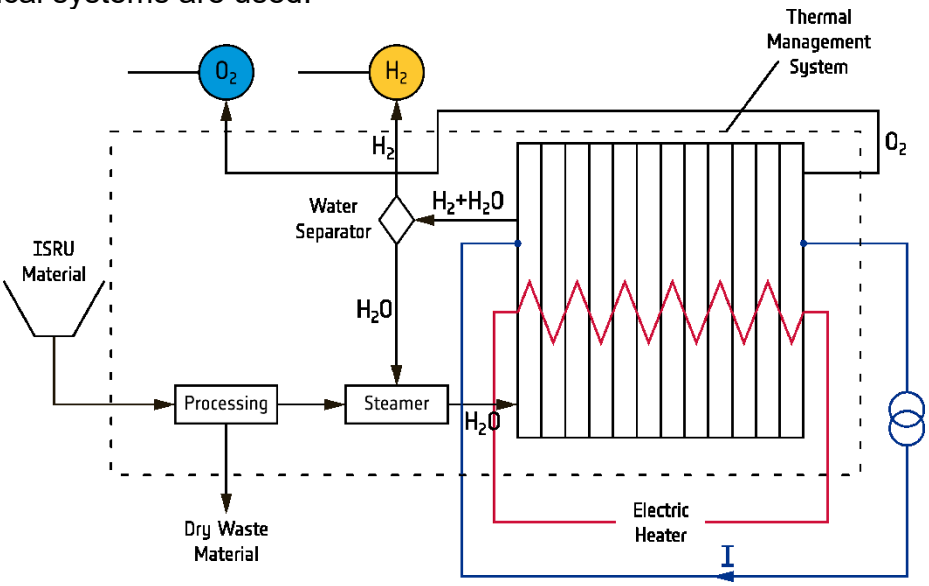

Figure 4 Draft concept of the HP-SOE system that is to be developed in [26]

Electrochemical pumping can also be used for separating oxygen from other gases or for purifying purposes. ESA is planning to issue an invitation to tender (ITT) in the coming months, in which the requirements and the statement of work will be defined. The objective of the activity will be to develop electrochemical O_2 pumping technologies and to demonstrate the performance at TRL 3.
Electrochemical pumping of H_2 using SOC technology is also seen as a very promising technology for space applications but it has to compete with PEM technology, which is already highly advanced. This option has currently not been studied yet for space applications by ESA.

https://doi.org/10.5281/zenodo.4550525

Electrochemical O_2 pumping has been demonstrated in 2007 by Spirin et al [27]. In 2016 researchers at NASA's Glenn Research center have built electrochemical O_2 compressors for space applications The TRL is not known and no information on the pressure level could be found.

Chemicals production

As already mentioned, the SOC technology is capable of converting dry CO_2 to CO and O_2. If the conditions are well controlled carbon formation by the Boudouard equilibrium can be avoided. The process allows to split the very stable CO_2 molecule and bring it to a more activated state for subsequent reactions. Similarly H_2O can also be electrolysed in an SOC electrolyser. If both CO_2 and H_2O electrolysis is combined at the fuel side of the reactor CO/H_2 (syngas) is formed, which can be used in a downstream extra reactor to produce different chemicals, which will be of use for future manned mission to Mars. Methane, methanol or synthetic fuels are some examples of the products that could be made on the Martian surface using in situ water from the ground and CO_2 from the atmosphere.

Water Propulsion System

Water propulsion is an innovative propulsion technology where water is split in orbit over a longer period with low electric power into hydrogen and oxygen at high pressures. These gases are stored and burned when a thrust is needed (e.g. for deorbiting a satellite at the end of mission). In the frame of an ESA R&D activity [28] different aspects of this technology were investigated. The activity is based on PEM technology but theoretically the SOEC technology could also be applied with the potential advantage of reaching a higher power and efficiency as compared to the PEM technology.

ESA Roadmap

The process of harmonising and elaborating a future strategy for the electrochemical energy storage has been completed in 2019 [29]. As well as batteries and supercapacitors, also fuel cells are included. The most recent roadmap agreed with industry and ESA member state delegations is shown in Figure 5. As mentioned in the electrochemical energy storage dossier, the current fuel cell and electrolyser technology is at a relatively low TRL in Europe for space applications. Most of the activities are on fuel cells in general not prescribing a technology. An evaluation of solid oxide cell based RFCS system for HAPS is foreseen as well as the already mentioned electrochemical pumping.
The roadmap activities are subject to constant revision and reconsideration and if an activity is not foreseen in it, it is still possible to launch an activity that is deemed important.
Similar to batteries there is a market focus on the larger terrestrial industry and it can be a challenge to focus commercial organisation on the relatively small volume applications in space, especially given the long-term application horizon on exploration fuel cell usage. Because of this, the progress through the TRL spectrum is slow and the relative cost projection for new systems can be prohibitive. Space fuel cells can bring benefits for terrestrial R&D and vice-versa. It must be ensured that the developments will bring benefits to both sector of activities.

https://doi.org/10.5281/zenodo.4550525

Summary and Conclusion

This paper has given an overview of the past, current and future ESA activities in the domain of fuel cells, electrolysers and regenerative fuel cell systems. ESA has been active in the field of space fuel cells in the past decades. An increased interest for fuel cell systems in space applications can be noticed. It appears that different companies are interested to assess their fuel cell, electrolyser and balance of plant components for space applications. The endorsement of the harmonisation dossier [29] in the field of fuel cells by industry and delegations also confirms the increasing interest in these technologies. More than 16 fuel cell related activities with a planned budget of above 12 million Euros have been endorsed in the harmonisation dossier of electrochemical energy storage in 2019.
A point of utmost importance is the spin-in from terrestrial technologies for space applications, taking into account the space requirements like high performance, reliability, mechanical resilience, radiation, vacuum, thermal management and lifetime.

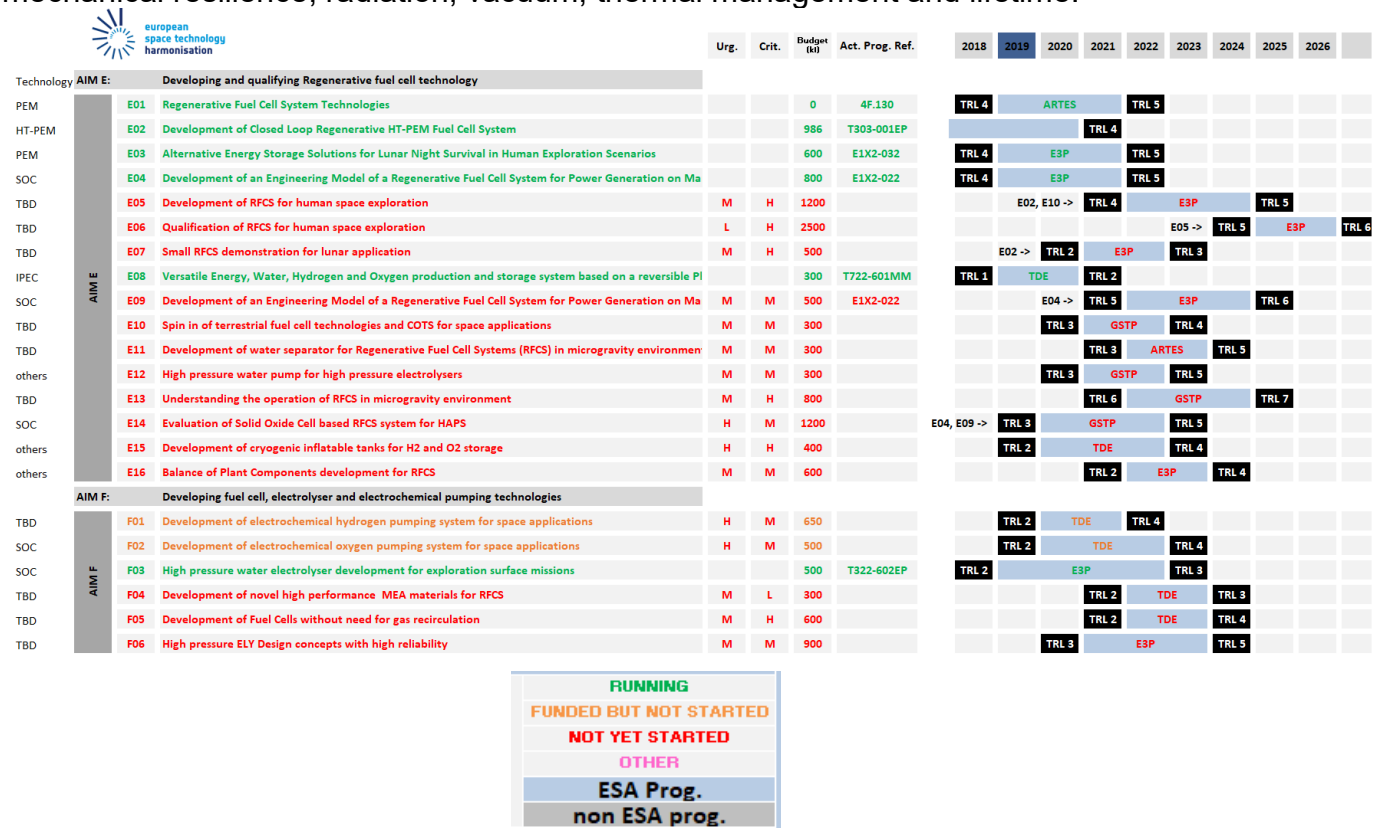

Figure 5 The fuel cell activities as agreed during the European Space Technology Harmonisation process in 2019

Many of the current terrestrial developments in SOC technology like dry electrolysis, water electrolysis, co-electrolysis, reversible SOCs that have gained momentum in the past years. The vision that is being followed is that a diverse set of companies and organisations from ESA member states contribute to future space endeavors that will rely on fuel cell/electrolyser technologies.

https://doi.org/10.5281/zenodo.4550525

Acknowledgements

ESA is grateful for the contribution and work of many partners such as (the list might not be complete): Prototech, CERTH, FORTH, EPFL, Haldor Topsoe, Omnidea, Airliquide, EH Group, ET EnergieTechnologie, Almatech and the large system integrators such as: Airbus Toulouse, Airbus Friedrichshafen, TASI, TASF, Ariane Group Lampoldshausen, Blue Horizon Deutschland GmbH (OHB SE).
Many thanks also to all the ESA colleagues from different directorates interested and supportive in advancing the technologies described in this paper.

References

[1] Asbjorn Strand and Helge Weydahl, "Regenerative Fuel Cell Systems for Satellites", in *8th European Space Power Conference*, Constance, Germany, 2008.
[2] "Alternative Energy Storage Solutions for Lunar Night Survival in Human Exploration Scenarios", ESTEC/Contract No. 4000127686.
[3] Final Report "Feasibility of Regenerative PEM Fuel Cells for Space Applications", ESTEC/Contract No. 400021113, 2009.
[4] Final Report "Regenerative PEM Fuel Cells", ESTEC/Contract No. 4200022329, 2012.
[5] Final Report "Demonstration of a closed loop H2/O2 fuel cell system", ESTEC/Contract No. 400022556, 2013.
[6] Final Report "Fuel Cells for Extra Lager Telecommunication Satellites", ESTEC/Contract No. 4000112010, 2016.
[7] Jarle Farnes, Arild Vik, Dmitry Bokach, Tjalve Svendsen, Max Schautz, and Xavier Geneste, "Recent Development of Regenerative Fuel Cell Systems for Satellites", in *10th European Space Power Conference*, Noordwijkerhout, The Netherlands, 2014.
[8] Jarle Farnes, Dmitry Bokach, Sander ten Hoopen, Kim Skatun, Max Schautz, Xavier Geneste*, et al.*, "Optimized High Temperature PEM Fuel Cell & High Pressure PEM Electrolyser for Regenerative Fuel Cell Systems in GEO Telecommunications Satellites", in *11th European Space Power Conference*, Thessaloniki, Greece, 2016.
[9] "Regenerative Fuel Cell System Technologies Development", ESTEC/Contract No. 4000126860.
[10] International Space Exploration Coordination Group "The Global Exploration Roadmap", 2018.
[11] Final Report "Regenerative Energy Storage Systems for Space Missions", ESTEC/Contract No. 4000105059, 2014.
[12] Final Report "High Temperature Fuel Cells", ESTEC/Contract No. 4200021767, 2010.
[13] Final Report "Regenerative Fuel Cell System for Mars Exploration", ESTEC/Contract No. 4000108849, 2018.
[14] Ivar Waernhus, Arild Vik, Asbjorn Strand, Dimitrios Tsiplakides, Stella Balomenou, and Kalliopi Papazisi, "High Temperature Fuel Cells for Future Mars Missions", in *9th European Space Power Conference*, Saint Raphael, France, 2011.
[15] Ivar Waernhus, Crina S. Ilea, Arild Vik, Dimitrios Tsiplakides, Stella Balomenou, Kalliopi-Maria Papazisi*, et al.*, "Regenerative Energy Storage for Space Exploration Missions", in *11th European Space Power Conference*, Thessaloniki, Greece, 2016.
[16] Ivar Waernhus, Crina S. Ilea, and Arild Vik, "Regenerative Energy Storage for Mars Exploration", in *12th European Space Power Conference*, Juan-Les-Pins, France, 2019.

[17] Kalliopi Papazisi, Dimitrios Tsiplakides, Stella Balomenou, Ivar Wærnhus, Crina Suciu, Arild Vik*, et al.*, "Carbon Tolerant Fuel Electrodes for Reversible Sofc Operating on Carbon Dioxide", *E3S Web of Conferences,* vol. 16, p. 09003, 01/01 2017.
[18] "Development of an Engineering Model of a Regenerative Fuel Cell System for Power Generation on Mars", ESTEC/Contract No. 4000127311.
[19] Forrest E. Meyen, Michael H. Hecht, and Jeffrey A. Hoffman, "Thermodynamic model of Mars Oxygen ISRU Experiment (MOXIE)", *Acta Astronautica,* vol. 129, pp. 82-87, 2016/12/01/ 2016.
[20] Gerald Sanders, Aaron Paz, Lara Oryshchyn, Koorosh Araghi, Anthony Muscatello, Diane L. Linne*, et al.*, "Mars ISRU for Production of Mission Critical Consumables - Options, Recent Studies, and Current State of the Art", presented at the AIAA Conference and Exposition, 2015.
[21] M. Ralphs, B. Franz, T. Baker, and S. Howe, "Water extraction on Mars for an expanding human colony", *Life Sciences in Space Research,* vol. 7, pp. 57-60, 2015/11/01/ 2015.
[22] Anthony C. Muscatello and Robert J. Gustafson, "Comparison of Direct Solar Energy to Resistance Heating for Carbothermal Reduction of Regolith", *NASA Technical Reports Server (NTRS) 20110004888,* 2011.
[23] K. R. Sridhar, J. E. Finn, and M. H. Kliss, "In-situ resource utilization technologies for Mars life support systems", *Advances in Space Research,* vol. 25, pp. 249-255, 2000/01/01/ 2000.
[24] James Carpenter, Richard Fisackerly, and Berengere Houdou, "Establishing lunar resource viability", *Space Policy,* vol. 37, pp. 52-57, 2016/08/01/ 2016.
[25] Carsten Schwandt, James A. Hamilton, Derek J. Fray, and Ian A. Crawford, "The production of oxygen and metal from lunar regolith", *Planetary and Space Science,* vol. 74, pp. 49-56, 2012/12/01/ 2012.
[26] "High Pressure Water Electrolyser Development for Exploration Surface Missions", ESTEC/Contract No. 4000128887.
[27] Alexey Spirin, Alexandr Lipilin, V. V. Ivanov, S. Paranin, Alexey Nikonov, V. R. Khrustov*, et al.*, *Solid Oxide Electrolyte Based Oxygen Pump* vol. 65, 2010.
[28] "Water propulsion system", ESTEC/Contract No. 4000119185.
[29] Technology Harmonisation Advisory Group (THAG) "European Space Technology Harmonisation Dossier "Electrochemical Energy Storage", ESA/IPC/THAG(2019)6, 2019.

Keywords: EFCF2020, SOx
Session A05: Technology status at industry and major groups II

A0604

Practicality Evaluation of Solid Oxide Fuel Cell (SOFC) – Micro Gas Turbine (MGT) Hybrid Power Generation System

Yasuharu Kawabata (1,3), Daishiro Takeda (3), Kazuyoshi Ochi (3), Hiroshi Fujiki (3)
Toshihiro Oshima (2), Yuya Tachikawa (1), Shunsuke Taniguchi (1,2)
Yoshio Matsuzaki (1,2,3), Kazunari Sasaki (1,2)
(1) Center for Coevlolutionary Research for Sustainable Communities, Kyushu University
Motooka 744, Nishi-ku, 819-0395 Fukuoka/Japan
(2) Next-Generation Fuel Cell Research Center (NEXT-FC), Kyushu University
Motooka 744, Nishi-ku, 819-0395 Fukuoka/Japan
(3) Tokyo Gas Co., Ltd.
Kaigan, 1-5-20, 105-8527 Minato-ku/Japan

Contact authors: www.EFCF.com/ContactRequest

Abstract

Solid oxide fuel cell (SOFC) and micro gas turbine (MGT) hybrid power generation system (SOFC-MGT HPGS) is highly expected as one of the key technologies which can achieve energy saving and less CO_2 emission for a sustainable low-carbon society.

Mitsubishi Hitachi Power Systems Co., Ltd. (MHPS) has developed a 250kW-class SOFC-MGT HPGS for market introduction, and practicality evaluation from a user-side view with multiple evaluation points is required towards wide-spread use of such systems.

Here, we practically evaluate the newly developed SOFC-MGT HPGS including basic performance, system safety, environmental properties of noise and exhaust, and long-term durability under various environmental conditions through various kinds of field tests of the developed systems. As the results, we have confirmed high performance and sufficient applicability of the system, which led to deregulation of operators' continuous monitoring and the world's first market introduction and commercialization of SOFC-MGT HPGS.

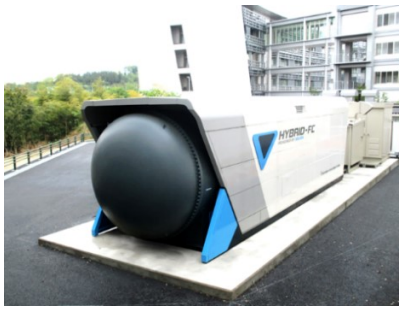

Fig.1 Field test of SOFC-MGT HPGS (NEXT-FC, Kyushu University)

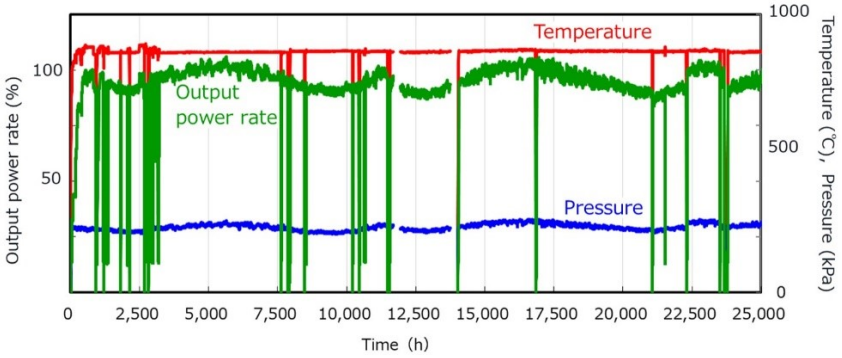

Fig.2 Over 20,000-h field test data of SOFC-MGT HPGS at NEXT-FC, Kyushu University

https://doi.org/10.5281/zenodo.4550554

Introduction

Under the actualizing global warming effect, it is indispensable and urgent to develop a highly efficient power generation system that contributes to the simultaneous realization of energy saving and low-carbon fossil fuel utilization. As an effective solution to this issue, a hybrid power generation system combining solid-oxide fuel cells and micro gas turbine is expected to put into practical use and introduced into the market [1].

However, in order to put newly developed power generation system into practical and widespread use, it is necessary to evaluate its' practicality and social benefit from a user-side perspective [2]. For user-side evaluation of new technology, it is quite important to verify not only basic performance, but also safety including the event of anomalies, environmental properties such as noise and emissions, long-term durability and reliability including robustness to environmental changes such as air temperature, rain, and snow, etc.

In this study, various practicability evaluation tests were carried out on SOFC-MGT HPGS developed by MHPS using several demonstration systems with different installation and operation conditions. Through long-term field tests of the systems, practicability of the developed SOFC-MGT technology were confirmed, that leads to the world's first commercialization of SOFC-MGT HPGS through an installation at a building in Tokyo.

1. Practicality Evaluation

In this study, various evaluations were conducted using three systems shown in Figure 1.

In October 2012, the first prototype system was installed in a building at Tokyo Gas test site. Long-term continuous rated power generation in an indoor installation environment and safety verification tests were conducted in the event of an anomaly in preparation for review of deregulation of continuous monitoring regulations of the Electrical Utilities Act in Japan.

A new SOFC-MGT HPGS powered by improved cell stack was installed outdoors at Next-Generation Fuel Cell Research Center at Kyushu University in March 2015. Long-term rated power generation has been carried out including a long-term durability evaluation that consists of environmental robustness with extreme hot and humid condition in summer, heavy snow in winter, typhoons, heavy rains, and big earthquakes.

Furthermore, in 2016, the same type was installed at the indoor test site of Tokyo Gas, and various evaluations such as the basic performance and load-following performance evaluation as a cogeneration system, the evaluation of the durability against repeated normal startup and abnormal shutdown.

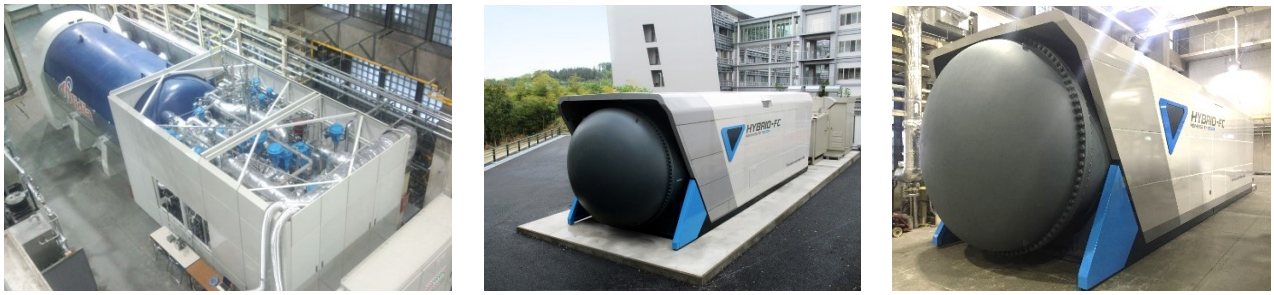

Fig. 1 Test systems for practicality evaluations
(Indoor prototype at Tokyo Gas, Outdoor system at Kyushu Univ., Indoor system at Tokyo Gas)

https://doi.org/10.5281/zenodo.4550554

2. Practicality Evaluation Method

To evaluate the practicality of a power generation system, not only its basic performance, but safety, durability, and reliability under actual operation conditions are quite important. Confirming the state of compliance with relevant regulations related to national or international codes and standards are also required for proper installation and operation. Therefore, evaluation tests were performed and results were evaluated judged on the basis of regulations and standards for related system such as JIS C 8841-2 "Small Solid Oxide Fuel Cell Systems-Part 2: Safety Standards and Safety Testing Methods" [3] and JIS C 8841-3 "Small Solid Oxide Fuel Cell Systems-Part 3: Performance Testing Methods and Environmental Testing Methods" [4]. However, these standards apply to small scale systems (rated power less than 10 kW), and are intended for installation in houses or small buildings. Furthermore, these standards are not applied to pressurized SOFC module and combined system with gas turbines. Therefore, this study also evaluate and verify the applicability of existing test methods and standards of small stationary SOFC systems to large-scale pressurized SOFC-MGT hybrid power generation systems.

In this study, we proposed multi-point evaluation including not only basic performance and safety, but also operability such as durability and environmental durability of 10-year-actual indoor or outdoor operation. The following is a summary of the main items for evaluation.

2.1 Rated Operation Performance

In evaluating the performance of a power generation system, the output and efficiency at rated operation are the most important indicators. In this study, the basic performance was evaluated based on the standard performance test method specified by JIS C 8841-3. The rated power generation status was maintained for 3 hours or more with the rated power generation held for 3 hours or more, and the total electric output of the hybrid power generation system measured at the outlet of the inverter of the power generation unit for 3 hours, and the time average data was taken as the power generation output. During the measurement of the output, the flow rate of city gas flowing through the Azbil Kimmon Co., Ltd.'s Gas Meter RA65TPCK. The flow rate was converted to the standard condition using the data of temperature and pressure of the gas.

Power generation efficiency was calculated by measured output power and gas flow rate. Regarding the exhaust heat recovery performance, water was circulated to the exhaust gas heat exchanger attached to the exhaust gas line, and the amount of waste heat recovery was calculated from the circulating water temperature and circulating water flow rate at the inlet and outlet of the heat exchanger. The exhaust heat recovery efficiency was also calculated from gas flow rate. In this study, the basic performance evaluation was carried out by the improved demonstration system installed in 2016 at Tokyo Gas test site.

2.2 Load Following Performance

Load variable range and load following speed of power generation systems are becoming to an important performance for output-adjusting distributed power sources in the future of unstable renewable energy popularization. This performance was also evaluated according to the load following characteristics test of JIS C 8841-3. In this test, the load was decreased to the 50 % of the rated output, which is the lowest load of this system, and the load-following-ability at the time of load decreasing was evaluated by the

time from the start of load decreasing operation at the rated power generation to the arrival of the indicated output.

In addition, by keeping 50 % output for 3 hours or more, after evaluating and confirming the stability of the system in the lowest load operation, an operation to increase the load to the rated output was taken, and the load-following-ability at the time of load increase was evaluated by the time from the start of load increasing operation to reaching the rated output.

2.3 Environmental Friendliness

In evaluation of the effect of the power generation system to the surrounding environment is also quite important for social implementation. The cleanliness of the exhaust gas, such as the concentration of nitrogen oxides (NOx), unburned hydrocarbons (THC), sulfur oxides (SOx), and dust, as well as noise and vibration generated during operation are important evaluation index, which should be referred to local regulations, codes, and standards.

Among these items, the exhaust gas property was evaluated based on the JIS environmental test methods by measuring the concentrations of NOx and THC using exhaust gas analyzer MEXA-7100 of Horiba Co., Ltd.,. Hazardous substances such as sulfur oxides and dust are also analyzed using gas chromatograph by Chugai Technos Co., Ltd.

In order to measure the noise and vibration under the condition of minimizing background noise and vibration, we measured the noise and vibration under the steady condition of the rated power generation in accordance with the environmental test methods stipulated in JIS C 8841-3 using the test system installed at the indoor test site of Tokyo Gas. Specifically, noise levels at steady-state power generation were measured by using a sound level meter NL-52 manufactured by Rion Co., Ltd. by setting 16 measuring points so as to surround the power generation system, using a position of 1 m on the generator side and 1.2 m in height as a measuring point. Further, surface vibration of the power generation system near the noise measurement point is analyzed with attaching element of the vibration meter VA-12 manufactured by Rion Co., Ltd.

2.5 System Safety under Normal Operation

Although it is important that the power generation system has beneficial basic performance, it is necessary to operate safely even in the case of various environmental and operational conditions. Therefore, safety in normal operation is an important evaluation item that should be verified in an actual installation and operational conditions before market introduction.

In particular, SOFC-MGT HPGS must have adequate safety measures in the power generation system because cell stack is operated at a high temperature of around 900 °C, and highly-reactive hydrogen and toxic carbon monoxide, which is at risk of generating gas poisoning in the event of a leak. In addition to these hazards, the system also has the additional hazards of pressurized SOFC operation and hybrid power generation using MGT.

Therefore, the surface temperature and exhaust gas temperature were measured from the viewpoint of fire and burn prevention, and the composition of the exhaust gas was analyzed from the viewpoint of confirming the risk of carbon monoxide poisoning. All of index are evaluated through comparing the existing national and international codes and standards.

2.6 System Safety in the Event of Internal Error

Regarding the safety evaluation of power generation systems, it is necessary not only to evaluate the systems during normal operation, but also abnormal condition including shutdown due to internal malfunction or external troubles. Considering SOFC-MTG HPGS with pressurized SOFC, the module stores more amount of high-temperature hazardous gases than non-pressurized systems, which could lead to higher risk and more damage in accidents.

Therefore, safety verification in case of internal error in the actual system was also carried out. To verify system safety under the most severe accidental condition, we intentionary input a signal of internal abnormality occurrence shifting to emergency shutdown mode during rated power operation and analyzed transition of operation data after error detection.

2.7 Safety in the Event of External Disturbance Error

Regarding abnormal occurrences during operation, abnormalities of external environment at the installation site, such as lightning blackouts or earthquakes, should be considered. It is also necessary to maintain safety even in the event of such conditions.

In this study, long-term outdoor power generation demonstration was conducted at Kyushu University to accumulate data of various external error conditions. As a specific example, we evaluated the data obtained when a big earthquake with seismic intensity of 4 was observed at the installation site during the Kumamoto Earthquake that occurred in April 2016.

2.8 Long-term Durability under Various Environmental Conditions

It is also important that the performance and safety of a power generation system can be maintained over a life time of the system. In addition, this long-term durability needs to include robustness to various environmental conditions. Especially for outdoor installed systems, stable operation and performance maintenance are required even under various environmental changes such as rising temperature and humidity in summer, heavy rain and strong wind in the case of typhoons, and snow coverage in winter. This item was also evaluated through long-term outdoor field test at Kyushu University.

2.9 Normal Start and Stop Cycle Durability

In the actual operation of the power generation systems, the periodic inspection and maintenance work of the system should be required based on the operating plan. Scheduled stopping according to the installation environment or needs of the users should be considered during life-time operation. Therefore, it is necessary to confirm the durability of normal start-up and shutdown operation cycle during the operation period because thermal cycling of SOFC deteriorates the materials and structures of cell stacks, resulting in performance degradation or malfunction of power generation system.

In this study, we evaluated the durability of SOFC cell stack by performing 30-time-repeated start and stop operations with assuming that a relatively large number of normal shutdowns and restarts are performed (3 times a year in estimated life time of 10 years). Specifically, after starting from the cold state of the power generation system and continuing the rated power generation for 3 hours or more to obtain the operation data, the shutdown operation was performed to automatically shut down the power generation module, including the cell stack, and after confirming that the maximum temperature in the

power generation module, including the fuel cell stack, had shifted to the shutdown completion state of 100 °C or less. The power output transition and its stability during the rated power generation from the first time to 30 times and the durability against repeated start-ups and shutdown were evaluated and verified.

2.10 Abnormal Shut-down and Restart Cycle Durability

In the actual use of power generation systems, a certain times of emergency stops due to disturbances such as power outage or earthquakes are also expected. Therefore, it is important to evaluate and confirm the durability of repeated abnormal shutdowns assumed during the operation period. In the emergency stop accompanied with the abnormal conditions, steep current changes due to the load shutdown, such as a sudden change in temperature and gas composition in the cell stack due to the emergency shut-off of the fuel or immediate supply of purge gas are all affective to the cell stack durability.

Therefore, the durability characteristics against repeated abnormal shutdown and restart operation were evaluated based on the operation data of actual abnormal shutdowns and restart which occurred during a long-term demonstration in Kyushu University. The durability was evaluated and verified by comparing the average output power of 3 hours rated power generation before abnormal stop and 3-hour-average output after restarting after abnormal shutdown during rated power generation.

3. Results of Practicality Evaluation

3.1 Rated Operation Performance

Table 1 shows the results of the rated operation performance test. As shown in the table, it was confirmed that this system has a high power generation efficiency of 53.6 % LHV, which is equivalent to the latest 1,000 MW class gas turbine combined power generation, even though the power output is 200 kW class. Unlike large centralized power plants, this power generation system can be introduced as a distributed power source close to the demand area. Therefore, it is not necessary to consider the transmission loss and the risk of grid failures can be reduced, thus enabling highly efficient on-site power generation.

It was also confirmed that this system can be operated as a co-generation system in which 20.5 %LHV waste heat can also be effectively utilized by 85 °C hot water recovering with the use of MGT exhaust heat. Therefore, this system has high potential for energy saving and CO_2 reduction, which can realize an on-site energy supply with a total efficiency of 74.1 %LHV by hybrid power generation and waste heat utilization.

Table 1 System performance at rated-output operation of 15-type SOFC-MGT HPGS.

Fuel input [kW-LHV]	381	City gas:33.8 Nm^3/h
Electrical power output [kW]	204	SOFC + MGT
Power generation efficiency [%-LHV]	53.6	
Heat recovery output [kW]	87.6	85 °C Hot water
Heat recovery efficiency [%-LHV]	20.5	
Total efficiency [%-LHV]	74.1	

3.2 Load Following Performance

Figure 2 shows the results of load following performance tests of the power generation system. Figure 2 (a) is the result of the load increasing test, and Figure 2 (b) is the result of the load decreasing test. As results of these tests, the load increasing speed of 10.2 kW/min (equivalent to 5.7 %/min of the rated power generation output) and the load

decreasing speed of 10.1 kW/min (equivalent to 5.5 %/min) were confirmed. Those are the same level of existing gas turbine combined power generation system despite of complex system configuration of hybrid power generation system of SOFC and MGT. From the results, it was proven that this system is suitable for distributed power generation with high efficiency and high flexibility which can cope with the increasing unstable renewable energy resources.

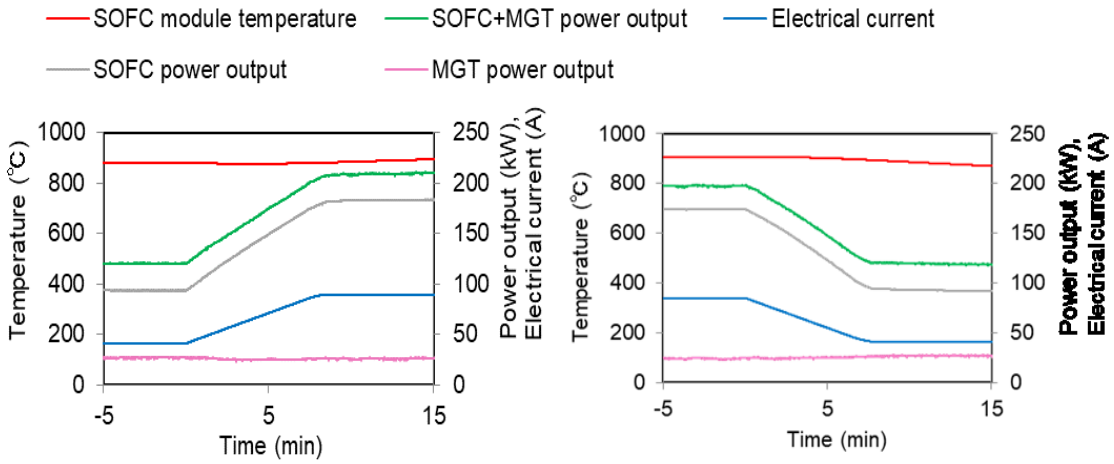

(a) Load increase operation (b) Load decrease operation

Fig.2 Load following characteristics of SOFC-MGT HPGS

3.3 Environmental Friendliness

Table 2 shows the results of noise and vibration characteristics. It was confirmed that the average noise is 66.8 dB-A, which is equivalent to existing power generation systems. The measured vibration was 43.6 dB, which was lower than the sensible vibration of 55 dB.

Table 3 also shows the results of the exhaust gas composition. As shown in the table, NOx concentration in the exhaust was 1.0 ppm (O_2=16%), that was much less than conventional power generation systems without de-NOx catalyst. This is because the operating temperature of SOFC and off-gas combustion temperature in MGT are lower than thermal NOx increasing temperature of 1,500 °C. On the other hand, it was confirmed that the unburned hydrocarbon was 833 ppm-C, the SOx concentration was less than 0.02 ppm, and the dust concentration was less than 0.0009 g/m^3. From these results, it was confirmed that this system has a high environmental property that can be installed even in urban areas.

Table 2 Noise and vibration characteristics of 15-type SOFC-MGT HPGS.

Noise [dB-A]	66.8	Under 70 dB-A
Vibration [dB]	43.6	Under 55 dB

Table 3 Exhaust gas characteristics of SOFC-MGT HPGS.

N_2 [vol ppm]	81.6	
O_2 [vol %]	15.2	
CO_2 [vol %]	3.29	
THC [vol ppm-C]	83.3	O_2= 0 %
CO [vol ppm]	25.3	O_2= 0 %
NOx [ppm]	1.0	O_2= 16 %
SOx [ppm]	<0.2	
Dust [g/m^3]	<0.0009	

https://doi.org/10.5281/zenodo.4550554

3.5 System Safety under Normal Operation

Table 4 shows the temperature of the system surface, exhaust gas, and the carbon monoxide concentration in the exhaust gas, which were measured as safety evaluation items during rated power generation. The results shows that all items satisfied the standards for small stationary SOFC systems, which are required higher-safety for residential or small building installation. Generally, SOFC operate at a high temperature, while ensuring the safety with the aim of minimizing heat radiation, the cell stack is covered with a sufficiently thick heat insulating material. Therefore, even if the inside of the module is hot, the temperature on the surface is usually kept around 50 °C, and it was also confirmed that the temperature was 56.5 °C even when the module was exposed to direct sunlight during the daytime in midsummer. At the same time, exhaust gas temperature was 185 °C, which was lower than 260 °C of the safety standard. This result shows that sufficient safety is ensured even in the mono-generation system without heat recovery. In this system, most of the heat of MGT combustor is effectively utilized for the compression and preheating to supply pressurized SOFC cathode air. Therefore, the exhaust temperature of MGT is lower than conventional MGT systems and also lower than safety standard.

The CO concentration in the exhaust gas was also 0.0025 vol% (O_2=0%), well below the safety standard of 0.14 vol% for small SOFC systems to be installed outdoors around houses, etc. This is because reformed CO is not only utilized for SOFC modules, but also well-consumed in MGT combustor and effectively utilized for MGT power generation and heat exchange.

Table 4 Safety validation data during rated-output power operation of SOFC-MGT HPGS.

SOFC module surface temp. [°C] at ambient temp. is 38.2 °C	56.5	≦ 95 °C (Codes of Japanese small scale stationary fuel cell system and IEC)
Exhaust gas temp. [°C] at ambient temp. is 38.2 °C	185	≦ 260 °C (Japanese small scale stationary fuel cell system codes : JEMA)
Exhaust CO concentration [vol%] (O_2=0%, 15-minutes-average)	0.0025	< 0.14% (Japanese small scale stationary fuel cell system codes : JEMA)

3.6 System Safety in the Event of Internal Error

Figure 3 shows the transition of the voltage of SOFC cell stack and the temperature and pressure in SOFC module during the "emergency stop mode" in which both inlet and outlet valves of the module are urgently closed. It is clear that in this shutdown mode, SOFC is automatically disconnected from the electrical grid, the current of SOFC becomes zero with an open circuit state, since there is no voltage drop due to the internal resistance, the voltage rises immediately after the emergency stop, the voltage remains because there is an electromotive force due to the gas compositional difference between anode and cathode, and decreases gradually thanks to the sealing. It is also confirmed that there is no sudden voltage change or destabilization that could lead to a safety issue.

Regarding to the temperature transition of the module, it is clear that the temperature gradually decreases because exothermic reaction in SOFC stops since emergency stop. Furthermore, it is also clear that there is no abnormal increase or decrease of SOFC

https://doi.org/10.5281/zenodo.4550554

module pressure. From the results, it is confirmed that this system can automatically and safely stop at an internal error occurrence. We also submitted these safety validation data to a committee that discuss deregulation of the Electrical Utility Act, so that all-time operator's monitoring regulation to pressurized SOFC system have been deregulated, and that enabled easy market introduction and future commercialization of pressurized SOFC power generation systems.

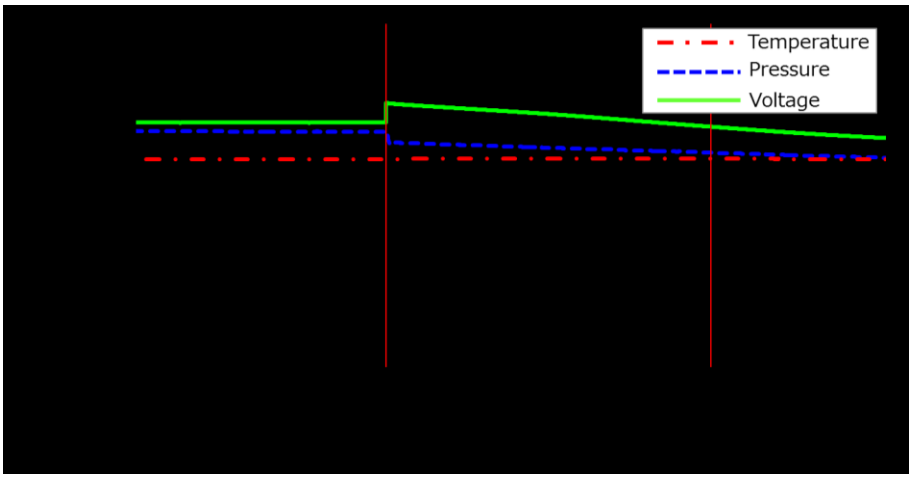

Fig.3 Safety validation data of SOFC-MGT HPGS

3.7 Safety in the Event of External Disturbance Error

As a result of safety verification at the occurrence of external disturbance error, Fig.4 shows output transition before and after big earthquake during the long-term operation in Kyushu University. Despite the seismic intensity of 4 was observed at the installation site, the system stopped safely by immediate detection of system disturbances. At detection of disturbance, the system automatically and promptly disconnected to the grid, while maintaining the temperature of SOFC module by shifting operation mode to the hot-standby state that can be easily and speedy restarted. In the period from detection of disturbance to the transition to the hot stand-by state, no rapid increase in temperature or pressure was observed, and it was confirmed that the safety of the system was also maintained. Furthermore, it was confirmed that the output power is the same as that before the earthquake.

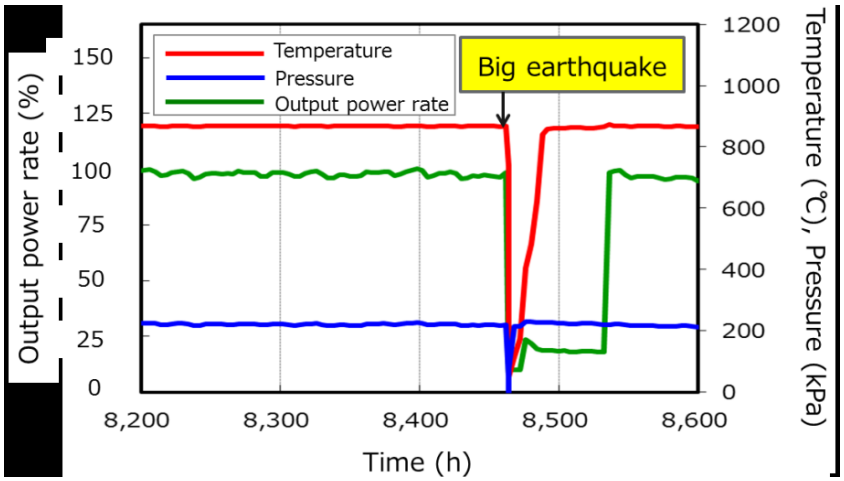

Fig.4 Emergency stop and restart of SOFC-MGT HPGS (Earthquake in Kyushu area)

https://doi.org/10.5281/zenodo.4550554

3.8 Long-term Durability under Various Environmental Conditions

Figure 5 shows the results of long-term power generation demonstration of the system installed outdoors at Kyushu University. Since the system started its power generation in May 2015, power generation operation continued while repeating the emergency shutdown and restart due to various abnormal disturbance with multiple normal shutdown and restart for yearly maintenance. As of June 2020, the long-term rated power generation operation reached to 25,000 hours without exchanging and degradation of SOFC cell stacks. Therefore, it was confirmed that this system should be expected to have sufficient long-term durability including various environmental conditions of outdoor installation.

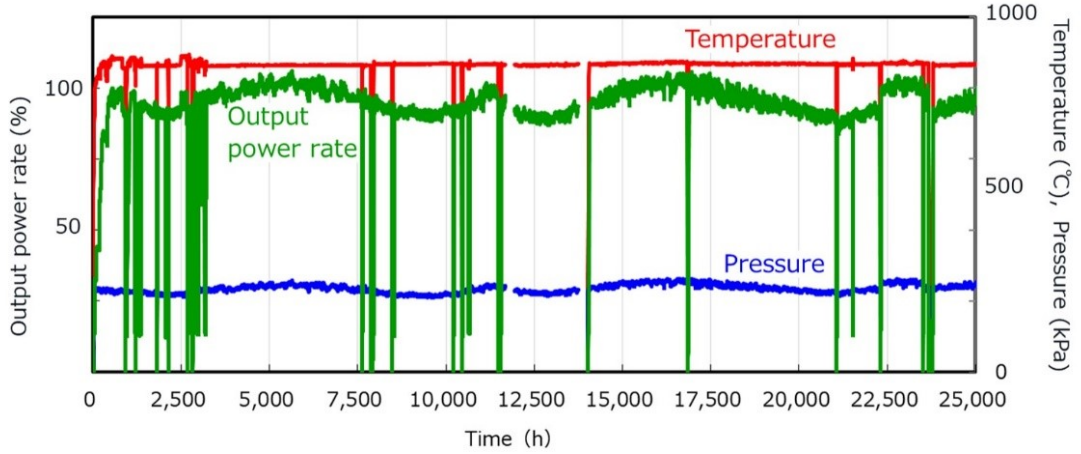

Fig.5 25,000-hour long-term field test data of the outdoor-installed SOFC-MGT HPGS in Kyushu University

3.9 Normal Start and Stop Cycle Durability

Figure 6 shows the results of the output power transition in the normal start-stop cycling test performed with the system installed in Tokyo Gas. The output power at the time of rated generation shown in the figure is plotted with the average output in the state where the rated generation is held for 3 hours or more according to the JIS performance test method. This evaluation is assuming 3 times a year during 10-year operation, so 30 times of normal startup and shutdown were repeated. It is clear that the rated output power does not drop significantly as the number of restart. Through the test, it was found that the rated power reduction rate at the final startup was only 0.74%. From these results, it was confirmed that this system has excellent thermal cycle tolerance which can sufficiently withstand 10-year operation with several start and stop according to the users request, etc.

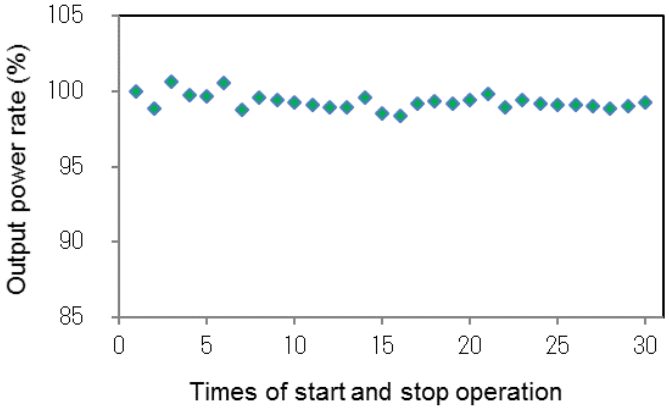

Fig.6 Start-and-stop cycle operation data of SOFC-MGT hybrid power generation system

https://doi.org/10.5281/zenodo.4550554

3.10 Abnormal Shutdown and Restart Cycle Durability

Figure 7 shows the result of output power at rated power operation after an abnormality detection shutdown during rated power generation. This evaluation data summarizes the recovery results after various abnormal detection stops due to external and internal factors that occurred during the long-term power generation demonstration in Kyushu University.

As shown in the figure, 17 times shutdown and restart were repeated, but the rated power output did not decrease. It was also confirmed that the rated output power at the latest restoration were only 0.06% below than the first data. Assuming abnormal shutdown occurs once a year during 10-year life time, this system is also expected to have sufficient durability even for abnormal shutdown. As the result of three kinds of durability assessment, it was confirmed that this system can be expected sufficient durability for 10-year actual outdoor operation without exchange of SOFC cell stack.

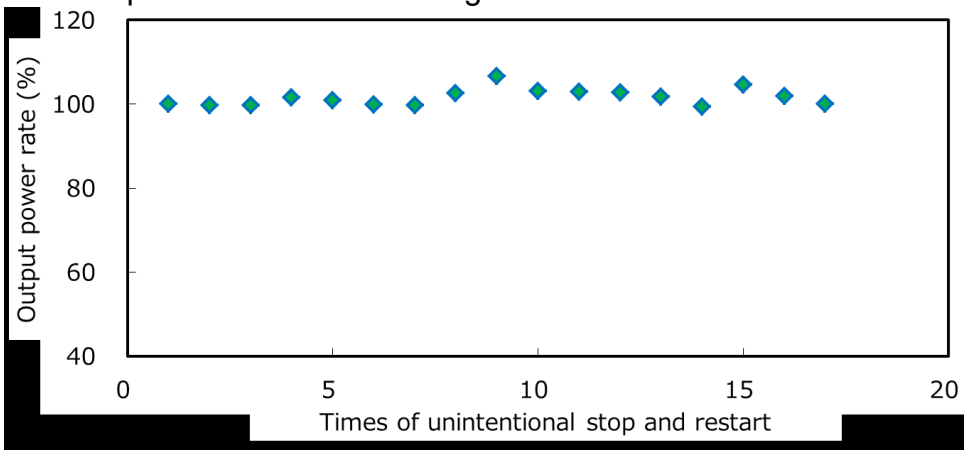

Fig.7 Unintentional stop-and-restart operation data of SOFC-MGT HPGS

4. Conclusions

A practicability evaluation for commercialization of SOFC-MGT hybrid power generation systems was conducted from a user-side perspective based on 10-year-actual operation. Through evaluation tests using several demonstration systems with different installation and operation conditions, the following results and outcomes have been obtained.

(1) Evaluated SOFC-MGT hybrid power generation system has a high power generation efficiency of 53.6 %LHV, which is equivalent to the 1,000 MW–class state-of-the-art gas turbine combined cycle despite of 200 kW-class output. It was also confirmed that this system combines excellent energy saving as cogeneration and environmental friendliness with 1.0 ppm NOx (O2=16%) concentration in the exhaust gas and lower noise and vibrations than standards that enable installation even in the urban area.

(2) System safety verification using a demonstration system was also carried out for two cases consists of internal malfunction and external disturbance detection. Through the tests, it was confirmed that system safety based on the relevant standards can be secured in both cases. By utilizing the safety verification data, the continuous-monitoring-regulation for some pressurized SOFC systems were deregulated, that leads to easy installation and operation for commercialization.

https://doi.org/10.5281/zenodo.4550554

(3) Outdoor demonstration with long-term continuous power generation including environmental durability evaluations has been performed. 25,000-hour outdoor operation with practical 10-year durability evaluations including 30 times start-stop operation and 14 times shutdown and restart operation without stack exchange were also confirmed.

(4) Through the practicability evaluation tests based on the assumed 10-year outdoor or indoor installation and actual operation, it was confirmed that the evaluated system meets the requirements for commercial and industrial applications, which leads to the world's first SOFC-MGT HPGS commercialization.

References

(1) Irie, H., Miyamoto, K., Teramoto, Y., Nagai, T., Endo, R., and Urashima, Y., Mitsubishi Heavy Industries Technical Review, Vol. 54, No. 3, Page 69-72 (2017).

(2) Ochi, K.,Kawabata, Y. and Fujiki, H.,Present status of residential and commercial fuel cell systems, Journal of the Gas Turbine Society of Japan,No.4(2016),pp.253–258 (in Japanese).

(3) Japanese Industrial Standard C 8841-2, Small-scale solid oxide fuel cell systems-No.2, Safety codes and standards for safety evaluation test method (2011), (in Japanese).

(4) Japanese Industrial Standard C 8841-3, Small-scale solid oxide fuel cell systems-No.3, Standards for basic performance and environmental performance test method (2011), (in Japanese).

Keywords: EFCF2020, SOx
Session A06: Products and demonstrations

https://doi.org/10.5281/zenodo.4550554

A0807

Experimental analysis of a pressurized 30 kW SOFC system with fuel gas recirculation at reaction temperature

Marius Tomberg (1), Matthias Metten (1), Christian Schnegelberger (1), Marc P. Heddrich (1), S. Asif Ansar (1), K. Andreas Friedrich (1, 2)
(1) German Aerospace Center (DLR), Institute of Engineering Thermodynamics Pfaffenwaldring 38-40, 70569 Stuttgart/Germany
(2) University of Stuttgart, Institute for Building Energetics, Thermotechnology and Energy Storage, Pfaffenwaldring 31, 70569 Stuttgart/Germany

Contact authors: www.EFCF.com/ContactRequest

Abstract

Solid oxide cells (SOCs) are flexible and efficient energy conversion devices. Due to their multiple usage possibilities, like electricity generation and syngas production, they can support the global energy transition. However, to play a significant role in the future energy system SOC reactors have to reach the megawatt and multi-megawatt range.

To address process system issues expected in the higher power range, a 30 kW solid oxide fuel cell (SOFC) system with multiple reactors was set up at the German Aerospace Center in Stuttgart, Germany. This system can be operated under pressure and is equipped with a recirculation blower that recirculates the fuel electrode off-gas at reaction temperature. The system can be used to investigate the behavior of multi-reactor modules in a process system. Multi-reactors are necessary for scaling to higher power ranges and behave differently compared to single reactors. Furthermore, the test rig is capable of emulating gas turbine (GT) components to investigate the operation of a SOFC reactor in a GT/SOFC hybrid power plant.

This work will present experimental results to help clarify the above mentioned multi-reactor issues. The focus will be on the heat losses and unequal flow distribution inside the reactor, which result in different temperature and reactant conversion rates for the single reactors. Various methods, like fuel and pressure variation, are used to characterize these effects. It will be shown how these effects limit the operability of the system and affect the design and operation of process systems. Furthermore, it will be analyzed how process systems should be designed and operated to overcome these problems. Control approaches that improve operability are elaborated and their impact is discussed. Assuming that similar multi-reactor modules will constitute the building blocks of future multi-megawatt systems, generic operation strategies that are derived from the extensive experiments are presented.

https://doi.org/10.5281/zenodo.4550589

Introduction

The growing global demand for energy from renewable sources is leading to new challenges for energy systems. Energy converters need to be developed to meet these challenges. On the one hand, the generation of electrical energy must be efficient and flexible. On the other hand, it is also necessary to develop solutions for hydrogen and syngas gas production from renewables in order to decarbonize industry and transport.

Electrochemical reactors with solid oxide cells can provide a solution due to their flexibility. First, these reactors can provide electrical energy efficiently and are both load and fuel flexible. Second, hydrogen and syngas can be produced in electrolysis mode (SOEC). Third, this flexibility can also be used to provide grid services and for energy storage in reversible mode (rSOC). With these features, SOC reactors can represent an important component for the energy transition. However, the power of commercially available modules is still too low. In order to have a significant impact on the future energy system, large modular SOC reactor modules with multi-megawatt output must be implemented [1, 2]. Up to now, academia has focused primarily on material development and the investigation of cells and their components. In order to address the fundamentals of modular multi-reactors the Institute of Engineering Thermodynamics of the German Aerospace Center in Stuttgart set up a test rig [3, 4] to investigate a 30 kW SOFC reactor module with 48 stacks under pressurized conditions including fuel off-gas recirculation at SOC reaction temperature.

The experimental results show that heat losses and flow distribution have a significant impact on the system's performance. This results in temperature profiles across the reactor and locally varying reactant utilizations. This work presents the test rig used and gives an overview of the experimental results.

1. Scientific Approach and Experimental Set-Up

Large SOC reactors are needed to increase the impact of SOC technology on the energy system. To investigate these in a system environment the DLR set up a test trig in Stuttgart that is presented in figure 1. The test rig is designed in such a way that various aspects can be investigated. It contains a recirculation device, which recirculates the fuel off-gases at reaction temperature. A reformer allows the usage of natural gas or simulated biogas (natural gas & carbon dioxide) as fuel. Furthermore, the SOFC reactor, the recirculation device and the reformer are located inside a pressure vessel for pressurized operation. The test rig is designed that it can emulate the interactions with a gas turbine (GT) to investigate SOFC/GT hybrid power plants.

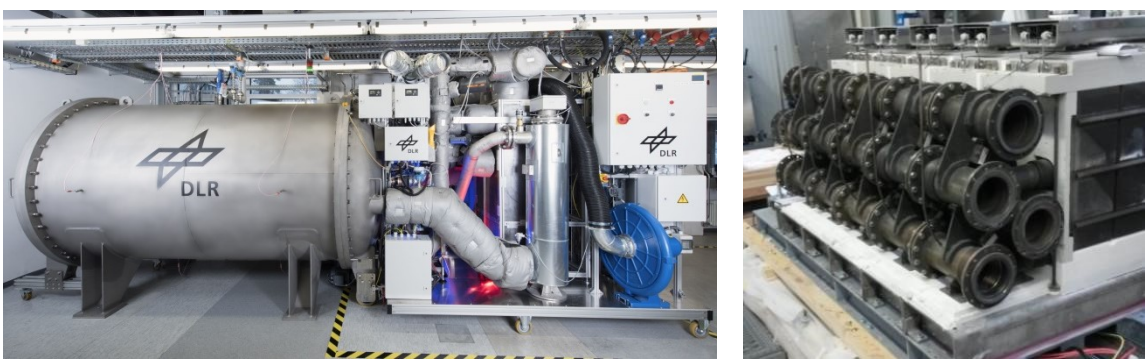

Figure 1: The pressurized 30 kW SOFC system with fuel gas recirculation at reaction temperature. It contains the shown 30 kW SOFC reactor.

https://doi.org/10.5281/zenodo.4550589

The SOFC reactor module consists of 1440 electrolyte supported cells grouped in six sub-reactors with six 30 cells stacks. Each sub-reactor is equipped with a separate power electronics channel to control their electrical currents. A sensor compartment at the bottom of the rector module contains the sensor and power cables.

Figure 2 shows a simplified process flow diagram of the test rig. The incoming pressurized air is controlled by three separate mass flow controllers. First, an air flow is led through the sensor compartment for cooling. The pressure inside this compartment is controlled by a valve. The pressure vessel is purged and pressurized by the second air flow. The inlet temperature can be controlled by an electrical heater. The third air flow is preheated via a heat exchanger by a natural gas burner and led to the oxide side of the SOFC reactor. The incoming fuel is led through a desulfurizer. Subsequently it is mixed with the recirculated fuel off-gases and enters the reformer. Both air and fuel gas flow are cooled outside the vessel and then merged to minimize the pressure difference between air and fuel gas electrodes. A valve controls the system pressure. Afterwards, the remaining combustible molecules are oxidized and cooled.

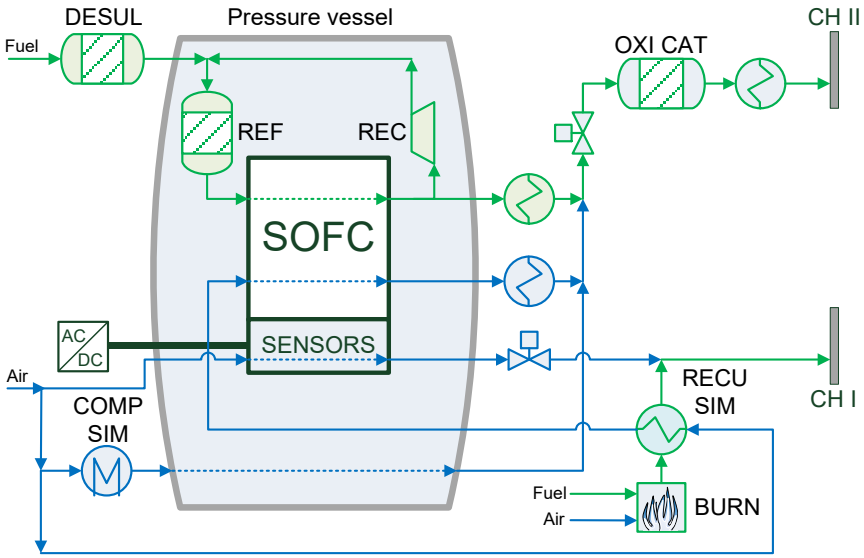

Figure 2: Process flow diagram of the test rig [4] showing the main components and fluid flows.

With this set-up the temperature and voltage distribution inside the SOFC reactor is analyzed. Furthermore, the impact of the recirculation on the reactor as well as system performance is investigated. By varying the pressure the effect of pressurization on the electrochemistry, the overall system and the controllers is examined.

2. Experimental Results

The aim of the experimental investigations was to characterize the operating behavior of the SOFC reactor module through the variation of temperature, pressure, electrical power, fuel gas, its utilization and the recirculation rate. A control concept was developed to achieve this [3, 4]. In addition to the basic controllers, such as power and temperature controllers, also controllers were developed, which were necessary due to the specific layout of the system.
An example is the differential pressure controller for the pressure in the sensor compartment. Since the cooling flow of the sensor area is leaving through another

chimney, a second pressure control valve is necessary (cf. Figure 2). Pressure differences between sensor compartment and reactor volume are potentially damaging the reactor. Therefore, the controller must be robust and fast. This was achieved by means of a feed-forward controller that considers the characteristic of the valve as well as the flow entering the valve. A PI-controller only corrects the error of the feed-forward approach. The analysis in Figure 3 shows that the pressure difference is sufficiently small. Normally it is 1 mbar around the set point of 1 mbar (respectively 2 mbar for a short period).

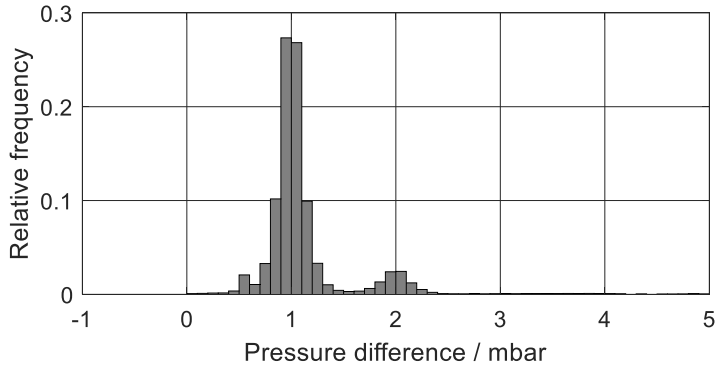

Figure 3: Accuracy of the difference pressure controller over a period of more than 1000 h. The set value changes from 1 to 2 mbar for a short period.

An important aspect of the studies is the analysis of the temperature distribution within the reactor module. Figure 4 shows such a temperature distribution. Each temperature measurement represents a 30 cell stack. The top stacks have the highest temperatures and the bottom stacks are the coldest. The maximum difference can be up to 50 K. One reason for this is that the fuel gas flow is supplied from the bottom of each tower and has a high heat capacity due to the recirculation. The large temperature differences in combination with the flow distribution inside the reactor leads to different flow operating points for the cells inside the reactor. Furthermore, a broad variation of the operating temperature is not possible in a multi-reactor as the lowest and the highest temperature are near the limits of the design range of the cells.

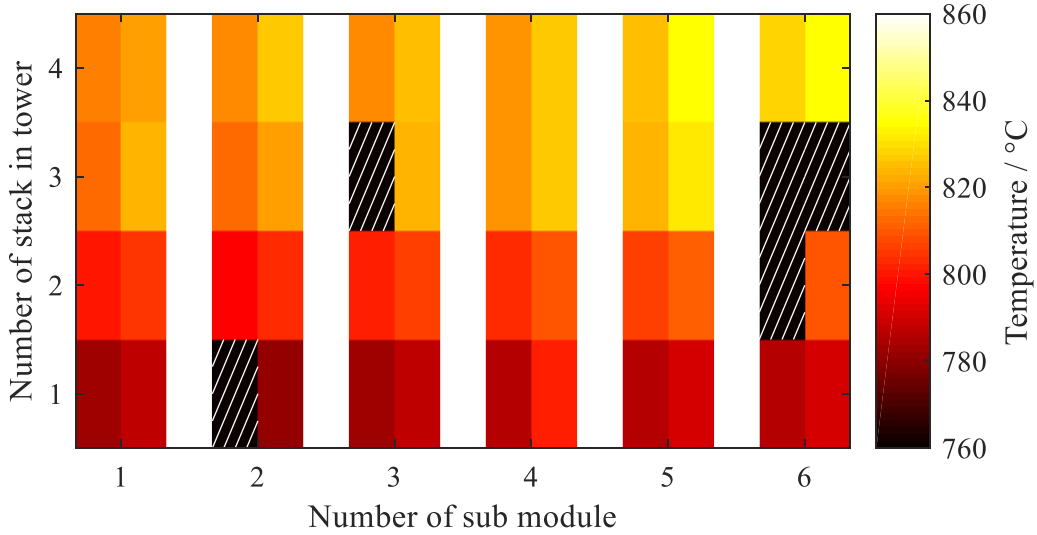

Figure 4: Distribution of air outlet temperatures of the stacks during a stationary operating point. The hatched white-black pattern indicates thermocouples out of operation [7].

The fuel gas utilization was usually set between 70 and 90 %. The recirculation rate is determined by the thermal energy required for fuel gas preheating and steam methane

reforming. A fuel gas variation was performed. In addition to operation with hydrogen, natural gas and biogas (simulated by natural gas and carbon dioxide) were also used as these are attractive SOFC fuels. Unfortunately the pure operation with 100% natural gas was not possible in this arrangement. The temperature at the inlet of the reactor module was too low due to heat losses and the reforming reaction. Therefore hydrogen was added to the natural gas. Figure 4 shows impact of the CO_2 content in biogas on the SOFC reactor module's efficiency. As expected the efficiency drops with a higher share of CO_2.

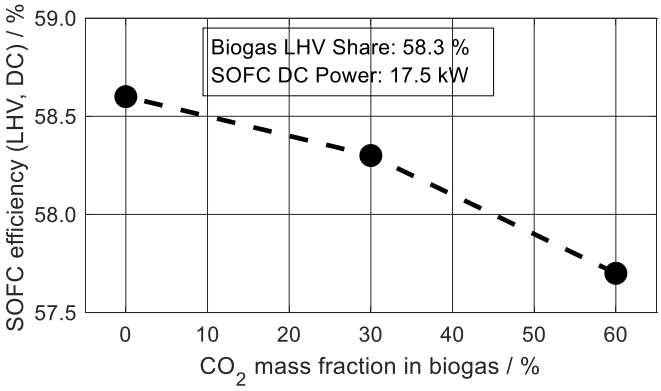

Figure 5: Impact of the CO_2 content in the simulated biogas on the efficiency of the SOFC reactor module.

Due to the temperature distribution shown in Figure 4 the operation of such reactors is challenging. Therefore, a transient simulation model for large SOC reactors is under development [7] based on [8]. Figure 6 shows the simulation results for a similar reactor module. Each sub-reactor is constituted as an 1D+1D model. Each cell is discretized in flow direction and these cells are stacked. Besides fuel cell operation, the model will also be able to simulate water, co- and CO_2 electrolysis.

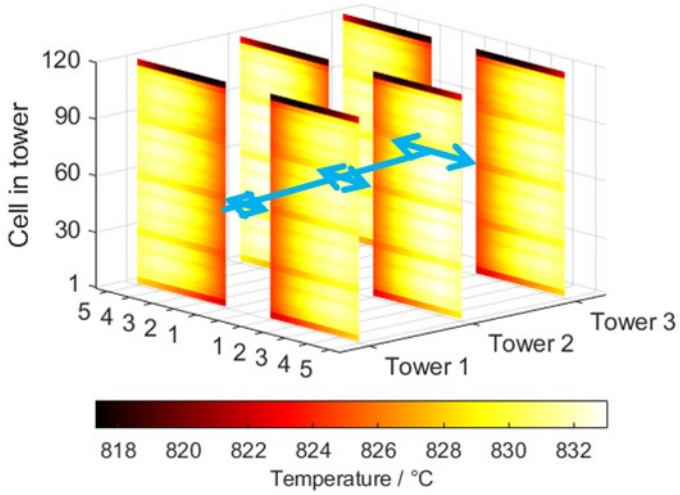

Figure 6: Simulation result of a similar SOC reactor module.

With this model it will be possible to increase the understanding of the behavior of large SOC reactor modules. Furthermore the simulations can be used to improve the operation strategies and develop control strategies and approaches.

https://doi.org/10.5281/zenodo.4550589

3. Conclusions

The DLR's Institute of Engineering Thermodynamics is working on SOC systems. A pressurized 30 kW SOFC system was built and operated to investigate SOC reactors and their behavior in process systems. The system features fuel off-gas recirculation, is fuel flexible and can replicate gas turbine components to study the behavior of a SOFC in a SOFC/GT hybrid.

The experimental results show that heat losses and pressure losses lead to a temperature, reactant utilization and voltage distribution across the reactor module. For example, the difference between the stack with the highest and the stack with the lowest temperature can be up to 50 K. Due to these distributions, each stack operates at a different operating point. These effects can limit the operating range and cause the reactor to degrade faster.

To further investigate these effects, a transient 1D+1D simulation model is being developed, which can also be used to develop efficient and robust operation and control strategies.

Acknowledgements

This project has received funding from the European Union's Horizon 2020 research and innovation program under grant agreement No 641073 (www.bio-hypp.eu). This work was financially supported by the project "SynLink – Energy: Synthetic e Fuels as key enabler for Sector Linking" of the Federal Ministry of Economic Affairs and Energy (BMWi, funding code 03EIV031C). The responsibility for the contents lies with the authors. Furthermore, the support from the German Federal Ministry of Economic Affairs and Energy for the project "DemoHydra" is gratefully acknowledged (support code: 03ET6032).

References

[1] Alexander Buttler, Hartmut Spliethoff, Current status of water electrolysis for energy storage, grid balancing and sector coupling via power-to-gas and power-to-liquids: A review. Renewable and Sustainable Energy Reviews, 82 (3), 2440-2454, 2018

[2] Thomas A. Adams II, Jack Nease, David Tucker, Paul I. Barton, Energy conversion with solid oxide fuel cell systems: A review of concepts and outlooks for the short-and long-term. Industrial & Engineering Chemistry Research, 52 (9), 3089-3111, 2013

[3] Moritz Henke, Mike Steilen, Christian Schnegelberger, Marc Riedel, Martina Hohloch, Sandro Bücheler, Melanie Herbst, Andreas Huber, Josef Kallo, K. Andreas Friedrich, Construction of a 30kW SOFC Gas Turbine Hybrid Power Plant. ECS Transactions, 68 (1), 85-88, 2015

[4] Matthias Metten, Marius Tomberg, Marc P. Heddrich, K. Andreas Friedrich, Analysis of experimental results of a Pressurized Solid Oxide Fuel Cell System simulating a Hybrid Power Plant. 3S Web of Conferences, Savona, Italy, September 2019

[5] Moritz Henke, Mike Steilen, Ralf Näke, Marc P. Heddrich, K. Andreas Friedrich, Control strategy for a SOFC gas turbine hybrid power plant. 12th European SOFC & SOE Forum, Luzerne, Switzerland, 2016

[6] Anna Marcellan, Alessio Abrassi, Marius Tomberg. Cyber-Physical System of a Solid Oxide Fuel Cell/Micro Gas Turbine Hybrid Power Plant. 3S Web of Conferences, Savona, Italy, September 2019

[7] Marius Tomberg, Srikanth Santhanam, Marc P. Heddrich, K. Andreas Friedrich, Transient Modelling of Solid Oxide Cell Modules and 50 kW Experimental Validation. ECS Transaction, 91 (1), 2019

[8] Srikanth Santhanam, Marc P. Heddrich, Sanchit Gupta, K. Andreas Friedrich, Transient reversible solid oxide cell reactor operation – Experimentally validated modeling and analysis. Applied Energy, 232, 473-488, 2018

Keywords: EFCF2020, SOx
Session A08: System design & performance

https://doi.org/10.5281/zenodo.4550589

A0808

The impacts of collaborations in the development of Solid Oxide Fuel Cell technologies from 2000 to 2019: A bibliometric analysis

Osaze Omoregbe, Ahmad El-kharouf, Robert Steinberger-Wilckens
Centre for Fuel Cell and Hydrogen Research, School of Chemical Engineering, University of Birmingham, Edgbaston, B15 2TT Birmingham/UK

Contact authors: www.EFCF.com/ContactRequest

Abstract

Solid Oxide Fuel Cell (SOFC) technologies are receiving considerable interest due to their promising properties of achieving high-efficient and clean energy generation from a variety of fuels. Notwithstanding, the collaborative roles among researchers, institutions and countries in the development of SOFC technologies cannot be ignored. Accordingly, a bibliometric analysis was employed in this work to evaluate the global trends in SOFC research in terms of the numbers of output (number of publications) through scientific collaboration among authors and countries. A total of 14,330 publications including research articles and paper proceedings from 2000 to 2019 were obtained in the Web of Science database, with 90 countries actively contributing to SOFC research. Among these countries, China (3,164) had the strongest participation in terms of number of publications followed by the U.S.A. (2,566), Japan (1,387), South Korea (1,099) and Germany (777). The Asian continent had the highest percentage (45.77%) followed by Europe (30.85%) and North America (19.21%), while Africa had the least participation (0.59%). Additionally, the strongest partnership was seen between USA-China followed by China-Australia, USA-S.Korea, China-Sweden, and China-Japan. This study presents the likely factors influencing the active involvement of some countries and why others have low productivity in published SOFC research.

https://doi.org/10.5281/zenodo.4550616

1. Introduction

The rapid population growth and the expansion of the world economy are greatly influencing global energy demand. Meanwhile the balance in the amount of energy demand is mainly covered by fossil fuel resources. For instance, the rise in energy demand in 2017 was reported to be 2.1%, whilst fossil fuels still accounted for about 81% of the total energy supply [1]. However, greenhouse gases such as CO_2 are emitted into the atmosphere during the combustion of fossil fuels, considerably impacting on climate. Moreover, the fluctuation in global oil prices and the uncertainty in the quantity of oil reserves are causing serious economic and energy security challenges to the world. Therefore, research into alternative and clean energy sources such as solar [2] and wind [3,4] has been intensified in recent times. Meanwhile, the need for an integrated system that uses a renewable energy source to produce hydrogen has been suggested since the energy generated from most of the alternative energy sources cannot be easily stored. The excess energy generated from these alternative sources is stored in form of hydrogen. Hydrogen is considered a feasible means of replacing fossil fuels and achieving a carbon-neutral economy [5,6]. The improved integration of renewable energy will also help in the smooth transitioning from fossil fuels into renewable energy or clean energy society.

In this regard, technologies that can utilise hydrogen for the production of clean and reliable power, such as fuel cells, are gaining increasing attention. Fuel cells have the advantages of improved efficiency, no moving parts, and potentially zero emissions at the point of use [7,8]. In particular, solid oxide fuel cell technology (SOFC) which was first initiated after Nernst discovered solid oxide electrolytes in 1899 [9], is considered an attractive technology for its high efficiency energy conversion [10], easy mode of operation since it does not require a liquid electrolyte [11] and its ability to operate with a wide range of fuels [12,13]. Solid oxide cells are operated at high temperature (700 to 900^{o}C) which gives them the higher efficiency when employed compared to their counterparts when operated either as a fuel cell or as solid oxide electrolyser in reverse polarisation [14]. In addition to the high efficiency in electric energy generation, SOFCs generate high quality heat which can be utilised in other applications such as in heating for both domestic and industrial applications [15]. This unique feature of SOFC enables a broader modulation of heat/electricity ratio regardless of size [14]. Finally, the fuel flexibility and high efficiency of SOFC makes them attractive to countries with high dependency on fuel imports, since fuel use can be reduced and a range of renewable fuels exploited [16].

Nevertheless, SOFC technologies have not yet reached their full potential since they are preferably employed in stationary applications with very long required lifetimes (10 years, 40,000 hours of operation) [17]. Other factors include high manufacturing costs resulting in a still high product selling price. Although intensive research is ongoing to resolve the technical and economical issues associated with SOFC, factors such as funding, regulatory framework, market introduction subsidies, and government policies must also be considered and addressed in order to achieve full-scale commercialisation and global acceptability of these technologies. Collaboration among research groups in different countries is key to a technological success at as global level.

Therefore, this paper aims to study the influence of collaborative activity in the development of SOFC. Specifically, a bibliometric analysis was conducted by considering the research activities of countries and institutions around the world within a period of 20 years (2000 to 2019). In this study, the number of research publications and citations were employed as criteria for productivity in the area of SOFC technologies.

https://doi.org/10.5281/zenodo.4550616

2. Methodology

Data for SOFC research was retrieved from the Web of Science (WoS) Core Collection Database on the 16th of July 2020. The WoS database was used for data collection since it is believed to hold relatively large volumes of data when compared to other sources [18,19]. The search for SOFC research outputs was restricted to research articles and proceeding papers to ensure that only research activity within the specified timeline was captured. The following search command was used in WoS to retrieve the required data:

Title: ("solid oxide fuel cell*" OR SOFC* or (solid AND Oxide AND Fuel AND Cell*)) AND Year published: (2000-2019) AND Document types: (Article OR Proceedings Paper) Timespan: 2000-2019. Indexes: SCI-EXPANDED, SSCI, A&HCI, CPCI-S, CPCI-SSH, BKCI-S, BKCI-SSH, ESCI, CCR-EXPANDED, IC.

The asterisk on some of the searched words was to ensure all possible forms of the keywords were included. For example, SOFC* can be SOFC or SOFCs while cell* can be cell or cells. The quotation mark is to search for exact phrases in the keywords. After retrieving the data from WoS, it was imported to MS Excel where the total number of publications and citations were obtained. Furthermore, the data from WoS was also imported into the VOSViewer software where network visualisation of the co-authorship of individuals, countries, and institutions were created. In addition, the VOSViewer software was used to obtain the collaboration strengths of the participating countries and institutions. It should be noted that “title” was used rather than “topic” for the keywords search because “title” will give an approximate value of the total publications while topic may give an over-estimated value or what is known as false positive results [20,21]. This is because a keyword search using “topic” will include papers where the keywords appeared in abstracts and authors’ keywords which may not be related to SOFC.

3. Results

In this section, findings from the bibliometric analysis conducted on SOFC research in the 2000 to 2019 period are presented.

3.1. Publication volume

The search for SOFC research based on articles and proceeding papers in WoS gave 14,330 total publications (TP) and 281,417 total citations (TC) as shown in Figure 1. As seen, there was a general rise in the number of citations per year, which indicates an increasing interest in SOFC research. This trend was likely triggered by the rising commercial interest in and expectations towards the technology. Moreover, the projected increase in the global market size of SOFC to reach USD 2.00 billion by 2026 may have been a driving force propelling research into this technology [22]. Similarly, there has been a relative increase in the number of publications since the year 2000 with a slight drop after 2011. This is probably due to a move of development into industry and therefore fewer publications.

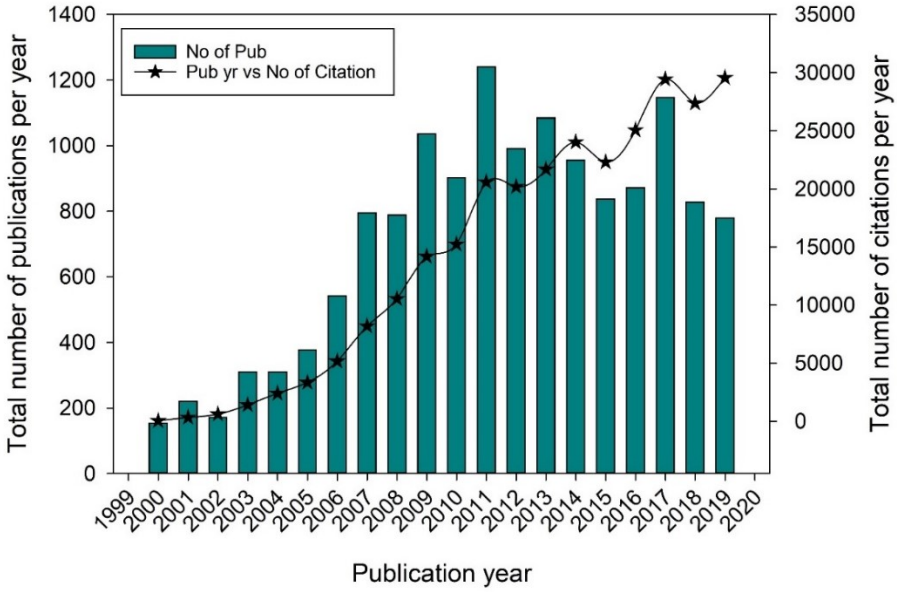

Figure 1: Total number of publications and citations per year for SOFC research during 2000-2019.

3.2 Participating countries

90 countries were obtained from the retrieved documents. Among these countries, China had the highest number of publications (3,164) followed by the U.S.A. (2,566), Japan (1387), S.Korea (1099), and Germany (777). The size of the circles in the co-authorship network visualisation shown in Figure 2 indicates publication volume, and the thickness of the lines connecting the countries indicates the collaboration strengths among them [21]. In addition, the analysis of results using VOSViewer revealed that China had the strongest collaboration record (total link strength = 931) followed by the U.S.A. (741), and Germany (305). Considering the strength of the link between two countries (Table 1), the strongest collaboration was between China and the U.S.A., followed by China and Australia, U.S.A. and S.Korea, China and Sweden, and China and Japan. In terms of total citations, the U.S.A. was the most cited country (59,006), followed by China (53,007), Japan (20,069) and Germany (16,414).

Table 1: List of top 20 countries and top 20 co-authored countries in the order of decreasing collaboration strengths.

S/N	country	Total link strength per country	Collaboration between countries	Link strength between countries
1	China	931	China-U.S.A.	276.42
2	U.S.A.	741	China-Australia	157.83
3	Germany	305	U.S.A.-S.Korea	99.58
4	France	303	China-Sweden	75.37
5	Italy	290	China-Japan	67.67
6	S.Korea	257	U.S.A.-Japan	50.58
7	England	255	U.S.A.-Italy	48.00
8	Japan	246	China-Canada	47.83
9	Australia	234	China-France	47.33
10	Spain	203	China-Singapore	41.67
11	Canada	187	France-Spain	40.75
12	Sweden	168	France-Germany	36.62
13	Switzerland	150	Italy-England	33.33
14	Scotland	117	England-Spain	32.08
15	Denmark	108	Germany-Austria	30.20
16	Poland	94	China-England	29.58
17	Singapore	80	Germany-Switzerland	28.32
18	India	78	France-Italy	26.12
19	Brazil	75	Italy-Switzerland	25.33
20	Netherlands	75	U.S.A.-Germany	24.25

https://doi.org/10.5281/zenodo.4550616

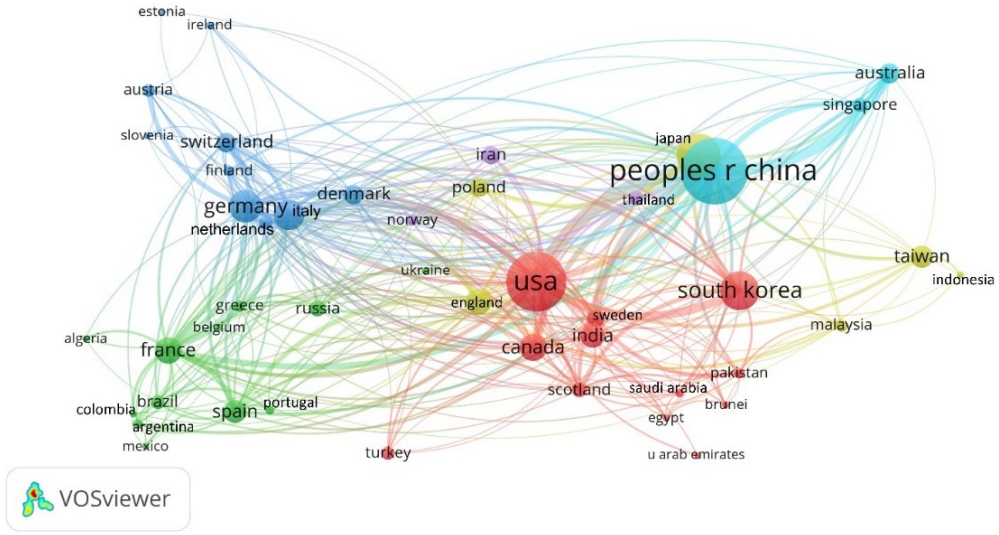

Figure 2: Co-authorship network visualisation of countries with a minimum of 20 publications on SOFC research within the time span 2000 to 2019.

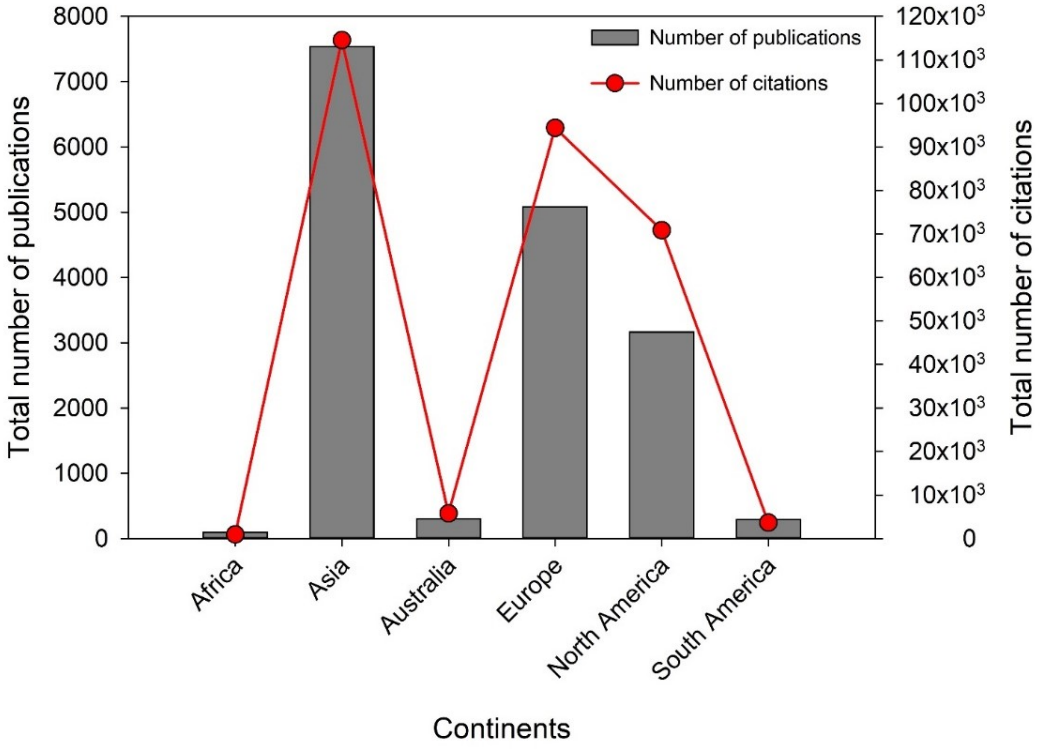

Figure 3: The activities of continents in SOFC research within 2000 to 2019.

One of the factors that influences the development of SOFC technologies in any country will be government policies, which help in changing the public perception and acceptability, but also the economic viability of technologies. For instance, Japan is among the top ranked countries that are actively involved in SOFC development. Due to the scarcity of indigenous energy resources, Japan has been conducting an intensive funding programme in alternative and efficient energy solutions over the past two decades, in which SOFC gained focus in the country. Today, Japan is strongly established in SOFC technologies. SOFC technologies became popular owing to the flexibility of fuels,

specifically being able to use natural gas with no or minimal processing. The least participating countries, especially the developing countries, must take decisive steps and efforts to invest heavily in hydrogen, green fuel, and fuel cell technologies as an alternative to the conventional fossil fuels based energy system in order to join the efforts for tackling climate change.

High productivity is seen in continents such as Asia, Europe, and North America in SOFC development (Figure 3) and is mainly due to factors such as government policies which include strict regulations on emission of greenhouse gases, market introduction incentives, and funding in research relating to green energy [23,24]. For instance, the U.S.A. recently announced a new funding through the US Department of Energy's Office of Fossil Energy of up to $30 million for the improvement of small-scale SOFC systems and hybrid energy systems [25]. This fund will further strengthen the participation of the U.S.A., which is already among the leading countries in SOFC research. Similarly, China, Japan, and other leading countries have a set of incentives in the form of subsidies to local manufacturers and key players in the energy sector, which has helped in consolidating their progress in advanced energy research and associated technologies over the years. Lastly, there is a strong collaboration among the leading countries as seen in the visualisation network represented in Figure 2 and Table 1. Meanwhile, the aforementioned factors, especially research collaboration, are lacking in African countries, which is why the region has low productivity in this aspect.

Notwithstanding, it will be economically important to look into the low participating continents, especially Africa, considering the enormous natural gas present in the region. The competition among the leading continents may get stiffer due to the projected boom in the market size of SOFC. The penetration of SOFC technology into Africa will require strong collaboration among the large international and local companies, an increased funding into SOFC research, government policies and incentives, and increased awareness in order to boost the acceptability of the technology. A successful penetration will greatly influence the global market size since Africa has the advantage of large population, which means potentially high selling volume of SOFC units in the region.

3.3 Participation of institutions

The initial result obtained from WoS indicated that 3,674 institutions participated in SOFC research. This value dropped to 3,624 after vetting the results due to some repeated institutions whose names appeared in different variations. The Chinese Academy of Science had the highest productivity in terms of number of publications followed by the University of Science & Technology China, Harbin Institute of Technology, and Forschungszentrum Juelich (Table 2). Overall, the highly active institutions were found in Asia, Europe, USA, and Australia while none of the institutions in Africa made it to the top 20. Moreover, the collaboration strengths of the various institutions followed a similar pattern as shown in Table 3. This trend further iterates the importance of collaboration in the development of SOFC. In order to demonstrate the general importance of cooperation, the following partnerships that were announced in 2016 shall be listed here, although they mostly do not refer to SOFC technology [26]:

- PowerCell Sweden AB and Swiss Hydrogen SA collaborated to manufacture and sell fuel cell systems according to the PowerCell's stacks for mobile and stationary applications.
- Ballard Power Systems and Toyota Tsusho Corporation partnered to enable Toyota Tsusho Corporation be a distributor of Ballard fuel cell products in Japan through 2020.

- US Hybrid and Sumitomo Corporation entered into a partnership for the increase in production capacity of fuel cell stacks for fuel cell engines and integrated vehicle technologies.
- IMS ECUBES and Arcola Energy announced a Joint Venture to develop hydrogen and fuel cell energy and mobility solutions for Europe and South Asia.
- Honda R&D Co. Ltd. and Ceres Power started collaborating to develop SOFC stacks using Ceres Power's Steel Cell technology.

The collaborative plan between Ceres Power, a UK-based company in the frontline of SOFC technology, and Weichai Power, a leading automobile and equipment manufacturing company in China, first announced in May 2018, has been concluded. The agreement included the commitment to establish a fuel cell manufacturing joint venture (JV) in Shandong Province, China [27]. Ceres Power also entered into a licensing agreement estimated as £8 million with Doosan Corporation, a Korea-based company in July 2019 to jointly develop SOFC power systems that are expected to balance the excess demands of S.Korea's commercial building market [22]. In the same month of July 2019, two companies in Japan, Mitsubishi Hitachi Power Systems and NGK Spark Plug entered into a partnership for the manufacturing and sale of cylindrical cell SOFC stacks which are the main components in power generation systems [22]. It is noteworthy that the aforementioned partnerships are only a few of the numerous ones entered among large companies, which are mainly based in the continents that are highly active in SOFC research.

On the other hand, only few countries in Africa have been able to enter into partnerships with some of the leading companies in SOFC technologies. For example, U.S.A.-based Dominovas Energy entered into a partnership with Delphi Automotive Systems to provide a 3 MW electricity plant to the City of David (a public-private partnership) in the Democratic Republic of Congo by employing its modular, off-grid Rubicon™ solid oxide fuel cell system [28]. In 2016, Dominovas Energy and a South Africa-based Edison Power Group, in partnership with Austria-based AVL GmbH (for system integration) and Italy-based SOLIDpower (for stack supply), launched a 50 kW unit RUBICON™ system in South Africa [29]. Dominovas Energy and Edison Power Group also entered into a partnership to develop a fuel cell system with a minimum of 50 MW capacity operating in sub-Saharan Africa over a period of 5 years, based on Dominovas Energy's RUBICON™ fuel cell system [29].

For a rapid development to take place in the area of SOFC technologies globally, considerable financial incentives, and strong partnership is required. In particular, African countries must implement policies that encourage technologies that enable the scale up of renewable energy supply, the introduction of more efficient energy conversion, and discourage energy from fossil fuels. In addition, more collaboration and technology transfer should be encouraged among the leading institutions or companies and the low participating countries to ensure speedy progress in SOFC research worldwide. It is worth mentioning that some challenges are encountered when conducting a bibliometric analysis. First, institution names can appear in both full and abbreviated forms which will caused WoS to treat them as separate institutions, which can lead to false positive results [20]. Secondly, not all journals are indexed in WoS. Consequently, those journals not indexed in WoS will be unintentionally omitted in a bibliometric analysis where WoS database was employed. The authors identified these challenges and ensured that they are minimised to an acceptable level.

Table 2: Publication status of the top 20 institutions that are actively participating in SOFC research according to number of publication within the timeline 2000 to 2019.

S/N	Names of Institutions	Country of Institution	Total Publications (TP)	Total Citations (TC)
1	Chinese Acad Sci	China	406	6908
2	Univ Sci & Technol China	China	349	8102
3	Harbin Inst Technol	China	277	4723
4	Forschungszentrum Julich	Germany	277	6744
5	Huazhong Univ Sci & Technol	China	268	4577
6	Natl Inst Adv Ind Sci & Technol	Japan	252	4527
7	Kyushu Univ	Japan	250	3390
8	Imperial College London	England	248	6946
9	Univ South Carolina	U.S.A.	215	4696
10	Tech Univ Denmark	Denmark	207	4966
11	Curtin Univ	Australia	194	3333
12	Georgia Inst Technol	U.S.A.	176	6245
13	Korea Inst Sci & Technol	S.Korea	162	2712
14	Pacific Nw Natl Lab	U.S.A.	159	4016
15	Jilin Univ	China	151	3957
16	Nanjing Univ Technol	China	146	4415
17	Nanyang Technol Univ	Singapore	145	5435
18	Tsinghua Univ	China	138	2434
19	Univ St Andrews	Scotland	136	3819
20	Univ Alberta	U.S.A.	130	2940

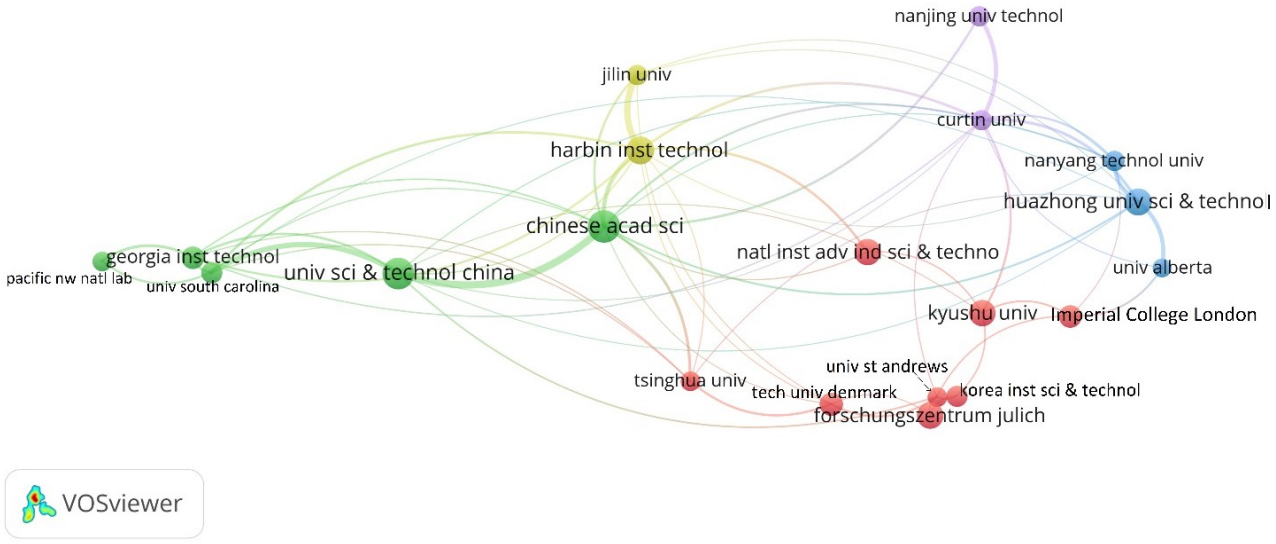

Figure 4: Co-authorship network of the top 20 institutions actively participating in SOFC research according to number of publication within the timeline 2000 to 2019.

Table 3: Top 20 institutions with strong collaboration strengths in SOFC research within the timeline 2000 to 2019.

S/N	Institutions	Country of Institution	Total link strength
1	Chinese Acad Sci	China	239
2	Univ Sci & Technol China	China	211
3	Harbin Inst Technol	China	163
4	Huazhong Univ Sci & Technol	China	161
5	Natl Inst Adv Ind Sci & Technol	Japan	152
6	Curtin Univ	Australia	133
7	Forschungszentrum Julich	Germany	130
8	Korea Inst Sci & Technol	South Korea	124
9	Georgia Inst Technol	U.S.A.	120
10	Jilin Univ	China	120
11	Kyushu Univ	Japan	113
12	Csic	Spain	103
13	Tsinghua Univ	China	98
14	Imperial College London	England	94
15	Nanyang Technol Univ	China	94
16	Univ St Andrews	Scotland	94
17	Tech Univ Denmark	Denmark	92
18	Univ S Carolina	U.S.A.	87
19	Chulalongkorn Univ	Thailand	87
20	Univ Alberta	U.S.A.	82

4. Conclusions

A bibliometric analysis was conducted to identify the impacts of collaborations in the development of solid oxide fuel cell technologies within the timeline 2000 to 2019. It was found that the most productive countries were from Asia, Europe and North America, while African countries had the least productivity in SOFC research. Findings further revealed that the leading countries have strong collaboration among themselves, which is most likely responsible for the very high productivity. The level of partnership between the top countries and institutions with those in Africa is very low which is due to unfavourable government policies and fear of uncertainties in investment. Therefore, the governments of the countries low in participating numbers must implement policies that enable investment in SOFC technologies and support international collaboration.

References

[1] IEA, Global energy demand grew by 2.1% in 2017, and carbon emissions rose for the first time since 2014, (2018). https://www.iea.org/news/global-energy-demand-grew-by-21-in-2017-and-carbon-emissions-rose-for-the-first-time-since-2014 (accessed December 17, 2019).

[2] A. Wahab, A. Hassan, M.A. Qasim, H.M. Ali, H. Babar, M.U. Sajid, Solar energy systems – Potential of nanofluids, J. Mol. Liq. 289 (2019) 111049.

[3] M. Shoaib, I. Siddiqui, S. Rehman, S. Khan, L.M. Alhems, Assessment of wind energy potential using wind energy conversion system, J. Clean. Prod. 216 (2019) 346–360.

[4] E. Rosales-Asensio, D. Borge-Diez, J.-J. Blanes-Peiró, A. Pérez-Hoyos, A. Comenar-Santos, Review of wind energy technology and associated market and economic conditions in Spain, Renew. Sustain. Energy Rev. 101 (2019) 415–427.

[5] I. Staffell, D. Scamman, A.V. Abad, P. Balcombe, P.E. Dodds, P. Ekins, N. Shah, K.R. Ward, The role and status of hydrogen and fuel cells across the global energy system, Energy Environ. Sci. (2018).

[6] P.E. V. De Miranda, Hydrogen energy: Sustainable and perennial, in: Science and Engineering of Hydrogen-Based Energy Technologies, Academic Press, 2018: pp. 1–38.

[7] D.K. Niakolas, M. Daletou, S.G. Neophytides, C.G. Vayenas, Fuel cells are a commercially viable alternative for the production of “clean” energy, Ambio. 45 (2016) 32–37.

[8] M._ Inci, O. Türksoy, Review of fuel cells to grid interface: Configurations, technical challenges and trends, J. Clean. Prod. 213 (2019) 1353–1370.

[9] R.M. Ormerod, Solid oxide fuel cells, Chem. Soc. Rev. 32 (2003) 17–28.

[10] A. Aarva, S.J. McPhail, A. Moreno, From Energy Policies to Active Components in Solid Oxide Fuel Cells: State-of-the-Art and the Way Ahead, ECS Trans. 25 (2019) 313–322.

[11] X. Wang, Solid Oxide Fuel Cell, in: K. Kuang, K. Easler (Eds.), Fuel Cell Electronics Packaging, Springer US, Boston, MA, 2007: pp. 97–111.

[12] K. Lee, S. Kang, K.Y. Ahn, Development of a highly efficient solid oxide fuel cell system, Appl. Energy. 205 (2017) 822–833.

[13] M. Rafique, H. Nawaz, M. Shahid Rafique, M. Bilal Tahir, G. Nabi, N.R. Khalid, Material and method selection for efficient solid oxide fuel cell anode: Recent advancements and reviews, Int. J. Energy Res. 43 (2019) 2423–2446.

[14] M.P. Carpanese, M. Panizza, M. Viviani, E. Mercadelli, A. Sanson, A. Barbucci, Study of reversible SOFC/SOEC based on a mixed anionic-protonic conductor, J. Appl. Electrochem. 45 (2015) 657–665.

[15] S.J. McPhail, B. Conti, J. Kiviaho, The Yellow Pages of SOFC Technology - International Status of SOFC deployment 2017, VTT Technical Research Centre of Finland Ltd, Finland, 2017.

[16] I. Staffell, D. Scamman, A. Velazquez Abad, P. Balcombe, P.E. Dodds, P. Ekins, N. Shah, K.R. Ward, The role of hydrogen and fuel cells in the global energy system, Energy Environ. Sci. 12 (2019) 463–491.

[17] D. Bhattacharyya, R. Rengaswamy, A review of solid oxide fuel cell (SOFC) dynamic models, Ind. Eng. Chem. Res. 48 (2009) 6068–6086.

[18] S.H. Zyoud, W.S. Waring, S.W. Al-Jabi, W.M. Sweileh, Global cocaine intoxication research trends during 1975-2015: A bibliometric analysis of Web of Science publications, Subst. Abus. Treat. Prev. Policy. 12 (2017) 1–15.

[19] L. Šubelj, D. Fiala, M. Bajec, Network-based statistical comparison of citation topology of bibliographic databases, Nature Publishing Group, 2015.

[20] W.M. Sweileh, A bibliometric analysis of global research output on health and human rights (1900–2017), Glob. Heal. Res. Policy. 3 (2018) 30.

[21] O. Omoregbe, A.N. Mustapha, R. Steinberger-Wilckens, A. El-Kharouf, H. Onyeaka, Carbon capture technologies for climate change mitigation: A bibliometric analysis of the scientific discourse during 1998–2018, Energy Reports. 6 (2020) 1200–1212.

[22] Fortune Business Insights, Solid Oxide Fuel Cell Market to reach USD 2.00 Billion by 2026; Growing Need to Reduce GHG Emissions to Boost the Market: Fortune Business Insights, GlobeNewswire News Room. (2019). https://www.globenewswire.com/news-release/2019/12/16/1960725/0/en/Solid-Oxide-Fuel-Cell-Market-to-reach-USD-2-00-Billion-by-2026-Growing-Need-to-Reduce-GHG-Emissions-to-Boost-the-Market-Fortune-Business-Insights.html (accessed July 20, 2020).

[23] MarketsandMarkets, Solid Oxide Fuel Cell Market by Type (Planar and Tubular), Application (Power Generation, Combined Heat & Power, and Military), End-Use (Data Centers, Commercial & Retail, and APU), Region (North America, Asia Pacific, and Europe) - Global Forecast to 202, Solid Oxide Fuel Cell Mark. (2017). https://www.marketsandmarkets.com/Market-Reports/solid-oxide-fuel-cell-market-39365796.html (accessed August 1, 2020).

[24] E. Weidner, R. Ortiz Cebolla, J. Davies, Global deployment of large capacity stationary fuel cells, 2019.

[25] DOE, DOE to Provide $30 Million to Develop Small-Scale Solid Oxide Fuel Cell Systems and Hybrid Energy Systems, (2020). https://www.energy.gov/articles/doe-provide-30-million-develop-small-scale-solid-oxide-fuel-cell-systems-and-hybrid-energy (accessed July 22, 2020).

[26] S. Curtin, J. Gangi, Fuel Cell Technologies Market Report 2016, 2017. doi:Department of Energy.

[27] Ceres Power, Weichai finalise strategic collaboration, JV deal, Fuel Cells Bull. 2019 (2019) 11.

[28] Dominovas signs MW SOFC deals in Congo, joins Power Africa, Fuel Cells Bull. 2015 (2015) 7–8.

[29] Dominovas launches first Rubicon SOFC project in South Africa, Fuel Cells Bull. 2016 (2016) 6–7.

Keywords: EFCF2020, SOx
Session A08: System design & performance

A0911

Lifetime prediction of SteelCell® stacks using advanced multiphysics modelling

Ameir Mahgoub, Robert Leah, Duncan Gawel, Gavin Reade, Jack Howlett, Nick Lawrence, Subhasish Mukerjee, Mark Selby
Ceres Power Ltd.
Viking House, Foundry Lane, RH13 5PX Horsham/UK

Contact authors: www.EFCF.com/ContactRequest

Abstract

A major challenge in the development of SOFC stacks designed for long operating lives of the order of 50-100kh is predicting through-life performance without running durability tests under a particular set of operating conditions for 5-10 years. Whilst this is the final aim it is not practical for system design purposes or in the situation where product lifecycles are much longer than product development cycles. A particular challenge is that Ceres Power provides stack technology to multiple customers, most of whom have their own requirements for stack operating conditions, which means that degradation rates measured under one set of operating conditions are not necessarily directly applicable to a different set, and undertaking long term verification testing under every set of stack boundary conditions is not practical.

To address this issue, Ceres Power has invested significant effort into understanding mechanisms of performance degradation at the fundamental cell level, generating models of degradation as a function of time, temperature and current density. Most degradation mechanisms observed are common to all SOFC cells, such as poisoning of both electrodes and increases in ohmic resistance due to oxide scale growth.

These degradation models are not in themselves sufficient to enable through life performance simulation, as in a full stack there are significant variations in temperature and local current density, meaning different areas of the cell will be degrading at different rates. In addition, because of performance degradation through life, significant changes in the local temperature and current density distribution may occur, and the stack will often generate more heat meaning the air flow and/ or inlet temperature will need to change to maintain the nominal stack temperature.

To allow simulation of these effects, a full multiphysics stack model has been developed using COMSOL Multiphysics, incorporating fluid dynamics, heat transfer, electrochemical and heterogeneous chemical reactions. The electrochemical model at start of life is calibrated from extensive experimental performance mapping using coupon cells with high resolution AC impedance spectroscopy, and the resulting full multiphysics stack model validated against test data from real stacks.

A dynamic solver has then been applied to the multiphysics model applying the models of cell degradation to be applied to a full stack, including changing the air flow through life to maintain a constant nominal stack temperature. The model has been validated against through-life performance tests. This is a powerful tool which allows rapid evaluation of the likely impact of operating a stack in a condition other than ones in which extensive test data already exist.

https://doi.org/10.5281/zenodo.4550634

Introduction

A considerable amount of work has been undertaken over the last few years to understand the performance degradation mechanisms of the Ceres Power metal-supported SteelCell® technology. The approach adopted has been broadly modelled on the Japanese NEDO project [1,2], although work has largely been undertaken internally at Ceres Power and not published.

The conclusions of that work to date are that Ceres technology is subject to similar performance degradation mechanisms to those widely reported in the literature for SOFC technology generally, and in the current generation of technology there are no technology-specific degradation mechanisms; those which have been identified in the past have been addressed by design changes to the cell/stack. Issues with substrate corrosion which have been widely reported for other metal-supported designs are not present in the SteelCell design. As reported elsewhere [3], Ceres technology is highly resistant to REDOX and thermal cycling by comparison with other SOFC designs due primarily to the inherent mechanical robustness of the metal supported design and the low operating temperature (<650°C). Also, primarily because of the low operating temperature performance degradation due to microstructural changes in the anode is negligible.

The latest V5 generation of SteelCell® technology has been demonstrated to have sufficiently low performance degradation for predicted lifetime to not be a limiting factor on commercialization, with experimental verification up to 27kh on a single stack, and multiple stacks at 20-25kh. The work described in this paper is focused on accelerated validation of operation under different operating conditions and identification of scope for future improvements, as the technology is already sufficiently robust and reliable for commercialization

As with most fuel cell developers, Ceres Power makes extensive use of AC impedance spectroscopy (ACIS) to characterize the breakdown of cell resistance and how it changes over time. Resistance contributions are broadly separated into ohmic resistances (non frequency-dependent) and frequency dependent polarization resistances. The main causes of performance degradation identified in SteelCell technology are.

- Ohmic resistance degradation (cathode current collection resistance degradation, electrolyte ionic conductivity degradation and anode-substrate interfacial resistance degradation primarily).
- Anode-side polarization resistance degradation through sulphur poisoning of internal steam reforming (the anode electrochemical reaction is fairly sulphur tolerant, as has been reported elsewhere [4] for Ni/CGO-based anodes).
- Cathode polarization resistance degradation through strontium segregation and poisoning by sulphur dioxide and chromium.

Mathematical models have been generated for resistance degradation as a function of time, current density and temperature based on long-duration short (17-layer) stack tests which readily allow ACIS measurements to be performed regularly on all layers, and are relatively isothermal. The functions chosen can be extrapolated to much longer test durations, with increasing uncertainty the further the functions are extrapolated beyond the experimental data on which they were calibrated.

A challenge common to the development of most fuel cell systems for stationary power generation is that the design life of the system is typically 60-100kh, which is commercially

https://doi.org/10.5281/zenodo.4550634

impractical to verify experimentally within an acceptable timescale, so lifetime prediction inevitably involves a significant degree of extrapolation of data.

A further challenge related to lifetime prediction on full-size stacks operating in systems is that as the stack performance degrades, the operating voltage of the stack falls increasing the internal heat generation. To maintain the stack at its desired operating temperature, this needs to be compensated for by either increasing the cathode air flow or increasing the temperature gradient across the stack. Both control reactions will potentially change the internal temperature and current density distribution within the stack, and the degradation rate assuming the local resistance degradation rate varies with local temperature and current density. In addition, changing the cooling air flow through the stack has an impact on the net power output of a system by changing the parasitic power demand from the air blower, which potentially means the net performance loss from stack degradation is greater than the loss of stack power output alone.

It has also been established that polarization resistance degradation mechanisms related to poisoning/strontium depletion do not affect the cell uniformly, but preferentially affect the area of the electrodes nearest the air/fuel inlets first, gradually moving along the direction of gas flow with time as the electrodes become saturated with poison. This observation is in line with reports in the literature [5] in other SOFCs about the effect of sulphur on perovskite cathodes. This means that electrode degradation is not spatially uniform, but forms a moving front with the performance degradation being much greater at the inlet region of the cell. This again will distort the temperature and current density profile within the stack with time. Modeling and experimental testing has however demonstrated that provided the specified requirements for reactant feed quality are maintained these mechanisms should not be life-limiting.

The implication of spatially-dependent cell performance degradation is that a high-resolution mathematical model is required to predict through life performance, capturing most of the physics occurring within the stack both at start-of-life and through life. This is particularly useful for screening new stack designs and/or making predictions about the implications of changing the stack operating boundary conditions on degradation.

1. Scientific Approach

A high resolution multiphysics model of a Ceres Power stack has been developed using the COMSOL Multiphysics simulation package. The model uses a spatially averaged approach in the active volume of the stack to avoid computationally prohibitive simulation of the gas flows, heat flows and electrochemistry of each individual layer of a large stack, whilst still producing physically realistic predictions of the internal temperature and cell voltage profiles.

The model can be run at various levels of resolution between ‘box model’ where the active area of the stack is treated as a box with adiabatic thermal boundaries, and full simulation involving the actual stack geometry, full fluid dynamics in the manifolds and heat transfer through the stack walls. The full set of physics/chemistry simulated by the model is listed below.

- Turbulent computational fluid dynamics of the air and fuel flows in the manifolds.
- Porous media simulation of the fluid dynamics within the active area of the stack.
- Local current density.

- Local cell resistance.
- Local heat release due to the electrochemical reaction
- Local heat absorption due to the internal steam reforming reaction, with a kinetic model.
- Local gas composition in the air and fuel channels.
- Heat transfer between the air and fuel and the solid components of the stack.
- Heat transfer through conduction within the solid components of the stack.
- Heat transfer between the stack walls and the surroundings.

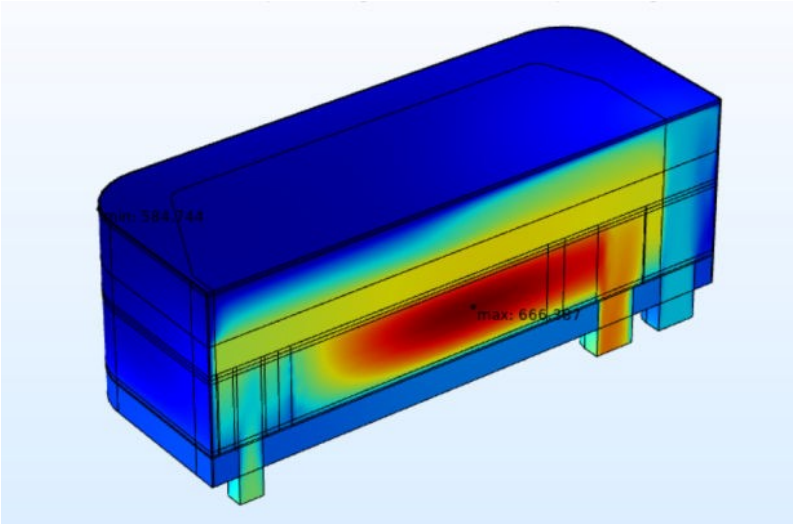

Figure 1: Example multiphysics simulation of a 17- layer short stack in a furnace showing 3D temperature profile. The stack is symmetrical along its centerline so only half the stack is meshed.

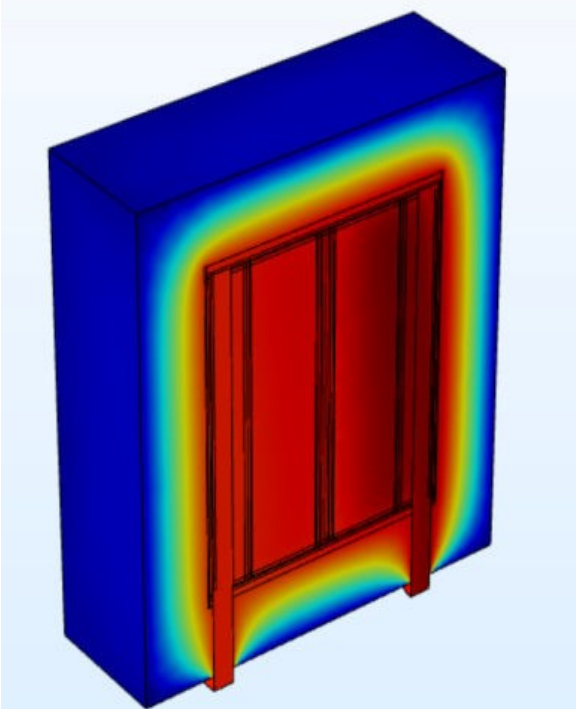

Figure 2: Example multiphysics simulation of a 250-layer 5kW stack surrounded by thermal insulation showing 3D temperature profile.

https://doi.org/10.5281/zenodo.4550634

The electrochemistry model incorporated into the multiphysics model is calibrated from numerous button-cell measurements of the area-specific resistance (ASR) of the cell as a function of temperature, current density and hydrogen/oxygen partial pressures. The use of button cell measurements means the intrinsic cell performance can be measured independent of reactant utilization and temperature effects present in a stack.

The kinetics of internal steam reforming and the water-gas shift reaction have also been calibrated from experimental data.

The multiphysics models have been extensively validated at start-of-life against heavily instrumented experimental stacks, so there is good confidence in the accuracy of model predictions.

The initial multiphysics model is essentially a steady-state model. To simulate degradation some degree of dynamic modelling is required. An issue arises in that a degradation simulation requires being able to simulate the entire operating life of the stack in a reasonable computation time, and thus the model needs to be able run at thousands of times faster than real time. As many of the processes within the stack have very fast dynamics which would be impossible to simulate whilst also simulating tens-of-thousands of hours of operation, these have essentially been treated as instantaneous.

The only equations with a time dependent term are the heat balance of the solid parts of the stack and the equations governing degradation. In addition, to be realistic, it is necessary to modify the stack boundary conditions through simulated time to counteract the effect of increased heat release as the stack degrades to maintain a constant temperature. A simulated control loop using proportional control, with a tolerance band to limit the frequency of control interventions, has been implemented to achieve this This approach has been shown to achieve acceptably stable simulated stack temperatures as a function of time whilst allowing practical simulation of 60kh of 5kW stack operation within a few days of CPU time.

Ohmic resistance degradation is simulated using an empirical model calibrated from multiple short stack tests giving ohmic resistance change as a function of temperature, current density and time.

Polarization resistance degradation through electrode poisoning is simulated by a moving front which progresses along the active cell area with time as the electrode becomes deactivated, at a rate calibrated from experimental measurements of cathode and steam reforming degradation as a function of temperature, reactant flow and poison concentration.

https://doi.org/10.5281/zenodo.4550634

2. Results and Discussion

Figure 3 shows the predicted ohmic resistance degradation (in arbitrary units) as a function of time, temperature and current density over a range of 166-255 $mAcm^{-2}$, calibrated from experimental measurements for up to 25kh. Note that degradation follows a parabolic pattern, and long-term degradation rates are very low.

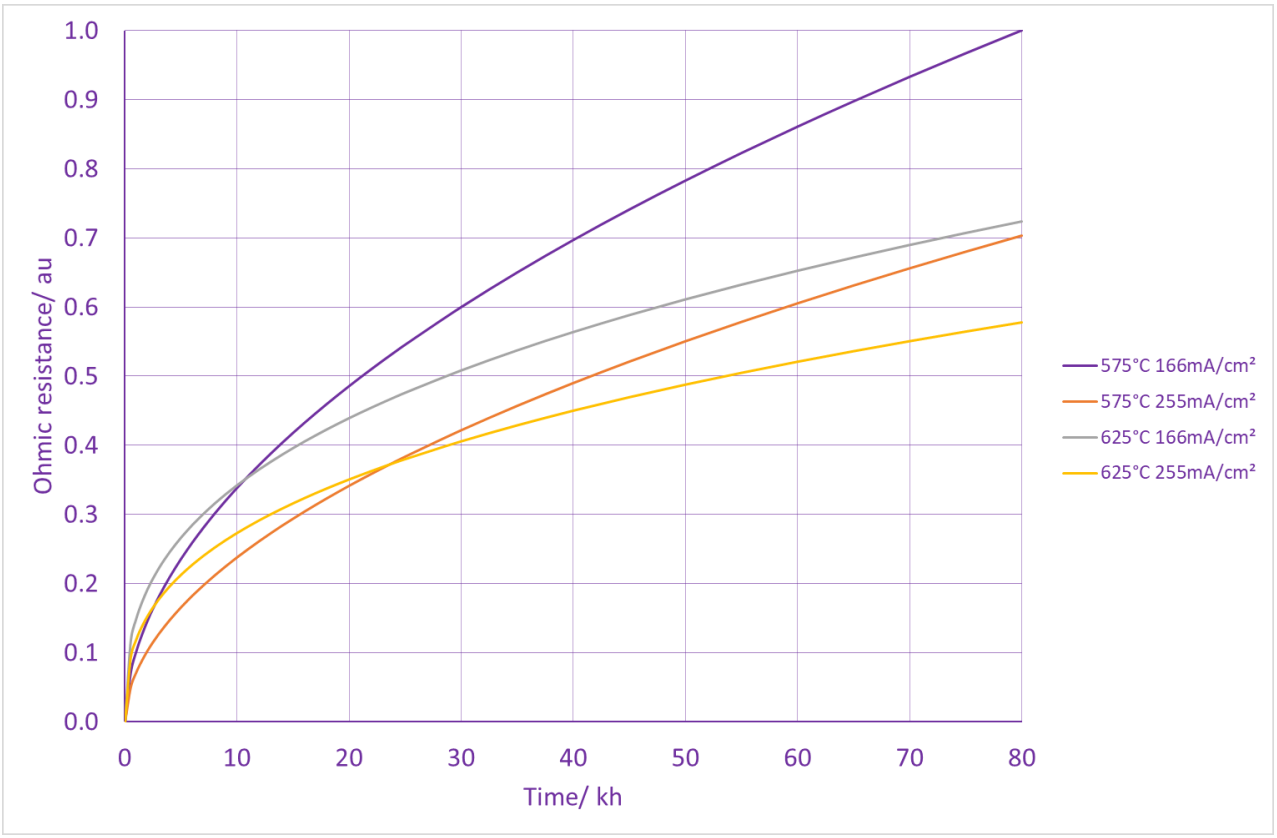

Figure 3: Predicted normalized ohmic resistance degradation as a function of temperature and current extrapolated to 80kh

https://doi.org/10.5281/zenodo.4550634

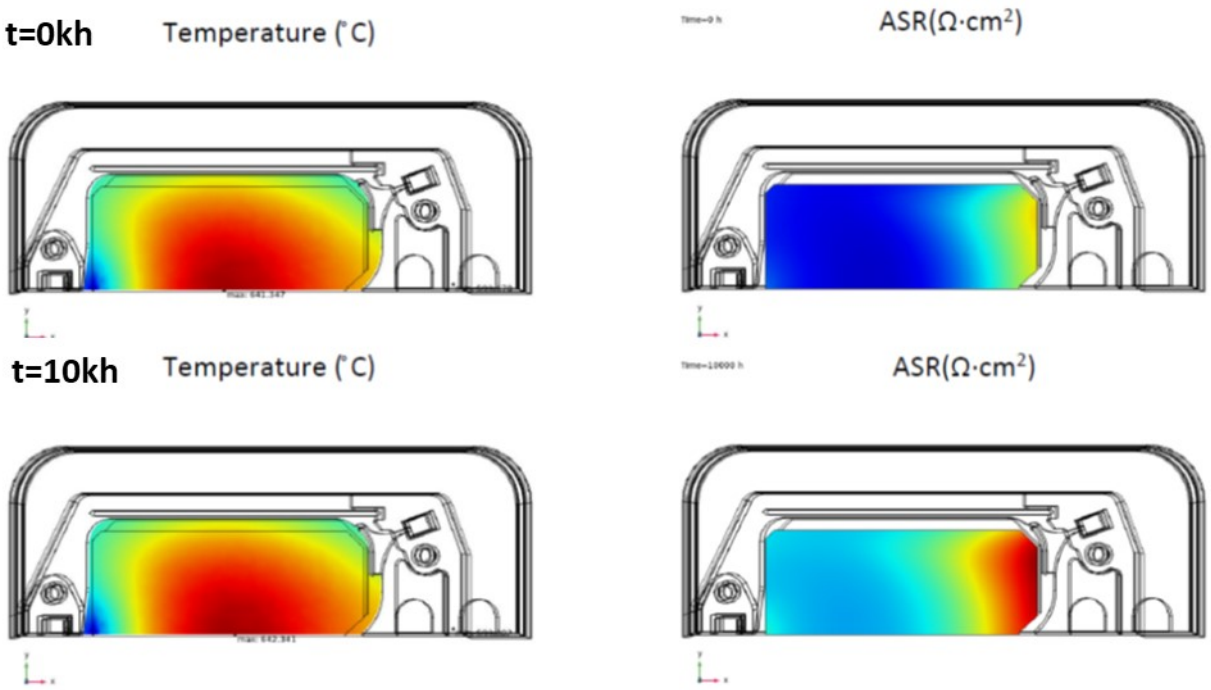

Figure 4: Model output for a 1kW-type short stack simulation showing predicted local temperature and ASR at start of life (top) and after 10kh of operation (bottom) due to ohmic resistance degradation.

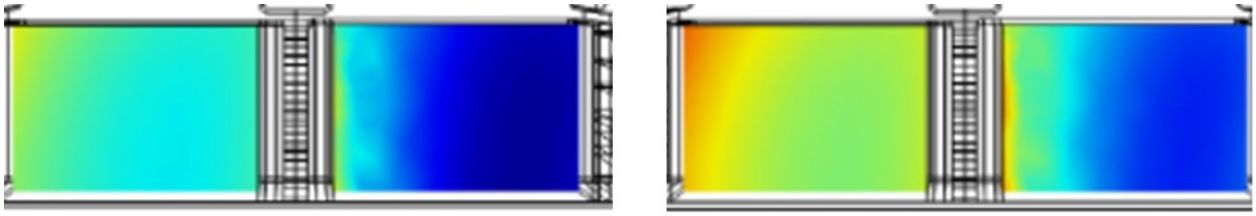

Figure 5: Predicted change in local ASR due to ohmic resistance degradation in middle cell of 5kW stack between start of life (left) and 60kh of operation (right).

Figure 4 shows the predicted change in local ASR and temperature for a 1kW-type short stack over 10kh of operation, applying the ohmic resistance degradation model shown in Figure 3.

Figure 5 shows the equivalent predicted change in local ASR due to ohmic resistance degradation in a 5kW stack over 60kh of operation. In both Figure 4 and Figure 5 the same color scale has been used for both initial and degraded plots, with the values and geometric detail of the 5kW stack obscured for reasons of commercial confidentiality.

https://doi.org/10.5281/zenodo.4550634

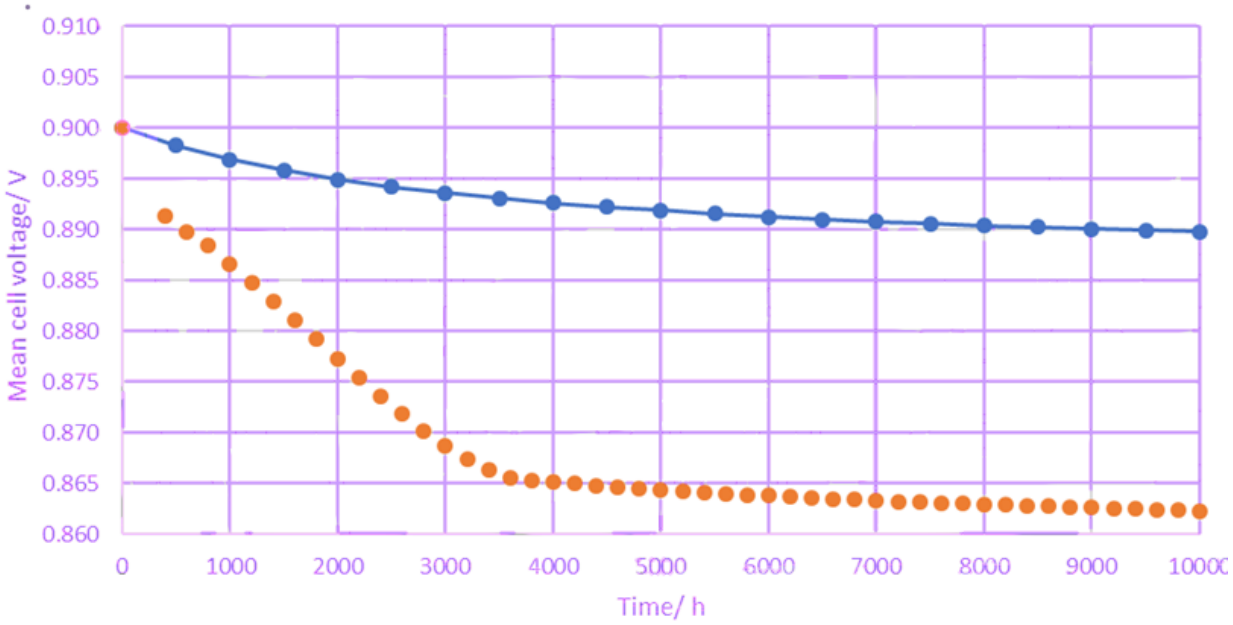

Figure 6: Predicted voltage degradation for a short stack with only ohmic resistance degradation (blue line) or ohmic resistance degradation and highly accelerated internal steam reforming poisoning due to H_2S.

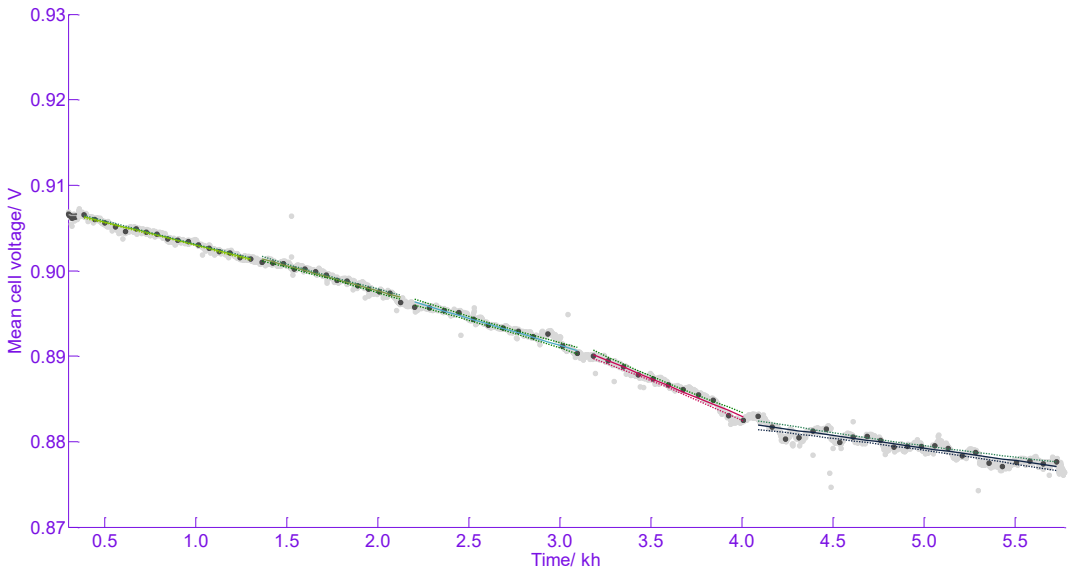

Figure 7: Experimental voltage degradation of a short stack with the equivalent level of H_2S in the fuel as the simulation.

Figure 6 shows the predicted effect of H_2S poisoning progressively deactivating the internal steam reforming of methane in a highly accelerated test where the H_2S concentration in the feed was well above the allowable limit for continuous operation. The blue line shows the predicted effect of ohmic resistance degradation only (the same data as shown in Figure 5), and ohmic resistance degradation with the addition of sulphur poisoning of the internal reforming reaction (orange line). The important point to note is that sulphur poisoning of the steam reforming reaction results in rapid initial degradation as the reforming kinetics are poisoned as a moving front along the fuel flow path of the cell. After around 4kh the degradation rate stabilizes as an equilibrium between the H_2S in the

https://doi.org/10.5281/zenodo.4550634

fuel and surface coverage on the catalyst is achieved, provided the H_2S concentration is low enough.

Figure 7 shows the equivalent experimental data at the same H_2S concentration in the fuel as the simulation in Figure 6. Note that it has been verified that poisoning is almost exclusively due to loss of internal steam reforming, as switching the fuel feed to the stack from reformate to hydrogen/steam whilst maintaining the same concentration of H_2S almost completely reverses the performance degradation, showing that the electrochemical reaction is largely unaffected.

3. Conclusions

An extensive program of work has identified the major performance degradation mechanisms in Ceres Power SteelCell® technology, which are broadly similar to other SOFC technologies. The most recent version 5 release of the technology, which is now in commercial production shows intrinsic performance degradation compatible with an 80kh operating life. Mathematical models of the performance degradation associated with the known degradation mechanisms

An advanced multiphysics model of Ceres stacks has been developed in COMSOL Multiphysics, and extensively validated against experimental data at start-of-life for several different stack variants.

Mathematical models of the main degradation mechanisms have been incorporated into the stack multiphysics model, and a dynamic solver has been developed which allows the stack temperature to be controlled by adjusting the cathode air flow as the heat release increases over simulated time due to degradation. This solver runs at up to 1000 times real-time, and allows simulation of the entire operating life of the stack in a few days CPU time. This allows the simulation of through-life stack performance under a variety of operating conditions, and allows the likely lifetime impact of stack design changes or changes in operating conditions to be rapidly evaluated, without the need for an expensive and time-consuming experimental validation program.

The lifetime degradation model is a valuable tool which Ceres can use to accelerate design and market launch of products utilizing SteelCell® technology for multiple customers with differing requirements and system architectures.

References

[1] H. Yokokawa, Achievements of NEDO Projects on SOFC Durability, ECS Trans., 78(1), 2211-2221, (2017).

[2] H. Yokokawa, A0304 Achievements of NEDO Durability Projects on SOFC Stacks in the Light of Physicochemical Properties (Diffusion and Chemical Reaction). Proceedings of the 13th European SOFC and SOE Forum, A03-32, (2018).

[3] R. Leah, M. Lankin, A. Bone, A. Selcuk, R. Pierce, L. Rees, D. Corcoran, P. Muhl, Z. Dehaney-Steven, C. Brackenbury and S. Mukerjee, Towards a Fully REDOX Stable SOFC: Cell Development at Ceres Power, ECS. Trans, 57(1), 849-856, (2013).

[4] P. Boldrin, E. Ruiz-Trejo, J. Mermelstein, J.M. Bermudez Menendez, T. Ramirez Reina and N.P. Brandon, Strategies for Carbon and Sulfur Tolerant Solid Oxide Fuel Cell Materials, Incorporating Lessons from Heterogenous Catalysis, Chemical Reviews, 116, 13633-13684, (2016).
[5] H. Iwai, K. Maejima, M. Kishimoto, M. Saito, H. Yoshida, H. Kishimoto, K, Yamaji and H. Yokokawa, Numerical Model of Sulfur Poisoning on LSCF Cathode and its Application to a 2-D Single Cell Simulation, ECS Trans. 91(1), 2115-2125, (2019).

Keywords: EFCF2020, SOx
Session A09: Emerging SO technology electrode investigation and modelling

https://doi.org/10.5281/zenodo.4550634

A0912

Model based engineering for improved SOFC system development

Raphael Neubauer, Thomas Krauss, Bernd Reiter, Juergen Rechberger
AVL List GmbH
Hans-List-Platz 1, AT-8020 Graz

Contact authors: www.EFCF.com/ContactRequest

Abstract

SOFC system development is an interdisciplinary task with some challenging goals to combine: fast heat-up, high efficiency, controllability, part-load operation, high power density, and on top - fuel flexibility. To reach all mentioned goals extraordinary expertise in a broad field of disciplines is required on system, sub-system, and component level. Hence, a model based engineering approach provides the possibility not only to achieve the goals, but also to achieve them in a more cost and time efficient manner by.

AVL has more than 50 years of experience in drive train and drive train component development. Using a classical automotive V-Model approach, the application requirements will be used as an input, to define the requirements of the SOFC system. All further development tasks are than coordinated by the model based engineering approach. For system simulation, AVL has a comprehensive library of physical models for all components necessary and typically used within SOFC/SOEC systems. This library can be easily updated by empirical models using neuronal networks (NN) for fast and efficient implementation. Using the AVL integrated open development platform (IODP) allows to better connect all mentioned and addition tools, such as active design of experiments (active DoE) and pinch analysis independently from both virtual and real world. Further, any experimental validations are fed back to the model based engineering approach via IODP. Having this feedback, the design process is driven by the latest performance data available. This approach provides the possibility of highly efficient SOFC system development from the first idea to serial production; limited only by the boundaries of the real world.

https://doi.org/10.5281/zenodo.4550656

Introduction

SOFC system development is an interdisciplinary task. When starting from a blank paper the following stages are usually be part of the development approach: (i) development of system architecture, (ii) process simulation, (iii) design integration, (iv) design implementation, (v) control strategy, and (vi) system validation. The described order does not necessarily have to follow the before mention one but is influenced by logical sequence and development philosophy. However, these different stages are usually processed by different people with different background and technical knowledge. Hence, a clear process and work flow, as well as good communication within the development team is crucial in order to keep the cost to a minimum and to avoid errors appear late in the development process. Because such late detected errors are typically more costly than errors corrected early in the process [1].

The broad scope of application of the SOFC/SOEC technology (e.g. combined heat and power, range extender, electrolyzer) [2] is further challenging because different applications require different system architectures, design integrations, design implementations, etc. with varying focuses on e.g. efficiency, durability, controllability, etc. This complex structure of influence parameters on the development approach require a more flexible work flow without losing its clear structure.

Modeling of complex systems such as SOFC/SOEC systems is crucial to better understand influence parameters and detect errors in an early stage of the development process. The modeling is thereby not limited to any level of detail but usually starts at high-level (very little details) and ends at low-level including already specific component characteristics such as mass, geometry, and e.g. temperature limitations. The change in level of detail can thereby take place at different stages within the development process and needs to be coordinated in an effective manner.

Within this paper the V-model from the automotive industry is used to describe and define the work flow for improved SOFC system development by using high- and low-level simulation at various stages.

1. Scientific Approach

Increasing complexity of SOFC systems require new development approaches. This becomes even clearer when considering the increasing demand in efficiency, controllability, and life time. Hence, traditional mechanical-oriented development approaches are overtaken. Such change in development strategies has already taken place in the automotive industries and new comprehensive approaches, such as the so-called V-model, have been implemented [3]. These comprehensive approaches are able to support simultaneous development of mechanical, electrical, and electronics systems including software. In addition, the support starts at system specification and follows all way down to component level and up again to the final product as illustrated in Figure 1.

Mathematical modeling of components and their thermodynamic behavior is crucial in order to connect the mechanical, electrical, and electronics systems from the very beginning of the development approach. AVL has more than 50 years of experience in drive train and drive train component development including the transition from mechanical-oriented development approaches to new comprehensive approaches. This experience is used to apply the V-model approach onto SOFC and SOEC system

https://doi.org/10.5281/zenodo.4550656

development where the integrated open development platform (IODP) of AVL supports to coordinate the different tasks.

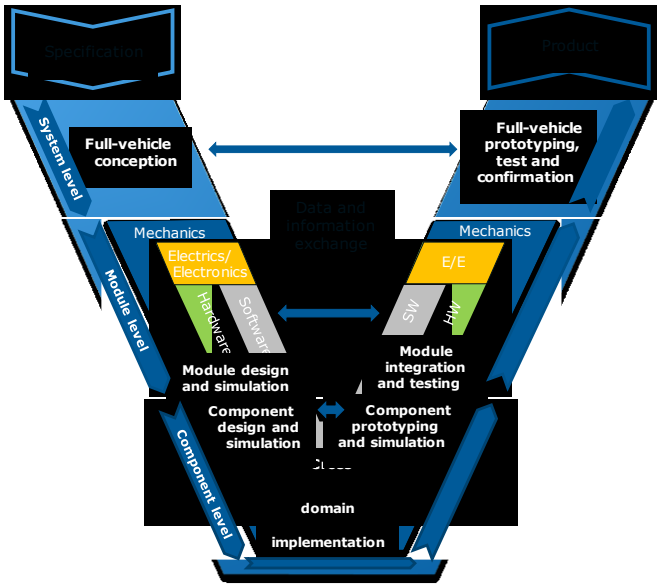

Figure 1. Exemplary V-model approach from the automotive industry

2. Simulations

For system simulation, a comprehensive library of physical models was developed in recent years and are constantly further developed and improved for all relevant components of SOFC and SOEC system. Within this library several models are available for the same component but with different degree of detail as illustrated in Figure 2.

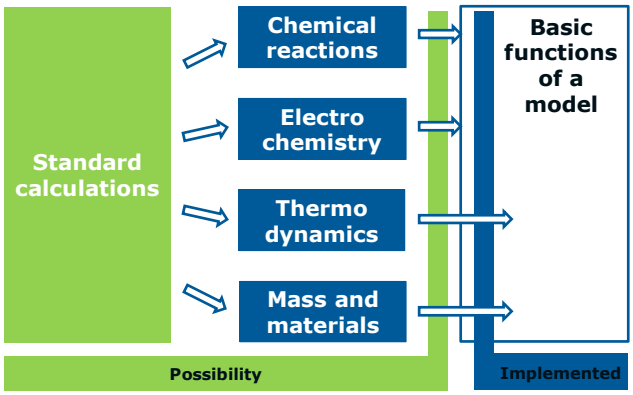

Figure 2. Structure and pathway to set up new models with different degree of detail

This is of great benefit in terms of model calibration and calculation time. At an early stage of a system development e.g. the mass and material properties of a heat exchanger might not be defined or available. However, system layout and heat management need to be developed and validated. At this stage, a simpler model without mass and materials (cf. Figure 2) can be used. However, all models of the same component do have the same interfaces and thus can be exchanged by each other within the development phase. This is important to feed back new boundaries from e.g. supplier or test results back into the simulation and development.

https://doi.org/10.5281/zenodo.4550656

Such system simulations are set up by just simply drag and drop the components into the simulation environment and connect them according to a flow chart. Additional tools allows to get out as much as possible from one simple simulation. This includes e.g. component specifications, empirical models of individual and system behavior, software verification and validation, optimized operations strategies, and many more. This already describes the importance of such mathematical models in order to connect the different branches within the V-model (cf. SW, HW, and mechanics in Figure 1).

3. Results

Within this chapter the above descripted approach and tools are presented by the example of three different cases: Case (i): Figure 3 shows the result of a stack test and the related simulation data based on a simple 0D model. The 0D model is a physical model considering cell number and active surface are as input and the area specific residence (ASR) as calibration parameter. The results show that the deviation between experimental data and simulation is within 2% and confirm that such a simplified stack model can be perfectly used for system architecture development.

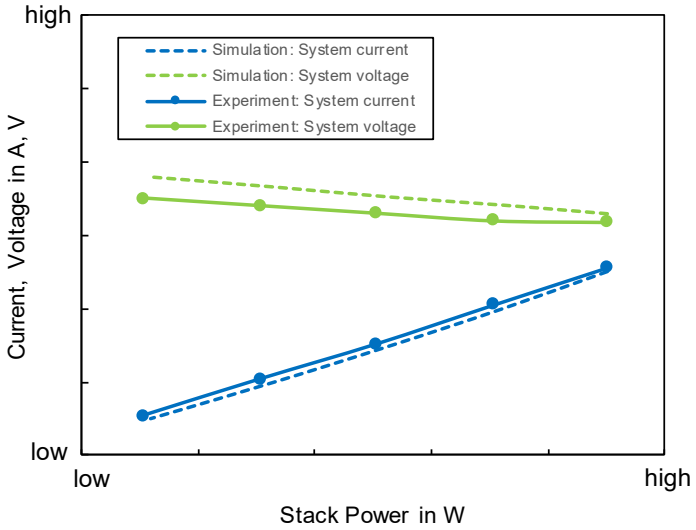

Figure 3. System current and voltage of a anode supported cell stack based on a real world experiment and virtual characterization via a simple 0D model

Case (ii): A routine of Computational Fluid Dynamics (CFD) and neuronal network (NN) is used within AVL for designing system specific ejectors for passive anode recirculation. This routine includes a 2D model for designing the nozzle geometry and a 2D CFD model for the whole ejector design (incl. nozzle, mixing chamber, and diffusor). Figure 4 shows a typical contour plot of the velocity and pressure within an ejector for a defined nozzle geometry. Out of several CFD simulations with different boundary conditions and design variations NN are used to identify the correlation between change of parameters and ejector performance.

https://doi.org/10.5281/zenodo.4550656

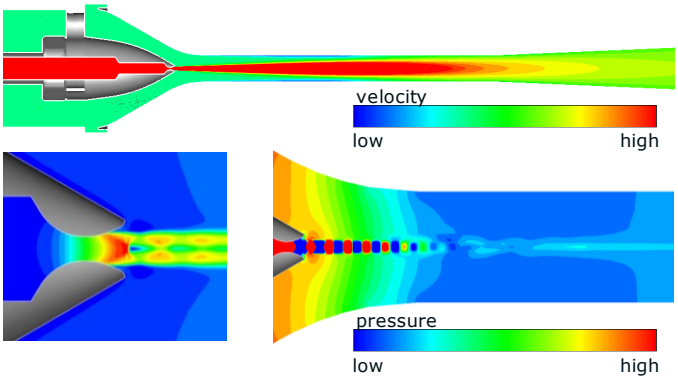

Figure 4. Typical contour plot of velocity and pressure within an ejector at full load operation point.

The output of the routine is a performance map of the ejector with any number of supporting points. Depending on the number of supporting points an empirical model (large number of supporting points) can be set up by NN. In addition, the performance map can also be used to calibrate a physical model (only few supporting points). Both can than be used within the system or sub-system simulation environment. This approach allows to even include complex components within plant and system models for control strategy and software validation and thus allows precise pre-calibration of a complex system and significant reduction on test bed operation and cost. In addition, the risk of component damage (in a thermal, mechanical or electric manner) is significantly reduced.

Case (iii): Within the development of a SOFC or SOEC system even small changes in efficiency of a component can have a significant influence on the overall efficiency, controllability, and life time of the overall system. Parameter studies are an excellent approach to evaluate and optimize system architectures and operating strategies. Figure 5 shows the outcome of such a parameter study for a 0D/1D system simulation including all relevant components. Within this study the efficiency of the air heat exchanger, the system pressure, as well as the stack temperature was varied via design of experiment (DoE).

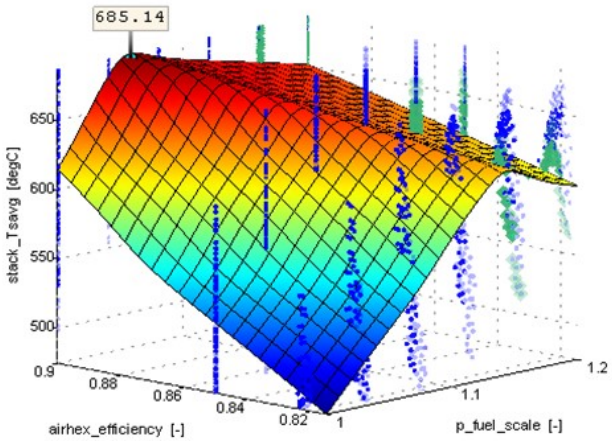

Figure 5. Parameter study on system level based on DoE

Such results, as shown in Figure 5, are indispensable for system optimization and identification of crucial control parameters to keep the system within its boundary conditions. Without the support of such a strong simulation tool and environment, the connection via the different branches within the V-model is not possible and significantly reduces the benefits of such a modern development approach.

https://doi.org/10.5281/zenodo.4550656

References

[1] Tom L. Roberts Jr., Micahel L. Gibson, Kent T. Fields, and R. Kelly Rainer Jr., Factors that Impact Implementing a System Development Methodology. IEEE Transactions of Software Engineering, vol. 24, no. 8, August 1998

[2] F. Ramadhani, M.A. Hussain, M. Mokhlis, S. Hajimolana, Optimization strategies for Solid Oxide Fuel Cell (SOFC) application: A literature survey, Renewable and Sustainable Energy Reviews, 76, 2017, 460-484

[3] Mario Hirz, An approach supporting integrated modeling and design of complex mechatronics products by the example of automotive applications, July 2018

Keywords: EFCF2020, SOx
Session A09: Emerging SO technology electrode investigation and modelling

https://doi.org/10.5281/zenodo.4550656

A1212

Sn Electrodeposition on Gas Diffusion Electrodes for the Electrochemical CO_2 Reduction

Mila Manolova(1), Renate Freudenberger(1), Joachim Hildebrand(2), Elias Klemm(2), Fabian Bienen(3), Dennis Kopljar(3), Norbert Wagner(3)
(1) fem - Research Institute for Precious Metals & Metals Chemistry
Katharinenstrasse 17, D-73525 Schwäbisch Gmünd/Germany
(2) ITC - Institute of Chemical Technology, University of Stuttgart
Pfaffenwaldring 55, D-70569 Stuttgart/Germany
(3) DLR – German Aerospace Center, Institute of Engineering Thermodynamics
Pfaffenwaldring 38-40, D-70569 Stuttgart/Germany

Contact authors: www.EFCF.com/ContactRequest

Abstract

The electrochemical reduction of CO_2 to diverse useful chemical products is a promising way to transform chemical industry to CO_2-neutral production. The gas diffusion electrodes (GDE), which enhance the gas/liquid and the liquid/solid interface tremendously, are very suitable for the CO_2 electroreduction. Even if no real contact of all three phases – gas, liquid, solid – occurs it is often referred to as triple-phase-boundary (TPB). This term will also used throughout this paper because even if not entirely correct it is well-established in literature. The high diffusivity of gaseous CO_2 and shorter diffusion lengths of solved CO_2 in such electrodes enable the utilization of high process current densities. Tin based catalysts are of interest for CO_2 electroreduction due to the low cost, non-toxic properties and ability to produce formic acid/formate at high selectivity.
In this presentation we will show the electrochemical deposition of Sn onto commercial and in-house fabricated carbon based GDEs from different electrolytes. Focused ion beam (FIB) etching was utilized to build a 3D model of the porous GDE. Scanning electron micrographs (SEM) of the electrodeposits showed that different layer morphologies are attainable by changing the deposition mode. A new method was developed for cleaning the GDE after electrochemical deposition. The distribution of Sn throughout the thickness of the GDE was investigated with computer tomography (CT). The initial electrochemical characterization tests of the Sn-loaded GDE, under laboratory operating conditions demonstrated promising results.

https://doi.org/10.5281/zenodo.4550671

Introduction

The main goal of the European Green Deal is for the European Union to become the world's first "climate-neutral bloc" by the year 2050. The global chemical manufacturing could accommodate only a few percent of the worldwide emitted CO_2. However, the chemical industry possess many technologies, which could support the goal of zero greenhouse gas emissions for this sector. The electrochemical CO_2 reduction reaction (CO_2RR) is one potential technology, which can converse under ambient conditions at least a part from the CO_2 into diverse spectrum of chemicals. Two of them – CO and formic acid are comparably easy to produce, because in the reduction process only two electrons are involved. These products could be further used as chemical feedstock in the chemical manufacturing industry [1].

The selectivity of the CO_2 reduction reaction is dependent on the catalyst used. Sn-based catalysts are suitable candidates for the electro-reduction of CO_2 to formate due to their non-toxic properties, low cost and ability to produce (s.o.) [2-8]. For preparing the cathode Sn/SnO_2 nanoparticles are usually mixed with carbon black [9,10], brushed or sprayed onto carbon paper [11-14].

Electrodeposition is well known for being an economical and uncomplicated method for creating metal films. The morphology and thickness of the films can be varied through the applied current density or deposition potential. Beside galvanostatic deposition (DC), pulse current deposition (PP) is one of the techniques commonly used in electroplating. It is known that morphology, microstructure, hardness, ductility, porosity and surface roughness of electrodeposits are impacted by the process parameters [15]. PP also yields a finer homogeneous surface appearance because it is possible to achieve higher instantaneous current densities during electrodeposition.

The efficiency of the CO_2RR is very low due to the low solubility of CO_2 in water and therefore related diffusion limitations. Increasing current density beyond 5 mA/cm^2 on planar electrodes leads to increasing the hydrogen evolution reaction (HER) which is competitive in aqueous solutions. The current density could be appropriately increased with the use of Gas diffusion electrodes (GDE) as shown in numerous literature studies. Due to their porous structure such electrodes can manage gas, liquid, electron and heat transport at electrochemical surfaces [9]. In such case, the increase of the current density is due to the use of gaseous CO_2 as reactant (which can increase the diffusion rate), shorter diffusion lengths and an appropriate wettability, which facilitates the development of an extensive triple-phase boundary.

Electrodeposited Sn-films on different GDE are already successfully tested for the CO_2RR [16-21]. However, in the reported studies, the metal layers mostly covered only the outer surface area of the substrate as thin catalytic film. To achieve both a high catalyst surface area in contact with electrolyte and good accessibility of CO2, it should be beneficial if the catalyst is homogeneously distributed throughout the extended volume of the GDE in which gas- and electrolyte-wetted pores are in close contact.

1. Scientific Approach

In this study the electrodeposition of Sn film on commercial and in-house fabricated carbon based GDEs [9,10] from commercial electrolytes using different deposition techniques was investigated. The morphology of the samples was investigated with Scanning electron micrographs (SEM). The distribution of Sn throughout the thickness of the GDE was evidenced by computer tomography (CT). The initial electrochemical characterization tests of the Sn-loaded GDE, under laboratory operating conditions demonstrated promising results.

https://doi.org/10.5281/zenodo.4550671

2. Experiments/Calculations/Simulations

Chemicals. As substrates 29 BC (SGL CARBON GmbH) and in-house fabricated carbon based GDEs were used. To prepare the GDEs, carbon support (Acetylene Black, AB, Alfa Aesar, 100 % compressed, >99.9 %) was mixed with PTFE (Dyneon, TF 92070Z, $\bar{d}$p = 450 µm) in a ratio of 65 to 35 followed by dry-pressing at up to 7 t for 4 min [9, 10]. The samples were coated from commercial Sn electrolytes Solderon ST 200 (Room and Haas Electronic Materials L.L.C) and Slototin MT 1110 (Schloetter) at room temperature and different deposition times. As anode a Sn plate was used.

Apparatus.

Electrodeposition:

The electrochemical deposition experiments were conducted with a model SP-150 potentiostat/galvanostat (BioLogic) and controlled by EC-Lab Software (BioLogic). For galvanostatic and PP deposition were used current densities from 1 to 5 A.dm^2; the square-wave current pulses used in the PP experiments had an on-/off-time of ton/toff = 1 s/1 s. The potentiostatic deposition was carried out at – 1 V vs. Saturated Calomel Electrode (SCE).

The surface morphology and chemical composition of the electrodeposits were determined using high resolution scanning electron microscope (SEM, Gemini SEM 300, Zeiss) with energy dispersive spectroscopy (EDS) operated at 15 kV.

A Zeiss Auriga 60 XBeam work-station (Zeiss Microscopy GmbH, Oberkochen, Germany) was used for FIB serial-sectioning and SEM image acquisition. An advanced air-conditioning system minimized the variations in temperature (23 C ± 0.5°C during data acquisition). In order to minimize specimen drift, the stub was mounted on a high mass sample holder with a fixed tilt angle of 54°, which is why no stage tilting was required to position the sample perpendicular to the side mounted ion beam gun. Stage and sample holder were allowed to equilibrate for 3 h before the image acquisition routine was started. FIB milling was performed with a 30 kV, 600 pA gallium ion beam. SEM images were acquired in high current mode at 1.2 kV with an aperture of 60 µm. The in-column Zeiss EsB (energy selective backscattered) detector (Zeiss Microscopy GmbH) was shielded by an energy filtering grid set to 980 V, thus eliminating a large fraction of inelastically scattered electrons. All images were automatically tilt corrected with respect to the cross-section surface. The gradual change of working distance and the shift of the cross-section in the SEM field of view during milling were also corrected automatically. A stack of 108 slices with a nominal voxel size of 15 × 15 × 30 nm was acquired in 4 h. 3d models were evaluated with VG-Software.

VtomexL 450 was used for computer tomography measurements.

Electrochemical characterization:

The electrochemical characterisation of the electrodes was performed in a custom-made semi-batch cell made from PMMA. The electrodes were separated by a cation exchange membrane (Nafion® 117, DuPont). The experiments were conducted with a Gamry Inferface 1010E potentiostat. 2 M $KHCO_3$ with a pH-Value of 10 was used as electrolyte. Hg/HgO (1 mol/l KOH conduces as reference electrode. A platin wire was availed as counter electrode. The electrolyte was heated and monitored by an external heat exchanger. On the gas side, a nickel mesh was used as current collector. To protect the GDE from mechanical destruction by the nickel mesh, a GLD (SGL, Sigracet GDL 35AA) was placed between mesh and GDE.

The gaseous products (H_2, CO) were analysed by a thermal mass flow meter and online-GC (Agilent 7879A). To quantify the formate concentration a HPLC (Agilent Technology, 1280 Infinity) was used.

For the electrochemical characterization, the geometrical area of the GDE was limited to 1 cm^2 by a ABS mask. The characterisation was carried out at 50 °C and a CO_2 flow rate of 5 ml/min.
To characterize the GDE the current was increased in 60 s from 0 mA to -200 mA as preconditioning. This was followed by a galvanostatic hold for 1 h at -200 mA.

3. Results

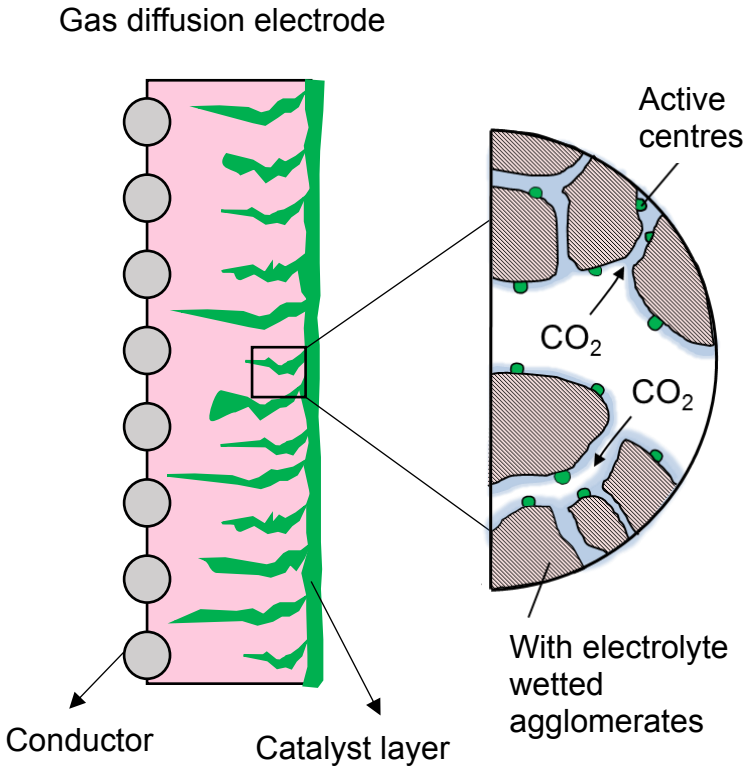

Fig. 1. Schematic representation of the GDE, covered with catalytic layer.

Electrodeposition:

In this work two types of substrates were used: commercial and in-house fabricated carbon based GDEs. For improved CO_2RR catalyst grains or particles should be located not only on the top of the electrode. They must be positioned also inside the substrate, homogeneously distributed into the pores of the substrate where gaseous CO2 and liquid electrolyte are in contact, i.e. at the so-called triple-phase boundary (TPB). One possibility to place catalyst nanoparticles specifically at these positions into the three-dimensional substrate structure is provided by the electrochemical deposition (Fig. 1). The morphology of the layers, their orientation and the grain size can be varied through the parameters of this technique. This is of big interest, because in the recent years it was demonstrated in the literature, that the orientation of the catalyst material and its morphology has a large influence on the produced products [16,18,22,23].
During the CO_2 electrolysis the location and extent of the TPB and, accordingly, the wetting of the electrode is the decisive factor for its local selectivity. When the wetting zone during the deposition is the same as the wetting zone during the electrolysis, there will be

efficient catalyst utilization directly in the three-phase area. Hence, optimizing the porosity, structure, hydrophobicity and the three-dimensional design of the substrate is crucial and has to be aligned with the catalyst deposition.

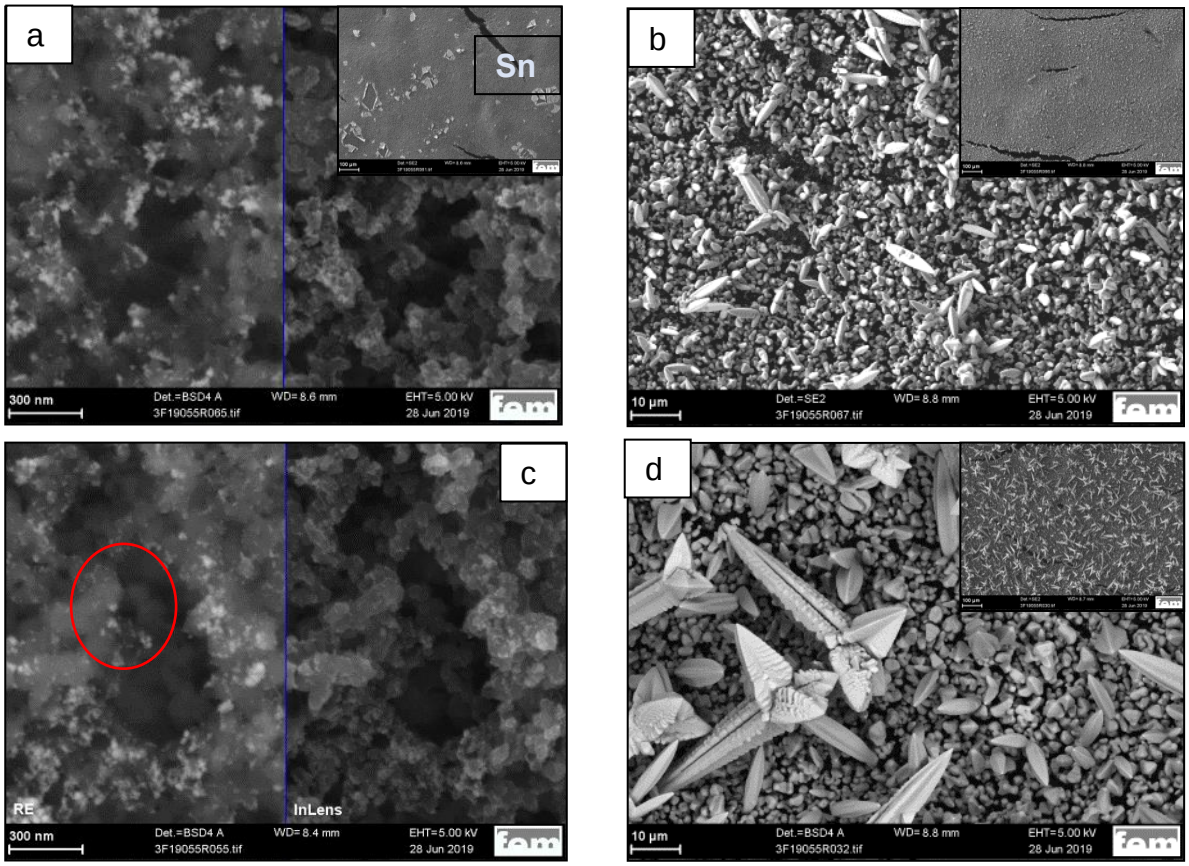

Fig. 2. Sn-electrodeposition on commercial substrate with different deposition techniques. a) DC, = - 1 A.dm^{-2}; b) DC = - 1 A.dm^{-2}; c) PP = - 1 A.dm^{-2} t_{on}/t_{off} = 1:1 ms; d) Potentiostatic deposition (PD) E = - 1 V.

Figure 2 presents SEM investigations of commercial substrate after Sn-electrodeposition. Using different deposition techniques it was possible to produce layers with different morphology. After applying DC with lower current density the surface is covered with a very tin Sn-layer (insert in Fig. 2 a). Detailed investigations showed that this tin film consists of separate Sn agglomerates (Fig. 2 a) which are distributed only on the substrate interface. The images 2a and 2c are separated in two parts. The deposited metal is better imaged with the back-scattered electrons (left part of the image) whereas the substrate structure is clearly imaged with InLens detector (right part of the image). A homogeneous film is deposited with increased current density (insert in Fig. 2 b). The whole sample surface is covered with large well-structured crystallites (Fig. 2 b). After PP deposition the sample is covered with a thin Sn-layer, which consists of separated agglomerates (Fig. 2. c). Only few Sn-particles could be observed inside the substrate (red circle in Fig. 2. c). The potentiostatically deposited sample is covered with a homogeneous thick film. Three-dimensional sharp-edged dendrites are regularly distributed on the surface (insert in Fig. 2 d). In-between big well oriented crystallites are grown (Fig. 2 d).

For increased process efficiency the catalyst particles should be evenly distributed inside the substrate (see Fig. 1). The samples shown in Fig. 2 did not meet these requirements. Both investigated substrates were thick and PTFE is part of the structure. Its hydrophobic properties are useful for the CO_2RR, but complicate the penetration of electrolyte for Sn-deposition inside the substrate. To enhance this process ultrasonic bath was used for

substrate preparation. Two different electrolytes were tested. In both cases Sn was indeed detected inside the probes (Fig. 3 a and 3 b) as targeted. It was possible to deposit in the inner substrate layers very fine Sn-films (Fig. 3 a) or well-structured Sn-layers with big crystallites (Fig. 3 b).

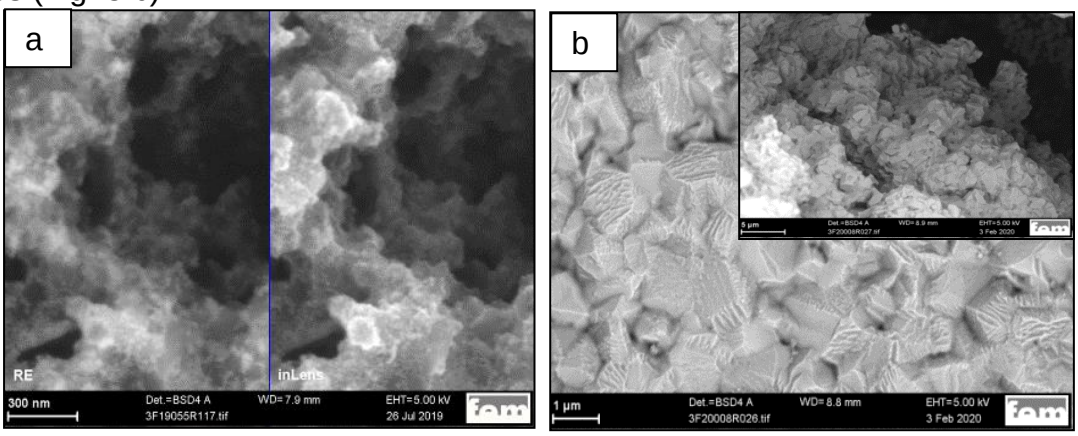

Fig. 3. Sn-electrodeposition on commercial substrate from different electrolytes. PP = - 1 A.dm^{-2} t_{on}/t_{off} = 1:1 ms a) SOLDERON b) SLOTOTIN.

Consequently, to get a better insight into how the catalyst is distributed inside the electrode, computed tomography (CT) scans were performed. CT is an imaging procedure that uses computer-processed combinations of an array of X-ray measurements taken from different angles. Thereby, it is possible to produce three-dimensional internal and external representations of a scanned object. With this non-destructive method various levels in different directions inside the probe can be investigated.

Such a CT scan of the pure commercial substrate is represented in Fig. 4 a. The blue line in the upper part of the image shows which area from the sample is investigated with a cross-section in the lower part of the image. Holes and elongated cracks are evenly distributed on the whole sample and they reach the back of the sample (not shown in the figure).

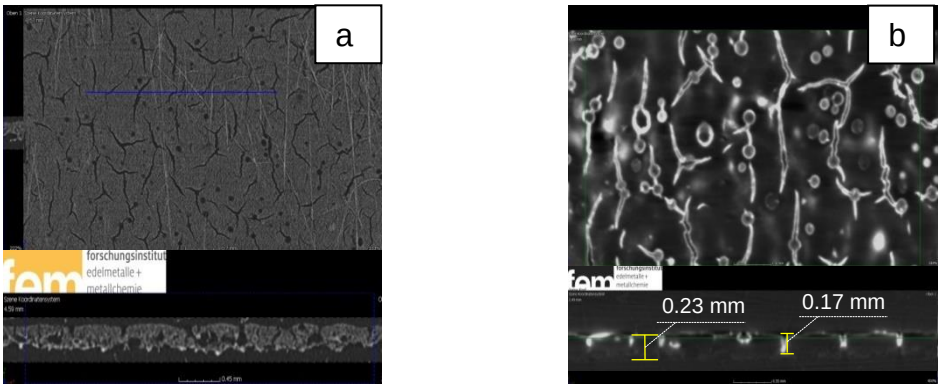

Fig. 4. CT scans of commercial substrate inside the sample. a) pure substrate and b) after Sn-electrodeposition.

CT-images of the sample, shown in Fig. 3 b are presented in Fig 4 b. The green line in the image in the lower part of Fig 4 b shows which level from the sample is investigated in the upper image in the figure. The whole substrate thickness is 2.3 µm. At above mentioned current parameters it was possible to deposit Sn at lower levels until 1.7 µm – more than 2/3 from the whole substrate thickness. Sn is deposited more uniform inside the volume and a thicker layer is detected around the pores. The white agglomerates between them are from thinner Sn-film (upper image in Fig. 4b).

Focused ion beam (FIB) is a technique that resembles a scanning electron microscope (SEM) and uses a finely focused beam of ions (usually gallium) to image the investigated sample. One tool of this technique is the FIB Tomography. The process is destructive because the probe is being sequentially milled away after each image. FIB has nanometer-scale resolution and can determine the distribution of the object's elements. The collected series of images could be reconstructed to a 3D model of the exact region of interest.

Fig. 5. FIB cuts (15 x 15 x 30 nm^3) of in-house fabricated substrate, evaluated with VG-Software. a) graphite b) pores and c) PTFE.

The in-house fabricated substrates are manufactured by a dry pressing method as described in [9]. For that purpose the powder components are mixed in a dry state and pressed with a hydraulic press. FIB characterization of these substrates shows the distribution of carbon black and the hydrophobic binding agent PTFE as well as the porous structure. Particularly, the inhomogeneous distribution of PTFE can be observed. The highly porous nature of the electrode substrate determined by the carbon black agglomerates and the electrode manufacturing is evidenced by Hg-porosimetry measurements which give a value of around 70%. The volume fractions were calculated: graphite = 69.4%; PTFE = 16.9%; pores = 13.7%. In this case the combined 3D-models evaluated with VG-Software do not give additional information about the element distribution into the probe and are not shown here.

During the investigations it was observed that with time the probes lose the silver metallic glossy colour. SEM investigations determined that 2 h after the deposition fast corrosive process takes place (Fig. 6 a). The Sn-crystallites were destroyed towards the axes of crystal lattice. With EDX a lot of sulphur on the surface was measured. After 5 days all the Sn-crystallites shrink and lose their structure (Fig. 6 b). On the surface remain only Sn-cuticle layers. It was supposed, that electrolyte residues are entrapped in the substrate pores and later dissolve the deposited film. For this reason it was developed a new rinsing method: changing 3 times hot and cold rinsing. After that the well-structured Sn-crystallites covered the surface (Fig. 6 c).

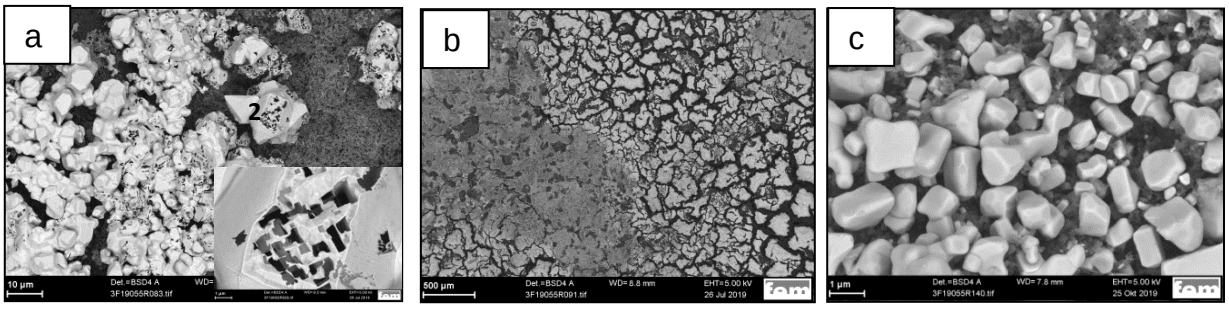

Fig. 6. SEM investigations of in-house fabricated substrate. a) 2 h after deposition b) 5 days after deposition and c) after new rinsing procedure.

https://doi.org/10.5281/zenodo.4550671

Electrochemical characterisation: As benchmark the performance of state of the art GDEs developed by Löwe et al. was analysed (A) [24]. For a comparison two electrodes with electrodeposited Sn were chosen. One electrode based on the commercial 29 BC substrate (B) and one based on the in-house fabricated GDE (C).
The faradaic efficiency (FE) for the product formate and the by-products H_2 and CO was picked as a mark for the performance of the electrodes.

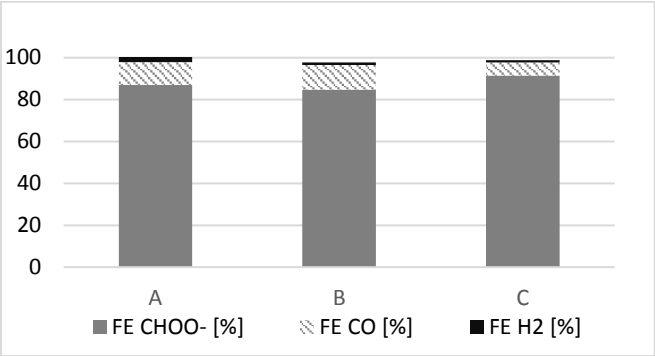

Fig. 7. Faradaic efficiencies of a state of the art GDE (A) and electrodes based on 29 BC (B) and on an in-house fabricated GDE (C).

The performance of the electrodes with electrodeposited Sn as catalyst is comparable with the performance the state of the art GDEs.
The FE for formate is even better than the state of the art electrodes by using an electrode with electrodeposited Sn as catalyst on an in-house fabricated GDE as substrate (C).

4. Summary

Sn layers were successfully deposited from commercial electrolyte onto GDE (commercial and in-house fabricated)
Using different deposition techniques it was possible to produce layers with different morphologies.
It was possible to deposit in the inner substrate layers Sn-films using ultrasonic bath for substrate preparation.
Computer tomography investigations prove the homogeneous Sn-distribution in the inner substrate layers.
The performance of the electrodes with electrodeposited Sn catalyst is comparable and even better for formate with the performance the state of the art GDEs.

References

[1] Pletcher, D., 2015, “The cathodic reduction of carbon dioxide - What can it realistically achieve? A mini review,” Electrochem. Commun., 61, pp. 97–101.
[2] Zhang, S., Kang, P., and Meyer, T. J., 2014, “Nanostructured tin catalyst for selective electrochemical reduction of carbon dioxide to formate,” J. Am. Soc., 136(5), pp. 1734-1737.
[3] Liu, Y., Fan, M., Zhang, X., Zhang, Q., Guay, D., and Qiao, J., 2017, “Design and engineering of urchin-like nanostructured SnO2 catalysts via controlled facial hydrothermal synthesis for efficient electro-reduction of CO2,” Electrochim. Acta, 248, pp. 123–132.

[4] Dutta, A., Kuzume, A., Kaliginedi, V., Rahaman, M., Sinev, I., Ahmadi, M., Cuenya, B. R., Vesztergom, S., and Broekmann, P., 2018, "Probing the chemical state of tin oxide NP catalysts during CO2 electroreduction: A complementary operando approach," Nano Energy, 53, pp. 828–840.
[5] Hu, H., Gui, L., Zhou, W., Sun, J., Xu, J., Wang, Q., He, B., and Zhao, L., 2018 "Partially reduced Sn/SnO2 porous hollow fiber: A highly selective, efficient and robust electrocatalyst towards carbon dioxide reduction," Electrochim. Acta, 285, pp. 70-77.
[6] Kong, Y., Wang, L., Jiang, H., Li, F., Zhao, T., Zhuo, M., Chen, Q., Mao, M., and Xu, Y., 2019, "Design of counter oxidation vs. CO2 electroreduction for efficient formate production on a tin cathode," J. Electroan. Chem., 847, 113264.
[7] Liu, S., Pang, F., Zhang, Q., Guo, R., Wang, Z., Wang, Y., Zhang, W., and Ou, J., 2018, "Stable nanoporous Sn/SnO2 composites for efficient electroreduction of CO2 to formate over wide potential range," Appl. Mater. Today, 13, pp. 135–143.
[8] Proietto, F., Schiavo, B., Galia, A., and Scialdone, O., 2018, "Electrochemical conversion of CO2 to HCOOH at tin cathode in a pressurized undivided filter-press cell," Electrochim. Acta, 277, pp. 30-40.
[9] Kopljar, D., Inan, A., Vindayer, P., Wagner, N., and Klemm, E., 2014, "Electrochemical reduction of CO_2 to formate at high current density using gas diffusion electrodes," J. Appl. Electrochem, 44, pp. 1107-1116.
[10] Kopljar, D., Wagner, N., and Klemm, E., 2016, "Transfering electrochemical CO_2 reduction from semi-batch into contionuous operation mode using gas diffusion electrodes," Chem. Eng. Technol, 39(11), pp. 2042-2050.
[11] Yang, H., Kaczur, J. J., Sajjad, S. D., and Masel, R. I., 2017, "Electrochemical conversion of CO2 to formic acid utilizing Sustainion™ membranes," J. of CO2 Utilization, 20, pp. 208-217.
[12] Yu, J., Liu, H., Song, S., Wang, Y., and Tsiakaras, P., 2017, "Electrochemical reduction of carbon dioxide at nanostructured SnO2/carbon aerogels: The effect of tin oxide content on the catalytic activity and formate selectivity," App. Catal., A, 545, pp. 159-166.
[13] Wang, Q., Wang, X., Wu, C., Cheng, Y., Sun, Q., and Yu, H., 2018, "Enhanced electroreduction of CO2 and simultaneous degradation of organic pollutants using a Sn-based carbon nanotubes/carbon black hybrid gas diffusion cathode," J. of CO_2 Utilization, 26, pp. 425–433.
[14] Mot, B. D., Hereijgers, J., Duarte, M., and Breugelmans, T., 2019, "Influence of flow and pressure distribution inside a gas diffusion electrode on the performance of a flow-by CO2 electrolyzer," Chem. Eng. J., 378, 122224.
[15] Puippe, J. C., and Leaman, F. H., 1986, "Theory and practise of pulse plating". Orlando: AESF Soc.
[16] Won, D. H., Choi, C. H., Chung, J., Chung, M. W., Kim, E.-H., and Woo, S. I., 2015, "Rational Design of a Hierarchical Tin Dendrite Electrode for Efficient Electrochemical Reduction of CO2,", Chem. Sus. Chem., 8, pp. 3092–3098.
[17] Sen, S., Skinn, B., Hall, T., Inman, M., Taylor, E. J., and Brushett, F., 2016, "Pulsed electrodeposition of tin electrocatalysts onto gas diffusion layers for carbon dioxide reduction to formate," MRS Fall Meeting, Manuscript ID MRSF16-2540220.R1 Manuscript Type: Symposium EC3
[18] Zhao, C., and Wang, J., 2016, "Electrochemical reduction of CO2 to formate in aqueous solution using electro-deposited Sn catalysts," Chem. Eng. J., 293, pp. 161–170.
[19] Alba, B. C. S., Camayang, J. C. A., Mopon, M. L. Jr., and Rosario, J. A. D., 2017, "Electrocatalytic reduction of carbon dioxide on electrodeposited tin-based surfaces," AIP Conference Proceedings 1879 https://doi.org/10.1063/1.5000469.
[20] Wang, Q., Wang, X., Wu, C., Cheng, Y., Sun, Q., and Yu, H., 2017, "Electrodeposition of tin on Nafion-bonded carbon black as an active catalyst layer for efficient electroreduction of CO2 to formic acid," Scientific Reports, 7, 13711.

[21] An, X., Li, S., Yoshida, A., Wang, Z., Hao, X., Abuliti, A., and Guan **G.,** 2019, "Electrodeposition of Tin-Based Electrocatalysts with Different Surface Tin Species Distributions for Electrochemical Reduction of CO2 to HCOOH," ACS Sustainable Chem. Eng., 7(10), pp. 9360-9368.
[22] Zhao, J., Sun, L., Canepa, S., Sun, H., Yesibolati, M. N., Sherburne, M., Xu, R., Sritharan, T., Loo, J. S. C., Ager III, J. W., Barber, J., Mølhave, K., and Xu, Z. J., 2017, "Phosphate tuned copper electrodeposition and promoted formic acid selectivity for carbon dioxide," J. Mater. Chem., A, 5, pp. 11905–11916.
[23] Reller, C., Krause, R., Volkova, E., Schmid, B., Neubauer, S., Rucki, A., Schuster, M., and Schmid, G., 2017, "Selective Electroreduction of CO2 toward Ethylene on Nano Dendritic Copper Catalysts at High Current Density," Adv. Energy Mater., 7, pp. 1-8.
[24] Löwe, A., Rieg, C., Hierlemann, T., Salas, N., Kopljar, D., Wagner, N., and Klemm, E., 2019, "Influence of Temperature on the Performance of Gas Diffusion Electrodes in the CO2 Reduction Reaction." ChemElectroChem, 6(17), pp. 4497–4506.

Keywords: EFCF2020, SOx
Session A12: SOC integration, Power-to-X, CO2 capture etc.

A1221

Integrating SOEs with a methanation reactor for methane gas production using an MCFC for CO_2 capture from biogas

Mohammed Kazeem Ayodeji, Robert Steinberger-Wilckens

School of Chemical Engineering
College of Engineering and Physical Sciences
University of Birmingham, Birmingham/UK

Contact authors: www.EFCF.com/ContactRequest

Abstract

This study reports a concept of coupling two Solid Oxide Electrolysers (SOE) directly and indirectly with a methanation reactor for production of methane-rich gas for either an electricity or heat storage application on a larger scale. The main idea is focussed on increasing the ratio of methane in the biogas by removing CO_2 using an MCFC.

Water and biogas are used as the input to an SOE and an MCFC respectively. The SOE produces pure hydrogen gas, delivered to the MCFC anode. Biogas is supplied to the MCFC cathode. Here, the CO_2 is captured and transferred to the anode from where it passes to the methanation reactor together with the water formed from the hydrogen oxidation. The methane-rich gas from the MCFC cathode effluent and the methanation reactor output are sent to storage or fed into the natural gas grid as pure methane. Pure Oxygen is released from the first SOE anode and will be mixed with the biogas input to the MCFC to supply the oxidant to the MCFC reaction. In this way, close control is kept of the reactant gas flow compositions.

On 'discharging' the gas storage by extracting methane from the gas grid and feeding this to the SOFC, the second SOE will be fed with the SOFC anode effluent composed mainly of CO_2 and H_2O. This in turn delivers synthetic gas ($CO + H_2$) for the methanation reactor. It is necessary to have a control over the admissible H_2/CO ratio of 1:3 which is optimal for methane production in the methanation reactor. The concept requires detailed electrochemical, chemical and thermal simulations.

https://doi.org/10.5281/zenodo.4550684

Introduction

The global generation of power from renewable energy sources continued to be on the increase (i.e. 71 mtoe) reaching about 14.5% of the 2017 record-breaking increase, which are responsible for a third of the net growth in power generation in 2018. A Large portion of the growth was achieved mainly by energy from wind and solar [1]. These trends are more than likely to continue in the future. Power produced from renewable energy sources such as wind and solar, however, mismatches the world electrical energy demand due to its fluctuating availability and nature. With the growth in renewable energy investments observed in recent times, proposing mitigation ideas to the inherent issues with the future energy infrastructure become increasingly necessary [2], [3].

The key issues are power fluctuation, flexibility of the system and the efficiencies. There is a need to systematically store the excess energy available in peak power production periods in compensative measures against the lower energy production periods in order to aid the scale-up of employability of energy from renewables [4]. As such, energy storage is considered a key technology as it can help provide an assuagement for the inherent deficiencies and inefficiencies when fully integrated with the existing electrical power grid [5], [6]. Various energy storage technologies based on their working principles are shown in Table 1.

Table 1: Energy storage techniques

Energy Form	Principles	Ref
Electrical	Superconducting magnetic energy storage (SMES), super-capacitors.	[7]
Mechanical	Flywheels, pumped storage and compressed air.	[8]
Thermal	Thermochemical, sensible heat and latent heat	[9], [10]
Chemical	Electrochemical, power-to-liquid/gas (P2L, P2G, P2X)	[11]–[13]

Asides the working principles, the techniques also differ in further aspects, such as mode of discharge, time requirement for start-up, capacity, operating conditions, bulkiness of the equipment involved, and efficiencies, involving the application of various disciplines to overcome the technical issues [14].

Energy storage by SMES, flywheels and super capacitors offer some advantages over the other storage technologies which includes high round-trip efficiency, low charging and response time, long life cycle, and high power density. However, the major drawback of SMES and super capacitor is the cost of installation in comparison with the storage capacity [15], while flywheels are affected by standby losses. Both flywheel and super capacitor suffer from low energy density [16].

Pumped hydro power energy storage has the capability of high energy storage duration (for over 6 months) but still contributes to the emission of greenhouse gasses due to the released of CO_2 from cement production during construction [16]. The major disadvantages of compressed air energy storage (CAES) are the dependence on geological formation and high installation cost [17].

The use of batteries for energy storage enjoin low maintenance requirement and high round trip efficiency, but lacks high energy capacity and density and has an issue of self-discharge. Therefore limiting their utilisation to short term storage [11].

Easy transportation of energy to where it is needed is another topic of interest and the necessities to store excess renewable energy cannot be overemphasised. High energy and power density, utilisable for extended period of time can be achieved by employing power-to-fuel technologies [14].

In regions, where there is abundant solar or wind energy sources, one profound way to store excess energy is to employ the concept of Power-to-Methane (P2M) [18], and

integrate it with high temperature fuel cells such as molten carbonate fuel cell (MCFC) and solid oxide fuel cells (SOFCs) in such a way as to exploit the stored renewable energy. A P2M plant basically consists of a water electrolyser, a CO_2 source, and a methanation module as shown in Figure 1 [19].

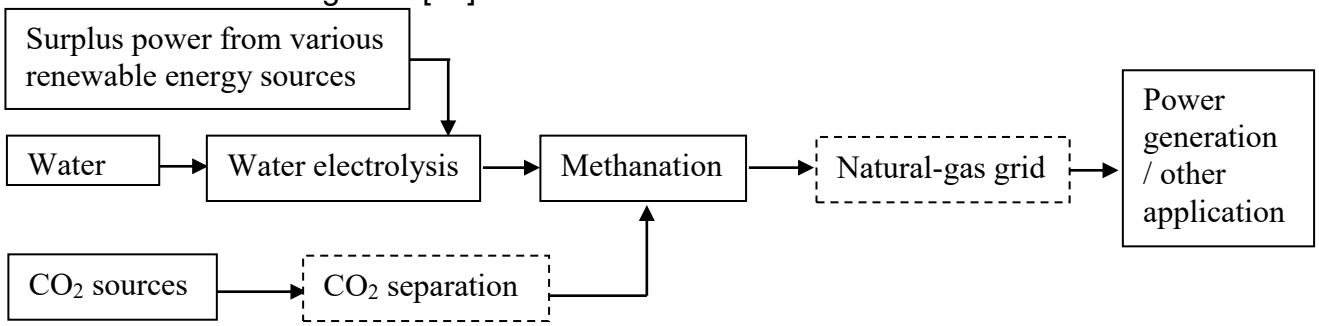

Figure 1: Principle of power-to-methane

Pure hydrogen gas is produced by the electrolyser from water and sent to the methanator. In the methanation unit, the pure hydrogen gas is reacted with CO_2 to generate a mixture of gasses which primarily consist of methane and steam [18]. The reaction equations are presented in Eqn. (10) - (12). The methane gas obtained can be sent to storage, or fed into the natural gas grid as pure methane to be later used, for example in SOFCs for power generation. Methane fuel is preferred because of its relatively higher hydrogen to carbon ratio compared to other hydrocarbon fuels [20].

CO_2 sources for the technology can include biomass plants (i.e. from biogas upgrading - approximately 100% (v/v) [21]), power generation plants (i.e. from combustion of coal – about 10-15% (v/v) [22], natural gas – about 3-5% (v/v), petroleum – about 3-8% (v/v), industrial processes (i.e. in the production of cement – about 14-33% (v/v) [23], production of ethylene oxide – approximately 100% (v/v), production of Iron and steel – about 20-30% (v/v) [23]) and ambient air – approximately 0.04% (v/v) [24].

The technical feasibility of CO_2 capture from these sectors is positive, however, the integration in the present technology is economically dependent on the CO_2 partial pressures in the exhaust gas due to the energetic and procedural effort for separation [23]. Common CO_2 sources, investigated in past studies are those from the combustion of coal, natural gas or petroleum. Their integration with fuel cell plants particularly SOFCs is a breakthrough in achieving concurrently a huge fuel conversion efficiency and very low pollutants emission [25]. This however eliminate the problem of transporting CO_2 to the site. Nevertheless, the energy requirement for the CO_2 separation still makes it somewhat less energy-efficient. Therefore, the incorporation of a molten carbonate fuel cell (MCFC) as the CO_2 separation unit could make the overall plant an energy-efficient one.

1. Literature Review

Many institutions and research institutes are geared towards the development of such technology i.e. integrated gasification fuel cell cycle (IGFC) that utilizes a low cost fuel to generate electricity with high efficiency and the annihilation of emission of greenhouse gases (GHG) or the incorporation of a carbon capture technology. One typical advantage of this concept is the electrochemical oxidation of the fuel that occur in the fuel cell, thereby leaving only CO_2 and H_2O as the exhaust unlike the combustion engines which leaves oxides of sulphur and nitrogen in the exhaust. Several thermodynamic studies of gas turbines and fuel cells (especially SOFCs and MCFCs) integration to form hybrid FC-GT cycle have been reported in literature in the last decades. Examples of such studies are concisely presented below.

Ghosh and De (2003) carried out a study on thermodynamic performance of a 20 MW_e IGFC system. The configuration included a gasifier through which oxygen was constantly

supplied, an air separating unit (ASU) and a slurry feed. A syngas purifier with the operating temperature of 673.2k was used for the initial removal of sulphur-containing compounds and particulates before being sent into the fuel cell. The authors reported 48 to 55% lower heating value (LHV) efficiencies, varying with the ratio of cycle pressure (i.e. 5 to 35) and cell potentials (i.e. 0.91 to 0.965V).

Kivisaari et al. (2004) carried out a feasibility study on a high temperature SOFC plant integrated with a coal gasifier. The group assessed a 30 MWe system operating on a dry coal feed, and oxygen blown gasifier to produce syngas. The exhaust gas from the SOFC was used to reheat the syngas after being quenched. The study revealed 43% LHV efficiency without SOFC anode gas recirculation, and 47% LHV efficiency with SOFC anode gas recirculation while assuming a cell voltage of 0.725V at fuel utilisation of 85%.

Verma, Rao, and Samuelsen (2006) reported a sensitivity analysis of a Vision 21 350 MWe coal power plant with CO_2 capture. The plant's configuration included a fluidised bed gasifier, a methanator, an ASU, WGS reactors, a membrane-based H_2 separator, a catalytic combustor, a heat recovery unit, a CO_2 compressor and a SOFC fed with methane and recirculated H_2. The authors reported 51 to 53% LHV efficiency, while assuming 85% fuel utilisation, 0.75V cell potential and an operating pressure ranging from 5.9 to 19.7 atm after optimising the parameters.

Romano et al. (2009) studied a coal gasifier integrated with an SOFC plant with the capacity of 590 MWe. The SOFC plant was fed with a syngas produced from the coal gasifier, and highly pressurised air produced by the gas turbine compressor. The study gave approximately 59% LHV efficiency while maintaining a fuel utilisation of 85%, cell voltage of 0.753V in the SOFC, with and without syngas expander, and a pressure ratio of 20 to 26.5 respectively. The plant configuration assessed could be improved by addition of units like methanation, or CO_2 capture to achieve even higher efficiencies passing the 60% limit.

Spallina et al. (2011) thermodynamically analysed an SOFC-based plant with Carbon capture. Herein, an air separator was used to produce pure oxygen feed for the gasification of coal. Syngas produced is passed directly to SOFC modules after being cleaned and passing through heat recovery. The remaining combustible gas form the SOFC's anode exhaust were combusted with the pure O_2 produced in the ASU, the product gas was used to generate steam by heat recovery before condensing and compressing the water and carbon dioxide (cryogenic separation), respectively. The author fed the coal with the captured CO_2 in the lock hoppers thereby avoiding the use of N_2 in order to achieve high CO_2 purity. Nevertheless, the study of the 520MW_e plant showed 47% LHV efficiency, and approximately 0.0211 kg/kWh emission of carbon dioxide while maintaining 89% and 0.747V of fuel utilisation and cell potential, respectively in the SOFC. Though, the study achieved reduced CO_2 emissions, the amount released will however increase over time and the assessed plant did not cater for it reabsorption back to the cycle.

Romano, Spallina, and Campanari (2011) also thermodynamically studied an SOFC-based IGFC (fuelled with coal) plant integrated with H_2 post firing, physical absorption carbon capture, and a methanator. The plant assessed gave 53% LHV efficiency and specific CO_2 emission of 30.9% for a 582 MW_e system while maintaining 74% fuel utilisation, and a cell potential of 0.812V in the SOFC module. Though a better CO_2 management with respect to net power was achieved with the configuration, the high complexity of the plant incurred high cost of the equipment required.

This study intends to report a concept of coupling two Solid Oxide Electrolysers (SOE) directly and indirectly with a methanation reactor for production of methane-rich gas for either an electricity or heat storage application on a larger scale. The main idea is focussed on this biogas upgrading by removing CO_2 using an MCFC. The plant will be

thermodynamically assessed, and a parametric sensitivity analysis will be carried out as regards to the overall efficiency.

2. Design of MCFC CO_2 capture plant layout

Figure 2 depicts the overall plant layout for a system using biogas input and CO_2 recycling via an MCFC unit. Water and biogas are used as the input to an SOE and an MCFC, respectively, as shown in the flow chart. The SOE produces pure hydrogen gas, delivered to the MCFC anode. Biogas is supplied to the MCFC cathode. Here, the CO_2 is transferred to the anode by facilitating the oxygen ion diffusion necessary for the hydrogen oxidation reaction. From where it passes to the methanation reactor together with the water formed from the hydrogen oxidation. The methane enriched gas from the MCFC cathode effluent and the methanation reactor output are sent to storage or fed into the natural gas grid as pure methane. Pure Oxygen is released from the first SOE anode (air electrode) and will be mixed with the biogas input to the MCFC cathode to supply the oxidant to the MCFC reaction. In this way, close control is kept of the reactant gas flow compositions.
On 'discharging' the gas storage by extracting methane from the gas grid and feeding this to the SOFC, the second SOE will be fed with the SOFC anode effluent composed mainly of CO_2 and H_2O. This in turn delivers syn gas (CO + H_2) for the methanation reactor. It is necessary to have a control over the admissible H_2/CO ratio of 1:3 which is an optimal ratio for production of methane in the methanator.
Explanations of reactions taking place in each unit and their significances in the configuration are discussed in the succeeding sections.

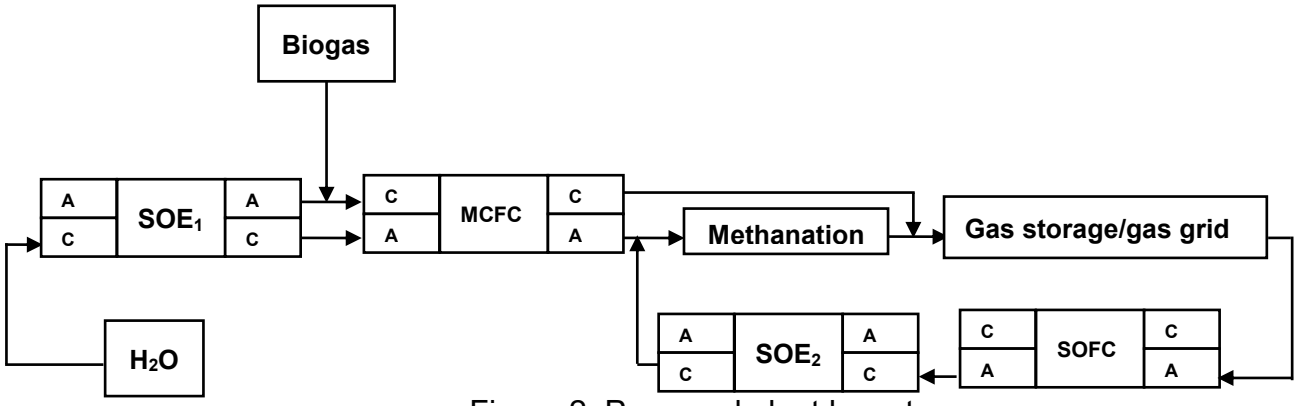

Figure 2: Proposed plant layout

The SOE

The first step as shown in Figure 2 is the co-electrolysis of water by the solid oxide electrolyser-1 (SOE_1), which can use power derived from excess renewable energy sources i.e. solar and wind energy to split water (H_2O) into hydrogen (H_2) and oxygen (O_2) [44]. A mixture of CO_2 and H_2O is processed in SOE_2 as shown in Figure 2.
Figure 3 shows the principle of SOEs. H_2 (as in the case of SOE_1) and / or CO (as in the case of SOE_2) evolves from the cathode of the SOE (i.e. the fuel electrode) while O_2 evolves from the anode (the 'air' or 'oxygen' electrode). A solid electrolyte separates the two electrodes is conductive only for oxygen ions (O^{2-}). The input gas stream for SOE_1 is composed of H_2O (steam) while for SOE_2, it includes both carbon dioxide and steam. Here, the feed gas would have access to the electrons delivered from the excess solar and wind power to produce either H_2 gas (in SOE_1 which delivers to the MCFC anode in Figure 2) or syngas (H_2 and CO) (in SOE_2 which delivers to the methanation unit) as well as the oxygen ions according to Eqn. (1) and (2) [45].

https://doi.org/10.5281/zenodo.4550684

$$CO_{2(g)} + 2e^- \rightarrow CO_{(g)} + O^{2-} \quad (1)$$
$$H_2O_{(g)} + 2e^- \rightarrow H_{2(g)} + O^{2-} \quad (2)$$

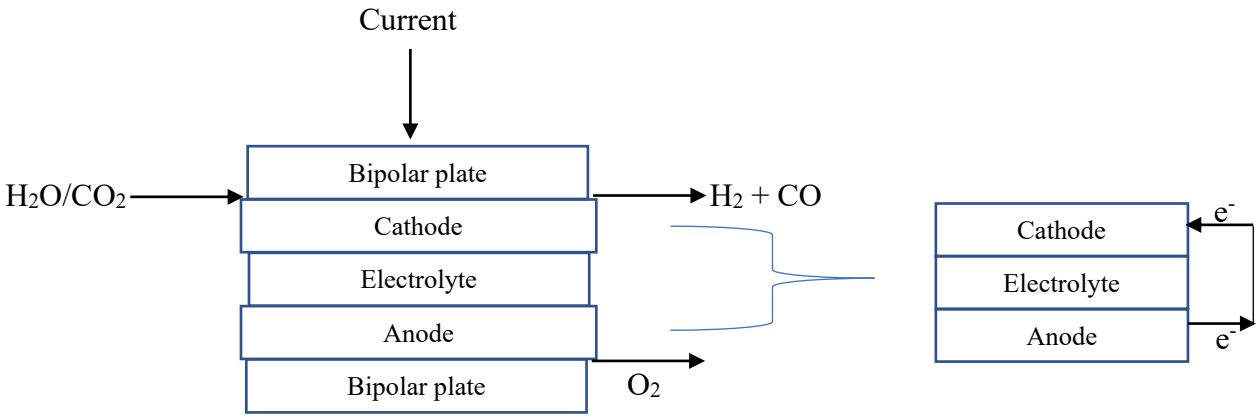

Figure 3: Schematic illustration of an SOEC

The oxygen ions are transported through the solid electrolyte to the anode where they are oxidized to oxygen gas as shown in Eqn. (3) and sent to either the MCFC cathode (as in SOE_1) or storage tank (as in SOE_2) which can later be used in the SOFC.

$$2O^{2-} \rightarrow O_{2(g)} + 4e^- \quad (3)$$

There is complexity in the SOEs co-electrolysis of the mixture of steam and carbon dioxide compared to individual electrolysis of the feed in SOEs. This is due to the following possible reactions represented in Eqn. (4) to (7) which could occur on the cathode [46]:

$CO_2 + H_2 \leftrightarrow CO + H_2O$ Reverse water-gas shift reaction (4)
$CO + 3H_2 \leftrightarrow CH_4 + H_2O$ Methanation reaction (5)
$2CO + 2H_2 \leftrightarrow CH_4 + CO_2$ Methanation reaction (6)
$CO_2 + 4H_2 \leftrightarrow CH_4 + 2H_2O$ Methanation reaction (7)

The high-temperature steam electrolysis (SOE) offers the benefit of a lower electric energy demand compared to low-temperature electrolysers (Alkaline and PEM), especially if the latent heat of water vaporisation is provided from an external source. Several studies in the literature ascertained that the electrolysis of steam at temperature of 1173.2K requires approximately 20% lower electrical energy than electrolysis of water at 353.2K. This high-temperature steam demand, however, aids the thermal integration with the methanation reactor and therefore reduces the need for additional cooling devices. Therefore, SOEs are promising technology for this purpose, albeit the effect of high temperature and long term operation on the integrity of the ceramic materials is questionable [47].

Molten carbonate fuel cell

This study proposes to use a Molten Carbonate Fuel Cell for supplying CO_2 captured from biogas to the methanation reactor. This solution gives pure CO_2 delivered directly to the reaction zone. The MCFC can at the same time be used to upgrade biogas through the removal of CO_2.

In general principle, an MCFC uses CO_3^{2-} as electron carrier through its molten carbonate electrolyte. When CO_2 gas is supplied to the MCFC cathode, it reacts with O_2 to form CO_3^{2-} which then diffuses to the MCFC anode where it is recovered as CO_2 again after reacting with a molecule of H_2 with the generation of two moles of electrons as shown in Eqn. (8) and (9).

Cathode: $\frac{1}{2}O_2 + CO_2 + 2e^- \rightarrow CO_3^{2-}$ (8)

Anode: $H_2 + CO_3^{2-} \rightarrow H_2O + CO_2 + 2e^-$ (9)

In other words, MCFCs can act as a gas filter which if employed in the present study for removing CO_2 from biogas, can help improve the heating value of the biogas and as well supply free CO_2 (i.e. nearly zero energy cost) for the methanation reaction.

Methanation unit

The syngas produced via the co-electrolysis of steam and CO_2 could as well be fed directly to the SOFC anode, instead of CH_4 but several studies [29], [30], [48] revealed low fuel conversion efficiencies and high rate of air flow requirement for cooling the SOFC device when pure syngas is used as the fuel gas.

However, if a fraction or the whole fuel gas is made up of CH_4, internal reforming of the CH_4 gas will be enhanced by the heat generated within the SOFC electrochemical reaction, this in turn causing cooling of the device. Therefore, more coolant like air would be required when fuel gas with zero percent methane is used which consequently reduces the efficiency of the fuel cell [29].

Methanation is an exothermic reaction [44] as shown in the following chemical equations (10) to (12) with the reactor temperature ranging from 503 to 1023K and the process pressures ranging from 4.4 to 84 atm [49].

$CO_{(g)} + 3H_{2(g)} \leftrightarrow CH_{4(g)} + H_2O_{(g)}$ $\Delta_r H^0_{298\,k} = -206.1\ {}^{kJ}/_{mol}$ (10)

$CO_{2(g)} + 4H_{2(g)} \leftrightarrow CH_{4(g)} + 2H_2O_{(g)}$ $\Delta_r H^0_{298\,k} = -165.0\ {}^{kJ}/_{mol}$ (11)

$CO_{(g)} + H_2O_{(g)} \leftrightarrow CO_{2(g)} + H_{2(g)}$ $\Delta_r H^0_{298\,k} = -41.2\ {}^{kJ}/_{mol}$ (12)

Thermodynamically, the reactions are favoured at low temperatures and high pressures.

The important criteria for designing an efficient methanator are listed as follows [50]:

(i) Operate at conditions that aid high methane yield and fast kinetics,

(ii) Avoid catalyst deactivation caused by sulphur poisoning.

(iii) Avoid conditions such as extremely low temperature or inadequate H_2:CO ratio which can deactivate the catalyst by deposition of carbon and formation of Nickel tetra carbonyl ($Ni(CO)_4$).

(iv) Avoid sintering of catalysts at high temperature.

Considering the exothermic nature of the methanation reaction, the temperature conditions would appear difficult to achieve [50]. Nevertheless, addition of Steam could help increase the H_2 and O_2 content of the feed syngas, thereby, lowering the risk of carbon deposition.

The SOFC

Solid oxide fuel cells (SOFCs) are high temperature (i.e. 500 to 900 °C) fuel-to-power devices [51] which accept directly not only hydrogen, but also hydrocarbons [52] such as CH_4, C_2H_5OH [53], C_3H_8 [54], [55], or reformed $CO(NH_2)_2$ [56] as fuel for generation of power. Syngas (CO, H_2) and ammonia (NH_3) are also potential fuels.

The SOFC will be fed with the gas stream generated at the methanation unit which consist mainly of CH_4 and steam together with some percentage of unreacted CO, H_2 and even CO_2. SOFC can internally reform the methane gas as shown in Eqn. (13), (14) and (15) [57] which practically overcomes the requirement for an external fuel reforming unit. External reforming will increase the cost and makes the operation complex, or could also reduce the plant's efficiencies [20].

$CH_4 + H_2O \rightarrow CO + 3H_2$ $\Delta_r H^0_{298\,k} = +206.1\ ^{kJ}/_{mol}$ Steam reformed (13)

$CO + H_2O \leftrightarrow CO_2 + H_2$ $\Delta_r H^0_{298\,k} = -41.2\ ^{kJ}/_{mol}$ WGS (14)

$CH_4 + CO_2 \rightarrow 2CO + 2H_2$ $\Delta_r H^0_{298\,k} = +247\ ^{kJ}/_{mol}$ Dry reformed (15)

The internal fuel reforming reactions represented in Eqn. (13) and (15) is enhanced by the heat generated by the electrochemical oxidation reactions of the fuel at the anode. However, in a typical SOFC operating condition, heat generated by the electrochemical reaction is higher than the heat required for the internal reforming reaction. This thereby still requires additional external cooling of the device but would have been lowered by 50% as compared to that required if external reforming reaction is used.
However, this mismatch in heat requirement and supply could give lead to non-uniformity in temperature distribution within the SOFC device which consequently could induced thermal stress on the cells and cause mechanical failure. Nevertheless, the above stated problem can be attenuated through the addition of little amount of O_2 to the feed fuel (i.e. CH_4) [58]. Product gas from the SOFC will be recycled by means of a blower and cooling the stream might not be necessary since high-temperature steam electrolysis (SOE) is employed.

Mole balance of the proposed plant

The mole balance of the proposed plant was carried out using the Aspen Plus™ as shown in figure 4.

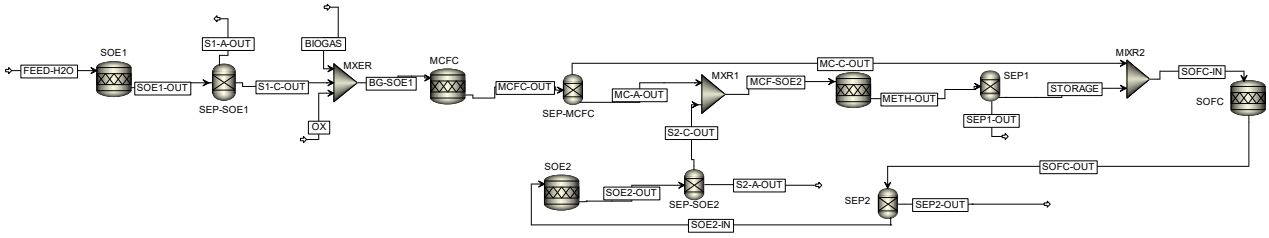

Figure 4: Mole balance of the MCFC CO_2 capture plant in Aspen Plus

1 mol/hr of water is fed into the SOE1 cathode and biogas containing 1 mol/hr of CH_4 and CO_2 each respectively is fed into the MCFC cathode. The stoichiometric chemical reactions elucidated in the preceding sections for each module were employed for the calculations.

3. Results

Table 2 shows the mole balance of the MCFC CO_2 capture plant. According to the performed analysis, the total number of electrons spent and generated are 20 and 28 respectively. It is worth to note that the extra 8 electrons generated is as a result of the 1 mol/hr of CH_4 captured form the biogas by the MCFC. It is assumed that Oxygen as oxidant for both MCFC and SOFC is abundantly available for the calculations.

	Mole flows										
Stream Name	Feed-H_2O	SOE1-out	Biogas	MCFC-Anode-out	MCFC-Cathode-out	MCFC-SOE2	Storage	SOFC-in	SOFC-out	SOE2-in	SOE2-Cathode - out
H_2O	1	0	0	1	0	1	0	0	6	6	0
H_2		1	0	0	0	6	0	0	0	0	6

CO_2	0	1	1	0	1	1	1	4	4	0
CH_4	0	1	0	1	0	2	3	0	0	0
CO	0	0	0	0	4	2	2	2	0	4

Table 2: Mole balance of the MCFC CO_2 capture plant

4. Conclusion

The study presents a concept of coupling SOEs with a MCFC and methanation reactor for an electricity storage application on a larger scale. The concept seems attractive as it includes storage of excess renewable energy, CO_2 capture, and temperature compatibility with methanation reactions and higher round trip efficiency as observed from the result. Detailed investigations based on mathematical modelling, thermodynamics and experiments will conducted in the next step of research.

References

[1] BP, "Statistical Review of World Energy 68th ed.," 2019.
[2] P. L. Joskow, "Challenges for wholesale electricity markets with intermittent renewable generation at scale: the US experience," *Oxford Rev. Econ. Policy*, vol. 35, no. 2, pp. 291–331, Apr. 2019.
[3] Y. Bilan, D. Streimikiene, T. Vasylieva, O. Lyulyov, T. Pimonenko, and A. Pavlyk, "Linking between Renewable Energy, CO_2 Emissions, and Economic Growth: Challenges for Candidates and Potential Candidates for the EU Membership," *Sustainability*, vol. 11, no. 6, p. 1528, Mar. 2019.
[4] E. I. Koytsoumpa, C. Bergins, and E. Kakaras, "The CO_2 economy: Review of CO_2 capture and reuse technologies," *J. Supercrit. Fluids*, vol. 132, pp. 3–16, Feb. 2018.
[5] D. Rekioua, "Storage in Hybrid Renewable Energy Systems," in *Hybrid Renewable Energy Systems. Green Energy and Technology*, Springer, Cham, 2020, pp. 139–172.
[6] F. Keck, M. Lenzen, A. Vassallo, and M. Li, "The impact of battery energy storage for renewable energy power grids in Australia," *Energy*, vol. 173, pp. 647–657, Apr. 2019.
[7] V. T. Tran, M. R. Islam, K. M. Muttaqi, and D. Sutanto, "A novel application of magnesium Di-boride superconducting energy storage to mitigate the power fluctuations of single-phase PV systems," *IEEE Trans. Appl. Supercond.*, vol. 29, no. 2, Mar. 2019.
[8] I. Stadler, F. Bauer, M. Budt, E. Heindl, and D. Wolf, "Mechanical Energy Storage," in *Handbook of Energy Storage*, Berlin, Heidelberg: Springer Berlin Heidelberg, 2019, pp. 483–561.
[9] U. Pelay, L. Luo, Y. Fan, D. Stitou, and C. Castelain, "Integration of a thermochemical energy storage system in a Rankine cycle driven by concentrating solar power: Energy and exergy analyses," *Energy*, vol. 167, pp. 498–510, 2019.
[10] S. Riahi, Y. Jovet, W. Y. Saman, M. Belusko, and F. Bruno, "Sensible and latent heat energy storage systems for concentrated solar power plants, exergy efficiency comparison," *Sol. Energy*, vol. 180, pp. 104–115, 2019.
[11] T. Liu *et al.*, "Exploring competitive features of stationary sodium ion batteries for electrochemical energy storage," *Energy Environ. Sci.*, vol. 12, no. 5, pp. 1512–1533, 2019.

[12] A. Afif, S. M. Rahman, A. Tasfiah Azad, J. Zaini, M. A. Islan, and A. K. Azad, "Advanced materials and technologies for hybrid supercapacitors for energy storage – A review," *J. Energy Storage*, vol. 25, p. 100852, 2019.
[13] S. Bellocchi, M. De Falco, M. Gambini, M. Manno, T. Stilo, and M. Vellini, "Opportunities for power-to-Gas and Power-to-liquid in CO_2-reduced energy scenarios: The Italian case," *Energy*, vol. 175, pp. 847–861, 2019.
[14] E. Moioli, R. Mutschler, and A. Züttel, "Renewable energy storage via CO2 and H2 conversion to methane and methanol: Assessment for small scale applications," *Renew. Sustain. Energy Rev.*, vol. 107, pp. 497–506, 2019.
[15] P. Mukherjee and V. V. Rao, "Superconducting magnetic energy storage for stabilizing grid integrated with wind power generation systems," *J. Mod. Power Syst. Clean Energy*, vol. 7, no. 2, pp. 400–411, 2019.
[16] B. R. Alamri and A. R. Alamri, "Technical review of energy storage technologies when integrated with intermittent renewable energy," in *1st International Conference on Sustainable Power Generation and Supply, SUPERGEN '09*, 2009.
[17] N. S. Hasan, M. Y. Hassan, M. S. Majid, and H. A. Rahman, "Review of storage schemes for wind energy systems," *Renew. Sustain. Energy Rev.*, vol. 21, pp. 237–247, 2013.
[18] M. Gotz *et al.*, "Renewable Power-to-Gas: A technological and economic review," *Renew. Energy*, vol. 85, pp. 1371–1390, 2016.
[19] S. K. Hoekman, A. Broch, C. Robbins, and R. Purcell, "CO_2 recycling by reaction with renewably-generated hydrogen," *Int. J. Greenh. Gas Control*, vol. 4, no. 1, pp. 44–50, 2010.
[20] T. M. Gür, "Comprehensive review of methane conversion in solid oxide fuel cells: Prospects for efficient electricity generation from natural gas," *Prog. Energy Combust. Sci.*, vol. 54, pp. 1–64, 2016.
[21] R. Muñoz, L. Meier, I. Diaz, and D. Jeison, "A review on the state-of-the-art of physical/chemical and biological technologies for biogas upgrading," *Rev. Environ. Sci. Biotechnol.*, vol. 14, no. 4, pp. 727–759, 2015.
[22] J. Ling, P. Xiao, A. Ntiamoah, D. Xu, P. Webley, and Y. Zhai, "Strategies for CO_2 capture from different CO_2 emission sources by vacuum swing adsorption technology," *Chinese J. Chem. Eng.*, vol. 24, pp. 460–467, 2016.
[23] B. Metz, O. Davidson, H. de Coninck, M. Loos, and L. Meyer, *Carbon dioxide capture and storage*. Cambridge University Press, Cambridge, 2005.
[24] M. A. Sakwa-Novak, C. J. Yoo, S. Tan, F. Rashidi, and C. W. Jones, "Poly(ethylenimine)-Functionalized Monolithic Alumina Honeycomb Adsorbents for CO_2 Capture from Air," *ChemSusChem*, vol. 9, no. 14, pp. 1859–1868, 2016.
[25] V. Spallina, M. C. Romano, S. Campanari, and G. Lozza, "A SOFC-Based Integrated Gasification Fuel Cell Cycle With CO_2 capture," *J. Eng. Gas Turbines Power*, vol. 133, pp. 683–693, 2011.
[26] S. Ghosh and S. De, "Thermodynamic performance study of an integrated gasification fuel cell combined cycle - An energy analysis," *Proc. Inst. Mech. Eng. Part A J. Power Energy*, vol. 217, no. 2, pp. 137–148, 2003.
[27] T. Kivisaari, P. Björnbom, C. Sylwan, B. Jacquinot, D. Jansen, and A. de Groot, "The feasibility of a coal gasifier combined with a high-temperature fuel cell," *Chem. Eng. J.*, vol. 100, pp. 167–180, 2004.
[28] A. Verma, A. D. Rao, and G. S. Samuelsen, "Sensitivity analysis of a Vision 21 coal based zero emission power plant," *J. Power Sources*, vol. 158, no. 1, pp. 417–427, 2006.
[29] M. C. Romano, S. Campanari, V. Spallina, and G. Lozza, "SOFC-Based Hybrid Cycle Integrated with a Coal Gasification Plant," in *Proceedings of ASME Turbo Expo 2009: Power for Land, Sea and Air GT2009 GT2009-59551*, 2009, pp. 1–10.

[30] M. C. Romano, V. Spallina, and S. Campanari, “Integrating IT-SOFC and gasification combined cycle with methanation reactor and hydrogen firing for near zero-emission power generation from coal,” *Energy Procedia*, vol. 4, pp. 1168–1175, 2011.

Keywords: EFCF2020, SOx
Session A12: SOC integration, Power-to-X, CO2 capture etc.

https://doi.org/10.5281/zenodo.4550684

A1301

SOFC technology for heavy-duty vehicle propulsion

Marcus Taylor, Ahmad El-Kharouf, Robert Steinberger-Wilckens
Centre for Fuel Cell & Hydrogen Research, School of Chemical Engineering
University of Birmingham, Edgbaston, B15 2TT Birmingham/United Kingdom

Contact authors: www.EFCF.com/ContactRequest

Abstract

Solid oxide fuel cell (SOFC) systems can be integrated into heavy-duty vehicle (HDV) powertrains for applications where the vehicles are regularly and intensively used, such as commercial vehicles for long-haul road freight, as well as in buses, taxis, ships, etc. In such applications, cold-start of the fuel cell system is rare and current start-up times for the SOFC system are acceptable.

Using SOFCs for commercial vehicle applications allows for compatibility with the current trends towards LNG in freight transport. Given that natural gas can be replaced by synthetic natural gas (SNG) with carbon dioxide from biomass sources, a fully decarbonised and carbon neutral transport concept is achieved. The advantage over a pure low-temperature/hydrogen system is the higher efficiency of the fuel cell system, higher volumetric energy density of the fuel and the benefits of the high temperature off-heat. The phasing-in of such a system would occur without any disruption since it would use the current natural gas (methane) infrastructure. The application on commercial vehicles also includes refrigerated goods transport where the off-heat available from the SOFC system can power a vapour absorption refrigeration system.

This paper presents a zero-dimensional (0D) dynamic model of an SOFC stack with direct internal reforming (DIR) of methane, suitable for the integration into a vehicle powertrain. The area and number of cells define the stack size to meet the vehicle load requirements. The model uses an area specific resistance (ASR) approach to estimate polarisation losses and defines a lumped solid heat capacity to determine dynamic thermal response to a step change in load. The model shows good agreement with experimental data in the literature.

https://doi.org/10.5281/zenodo.4550700

Introduction

Advantages of SOFC technology for vehicle propulsion

SOFCs are attractive for stationary power and heat applications, but there has been limited development in automotive SOFC systems. We identify a number of advantages of SOFCs for vehicle propulsion:

1. High efficiency: The electrical efficiency of an SOFC—system (64%, LHV, DC [1]) and stack (74% [2])—is significantly higher that than of an internal combustion engine (ICE) or polymer electrolyte fuel cell (PEFC), resulting in reduced fuel consumption and lower emissions.
2. Fuel flexibility: SOFC vehicles run on existing natural gas infrastructure. There are over 4000 CNG or LNG refuelling stations and 1.4 million NG vehicles in Europe [3]. Renewable energy and biomass-derived carbon dioxide can be co-electrolysed to produce the feedstock for synthetic natural gas (SNG) production. SOFC drivetrains with the phase-in of SNG offer a fully decarbonised transport solution.
3. Electric: The electric motor employed in electrified vehicles delivers high torque at low speeds, ideal for HDVs, giving superior performance to ICEs. A hybrid battery can be included to meet transient load requirements, enabling SOFC downsizing and energy recuperation.
4. Off-heat availability: High-temperature heat used for ancillary services, e.g. a vapour absorption refrigeration system [4] for refrigerated goods transport, or air conditioning for off-road construction vehicles.

Modelling of SOFCs in automotive applications

SOFCs have been demonstrated as an auxiliary power unit (APU) onboard diesel heavy-duty vehicles (HDVs) [5], and for battery charging onboard an electric car [6] or an electric bus [7]. A number of authors have simulated SOFC concept vehicles [8]–[11], typically focussing on the SOFC hybridisation strategy. To the author's knowledge, few have studied the SOFC thermal dynamics on a vehicle. To investigate this, an SOFC model is required.

We consider direct internal reforming (DIR) SOFCs advantageous to systems with external reforming, due to their lower system complexity and the cooling DIR provides to the stack through the endothermic methane steam reforming (MSR) reaction. Models of DIR-SOFCs often calculate the rate of MSR reaction on the SOFC anode with chemical kinetics, with the fast water-gas-shift (WGS) reaction at chemical equilibrium and the relatively slow CO oxidation neglected [12].

In a DIR-SOFC, current density, temperature and reactant profiles are non-linear, therefore partial pressures and chemical kinetics are challenging to determine accurately. A 0D modelling approach can simplify the model with two assumptions (i) that the MSR reaction goes to completion [13], and (ii) that the partial pressures in the stack are equal to those at the exit [14]. Two authors published hierarchical models to work around this limitation of 0D models with DIR [15], [16]. They reduced one-dimensional (1D) profiles to 0D averages to study the dynamic performance. This approach combined the accuracy of 1D modelling with the fast computation of 0D modelling; however, is valid only for fixed inlet conditions.

During standard operation of SOFCs, ohmic losses dominate over other polarisation losses due to the high operating temperature. Therefore, some 0D models employ a

temperature-dependent ASR approach that lumps all polarisation losses into a single linear correlation [17]. The ASR approach is useful for 0D grey-box modelling because it requires no knowledge of the SOFC geometry. However, the uniform current density assumed in 0D modelling means that the low and high current densities, seen in a 1D DIR-SOFC model at the stack entrance and exit, respectively, are not depicted in the model.

Many DIR-SOFC models calculate polarisation contributions separately. However, such models involve estimating parameters that are difficult to determine accurately and are specific to stack design. For example, many authors calculate ionic and electronic conductivities using experimental data from IEA benchmark testing for planar SOFCs [18] and from Siemens Westinghouse for tubular SOFCs [19], even if the SOFC stack they model is rather different.

Thermal dynamics are of interest to SOFC researchers since they have a large impact on SOFC degradation rates in transient operation. Some authors have neglected gas mass transfer and electrochemistry dynamics, since thermal dynamics are far slower and dominate SOFC transient behavior [16], [20].

To the authors' knowledge, experimental set-ups or models in the literature where the majority of methane is reformed internally are rare. However, such experimental data is required for model verification. Forschungszentrum Jülich (FZJ) ran long-term SOFC tests with 90% of methane reformed internally, however current-voltage behaviour was characterised only with wet hydrogen [21]. The Korea Institute of Energy Research (KIER) published the current-voltage behaviour of a FZJ 5 kW stack operating up to 3.5 atm (absolute) with 90% of methane reformed internally [22].

1. Scientific Approach

This paper presents a 0D DIR-SOFC model suitable for estimating the dynamic performance during transient operation onboard a vehicle, as depicted in Figure 1. The model has a number of assumptions:

- Current density, stack temperature and reactant profiles are all uniform,
- Gases in SOFC channels are ideal gas mixtures at constant pressure (at 1 atm),
- The SOFC operates adiabatically,
- Three internal reactions take place within the SOFC; MSR (1), WGS (2), and hydrogen oxidation (H2OX) (3).
    - All methane fed to the stack reacts via MSR reaction [13],
    - The WGS reaction is at thermodynamic equilibrium [12],
    - Rate of CO oxidation is negligible [12],
- Only thermal dynamics are considered, pressure dynamics neglected [16]
    - Thermal mass of the fluid in the channels negligible to thermal solid mass,
- All polarisation losses may be approximated by a lumped ASR approach [17].

$$CH_4 + H_2O \rightarrow CO + 3H_2 \quad (1)$$

$$CO + H_2O \rightarrow CO_2 + H_2 \quad (2)$$

$$H_2 + 0.5\,O_2 \rightarrow H_2O \quad (3)$$

A steam-to-carbon ratio above two and an air-fuel equivalence ratio above three prevent carbon deposition. The stack operates at constant fuel utilisation. Single-cell experiments at FZJ estimated the ASR as a function of temperature [17]. The results of the model have been compared to experimental testing of the F' design FZJ stack at KIER [22].

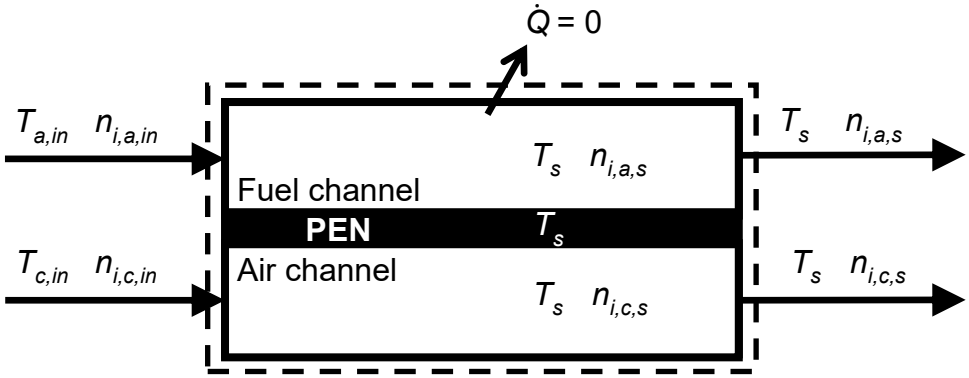

Figure 1: SOFC modelling approach.

2. Experimental

The 0D DIR-SOFC model is described by Equations (4) to (15), with parameter values shown in Table 1. Table 2 shows the operating conditions for model verification, and Table 3 shows the conditions for investigating the transient response of the model.

Rate of reaction

$$r_{MSR} = \dot{n}_{CH_4,in} \qquad r_{H2OX} = \frac{i}{nF} \tag{4}$$

WGS equilibrium

$$K_{WGS} = \prod_i a_i \, \upsilon_{i,WGS} = \exp\left(-\frac{\Delta G^o_{WGS}(T)}{RT}\right) \tag{5}$$

Material balance

$$\dot{\boldsymbol{n}}_{i,\,out} = \dot{\boldsymbol{n}}_{i,\,in} + \boldsymbol{\upsilon}_{i,k}\, \boldsymbol{r}_k \tag{6}$$

The model calculates r_{WGS} by solving Equations (4) to (6).

Activity

$$\boldsymbol{a_i} = \boldsymbol{y_i}\, \boldsymbol{P_i} = \frac{\dot{\boldsymbol{n}}_{i,out}}{\sum_i n_{i,out}}\, \boldsymbol{P_i} \tag{7}$$

Fuel utilisation

$$U_f = \frac{r_{H2OX}}{3\, r_{MSR} + r_{WGS}} \tag{8}$$

Cell voltage

$$V = V_0 - ASR \cdot i \tag{9}$$

Nernst potential

$$V_0 = -\frac{\Delta G^o_{H2OX}(T)}{n\,F} - \frac{RT}{n\,F} \ln\left(\prod_i a_i \, \upsilon_{i,H2OX}\right) \tag{10}$$

Area specific resistance

$$ASR = ASR_0 \cdot \exp\left[\frac{E_a}{R}\left(\frac{1}{T} - \frac{1}{T_0}\right)\right] \tag{11}$$

Energy balance

$$m_s\, \widehat{C}_p\, \frac{\mathrm{d}T}{\mathrm{d}t} = \dot{E}_{in} - \dot{E}_{out} - Q - iV \tag{12}$$

Energy flux in

$$\dot{E}_{in} = \dot{\boldsymbol{n}}_{c,i,in} \cdot \int_{T_{ref}}^{T_{c,in}} \boldsymbol{C_{p,i}}(T)\, \mathrm{d}T + \dot{\boldsymbol{n}}_{a,i,in} \cdot \int_{T_{ref}}^{T_{a,in}} \boldsymbol{C_{p,i}}(T)\, \mathrm{d}T \tag{13}$$

Energy flux out

$$\dot{E}_{out} = \dot{\boldsymbol{n}}_{i,out} \cdot \int_{T_{ref}}^{T_s} \boldsymbol{C_{p,i}}(T)\, \mathrm{d}T \tag{14}$$

Heat of reaction

$$Q = \boldsymbol{r}_k \cdot \Delta \boldsymbol{H}_{\boldsymbol{r},i,k} = \boldsymbol{r}_k \cdot \left[\left(\Delta \boldsymbol{H}_{\boldsymbol{f},i} + \int_{T_{ref}}^{T_s} \boldsymbol{C_{p,i}}(T)\, \mathrm{d}T\right) \boldsymbol{\upsilon}_{i,k}\right] \tag{15}$$

https://doi.org/10.5281/zenodo.4550700

Table 1: SOFC model parameters

Parameter	Value	
Area specific resistance at temperature T_0, ASR_0	0.29 Ω cm^2	[17]
ASR reference temperature, T_0	1073 K	[17]
Activation energy of H2OX reaction, E_a	0.65 eV	[17]
Mass of the solid per unit cell area, m_s	1.9 g cm^{-2}	
Specific heat capacity of fuel cell stack, $\widehat{C}_p$	0.4 J g^{-1} K^{-1}	[23]

Table 2: Experimental conditions for model verification [21]

Parameter	Value
Degree of pre-reforming	10%
LNG composition (simplification)	100% CH_4
Steam-to-carbon ratio	2.1
Fuel utilisation	0.705
Air-fuel equivalence ratio	3
Temperature of air and fuel at stack inlet	700°C

Table 3: Simulation conditions for investigating transient response

Parameter	Value
Degree of pre-reforming	0%
LNG composition	100% CH_4
Steam-to-carbon ratio	2
Fuel utilisation	0.70
Air-fuel equivalence ratio	6
Temperature of air and fuel at stack inlet	750°C

3. Results

SOFC characterisation

Overall, both the voltage and power characteristics show good agreement with the experimental data in Figure 2 at current densities of 0 A cm^{-2} to 0.44 A cm^{-2} with the stack temperature at 750°C. The point of inflection in voltage displayed around 0.03 A cm^{-2} is unexpected. It could be an artefact of the model caused by poor estimation of polarisation at low current densities using the ASR approach. However, this behaviour is acceptable, since it is outside the normal operational range of an SOFC stack. DIR reduces the Nernst potential (10) relative to operation with hydrogen fuel. The approximation that the uniform molar composition in the fuel channel is equal to that at the stack outlet, may be inaccurate, altering the Nernst potential, and shifting the voltage characteristic in Figure 2 vertically.

The gradient of the voltage characteristic is the ASR, a function of temperature. The parameters of the ASR equation (11)(11) were determined from single cell experiments at FZJ at low fuel utilisations and constant temperature [17]. Whilst cell-level results may have limited accuracy in predicting stack-level behaviour, the results in Figure 2 suggest they are useful to estimate the trend.

In Figure 2, the voltage and power calculated by the model are lower than the experimental data, particularly at higher current densities. It would be useful to have

experimental data under different operating conditions and at higher current densities (at least up to 1 A cm^{-2}) to better validate the model.

Overall, the SOFC model matches the experimental data well, suggesting that the model is suitable for integration into an electric drivetrain model.

SOFC dynamic response

A step increase in current density from 0.4 A cm^{-2} to 0.7 A cm^{-2} is simulated under the operating conditions tabulated in Table 3. Figure 3 shows a temperature increase of 25°C in response to the step increase in current density. The increased rate of the electrochemical oxidation of hydrogen, which is an exothermic reaction, causes this increase in temperature.

Figure4 shows an immediate voltage drop of 0.096 V in response to the step in current density. The increased polarisation losses that occur at increased load cause this drop in voltage. However, as the temperature of the stack increases, the ASR decreases and the voltage recovers by 0.025 V.

The relaxation time of the voltage and temperature response is analysed using the approach used in Sorrentino et al. [16]. The authors defined relaxation time as the time to recover 90% of the voltage drop, and 90% of the temperature increase, respectively. The voltage relaxation time is 650 s and the temperature relaxation time is 690 s.

The magnitude of the temperature and voltage response is dependent not only on the load change and on the ASR, but also on the chemical reaction kinetics and operating point (temperature, inlet composition, etc.). The relaxation time is dependent on the estimated mass and heat capacity of the stack (12). The relaxation times here are of similar order of magnitude to simulations presented in Sorrentino et al. [16].

Similar stack current step experiments conducted for an SOFC stack within an insulated integrated system module (ISM) from SOLIDPower SA, indicated relaxation times one to two orders of magnitude higher [14] due to the far larger thermal mass of system components in the HotBox, which is not considered in this simulation.

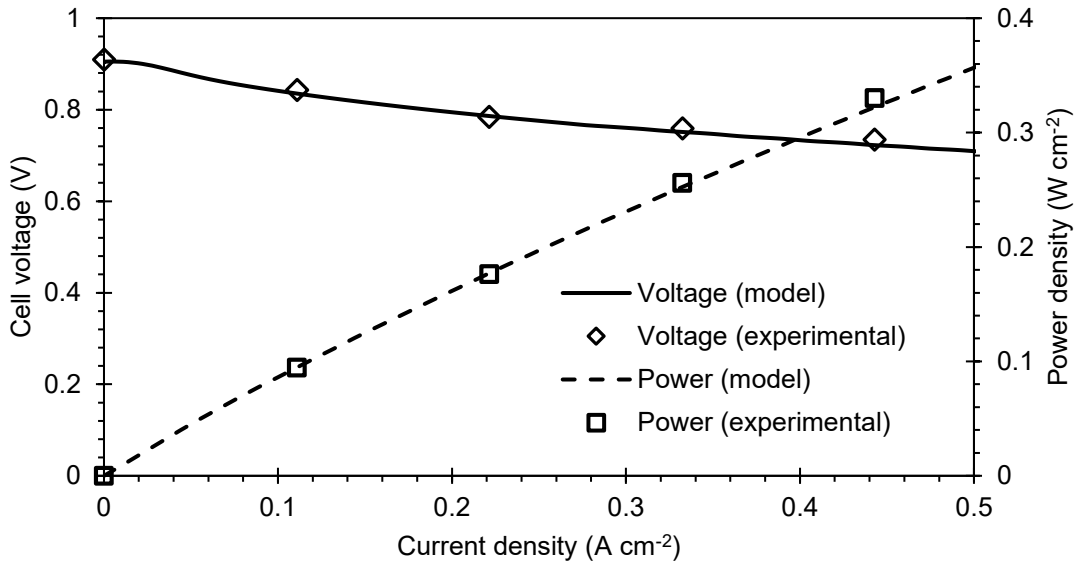

Figure 2: Verification of voltage and power characteristics.

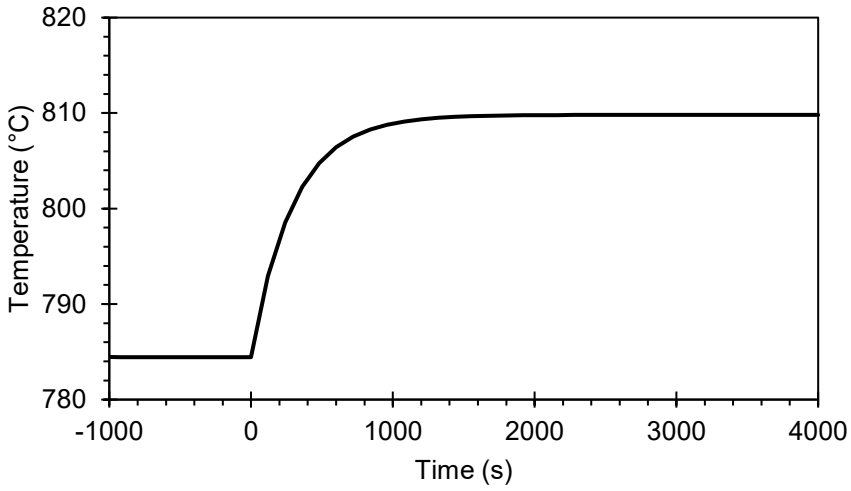

Figure 3: Temperature response to step change in current.

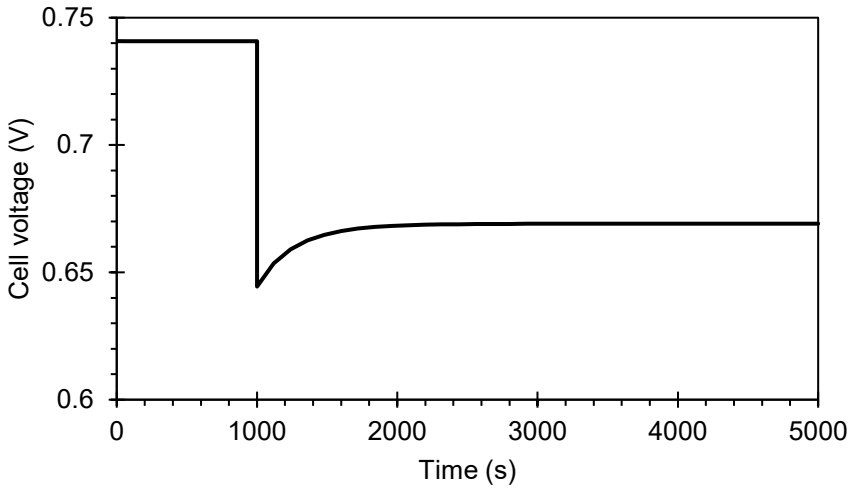

Figure 4: Voltage response to step change in current.

Conclusions

This paper displays a DIR-SOFC stack model suitable for integration into a system model on a commercial vehicle, with good agreement with experimental data in the literature. The results presented the thermal response of the stack during transient operation, which acts as a constraint in an SOFC control strategy. Additionally, only the current density, the number of cells and the cell area need be defined to meet a required load cycle.

However, there are some limitations to the thermal model: (i) the assumption that outlet temperatures on the anode- and cathode-side are equal and (ii) the 0D modelling approach does not account for temperature gradients within the stack. Moreover, the SOFC system from KIER used for experimental validation is significantly heavier than a system suitable for integration on-board a vehicle.

The lumped 0D modelling approach has the advantage of being computationally quick and requires knowledge of a limited number of variables. Therefore, it is considered an efficient means to estimate the behaviour of an SOFC within a vehicle drivetrain.

https://doi.org/10.5281/zenodo.4550700

Nomenclature

a	activity, species i	
ASR	area specific resistance	$\Omega\ m^2$
ASR_0	area specific resistance at temperature T_0	$\Omega\ m^2$
$\boldsymbol{C_p}$	molar heat capacity of species i	$J\ mol^{-1}\ K^{-1}$
$\widehat{C}_p$	specific heat capacity of fuel cell stack	$J\ kg^{-1}\ K^{-1}$
E_a	activation energy of H2OX reaction	$J\ mol^{-1}$
$\dot{E}$	enthalpy rate	$J\ s^{-1}$
F	Faradays constant	$C\ mol^{-1}$
$G°$	Gibbs free energy of reaction k at standard pressure	$J\ mol^{-1}$
i	current density	$A\ m^{-2}$
K	equilibrium constant, reaction k	
m_s	mass of the fuel cell stack per unit area	$kg\ m^{-2}$
n	moles of electrons transferred per mole H2OX reaction	
$\dot{\boldsymbol{n}}$	molar flow rate, species i	$mol\ s^{-1}\ m^{-2}$
P	partial pressure	Pa
R	universal molar gas constant	$J\ mol^{-1}\ K^{-1}$
$\boldsymbol{r}$	rate of reaction, reaction k	$mol\ s^{-1}\ m^{-2}$
T	temperature	K
T_0	ASR reference temperature	K
T_{ref}	enthalpy reference temperature	K
U_f	fuel utilisation	
V	cell voltage	V
V_0	open circuit voltage	V
$\boldsymbol{\upsilon}$	stoichiometric coefficient, species i, reaction k	

Subscripts

a	anode-side
e	electric
c	cathode-side
i	species i
in	inlet
k	reaction k
out	outlet
s	stack

References

[1] B. P. Borglum and H. Ghezel-Ayagh, 'Development of Solid Oxide Fuel Cells at Versa Power Systems and Fuel Cell Energy', *ECS Trans.*, vol. 57, no. 1, p. 61, Oct. 2013.

[2] Elcogen, 'Solid Oxide cell stack'. https://elcogen.com/products/solid-oxide-cell-stacks/ (accessed Jul. 25, 2020).

[3] NGVA Europe, 'Natural Gas Vehicle Catalogue 2019', Brussels, Aug. 2019.

[4] V. Venkataraman, A. W. Pacek, and R. Steinberger-Wilckens, 'Coupling of a Solid Oxide Fuel Cell Auxiliary Power Unit with a Vapour Absorption Refrigeration System for Refrigerated Truck Application', *Fuel Cells*, vol. 16, no. 3, pp. 273–293, 2016.

[5] J. Rechberger, A. Kaupert, J. Hagerskans, and L. Blum, 'Demonstration of the First European SOFC APU on a Heavy Duty Truck', *Transportation Research Procedia*, vol. 14, pp. 3676–3685, Jan. 2016.

[6] M. Matsumoto, 'e-Bio Fuel-Cell', presented at the World Congress on Industrial Biotechnology, Montreal, Canada, Jul. 2017.

[7] A. Ballard *et al.*, 'Development of the 5kWe SteelCell® Technology Platform for Stationary Power and Transport Applications', *ECS Trans.*, vol. 91, no. 1, p. 117, Jul. 2019.
[8] Y. Bessekon, P. Zielke, A. C. Wulff, and A. Hagen, 'Simulation of a SOFC/Battery powered vehicle', *International Journal of Hydrogen Energy*, vol. 44, no. 3, pp. 1905–1918, Jan. 2019.
[9] A. Chaudhari, A. Plianos, and R. Stobart, 'Modeling and Control Design of a SOFC-IC Engine Hybrid System', Apr. 2008, pp. 2008-01–0082.
[10] Z. Wu *et al.*, 'Dynamic modeling and operation strategy of an NG-fueled SOFC-WGS-TSA-PEMFC hybrid energy conversion system for fuel cell vehicle by using MATLAB/SIMULINK', *Energy*, vol. 175, pp. 567–579, May 2019.
[11] D. J. L. Brett, P. Aguiar, and N. P. Brandon, 'System modelling and integration of an intermediate temperature solid oxide fuel cell and ZEBRA battery for automotive applications', *Journal of Power Sources*, vol. 163, no. 1, pp. 514–522, Dec. 2006.
[12] E. Achenbach, 'Three-dimensional and time-dependent simulation of a planar solid oxide fuel cell stack', *Journal of Power Sources*, vol. 49, no. 1, pp. 333–348, Apr. 1994.
[13] S. Campanari, 'Thermodynamic model and parametric analysis of a tubular SOFC module', *Journal of Power Sources*, vol. 92, no. 1, pp. 26–34, Jan. 2001.
[14] M. Gallo, D. Marra, M. Sorrentino, C. Pianese, and S. F. Au, 'A versatile computational tool for model-based design, control and diagnosis of a generic Solid Oxide Fuel Cell Integrated Stack Module', *Energy Conversion and Management*, vol. 171, pp. 1514–1528, Sep. 2018.
[15] X. Zhang, J. Li, G. Li, and Z. Feng, 'Development of a control-oriented model for the solid oxide fuel cell', *Journal of Power Sources*, vol. 160, no. 1, pp. 258–267, Sep. 2006.
[16] M. Sorrentino, C. Pianese, and Y. G. Guezennec, 'A hierarchical modeling approach to the simulation and control of planar solid oxide fuel cells', *Journal of Power Sources*, vol. 180, no. 1, pp. 380–392, May 2008.
[17] A. Gubner, 'Non-Isothermal and Dynamic SOFC Voltage-Current Behavior', *Proc. Vol.*, vol. 2005–07, no. 1, p. 814, Jan. 2005.
[18] U. G. Bossel, 'Final report on SOFC Data: Facts and Figures', International Energy Agency, Berne, Switzerland, Apr. 1992.
[19] N. F. Bessette, W. J. Wepfer, and J. Winnick, 'A Mathematical Model of a Solid Oxide Fuel Cell', *J. Electrochem. Soc.*, vol. 142, no. 11, p. 3792, Nov. 1995.
[20] R. Bove and S. Ubertini, Eds., *Modeling Solid Oxide Fuel Cells: Methods, Procedures and Techniques*, 1st ed. Springer Netherlands, 2008.
[21] Q. Fang, L. Blum, P. Batfalsky, N. H. Menzler, U. Packbier, and D. Stolten, 'Durability test and degradation behavior of a 2.5 kW SOFC stack with internal reforming of LNG', *International Journal of Hydrogen Energy*, vol. 38, no. 36, pp. 16344–16353, Dec. 2013.
[22] T. Lim *et al.*, 'Operating characteristics of a 5kW class anode-supported planar SOFC stack for a fuel cell/gas turbine hybrid system', *International Journal of Hydrogen Energy*, vol. 33, no. 3, pp. 1076 – 1083, Feb. 2008.
[23] A. M. Murshed, B. Huang, and K. Nandakumar, 'Control relevant modeling of planer solid oxide fuel cell system', *Journal of Power Sources*, vol. 163, no. 2, pp. 830–845, Jan. 2007.

Keywords: EFCF2020, SOx
Session A13: Products, demonstrations, novel concepts & BoP

A1308

Solid oxide electrolyze cells prototype based on self-produced electrode supported tape cast cells and powder metallurgy interconnects: The CO_2Sin Project

M. Carmen Monterde (1, 2, 3), L. Bernadet (2), A. Rodriguez (1), J. Arcos (1), F. Ramos (4), A.Tarancón (6), J. A. Calero (1), E. Jimenez-Pique (3,5), M. Torrell (2)
(1) AMES S.A., 8 Camí Can Ubach, Barcelona/Spain
(2) IREC, Catalonia Institute for Energy Research, Dept. Advanced Materials for Energy Jardins de les Dones de Negre 1, 2ª pl. 08930 Sant Adrià de Besòs Barcelona/Spain
(3) Department of Material Science and Engineering. Universitat Politécnica de Catalunya, C/Eduard Maristany 16, 08019 Barcelona/Spain
(4) FAE, Políg. Ind. Gran Vía Sud, Carrer de Rafael Barradas, 19, 08908 Barcelona
(5) Barcelona Research Center in Multiscale Science and Engineering. Universitat Politécnica de Catalunya, C/Eduard Maristany 16, 08019 Barcelona/Spain
(6) ICREA, Passeig Lluís Companys 23, 08010 Barcelona/Spain

Contact authors: www.EFCF.com/ContactRequest

Abstract

The present work presents the advances on the development of a solid oxide electrolyze (SOE) prototype based on the own production of electrode supported tape cast cells combined with powder metallurgy interconnects (PM-IC). This progress has been developed by a consortium of two companies FAE producing the fuel electrode supported cells and AMES producing the PM-IC. IREC, as a research center is in charge of the testing and validating of the developed stacks. Single repetition units (SRU) and sub-stacks have been already produced and recently tested achieving 300 mA/cm^2 of injected current density at 1.4V under steam electrolysis and coelectrolysis modes. A SOEC prototype has been build and validated with 1kW commercial stacks. This prototype has been tested on a real industrial environment by coupling to a water treatment plant. As water is converted into hydrogen, values of 80% conversion have been obtained under a total injected current of 18 A and a voltage of 42 V, which corresponds to a production of more than 180L/h of hydrogen for SOEC prototype validation with the commercial stack coupled to the CO_2 outstream of the digesters of a water treatment plant to produce synthetic methane.
All these activities have been carried out under the frame of the CO_2SIN project (EU-RIS3-COMRDI15-1-0037-06).

https://doi.org/10.5281/zenodo.4550716

Introduction

Electrolyser devices are fundamentally based on SOFC technology operating in reverse mode. In an electrolyser stack, the cells determine the final performance, and therefore, a strong emphasis on increasing the cell quality should be carried out. The improvement of cell performance may be tackled on three different levels: i) materials selection, ii) microstructure of the electrodes, and iii) quality and adhesion of the interfaces [1,2]. In addition, the stability of used materials becomes very important for the good operation and durability of the SOC systems. SOEC cells are commonly derived from cells developed for SOFC operation. In general, such cells can stably operate in SOEC mode with no or minor modifications. However, an oxygen electrode that works stably in SOFC mode may experience rapid performance decay in electrolysis mode due to electrode delamination caused by oxygen evolution at the oxygen electrode/electrolyte interface [3].

This work presents the advances on the development of solid oxide electrolysis fuel electrode supported tape cast cells, the production of powder metallurgy based interconnects (PM-IC) and the preliminary validation of the balance of plant of a 1kW electrolyze prototype based on the own technology. The manufactured SOEC prototype was validated with a commercial 1kW stacks and tested on a real industrial environment by coupled with the CO_2 rich biogas outstream of the digesters of an industrial water treatment plant to produce synthetic methane. All these activities have been carried out under the frame of the CO_2SIN project (EU-RIS3- COMRDI15-1-0037-06)

1. Scientific Approach

The main research topics here presented are the design, manufacturing and validation of components to fabricate a stack based on fuel electrode supported (FES) solid oxide cells and PM interconnects, and the development of the balance of plant and the validation of an electrolyzer prototype based on SOEC technology.

In this work, fuel electrode supported solid oxide cells made using aqueous-based tape casting and screen-printing techniques were fabricated for fuel cell (SOFC) and electrolysis (SOEC) modes by FAE Company. Afterwards, cells of 36 cm^2 of active area were produced and tested in Single Repeating Unit (SRUs) and short-stack configurations SOEC (steam electrolysis) and Co-SOEC (steam and CO2 co-electrolysis) modes, offering remarkable performance results. Metallic interconnects made have been obtained by means of powder metallurgy technology (PM-IC) from ferritic stainless steels powders at AMES Company with 36 cm^2 of active area and tested in SRU at 750ºC in SOEC mode.

New developments have been incorporated in the FES cells production to obtain a co-sintered half cell using aqueous-based tape casting to finally deposit the CGO barrier layer and LSCF oxygen electrode by screen printing techniques at industrial scale at FAE Company. PM-IC have been obtained by means of powder metallurgy technology from ferritic stainless steels powders at AMES Company. Fabricated cells have been structurally and electrochemically characterised under electrolysis (SOEC) and coelectrolysisi (CO-SOEC) modes. Fuel electrode supported solid oxide cells and metallic interconnect, have been tested in single repeating unit (SRU) offering remarkable performance results. The Area Specific Resistance (ASR) values were measured with four-probe method under an isothermal condition at 770ºC. ASR was calculated using Ohm's law from the slope of the curve, obtained by plotting the measured voltage as a function of the applied current normalized by area.

https://doi.org/10.5281/zenodo.4550716

Another major objective of this study was the design, construction and validation with a commercial 1 kW stack tested on a real industrial environment and the development of the required balance of plant. The SOEC prototype is being installed to be operated under electrolysis and co-electrolysis mode coupled to the biogas out stream of an industrial water treatment plant [5].

The manufacturing of the electrolyzer prototype as well as its components (cell and interconnector) are part of the CO_2SIN project (fig.1) which aims to validate the production of renewable synthetic natural gas in a water treatment plant based in the Barcelona area. This project considers two types of electrolysis technologies for hydrogen generation: 37 kW of a commercial alkaline electrolyzer that operates at pressure (12 Bar) and the prototype solid oxide electrolysis system (SOEC) with higher efficiency to operate in electrolysis and coelectrolysis mode that is part of this study. The project also includes a biogas cleaning unit and a catalytic methanization reactor.

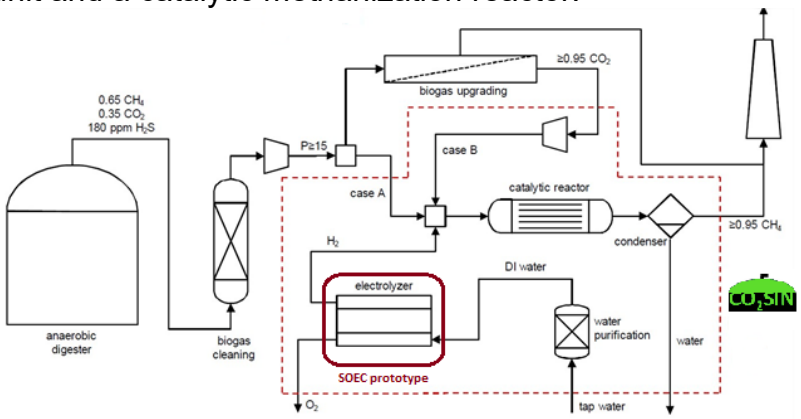

Fig. 1: Scheme of the CO_2SIN project

2. Experimental procedure

Nickel-yttria-stabilized zirconia (Ni-YSZ) fuel electrode supported solid oxide cells are composed of a Ni-YSZ support and fuel functional layer (FFL), a dense YSZ electrolyte, a CGO barrier layer and a LSCF cathode. The half cells that includes the Ni-YSZ support, the FFL and electrolyte were fabricated by aqueous multi-layered tape-casting process at industrial scale in FAE Company. YSZ (8% Y_2O_3-ZrO_2 by Kceracell), NiO (Kceracell) and a pore former (Sigma-Aldrich) were used to prepare FES, FFL and electrolyte. PEG 400, Duramax B1000 and Dolapix PC75 were employed as a plasticizer, binder and dispersant, respectively and water as a solvent. The YSZ slurry ratio in terms of powder:solvent:binder:plastizer:dispersant was 23:5:4:1:1. FFL slurry was prepared following the same approach, mixing NiO:YSZ in a 1:1 ratio by ball milling and the slurries prepared as YSZ slurries. FES slurry was prepared by a mixture of NiO:YSZ:PMMA (as pore former) in a 4:4:1 ratio by ball milling and the slurries prepared as YSZ and FFL ones. The half-cells were subsequently co-sintered at >1300ºC presenting an area of 8 x 8 cm^2 and a total thickness around 600 um. Afterwards, a cation diffusion barrier layer CGO ($Gd_{0.2}Ce_{0.8}O_2$) was deposited by scree-printing and sintered at >1200ºC. Finally, a LSCF ($La_{0.6}Sr_{0.4}Co_{0.2}Fe_{0.8}O_3$ oxygen electrode was deposited by screen-printing and subsequently sintered (Fig. 2 a)) [6]. Cells were tested in the IREC test bench equipped with a DC power supply and electronic loads that allowed reversible operation able to measure either single cells or stacks.

In this work the Interconnect has produced from a 22%wt Cr, 0.6%wt Mn, 1%wt Mo, Fe rest alloy manufactured by Epson Atmix Corporation from Japan which was compacted in a die at a pressure of 3 Tm/cm^2. Ferritic stainless steel (FSS) are good candidates as metallic interconnects in SOC technology at high temperatures (800ºC) as they offer simultaneously high electronic conductivity, high thermal conductivity, gas tightness and thermal expansion coefficient matching that other stack components [7]. P/M interconnects has some advantages over traditional manufactures (casting-rolling-forging route) such as near-net shape production, fast and high production rates, elimination and reduction of machining step and scrap material [8]. After a compacting process the samples were thermally treated in a continuous belt furnace under a reducing atmosphere at 1250ºC to 300 seconds/drawer has been performed to sinter the final piece (8 x 8 cm^2). In the present case, the samples fabricated to test the interconnect functionality and needs, have a continuous peaks and valley geometry. In the sintered interconnect (fig. 2 b)), a final density of 7.32 g/cm^3 has been achieved for all the fabricated pieces. This final density, represents a 95% of the same chemical composition that the solid with a 29% in dimensional change (shrinkage) due to thermic process. In order to minimise the Cr-poisoning effect, a protective $(Mn,Co)_3O_4$ spinel coatings has been applied on the sintered interconnect by roll painting of a commercial powder suspension in terpineol (Sigma-Aldrich) with sintering cycles (reduction and oxidation treatment) for the coating sintering. The ASR values of interconnectors were measured with four-probe method under an isothermal condition at 770ºC for 500h in air for one side and a mix of 90% N_2/10% H_2 on the other side. Heating and cooling rates were set to 1ºC/min to reproduce the operating conditions for solid oxide cell operations. Area Specific Resistance (ASR) was calculated using Ohm's law from the slope of the curve, obtained by plotting the measured voltage as a function of the applied current (from -5 A to 5 A) normalized by area.

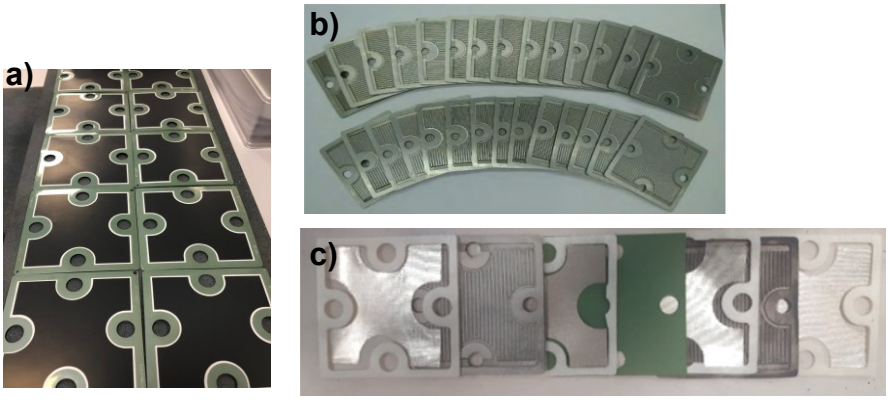

Fig 2: a) ASC manufactured at FAE, b) PM-IC manufactured at AMES and c) SRU components

The cells are assembled into single repeating unit (SRU) to build up a stack [2,7]. A single repeating unit consisting on a cell and two interconnectors, glass sealing, Ni foam at the fuel electrode and Ag mesh.

The high temperature electrolyze prototype (Fig.3) is completely designed and developed in Spain through the collaboration of research centers (IREC, UPC) and companies (FAE, AMES). The main components of the prototype are the oven or heating system, the mass flow controller and meter system for fuel gas (H_2O or CO_2) and waste or product gases (air, oxygen and H_2), the controlled evaporator mixer (CEM) to obtain the water vapor. The control and program system as well as the planning of the various working methods, the possible actions in case of emergency and the continuous data collection and graphing

has been designed, programmed and assembled internally at AMES. The SOEC prototype was validated with a commercial 1kW stacks and tested on a real industrial environment by coupling to an industrial water treatment plant. The commercial stack (SOFCMAN company) is composed by 30-cell planar 8 x 8 cm^2 cathode supported cells made with Ni-YSZ, YSZ electrolyte, CGO barrier layer and LSCF-CGO oxygen electrodes with a total active area of 1900 cm^2 and has been tested as water electrolyser at 750ºC on the water treatment plant.

Fig. 3: SOEC prototype on the water treatment plant

3. Results

SRU electrochemical test

Developed cell were assembled in SRU between two PM-IC and one cell with ceramic sealing, Ni foam and Ag mesh in order to ensure de current contact and to facility the assembly. Figure 4 shows the I-V polarization curve for the SRU under SOEC and Co-SOEC mode at 750ºC. The presented I-V curves have been obtained under 50 $NmL \cdot min^{-1} \cdot cm^{-2}$ of 90/10 H_2O/H_2 for the SOEC measurement and 65/25/10 $H_2O/CO_2/H_2$ for the Co-SOEC measurement at the fuel electrode, and 150 $NmL \cdot min^{-1} \cdot cm^{-2}$ of synthetic air at the oxygen electrode. The SRU present the expected OCV (>1.1) and a maximum injected current density around 0.3A/cm^2 for both cases at 1.4V.

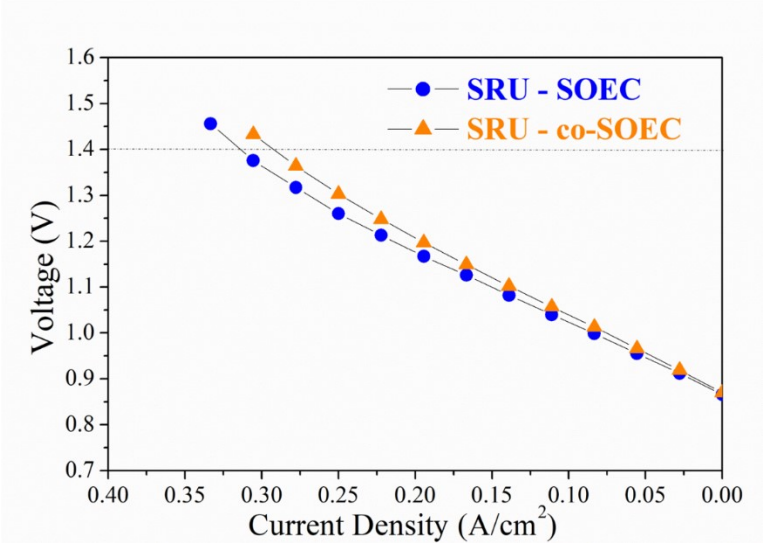

Fig. 4: I-V polarization curve of SRU under SOEC and Co-SOEC mode for a single fuel electrode cell and two PM interconnector SRU

https://doi.org/10.5281/zenodo.4550716

SRU Characterization after testing

The SRU was characterized by EDS-SEM after 150h of tests in order to find Cr poisoning to due to the high chromium content of the IC-PM (figure 5 a) and to verify the MnCo protective barrier layer functionality. The line scan analysis of the cell confirms that after 150 h of testing there is no chromium poisoning on the cell showing the desired stability at high temperatures.

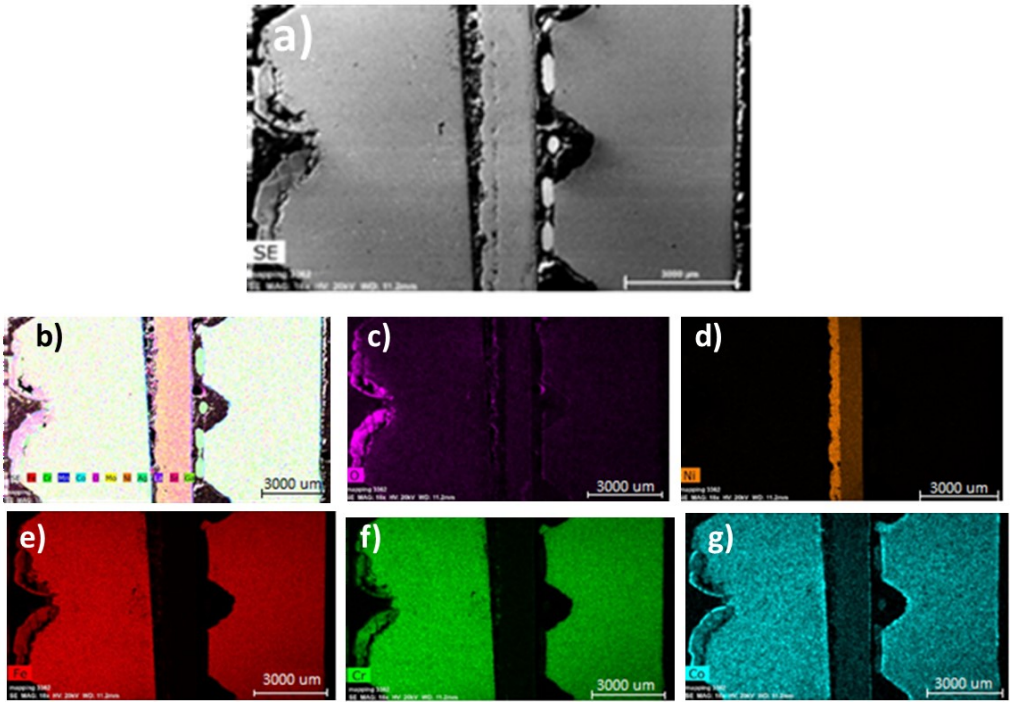

Fig. 5: a) SEM image and b) chemical compounds mapping of SRU cross-section tested and the different elemental compositional EDS maps of c) oxygen, d) nickel, e)Iron, f)chromium, g) cobalt.

SOEC Prototype validation in water treatment plant

The SOEC prototype was validated in the laboratory with a commercial 1kW stacks at 750ºC under 80% of FU (atmosphere condition shows in the figure 6). This test confirms that the designed balance of plant of the prototype was working at the operation conditions of 750ºC achieving 80% of steam conversion under an injected current of 32A and a voltage of 39 V that correspond to 400L/h of hydrogen in SOEC mode.

https://doi.org/10.5281/zenodo.4550716

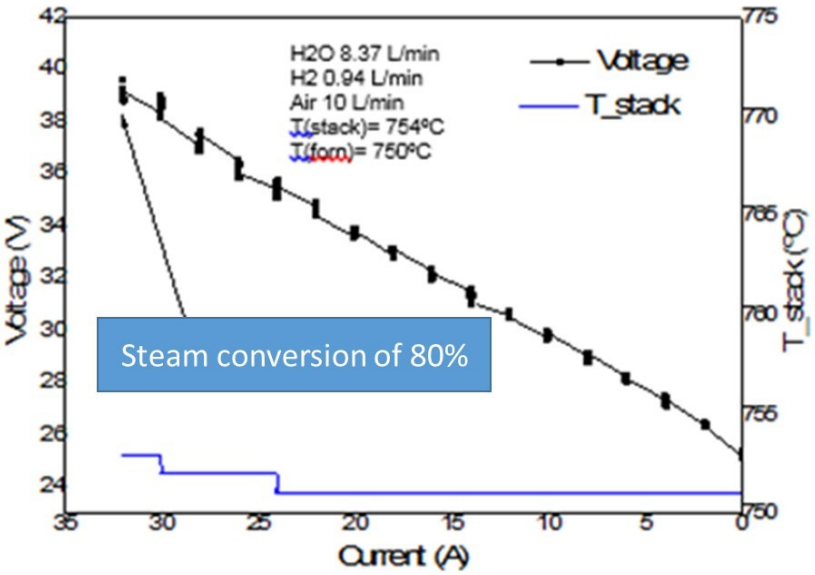

Fig. 6: I-V polarization curve of 1 kW commercial stack at SOEC prototype at 750ºC

SOEC Prototype tested

Once the electrolyze prototype was coupled to the water treatment plant, its behavior was validated in electrolysis mode for the generation of H_2 in the plant. Different types of operation regime were studied. Focusing on the analysis of the effect of variable current injection with I-V curves made at 750ºC in steam electrolysis mode (Fig.7). Values of 80% conversion have been obtained under a current of 18 A and a voltage of 42 V, showing a lower performance than the obtained on the laboratory tests. Further experiments are needed to optimize the operation on the real industrial environment.

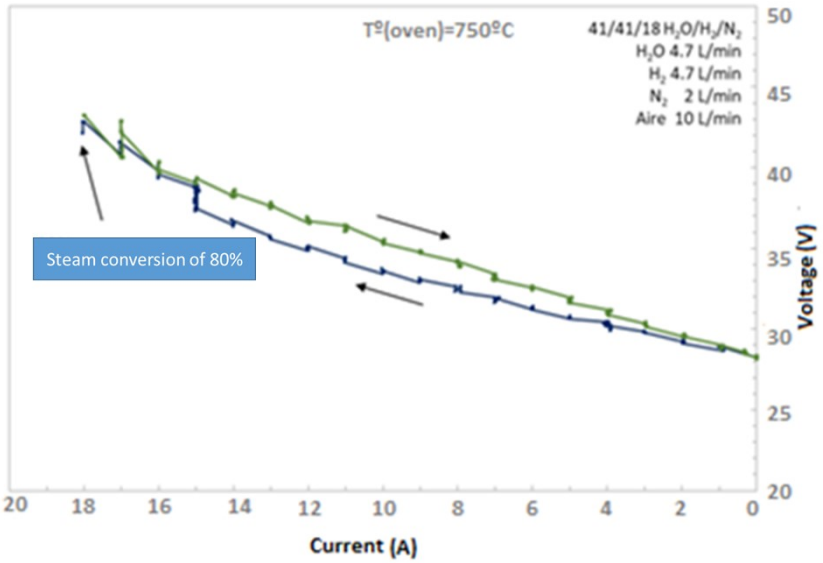

Fig. 7 – I-V polarization curve in electrolysis obtained in the water treatment plant at 750ºC

4.-Conclusions

Functional fuel electrode supported tape cast cells and coated powder metallurgy based interconnects (PM-IC) have been obtained and tested as SRU for solid state electrolyzer (SOEC) systems. The coating applied to the interconnector after 150h of testing at 770ºC demonstrates its effectiveness as a barrier to chrome, preventing cell poisoning.

https://doi.org/10.5281/zenodo.4550716

The 1kW electrolyze prototype has been designed, built and validated with a commercial stack. 32A have been injected at 39 V with a commercial stack (1kW) in the laboratory tests while a lower performance of 18A at 41V has been obtained on the validation of the integrated prototype at the water treatment plan.

5.-Aknowledgements

The authors are grateful for to the financial support of EU-RIS3 (FEDER) within the framework of the projects (CoSin)-COMRDI-15-1-0037 and HyBCN project 19S01452 - 006, and the “Institut de Cultura de Barcelona” for the financial support of the project HY-BCN (19S01452-006). M.C.Monterde would like to acknowledge the Generalitat de Catalunya through AGAUR for the project Industrial Doctorate ref.2017 DI

References

[1] J. T. S. Irvine, et al. Evolution of the electrochemical interface in high-temperature fuel cells and electrolysers. Nat. Energy 1 (2016) 15014.

[2] N. Mahato, et al. Progress in material selection for solid oxide fuel cell technology: A review. Progress in Materials Science 72 (2015) 141-337

[3] GE Hybrid Power Generation Systems. High Performance Flexible Reversible Solid Oxide Fuel Cell, Final Technical Report (2008).

[4] C. Graves, S.D. Ebbesen, M. Mogensen and K.S. Lackner, *Renew. Sustain. Energy Rev.*, 2011, 15, 1-23.

[5] R. Bhandari, C.A. Trudewind and P. Zapp, *J. Clean. Prod.*, 2014, 85, 151-163.

[6] Miguel Morales, Marc Torrell, Álex Morata, Eduard de Paz, Mari Carmen Monterde, Maria Sierra, Francisco Ramos and J.Antonio Calero “Development of an electrolyzer stack module of fuel electrode supported solid oxide cells fabricated by aqueous multilayered tape-casting and metallic interconnects by powder metallurgy” 13th SOFC-SOE Forum 2018.

[7] N. Shaigan, W. Qu, D. G. Ivey, W. A. Chen. Review of recent progress in coatings,surface modifications and alloy developments for solid oxide fuel cell ferritic stainless steel interconnects. Journal of Power Sources 195(6) (2010) 1529-1542

[8] H. Herchen, C. Karuppaiah, T. Armstrong. Method of making fuel cell interconnect using powder metallurgy. United States Patent App. Public (2013) US 2013/0129557 A1.

[9] J. C. W. Mah, A. Muchtar, M. R. Somalu, and M. J. Ghazali, “Metallic interconnects for solid oxide fuel cell: A review on protective coating and deposition techniques,” *Int. J. Hydrogen Energy*, vol. 42, no. 14, pp. 9219–9229, 2017.

Keywords: EFCF2020, SOx
Session A13: Products, demonstrations, novel concepts & BoP

A1501

Fabrication of Porous Structure with 3D Printing Technology

Kotaro Miyamoto (1), Hirotaka Koga (1), Masaaki Izumi (1), Masahiko Mizui (2), Hidekazu Nishiguchi (3)
(1) The University of Kitakyushu
1-1, Hibikino, Wakamatsu-ku, Kitakyushu, Fukuoka/Japan
(2) Kyushu Kyoritsu University
1-8, Jiyugaoka, Yahatanishi-ku, Kitakyushu, Fukuoka/Japan
(3) Meiryo Corporation
1-2, Kurosaki shiroishi, Yahatanishi-ku, Kitakyushu, Fukuoka/Japan

Contact authors: Try www.EFCF.com/ContactRequest

Abstract

The porous structure of electrodes in SOFCs is the key factor to improve its performance and the manufacturing method to control its design needs to be established. Additive manufacturing, so-called 3D printing technology can be a prospective method for the fabrication of electrodes of SOFCs. In this experiment, stereolithography, which is a form of 3D printing technology using UV-light with approximately 365nm wavelength and photo-curable resin, is applied. The UV-light that goes through pinholes enables the production of multiple cylindrical objects at once. As a result, the objects and the empty spaces between them make the porous structure. Moreover, by changing the size and the number of holes and distance between them, the fabrication of electrodes with the desired microstructure can be expected.

https://doi.org/10.5281/zenodo.4556828

Introduction

Solid oxide fuel cells (SOFCs) are considered as prospective power generators because of their high efficiency and less emissions of CO_2 and other air pollutants such as NOx and SOx. These advantages increase the attention towards fuel cells and better improvement is required in terms of environmental load [1]. The microstructure (porosity) of an anode in SOFCs in particular, is responsible for the cell reaction, transfer phenomenon of hydrogen, water vapour and electron, and affects not only its performance but also durability. Especially the most important areas of solid oxide fuel cell anodes are the Triple Phase Boundary (TPB), where oxide ion meets hydrogen and chemical reaction occurs. It is necessary to produce the microstructure with multiple pores that transfer the fuel into electrochemical reaction zones (TPB) and let water vapour flow out smoothly. Therefore, the optimisation of the microstructure is crucial for the improvement of the performance [2]. A conventional method, which is wet processing, makes the irregular pore distribution by heat-treating the mixture of YSZ and NiO with pore formers is widely used [3]. However, this does not enable to control the distribution of gas channels and the size of each pore. Hence, an alternative way to realise the fabrication of microstructure of an anode, controlling its porosity, needs to be established.
Additive manufacturing, so called 3D printing technology is considered as a prospective method because of its flexibility to change the design although manufacturing time tends to be extremely long to improve the modeling accuracy [4]. The optimization of cell components including electrodes with Selective Laser Melting technology (SLM) proved the possibilities of better production of the porous structure in electrodes [5]. This research aims to fabricate electrodes with microstructure by adopting and advancing a type of 3D printing technology, especially stereolithography. In order to improve modeling accuracy while shortening manufacturing time, some basic experiments have been conducted. This paper, in particular, mentions objects, which are fabricated with an original 3D printer and consist of multi-cylinders and pores.

1. Apparatus and experimental method

Figure 1 shows the schematic diagram of the 3D printer which was specifically designed for this research. UV-LED light irradiates a mixture of electrode powder and photo-curable resin in the pool. The glass plate is attached at the bottom of the pool in order for the light to pass through and reach the substrate, which is connected to the upper XYZ-stage. The UV-LED light with a wavelength of 365nm cures the resin on the surface of the substrate. For the light source, Omuron ZUV-H2OMC and ZUV-C2OH are used as a head and a controller respectively. For the optical system from the light source, whose output power is 540mW, to the pinhole plate, the compact microscope CM-30L2 made by Nikon with various lenses is used. Two types of pinhole plates (Fig. 3) : one with 16 (4×4) holes with 200μm diameter and the other one with 9 (3×3) holes with 300μm diameter are designed to fit in the 1.6mm diameter, which is the irradiation area when the objective lens is utilised. Electrode material is a mixture of NiO and YSZ, which are commonly used for anodes, and photo-curable resin, Henkel LOCTITE363 is added. Mixing ratio of the electrode material by volume is 5%, 10% and 20%. Though forming with the mixture of 5% and 20% are verified, 10% one is mainly employed because of its stability for forming.

https://doi.org/10.5281/zenodo.4556828

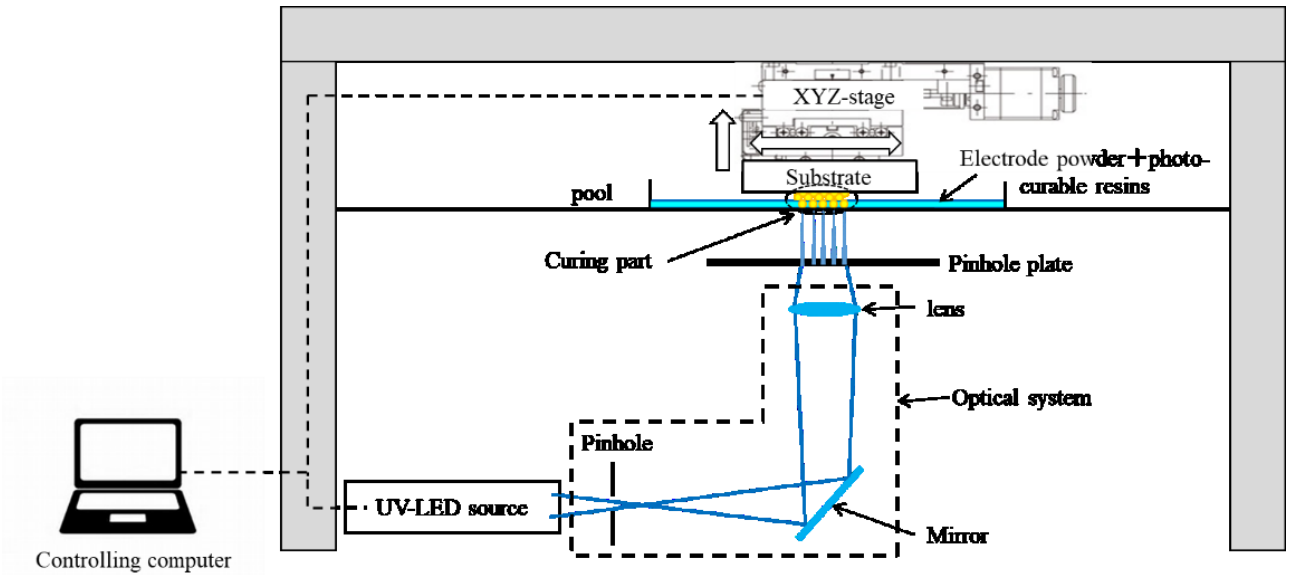

Fig. 1 Schematic diagram of the 3D printer

Figure 2 shows the position of the pinhole plate in the equipment. At the beginning, it was set under the glass plate at the bottom of the pool but it is put on the glass and covered with 50μm thickness coating film on it. This change decreases light scattering and enables to obtain the cylindrical objects, whose diameter is almost equal to pinholes'. Coating film prevents the formed objects from adhering to the glass not the substrate.

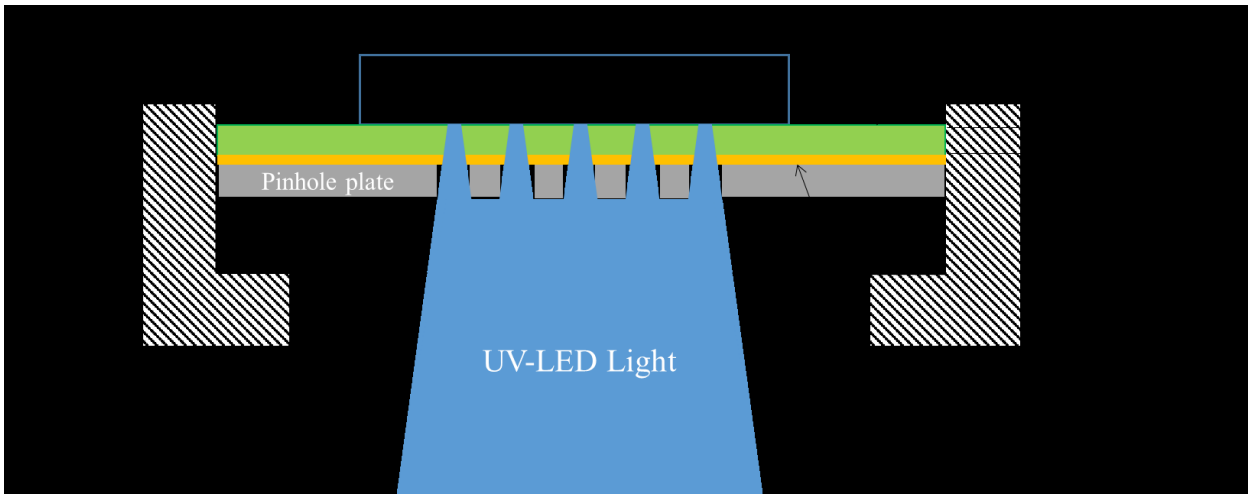

Fig. 2 Position of the pinhole plate

The space called "clearance" between the coating film and the substrate affects the height of the objects. The "clearance" is measured by the high precision laser displacement meter (OPTEX CDX-LE15) with accuracy of 0.1 μm and controlled by the automatic XYZ-stage in 1μm increments in advance. The displacement meter is fixed at the same position as the optical system and replaced after completing measurement.

The pinhole plates are made of stainless and have a thickness of 100μm. As shown in Figure 3, Φ200μm pinhole plate has 16 holes and Φ300μm pinhole plate has 9 holes. The centre-to-centre distance between each hole is 300μm for Φ200μm pinhole plate and 400μm for Φ300μm pinhole plate. The number of pinholes is limited because of the

irradiation area, which is a circle with 1.6mm diameter when the objective lens of 10 magnification is applied. The irradiation area can be expanded by adopting another type of lens.

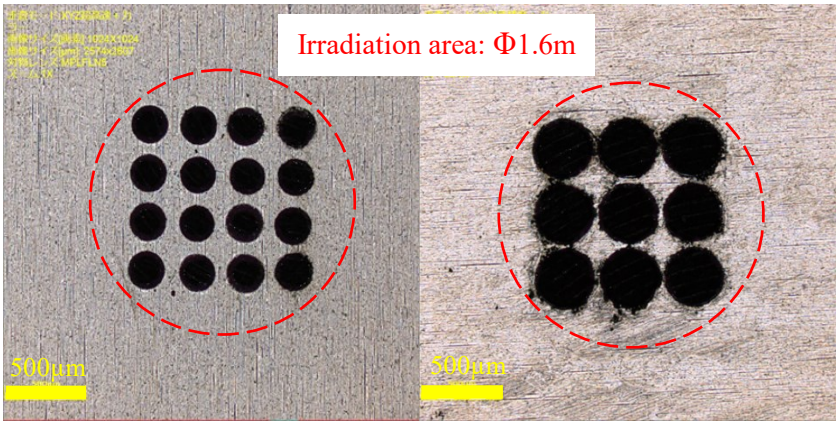

(a) Φ200μm pinhole plate (b) Φ300μm pinhole plate

Fig. 3 Pinhole plates

Figure 4 illustrates the procedure of forming multi-cylindrical objects and stacking layers. The UV-LED light goes though the pinholes and divided lights irradiate the mixture of electrode powder and photo-curable resin. After the irradiation, photo-curable resin is cured and cylindrical objects are formed on the surface of the substrate above. Once multi-objects of the 1st layer are formed, the substrate connected to the XYZ-stage moves up to make some space between the pinhole plate and the substrate so that the objects of the next layer are ready to be formed. By repeating this process, pores are obtained between each cylindrical object and layer and a mass with microstructure (porosity) is fabricated. This mass that consists of tiny cylindrical objects with gas channels can work as a part of a SOFC anode or an anode itself. In addition, by changing the design of the pinhole plate, it is possible to control porosity and pore distribution.

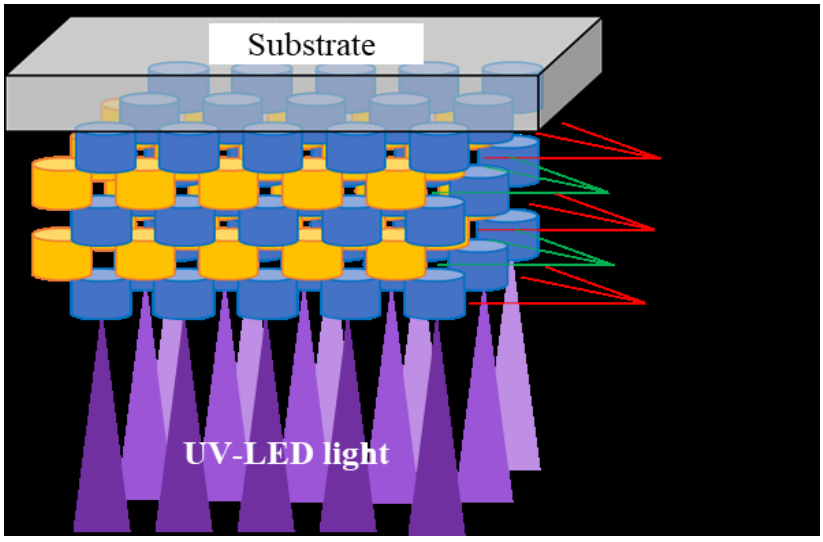

Fig. 4 Forming objects

https://doi.org/10.5281/zenodo.4556828

2. Results and Discussion

Cure conditions

In order to determine the conditions that enable the perfect cure of the mixture of resin and electrode powders (mixture ratio 10%), experiments with Φ300μm pinhole were conducted, changing the light source power and irradiation time. The range of the light source power is 50 to 100%. Figure 5 reveals the conditions where 9 cylindrical objects were successfully formed and where the formation failed or defect can be seen. As the results show, in order to form 9 cylindrical objects completely, at least 230 seconds duration is required with 80% light source power while only 100 and 80 seconds are the minimum irradiation times with 90% and 100% light source power respectively. Irradiation with 50 to 70% light source power for 240 seconds were unable to cure any cylindrical object.

Between 80% and 90% of the light source power, the cause of the rapid change in irradiation time required to obtain the perfect cure is not clear, it is currently under investigation.

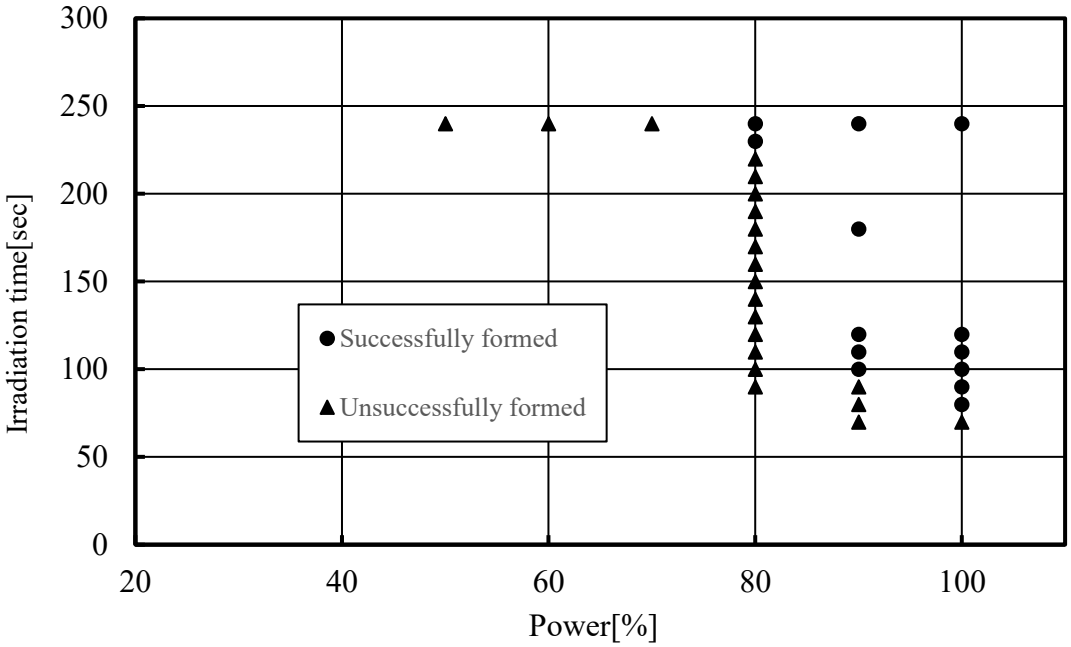

Fig. 5 Relation between light source power and irradiation time

Multi-layer objects

Some samples of multi-layer objects were fabricated to demonstrate that the mass of cylindrical objects has the pores that can be gas channels of the electrode. These samples were successfully formed after the arrangement of automatic control system that controls the move of the substrate and the irradiation timing of the light.

Figure 6 shows the sample of 6-layer objects, which has 36 (6×6) cylindrical objects per layer. Each layer is about 2.4mm square and the average height of the whole mass is 142μm. The calculated porosity is 54%, which is higher than the design value because each cylindrical object shrunk compared to the size of pinholes.

Figure 7 shows the sample of 10-layer objects. Each layer has 36 (6×6) cylindrical objects. The average height of the mass is 231μm and the distance between each object is 68μm on average.

https://doi.org/10.5281/zenodo.4556828

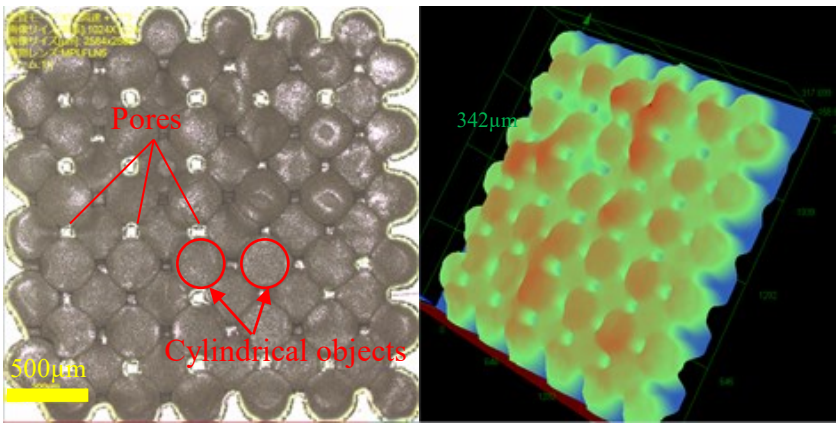

(a) Colour image (b) 3D image

Fig. 6 3D printed 6-layer objects

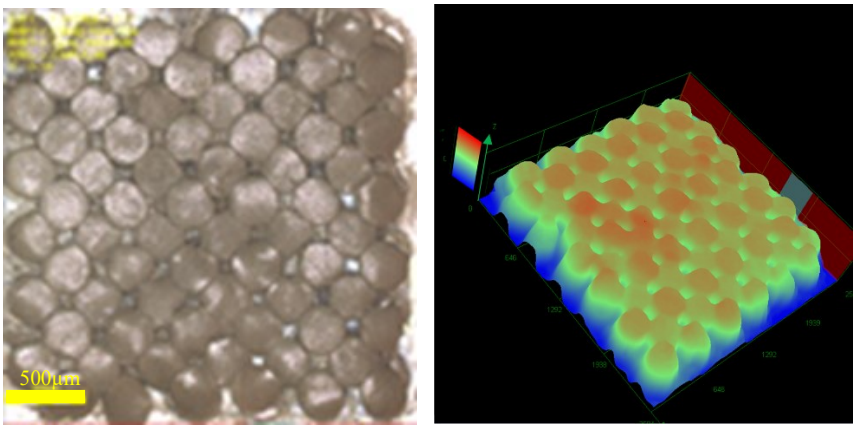

(a) Colour image (b) 3D image

Fig. 7 3D printed 10-layer objects with microstructure

Figure 8 shows the optical microscopy image of the cross-section of multi-layer object. The gray area in the figure shows the void between layers. The gap seen at the centre of the image is surrounded by cured parts and has approximately 25μm height as designed. This proves that gas channels were successfully formed between each layer and enabled the fabrication of porous structure without the mixture of resin and electrode powder filling these gaps.

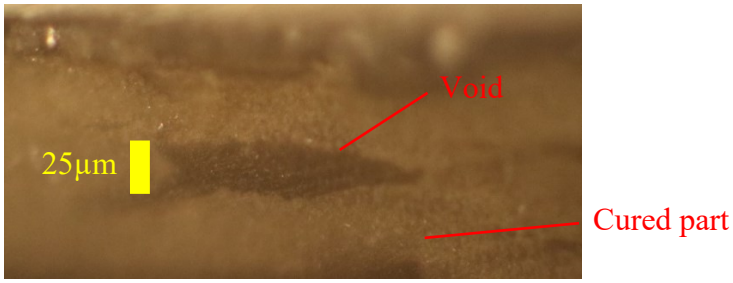

Fig. 8 Void between layers

3. Conclusions and future prospects

In this study, the original 3D printer enabled the production of multiple cylindrical objects and the mass with porous structure. The mixture of electrode powder and photo-curable resin was successfully cured with UV-LED light whose wavelength is 365μm. The size and

shape of each cylindrical object depends on those of pinholes. Also, the possibility of curing is affected by the light source power and the irradiation time. The mass with 6-layer and 10-layer objects demonstrate the formation of pores between each cylindrical object and layer.
In order to fabricate a decent-sized mass, the area in a plane direction needs to be extended. Further experiments will be done to increase layers and shorten the irradiation time for more rapid fabrication. Increase of the volume fraction of electrode material is also required. The final aim of this study is to produce more efficient and durable anodes for SOFCs that perform better than ones fabricated in a conventional way. This novel method using stereolithography will be an alternative technology because of its advantages, especially the flexibility to change or control the design of microstructure.

References

[1] Lucy Smith, et al, Comparative environmental profile assessments of commercial and novel material structures for solid oxide fuel cells, Applied Energy, 235, 1300-1313, 2019.
[2] PaulA. Connor, et al, Tailoring SOFC Electrode Microstructures for Improved Performance, Advanced Energy Material, 8(23), 2018.
[3] Masaaki Izumi, et al, Effect of pre-sintering of raw material powder on properties of solid oxide fuel cell electrolyte prepared by dip-coating method, Journal of the Ceramic Society of Japan 118, 944-947, 2010.
[4] N.P.Kulkarni, et al, Fuel cell development using additive manufacturing technologies - A review, Journal of sustainable manufacturing and renewable energy , 686-689, 2009.
[5] L.F. Arenas, C. Ponce de León ⁎, F.C. Walsh, Electrochemistry communications 77, 133-137, 2017.

Keywords: EFCF2020, SOx
Session A15: Cell, stack & system modelling and optimization

https://doi.org/10.5281/zenodo.4556828

A1502

A methodology for the assessment of sealing joints in high-temperature SOFC stacks

Sophia Bremm (1), Sebastian Dölling (1), Wilfried Becker (1), Ludger Blum (2), Roland Peters (2), Jürgen Malzbender (2)
(1) Technische Universität Darmstadt, Fachgebiet Strukturmechanik, Franziska-Braun-Straße 7, D-64287 Darmstadt/Germany
(2) Forschungszentrum Jülich GmbH, D-52425 Jülich/Germany

Contact authors: www.EFCF.com/ContactRequest

Abstract

High-temperature Solid Oxide Fuel Cells (SOFCs) enable an efficient and economical way to convert chemical energy, stored in fuels, directly into electrical energy. A decisive factor for the reliable long-term operability of the stack is the hermetic sealing and thus a separation of oxidant and fuel gas. The design of the sealing, commonly made of glass ceramics is very demanding since it has to withstand high temperature loadings. The load on the sealing results from the inhomogeneous temperature field and the mismatch of thermal expansion coefficients yielding an inhomogeneous stress field. Furthermore, time-dependent effects have to be considered as well. In the present work a methodology for the assessment of glass ceramic sealings is presented and applied to a recent SOFC design, developed by Forschungszentrum Jülich.
Using simplified two-dimensional models and where necessary a parameterized three-dimensional full scale finite element model, stationary in operation load cases as well as cooling down to ambient temperature are investigated.
Particular emphasis is placed on the discussion of the physical mechanisms causing stresses within the sealing. If the temperature is below the glass transition temperature, time-invariant material behavior may be postulated. Hence, crack initiation in the sealing yielding leakage may be predicted using the coupled stress and energy criterion within the framework of finite fracture mechanics. If the temperature is larger than the glass transition temperature viscoelastic behavior has to be taken into account. Finally, on the basis of sensitivity analyses possibilities for an improved design are discussed.

https://doi.org/10.5281/zenodo.4556841

Introduction

Solid Oxide Fuel Cells are operating in a temperature range from about 600°C to 1000°C. Due to the high operating temperatures, they allow solid ceramics, often yttria-stabilised zirconia, as cost-efficient electrolyte. Moreover, SOFCs exhibit energy conversion rates that exceed those of other fuel cell concepts [1]. Nevertheless, also difficulties associated with high operating temperatures arise. Especially for planar SOFC designs the hermetic sealing of the fuel cell stacks is challenging [2]. The seals are subjected to high operating temperatures, inhomogeneous temperature fields, and reactive atmospheres. Thus, the seals can significantly reduce the lifespan of the fuel cell stacks since even weak leakage can markedly affect the cell performance [3]. As a consequence, the sealing development plays a major role in a potential industrial SOFC application. Different sealing concepts were proposed. They can be roughly distinguished between compressive and rigid seals. A compressive seal is a compliant high temperature material that is placed between the sealing surfaces. The seal effect is reached by compressing the seal by external forces on the fuel cell top. That type of sealing is not materially bonded to the surfaces and therefore allows a relative movement between the sealing surfaces such that different thermal expansion behavior of the stack components can be handled. A drawback of that type of seals is that a certain leakage cannot be avoided, as shown by many authors.
More widespread is the concept of rigid seals since it exhibits several advantages. Typically, rigid seals consist of glasses or glass ceramics [4]. As a matter of principle, rigid seals avoid leakage effectively. The sealing has to fulfill several complex requirements in order to ensure proper SOFC operation. At the same time, it has to withstand thermal stresses caused by differences in coefficients of thermal expansion (CTEs) or temperature gradients, stresses induced by the stack weight or gas pressure, thermal cycling between ambient temperature and operating temperature, creeping and chemical reactions [4]. Due to the high relevance of rigid seals, numerous studies have been conducted. For an initial overview the interested reader is referred to [2, 4, 5].
However, the reliability of the sealing has a major impact on the lifespan of the SOFC stack. Hence, the failure assessment of seals comes to the fore. The mechanical properties of glass ceramics sealants change significantly depending on whether the temperature T is above or below the glass transition temperature T_g. Within the failure assessment this change has to be taken into account. Several authors proposed to operate the SOFC above the glass transition temperature of the sealant in order to reduce stresses that occur due to a CTE mismatch by means of viscosity [6, 7]. But there is evidence that creep damage may occur in the long run [8]. Below the glass transition temperature brittle material behavior is expected involving different failure modes. Typically, stress based criteria are used for the failure prediction. Due to the fact that the occurring stress fields are highly inhomogeneous particularly at the junction between the sealant and the adjacent metal layers, where a so-called free-edge effect occurs, classical strength-of-material approaches are not suitable.
As alternative approach, failure criteria based on linear elastic fracture mechanics (LEFM) were proposed. Those criteria require the existence of a pre-existing crack or inherent flaw. As a consequence, assumptions must be made regarding a fictitious crack size.
To surpass the mentioned limitations Leguillon [9] proposed a combination of the strength-of-material approach and linear elastic fracture mechanics in form of a coupled stress- and energy criterion.

In the present work, a methodology for the assessment of glass ceramics seals failure is proposed. Since the temperature during operation can be both above and below the glass transition temperature, both cases must be considered within the failure prediction.
The suggested procedure is explained using a current SOFC design developed by Forschungszentrum Jülich, but also using simple examples. Furthermore, the mechanisms

responsible for the occurrence of the stresses are investigated and their influence on the failure behavior is discussed.

1. Scientific Approach

In the following the methodology for the assessment of the glass-ceramics seals is discussed. As depicted in Fig.1 the failure assessment can first be classified according to the type of load.

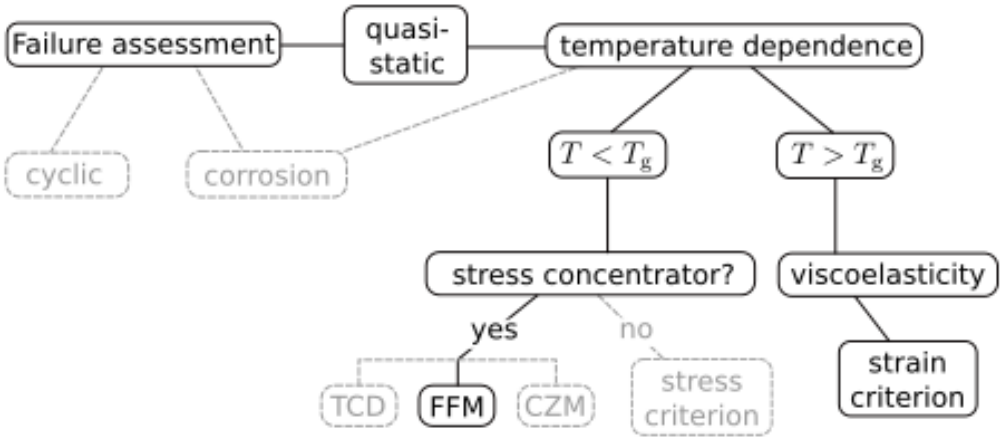

Figure 1: Methodology for the investigation of glass-ceramics seal failure.

During its lifetime the SOFC stack is exposed to a variety of different loads as, for instance, cyclic loading due to the cool-down to room temperature and heat-up to the operating temperature, or the static stationary operation. In the following only the latter load case is considered. As previously mentioned, the failure behavior of the glass-ceramics depends on the temperature. Hence, within the failure assessment a distinction must be made whether the operating temperature is above or below the glass transition temperature.
Below the glass transition temperature brittle fracture occurs. If the stress field is homogeneous a classical stress based criterion is suitable for failure prediction. Generally, highly inhomogenous stress fields are expected for SOFCs since the temperature field in operation behaves also inhomogeneously and differences in the coefficients of thermal expansions between the involved materials occur. In these cases the use of a simple stress criterion is not appropriate. The stress gradient has to be taken into account. Therefore, several approaches exist. The Theory of Critical Distances (TCD), as proposed by Taylor, summarizes all non-local approaches where the stresses are evaluated in a certain distance away from the stress concentration or criteria based on linear elastic fracture mechanics where the existence of an inherent flaw of a certain size is assumed. These approaches have in common that they are simple to use, but depend on a length scale with unclear physical meaning. Alternatively, Cohesive Zone Models (CZM), based on damage mechanics, are widely used. As the latter approach leads to a nonlinear problem the computational costs are high.
Besides the described approaches, Hashin [11] postulated the instantaneous formation of a finite sized crack an approach denoted as Finite Fracture Mechanics. Based on this

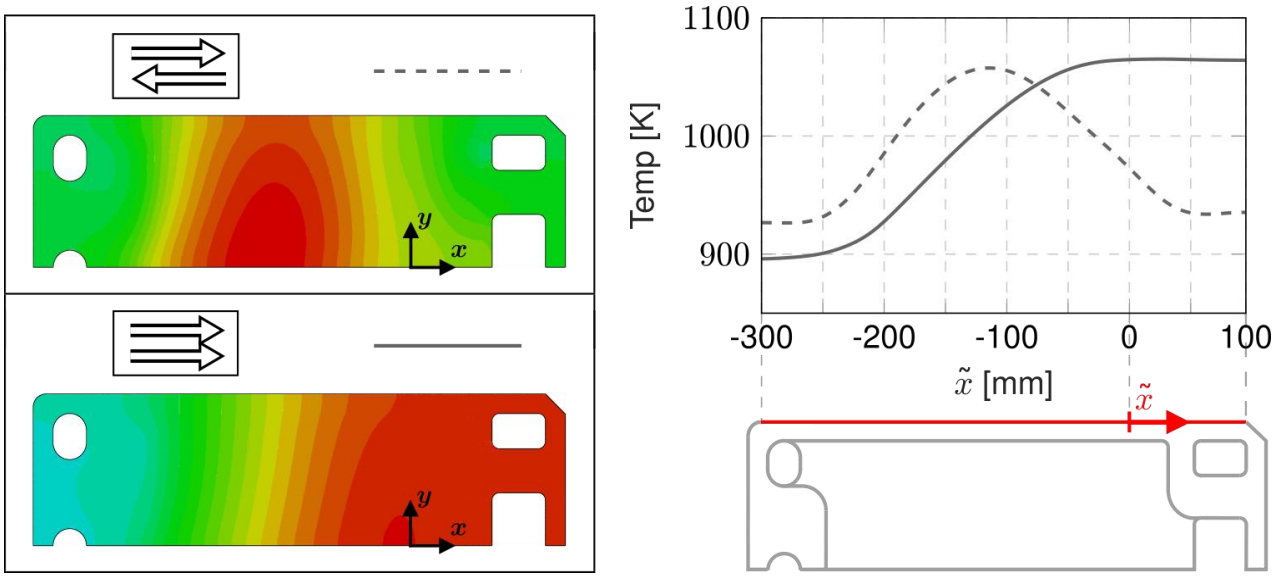

Figure 2: The temperature fields for co and counter gas flow operation (fuel gas methane) are depicted. The results were obtained by CFD-simulations and are provided by Forschungszentrum Jülich.

framework, Leguillon [9] proposed a coupled stress and energy criterion for the investigation of brittle fracture. It is postulated that two necessary and sufficient conditions in form of a stress and an energy criterion have to be fulfilled simultaneously. Evaluating the so-called coupled criterion only requires solving linear problems, which has a beneficial effect on the computing time. Moreover, only intrinsic material properties in terms of the strength and the fracture toughness are required. Finally, the failure load as well as the corresponding crack length are obtained by evaluating the coupled criterion.
Above the glass transition temperature, viscous material behavior occurs. Hence, stresses induced, for instance by differences in the coefficients of thermal expansion vanish after some time. But dead loads, as the weight of the stack, yield increasing deformations of the glass-ceramic seals. Since a material can not bear unlimited deformations, a crack may occur in the long run.

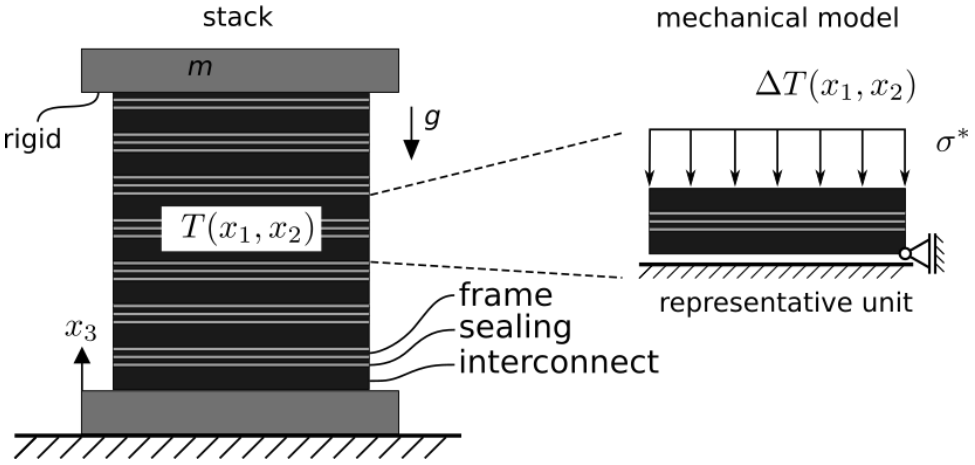

Figure 3: Deduction of the representative unit.

https://doi.org/10.5281/zenodo.4556841

2. Mechanical and Numerical Modeling

In the following the mechanical model is introduced. It is assumed that the mechanical response of the stack does not depend on the out-of-plane direction x_3. Especially, the temperature field (depicted in Fig. 2) only depends on the in-plane coordinates x_1 and x_2. Based on the assumptions, only a representative unit consisting of two interconnects, the different layers of glass-ceramic seals and the metal frames, are further taken into account (Fig. 3 and Fig. 4).

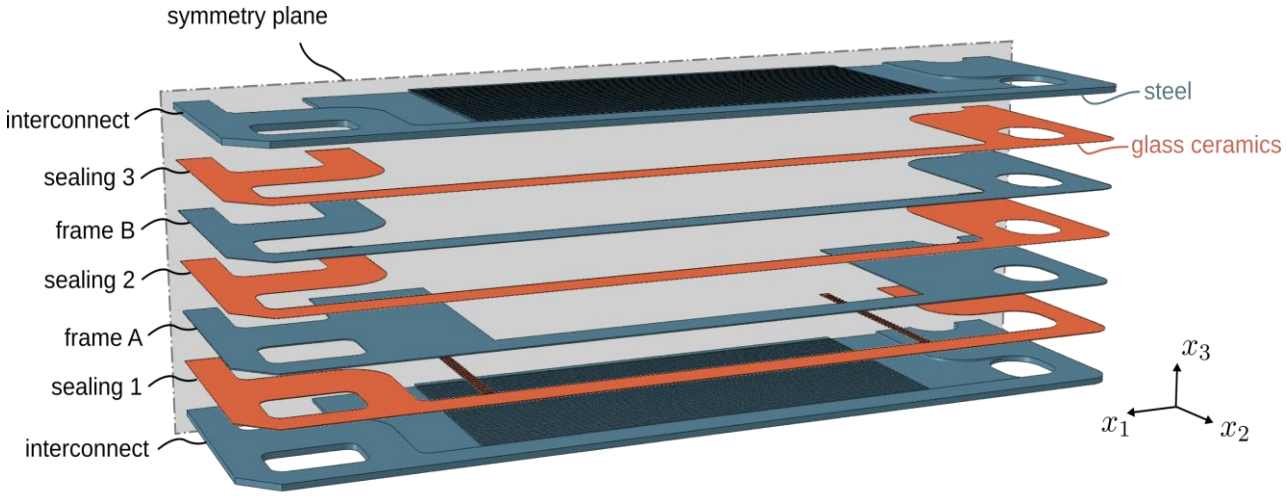

Figure 4: Representative unit of the SOFC stack. In order to reduce the numerical effort the shown symmetry plane is used.

The weight on the top of the stack is considered in terms of a stress boundary condition. Furthermore, it is assumed that the thermal stresses within the representative unit are zero at the joining temperature of 1073 K. The representative unit, shown in Fig. 4 is modeled in the commercial finite element software *Abaqus.* The symmetry with respect to the x_1-x_3-plane is used in order to reduce the numerical effort by half. The finite element model is fully parameterized using a *Python* script. The model contains about 4.000.000 degrees of freedom and is discretized using fully integrated three-dimensional brick elements with bi-quadratic shape functions. The discretization is shown exemplarily in Fig. 5. Within the three-dimensional finite element model linear elasticity is presumed.

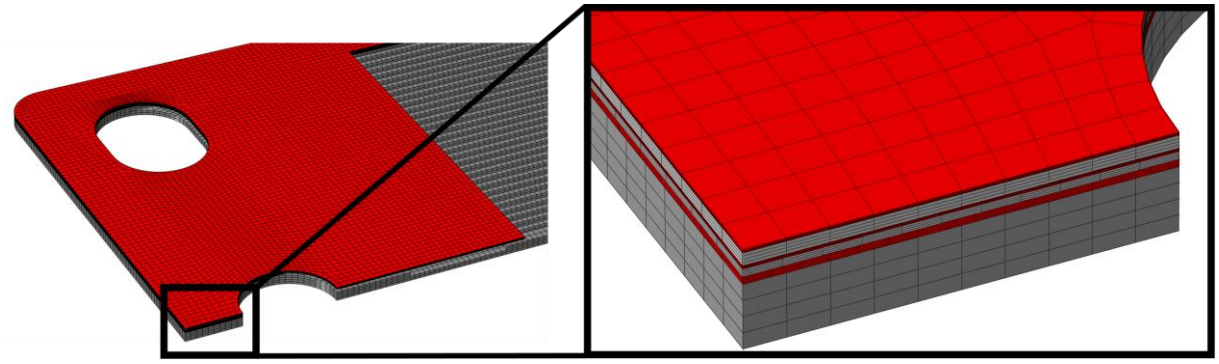

Figure 5: Discretization of the repeating unit (second interconnect is not depicted). The seals are shown in red, the interconnect and frames are grey.

https://doi.org/10.5281/zenodo.4556841

3. Results

In the following, the stresses obtained by the three-dimensional finite element analyses are discussed. Three different mechanisms are responsible for the occurring stresses: the inhomogeneous temperature field, a mismatch in the coefficients of thermal expansion between the glass-ceramic sealant and the steel components (interconnect and frames), and the dead load in terms of the weight on the top of the stack. The obtained results are shown exemplarily in Fig. 6 for sealing 2.

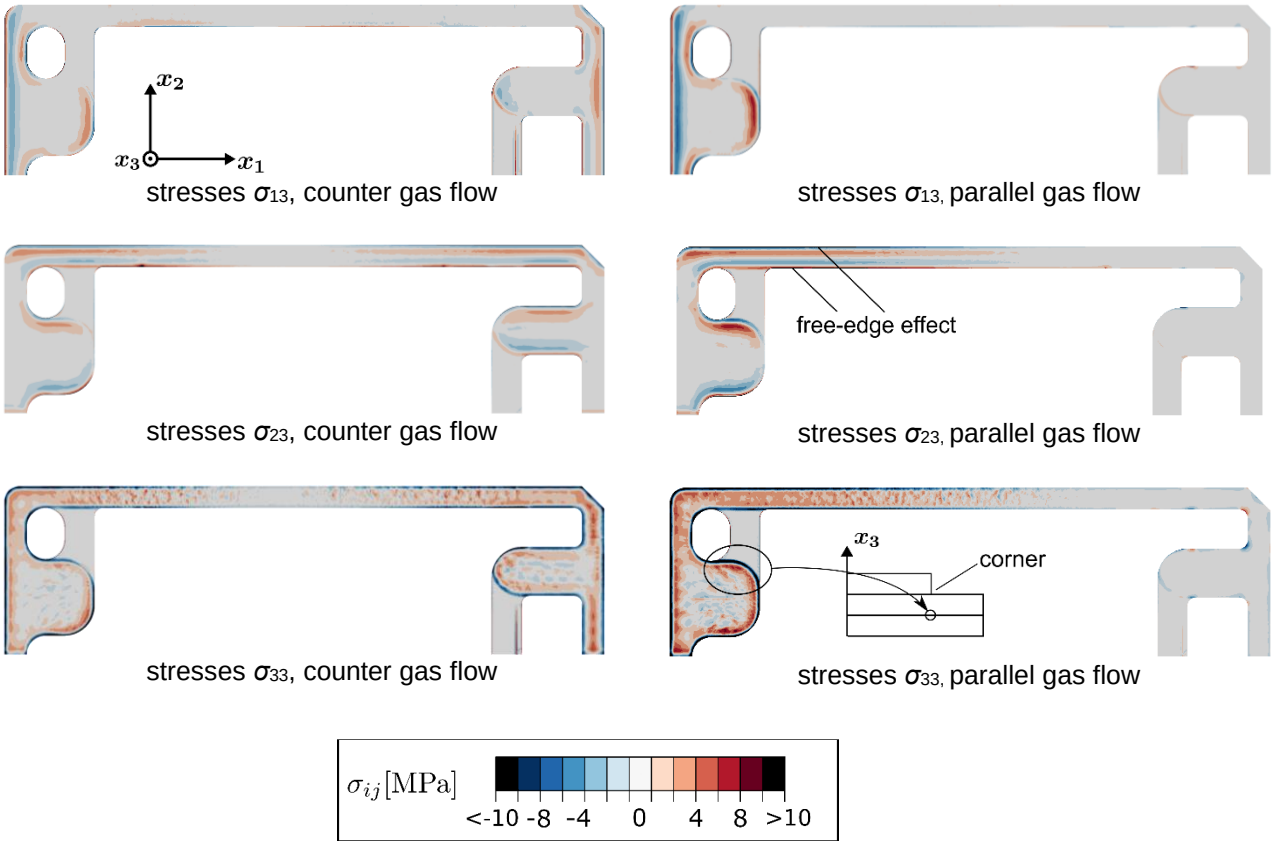

Figure 6: The interlaminar (out-of-plane) stress components are depicted exemplarily for sealing 2.

It can be observed that stress concentrations at the junctions of the adjacent layers occur (so-called free-edge effect). Following elasticity theory the stresses become theoretically infinite at the junction. The reason for the observed behavior is the mismatch of the elastic constants between the sealant and the steel components. Besides the mismatch in elastic constants, also geometric discontinuities like corners cause stress concentrations as shown exemplarily for parallel gas flow. Moreover, for both load cases it can be observed the higher the temperature gradient the higher the stresses.

https://doi.org/10.5281/zenodo.4556841

4. Sealing Failure Assessment

It has to be distinguished whether the temperature is above or below the glass transition temperature. For the investigated structural situation, both cases occur simultaneously as the glass transition temperature is about 873 K to 1053 K [12]. In the following both cases are discussed. Therefore, a minimal example is used in order to examine the elementary physical effects. In Fig. 7 the minimal example in form of a finite element model is depicted.

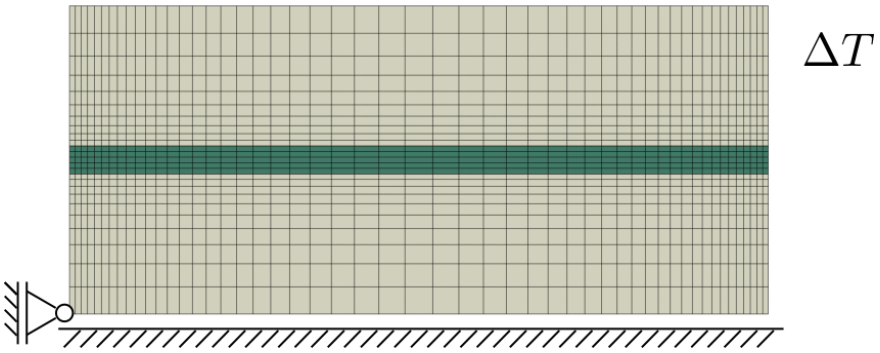

Figure 7: The finite element model for the used minimal example is shown. The glass-ceramic seal is shown in green and the steel components are grey.

4.1 Failure assessment for $T < T_g$

As shown exemplarily in Fig. 6, the stresses within the seals are highly inhomogeneous. Hence, the evaluation of a simple stress criterion is not sufficient. Instead, the coupled stress and energy criterion within the framework of finite fracture mechanics is employed. The solution of the coupled criterion in form of a quadratic interaction relation for the stresses and a linear interaction relation for the energy criterion is shown in Fig. 8.

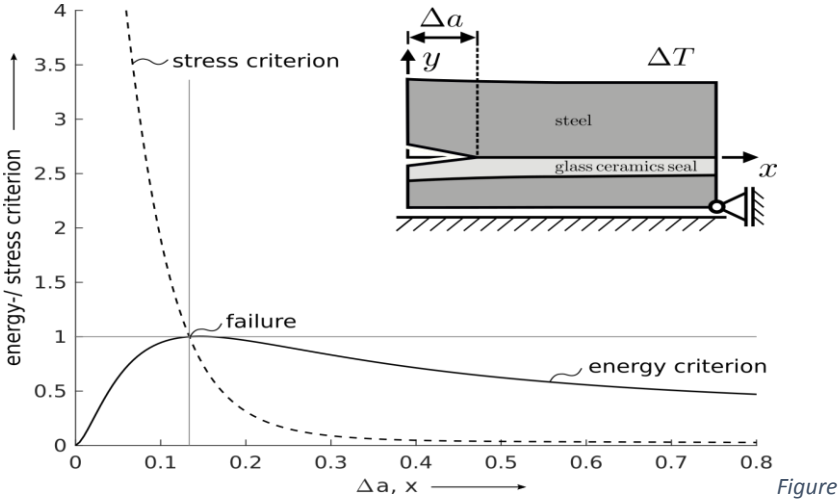

Figure 8: Coupled stress and energy criterion. If both criteria are fulfilled simultaneously failure in form of instantaneous crack formation occurs. In the depicted case is the critical temperature difference at failure ΔT_f = -768 K.

In the minimal example a rather high temperature difference is required for failure. Thus, it is expected that failure does not actually occur in operation. However, cooling down to

room temperature may lead to brittle fracture within the glass-ceramic seals since the temperature difference is of the same magnitude as the critical temperature difference predicted by the coupled criterion.

4.2 Failure assessment for $T > T_g$

For areas where the temperature is higher than the glass transition temperature viscous effects may play a fundamental role for failure. Especially, if the failure occurs not instantaneously but after a certain time viscous effects should be considered. On the one hand it is expected, that stress concentrations induced by differences in the coefficients of thermal expansion of the involved materials, the inhomogeneous temperature field or geometric discontinuities decrease due to viscous relaxation processes. On the other hand, dead loads as the weight on the top of the SOFC stack yield shear deformations. The shear deformations increase continuously over time. If the shear deformations exceed the deformability of the glass-ceramic sealant cracks can occur.

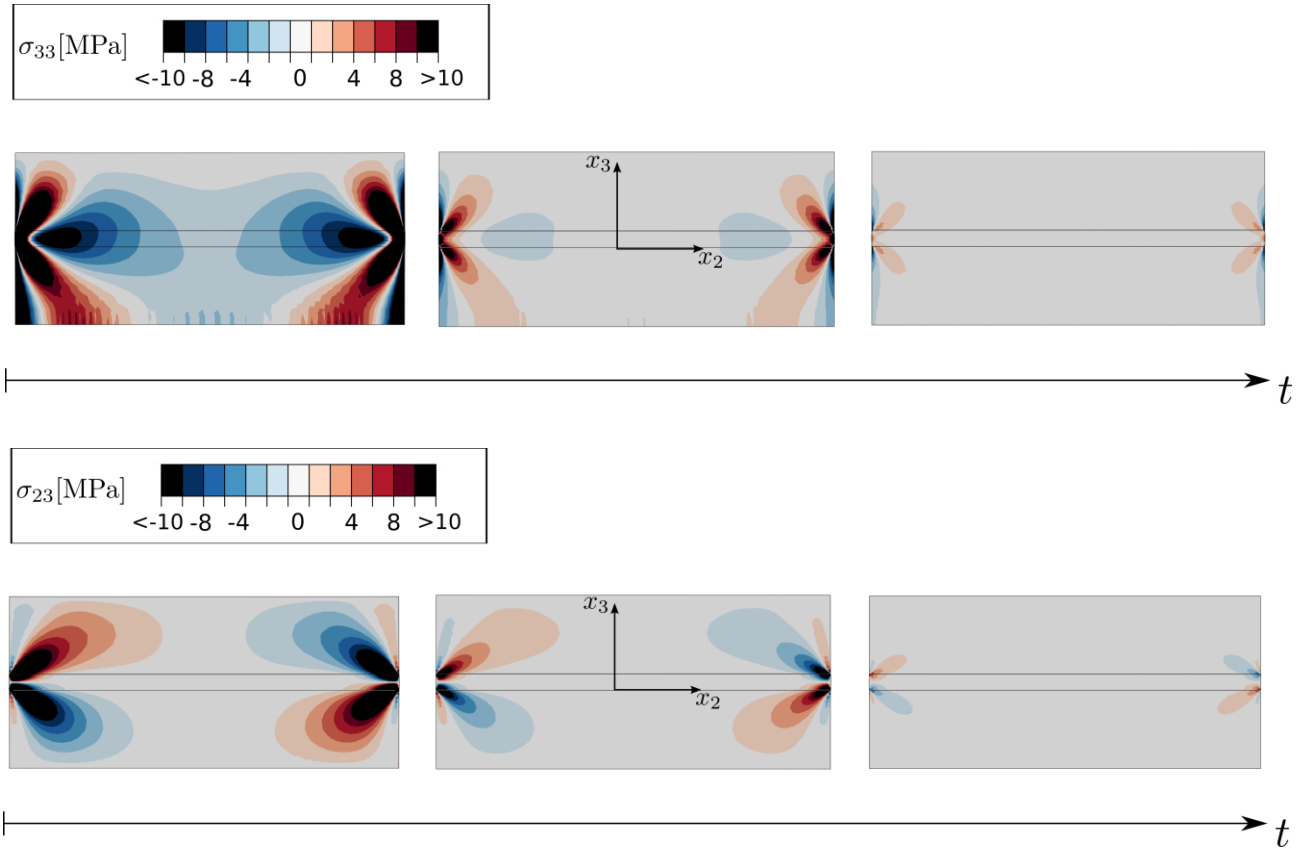

Figure 9: Development of the interlaminar stress components with respect to the time assuming viscous material behavior. The stresses are induced only by the differences in the coefficients of thermal expansion. The stress boundary condition, representing the weight on the top of the SOFC stack is neglected.

https://doi.org/10.5281/zenodo.4556841

In Fig. 9 the development of selected interlaminar stress components is depicted. Due to the viscous relaxation the stresses are reduced over the time. This behavior can be used selectively to reduce the stresses and this is the reason why an operating temperature above the glass transition temperature of the glass-ceramic sealant is recommended in literature. However, this recommendation is based on an incomplete consideration. In Fig. 10 an example of creep deformation is shown.

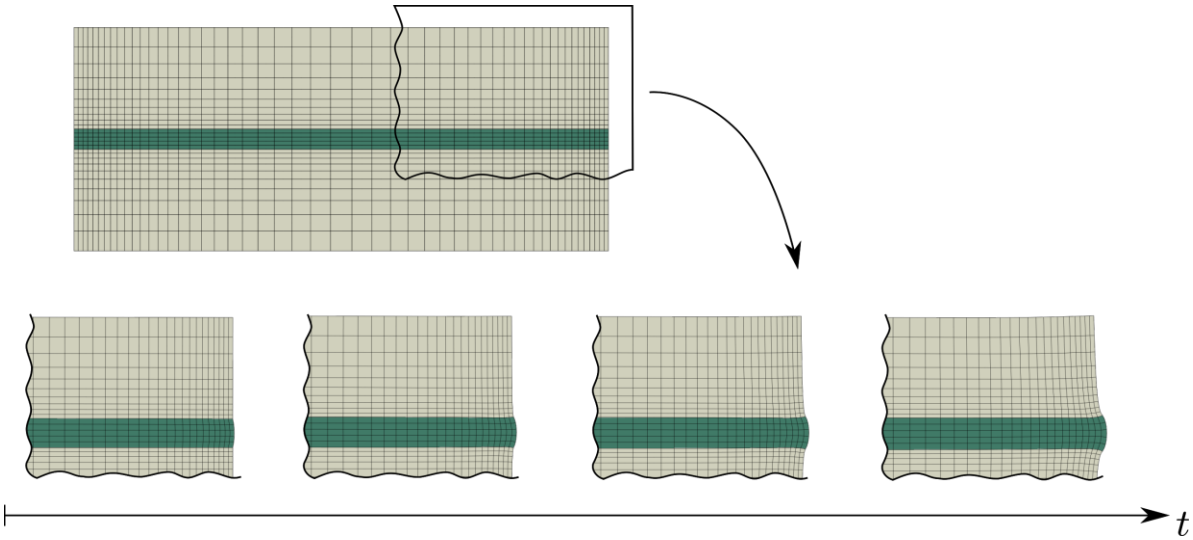

Figure 10: The creep deformation of the glass-ceramic seal is shown with respect to the time. The deformation is induced by the dead load on the top of the SOFC stack.

An unlimited increasing creep deformation is observed. If the viscous material behavior is known exactly, a prediction of creep failure seems to be possible.
As a consequence, the recommendation of viscoelastic seals should be viewed with skepticism. The viscous behavior necessarily has to be taken into account as possible failure mode.

https://doi.org/10.5281/zenodo.4556841

5. Conclusion

In the present work a methodology for the assessment of sealing failure in SOFC applications has been proposed. It has to be distinguished whether the operating temperature is above or below the glass transition temperature as the mechanical properties of the sealant change significantly reaching this critical value.
Below that temperature the sealant behaves brittle but occurring stresses are unequally distributed yielding highly localized stress concentrations. Hence, for the assessment of failure below the glass transition temperature the coupled stress and energy criterion is the method of choice. It provides the critical temperature at crack initiation as well as the corresponding crack length. The investigation revealed that for the underliying SOFC design no brittle failure has to be expected for areas where the operating temperature is below the glass transition temperature. But if the SOFC stack is cooled-down to room temperature brittle failure seems to be in reach. For that load case further investigations are recommended.
As the operating temperature is locally above the glass transition temperature, viscous effects have to be considered. Besides the advantageous relaxation of local stress concentrations dead loads as the weight of the SOFC stack and the internal pressure within the manifold yield increasing deformations over time. Those creep deformations can exceed the deformability of the glass ceramics sealant. As a consequence, creep failure may occur after some time.

References

[1] Yamamoto, O., Solid oxide fuel cells: fundamental aspects and prospects. Electrochimica Acta 45, 2423–2435, 2002.
[2] Fergus, J.W., Sealants for solid oxide fuel cells. Journal of Power Sources 147, 46–57, 2005.
[3] Bram, M., Reckers, S., Drinovac, P., Mönch, J., Steinbrech, R.W., Buchkremer, H.P., Stöver, D., Deformation behavior and leakage tests of alternate sealing materials for SOFC stacks. Journal of Power Sources 138, 111–119, 2004.
[4] Mahapatra, M., Lu, K., Seal glass for solid oxide fuel cells. Journal of Power Sources 195, 7129–7139, 2010.
[5] Lessing, P.A., A review of sealing technologies applicable to solid oxide electrolysis cells. Journal of Materials Science 42, 3465–3476, 2007.
[6] Ley, K.L., Krumpelt, M., Kumar, R., Meiser, J.H., Bloom, I., Glass-ceramic sealants for solid oxide fuel cells: Part I. Physical properties. Journal of Materials Research 11, 1489–1493, 1996.
[7] Chang, H.T., Lin, C.K., Liu, C.K., High-temperature mechanical properties of a glass sealant for solid oxide fuel cell. Journal of Power Sources 189, 1093–1099, 2009.
[8] Lin, C.K., Lin, K.L., Yeh, J.H., Shiu, W.H., Liu, C.K., Lee, R.Y., Aging effects on high-temperature creep properties of a solid oxide fuel cell glass-ceramic sealant. Journal of Power Sources, 241, 12–19, 2013.
[9] Leguillon, D., Strength or toughness? A criterion for crack onset at a notch. European Journal of Mechanics – A/Solids 21, 61–72, 2002.
[10] Taylor, D., The theory of critical distances, Engineering Fracture Mechanics 75 (7), 1696–1705, 2008.
[11] Hashin, Z., Finite thermoelastic fracture criterion with application to laminate cracking analysis. Journal of the Mechanics and Physics of Solids 44, 1129–1145, 1996.

[12] Osipova, T., Wei, J., Pecanac, G., Malzbender, J., Room and elevated temperature shear strength of sealants for solid oxide fuel cells. Ceramics International, 42 (11), 12932-12936, 2016.

Keywords: EFCF2020, SOx
Session A15: Cell, stack & system modelling and optimization

https://doi.org/10.5281/zenodo.4556841

A1503

Multi-scale model to describe the local degradation and mechanical failures in an SOC stack

Henrik Lund Frandsen, Omid Babaie Rizvandi, Xing-Yuan Miao
Department of Energy Conversion and Storage, Technical University of Denmark (DTU), Building 310, Fysikvej, DK-2800 Kgs. Lyngby/Denmark

Contact authors: www.EFCF.com/ContactRequest

Abstract

A multi-physical 3D model of the stack is a useful tool to increase the lifetime of an SOC stack, as this can be used to study the impact of modifying operating parameters, design and/or predict the requirements to the stack component materials. The multi-physics model can estimate the variation of physical quantities (e.g. temperature, overpotentials, thermal stresses), which could be used to assess local degradation or mechanical failures.

Multi-physical 3D models describing all relevant physical phenomena (current, gas flows, heat transport, mass balances and mechanical stresses) with the geometric details are computationally expensive to run, i.e. days on a cluster is required for a single steady-state simulation. However, by using multi-scale models or so-called homogenized models, the computational resources are tremendously decreased, such that a steady-state model can be solved within minutes on a workstation.

A wide range of models have been developed to describe the degradation and failure of cells and other components in the stack for both electrolysis and fuel cell modes of operation. These include Ni migration and agglomeration, Chromium poisoning, corrosion and failure in the oxygen electrode / interconnect interface. Most of these relate simple physical models or empirical models to the observed degradation in actual cells and stacks by fitting a few unknown parameters. These models are rather useful to describe the *local* degradation in SOC stack, but the local evolution will influence the entire stack, and a full 3D stack model is needed to predict the spatial variation of the degradation.

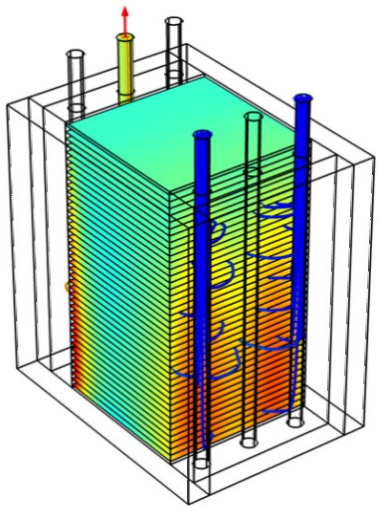

Figure 1 Temperature of air flow and thermo-mechanical stresses in an SOFC stack simulated by a homogenized model.

In this paper, we present a 3D model of an SOC stack, where the local degradation and mechanical failures are described everywhere in the stack over the stack lifetime. The model is thus able to describe all relevant physics (currents, gas flows, heat transport, mass balances and mechanical stresses) coupling in space *and* time. Simulations of tens thousands of hours of operation can be computed within an hour or two on a high-end workstation, a task that would have taken months of simulation time with conventional models. This makes it possible to assess the lifetime, effect of design modifications and material requirements for the SOC stack technology.

https://doi.org/10.5281/zenodo.4556872

Introduction

To increase the lifetime of an SOC stack testing is eventually a necessity. However, to explore the impact on the degradation of various operating conditions a multi-physical 3D model of the stack is a useful tool. A 3D stack model can be used to study the impact of modifying operating parameters, design and/or predict the requirements to the stack component materials. The multi-physical model can estimate the variation of physical quantities (e.g. temperature, overpotentials, thermal stresses), and with those, it is possible to assess local degradation or mechanical failures.

Multi-physical 3D models describing all relevant physical phenomena (current, gas flows, heat transport, mass balances and mechanical stresses) with the geometric details are computationally expensive to run. For instance, Li, Song and Lin [1] presented a fully-coupled SOC stacks model made in Ansys-Fluent model of a 30 cell stack with a relatively simple geometry, for which steady-state operation could be simulated in 40 hours on a work station. Similar computational efficiency was achieved in the model by Nishida, Beale and Pharoah [2] using OpenFoam. Thus, if a set of equations from such a stack model should be solved for each time step in a transient model, describing the lifetime of a stack, then the solution time would be at least 500 hours, and thus not practically feasible to use for this type of studies.

In Frandsen, Navasa et al. [3,4] a novel approach for simulating the SOC stacks were presented, where the multi-physics of an SOC stack could be simulated in steady-state within 15 minutes using a workstation. To achieve this, so-called homogenization was employed to indirectly include the geometric details of the real stack. By replacing the actual geometry with homogeneous media, with the same physical properties, it is possible to represent the response of the stack. An example of this is shown in Figure 1. The physical properties of the homogeneous media is obtained by extracting the average physical response of the repeating for the different physics [4]. By doing this, the many computational units (finite elements, control volumes, etc.) needed to describe the repeating unit can be replaced by a homogeneous medium. And as it is a homogeneous medium, the discretization can be chosen according to the gradients of the free variables, which is solved for. Thus, Navasa et al. achieved computational time of approximately 15 minutes for a 100 cell stack [4]. With a steady-state solution time of 15 minutes iterative time stepping suddenly appears feasible and thus also the possibility of simulating the degradation over the lifetime of a stack.

Modeling of the SOFC degradation is an important tool for analyzing its long-term performance, investigating effects of the operating and geometric parameters on the lifetime of the SOFC, and so mitigation techniques to improve its lifetime. A limited number of studies have been devoted to numerical modeling of the degradation phenomena of the SOFC. Nakajo et al. [5] integrated degradation phenomena of Ni particle coarsening, Cr poisoning, interconnect oxidation, reduction of the electrolyte conductivity, and formation of insulating phases into a 2D model of a repeating unit of a SOFC stack. Miyoshi et al. [6] applied the Cr poisoning model proposed by Nakajo et al. [5] to a 3D model of the electrodes and electrolyte of a single cell. Moreover, Zhu et al. [7] studied the degradation phenomena of Ni coarsening, electrolyte conductivity reduction, and interconnect corrosion through a 3D model of a single cell. The effects of the model variables such as species concentrations and temperature distribution on the degradation rates over the cell were investigated. Nonetheless, it is obvious that the modeling variables vary over the stack and not all the cells experience the same condition. Therefore, stack-scale modeling of the

https://doi.org/10.5281/zenodo.4556872

degradation phenomena is necessary to investigate the degradation distribution over the stack and analyze the long-term performance of the SOFC stack.

One of the drawbacks of using a homogenized model is that the local parameters like overpotentials, stress intensities at assemblies are not directly obtainable, as the geometric features within a repeating unit and thus the detailed physical response is not directly represented in the model. An analogy to this is that for full cell models, the microstructure of the electrodes is not represented, as the number of computational units would be far too high for current computers. However, the overall response of the homogenized response can be used to achieve the local details in the substructure of the SOC stack again, but so-called localization. In localization, the submodel of the repeating unit is employed with physical parameters (e.g. temperature, currents, flows, stresses, etc.) in a single point in a solution of the homogenized model. The physical parameters at the single point are applied as boundary conditions to the repeating unit submodel and by solving this, the local conditions at the point of interest can be retrieved. With this approach, a multi-scale, multi-physics model can be achieved.

In this paper, an overview of the recent developments of the multi-physics, multi-scale model developed at DTU Energy is presented. These consist of two main contributions, i.e. 1) adding a novel localization approach, which can be used to model the local mechanical failures in the stack using so-called fracture mechanics, 2) making the model transient and able to simulate the degradation of a full-stack in 3D over the full lifetime of a stack (~40,000 hours) in practical feasible time-span, i.e. 1 hour and 15 minutes. The overall approach will be described and examples of results provided.

1. Scientific Approach

The approach in this work is purely modelling. Modelling cannot stand on its own in a true investigation of a phenomenon, but this concerns the development of a new type of models, which will solve a class of problems, which have not been possible until this point, and thus stands for itself. The onwards approach is to ensure that the model provides correct results and work together with SOC stack providers to validate the model for one or more specific stack technologies.

The current stack model relies on homogenization as described in the introduction, and following physical phenomena are simulated in parallel: 1) flow distributions for the fuel and air; 2) turbulent variables for the airflow in the air manifolds; 3) mass transport and electro-chemical reaction of the species; 4) current, voltage, overpotentials, and degradation variables; 5) heat transfer in the solid and fluids; and 6) mechanical streses in the solids and local energy release rate for fracture in the cell-interconnect interface.

1.1 Modelling localized fractures in SOC stacks

In Navasa et. al. [4]. it was shown how the average stresses could be obtained in the stack based on the temperature profile, thermal expansions and external loadings. Also, it was shown how it would be possible to estimate the stresses in the cell by an analytical model mapping the average stresses to the local stresses in the different cell layers. This was possible because of a simple interconnect geometry for which a simple average stiffness could be deducted.

For more complex interconnect geometries, it is not possible to use an analytical model and the sub-model of the repeating unit must be made numerically. This is certainly also possible and is done e.g. in Refs. [8,9]. In Miao et. al. [8] the effective properties for the homogeneous media are obtained by imposing an increment in the free variable e.g. temperature as boundary conditions to the sub-model and integrating the heat flux, to obtain the heat conductivity.

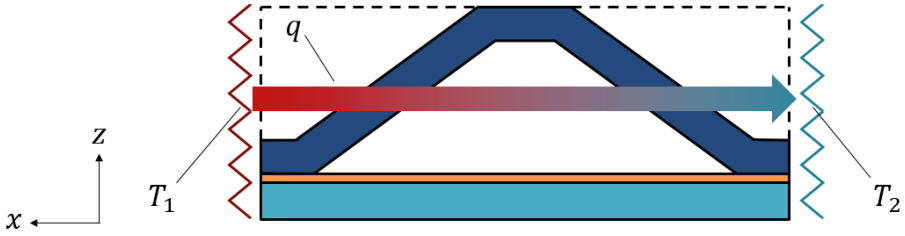

Figure 2 Concept for retrieval of material parameters for homogeneous media by nummerical modelling *[8]*.

The same sub-model used to retrieve the homogeneous parameters can also be used for so-called localization. Once the stack model with homogenization has been run the details in the repeating unit cell geometry is not resolved by the model. For many phenomena, a very high local number of computational elements are needed to resolve for instance variations in overpotentials in the electrodes or stress concentrations at the junction between the cell and interconnect. This can be handled by imposing e.g. the average stress $\bar{\boldsymbol{\sigma}}$ from the homogenized stack model as boundary conditions in the form of tractions (Figure 3b) on the sub-model (Figure 3c).

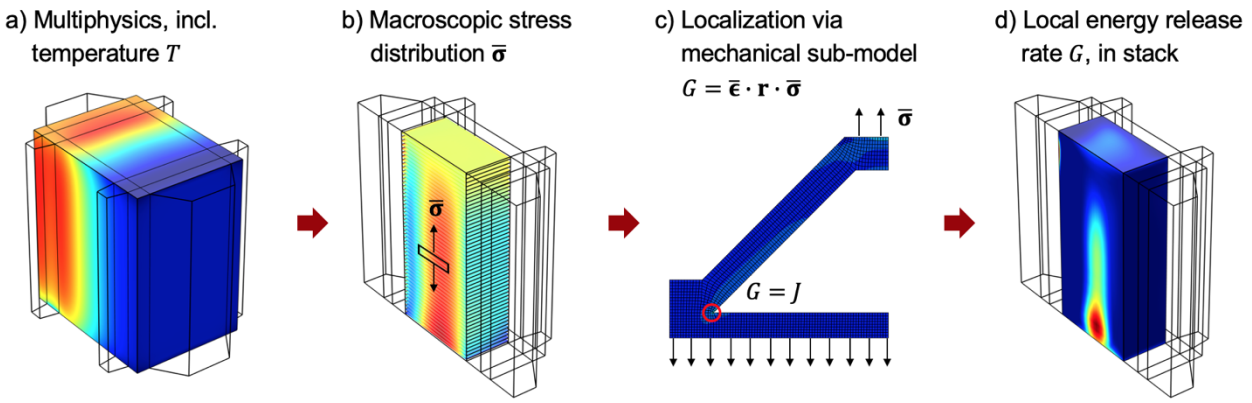

Figure 3 Concept of the modelling approach, linking the homogenized multiphysics model (homogenized stack model) (a) to the average calculation of stresses (b), which are then connected via a mechanical sub-model (c) to the examination of local fracture energy in the entire stack (d) *[8]*.

To evaluate if a local failure will occur there are two approaches; 1) the statistical approach, where the stresses are evaluated and based on this probability for failure is evaluated (see e.g. [10,11], and 2) the fracture mechanical approach where the Griffith criteria is investigated, i.e. if the energy release rate G for generating a crack is lower than the critical energy release rate (/fracture energy) G_c. The latter has primarily been used for the characterization of SOC materials but to the authors' knowledge not been applied in the analysis of SOC stacks.

For both approaches, a consistent set of models and measurements needs to be feasible to evaluate the risk of failure. Whereas, it is less complicated to measure the strength of

bulk materials, the strength of interfaces is difficult to characterize consistently [12]. The reason is that stress across the assembly varies significantly for the different testing methods, and when assuming uniform stress distribution the assumption leads to large variations of apparent strength. Some researchers therefore carefully treat the edges of the specimens used, see e.g. Ref. [13]. However, when producing stacks, the edges of the assemblies are not polished, and the strength measurement will thus result in higher strength than what is reached in practice. A non-conservative approach would be to have samples where a sharp crack is pre-initiated before the mechanical testing.

Thus, for characterizing the mechanical robustness of an interface, we believe that the fracture mechanical approach is more suitable as it is possible to manufacture specimens with the materials and methods used in actual stacking [14,15]. This does however imply that the more advanced fracture mechanical models must be employed in the modelling of the SOC stack. In Miao et al. [8] a simple approach for this was however developed using the sub-model concept. Here, the stresses from the homogenized model are applied as boundary conditions on the sub-model, as described above (Figure 3c). For a certain set of stresses, the stress variation in the repeating unit can be evaluated, and by introducing an initial crack at the critical spot, the local energy release rate *G* can be evaluated by use of the so-called J-integral [16].

Making this mapping of a certain set of average stresses onto the sub-model to compute the local *J*-integral can be done easily once, and a sub-routine could easily be set up to evaluate the *J*-integral for a finite number of points within the SOC stack. However, with this, the computational effort would again increase, although this process could easily be parallelized and solved on a cluster.

In [8], a far more computational efficient scheme is however suggested. In this, the *J*-integral can be determined by a closed form expression for a 2D loading case (explained in later)

$$J = r_{xx}\bar{\sigma}_{xx}\bar{\epsilon}_{xx} + r_{zz}\bar{\sigma}_{zz}\bar{\epsilon}_{zz} + r_{xz}\bar{\sigma}_{xz}\bar{\epsilon}_{xz} \quad (1)$$

where $\bar{\sigma}_{ij}$ and $\bar{\epsilon}_{ij}$ are average stress and strain components from the homogenized model, and r_{ij} are a set of coefficients, which have been determined using the submodel (as explained in the following). By this approach, it is possible to achieve the *J*-integral at any point in the stack directly from the average stress and strain field from a simple closed form expression (Figure 3d).

The r_{ij} coefficients are determined by imposing the submodel by each of the fundamental stress conditions as boundary conditions (tractions), i.e. two axial loading conditions (x-direction, z-direction) and a shear loading condition (in xz plane). For each of the fundamental stress condition, the *J*-integral is evaluated by solving the finite element problem for the numerical sub-model (Figure 4a) and consequently evaluating the J-integral (Figure 4b). As no other loads are imposed on the sub-model, only one of the terms of Eq. (1) remains, and the relevant r_{ij} coefficient can now be obtained as it is the only unknown in Eq. (1). It is also shown in [8] that Eq. (1) applies to any combination of the fundamental stress conditions, why their contributions to J can be determined for any given combination.

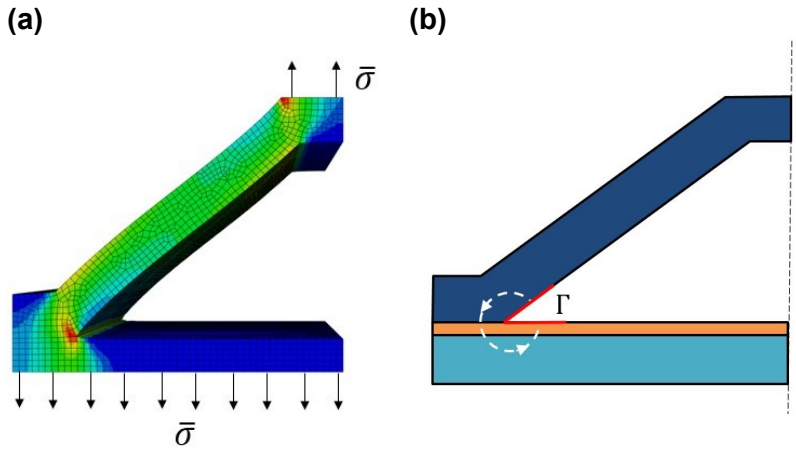

Figure 4 a) Stresses on sub-model of the repeating unit and b) path for the J-integral.

1.2 Modelling degradation in an SOFC stack

As mentioned in the introduction, the main challenge of describing the degradation over time of an SOC stack is the lack of computational resources for the conventional stacks. Using a homogenized stack model, the computational needs are far more moderate, making this possible.

Making the homogenized stack model transient was done in Rizvandi et al. [17], but the stack model was also improved by introducing manifolds in the stack and using a more effective computational scheme.

Setting up the model to be transient is possible within the Comsol Multiphysics environment since the standard partial differential equations (PDEs) with a transient version of them were used throughout the model framework. Only material parameters relating to the time dependency of the PDEs, such as heat capacity of the different structural components is needed to make the model transient. However, because of the slow degradation, phenomena such as double layer capacitance and other sub-second time-dependent responses of the cell can be neglected.

The integration of manifolds to the homogenized stack model was also done in Rizvandi et al [17]. The free flow in the manifolds was described by a separate PDE, i.e. Navier-Stokes equations. Because of the turbulent flows in the air flow manifolds, Reynold's average Navier-Stokes (RANS) was used to describe the turbulent flow in them. Specifically, the k-ω turbulence model with Wilcox's revised formulations [18] was used.

The current model is not specific towards a specific stack or cell technology, but is rather demonstrating what is now computationally feasible. Therefore, degradation models for the most common degradation mechanisms are implemented in the stack model, but with the origin from various groups on and various materials. The degradation phenomena considered in the stack model and the models used are:

- nickel coarsening in the fuel electrode [19],
- chromium poisoning of the oxygen electrode [6],
- and oxidation of the interconnect [20].

With respect to the oxidation of the interconnect, also the threshold for break-away oxidation was added to the model.

The computational efficiency of the stack model was further optimized by careful meshing, simulating only half the stack (symmetry) and by tuning the segregated solution approach in Comsol Multiphysics in Ref. [18]. Hereby the computational time of the full stack model with all the physics present including turbulent flows in the manifolds, but except from solid mechanics, could be brought down 5 minutes for a steady-state simulation on a high-end workstation (Intel Core i9 3.5 GHz 12-core processor, 128 Gb ram). Solving the same model transiently over 38,000 hours including degradation takes 1 hour and 15 minutes.

2. Simulations and results

The simulations were done on a stack operating with co-flow. The co-flow was established by having two external air manifolds, one at each end of the stack in the flow direction, and two external fuel manifolds to either side of the stack to distribute the flow across the stack before it enters the flow direction.

A stack of 100 cell was chosen for this example with an overall stack geometry as shown in Figure 5.

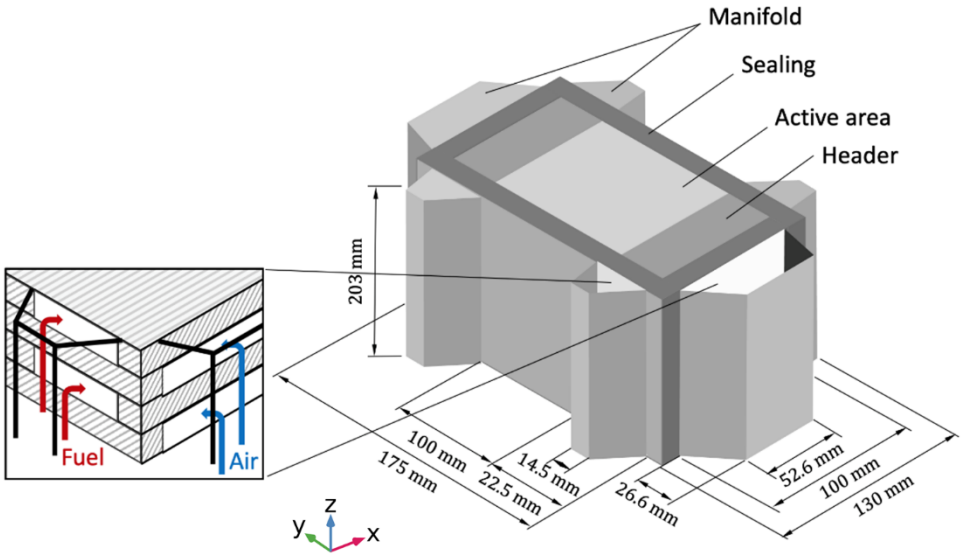

Figure 5 Schematics and overall geometry of the simulated stack *[8].*

Pressure boundary conditions were set to supply the flows of air and hydrogen with a pressure difference of 8 and 0.4 mbar, respectively. The current was adapted to the resulting flows to have a fuel utilization of approximately 70 %. The inlet temperature was 700°C and the load current was 25 A for the 10x10 cm^2 active area stack (0.25 A/cm^2 average current density).

2.1 Local fractures in an SOFC stacks

In Figure 6 an example of simulations with the stack model, analysing the average stresses based on the temperature distribution and using these to determine the local energy release rate, using the J-integral approach described in Section 1.1. It is seen that due to the relatively non-uniform hydrogen fuel distribution the current density and temperature distributions become non-uniform. This results in high vertical tensile stresses at the air inlet. These high vertical stresses results in corresponding high values for the J-integral, which would most likely induce failure (depending on the material toughness).

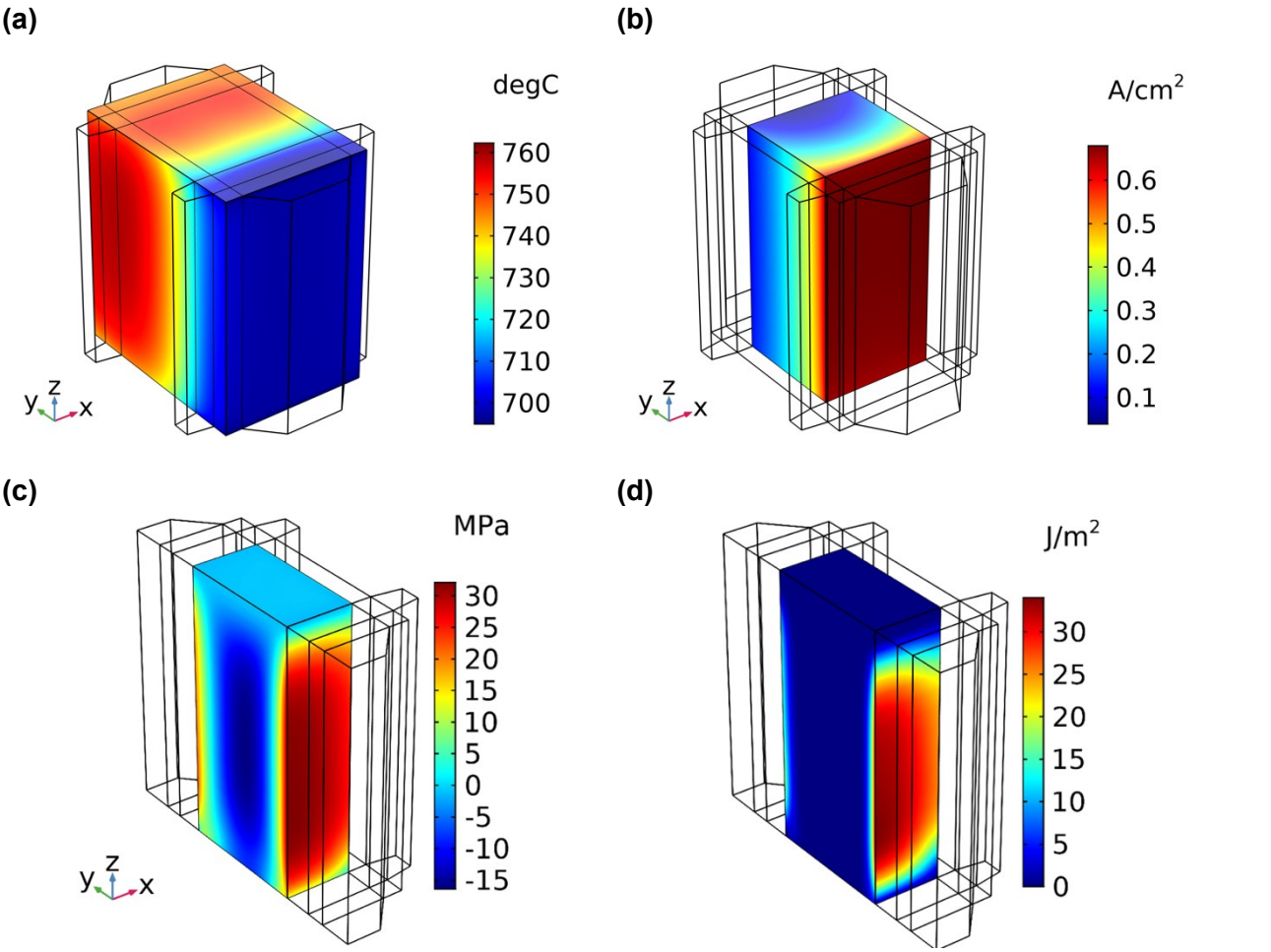

Figure 6 Examples of output from the stack model: a) Temperature distribution, b) Current density distribution, c) average vertical stress distribution, and d) local critical energy release rate for a crack between the oxygen electrode and interconnect.

2.2 Degradation in an SOFC stack

Figure 7 shows the evolutions of the spatial distribution of the area specific resistance (ASR) and the resulting current density distribution. Again, the impact from the uneven fuel flow and temperature distribution is seen to impact the distribution of degradation across the stack. After 37,000 hours, the simulation shows that, with the chosen geometry and operating temperature, it is Cr-poisoning of the air electrode, which increases the activation overpotential dramatically, resulting in a high ASR at the inlet, see Figure 7b''. For more details on the evolutions of the various overpotentials across the stack, please refer to [17].

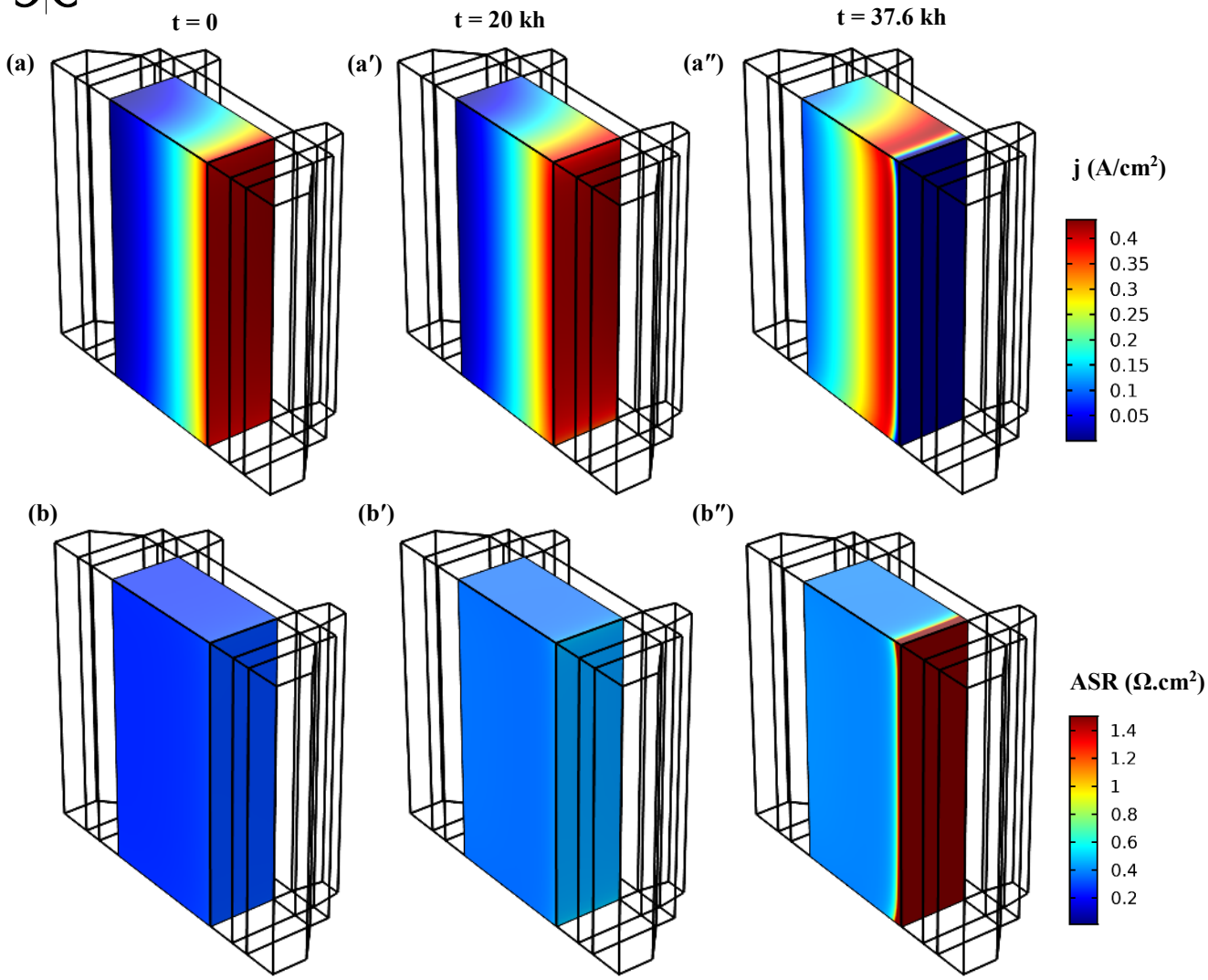

Figure 7: Evolutions of spatial distributions of (a, a′, and a″) current density and (b, b′, and b″) ASR over the stack.

4. Conclusions

In this paper, it shown how different model developments now make it feasible to simulate for *full* SOC stack: 1) very detailed local failures, 2) degradation over the lifetime of a stack.

It is made possible by using the so-called homogenization approach, which reduced the steady-state simulation time from ~40 hours to 5 minutes for a full stack with all relevant physical phenomena. This make the transient simulations of a full stack possible. Using state-of-the-art degradation models from the literature it is possible to simulate the degradation in a full stack over the lifetime of 37,600 hours of operation within 1 hour and 15 minutes. With this computation speed, it is possible to explore a high number of operating scenarios, but also look into the effect of dynamic operation (future work).

The drawback of the homogenization approach is that local details are not described directly, as e.g. the local stresses at the interface between the oxygen electrode and the interconnect. This was however made possible by introducing a simple function, which is used to map the available average stresses to the local so-called J-integral, with a swiftly evaluated closed form expression. The J-integral is a way to evaluate how much energy will be released by crack growth, which can be compared to the critical energy release rate

measured in experiments. This is thus a fracture mechanical approach, which in the authors opinion contemplate a more solid approach to analysing interfacial fractures, as interface strength measurements are hard to do right.

5. Acknowledgements

This research has been financed by the LOWCOST-IC project. This project has received funding from the Fuel Cells and Hydrogen 2 Joint Undertaking (JU) under grant agreement No 826323. The JU receives support from the European Union's Horizon 2020 research and innovation programme and Denmark, France, Austria, Belgium, Sweden, Germany, Italy.

References

[1] A. Li, C. Song, Z. Lin, A multiphysics fully coupled modeling tool for the design and operation analysis of planar solid oxide fuel cell stacks, Appl. Energy. 190 (2017) 1234–1244. doi:10.1016/j.apenergy.2017.01.034.

[2] R.T. Nishida, S.B. Beale, J.G. Pharoah, Comprehensive computational fluid dynamics model of solid oxide fuel cell stacks, Int. J. Hydrogen Energy. 41 (2016) 20592–20605. doi:10.1016/j.ijhydene.2016.05.103.

[3] H.L. Frandsen, M. Navasa, T.T. Molla, P.V. Hendriksen, Computational efficient 3D multiphysics models to estimate the long-term mechanical behavior of SOC stacks, in: Proc. 13th Eur. Fuel Cell Forum, Lucerne, Switzerland, 2018.

[4] M. Navasa, X.-Y. Miao, H.L. Frandsen, A fully-homogenized multiphysics model for a reversible solid oxide cell stack, Int. J. Hydrogen Energy. 44 (2019) 23330–23347.

[5] A. Nakajo, P. Tanasini, S. Diethelm, J. Van herle, D. Favrat, Electrochemical Model of Solid Oxide Fuel Cell for Simulation at the Stack Scale II: Implementation of Degradation Processes, J. Electrochem. Soc. 158 (2011) B1102. doi:10.1149/1.3596435.

[6] K. Miyoshi, H. Iwai, M. Kishimoto, M. Saito, H. Yoshida, Chromium poisoning in (La,Sr)MnO3 cathode: Three-dimensional simulation of a solid oxide fuel cell, J. Power Sources. 326 (2016) 331–340. doi:10.1016/J.JPOWSOUR.2016.06.110.

[7] J. Zhu, Z. Lin, Degradations of the electrochemical performance of solid oxide fuel cell induced by material microstructure evolutions, Appl. Energy. 231 (2018) 22–28. doi:10.1016/J.APENERGY.2018.09.127.

[8] X.-Y. Miao, O.B. Rizvandie, H.L. Frandsen, Modelling of local mechanical failure in solid oxide cell stacks, Rev. (n.d.).

[9] T.T. Molla, K. Kwok, H.L. Frandsen, Efficient modeling of metallic interconnects for thermo-mechanical simulation of SOFC stacks: Homogenized behaviors and effect of contact, Int. J. Hydrogen Energy. 41 (2016) 6433–6444. doi:10.1016/j.ijhydene.2016.03.002.

[10] A. Hagen, R. Barfod, P.V. Hendriksen, Y.-L. Liu, S. Ramousse, Degradation of Anode Supported SOFCs as a Function of Temperature and Current Load, J. Electrochem. Soc. 153 (2006) A1165. doi:10.1149/1.2193400.

[11] F. Greco, H.L. Frandsen, A. Nakajo, M.F. Madsen, J. Van herle, Modelling the impact of creep on the probability of failure of a solid oxide fuel cell stack, J. Eur. Ceram. Soc. 34 (2014) 2695–2704. doi:10.1016/j.jeurceramsoc.2013.12.055.
[12] A. Ventrella, M. Salvo, M. Avalle, M. Ferraris, Comparison of shear strength tests on AV119 epoxy-joined ceramics, J. Mater. Sci. 45 (2010) 4401–4405. doi:10.1007/s10853-010-4417-4.
[13] J. Malzbender, Y. Zhao, Flexural Strength and Viscosity of Glass Ceramic Sealants for Solid Oxide Fuel Cell Stacks, Fuel Cells. 12 (2012) 47–53. doi:10.1002/fuce.201100116.
[14] L. Han, B. Talic, K. Kwok, P.V. Hendriksen, H.L. Frandsen, Interface Fracture Energy of Contact Layers in a Solid Oxide Electrolysis Cell Stack, Appl. Energy Mater. 3 (2020) 2372−2385.
[15] M.C. Tucker, L.C. DeJonghe, V. García-Negrón, R. Trejo, E. Lara-Curzio, Mechanical and electrochemical performance of composite cathode contact materials for solid oxide fuel cells, J. Power Sources. 239 (2013) 315–320. doi:10.1016/j.jpowsour.2013.03.130.
[16] J.R. Rice, A path independent integral and the approximate analysis of strain concentration by notches and cracks, J. Appl. Mech. Trans. ASME. 35 (1964) 379–388. doi:10.1115/1.3601206.
[17] O.B. Rizvandie, X.-Y. Miao, H.L. Frandsen, Modeling of Degradation in Full Solid Oxide Fuel Cell Stacks, Rev. (n.d.).
[18] D.C. Wilcox, Formulation of the k-w Turbulence Model Revisited, AIAA J. 46 (2008) 2823–2838. doi:10.2514/1.36541.
[19] J.H. Zhu, H. Ghezel-Ayagh, Cathode-side electrical contact and contact materials for solid oxide fuel cell stacking: A review, Int. J. Hydrogen Energy. (n.d.). doi:10.1016/j.ijhydene.2017.08.005.
[20] J.G. Maillard, DEVELOPMENT OF MODELLING AND TESTING FOR ANALYSIS OF DEGRADATION OF NI-YSZ ANODE IN SOLID OXIDE FUEL CELLS, 2018. https://etheses.bham.ac.uk/id/eprint/8066/1/Maillard18PhD.pdf (accessed August 26, 2020).

Keywords: EFCF2020, SOx
Session A15: Cell, stack & system modelling and optimization

A1511

Computational analysis of mass transfer limitation in porous electrodes of solid oxide electrochemical cell

Marcin Blesznowski (1,2), Monika Sikora (1,3), Wojciech Orciuch (3), Lukasz Makowski (3), Jakub Kupecki (1,2)
(1) Institute of Power Engineering – Research Institute
01-330, Mory 8, Warsaw/Poland
(2) CTH2 - Center for Hydrogen Technologies, Institute of Power Engineering
Augustowka 36, 02-981, Warsaw/Poland
(3) Warsaw University of Technology, Faculty of Chemical and Process Engineering
Warynskiego 1, 00-645 Warsaw/Poland

Contact authors: www.EFCF.com/ContactRequest

Abstract

The limitations of mass transport at elevated temperature in porous electrodes of solid oxide cells (SOC) in conditions of significant concentration gradients of gas component is one of the key contributors to the performance operation of SOCs. Uneven and low porosity ~20% (after sintering process) affects the maximal performance and lifetime of electrodes. On the other side, high porosity (above 40%) reduces the mechanical stability of sintered SOC support layer.
Due to complex nature of the mechanism and scale of analyzed case, a detailed computational fluid dynamic (CFD) modeling of diffusion transport in porous electrode was performed in order to analyze limiting factors of the mass transport through porous media at operating conditions of SOCs. Numerical investigation supported by microstructure characterization enabled understanding and distinguishing contributing process according to their significance and impact on the overall transportation in porous structures. A set of mathematical models of diffusive mass transport were examined. In the final stage, Dusty Gas Model (DGM) and Knudsen diffusion were selected and implemented in Fluent solver for the purpose of numerical study.
The calculations done using CFD model will be verified during measurements of the pressure drop and gas composition in the flow field within the porous structures. Laboratory investigations and numerical analyses will be performed with supporting layer of SOC, fabricated in the Institute of Power Engineering in Poland. The influence of porosity will evaluated for a set of electrodes with porosity varied in the range from 15% to 35% (after sintering process), thickness from 0.55 mm to 1 mm.
Systematic analysis of these parameters and their effects on the overall operation of SOCs allow determination of the limitations of diffusion mechanisms in porous structures at high temperature, in the regime of significant concentration gradients of gaseous components. Results of this work extend the range of optimal operating conditions for fuel cells, high temperature membranes, separators, selective sieves or porous filters.

https://doi.org/10.5281/zenodo.4556881

Introduction

SOCs have ability to effectively convert electrochemically hydrocarbon fuels which are usually in gaseous state. However, it is also possible to fueled them with solid (carbon) fuels [1]. Nickel-based porous structure of anode (fuel electrode in SOFC mode) is responsible for intensification of the reactions at high temperatures (between 600°C and 1000°C). In SOFC mode three main polarizations are distinguished: activation, ohmic and diffusion [2]. The last one is strictly correlated with significant concentration gradients of gas component under high electronic load. Such operating conditions are detrimental to lifetime of SOC [3] and are classified as destructive testing. An anode is an example of porous medium which is typically characterized by porosity, tortuosity [4] and Knudsen number which is associated with the diameter of the pores. Mass transport mechanism in porous anode is approximated with different diffusion models. The most popular are Fick laws, modified Fick law, Maxwell-Stefan Model and Dusty Gas Model.

Ficks laws are one of the most willingly used [5-8]. The second Fick's law assumed that fluid is stationary in a porous fuel cell electrode and convective mass transport may be neglected [9]. Due to steady character of diffusive transport, equimolar counterdiffusion, with assumption that the concentration profile does not develop with time, the second Fick's law simplifies to the first Fick's law [10]. In case of SOFC technology, there are some restrictions which limit the applicability of Fick's law [11]. Application of the first Fick's law with incorporation of porosity and tortuosity influenced by introducing effective diffusion coefficient [12] is appropriate for binary system where delivered fuel is of 100% concentration.

Next model – Modified Fick's law is based on the assumption [13] that the factor limiting current density is surface diffusion of adsorbed fuel components to active centres of the electrochemical reaction at Triple Phase Boundary – TPB. The parameter that differs modified Fick's model from standard Fick's law is the formula of diffusion coefficient $D_{i,t}$ which incorporates influence of bulk and surface diffusion by exponential weighted average at high current densities [14]. Fitting the activation energy of adsorption and surface diffusion coefficients at zero and full surface coverage is a drawback because it cannot guarantee reliability in another reaction case. This model accurateness is determined by the compliance between values of fitted parameters and experimental data.

Maxwell-Stefan (MS) model is used to characterize diffusion in multicomponent systems where volume of single molecule of gas is negligible compered to system's volume. Maxwell-Stefan diffusivity (D_{ij}) considers concentration impact in isothermal and isobaric conditions. Standard SOFC performance conditions (close to atmospheric pressure, high temperature) are well above critical temperature of commonly used gases. In this case MS model can be simplified or solved analytically [15]. Researchers prefer to simulate with MS model diffusion in nonporous media [16]. According to Huang and Goodenough's work [17], this model is the most precise when pore size diameter is large enough to neglect Knudsen diffusion.

The last one, Dusty Gas Model (DGM) is a synthesis of previously described models: multicomponent diffusion, Knudsen diffusion and viscous flow coupled with the diffusion which triggers pressure gradient. In Dusty Gas Model porous medium is treated as large, spherical and motionless dust particles. The DGM equation is expressed by Eq. (1) [16].

$$\frac{N_i}{D_{K,i}^{eff}} + \sum_{\substack{j=1 \\ j\neq i}}^{n} \frac{y_j N_i - y_i N_j}{D_{i,j}^{eff}} = -\frac{P\nabla y_i}{RT} - \frac{y_i}{RT}\left(1 + \frac{1}{D_{K,i}^{eff}}\frac{B_0 P}{\mu}\right)\nabla P \quad (1)$$

On the left side of Eq. (1) all quantities are expressed in molar units whereas on the right side average mass velocity was used, in order to obtain pressure gradient (based on

Darcy's law). On the cathode side of SOFC this discrepancy can be neglected because molecular masses of mixture components are similar but on the anode side it may lead to some numerical errors in simulations [18]. In this case, molecular mass of hydrogen differs significantly from any other compounds.
To simplify full form of DGM an additional assumption of constant pressure in the porous medium is often used. The comparison of published results obtained from full DGM and DGM with constant pressure assumption demonstrated that neglecting the pressure gradient does not lead to considerable errors [16-19].

1. Mathematical model

Calculations of mass transport of pure hydrogen and pure carbon dioxide through porous anode in opposite directions were conducted with use of DGM in order to include diffusive transport as well as permeation and Knudsen diffusion. The aim of numerical campaign was to perform simulations in open circuit mode and isothermal conditions in order to examine solely mass transport and to identify how this process may affect the concentration polarization during SOFC performance. Knudsen number was obtained in the range of 0.2942÷0.5528, hence the transition flow was assumed [20].
Self-developed code with Dusty Gas Model was integrated into Fluent. The overall effective diffusivity determined Bosanquet (Eq. (2) [21]) where molecular and Knudsen diffusion coefficient is expressed by Chapman-Enskog formula (Eq. (3) [21]) and Eq. (4) [21] respectively.

$$D_{z,i}^{eff} = \left(\frac{1}{D_{ij}^{eff}} + \frac{1}{D_{K,i}^{eff}} \right)^{-1} \tag{2}$$

$$D_{ij} = \frac{1{,}86 \cdot 10^{-7} T^{\frac{3}{2}} \left(\frac{1}{M_i} + \frac{1}{M_j} \right)^{\frac{1}{2}}}{P \Omega_D \sigma_{ij}^2} \tag{3}$$

$$D_{K,i}^{eff} = \frac{\varepsilon}{\tau} \cdot \frac{d}{3} \sqrt{\frac{8RT}{\pi M_i}} \tag{4}$$

Porous anode was modelled by the addition of momentum source term (Eq. (5)) to the Fluent's standard fluid flow equations. Only viscous resistance term was applicable due to laminar flow. It was defined based on Darcy's law [22] and structure parameters of anode material.

$$S_i = -\left(\sum_{j=1}^{3} B_{ij} \mu v_j + \sum_{j=1}^{3} C_{ij} \frac{1}{2} \rho |v| v_j \right) \tag{5}$$

Furthermore, mass diffusivity coefficient was of the same value as diffusion coefficient relative to molar average velocity or volume average velocity in case of binary system [12,23].

2. Results

Co-current and counter-current – two configurations of flow design were investigated for a set of various volume flow values. The flow systematically was increased from 10 [ml/min]

to 200 [ml/min] in order to evaluate the impact of residence time in the system on the outlet concentrations.
The shorter residence time, the slower diffusion through the anode (Figure 1). Carbon dioxide requires longer residence time therefore the most noticeable changes occur for small rates, up to 60 [ml/min].In both cases hydrogen diffuses more effectively through the porous anode to upper channel. However, counter-current variant demonstrated slower diffusion process in comparison to co-current (Figure 1 and Figure 2). Velocity at the outlet of upper channel is increasing (Figure 3) as a result of hydrogen diffusion. Counter-current flow characterizes higher velocity uniformity in system.

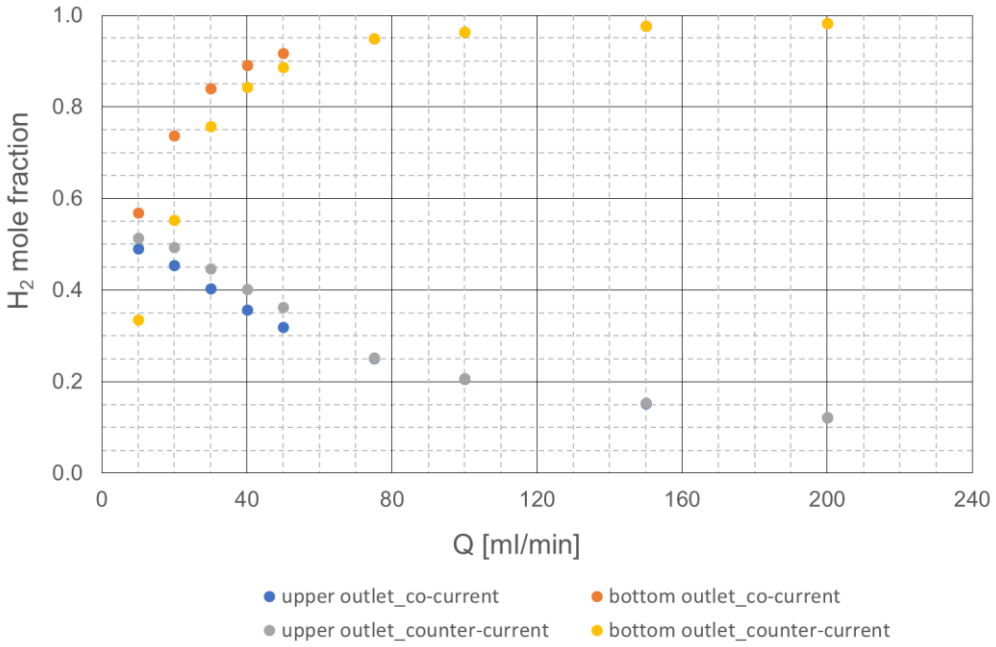

Figure 1 Mole fractions of hydrogen at outlets depending on the flow rate for co-current flow and counter-current flow

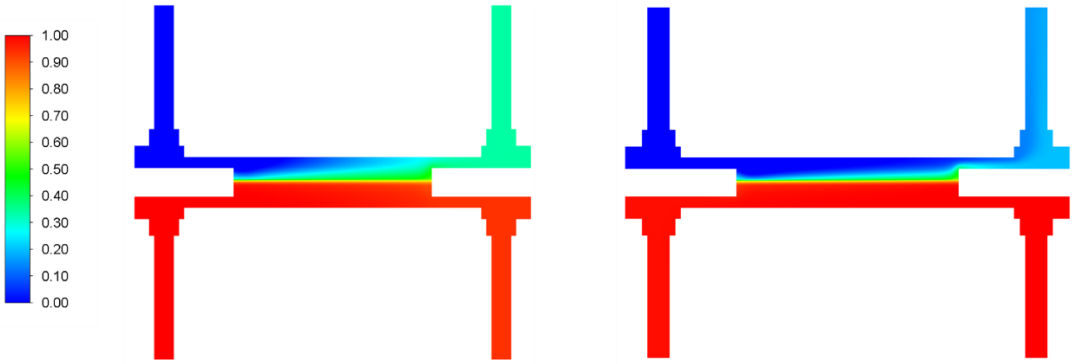

Figure 2 Mole fraction of hydrogen distribution for Q= 40 [ml/min] – comparison between co-current (left) and counter-current (right) flow

https://doi.org/10.5281/zenodo.4556881

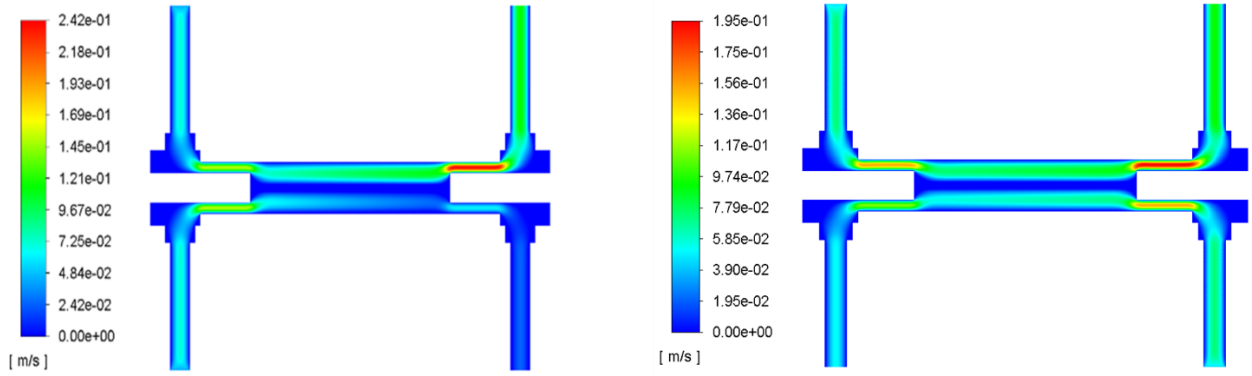

Figure 3 Velocity profile for Q= 40 [ml/min] – comparison between co-current (left) and counter-current (right) flow

3. Conclusions

The aim of this work was to investigate the limitations of mass transport at elevated temperature in porous electrode of solid oxide cells (SOC). The calculations were based on the fundamental conservation laws of mass with a usage of DGM in order to include diffusive transport as well as permeation. Moreover, in DGM Knudsen diffusion was also incorporated.

Carbon dioxide reflected steam – product of electrochemical reaction. It was determined that carbon dioxide diffusion was much slower than hydrogen diffusion. The counter-current flow demonstrated the slowest mass transport process for all analyzed flows. Calculations were performed in Ansys Fluent software for open circuit conditions in order to analyze mass transport phenomena not influenced by electrochemical reaction.

Developed numerical model enables the evaluation of mass transfer impact on overall process in porous anode of solid oxide cell. Further development of model depends on validation process which is planned to perform with a usage of a set of planar 50 x 50 mm anodes of SOC, delivered by Ceramic Branch CEREL of Institute of Power Engineering.

Acknowledgment

This work was financially supported by the National Science Centre, Poland, Grant No. 2016/23/N/ST8/01580.

References

[1] Dudek M., Skrzypkiewicz M., Moskała N., Grzywacz P., Sitarz M., Lubarska-Radziejewska I., The impact of physicochemical properties of coal on direct carbon solid oxide fuel cells, International Journal of Hydrogen Energy 2016, vol. 41, 18872-18883

[2] Monografia: Modeling, Design, Construction, and Operation of Power Generators with Solid Oxide Fuel Cells, editor J. Kupecki, 2018

[3] A. Ploner, A. Hagen, A. Hauch, Study of Operating Parameters for Accelerated Anode Degradation in SOFCs, Special Issue: 12th European SOFC & SOE Forum August 2017, Volume 17, Issue 4, 498-507

[4] Brus G., Miyawaki K., Iwai H., Saito M., Yoshida H., 2014, Tortuosity of an SOFC anode estimated from saturation currents and a mass transport model in comparison with a real micro-structure. Solid State Ionics, 265, 13–21.

[5] Cayan, F. N., Pakalapati, S. R., Elizalde-Blancas, F., Celik, I., 2009. On modeling multi-component diffusion inside the porous anode of solid oxide fuel cells using Fick's model. Journal of Power Sources, 192(2), pp.467–474.
[6] Ho, T. X., Kosinski, P., Hoffmann, A. C., Vik, A., 2009. Numerical analysis of a planar anode-supported SOFC with composite electrodes. International Journal of Hydrogen Energy, 34(8), pp.3488–3499.
[7] Ferguson, J.R., Fiard, J.M. & Herbin, R., 1996. Three-dimensional numerical simulation for various geometries of solid oxide fuel cells. Journal of Power Sources, 58(2), pp.109–122.
[8] Nikooyeh, K., Jeje, A.A. & Hill, J.M., 2007. 3D modeling of anode-supported planar SOFC with internal reforming of methane. Journal of Power Sources, 171(2), pp.601–609.
[9] Pohorecki R., Wroński S. K., 1979. Kinetyka i termodynamika procesów inżynierii chemicznej, Wydaw. Nauk. -Techn, Warszawa, 396
[10] Ho, W.S.W. & Webb, C.K., 2006. Gas Transport in Porous Media, Springer Netherlands, 10
[11] Krishna R., Wesselingh, J.A., 1997. The Maxwell-Stefan approach to mass transfer. Chemical Engineering Science, Great Britain, 52(6), 861–911
[12] E. L. Cussler. Diffusion: Mass Transfer in Fluid Systems. Cambridge University Press, Cambridge, 1995
[13] Williford, R. E., Chick, L. A., Maupin, G. D., Simner, S. P., Stevenson, J. W., Pacific Northwest National Lab., Richland, W., 2003. Diffusion Limitations in the Porous Anodes of SOFCs. Journal of the Electrochemical Society, 150(8), pp.A1067–A1072
[14] Gholaminezhad I., Paydar M. H., Jafarpur K., Paydar S., 2017. Multi-scale mathematical modeling of methane-fueled SOFCs: Predicting limiting current density using a modified Fick's model. Energy Conversion and Management, Iran, 148, p. 222
[15] Krishna, R. & Baur, 2004. Analytic solution of the Maxwell–Stefan equations for multicomponent permeation across a zeolite membrane. Chemical Engineering Journal, 97(1), pp.37–45.
[16] Fu Y., Jiang Y., Dutta A., Mohanram A., Pietras J., Bazant M., 2014, Multicomponent Gas Diffusion in Porous Electrodes, USA, 1-25
[17] Huang K. & Goodenough J.B., 2009. Solid Oxide Fuel Cell Technology, 7 – Voltage losses in a solid oxide fuel cell (SOFC), Woodhead Publishing Series in Energy, pp. 98-140
[18] Geisler, H. I., 2019, Finite Element Method (FEM) Model and Performance Analysis of Solid Oxide Fuel Cells, Karlsruher Institut für Technologie (KIT), 59-71
[19] Kookos, I.K., 2012. On the diffusion in porous electrodes of SOFCs. Chemical Engineering Science, 69(1), pp.571–577.
[20] Kong W., Zhu H., Fei Z., Lin Z., 2012. A modified dusty gas model in the form of a Fick's model for the prediction of multicomponent mass transport in a solid oxide fuel cell anode. Journal of Power Sources, 206, 171–178
[21] Jiang, Y. & Virkar, A., 2003. Fuel composition and diluent effect on gas transport and performance of anode-supported SOFCs. Journal of the Electrochemical Society, 150(7), pp.A942–A951.
[22] Fluent Theory Guide, 2019, Ansys Inc
[23] Bird, R. B., Steward, W. E., and Lightfoot, E. N., 1960., Transport Phenomena, Wiley, New York

Keywords: EFCF2020, SOx
Session A15: Cell, stack & system modelling and optimization

https://doi.org/10.5281/zenodo.4556881

A1513

Towards model-based optimization of CGO/Ni anodes

Philip Marmet (1), Thomas Hocker (1), Jan G. Grolig (2), Holger Bausinger (2), Andreas Mai (2), Joseph M. Brader (3), Lorenz Holzer (1)
(1) Zurich University of Applied Sciences, Institute of Computational Physics
8401 Winterthur/Switzerland
(2) Hexis AG
8404 Winterthur/Switzerland
(3) University of Fribourg, Department of Physics
1700 Fribourg/Switzerland

Contact authors: www.EFCF.com/ContactRequest

Abstract

Gadolinium doped Ceria (CGO) is a promising material for SOFC anodes because of its mixed ionic electronic conductivity, its high catalytic activity for the hydrogen oxidation reaction (HOR) and its robustness against degradation. In SOFC research, electrochemical impedance spectroscopy (EIS) is an essential characterization tool, which serves as a basis for materials optimization on the electrode, cell and stack levels. However, for CGO based electrodes, there is no consensus how to interpret the impedance spectra yet. In the literature, especially the low frequency arc is often either depicted as gas impedance or as chemical capacitance process, without conclusive evidence. Further uncertainties in the interpretation of impedance spectra arise with respect to the operating conditions (especially pO_2, pH_2O) and to their impact on the HOR resistance. Hence, reliable interpretation of impedance spectra for SOFC with CGO-based anodes requires a detailed model, which captures a) the relevant physico-chemical processes, b) the associated material laws and c) the dependencies on varying operating conditions.
In the present contribution, we present an approach for a systematic materials optimization for CGO-based anodes, including EIS measurements, microstructure analysis and finite element modelling with AC and DC mode. The model captures all previously mentioned effects and their impact on the performance of a CGO/Ni-based anode. The computational model is validated and calibrated with EIS-measurements and the impacts of the chemical capacitance and gas impedance on the EIS spectra are illustrated for button cell conditions. The calibrated model is exemplarily used to optimize the CGO/Ni layer thickness. DC results of the extension of the reaction zone are thereby used to understand the different resistive contributions (e.g. from electrochemical conversion, from transport of charge carriers or from gas diffusion) to the total anode impedance.
In summary, we present a model-based approach to link bulk material properties, fabrication parameters, microstructure effects and operating conditions with the cell performance on button cell level. Moreover, the model can be extended to different scales like thin film electrodes, used for fundamental material characterization, as well as to large area cells used for industrial devices with stack architecture. By using a stochastic model for virtual structure variation, also the influence of the microstructure can be assessed in a fully digital way (digital materials design). Hence, with the integration of detailed physico-chemical properties over different scales into a single model framework, findings from basic and applied research can be directly used for the industrial development, enabling a systematic optimization of SOFC devices.

https://doi.org/10.5281/zenodo.4556899

1. Introduction

SOFC technology is a promising solution for the efficient use of renewable fuels or natural gas for heat and power. Thereby, doped Ceria represents an excellent material for SOFC anodes because of its mixed ionic electronic conductivity, its high catalytic activity for the hydrogen oxidation reaction (HOR) on the two phase boundaries (gas/Ceria) and its robustness against degradation.
Ceria based anodes are widely studied with thin-film symmetric cell setup, but less rigorously for the case of porous high-performance electrodes. Nevertheless, Ceria-based anodes are now at the threshold of commercialization. The requirements of the market call for higher performance and efficiency, longer lifetime and lower system costs. In this context a detailed understanding of the processes involved in Ceria-based porous high performance anodes on button cell, large area cell and stack levels is crucial in order to perform a systematic evaluation and optimization of the corresponding cell concepts and materials systems.

In SOFC research, electrochemical impedance spectroscopy (EIS) is an essential characterization tool, which serves as a basis for materials optimization on the electrode, cell and stack levels. However, for CGO based electrodes, there is no consensus how to interpret the impedance spectra yet. With EIS, the response from different processes in CGO based anodes are often not distinguishable from each other because their frequency ranges overlap and because of their interdependencies. Especially, on button cell level, it is often unclear which EIS-signals originate from chemical capacitance, surface reaction resistance, gas diffusion impedance and/or transport resistance.

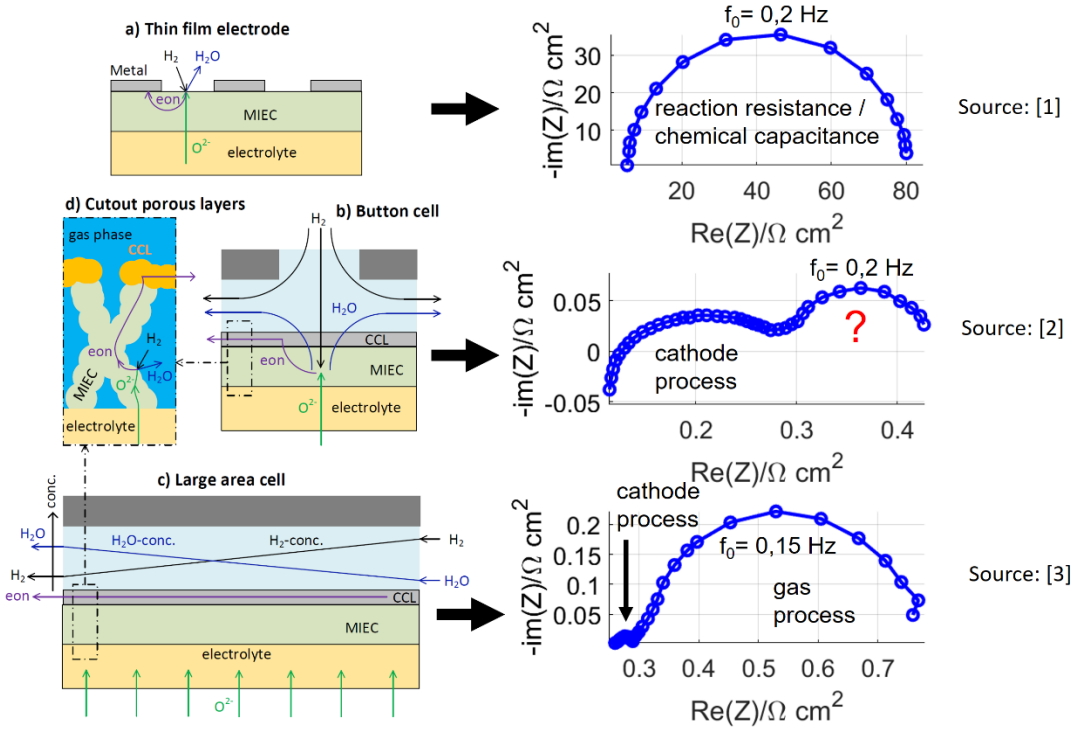

Figure 1: Illustration of the EIS-processes of Ceria-based electrodes on different levels, showing typical impedance spectra: a) from an SDC thin-film electrode (symmetric anode cell) showing a clear dominance of the chemical capacitance / surface reaction process, b) from a button cell (full cell with porous electrodes) with a CGO based anode, showing a low frequency process with non-obvious contributions from different processes and c) from a short stack consisting of large area full cells with CGO based anodes showing a clear dominance of the gas impedance process for the low frequency arc.

https://doi.org/10.5281/zenodo.4556899

In fact, there are some pitfalls when trying to link the impedance spectra of thin-film electrodes with those from porous high-performance electrodes. It is well accepted (e.g. [1], [4], [5]), that ceria based electrodes own a chemical capacitance, describing their ability to store energy by a change in stoichiometry. For ceria based thin film electrodes, other effects like the gas impedance and transport resistance of the charge carrier are negligible, and therefore the low-frequency arc can be attributed unequivocally to the chemical capacitance, which is linked with the electrochemical surface reaction (HOR) process. This mechanism is illustrated in Fig. 1 a), replotted from Chueh et al. [1]. On the other hand, for large area cells, the low frequency arc is clearly identified as a gas impedance process, because of the large gas conversion impedance due to the fuel consumption along the cell, as shown for a Hexis short stack in Fig. 1 c) with a CGO-Ni anode from Linder et al. [3]. In this case it is assumed that the (low frequency) contribution from chemical capacitance is relatively small and therefore hidden within the dominant gas impedance arc. In a button-cell setup with an excess fuel flow rate, the gas impedance is much smaller. In Fig. 1 b), a typical impedance spectrum for a button cell with a CGO based anode is shown from Riegraf et al. [2]. Whether this low frequency process in this case is dominated by the gas impedance, chemical capacitance / surface reaction process or even by a different process like the transport resistance of the charge carriers, is neither obvious nor trivial and different interpretations are found in the literature ([6], [7], [8], [9]).
In the present contribution, we will use a combined approach involving characterization methods like EIS and microstructure analysis as well as a simulation model to elucidate the contributions from gas impedance, chemical capacitance and surface reaction resistance and their interdependencies for button cell conditions.
A precise understanding and quantization of all the important physico-chemical processes involved is the basis for a systematic materials optimization of CGO-based anodes.

2. Approach for a systematic materials optimization of MIEC anodes

In Fig. 2, our approach for a systematic materials optimization of MIEC SOFC-electrodes is shown schematically.

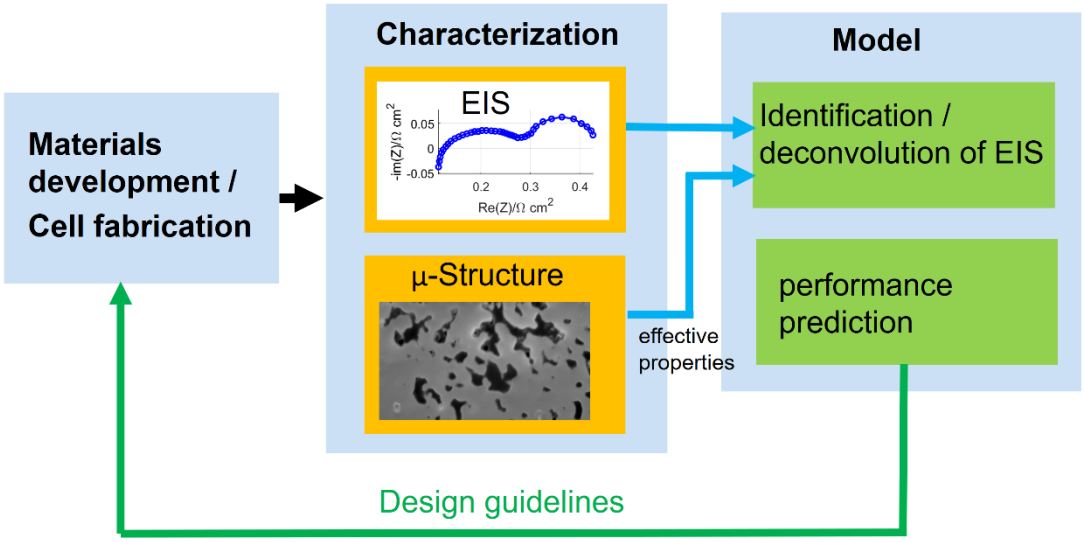

Figure 2: Approach for a systematic optimization of MIEC SOFC anodes with Materials development and cell fabrication on the button cell level (left), EIS characterization and quantitative 3D-microstructure analysis and determination of effective transport properties (centre), model for the deconvolution of EIS and identification of underlying (rate-limiting) processes and prediction of performance as a function of microstructure, operating conditions, cell architecture/layer thickness (right).

https://doi.org/10.5281/zenodo.4556899

The starting point for our systematic materials optimization approach is a batch of button-cells, which are fabricated based on detailed experimental know how at Hexis laboratories. The cell performance is characterized with electrochemical impedance spectroscopy (EIS). However, overlapping processes in the EIS spectra and lacking knowledge about the detailed physico-chemical processes makes it difficult to interpret the EIS-spectra correctly. Multi-physics simulation with AC and DC modes, enable the simulation of the EIS-spectra as well as the DC behavior during the normal cell operation. An essential prerequisite for an appropriate model is the knowledge about the effective properties of the microstructure. Microstructure analysis based on FIB-tomography enables to quantify morphological characteristics (tortuosity, porosity etc) and the associated transport properties. For details we refer to previous publications (e.g. Holzer et al. [17,18], Pecho et al [19], Neumann et al. [20,21], Stenzel et al.[22]).
Moreover, literature data for the bulk material properties is used in order to minimize the number of fit parameters. As illustrated below, this combination of characterization and modeling provides a basic understanding of the complex physico-chemical processes and enables the reliable deconvolution of EIS-spectra from fuel cells with ceria-based anodes.
The calibrated simulation model is then used to predict the impact of design adjustments (e.g. cell architecture, material and microstructure variations) on the cell performance. A key point thereby is to include the effects from the microstructure appropriately in the model. With the digital materials design (DMD) approach, the effect of microstructure variation on the cell performance can be assessed by generating virtual but realistic microstructures. By establishing the relation between material properties, microstructure, cell-design and performance, guidelines for a new anode materials design can be deduced. This allows for a faster and more systematic development of new SOFC electrodes. The different steps of the suggested approach are described in the following.

2.1 Cell fabrication and testing

The button-cells are fabricated by screen printing the anode and the cathode layers onto a 160 µm thick electrolyte disk from 6ScSZ (HEXIS). Both, the CGO and Nickel based anode layer and the double layered LSM/8YSZ and LSM cathode were prepared using the previously reported preparatory methods ([6],[10],[11]). The anode side is contacted with a Ni-mesh and the cathode side with a gold-mesh. The button-cells are operated on a seal-less button-cell test ridge at the laboratories of Hexis with a post-cell combustion zone. A more detailed description of the test ridge can be found in the work of Price et al. [6]. An excess hydrogen fuel supply on the anode side and an excess compressed air supply on the cathode side are used in order to avoid gas conversion impedance effects. The OCV and therewith the water content are varied by changing the fuel flow rate, which results in a specific gas composition due to the leakage of the seal-less setup. For the EIS-measurements a Zennium PP241 from Zahner is used.

2.2 Microstructure analysis

3D reconstructions of the microstructures from anodes are obtained by performing serial-sectioning with focused-ion beam scanning electron microscopy (FIB-SEM). The image size of each cross-section is about 13x9 µm with a (x-y) pixel resolution and (z-) slicing distance of 5 nm (Fig. 3). The 3D image is then segmented using GeoDict software (www.geodict.com). By means of image analysis and numerical simulations, metrics like the porosity and specific surface area and the transport properties for the gas and solid phase were determined using GeoDict. Because of the fine porous microstructure Knudsen and bulk diffusion are both relevant. The effective properties of a characteristic anode microstructure are summarized in Tab. 1 and will be discussed in more detail in the results

section. For details about the microstructure property relationships, we refer to previous publications (e.g. Holzer et al. [17,18], Pecho et al [19], Neumann et al. [20,21], Stenzel et al.[22]).

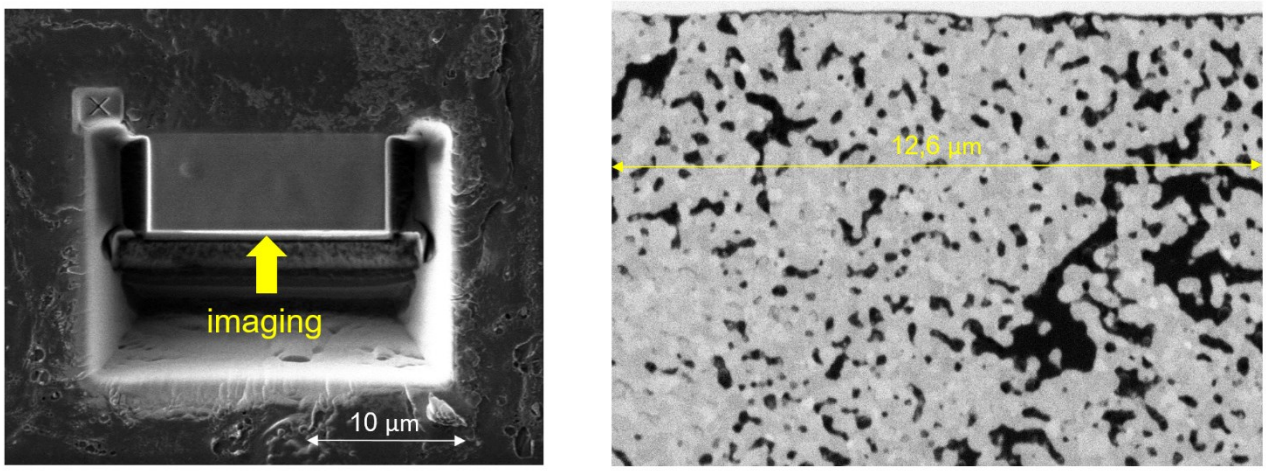

Figure 3: 3D imaging with FIB-tomography. a) Preparation of a cube for serial sectioning (top view, x-z-directions), b) SEM-cross-section with a voxel resolution of 5 nm (x-y).

2.3 Simulation model

For the simulation study, a 1D computational model is developed using the commercial software package Comsol Multiphysics [12]. The model consists of two computational domains as visualized schematically in Fig. 4.

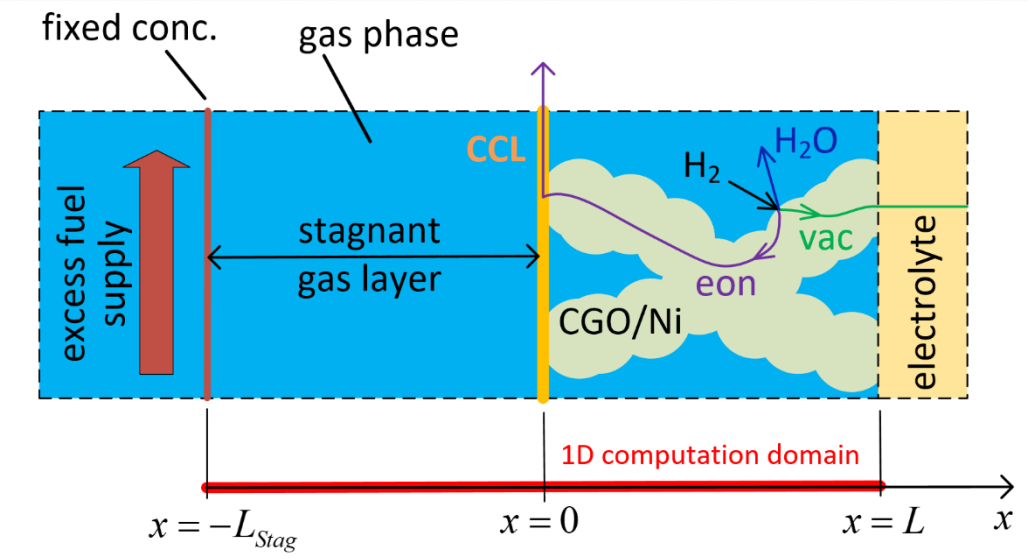

Figure 4: Illustration of the 1D simulation setup: eon = electrons, vac = oxygen ion vacancies, L_{Stag} = stagnant gas layer thickness, L = thickness of the porous CGO/Ni layer.

The domain from x = [0,L] is the porous CGO/Ni layer. It describes the transport of negatively charged Ce^{3+} ions (hereafter simply called electrons) and positively charged oxygen ion vacancies in the mixed ionic and electronic conductor (MIEC) CGO by drift and diffusion. Transport of gas species in the porous medium is described by a dusty gas model [13], which accounts for bulk and Knudsen diffusion. The hydrogen oxidation reaction (HOR) takes place at the CGO/pore interface, which is modelled as a source term as a consequence of the 1D setup.

The large volumetric chemical capacitance is a characteristic feature of (Ceria-based) MIEC-electrodes, which is associated by the storage of charges and a change of stoichiometry. The size of the chemical capacitance depends on the number of charge carriers. The number of charge carriers is a function of oxygen partial pressure and temperature and is implemented in the model according to experimental measurements from Wang et al. [14]. Also the ionic and electronic conductivities of CGO10 are implemented into the simulation model from Steele [15].
Based on the experimental setup, an excess fuel supply is assumed, resulting in a fixed gas species concentration at x = -L_{Stag}, avoiding any gas conversion impedance effect. Despite the excess fuel supply, there exists a stagnant gas layer above the electrode, where the gas transport is governed by diffusion and not by convection of the excess fuel supply. In the domain from x = [-L_{Stag},0], the gas species diffusion in a stagnant gas layer is thus modelled. For the combined effect of the diffusion in the stagnant gas layer and in the porous CGO/Ni electrode the term gas diffusion impedance is used.
The electrolyte at x = L and the current collector layer at x=0 are only modelled as boundary conditions and are not spatially resolved. This model is described in great detail in a separate publication in preparation (P. Marmet et al., to be submitted to PCCP (Physical Chemistry Chemical Physics), Royal Society of Chemistry).

3. Results

3.1 EIS-Results

The Nyquist-plot of the EIS-spectra from a button-cell measured at T=850°C operated with a current density of J = 0.2 A/cm^2 is shown in Fig. 5. The water content was calculated from the OCV to be x_{H2O} = 0.0844. The anode processes and the cathode-processes can be clearly distinguished. However, for the current study we are only intersted in the anode processes.

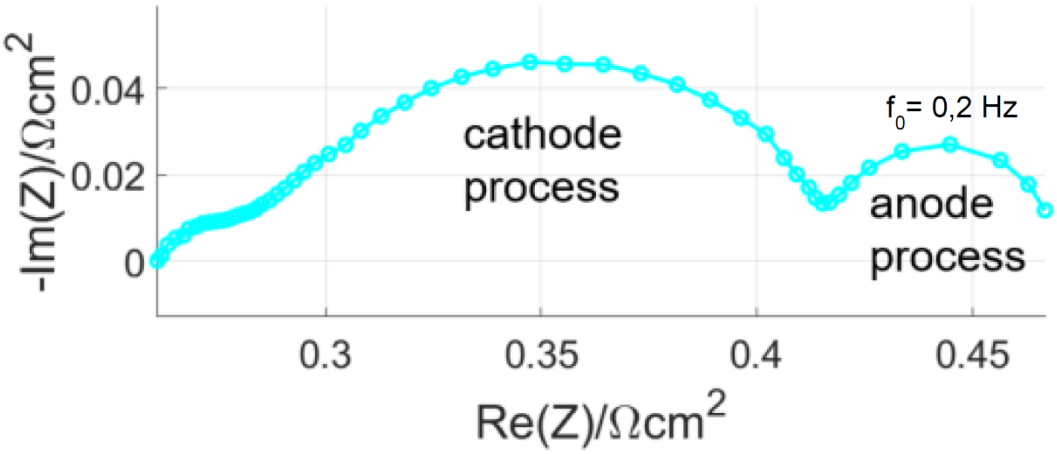

Figure 5: Nyquist-plot of the EIS-spectra measured at T=850°C, current density J = 0.2 A/cm^2 and a water content of x_{H2O} = 0.0844.

As mentioned in the introduction, the anode contributions to the EIS-spectra appear as only one single LF-arc and the different contributions can not be distinguished, which hinders a systematic optimization. Therefore, a physical model is needed to deconvolute these processes.

https://doi.org/10.5281/zenodo.4556899

3.2 Microstructure and effective properties

A crucial prerequisite for appropriate simulation results is the knowledge of the effective transport properties and other microstructure metrics, which are summarized in table 1. The CGO-Ni layer thickness was estimated to 20 µm, but was difficult to measure precisely because of a considerable variation of the thickness along the cell. The sample is quite dense and shows a porosity of ε = 0.213. The hydrogen oxidation reaction (HOR) scales proportionally with the surface of the CGO/gas interface. Because of the low porosity, the relative bulk gas diffusivity and the gas permeability are quite low (note: the relative properties are subsequently also named as microstructure factor, defined as M = (effective porous material property)/(bulk material property)). The characteristic pore diameter is about 125 nm and therewith, Knudsen diffusion is relevant and is even the dominant diffusion resistance as the effective Knudsen numbers for hydrogen and water are larger than one. The relative Knudsen diffusivity, which is determined by a random walk algorithm, is in the same order of magnitude but not identical to the relative bulk diffusivity, which is determined by solving the diffusion equation on the voxel mesh. All these effective properties for the pore phase enter into the dusty gas model, which describes the combined effects of bulk and Knudsen diffusion appropriately. Because of the high solid volume fraction, the relative electric conductivity is quite high. Using these effective properties, the effect of the microstructure can be captured reliably in the simulation model. However, an uncertainty of such an effective property model enters by the fact, that the CGO/Ni layer contains local cracks (not shown), which cross-cut the entire anode layer. As these cracks are not yet respected in the current model description, the transport resistance in the pore phase tends to be overestimated while the transport resistance in the solid phase tends to be underestimated.

CGO/Ni Layer Thickness / µm	20
Porosity (Epsilon) / -	0.213
Specific Surface Area (S) / μm^{-1}	4.29
Relative Bulk Gas Diffusivity (D_rel_sim) / -	0.0163
Gas Permeability (Kappa_sim) / m^2	9.79E-17
Characteristic pore diameter / nm	125.31
Relative Knudsen Diffusivity	0.0122
Effective Knudsen number Kn for H2	6.39
Effective Knudsen number Kn for H2O	4.86
Solid Volume Fraction (Phi) / -	0.787
Relative Electric Conductivity (Sigma_rel_sim) / -	0.623

Tabel 1: Summary of microstructure characteristics and effective properties.

3.3 Simulation results

The microstructure properties enter into the simulation model together with bulk material properties from literature. The only fit parameter in the model is the exchange reaction rate for the HOR, which is very hard to determine appropriately in an analytical way or from literature. This now allows for a deconvolution of the EIS-spectrum into the different contributions from distinct anode processes. The simulation results are plotted along with the experimental EIS-measurements in Fig. 6. The Nyquist-plot in Fig. 6 a) shows that the surface reaction resistance Z_{SR} of the HOR has the largest contribution from all anode processes (note: the surface reaction resistance is strongly linked with the chemical capacitance). The gas diffusion impedance Z_{gas} contributes also substantially to the anode

arc (due to low porosity and small pore size associated with the dense anode microstructure), while the resistance for the transport of the charge carriers $Z_{transport}$ is negligible for an anode with such a dense microstructure and relatively small CGO/Ni layer thickness.
The imaginary part of the impedance in Fig. 6 b) also shows a good agreement between simulation and EIS-measurement in the low frequency range. This result points out that the computed chemical capacitance is in a reasonable range. It must be emphasized that the chemical capacitance is not fitted, but instead it is determined directly with the model. Thereby, the result for chemical capacitance (and Z_{SR}, respectively) strongly depends on the charge carrier concentration, which is implemented from literature data.

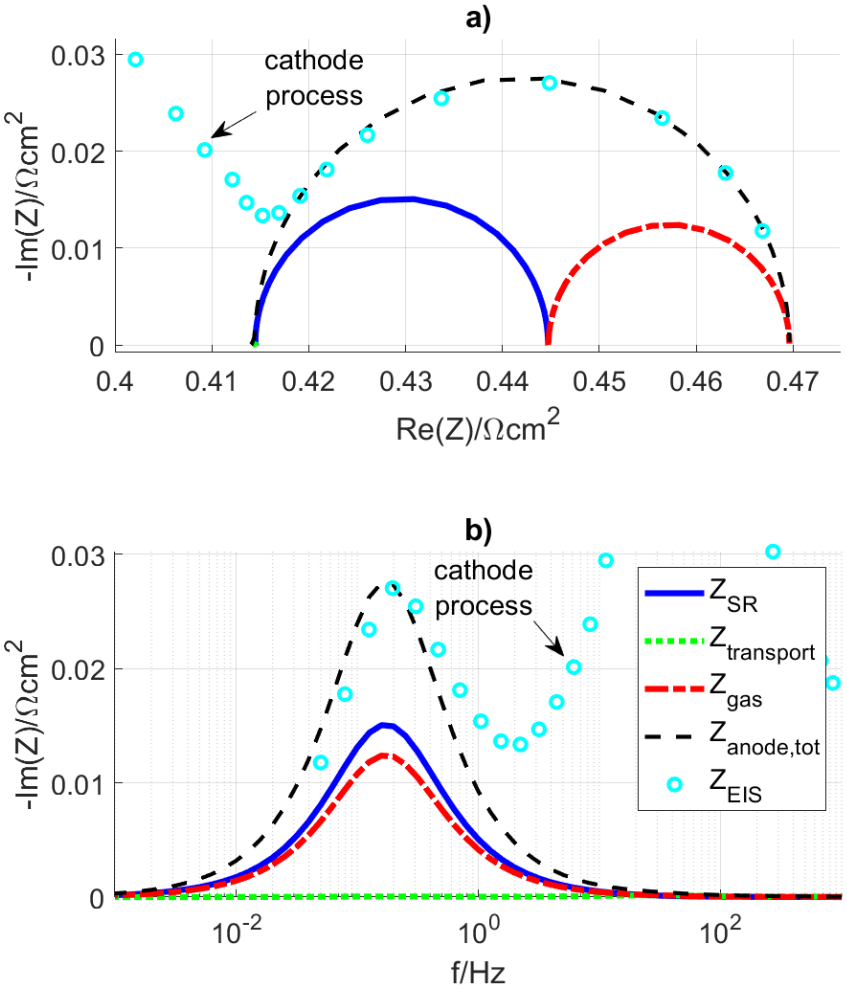

Figure 6: Simulation-based deconvolution of process-related contributions to the anode impedance spectrum and comparison with experimental data (Z_{EIS}). a) Nyquist impedance plot and b) imaginary part of the impedance for the surface reaction impedance Z_{SR}, impedance associated with the charge carrier transport in the CGO layer $Z_{transport}$, gas diffusion impedance Z_{gas}, total anode impedance $Z_{anode,\,tot}$ and experimental data (Z_{EIS}).
Moreover, the simulation shows, that the gas impedance Z_{gas} and the surface reaction impedance Z_{SR} have exactly the same characteristic frequency! This is not by chance, but a consequence of the way these two processes are coupled. An RC-like arc in an impedance spectra results always in bypassing the resistance by just oscillating the charge in the capacitor. For the surface reaction impedance that means, that the surface reaction resistance is bypassed and that there is no change in the surface reaction due to the applied perturbation at all, because the harmonic current is entirely stored in the chemical capacitance! And if there is no effect on the reaction anymore, there is also no effect on the gas concentration at the electrode surface. And if the concentration does not

change anymore, also the gas impedance is bypassed. Due to this strong coupling, the gas impedance process is forced to the same frequency as the surface reaction process and the two processes cannot be distinguished experimentally in an EIS-spectra of a button cell! The situation might be different for large area cells and stacks. Here, the anode arc is usually dominated by the gas impedance. If the characteristic frequency of the gas impedance is lower than the surface reaction / chemical capacitance impedance process, the two processes are theoretically distinguishable from each other.
Even if this deconvolution of distinct anode processes might appear as a detail for the overall cell performance, it is crucial for a systematic optimization of the anode electrode! If e.g. the anode ASR shall be optimized for a cell where the largest contribution is the surface reaction resistance, the layer thickness can be increased or the fabrication process can be tailored to a microstructure with higher active surface area, which then lowers the surface reaction resistance. At the same time the gas impedance may increase as a trade-off. For a cell, where the gas impedance represents the dominant contribution to the anode arc, the opposite measure (i.e. thinner and less dense anode) potentially leads to an improvement of the total anode performance. This example illustrates, that a systematic optimization is only possible with a detailed understanding of the relevant physico-chemical processes involved.

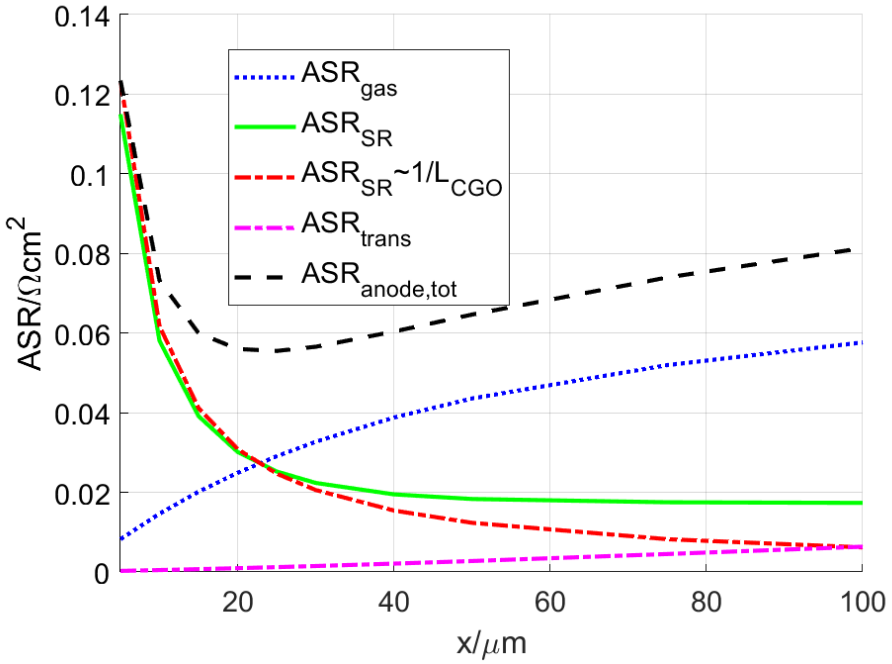

Figure 7: Simulation results of the different contributions to the total anode area specific resistance (ASR) as a function of the CGO/Ni layer thicknesses assuming identical microstructures for all thicknesses. ASR_{SR}: surface reaction resistance, ASR_{trans}: resistance associated with the charge carrier transport in the CGO/Ni layer, ASR_{gas}: gas diffusion resistance and $ASR_{anode,\ tot}$: total anode area specific resistance.

As a simple example for model based-optimization, the thickness of the CGO/Ni layer is changed continuously. Thereby, it is assumed that the operating conditions and microstructure properties remain identical for all thicknesses. The different contributions to the anode ASR extracted from AC simulations are shown in Fig. 7. The optimal thickness for the specific operating conditions and microstructure is about 25 µm. For smaller thicknesses, the total anode ASR rises steeply, because the active surface for the HOR reaction becomes too small. For thicknesses larger than 25 µm, the total ASR anode increases, but with a shallower slope. As a rule of thumb it is often assumed that ASR_{tot} with a minimum is due the two following thickness effects: the gas impedance ASR_{gas}

increases linearly with the thickness, and the surface reaction impedance ASR_{SR} decreases inverse proportional to the thickness (1/L). Our model calculations show that these rules are not precise:
The contribution of the gas impedance ASR_{gas} does not increase linearly but sub-proportional with the layer thickness. In addition, the contribution of the surface reaction impedance ASR_{SR} decreases less than inverse proportional to the layer thickness (the inverse proportional line is plotted as a reference in Fig. 7). This behaviour can be easily understood by considering the DC-result from the extension of the reaction zone in Fig. 8.

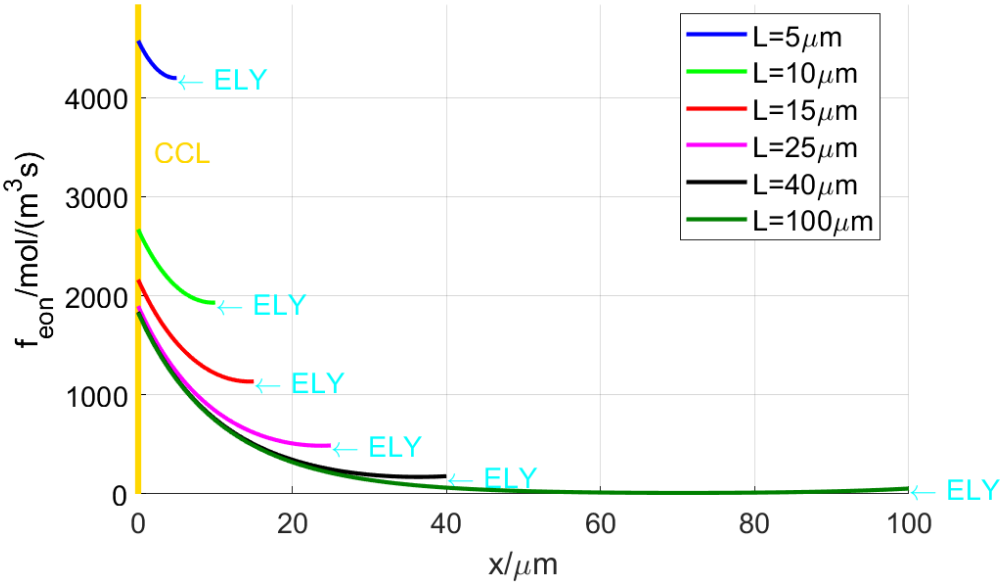

Figure 8: Surface reaction rate (source term of electrons) across the CGO/Ni layer for different CGO/Ni layer thicknesses.

For small CGO/Ni layer thicknesses (e.g. L = 5 µm) high reaction rate is distributed almost homogeneously over the entire CGO/Ni layer. For larger CGO/Ni layer thicknesses, the reaction zone (i.e. domain with high reaction rate) is concentrated close to the CCL in order to minimize the pathways for gas transport in the very dense microstructure. Hence, in thick anodes only a relatively small part of the CGO/Ni layer is electrochemically active and the surface reaction resistance only decreases slightly with increasing layer thickness. At the same time, the increase of the gas impedance with growing thickness is limited, as the gas species only have to be transported to the active zone. Note, that for higher porous microstructures, where the charge transport impedance is larger than the gas diffusion impedance, the reaction zone would be shifted towards the interface with the electrolyte in order to minimize the losses from charge transport (not shown here).

3.4 Influence of the operating conditions

In order to ensure a robust materials design, the dependency of the anode resistance on the operating conditions is investigated in a combined experimental/modeling approach. As shown in Fig. 9, the total ASR anode $ASR_{tot,exp}$ is fitted for experimental EIS-data for different water fractions at OCV. A large variation of about a factor of 3 can be observed, demonstrating the importance of paying attention to the dependency on operating conditions. The total anode $ASR_{tot,exp}$ essentially deconvolutes in a contribution of the surface reaction resistance / chemical capacitance process and the gas diffusion impedance process. The gas diffusion resistance ASR_{gas} can be calculated from the model and the results is plotted in Fig. 9. As mentioned before, the surface reaction resistance is difficult to be determined analytically and precise experimental characterizations describing the impact of gas composition (water content) are not available. Therefore, we estimate the dependency of the surface reaction resistance $ASR_{SR,estimated}$ as the difference between the experimentally measured total ASR of the anode $ASR_{tot,exp}$ and the simulated gas diffusion resistance ASR_{gas}, neglecting other contributions as e.g. the resistance from charge carrier transport. The result $ASR_{SR,estimated}$ is plotted in Fig. 9.
From literature it is known, that the surface reaction resistance depends on the oxygen partial pressure p_{O2} and water content x_{H2O} (e.g. [2,16]). Therefore, an expression for the surface reaction resistance as a function of p_{O2} and x_{H2O} shall be suggested. For the present case of humid hydrogen, the oxygen partial pressure varies according to the dissociation of water according the following law:

$$p_{O_2} = \left(\frac{p_{H_2O}}{p_{H_2}} \right)^2 \frac{1}{K_p} \quad \text{(Equation 1)}$$

where K_p is the equilibrium constant of the reaction. Therewith, we a have a relationship between p_{O2} and x_{H2O} available.

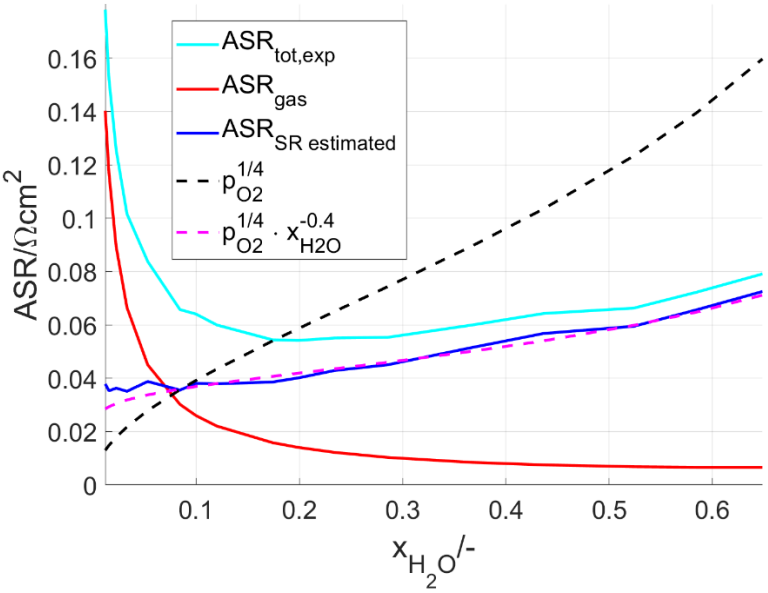

Figure 9: Dependency of the anode ASR on the water fraction at OCV. $ASR_{tot,exp}$: total anode ASR from experimental EIS-measurements extracted by circuit fitting, ASR_{gas}: simulated gas diffusion resistance, $ASR_{SR\ estimated}$: estimated surface reaction resistance calculated as $ASR_{SR\ estimated} = ASR_{tot,exp} - ASR_{gas}$, black dashed line: $p_{O2}^{1/4}$-law as reference, magenta dashed line: $p_{O2}^{1/4}\ x_{H2O}^{-0.4}$-law as reference.

As a reference, the $p_{O2}^{1/4}$-law, which is often reported as a dependency on the oxygen partial pressure of the surface reaction resistance of Ceria-based electrodes (e.g. Chueh et al. [16]), is plotted as black dashed line with x_{H2O} = 0.0844 as a reference point, which has been used for the study above. The oxygen partial pressure p_{O2} is thereby calculated from the water content according to equation 1. The curve of the $p_{O2}^{1/4}$-law is much steeper than the estimated curve for the surface reaction resistance that is fitted for varying p_{H2O}. This is in accordance with the observation of e.g. Riegraf et al. [2] according to whom the water concentration reduces the surface reaction resistance and therefore possibly acts as a catalyst for the HOR. A reasonable agreement for the current data set can be achieved by using a power law for the water fraction dependency with an exponent of approximately -0.4 (see the magenta dashed line with the $p_{O2}^{1/4}$ $x_{H2O}^{-0.4}$-law). In this way, the surface reaction resistance can be calibrated as a function of the water content based on a fitting-procedure with EIS-measurements.

4. Summary and Outlook

We present an approach for a systemtic materials optimization for CGO-based anodes including EIS-measurments, microstructure characterization and simulation models. The EIS-measurements and the effective properties of the microstructure can be used to achieve an appropriate simulation model, which is able to capture all relevant physico-chemical processes involved and to extract valuable information for the optimization of the electrode, which are blurred in the experimental impedance spectra. We especially point out, that the anode arc for button cell conditions often includes a gas diffusion impedance and a surface reaction resistance / chemical capacitance process, which are not distinguisable experimentally. The correct interpretation of the EIS-spectra with identification of the dominant, rate limitting process is only possible in combination with an appropriate model. For the situation of thin film electrodes, the surface reaction resistance / chemical capacitance process (Fig. 1 a)) and for large area cells, the gas impedance process (Fig. 1 c)) are typically dominant. We also show that the operating conditions have a large impact on the cell performance. EIS-measurements at different water contents show, that the total anode ASR changes about a factor of 3 as a function of the water content. We also present an approach to describe quantitatively the dependency on the water content of the different contributions of gas impedance and surface reaction resistance.

The knowledge about a) the relevant physico-chemical processes, b) the associated material laws and microstructure effects and c) the dependencies on varying operating conditions is a crucial prerequisite for a systemic materials optimization. If all those aspects are implemented in a comprehensive simulation model, the optimization process can be performed in a very efficient way, as it has been exemplarily shown for the optimization of the CGO/Ni layer thickness assuming a constant microstructure.

As an outlook, the full potential of the suggested model approach can be exploited in combination with the digital materials design (DMD) approach using virtual microstructures. Thereby, a stochastic digital twin of a reference microstructure from FIB-SEM imaging is deduced, which allows for a virtual but realistic variation of the microstructure. The effect of the microstructure variation on the cell performance can be assessed by the simulation model (virtual materials testing, VMT). Based on a set of experimental data this approach enables a fully digital materials optimization providing design guidelines for the next experimental steps, allowing for a faster and more systematic optimization of the next generation of MIEC-based anodes.

https://doi.org/10.5281/zenodo.4556899

References

[1] W. C. Chueh and S. M. Haile, “Electrochemical studies of capacitance in cerium oxide thin films and its relationship to anionic and electronic defect densities,” Phys. Chem. Chem. Phys., vol. 11, no. 37, pp. 8144–8148, 2009

[2] M. Riegraf, V. Yurkiv, R. Costa, G. Schiller, and K. A. Friedrich, “Evaluation of the Effect of Sulfur on the Performance of Nickel/Gadolinium-Doped Ceria Based Solid Oxide Fuel Cell Anodes,” ChemSusChem, vol. 10, no. 3, pp. 587–599, 2017.

[3] M. Linder et al., “A model-based approach for current voltage analyses to quantify degradation and fuel distribution in solid oxide fuel cell stacks,” J. Power Sources, vol. 288, pp. 409–418, 2015.

[4] J. Jamnik and J. Maier, “Treatment of the impedance of mixed conductors. Equivalent circuit model and explicit approximate solutions,” J. Electrochem. Soc., 1999.

[5] W. Lai and S. M. Haile, “Impedance spectroscopy as a tool for chemical and electrochemical analysis of mixed conductors: A case study of ceria,” J. Am. Ceram. Soc., vol. 88, no. 11, pp. 2979–2997, 2005.

[6] R. Price, M. Cassidy, J. G. Grolig, A. Mai, and J. T. S. Irvine, “ Preparation and Testing of Metal/Ce 0.80 Gd 0.20 O 1.90 (Metal: Ni, Pd, Pt, Rh, Ru) Co-Impregnated La 0.20 Sr 0.25 Ca 0.45 TiO 3 Anode Microstructures for Solid Oxide Fuel Cells ,” J. Electrochem. Soc., vol. 166, no. 4, pp. F343–F349, 2019.

[7] S. Primdahl and M. Mogensen, “Mixed conductor anodes: Ni as electrocatalyst for hydrogen conversion,” Solid State Ionics, vol. 152–153, pp. 597–608, 2002.

[8] P. V. Aravind, J. P. Ouweltjes, and J. Schoonman, “Diffusion impedance on nickel/gadolinia-doped ceria anodes for solid oxide fuel cells,” J. Electrochem. Soc., vol. 156, no. 12, 2009.

[9] T. Nakamura et al., “Determination of the Reaction Zone in Gadolinia-Doped Ceria Anode for Solid Oxide Fuel Cell,” J. Electrochem. Soc., 2008. [4] J. Jamnik and J. Maier, “Treatment of the impedance of mixed conductors. Equivalent circuit model and explicit approximate solutions,” J. Electrochem. Soc., 1999.

[10] R. Price et al., “Development and Testing of Impregnated $La_{0.20}Sr_{0.25}Ca_{0.45}TiO_3$ Anode Microstructures for Solid Oxide Fuel Cells“, ECS Trans., 78(1),1385 (2017).

[11] R. Price et al., “Screen Printed Porous $La_{0.20}Sr_{0.25}Ca_{0.45}TiO_3$ Fuel Electrode Scaffold Microstructures: Optimisation of Interaction with Impregnated Catalysts for More Durable Performance “, ECS Trans., 68(1), 1499 (2015).

[12] COMSOL Multiphysics® v. 5.5. www.comsol.com. COMSOL AB, Stockholm, Sweden.

[13] S. Liu, W. Kong, and Z. Lin, “Three-dimensional modeling of planar solid oxide fuel cells and the rib design optimization,” J. Power Sources, vol. 194, no. 2, pp. 854–863, 2009.

[14] S. WANG, H. INABA, H. TAGAWA, M. DOKIYA, and T. HASHIMOTO, “Nonstoichiometry of Ce 0. 9 Gd 0. 1 O 1. 95-x,” Solid state ionics, 1998.

[15] B. C. H. Steele, “Appraisal of Ce1-yGdyO2-y/2 electrolytes for IT-SOFC operation at 500,” Solid State Ionics, vol. 129, no. 1, pp. 95–110, 2000.

[16] W. C. Chueh, W. Lai, and S. M. Haile, “Electrochemical behavior of ceria with selected metal electrodes,” Solid State Ionics, vol. 179, no. 21–26, pp. 1036–1041, 2008.

[17] L. Holzer, B. Münch, B. Iwanschitz, M. Cantoni, T. Hocker, T. Graule, Quantitative relationships between composition, particle size, triple phase boundary length and surface area in nickel-cermet anodes for Solid Oxide Fuel Cells, J. Power Sources. 196 (2011) 7076–7089. doi:10.1016/j.jpowsour.2010.08.006.

[18] L. Holzer, B. Iwanschitz, T. Hocker, L. Keller, O. Pecho, G. Sartoris, et al., Redox cycling of Ni–YSZ anodes for solid oxide fuel cells: Influence of tortuosity, constriction and percolation factors on the effective transport properties, J. Power Sources. 242 (2013) 179–194. doi:10.1016/j.jpowsour.2013.05.047.
[19] O. Pecho, O. Stenzel, B. Iwanschitz, P. Gasser, M. Neumann, V. Schmidt, et al., 3D Microstructure Effects in Ni-YSZ Anodes: Prediction of Effective Transport Properties and Optimization of Redox Stability, Materials (Basel). 8 (2015) 5554–5585. doi:10.3390/ma8095265.
[20] M. Neumann, O. Stenzel, F. Willot, L. Holzer, V. Schmidt, Quantifying the influence of microstructure on effective conductivity and permeability: Virtual materials testing, Int. J. Solids Struct. 184 (2020) 211–220. doi:10.1016/j.ijsolstr.2019.03.028.
[21] M. Neumann, O. Furat, D. Hlushkou, U. Tallarek, L. Holzer, V. Schmidt, On Microstructure-Property Relationships Derived by Virtual Materials Testing with an Emphasis on Effective Conductivity, in: Sim Sci, Commun. Comput. Inf. Sci., 2018: pp. 145–158. doi:10.1007/978-3-319-96271-9_9.
[22] O. Stenzel, O. Pecho, L. Holzer, M. Neumann, V. Schmidt, Big data for microstructure-property relationships: A case study of predicting effective conductivities, AIChE J. 63 (2017) 4224–4232. doi:10.1002/aic.15757.

Keywords: EFCF2020, SOx
Session A15: Cell, stack & system modelling and optimization

A1515

Characteristics of a Planar SOFC With Load Variation

Hiroyuki MISE (1), Masahiro NAKAMURA (2), Yuya TACHIKAWA (1,3), Hironori NAKAJIMA (1,3), Kohei ITO (1,3)
(1) Department of Hydrogen Energy Systems, Graduate School of Engineering, Kyushu University
744 Motooka, Nishi-ku, 819-0395 Fukuoka/Japan
(2) International Research Center for Hydrogen Energy, Kyushu University
744 Motooka, Nishi-ku, 819-0395 Fukuoka/Japan
(3) Department of Mechanical Engineering, Faculty of Engineering, Kyushu University
744 Motooka, Nishi-ku, 819-0395 Fukuoka/Japan

Contact authors: www.EFCF.com/ContactRequest

Abstract

Renewable energy such as solar power and wind power has been widely introduced to mitigate environmental impacts in energy consumption, but it needs power output leveling for demand. SOFCs can be a candidate for the component thanks to their high efficiency. However, load variation for the leveling gives rise to time variation in distributions of fuel/oxidant concentration, current, and temperature in a cell, affecting the power output stability and the durability of a cell. We have therefore developed a finite element method model of a planar SOFC verified with measurement using segmented electrodes (Figs.1, 2) (1), (2), and investigated corresponding cell behavior assumed in a model of a stationary combined heat and power (CHP) system (3) and limitation of load variation for durable cell/interconnector designs and operating conditions.

Fig.1.Segmented cathode of the planar SOFC

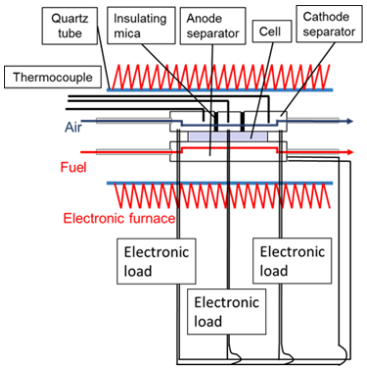

Fig.2. Experimental set-up

Acknowledgments:
This work was supported by the New Energy and Industrial Technology Development Organization.

1. Ö. Aydin, T. Koshiyama, H. Nakajima, and T. Kitahara, J. Power Sources, 293, 1053 (2015).
2. H. Nakajima, T. Kitahara, and E. Tsuda, ECS Trans., 78(1), 2109 (2017).
3. R. Torii, Y. Tachikawa, K. Sasaki, and K. Ito, J. Power Sources, 325, 229 (2016).

https://doi.org/10.5281/zenodo.4556918

Introduction

Renewable energy such as solar power and wind power has been widely introduced to mitigate environmental impacts in energy consumption, but it needs power output leveling for demand. SOFCs can be a candidate for the component thanks to their high efficiency. However, load variation for the leveling gives rise to time variation in distributions of fuel/oxidant concentration, current, and temperature in a cell, affecting the power output stability and the durability of a cell. We have therefore developed a finite element method (FEM) model of a planar SOFC verified with measurement using segmented electrodes (1-4), and investigated corresponding cell behavior assumed in a model of a stationary combined heat and power (CHP) system (5) and limitation of load variation for durable cell/interconnector designs and operating conditions.

1. Finite Element Modeling

COMSOL Multiphysics (COMSOL, Inc.) was used to develop an FEM model to obtain the hydrogen partial pressure, current and temperature distributions in an anode-supported cell (1,2). Butler-Volmer type kinetic equation and Ohm's law were used for the charge conservation. We employed the Stefan-Maxwell equation for the multicomponent diffusion, the Navier-Stokes equation for non-porous fluid in the gas stream, and the Brinkman equation for fluid in the porous electrodes (1, 2). FEM modeling was carried out for a single channel (width: 2 mm, depth: 0.5 mm) and rib (width: 2 mm) of the anode and cathode separators in a co-flow configuration.

2. Experiments

2.1 Cathode segmentation

We have applied segmented electrode method that cathode was segmented into three parts of upstream, midstream, and downstream parts (1-4) to a planar SOFC (ASC-10B, Elcogen, Estonia) consisting of a Ni/8YSZ (8mol%YSZ) anode support, an LSC cathode, an 8YSZ electrolyte, and a GDC interlayer. The anode geometrical area was 19.5 (6.5×3.0) cm^2 while the cathode geometrical area was 2.25 (1.5×1.5) cm^2 each in the upstream, midstream and downstream parts. In this study, we mainly focus on the current and partial pressure distributions in the anode, so that only the cathode were segmented to prevent the influence of the anode segmentation on the fuel flow in the in-plane direction. The anode and cathode separators made of stainless steel (Crofer 22 APU, VDM Metals GmbH, Germany) had flow channels with a width of 1 mm and a depth of 1 mm (MAGNEX Co., Ltd., Japan). The anode separator had 8 parallel flow channels having a length of 4.9 cm. Silver paste (Silvest P-248, Tokuriki Honten Co. Ltd., Japan) and mesh (Nilaco Corp., Japan) were used for current collection.

2.2 Current-voltage measurement

Three electronic loads were used to measure current-voltage (IV) characteristics under voltage control so that each segmented electrode had the same potential (equipotential) to reproduce a normal single cell condition (1-4). Temperature of the cell was 650°C at open circuit voltage (OCV) using a tubular electric furnace. For the measurement, four-terminal

method was used, where the current and voltage lines were separated. After reduction of the anode, IV measurements were carried out with feeding dry H_2/N_2 mixture (H_2: 17 cm^3min^{-1}, N_2: 7 cm^3min^{-1} (at 25°C, 1 atm)) and air (air: 100 cm^3min^{-1} (at 25°C, 1 atm)). Current density and cathode separator temperature transients were measured in the upstream, midstream and downstream parts.

3. Results

Figure 1 shows a transient response of the current density derived from the FEM modeling with stepwise changes of the cell voltage at constant fuel and air flow rates.

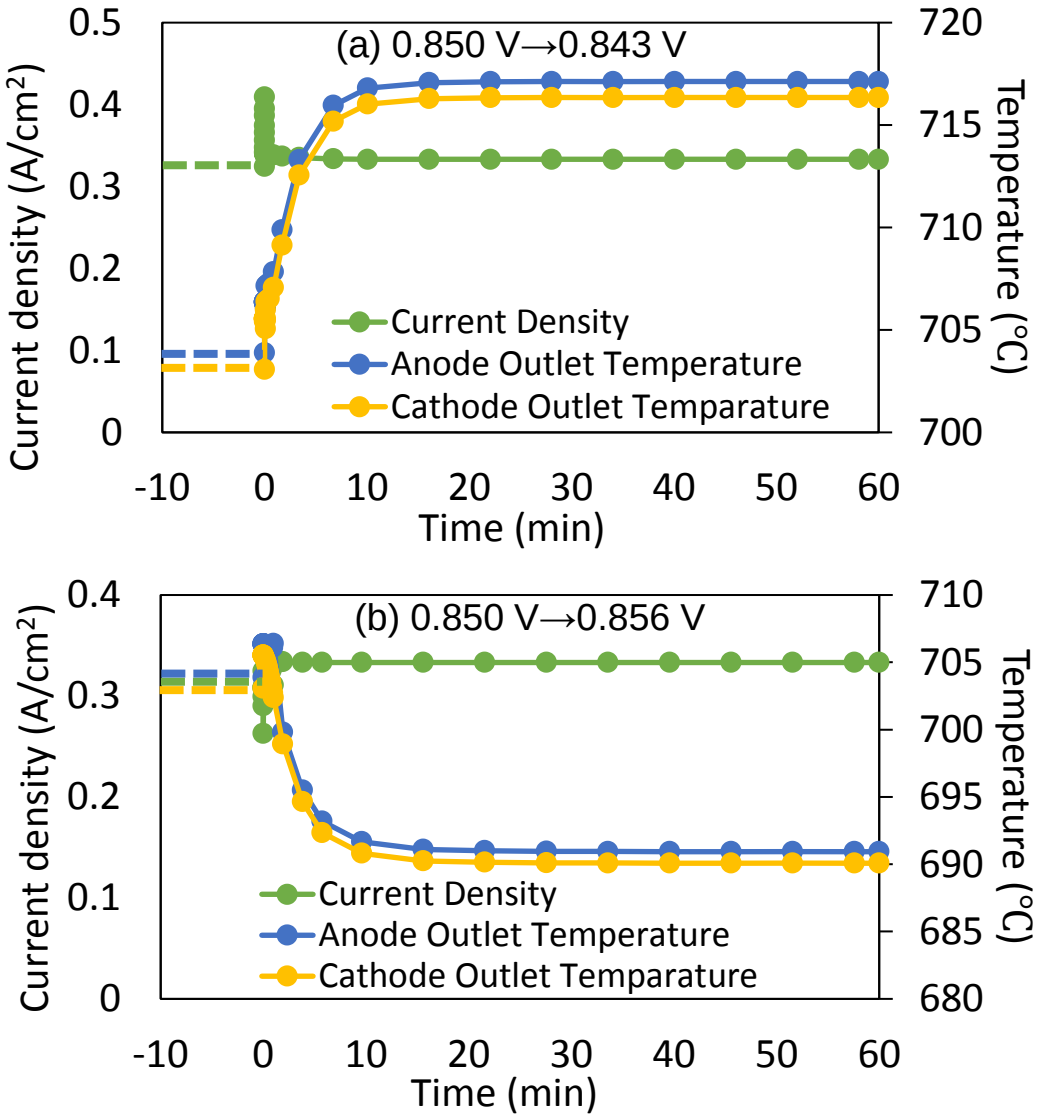

Fig. 1. Time variation of the current density and outlet temperatures derived from the FEM model with the cell voltage change (a) from 0.850 V to 0.843 V (output power from 100% to 120%) and (b) from 0.850 V to 0.856 V (output power from 100% to 80%).

Fuel and air utilizations are 70% and 37.2 %, respectively at 0.85 V, an output power of 100%. The cell voltage changes were assumed in conjunction electrically and thermally

(uniform heat flux through the separators) with a CHP system model (5) using a process simulator, Aspen Plus so that the output power became 120% (0.843 V) and 80% (0.856 V). The current density with the voltage drop spikes within 0.5 s and then transitions to a steady-state (Fig. 1(a)). A similar spike in current drop appears with the voltage rise (Fig. 1(b)). These spikes can be explained similarly as chronoamperometry reflecting current transient response represented by the Cottrell equation corresponding to local hydrogen partial pressure variations (6). It is interesting to note that a slight increase in the current density can be seen after the spike with the voltage rise owing to more uniform current distribution along the flow channel with decreased overpotential.

Figure 2 shows the transient response of the current density with the cell voltage changed in a stepwise manner from 0.85 V to 0.75 V and from 0.75 V to 0.85 V in the IV measurement.

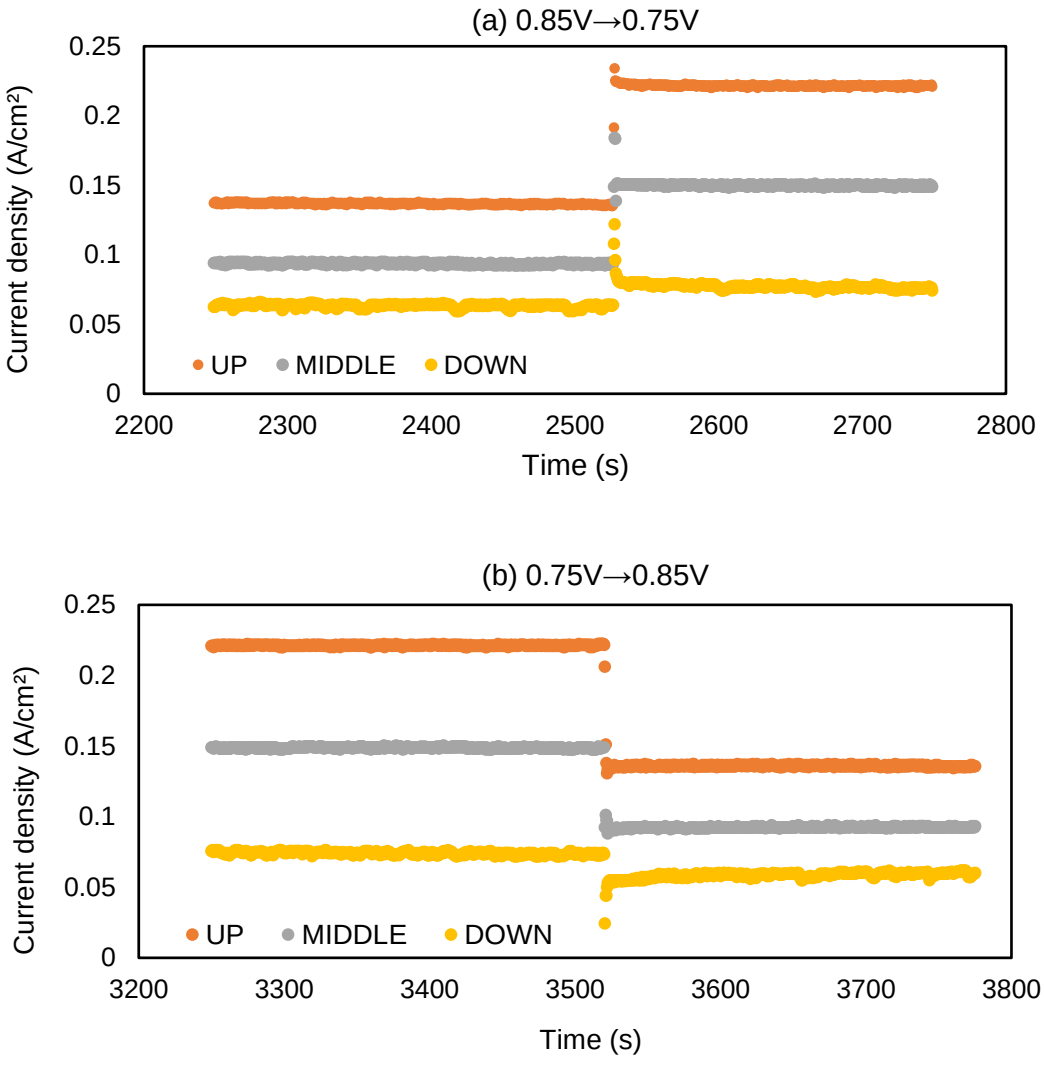

Fig. 2. Current transient along the anode flow channels with the stepwise voltage changes (a) from 0.85 V to 0.75 V and (b) from 0.75 V to 0.85 V at 650°C. (H_2: 17 cm^3min^{-1}, N_2: 7 cm^3min^{-1} (at 25°C, 1 atm)) and air (air: 100 cm^3min^{-1} (at 25°C, 1 atm)).
Both the voltage drop (Fig. 2(a)) and the voltage rise (Fig. 2(b)) give current spikes in each part along the anode flow channels, reproducing and verifying the FEM modeling.

https://doi.org/10.5281/zenodo.4556918

Acknowledgments

This work was supported by the New Energy and Industrial Technology Development Organization.

References

[1] Ö. Aydın and H. Nakajima, J. Electrochem. Soc., 165, F365 (2018).
[2] Ö. Aydın, T. Ochiai, H. Nakajima, T. Kitahara, K. Ito, Y. Ogura, and J. Shimano, Int. J. Hydrogen Energy, 43, 17420 (2018).
[3] Ö. Aydın, H. Nakajima, and T. Kitahara, J. Power Sources, 293, 1053 (2015).
[4] H. Nakajima, T. Kitahara, and E. Tsuda, ECS Trans., 78(1), 2109 (2017).
[5] R. Torii, Y. Tachikawa, K. Sasaki, and K. Ito, J. Power Sources, 325, 229 (2016)
[6] A. J. Bard, L. Faulkner, Electrochemical Methods, 2nd ed., John Wiley & Sons (2008).

Keywords: EFCF2020, SOx
Session A15: Cell, stack & system modelling and optimization

https://doi.org/10.5281/zenodo.4556918

A1601

Results of 5 kW SOFC CHP system development in the SOFC5-60 project

Martin Hauth (1), Christopher Sallai (1), Stephan Weißensteiner (1), Stephan Pickelberger (1), Peter Thonhofer (2), Ingwald Obernberger (2), Claudia Benesch (2), Christian Heschl (3), Roman Stelzer(3), Dominik Heitzinger (4), Stefan Megel (5), Stefan Rothe (5), Jens Schnetter (5), Mihails Kusnezoff (5), Andreas Mai (6), Moritz Becker (7), Stefan Stauch (7)

(1) AVL List GmbH
Hans-List-Platz 1, AT-8020 Graz/Austria

Contact authors: www.EFCF.com/ContactRequest
(2) BIOS BIOENERGIESYSTEME GmbH
Hedwig-Katschinka-Straße 4, AT-8020 Graz/Austria
(3) Forschung Burgenland GmbH
Steinamangerstraße 21, AT-7423 Pinkafeld/Austria
(4) High Tech Coatings GmbH – a Miba Group company
Dr.-Mitterbauer-Str. 3, A-4655 Vorchdorf/Austria
(5) Fraunhofer IKTS
Winterbergstraße 28, 01277 Dresden/Germany
(6) HEXIS AG
Zum Park 5, CH-8404 Winterthur/Switzerland
(7) AVL Schrick GmbH
Dreherstraße 3-5, 42899 Remscheid/Germany

Abstract

Continuous improvement of AVL's natural gas operated SOFC CHP platform towards residential and small industrial applications led to first operational tests of a completely new hardware generation, targeting 5 kW_{EL}, 55 % AC net electrical efficiency and 5000 h of operation. Within the scope of the publicly funded project "SOFC5-60" (FFG: 864851 / PtJ: 03ET6120A), conducted in cooperation with Fraunhofer IKTS, High Tech Coatings, BIOS Bioenergiesysteme GmbH, Viessmann, AVL Schrick and Forschung Burgenland from 2017 to 2021, the aim is to fully integrate and operate the system in an office building for the provision of electricity and hot water. Further target applications are hotels and apartment buildings. Therefore, electricity and heat demand profiles of such applications were analyzed to identify the optimal building sizes for a 5 kW system as well as the requirements for the operating procedure. AVLs existing system architecture based on hot anode gas recirculation, steam reforming and a modular interface between the gas processing unit and the stack module has been expanded with functionalities like a heat recovery for hot water production, an exhaust gas condensate recovery unit, and power electronics for grid feed-in. Besides that, an optimized integration of the BoP components such as the hot anode gas recirculation blower, development of periphery components for stand-alone applications, activities towards design to manufacture as well as load following operation capabilities and long term operational durability are in the center of development activities. This work gives an insight into the development achievements that are the next step towards industrialized SOFC CHP systems as well as operational data for full- and part load operating points, as well as transient- and load following operation.

https://doi.org/10.5281/zenodo.4556937

Introduction

The SOFC5-60 project aims towards the development of a 5 kW_{el} SOFC CHP (Solid Oxide Fuel Cell Combined Heat and Power) system for residential and non-residential applications such as hotels, small industries and multi-family homes (see Figure 1). The project is funded in Germany (Projekträger Jülich, PNr.: 03ET6120A) and Austria (FFG, PNr.: 864851) and consists of following consortium; AVL List, BIOS Bioenergiesysteme, MIBA HTC, Forschung Burgenland (Austrian partners), Viessmann/Hexis, Fraunhofer IKTS and AVL Schrick (German partners). The project lasts from 04/2017 to 03/2021. The product targets at an electrical efficiency of 60 %. Furthermore, the heat recovery development aims at an overall plant efficiency of 95% (related to the NCV of natural gas input into the SOFC) by using the recovered heat from the exhaust gas of the SOFC for domestic hot water supply of the customers (e.g. apartment buildings, hotels). Within the SOFC5-60 project an electrical efficiency of 55 % is targeted since not all components can be customized as required to meet the product requirements (e.g.: power electronics). However, the resulting system design will be the basis for an industrialization.

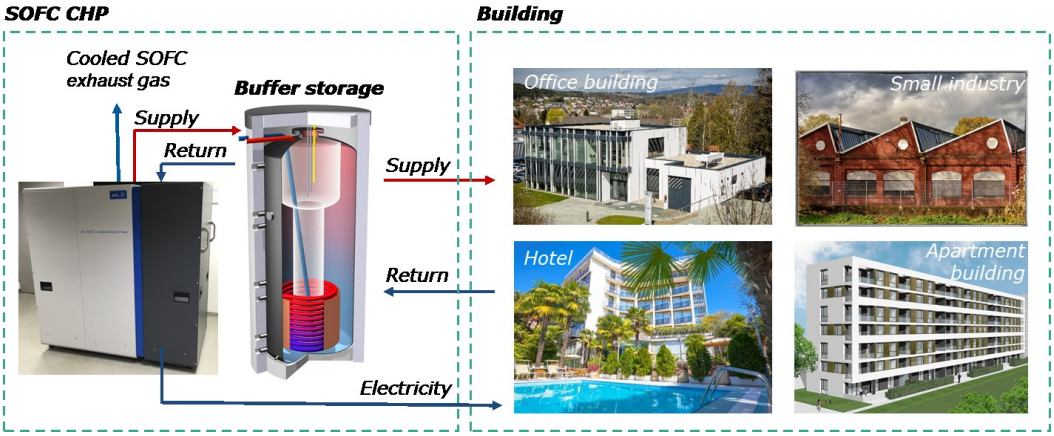

Figure 1: Target applications of SOFC CHP system

Further targets of the SOFC5-60 project and the related product can be seen in Table 1. The system operates on natural gas or bio methane and was designed with respect to low system CAPEX (Capital Expenditure <2000 EUR/kW_{el} based on high volumes), high lifetimes (80.000 h) and a wide power modulation range including load following capability to achieve a high number of full load hours over the year (>6000 h). The results of a previous functional demonstration platform formed the basis for further fundamental development and customization addressing the final power range and product requirements.

https://doi.org/10.5281/zenodo.4556937

Table 1: System targets

QUANTITATIVE TARGETS AND RESULTS		TARGETS Product	TARGETS SOFC5-60
Rated electrical power (BoL, AC, net)	[kW]	5	5
Electrical efficiency (BoL, AC, net, LHV)	[%]	60	55
Total efficiency (LHV)	[%]	95 [1)]	90 [1)]
Stack module lifetime	[h]	80,000	30,000 [2)]
System lifetime	[y]	20	5 [3)]
Demonstrated system lifetime	[h]	20,000	5,000
Power modulation	[%]	<50 %, t.b.d.	<50 %
CAPEX @ 1000 units/year	[EUR/kW]	<2000	prognosis
Emission limit (CO/NOx/SOx)	[mg/kWh]	50/30/5	50/30/5
Noise emission (sound power level)	[dB(A)]	50	to be investigated

[1)] Based on 35 °C exhaust gas temperature
[2)] Will be extrapolated from 5000 h test
[3)] Lifetime of BoP components will be extrapolated from durability testing

Eventually, the system will be integrated in an office building at Forschung Burgenland and thus validated under real life environment conditions to achieve a field-test-ready system at the end of the project for a subsequently planned field test programme.

1. Scientific Approach

First, building load profiles were analysed in order to determine the appropriate target for power output (5 $kW_{AC,net}$) and system efficiency (55/90 %). Based on the system requirements and the CFY stack technology of IKTS a new SOFC system architecture in terms of the flow sheet design and the packaging was developed by AVL. The main features are (i) the integration of a customized stack module for the desired power output, (ii) an off-the shelf power electronics for DC/DC and DC/AC conversion, (iii) the mechanical and thermal integration of an improved hot anode gas blower for anode gas recirculation, (iv) the integration of highly efficient heat recovery unit for hot water production, (v) an exhaust gas blower for underpressure operation, (vi) a desulfurization unit for natural gas and (vii) a condensate cleaning unit for condensing water recycle. The main focus of the development is on the one hand the optimization of the electrical efficiency as well as the definition of manufacturing and certification requirements for the product development stage. Furthermore, a detailed lifetime analysis has been carried out in order to size the stack module in terms of the number of stacks to meet 30,000 h of stack lifetime. Eventually, the control system including control and operating procedures for a fully automated operation are developed by AVL.

2. Simulations, Experiments and Design

Building load profiles (Forschung Burgenland)
Load profile analysis is a decisive procedure for designing CHP-systems. Particularly the time-resolved electrical and thermal energy demand information are mandatory for determining the required range of capacity and heat to power ratio. The computation of representative load profiles for multifamily houses based on standardized consumptions or limited datasets can lead to a peak overestimation and statistically irrelevant outcomes. Stochastic models, which considers the occupancy pattern, different technical appliances,

seasonal effects, household categories etc., can overcome these drawbacks and can provide beneficial information about the energy demand on a sub-hourly time scale. Hence, for the requirement definitions of the SOFC-system individualized, stochastic load profiles were generated with the simulation tool synPRO ([1], [2]). The investigations were carried out for different residential buildings (2 single-family houses, 22 multi-family houses and 12 semi-detached houses) and year of construction (between 2002 and 2017).

The waste heat utilization for domestic hot water (DHW) production facilitate an efficient year-round operation and the exploitation of the high exhaust temperature level of the SOFC-system. Therefore, the DHW application is the most promising integration scenario for residential buildings. For such application the ideal heat to power ratio can be identified based on the analysis of the generated electrical and DHW load profiles. In order to get a more efficient CHP system solution, normally a buffer tank will be used to avoid peak loads and to decouple the electrical and hot water demand. For this reason the heat to power ratio distribution were computed based on daily-averaged values. The left diagram in Figure 2 represents a typical frequency distribution of the required heat to power ratios for one year. Accordingly, it can be expected that the most frequently heat to power ratio is near 0.6, which fit well the addressed product and project targets (cf. Table 1).

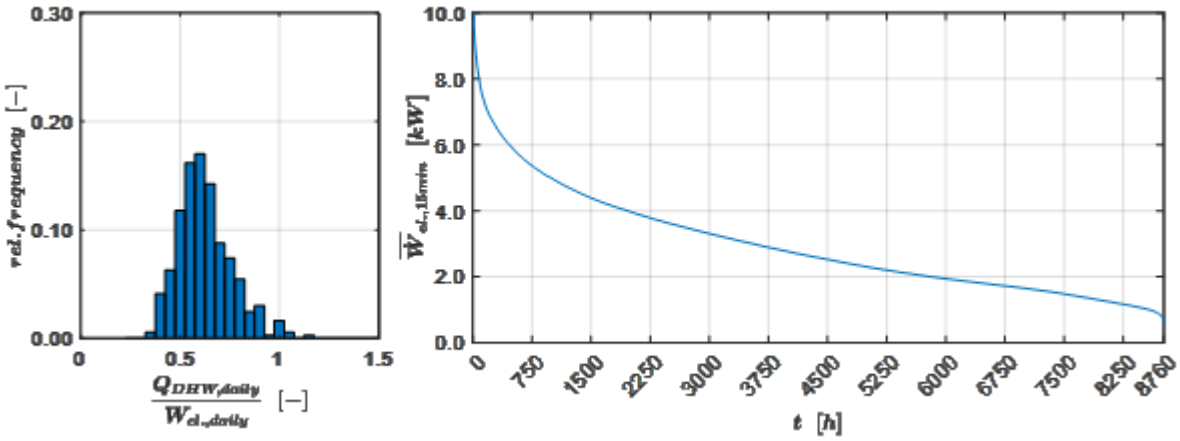

Figure 2: Left: Frequency distribution of the required heat to power ratio for CHP-system Right: Electrical load duration curve for one of the investigated residential building

In addition to the required heat to power ratios the load duration curves for the residential buildings were analyzed based on a time interval of 15 min. The right line plot in Figure 2 represents a typical load duration curve for a multi-family house with 9 apartments. The curve illustrates the required electrical capacity range of the SOFC-system. If a non-feed-in operation is aspired and the modulation range capture 2.5 to 5.0 kW_{el} the SOFC-system can cover 40% of the annual electrical energy demand. If the modulation range will be increased from 1.0 to 5.0 kW_{el} the cover ratio grows up to about 86%.

Process simulation of the SOFC CHP system (AVL)

A detailed 0/1D process simulation in matlab/Simulink was carried out to define the process conditions and component requirements. Different system architectures considering two different recirculation concepts (blower vs. ejector based), stack module size, component efficiencies and achievable lifetimes were investigated. Furthermore, full load, part load, beginning and end of life operating points were considered. The end of life criteria was defined to be 4 $kW_{AC,net}$ at constant current operation. The process is based on natural gas steam reforming. Figure 3 shows the Sankey diagram of the efficiency and power flow for the 100 % beginning of life (BoL) operating point. A DC gross efficiency of

63 % at 310 mA/cm^2 and 830 °C based on a global stack module ASR of 0.493 Ohm*cm^2 is achieved. Considering the power consumption of the blowers and other periphery components as well as the power conversion a AC net efficiency of 55 % is calculated. The heat in the exhaust gas is recovered down to 30.3 °C to make use of the condensing heat and thus achieve an overall efficiency of 90 %.

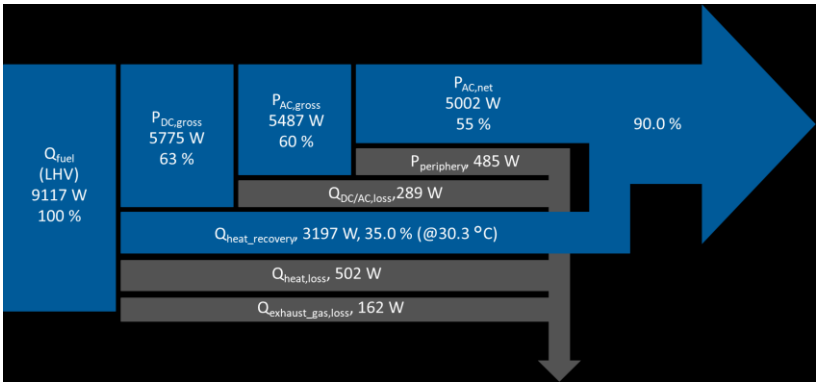

Figure 3: Sankey diagram of the efficiency and power flow

Further operating points at part load, heat-up and end of life were simulated as required for the following component developments.

Ejector development (AVL)

As an alternative to the hot anode gas recirculation blower an ejector based recirculation was considered in the beginning of the project. The ejector would be operated by an increased primary natural gas inlet pressure of >2 barg in order to achieve an anode gas recirculation ratio of 70 %. The ejector must overcome the pressure drop between the outlet and the secondary inlet. This pressure drop is mainly created by the reformer, the anode gas heat exchanger and the anode side of the stack module and amounts to 20 – 30 mbar. The relatively high pressure drop requires a well designed ejector geometry in order to reduce pressure losses between the primary inlet and the diffusor to a minimum. Only then a high efficiency of the ejector can be achieved. The ejector was simulated in AVL FIRE (CFD software tool) at various operating conditions in terms of primary pressure, temperature at primary and secondary inlet and gas compositions.

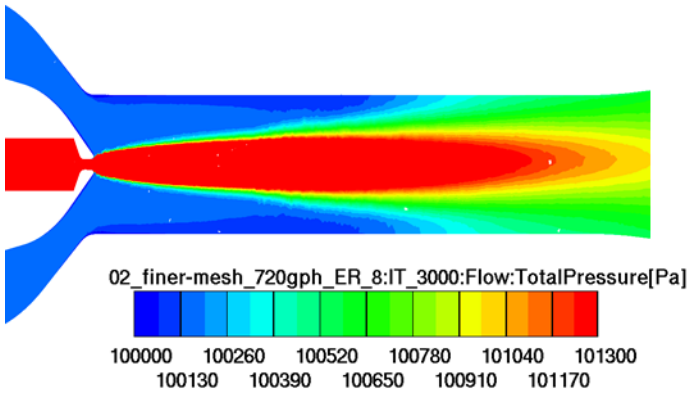

Figure 4: CFD simulation of ejector for anode gas recirculation

Figure 5 shows the comparison of the electric blower power needed for 70 % recirculation ratio at a pressure drop of 15 mbar between ejector outlet and ejector secondary inlet. The aim was to investigate which of the options leads to a lower electrical power consumption. Assuming a blower efficiency of 10 % for the hot anode gas recirculation blower (t_{in}=648 °C, m=1.119 g/s) and 20 – 30 % for a natural gas blower (t_{in}=20 °C, m=0.172 g/s) the

ejector would require a primary inlet pressures below 1.6 – 1.9 barg in order to be more efficient. Since CFD simulation has shown that a significantly higher pressure would be needed at the ejector inlet to reach the same recirculation ratio it was decided that the anode gas recirculation blower solution will be more efficient.

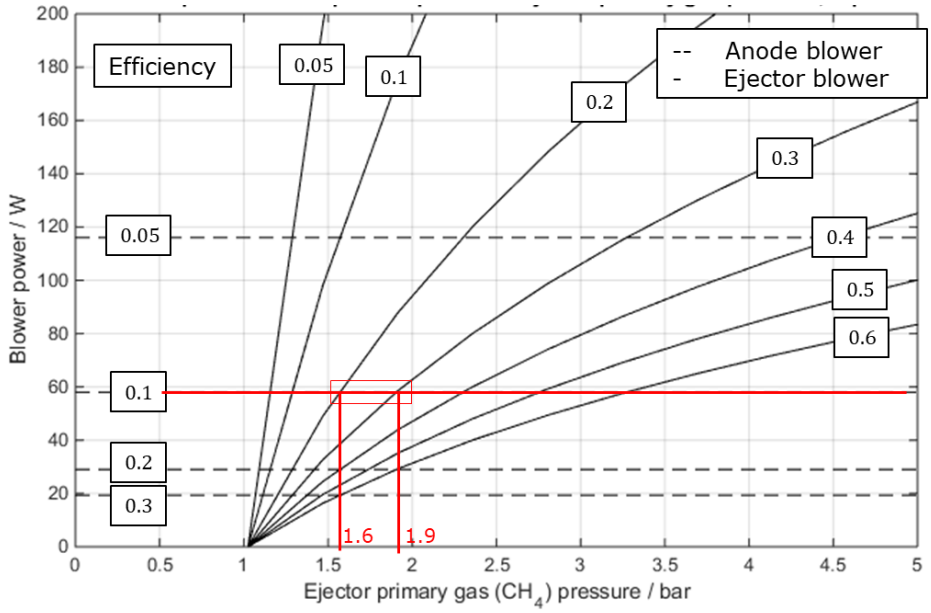

Figure 5: Comparison of blower power for ejector and hot anode gas recirculation blower

Hot anode gas recirculation blower development (AVL Schrick)

The development targets for the blower were and requirements of the SOFC5-60 blower have been:

- Recirculate temperatures up to 600°C
- >10% efficiency (electric-to-flow dynamic)
- Pressure ratio of 1,04 @ a recirculation mass flow of 2,1 g/s
- Liquid-cooling of e-motor stator
- Main accessibility from back-side due to installation requirements into the SOFC-system

While Figure 6 (left) shows the Mk1-design in a cross-section the prototype is displayed in Figure 6 (right).

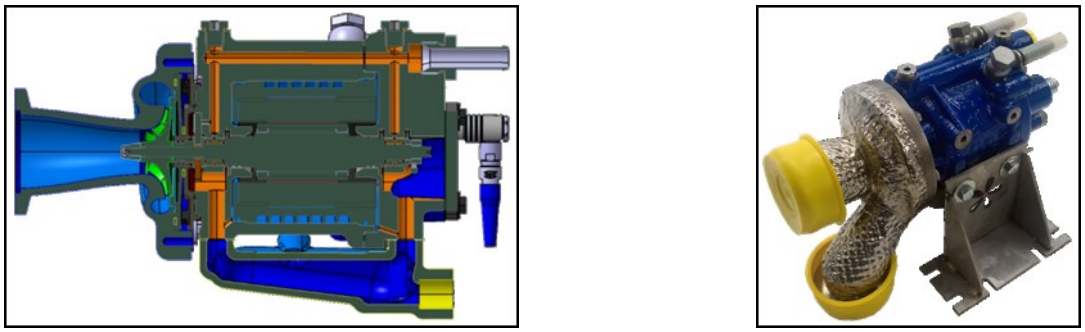

Figure 6: Blower Design Mk1 (left) and prototype (right)

As it can been seen in the cross-section the blower design utilizes an oil-based full-floating bearing concept. Main driver for choice of this bearing concept is the thermal management of the blower system as the maximum capable temperature of the e-motors permanent-magnets is far below the 600°C of the anode gas which is surrounding the compressor

wheel in a one-shaft design directly connected – and therefore conducting – to the rotor magnets. So, the lubrication mass flow of the compressor-side bearing sleeve is significantly contributing to shaft-cooling and therefore thermal protection of rotor magnets. Cooling of the e-motor stator – which is capable for maximum 120°C – is realized with an active coolant circuit which is integrated into the thermal circuit of the overall SOFC-system and therefore contributes to the hot water provision of the entire system.

Within initial testing of Mk. 1 of hot anode recirculation blower general functionality could be proven but it has been figured out that efficiency targets could not be reached. To improve the situation different optimization measures have been investigated and finally converted to a Mk. 2 design.
In Figure 7 a comparison of Mk. 1 and Mk. 2 design is shown.

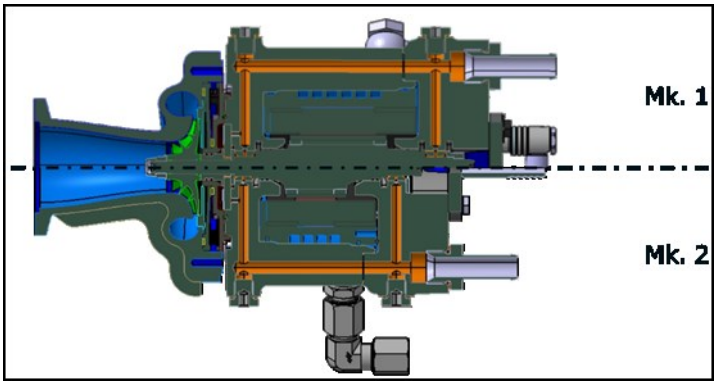

Figure 7: Comparison Mk1 and Mk2

The upgrades contain the following single measures:

- Reduction of active length of electric motor → load-point shift towards lower power consumption
- Re-work of bearing gap layout → feasible due to shortened rotor and therefore more robust rotordynamic behaviour
- Reduction of bearing diameters from 7mm to 6mm → reduction of frictional losses

Prototypes of Mk. 2 design are currently within assembly process and will afterwards prove the effectiveness of the taken measures to improve the efficiency of the hot anode recirculation blower.

Heat recovery development (BIOS)
In order to identify the suitable size of the heat consumers, typical electricity and heat demand profiles of residential buildings with 9 to 40 dwellings and 20 to 80 inhabitants have been selected for TRNSYS simulations. To reach highest annual full load operation hours and highest electricity generation, the simulations revealed, that the control strategy needs to be adapted to the consumer structure and that a heat controlled instead of an electricity controlled operation is more meaningful for residential clients. A 5 kW_{el} SOFC system is suitable for an apartment building with about 25-30 inhabitants. By the provision of domestic hot water, a heat controlled operation at high load during the whole year can be achieved. In addition, the option of domestic hot water production bears the advantage that the heat exchanger can operate in condensing mode because the return water temperature from the buffer storage tank typically amounts to only 20-25 °C and thus a high heat recovery potential of sensible and latent heat is given.
For the screening of suitable condensing heat exchangers (HX) 10 manufacturers of various HX types were asked whether their product portfolio contains heat exchangers

suitable for the given boundary conditions and the requested requirements such as reasonable pressure drop, low temperature difference and acceptable size.

At the end of the screening process two types, a plate HX and a radial HX remained and were further evaluated by means of CFD simulations. As one result of this work, the temperature distributions for the radial and the plate HX are shown in Figure 8.

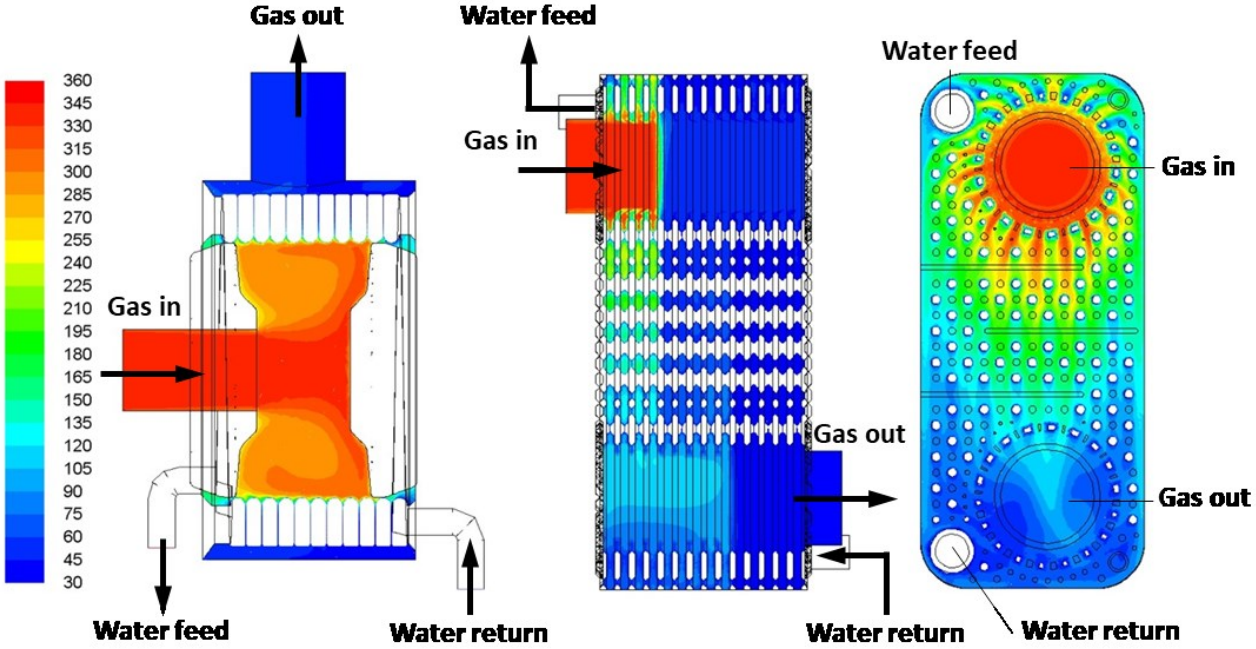

Figure 8: Iso surfaces of the exhaust gas temperature [°C] in a vertical axis cut through the radial HX (left) and a vertical axis cut and a first pass gas section cut through the plate HX (centre and right)

The temperature difference between exhaust gas outlet and water return is much smaller for the plate HX (<5°C) than for the radial HX (17°C), which leads to a considerably higher efficiency of the plate HX. In combination with the other advantages (more compact design, flexibility, price) this type of heat exchanger has been selected and subsequently has been further optimised by CFD simulations for the specific application in the SOFC system.
Subsequently the condensing HX has been built and tested. The performance evaluation was done at a specially designed heat exchanger test rig under representative operation conditions. The results show that the expected target design values regarding temperature difference between gas outlet and water return (4°C) and HX efficiency (79%; = thermal output/thermal input x 100) at a water return temperature of 30°C could be kept. According to TRNSYS simulations over a whole year, the HX efficiency will increase to 85%, considering a typical average domestic water return temperature of 24°C. This high efficiency of the HX results in an overall annual utilisation rate of the SOFC system of close to 95% (meeting the target design value).
The condenser has now been implemented in the overall SOFC testing unit and will be evaluated regarding its performance under real system conditions in steady state as well as in transient operation as a next step.

Stack module development (IKTS)
The development includes efforts on interconnect, cell and stack level to decrease degradation and increase power density of the stacks as well as on process design,

mechanical and electrical balance of plant component development and system packaging. The main interest of the IKTS MK35x stack development is reducing costs by new method of interconnect manufacturing and improving long term stability by new protection layer. A more stable electrode with less reforming capability will be developed and validated. For validation of components for stacks a standard procedure were specified based on performance map, 3000 h long term operation and start stop cycling tests. The quality of measurements were improved and tests were focused on the uncertainty of measurement to separate measurement or infrastructure errors from real degradation [3]. Under consideration of these impacts it is possible to use acceleration parameters for tests to shorten the validation period and estimate durability for 30,000 h or more.
Stacks will be combined to a stack module to reach the estimated power output based on existing know how with the focus on a design which is easy to scale up.

Experiments with new stack components for MK35x and reference tests for durability were conducted on the actual MK352 design, the new design Mk353 and were flanked with sample tests. Based on the performance map of a 10 cell MK352 stack with defined gases from simulation, 200 layers were an optimal size for the stack module of the system to get an power output of 5.7 kW_{el} at 100 % BoL. Furthermore, the number of cells were chosen with respect to the lifetime target.
For reasons of mechanical compression, easier assembly and tightness a “one tower assembly” were chosen. CFD-simulation have shown that an external gas manifold parallel to the internal stack manifold is necessary to reach an adequate uniformity. With the separate manifolding of two packages of 100 cells (see Figure 9) the maximum fuel utilization of the 200 cell configuration is only 2 % higher than the average.

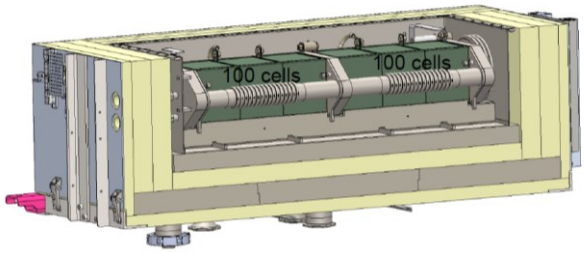

Figure 9: Sliced CAD model of the stack module showing each 100 cell towers

Two separate stack modules were successfully assembled and tested with power output BoL 100 %, 5.74 kWel and BoL 50 % 2.7 kWel at IKTS. Both modules have comparable quality of power output with a difference of only 51 W (1 %) contributed to an optimized thermal insulation of one of the two stack modules. The variation of fuel utilization η_{FU}= 60-85% at the 100% operation point (BoL) with 39.4 A shows a minor dependency on the electrical power output from 5.9 to 5.6 kW_{el}.
The median ASR of the stacks were calculated with 0.50-0.58 Ohm*cm^2 and therefore is a little bit higher than estimated at the simulation.

https://doi.org/10.5281/zenodo.4556937

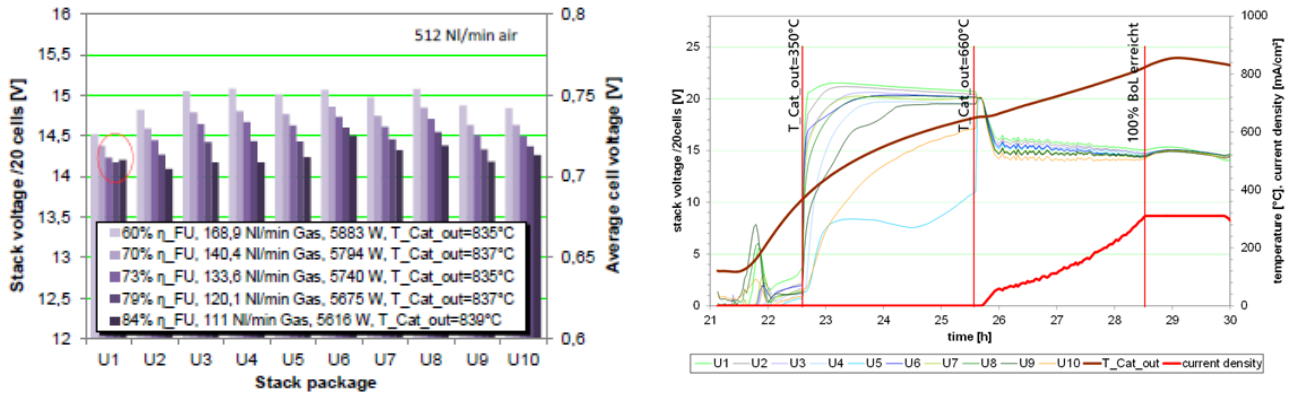

Figure 10: Left: Power output of stack module @100% BoL, 39.4 A, reformat gas and different η_{FU}, Right: Heat-up of stack module from room temperature to 100 % BoL

The startup procedure (see Figure 10 right) was adjusted to proceed as fast as possible from room temperature into operation based on system conditions. After 7,5 hours a stable operation point at 100% BoL was reached. The operating strategy was developed with regard to system operation focusing on the minimum stack temperature at which current drawing can be started. The transition from a heat-up through heated cathode gas to a thermally self-sustaining power generation and thus stack internal heat production was optimized in order to accelerate the heat-up time until full load. The performance characteristics of the stack at lower temperatures also define the dynamics of the system operation in low part load as well as for a re-start from hot stand-by conditions.

System design (AVL)

Based on the results of the process simulation and the individual component developments a completely new design for the 5 kW SOFC system was developed (see Figure 11). The design aims at a highly integrated packaging with at the same time good accessibility for service and maintenance.

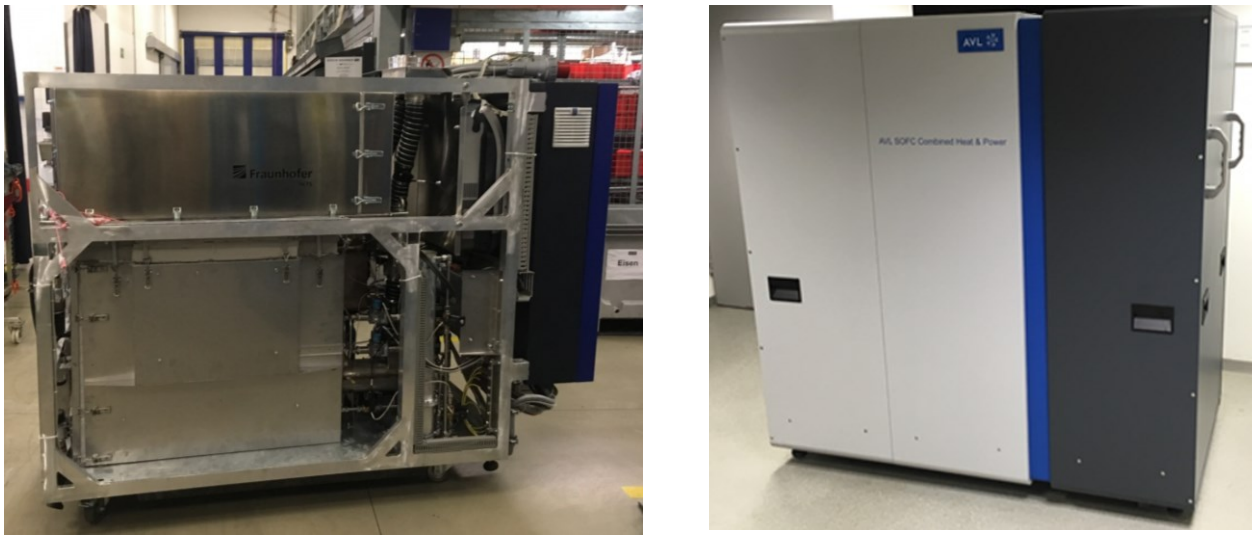

Figure 11: 5 kW SOFC CHP system

https://doi.org/10.5281/zenodo.4556937

System commissioning (AVL)
The Gen.1 system including all new features focusing on the stack module, hot anode gas recirculation blower, heat recovery and the power conversion was commissioned. Various operating functions such as the heat-up, the anode gas blower operation in underpressure conditions, the reforming, the condensate removal and recycle path from the heat recovery, the power conversion path from stack module DC output to grid AC input as well as different operating points up to 50 % part load were tested. The results are the basis for the design of the planned Gen.2 within the project.

4. Conclusion and Outlook

The electricity and heat demand profile of building consumers were investigated in detail in order to define the system requirements in terms of power output, power modulation and the optimal split between electricity and heat production. Further, product and system requirements were defined as basis for the system development. A new process design, component development as well as the system design and build-up for the Gen.1 5 kW SOFC CHP system was completed and commissioned. An anode gas blower based recirculation concept was chosen over an ejector based solution due to the higher efficiency potential based on the specific boundary conditions for the application. A highly efficient heat recovery was successfully simulated and tested. An off-the shelf power conversion system was integrated and operated in grid feed-in operation mode. The MK35x stacks and the assembled stack modules are a robust component for the CHP system and fulfil the requirements of operation from Gen.1. The target power output of the stack module of 5740 W_{el} at the conditions for the 100 % BoL was successfully reached. Optimization of air supply and isolation will lead to homogeneous temperature distribution inside the stack module and an increased operation window. Improved stack components with lower ASR and degradation rates as well as better connection between the stacks by an optimized electric- and gas interface will be the focus of Gen.2. The one tower stack module design opens an easy adaption of power output by variation of cells in one tower and in mirroring to two or four tower configuration. The findings are currently implemented in the design of the Gen.2. build-up and full validation is planned to be started later this year.

References

[1] David Firscher, Andreas Härtl, Bernhard Wille-Haussmann, Model for electric load profiles with high time resolution for German households, Energy and Buildings 92, 2015
[2] David Firscher, Tobias Wolf, Johannes Scherer, Bernhard Wille-Haussmann, A stochastic bottom-up model for space heating and domestic hotwater load profiles for German household. Energy and Buildings 124, 2016
[3] S. Megel S. Rothe, V. Sauchuk, N Trofimenko, J. Schilm, M. Kusnezoff, M. Hauth, C. Sallai, Degradation analysis of CFY-stacks MK35x and Illusiveness of accuracy – a guide for exact measurement, 14th European Fuel Cell Forum, Lucerne, CH (B0906), 2020

Keywords: EFCF2020, SOx
Session A16: System design & performance & BoP

A1603

Results from the operation of the first industrial size biogas-fed SOFC plant in Europe

M. Acri (1), M. Gandiglio (2), T. Hakala (3), A. Hawkes (4), M. Rautanen (5), M. Santarelli (2)
(1) SMAT – Società Metropolitana Acque Torino S.p.A.
Corso XI Febbraio, 14 - 10152 Torino (IT)
(2) Department of Energy, Politecnico di Torino
Corso Duca degli Abruzzi, 24 - 10129 Torino (IT)
(3) Convion Oy
Tekniikantie 12, 02150 Espoo (FI)
(4) Imperial College of London
South Kensington Campus, London SW7 2AZ (UK)
(5) VTT Technical Research Centre of Finland Ltd
P.O. Box 1000, FI-02044 VTT (FI)

Contact authors: www.EFCF.com/ContactRequest

Abstract

The EU-funded DEMOSOFC project (www.demosofc.eu), currently running, has spent the last 4 years in demonstrating the technical and economic feasibility of operating an industrial-size SOFC system (100 kW_e, 2x50 kW_e modules) in a wastewater treatment plant (WWTP). The fuel for the SOFC modules is biogas, which is available on-site from the anaerobic digestion of sludge collected from the treated wastewater. A heat-recovery loop allows to recover useful thermal energy from the hot SOFC exhaust gases (90 kW_{th}), transferred through a water loop to the sludge.
The plant includes 2 SOFC modules started respectively in October 2017 and October 2018. The first SOFC module has reached more than 5500 hours of operation on site (+1000 at Convion facilities) and the second SOFC module more than 9800 hours. Results from the operation of these modules confirmed the expected high-level performance of the fuel cell system: average measured SOFC efficiency from compressed biogas to AC power is 49-50%, with peaks at 56% at partial power (40 kW_e).
A dedicated emissions measurements campaign has been performed in December 2017. Results show no NO_x (detection limit of the method 20 mg/m^3) or SO_2 (d.l. 8 mg/m^3) and particulate lower than ambient air values (< 0.01 mg/m^3).
A deep economic analysis has been also performed, together with the plant owner SMAT s.p.a., to understand the current site preparation and the potential reduction of a second replication, thanks to the lesson-learned from the demonstration site. A total potential reduction of costs of 56% could be achieved according to the analysis performed.

https://doi.org/10.5281/zenodo.4556955

Introduction

The DEMOSOFC plant [1] is the first industrial-size Solid Oxide Fuel Cell (SOFC) system installed in a real site in Europe, and fed by biogas from waste water treatment. Industrial-size fuel cell systems, usually Molten Carbonate Fuel Cells (MCFCs) are already available outside Europe, especially in USA [2], Japan and South Korea [3], but not yet in EU. Key advantages of fuel cell based industrial systems in biogas plants have been deeply demonstrated in the authors' previous works [4]–[8] and include:

- High efficiency increase with respect to traditional biogas-fed Internal Combustion Engines (ICEs), especially for low-medium size systems. ICEs usually show electrical efficiency ranging from 35-38% to 43% [9], when the plant size increases from tens of kW to MW size. SOFC systems can indeed provide values higher than 55% from few kW to MW size.
- Zero emissions to atmosphere in terms of NO_x, SO_x, VOC and PM, which are traditionally a criticality in standard combustion engine (many ICEs need the installation of post-combustors to comply with local strict rules on emissions).

The scientific and research activity of the DEMOSOFC project focused on the analysis of the performance and management of the entire demo, including the biogas purification system (specifically designed for FC applications in the framework of the project), on the economics of the plant and on the replication potential in the EU area.

1. The DEMOSOFC plant layout

The DEMOSOFC site WWTP is located in Collegno, in the Torino premises (IT). The Collegno plant has a nominal capacity of 250'000 Person Equivalent (P.E.) and it is currently serving around 180'000 P.E., both residential and industrial.

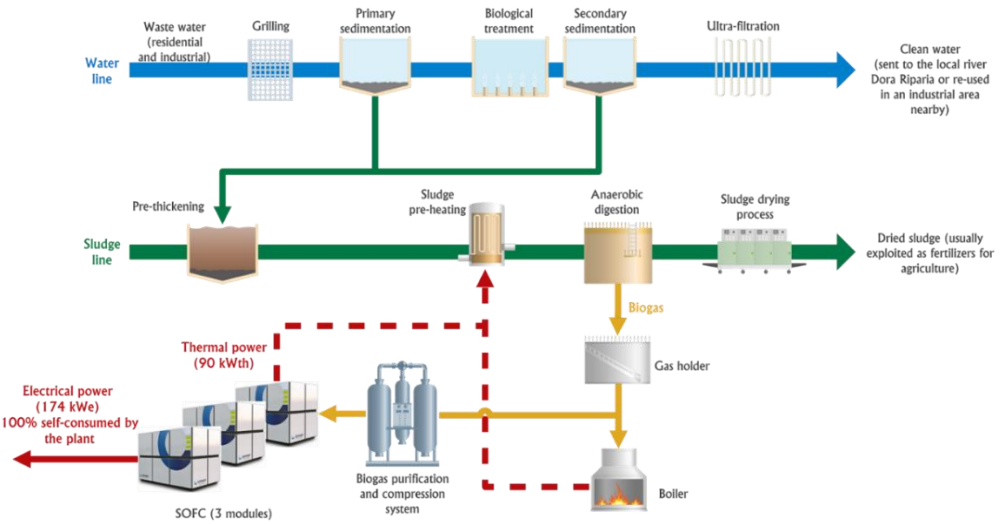

Figure 1. DEMOSOFC plant layout.

The plant is using the as-produced biogas for electrical and thermal energy production in a SOFC-based cogeneration system. The DEMOSOFC plant comprises of three main sections: 1) the biogas clean-up and compression section, 2) the SOFC power modules, and 3) the heat recovery loop. Figure 1 shows a schematic layout of the WWTP process and its integration with the DEMOSOFC plant.

Biogas clean-up and compression section

The biogas clean-up system aims at removing trace compounds (mainly sulphur and silicon based) from the raw biogas, since they could be detrimental for the SOFC module (both for the reformer catalyst and the FC anode). Required purification level, given by the

SOFC producer and used to design the cleaning unit, were max. 30 ppb of total Sulphur (including H_2S) and 10 ppb if siloxanes.
The system includes also other components like blowers and chillers to flow the gas until the DEMOSOFC area and remove condensing water; furthermore, a compressor is installed to provide inlet biogas to the SOFC at 4 bar(g), as requested by the SOFC manufacturer (Figure 2). A more detailed description of the cleaning section is available in [10]. The biogas cleaning and compression section (Biokomp, [11]) has been designed after a one-year monitoring of biogas composition in Collegno, where H_2S (average 20 ppm) and siloxanes (average 1 ppm) have been detected as the most harmful components to be removed. An in-line and real-time gas analysis (supplied by Qualvista LTD [12]) is installed to monitor the removal efficiency of the biogas clean-up unit. The online gas sensor can detect continuously both macro-composition (CH_4, CO_2, O_2) and contaminants (H_2S and total Silicon).

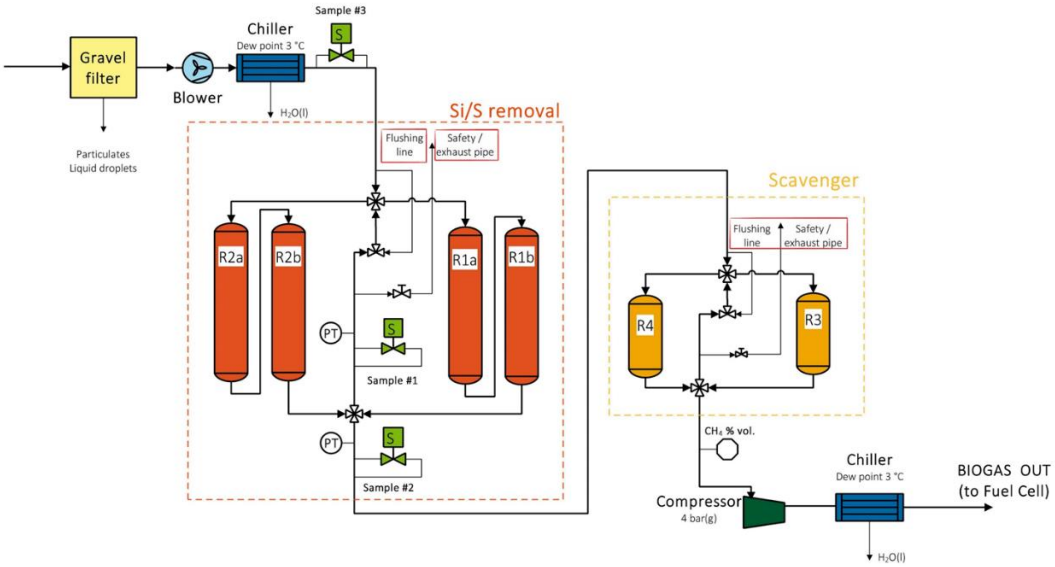

Figure 2. Biogas cleaning and compression section layout.

SOFC Modules

The core of the DEMOSOFC plant are the SOFC units supplied by Convion Oy [13], partner of the DEMOSOFC project. The modules can provide up to 55% electrical efficiency and 30% thermal efficiency.

Figure 3. SOFC modules and the DEMOSOFC site.

The two SOFC modules (Figure 3) produce around 100 kW_e, which cover around 25-30% of the WWTP electrical consumption [6]. The SOFC units are fed by biogas during nominal operation and are connected to the heat recovery system (water-glycol loop). Compressed air is required during start-up and an N-H mixture (95% N_2, 5% H_2) is available for standby

operation (maximum 24 hours maintenance on the biogas line – e.g. compressor maintenance – with the SOFC system in hot stand-by, avoiding shutdown).

Heat Recovery Section

Heat recovered from the SOFC units is completely transferred to the sludge entering the anaerobic digester through an intermediate water-glycol loop (30% glycol in water). Circulation pumps (twin pumps to avoid stops during maintenance) and three-way valves for regulation have been installed and a new sludge-water heat exchanger is supporting the existing one.

The DEMOSOFC plant has been in operation since October 2017 and the project will end in October 2020. During the 3 years of operation the DEMO site has reached in total more than 13'700 hours of operation with SOFC 1 or 2 running (1'500 hours only were performed with two modules in parallel). The following chapter aims to analyze results from the operation of the entire system, including the biogas cleaning unit and the overall DEMO site performance.

2. Results

Biogas raw composition is measured once per day by the online Qualvista analyzer (sample #3 in Figure 2). Clean biogas (both between and after the *lead-and-lag* reactors, respectively sample#1 and sample #2 in Figure 2) is indeed measured continuously for the other hours of the day. Each measurement (performed in batch mode) takes 40 minutes and N_2 is flushed after raw gas analysis. Results on the raw biogas composition (in terms of contaminants) are shown in Figure 4.

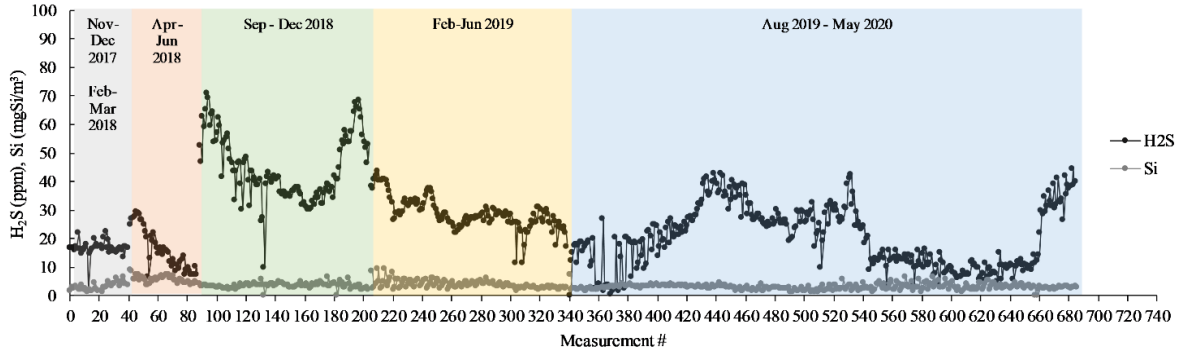

Figure 4. Raw biogas micro-composition (H_2S and total Silicon).

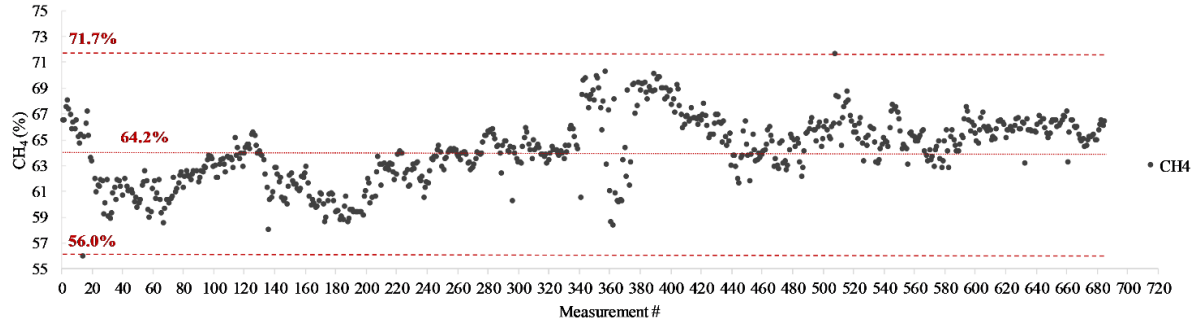

Figure 5. Methane content in raw biogas.

H_2S level has always been in line with historical trends with an average value of 26 ppm (min 0 ppm – max 71 ppm). Siloxanes are also varying in a limited rage with an average value in of 3.6 mg/m^3 (min 0 mg/m^3 – max 9.4 mg/m^3). Variation in the sulphur levels can be detected during the different operation periods: this is due to fluctuations in the iron chloride dosing in the water line (iron oxide is used to precipitate phosphorus, but it also reduces the sulfur content in the water). Siloxanes indeed shows some seasonal variations

[14]–[16]. Average methane content in the same period has been 64% (min 56% - max 72%). Methane content is stable on an hourly basis while weekly-monthly variations have been detected. Anyway, the SOFC was continuously monitoring the methane level (with a second continuous and fast-response sensor installed close to the main gas analyzer) and was able to keep the power output stable despite the fluctuations.

During the entire analyzed period, until today, no breakthrough of contaminants has been detected by the gas analyzer. The main reason for this is the under-utilization of the system compared to the design stage: the cleaning unit was designed for 3 SOFC modules running in parallel while, during the project, except for 1500 hours with 2 modules in parallel, only one module per time was in operation with a capacity factor between 40 and 60%.

A further analysis has been performed to compare the current loaded sulphur and silicon on the cleaning vessels with the maximum loading rate measured in the experimental phase during the design of the cleaning system. For what concerns H_2S, the adsorption capacity measured in the laboratory (in conditions similar to the site ones but with simulated gas) was around 84 mgS/g (expressed as mass of sulphur on mass of sorbent), while the current loaded sulphur amounts to 7.4 kg. Looking at only the first vessel in the series (Figure 2), filled with 250 kg of sorbent, only 35% of the potential loading capacity has been exploited. The same calculation can be performed with silicon (estimated adsorption capacity was 151 mgSi/g and loaded amount is 0.67 kg): in this case the exploited loading capacity amounts to only 1.8%.

Sulphur will thus probably be the first component reaching the breakthrough (as expected from the lower adsorption capacity of the sulphur-dedicated sorbents) but the system still seems far from the sorbent replacement activity.

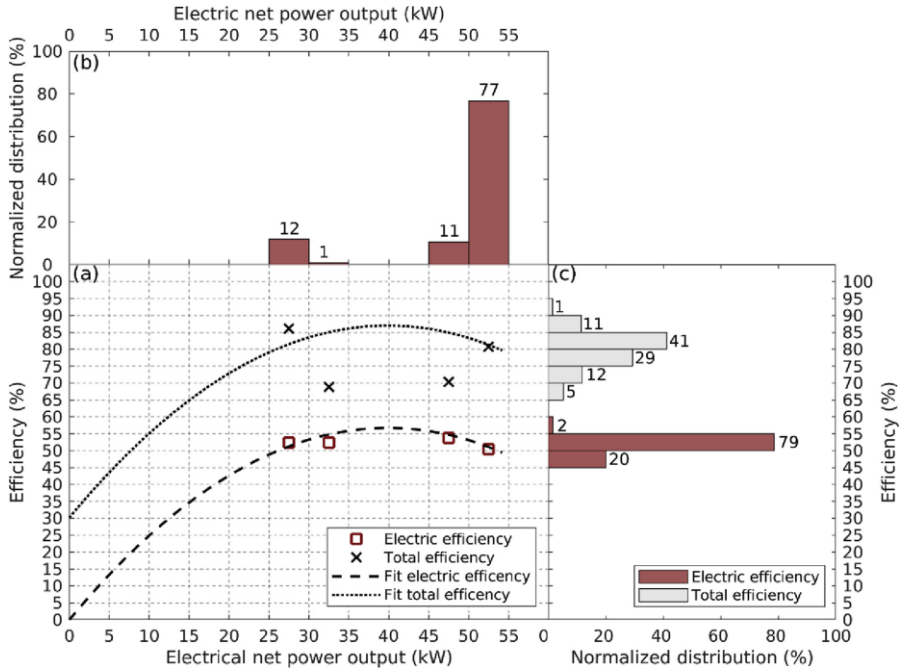

Figure 6. Electric and total efficiencies of the first Convion C50 SOFC system as function of the electrical net power output and corresponding normalized distributions. a) Electric (red squares) and total (black crosses) efficiency mean values for electrical net power output segments during stable operation. Segments are represented by the vertical dashed lines. Black dashed and dotted lines represent second order polynomial fits of the electric and total efficiencies for electric net power output values greater zero. b) Normalized distribution of the electric net power output. c) Normalized distribution of the electric and total efficiencies. Combined standard uncertainties were around 3% for the electric and around 6% for the total efficiency. [17]

For what concerns the SOFC modules, the 1st one was started in October 2017 and has now reached 5500+ hours of operation onsite (plus 1000 hours at Convion facilities during

the testing phase), while the 2nd was started in October 2018 and has reached 9800+ hours of operation onsite.

A detailed analysis of the SOFC modules operation has been performed and is available in [17]. This analysis was performed in late 2019 and was related to 9113 hours of operation, in which the modules provided electricity and heat to the plant. Results are here shown for what concerns only the 1st SOFC module (called SOFC1). Figure 6 shows the performance of the SOFC1. In Fig. 2a) the total electric efficiency and the total efficiency as a function of the electric net power output from 0 to 55 kW_e are illustrated. The SOFC system was operated stable in an electric net power output range between 25 kW_e and 55 kW_e. In this range the electric efficiency stayed stable between 50% and 55%. The black crosses show the total efficiency mean values which were between 67% and 87% during stable operation. The stable and high electric efficiencies over the operating net power output range (25–55 kW_e) illustrate an advantage of fuel cell technology in comparison to micro turbines and internal combustion engines. The results show that power modulation according to the site demand is possible while maintaining high efficiencies using SOFC systems. For most of the time (79%) the electric efficiency was between 50% and 55%. Around 2% of the time the electric efficiency was even higher with values between 55% and 60%.

Another analysis performed on the SOFC modules is the one related to the efficiency trend over time. Electrical and total efficiency for SOFC1 during year 2018 are shown in Figure 7. During the first two operating periods (from April to June and some days in August), the power output was kept stable at 53 kW_e electrical.

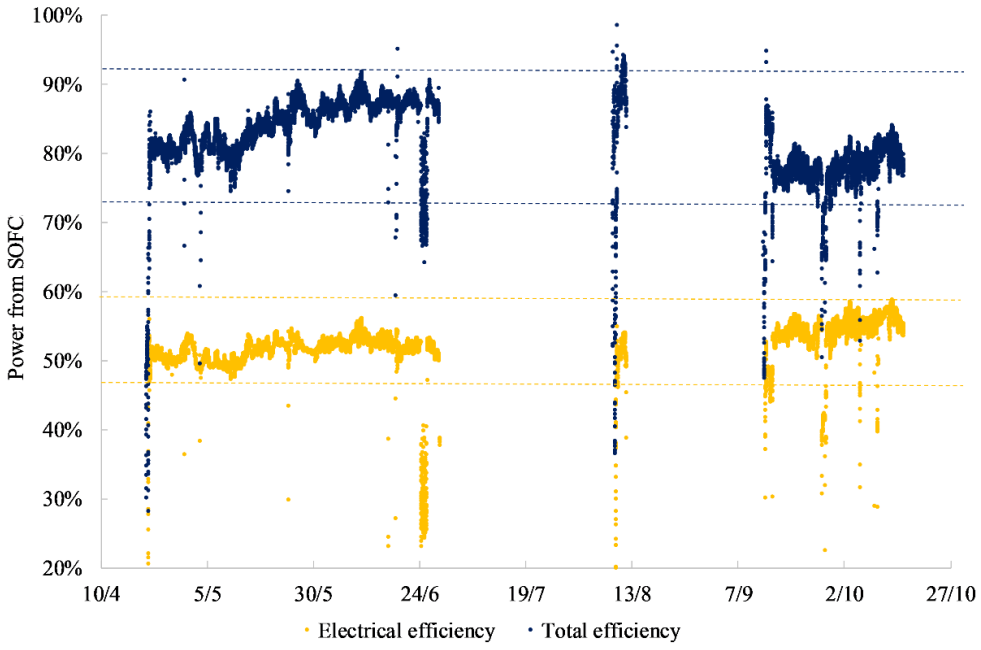

Figure 7. Efficiency of SOFC1 during 2018.

During this period, electrical efficiency was showing very good performance in the range 48 to 55%, with average values around 50-52% (electrical efficiency is here defined as net value from compressed biogas to AC power). Total efficiency shows an increase during time since the heat recovery system has been strongly optimized, comparing to the start-up phase, trying to maximize the thermal recovery; for this reason, thermal efficiency shows values up to 90% in the last part of the first operating period and in the second one. No efficiency degradation is visible from the graph shown. During the third operating period (September-October 2018) the system was operated at partial load for all the time (28 kW_e) and the efficiency shows an increase up to values close to 60%, while total

efficiency decreased a little bit due to the different thermal management within the SOFC module at partial load.
The two SOFC systems had cell stacks from two different suppliers, both representing the state of the art at the time of the design process. Cell voltage degradation, which is not reported here in quantitative terms because of confidentiality rights, is always a result of combined and cumulative effects of operational hours, operating profile and thermal cycles as well as potential influence of impurities. In steady operation, witnessed stack voltage degradation rate logged in field conditions with biogas was equal to that measured by the manufacturers in their test bench operation, indicating both design and operational success of the system and gas cleaning set-up. In post-mortem analysis of replaced stacks, anodes were found in good condition and proving that no breakthroughs of sulfur or siloxanes had taken place. Total rate of degradation including impact of thermal cycles was clearly higher than steady state degradation as operating history of stacks was particularly aggressive in the early stages of their lifetime. Towards the end of their useful lifetime, spread of voltages increased as a result of degradation and partial replacement of stacks in operation, limiting maneuverability of a system consisting of a large number of stacks exhibiting different voltage response to loading. This heterogenous condition was a reason behind downrating of power output at later stages.
Total electrical production from the DEMOSOFC plant was equal to 537 MWh, while thermal production was 356 MWh: all the energy produced was self-consumed within the plant. With the prices paid by the WWTP for electricity and heat, this is equal to a saving of more than 72'500€ for what concerning electricity and 21'900€ for what concerning saved natural gas from the grid. Average capacity factors (defined as the hours with SOFC modules on over the total project time) have been 43.5% for SOFC1 and 61% for SOFC2. Shutdown periods were due to authorization issues at the beginning (being a first-of-its-kind plant, local authority and grid operators requested more time to approve the authorization), together with instabilities in the cleaning system and heat recovery unit (solved by optimizing, during the first months, the operation and the control of these section).Later, during the stable operation, the long lead times for SOFC module maintenance were the main reasons for long shut down periods lowering the overall availability SOFC maintenance.

Section	Number of incidents
Clean-up section	4
SOFC modules	8
Control system & other sections	4
Gas analyser	1
Authorization process	2

Table 1. Number of incidents at the DEMOSOFC site. Not all the unexpected incidents caused a shutdown and lead time for maintenance/repair of the problems have been between few hours and different months.

During the operation of the SOFC modules, an analysis of the auxiliary equipment has been performed, to understand the impact of these components on the overall plant efficiency. Results are shown in Figure 8. The total auxiliary consumption with one SOFC module running (including all the biogas treatment section, heat recovery, electrical and control parts, conditioning of the technical building, etc.) is around 11.72 kW. The value is dominated by the biogas treatment section (two chillers, blower, compressor) and all the equipment within the container (especially ventilation and cooling during Summer). The two sections together account for 77% of the consumption, followed by small contributions of other components (the contribution of all the other section is always lower than 5%). An optimized design for future biogas-SOFC replications should thus focus on the biogas processing system. In quantitative terms, auxiliaries are currently counting for more than

20% on the electrical production but this is due to the off-design operation of the site (designed for 3 SOFC modules, 58 kW each) when working with 1 SOFC system only. Considering 174 kW total electrical production (design conditions) auxiliary are expected to impact for less than 10%.

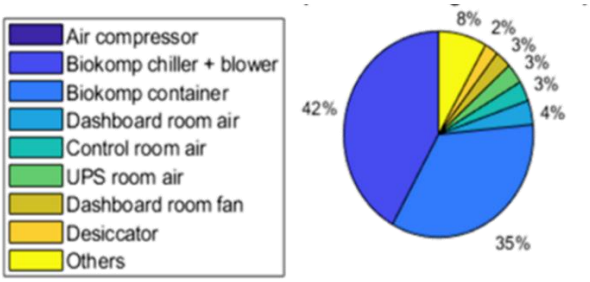

Figure 8. Auxiliary components for the DEMOSOFC site.

VTT Technical Research Centre of Finland [18], partner of the DEMOSOFC project, has performed onsite emissions analysis at the DEMOSOFC plant on December 7th, 2017. Results are shown in Figure 9 and discussed in detail in [17]. Results show that NO_x, SO_2, HCl, HF and organic compounds are all below the instrumentation detection limits see details in [10], [17], [19]). Particulate matter analysis (Figure 9) shows that particulate concentration in the surrounding ambient air is higher than the one in the SOFC module exhaust gases: the system is indeed filtering inlet ambient air and a ultra-low amount of particulate is added by the process.

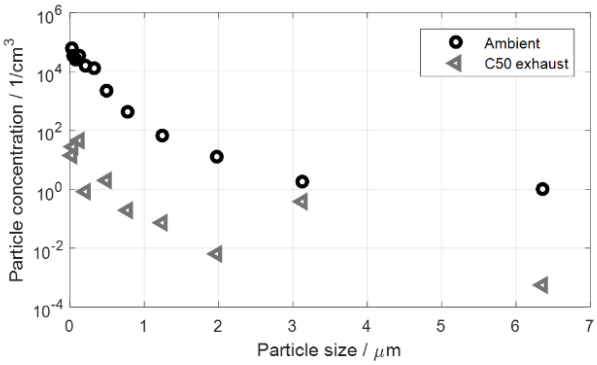

Figure 9. Results of the emissions analysis at the DEMOSOFC site (courtesy of VTT [18]).

A final evaluation was performed on the costs experienced during the DEMOSOFC project for what concerns the site preparation, defined as all the required components to be installed in order to run the SOFC modules. Results are shown in Table 2 and have been presented in [20]. Site preparation costs can be divided into mechanical works (piping, valves, sensors, etc.), electrical works (wires, power supply, control system, meters, etc.), civil works (basement preparation, pipe racks, technical buildings, etc.), biogas cleaning works (blower, chiller, container with compressor, chiller, cleaning vessel, etc.), auxiliary works (biogas analyzer, gas cylinders, gas cylinders box, etc.). The total cost for the site preparation during the DEMOSOFC project has been more than 850 k€, which account for around 4'500€/kW (considering the design system size of 174 kW). In order to reduce the impact of the site preparation on the overall plant cost, an optimization analysis was performed by the engineers from Politecnico di Torino and SMAT s.p.a responsible for the site construction.
The analysis focused primarily on the following elements:

- Excluding all the site-dependent costs (for example the WWTP needed a new electrical cabinet to host the CHP system, or the need of a blower because the plant was located far from the digester).
- Moving from underground pipeline to external (covered) pipeline.
- Removal of twin pumps (currently installed for guaranteeing a continuous operation even in case of pumps maintenance)
- Reduction of UPS size (currently over-sized for hours of operation, but required only for less than a second)
- Simplification of the technical building (moving to a simplified containerized solution)
- Optimization of the cleaning system (reduction of the number of vessels)

By means of these modifications the total costs could be reduced of 56% (with a specific impact close to 2'000 €/kW): the higher reductions are possible in the civil and mechanical works section. Furthermore, it should be underlined that this analysis is performed for a new construction, while many biogas plants already have a CHP unit and so many of these costs could be avoided.

	DEMOSOFC cost (€)	**Optimized cost (€)**	**Reduction (%)**
Mechanical works	174'562	65'502	-63%
Electrical works	173'913	100'819	-42%
Civil works	191'920	23'758	-88%
Biogas cleaning works	221'087	132'652	-40%
Auxiliary works	91'677	54'597	-40%
Total Costs	**853'159**	**377'328**	**-56%**

Table 2. DEMOSOFC site preparation costs in the current and optimized scenarios.

3. Conclusions

The DEMOSOFC plant has been in operation since October 2017 with 2 SOFC modules running (50 kW_e electrical each). During the 3 years of operation the DEMO site has reached in total more than 13'700 hours of operation with SOFC 1 or 2 running (capacity factor has been between 40 and 60% for SOFC1 and SOFC2 respectively). Shutdown periods were due to the authorization process in the first year of operation, followed by some unexpected maintenance on the cleaning system and the SOFC modules.

The presents work showed results from the operation of the entire system, including the biogas cleaning unit and the overall DEMO site performance, followed by economic perspectives.

The DEMOSOFC plant was able to demonstrate the possibility of operating an SOFC system within an industrial environment, fed by biogas from WWTP, keeping high electrical efficiency around 50% and total efficiency above 85%. Therefore, the efficiency targets connected to SOFC systems have been validated.

Biogas cleaning system and thermal recovery unit, after some months of optimization of the control, were found to be robust and reliable, and their design could be improved to reduce the costs.

Acknowledgments

This project has received funding from the Fuel Cells and Hydrogen 2 Joint Undertaking under grant agreement No 671470. This Joint Undertaking receives support from the European Union's Horizon 2020 research and innovation programme, Hydrogen Europe and Hydrogen Europe research.

References

[1] "DEMOSOFC project official website," 2016. [Online]. Available: www.demosofc.eu. [Accessed: 20-Dec-2015].

[2] P. Margalef, T. Brown, J. Brouwer, and S. Samuelsen, "Conceptual design and configuration performance analyses of polygenerating high temperature fuel cells," *Int. J. Hydrogen Energy*, vol. 36, no. 16, pp. 10044–10056, 2011.

[3] M. Gandiglio, A. Lanzini, and M. Santarelli, "Large Stationary Solid Oxide Fuel Cell (SOFC) Power Plants," Springer, Cham, 2018, pp. 233–261.

[4] M. Gandiglio, D. Drago, and M. Santarelli, "Techno-economic Analysis of a Solid Oxide Fuel Cell Installation in a Biogas Plant Fed by Agricultural Residues and Comparison with Alternative Biogas Exploitation Paths," *Energy Procedia*, vol. 101, no. September, pp. 1002–1009, 2016.

[5] E. Rillo, M. Gandiglio, A. Lanzini, S. Bobba, M. Santarelli, and G. Blengini, "Life Cycle Assessment (LCA) of biogas-fed Solid Oxide Fuel Cell (SOFC) plant," *Energy*, vol. 126, pp. 585–602, 2017.

[6] M. Gandiglio, A. Lanzini, A. Soto, P. Leone, and M. Santarelli, "Enhancing the energy efficiency of wastewater treatment plants through co-digestion and fuel cell systems," *Front. Environ. Sci.*, vol. 5, p. 70, 2017.

[7] M. Santarelli *et al.*, "Carbon recovery and re-utilization (CRR) from the exhaust of a solid oxide fuel cell (SOFC): analysis through a proof-of-concept," *J. CO2 Util.*, vol. 18, pp. 206–221, 2017.

[8] M. Sorace, M. Gandiglio, and M. Santarelli, "Modeling and techno-economic analysis of the integration of a FC- based micro-CHP system for residential application with a heat pump," *Energy*, 2016.

[9] B. Tjaden, M. Gandiglio, A. Lanzini, M. Santarelli, M. Järvinen, and M. Jarvinen, "Small-scale biogas-SOFC plant: Technical analysis and assessment of different fuel reforming options," *Energy and Fuels*, vol. 28, no. 6, pp. 4216–4232, 2014.

[10] M. Gandiglio, A. Lanzini, M. Santarelli, M. Acri, T. Hakala, and M. Rautanen, "Results from an industrial size biogas-fed SOFC plant (the DEMOSOFC project)," *Int. J. Hydrogen Energy*, vol. 45, no. 8, pp. 5449–5464, Sep. 2019.

[11] "Home Page | Bio-komp.com - official website." [Online]. Available: http://www.bio-komp.com/index.php. [Accessed: 08-Jan-2018].

[12] "Qualvista Ltd - official website." [Online]. Available: http://www.qualvista.com/. [Accessed: 08-Jan-2018].

[13] Convion Fuel Cell Systems, "Convion official website," 2017. [Online]. Available: http://convion.fi/. [Accessed: 11-Apr-2019].

[14] M. Gandiglio, A. Lanzini, M. Santarelli, and P. Leone, "Design and balance of plant of a demonstration plant with a Solid Oxide Fuel Cell fed by biogas from Waste-water and exhaust carbon recycling for algae growth," *J. Fuel Cell Sci. Technol.*, vol. 11, no. June, p. 14, 2013.

[15] A. Lanzini *et al.*, "Dealing with fuel contaminants in biogas-fed solid oxide fuel cell (SOFC) and molten carbonate fuel cell (MCFC) plants: Degradation of catalytic and electro-catalytic active surfaces and related gas purification methods," *Prog. Energy Combust. Sci.*, vol. 61, pp. 150–188, 2017.

[16] D. D. Papadias, S. Ahmed, and R. Kumar, "Fuel quality issues with biogas energy - An economic analysis for a stationary fuel cell system," *Energy*, vol. 44, no. 1, pp. 257–277, 2012.

[17] H. Langnickel *et al.*, "Efficiency analysis of 50 kWe SOFC systems fueled with biogas from waste water," *J. Power Sources Adv.*, vol. 2, p. 100009, Apr. 2020.

[18] "VTT | VTT Technical Research Centre of Finland Ltd Technology for business." .

[19] M. Rautanen, H. Vesala, T. Kajolinna, and T. Pellikka, "DEMOSOFC project - Deliverable number 4.3-a Analysis of the emissions from the DEMO," 2018.

[20] "DEMOSOFC web-seminar 2 - 'How to integrate an SOFC system in a biogas plant' - YouTube." [Online]. Available: https://www.youtube.com/watch?v=zF0HpwsWf1M&list=PLf5uOWQTy4DElcX5mlt32QrGPJdLLcMJv&index=3. [Accessed: 27-Aug-2020].

Keywords: EFCF2020, SOx
Session A16: System design & performance & BoP

https://doi.org/10.5281/zenodo.4556955

A1609

Consistent modelling and testing theory of high effectiveness heat exchanger performance by means of Shannon 1948 entropy

Jean-Paul Janssens (1), Michel Dubuisson (2)
(1) R&D BOSAL Energy Conversion Industries
Dellestraat 20 B-3560 Lummen/Belgium
(2) BOSAL Energy Conversion Industries
Kamerlingh Onnesweg 5 NL-4131PK Vianen/The Netherlands

Contact authors: www.EFCF.com/ContactRequest

Abstract

The components of the Hot Balance of Plant (H-BoP) of SOFC and SOEC (r-SOC) systems are in fact energy quanta managers. They organize the exchange of quanta in a well ordered way with heat exchanging processes or catalytic supported chemical conversions. Examples for stationary and mobile applications like electrical busses are Air Preheaters, Anode OffGas Coolers, Fuel Steam Humidifier, Fuel Reformers. Because considerations based on thermodynamics entropy could not offer a satisfactory explanation, a more fundamental definition of entropy based on the Shannon 1948 entropy is applied. A Shannon Isentropic Heat Exchanger shows insight in the formulation coming from Kays & London (1964) for compact heat exchangers. Starting from the laminar heat exchange model, it is enlarged towards heat exchangers with enhanced heat transfer due to micro-turbulences. A mathematical and graphical approach is discussed. A testing methodology is developed that offers the advantages to identify and quantify the performance quality accurately, and enables to discover links with the causes of performance degradation. A generalization towards catalytic supported reactions in the heat exchanger is touched to demonstrate the similarities. This approach delivers a clear different view on the thermodynamics in a high effectiveness heat exchanger, which can be characterized as a result of “thinking out of the box”.

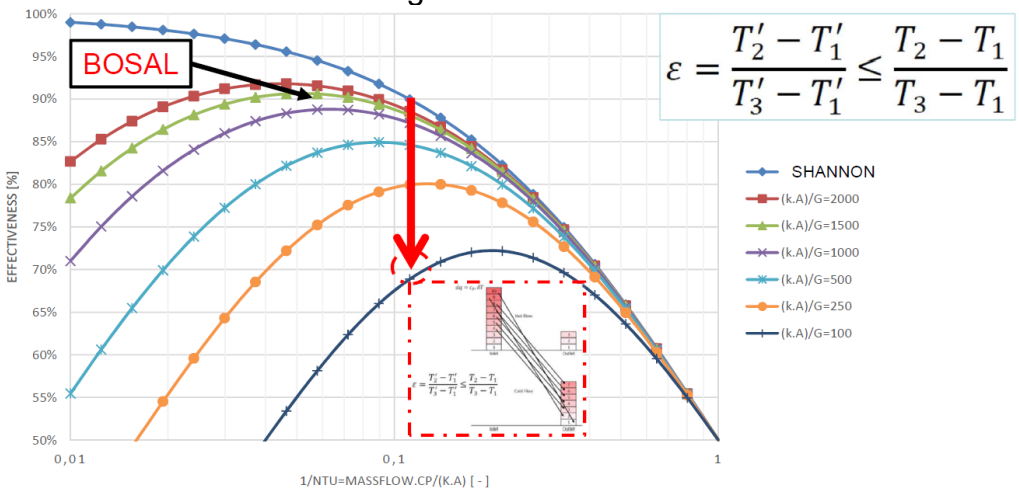

https://doi.org/10.5281/zenodo.4556973

Introduction

Until now the performance of high temperature counter-flow heat exchangers is mainly approached over the First Law of Thermodynamics (FLT) and the effectiveness definition which led in some cases to confusion and discussions in communications about expected performances. By start using the Second Law of Thermodynamics (SLT) and the notion entropy, a new approach and definitions are generated to facilitate communication regarding this matter.

Figure 1. Basic scheme of counterflow heat exchanger.

The basic scheme of a counter-flow heat exchanger shows two separated flows, a hot flow (highest inlet temperature T3) that provides heat and a cold flow (lowest inlet temperature T1) that receives heat. Hot flow travels on the top from left to right. Cold flow is traveling on the bottom from right to left. Effectiveness is defined as how close the target temperature is reached:

$$\varepsilon = \frac{T_{cold,out} - T_{cold,in}}{T_{hot,in} - T_{cold,in}} \quad [1]$$

Scientific Approach

A to the essence reduced non-dimensional model with no phase change is developed. This model is based on the following basics. According the thermodynamic approach, the following equations yield:

1) the continuity equation: “mass in” is “mass out”.

$$\int_A \rho.v.dA = 0$$

2) the first law of thermodynamics (FLT): conservation of energy. What disappears in the hot flow has to appear in the cold flow. The heat exchanger is considered as perfectly insulated, an adiabatic heat exchanger. In practice this means that the heat loss to the outside of the heat exchanger is significantly lower than 1% of the heat exchanging power between the hot flow and the cold flow.

$$\int_A \rho.v.h.dA = 0$$

3) the second law of thermodynamics (SLT). Entropy always increases over time. When a quantum leaves the hot flow, entropy reduces with a quantity equal to the ratio of the quantum energy divided by the absolute temperature where it leaves the hot flow. The quantum travels through the system to end up in the cold flow where it increases the entropy with a value equal to the ratio of the same quantum energy divided by the absolute temperature at that place, which is lower from where it started in the hot flow. Thus overall entropy increased.

$$ds_{hot} = \frac{dq}{T_{hot}}$$

$$ds_{cold} = \frac{dq}{T_{cold}}$$

$$dq = c_p.\delta T$$

https://doi.org/10.5281/zenodo.4556973

Well Managed Quanta Travel Schemes

It is wrong to assume that all the heat is provided at the same quality. You have to consider that the heat at the hot side inlet T3 is a pile of quanta, going from low temperature up to the high temperature. In figure 2, the inlet is set on the left side, outlet on the right side, the hot flow on the top, the cold flow below.

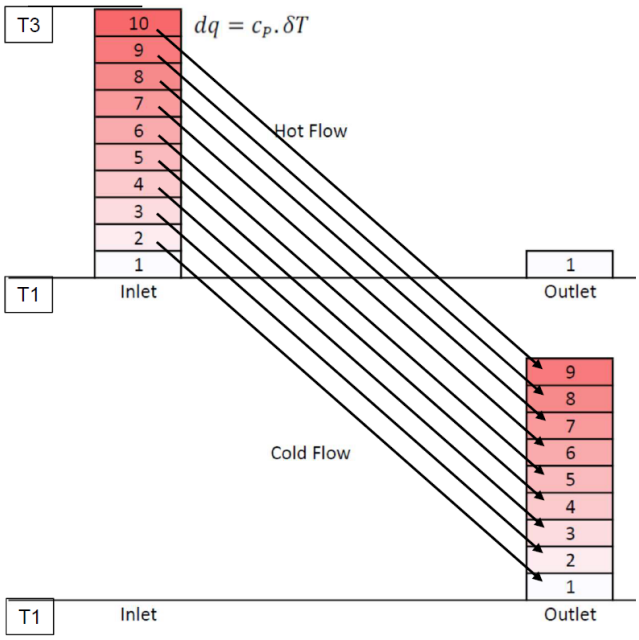

Figure 2. Quanta travel scheme H=0.

The resolution of this pile is arbitrary, at least 2 or higher. We select an arbitrary resolution of the quantum pile, assume here 10. We look at the situation where we have one quantum left in the hot outlet, which means that you have 9 quanta into the cold outlet according the first law of thermodynamics FLT.
The rule of the game is that each quantum can be used for a lower level, but not an equal or higher level. This is due to the thermal resistance 1/k of the main heat exchanging surface (3).

$$\frac{1}{k} = \left(\frac{1}{\alpha_1} + R_{f,1}\right).\frac{A_2}{A_1} + R_{wall} + \frac{1}{\alpha_2} + R_{f,2} \qquad [2]$$

This means level 9 on the cold side can only be delivered by level 10 from the hot side.
It also explains that we cannot get rid of level 1 on the hot side because there is no lower level available on the cold side.
Furthermore, because we have to transfer level 2 from the hot side, we need to use it for level 1 on the cold side.
However, level 2 from the hot side is not accessible. Nature reacts as if we only have access to the quantum on the top of the pile. So you have to put the quanta in a kind of register to have access to level 2 from the hot side and then build up the quanta on the cold side with the eldest quantum on the bottom and the youngest on the top.
This illustrates that these Hot BoP components work as quantum managers with well defined stucture.

https://doi.org/10.5281/zenodo.4556973

Shannon 1948 Entropy

Now the information theory of Shannon 1948 is introduced (1). Shannon defined the entropy H as the following two equations.

$$H = -\sum p_i . log_2(p_i) \quad with \sum p_i = 1 \qquad [3]$$

All cases must be considered so that the sum of all probabilities is one, and H is a summation of values of a function only depending on the probability itself of that case. The Shannon 1948 entropy is related to the amount of missing information. How many questions do I have to pose to solve the problem? Let us calculate the Shannon 1948 entropy of this situation.
Here we see that there is only one way to solve this situation, with the given rules of the game, thus the probability p_i is one , p_i=1. A second case does not exist. If we calculate the Shannon entropy H=1.Log$_2$(1) is zero. Shannon entropy is zero.

Although the Shannon entropy dH is a mathematical formulation out of the Information Theory, it reveals to be more basic than the definition of entropy in Thermodynamics ds. The link between both can be demonstrated by applying some straight forward mathematical operations. By using Lagrange multiplicators, we are able to find the condition with maximal disorder on the distribution of any set of energy holders or containers E_i. This leads to the link between Shannon and the Boltzmann distribution.

1. $\sum_i (p_i) = 1$
2. $\sum_i (p_i . E_i) = \langle E \rangle = average\ energy = constant$

$$L = H + \alpha . \left(\sum_i p_i - 1 \right) + \beta . \left(\sum_i (p_i . E_i) - \langle E \rangle \right)$$

$$L = -\sum_i \left(p_i . ln(p_i) \right) + \alpha . \left(\sum_i p_i - 1 \right) + \beta . \left(\sum_i (p_i . E_i) - \langle E \rangle \right)$$

$$\frac{dL}{dp_1} \rightarrow \ln(p_1) + \frac{p_1}{p_1} + \alpha + \beta . E_1 = 0$$

$$\frac{dL}{dp_i} \rightarrow \ln(p_i) + 1 + \alpha + \beta . E_i = 0$$

$$\ln(p_i) = -1 - \alpha - \beta . E_i$$

$$p_i = K . e^{-\beta . E_i}$$

$$K = e^{-1-\alpha}$$

$$p_i = K . e^{-\frac{E_i}{k.T}}$$

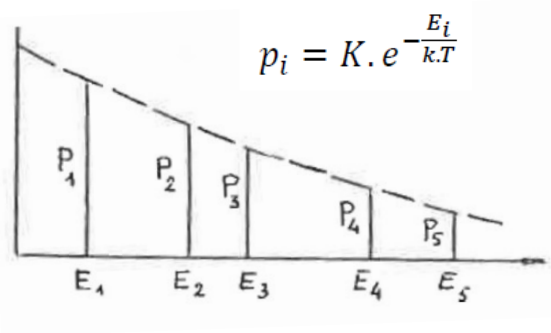

$$\beta = \frac{1}{k.T} \quad or \quad T = \frac{1}{k.\beta}$$

This distribution is linked with our definition of temperature. By further using differentiation techniques, one ends up with the link between dH and ds, being the Boltzmann constant:

$$dH = \beta . d\langle E \rangle = \frac{d\langle E \rangle}{k.T}$$

$$\boxed{ds = \frac{dE}{T} = k . \frac{dE}{k.T} = k . dH}$$

https://doi.org/10.5281/zenodo.4556973

Back to the heat exchanger formula's for ideal counter-flow heat exchanger [4] or H=0 "Shannon Isentropic heat exchanger" out of literature of Kays and London or VDI-Wärme Atlas, effectiveness is expressed as a function of NTU and z.

$$\varepsilon_{ideal,z=1} = \frac{NTU}{NTU+1} = \frac{T_2 - T_1}{T_3 - T_1}$$

$$\varepsilon_{ideal,z<1} = \frac{1 - e^{[(z-1).NTU]}}{1 - z.e^{[(z-1).NTU]}} = \frac{T_2 - T_1}{T_3 - T_1}$$

[4]

$$NTU = \frac{k.A}{(massflow.C_p)_{cold}}$$

$$z = \frac{(massflow.C_p)_{cold}}{(massflow.C_p)_{hot}}$$

The value z is the ratio of the thermal capacities of the flows determined by the product of mass-flow and c_p. The value z shows the effect of one quantum on the change in temperature in the hot flow and the cold flow. At z=1, the effect on temperature on both sides is the same. When z deviates from one, the effect on temperature increment is different.
NTU stands for Number of Transfer Units (2). It gives a relation between the main heat exchanging surface and the thermal capacity of the cold flow. Because we arbitrary selected a resolution of 10, we were able to transfer 9 units resulting in an effectiveness of 90%. If we arbitrary select a resolution of 2, we can only transfer 1 unit resulting in an effectiveness of 50%. This is fully in line with the formula's out of literature saying:

$$\varepsilon = \frac{NTU}{NTU+1} \qquad [5]$$

We put this behavior in figure 3. Y-axis is the effectiveness. X-axis is the reciprocal value of NTU, giving a non-dimensional mass-flow.

The right side is a high mass-flow and/or a rather small heat exchanger. The left side is low mass-flow and/or a very big heat exchanger.

Line z=1 is the behavior of the "Shannon Isentropic heat exchanger" in balance. At NTU=1 half of the pile (50%) remains in the hot flow resulting in an effectiveness=50%. At NTU=9 one tenth (10%) of the pile remains in the hot flow resulting in an effectiveness=90%. At NTU=19 one twentieth (5%) of the pile remains in the hot flow resulting in an effectiveness=95%. So each scheme is linked to a specific NTU-value on the X-axis.

https://doi.org/10.5281/zenodo.4556973

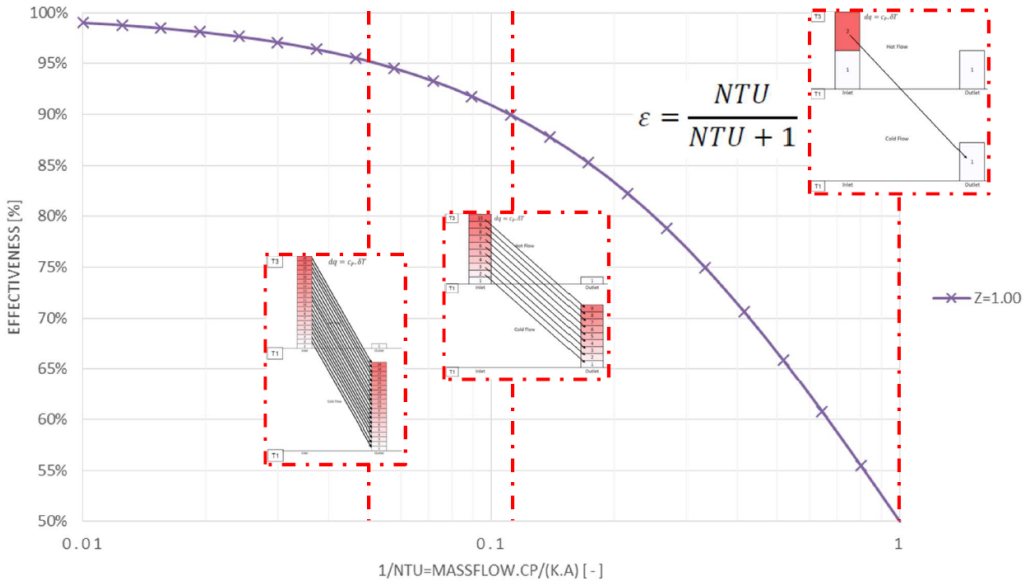

Figure 3. Effectiveness as a function of NTU at z=1.

Additional graphs are shown in figure 4 for multiple z-values. High effectiveness can easily be reached if more heat is available on the hot side (mass-flow or c_p), thus at z-values lower than 1. High effectiveness cannot be reached if less heat is available on the hot side (mass-flow or c_p), thus at z-values higher than 1. However, for all the points in figure 4 the Shannon 1948 entropy is zero: H=0. For each value of NTU the structured scheme of the quanta travel paths remains valid as discussed above. Only due to the changed value of z, the temperature scale for the cold outlet is no longer linear with the number of quanta.

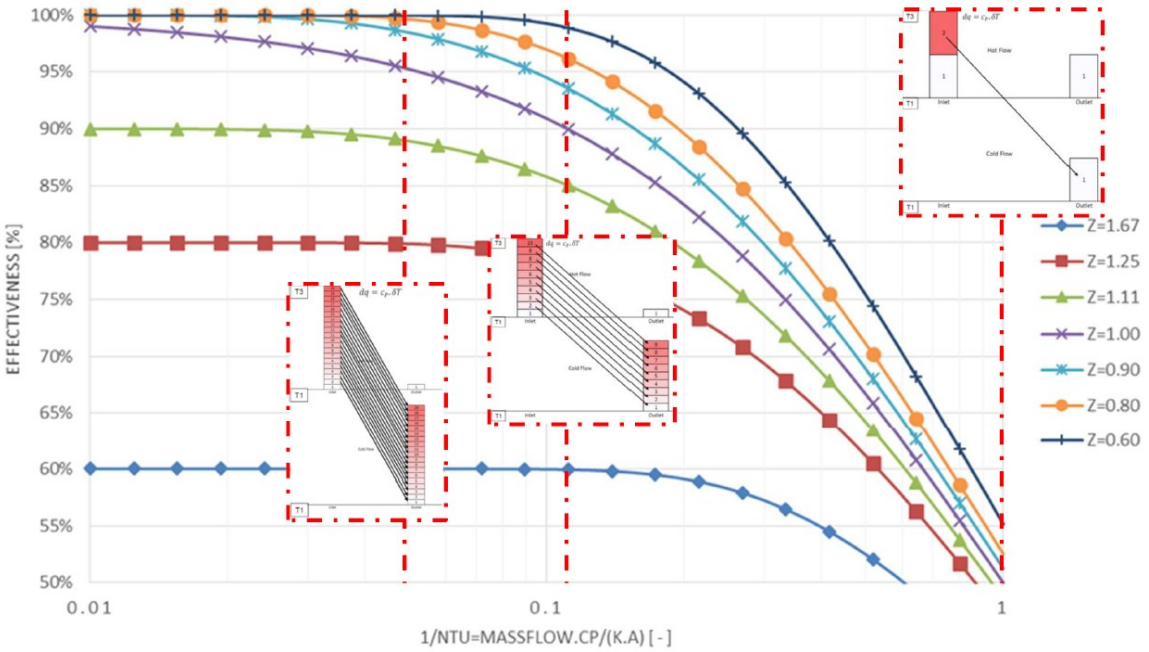

Figure 4. Effectiveness as a function of NTU for multiple z-values.

Quanta Travel Schemes with Amount of Disorder

What happens now in case where we could exchange nine quanta NTU=9, but only exchange 7, leaving 3 at the exit of the hot flow? This is correct according the first law of Thermodynamics. Now we have more possibilities to reach this result. For instance one could use 10 for 1, 9 for 2. From here onwards we do not have any choice. Because 4 has to go to the cold side, we have to use 4 for 3. The rest has to follow to come to the end result. But we could also start using 9 for 1, 10 for 2. Or we could use 8 for 1, 6 for 2 and so on. This results in multiple ways to come to this result.

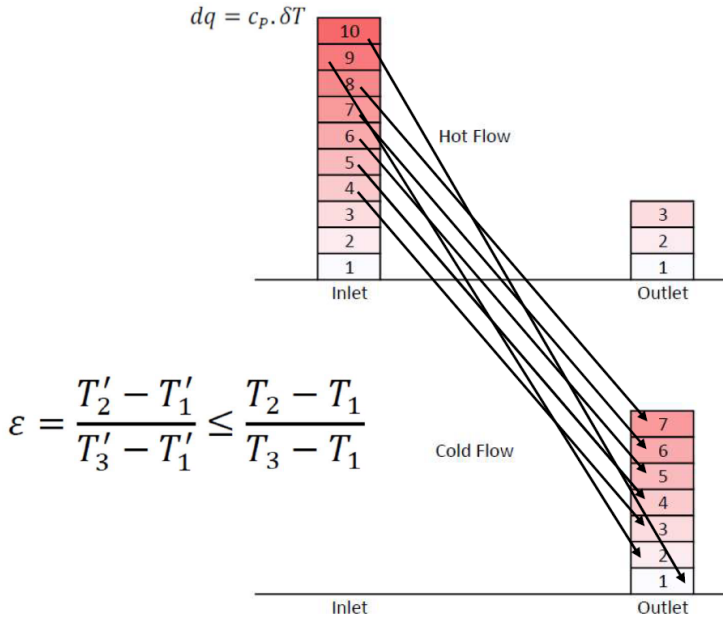

Figure 5. Quanta travel scheme H<>0.

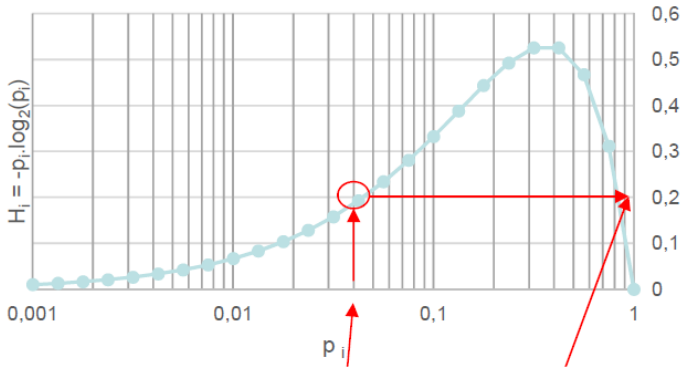

Figure 6. Shannon 1948 entropy contribution per case.

If we calculate the Shannon 1948 entropy now assuming we have 25 cases, (notice there are much more cases) all with equal probability, we have to look in figure 6 at the x-axis with p_i=1/25=0.04 resulting in a function value of 0.2. We have to sum this value over all the cases resulting in 25x0.2=5. Conclusion, the entropy increased.

https://doi.org/10.5281/zenodo.4556973

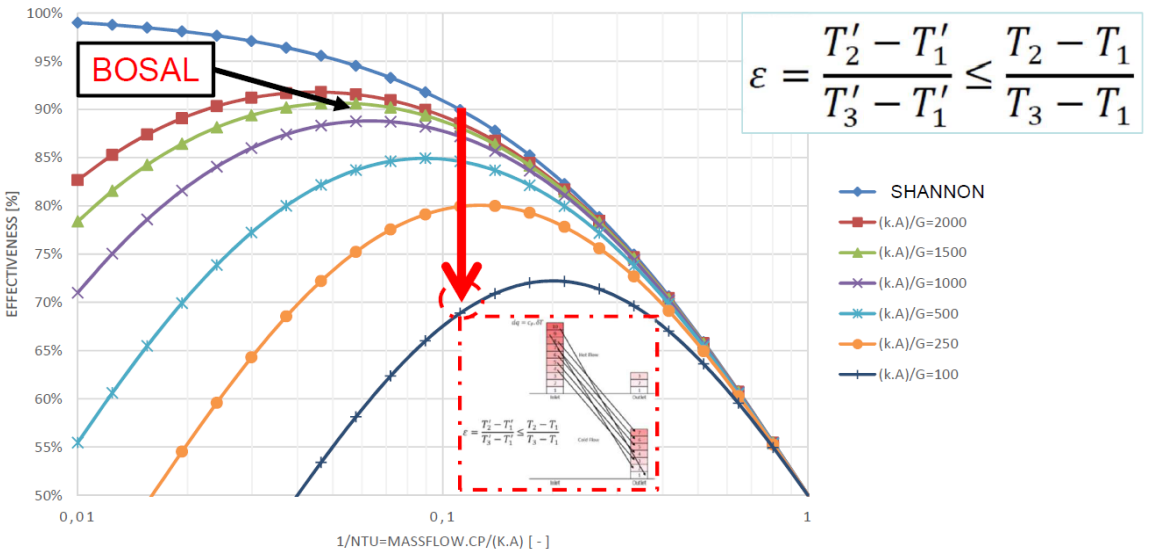

Figure 7. Performance chart of real heat exchangers with z=1.

If we integrate the previous case with NTU=9 in a performance chart of real heat exchangers with z=1 as shown in figure 7, we start from the Shannon curve out of figure 3 and identify the point with the structured exchange at 90% effectiveness down to 70% effectiveness according the red arrow.

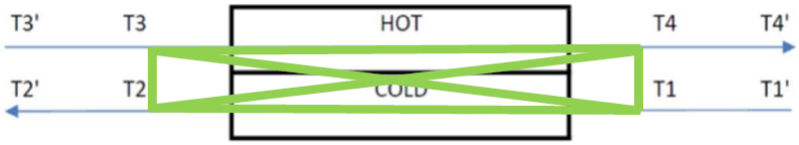

Figure 8. Structured Shannon heat exchanger embedded in 6 conductances G (green lines).

We composed a model with in the center a “Shannon Isentropic heat exchanger”, managing the quanta in a well structured way, embedded in six resistors, called G, linking all the ports of the “Shannon Isentropic heat exchanger” with each other. In this way quanta are able to travel in an unstructured way around the well structured core, for instance from T3 to T1 (10>1) or other possibilities. For the simplicity all the resistors are given the same conductance value G. Because G is a thermal conductance, just as k.A, the ratio of both results in the non-dimensional quality parameter (k.A/G). Now we do the math based on the continuity equation and first law of thermodynamics, and calculate the temperatures upstream and downstream of T1, T2, T3 and T4, expressing them as T’1, T’2, T’3 and T’4. To avoid transcendent calculations, it is assumed that the temperatures given by the “Shannon Isentropic heat exchanger” determine the quantum over the conductance G. If one deviates very far from the “Shannon Isentropic heat exchanger”, this simplification does not longer hold. For the case where G is zero, thus the quality factor (k.A/G) infinite, we end up in the Shannon H=0 case. All graphs with higher entropy are situated below this graph. The effect on effectiveness is: T3’ has to go up (T3’>T3) because it has to deliver quanta to all other ports. T1’ has to go down (T1’<T1) because it receives quanta from all other ports. And T2’ probably goes down as well (T2’<T2) because it normally receives less quanta from port 3 than it has to deliver to port 4 and 1. As a result, the real effectiveness goes down compared to the effectiveness of the “Shannon Isentropic heat exchanger” because the numerator does not change a lot while the denominator goes up. As a result a real heat exchanger shows a kind of maximum and will reduce performance significantly at lower mass-flows.

https://doi.org/10.5281/zenodo.4556973

Just as we cannot make an isentropic turbine, we are not able to build a ”Shannon Isentropic heat exchanger”, and certainly not better. The area above the Shannon H=0 case does not exist.

The BOSAL heat exchanger typically reaches effectiveness values of 90% at z=1. Expressed in quality factor this turns out to be around (k.A/G)=1200. This is a non-dimensional quantity factor. Later we will discuss a method to measure this quality factor accurately.
What are the parameters that influence the quality factor (k.A/G)? In general, the relative thermal resistance of the thermal bridges over the structured core must be as big as possible. This relative thermal resistance of the thermal bridges reflects all what can go wrong such as:

- Temperature gradient (dT/dx) along foils, not perpendicular to surface A
  - Choice of foil: highly alloyed material grade (austenitic and inconels)
  - Choice of foil: thickness in microns instead of millimeters
- Non-uniformity flows that deviate from balanced counterflow, cause heat exchange and mixing at higher different temperatures
- By-pass flow
- Thermal bridges between core/manifolds under different temperatures
- Radiation hot zones towards cold zones T^4(hot)-T^4(cold) (internal)
- Insulation between the manifolds and ducting
- Heat exchange in wedges (cross-flow type zone) at bigger temperature differences
- Manufacturing (tolerances, expertise and accomplishment)
- …

Performance Charts of Real Heat Exchangers at Different z Value

In the same way, for each z-value, the reduction of the performance can be plotted starting from the curve of the “Shannon Isentropic heat exchanger” on the top. This is done for Z values deviating from 1. Graphs are plotted, one for z-value lower than one and one for higher than one. Also here, the zone in the graph above the “Shannon Isentropic heat exchanger”-curve does not exist.

Until now we spoke about heating up the cold flow. Cooling down of the hot flow could also be the aim, to reach a certain temperature window for the process downstream of the hot outlet. This can be handled in the same way. More than that, only a small set of graphs is needed. One can speak about a set of mirrored graphs.

Considering heating up the cold flow, the effectiveness gives the degree how close the target, hot inlet temperature is reached. Considering cooling down the hot flow, the effectiveness gives the degree how close the target, cold inlet temperature, is reached.

https://doi.org/10.5281/zenodo.4556973

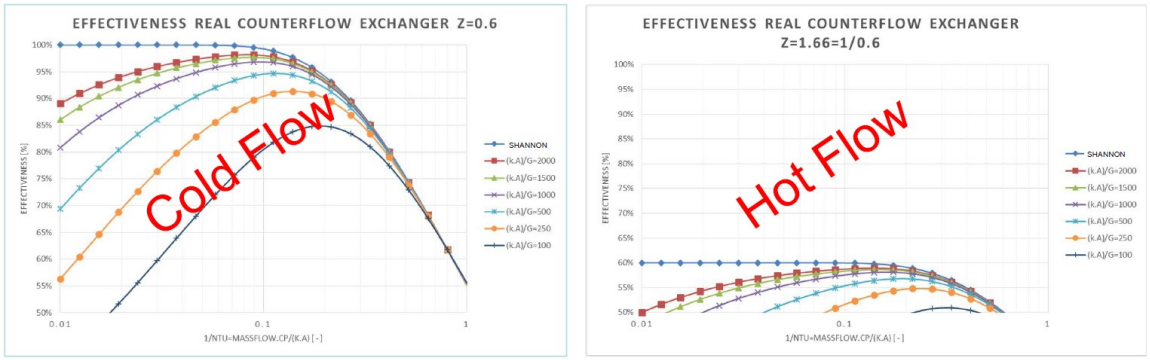

Figure 9. Mirrored graphs with z=0.6.

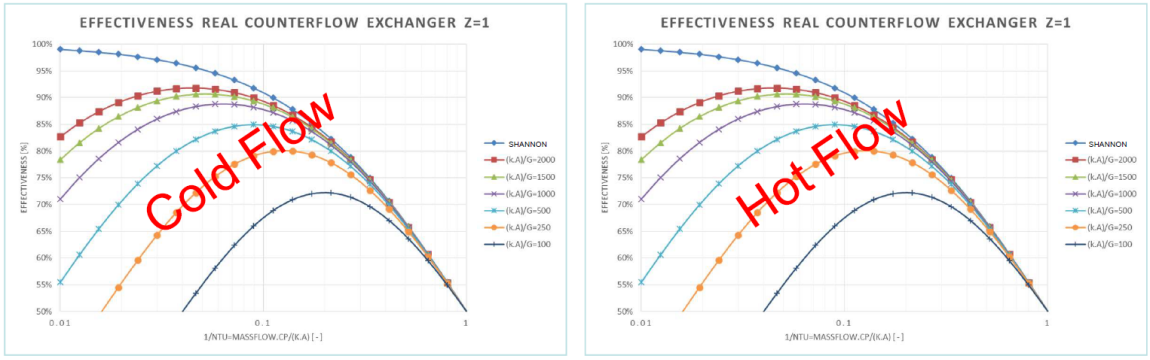

Figure 10. Mirrored graphs with z=1.0.

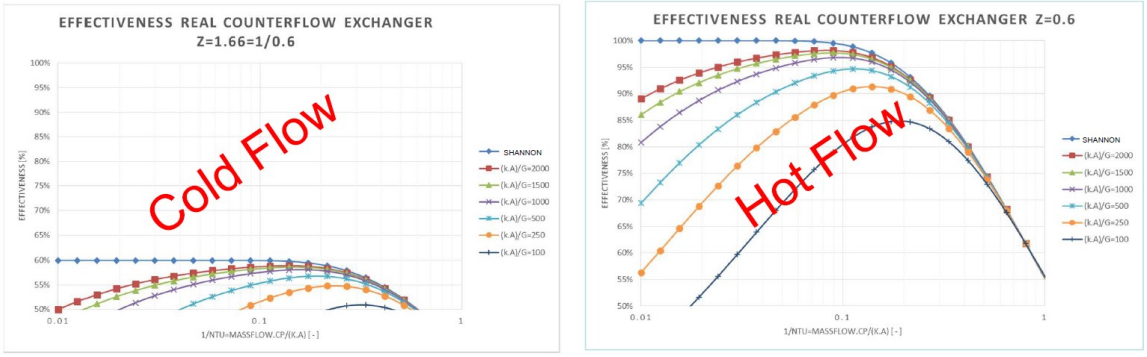

Figure 11. Mirrored graphs with z=1.66.

In case z=1, the first law of thermodynamics is the reason why the same graph can be applied on the hot side, interpreting this graph as the NTU determined on the hot side mass-flow and hot side c_p and the target is the cold inlet temperature. Because the graph only contains non-dimensional parameters, we end up with two identical graphs. If we reach 100%, the hot flow will fully reach the cold inlet temperature. When we now reduce the quality factor, k.A/G, the same reasoning holds for the hot side. So we can also use the same graph to determine the effect of the quality factor for the hot side.

In case z<1, there is more than sufficient heat available to reach high effectiveness values on the cold side. This situation is discussed in detail before. By reaching effectiveness values up to 100% cause a kind of saturation effect that stops the heat transfer which results in a high hot outlet temperature. This results in a low effectiveness value on the hot side. Due to the First Law of Thermodynamics we can prove that the graph of 1/z yields for the hot side, not only for the “Shannon Isentropic heat exchanger” but also for lower quality cases. Here it is important to use the hot side mass-flow and c_p to

determine the X-value. In this way you can see that the maxima in the graph of course fit with the maxima in the other graph, according to the FLT.

In case z>1, the same reasoning can be applied which leads to only 3 different graphs to describe the behavior of the cold and the hot flow for 3 cases of z and 6 cases of the quality factor (k.A/G). All these cases are visualized in figure 9 to 11. All these parameters are non-dimensional and this model can thus be used for any gas composition going from air, exhaust, CO, hydrogen or any combination.

Microturbulences and Reynolds Dependent Heat Transfer

The reciprocal value of NTU is proportional to the massflow when k.A is constant. This is the laminar case. When microturbulences enhance the heat transfer, k.A is a function of the Reynolds number to a certain power gamma. One can still use the graphs we discussed before by projecting the massflow axis on the 1/NTU axis in a double logarithmic graph. When gamma is zero, 1/NTU is proportional to the massflow, when gamma is one, the whole massflow axis is projected to one point on the 1/NTU scale, resulting in a singularity.

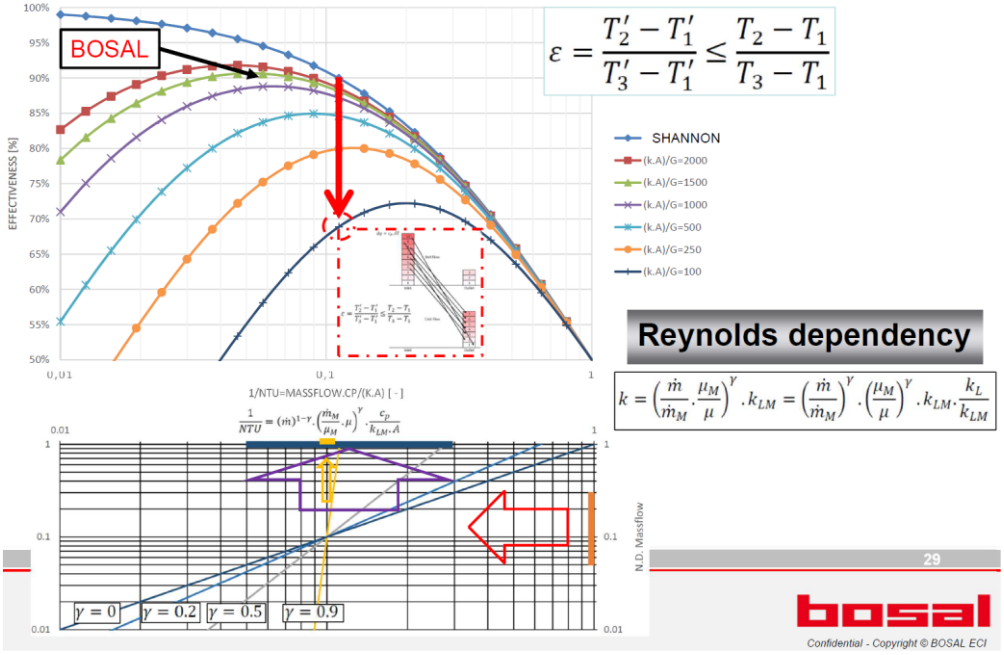

Figure 12. Microturbulences and Reynolds dependent heat transfer.

Curve Fitting Technique on Test Results

We have now a model available based on five non-dimensional parameters: effectiveness, z, NTU, k.A/G and gamma. One can determine effectiveness and z by

a) measuring the cold and hot mass-flow,
b) determine the c_p values of the cold and hot flows and
c) measure the temperatures on the real heat exchanger.

Use this input to apply curve fitting to find the best fit for NTU, k.A/G and gamma in the three dimensional space to determine not only on the value of the effectiveness but also on its curvature.

https://doi.org/10.5281/zenodo.4556973

This exercise is done for the BOSAL laser-welded solution in comparison with a brazed solution of a competitor. The exercise reveals that the quality factor of the BOSAL unit (quality=1204[-]) is more than five times higher as the competitor unit (quality=209[-]). This is realized based on better selection of a list of parameters mentioned in the next figure.

BOSAL	Description	Competitor
Laser welded		Brazed
1,0mm	Hydraulic diameter	2,5mm
150 microns	Plate thickness, highly alloyed	500 microns
I and Z Compliance	Channel geometry • Flow path, pressure drop and heat transfer • Stress (FEM detail)	U rigid
+	Uniformity: ways to optimize uniformity by manifold design.	-
More options	Symmetry versus a-symmetry.	One option
+	Heat exchanging volume: (heat exchanging surface) x (hydraulic diameter)	-
Thin foils	Transient behavior, low mass	Bulky, thick plates
1204	k.A/G	209

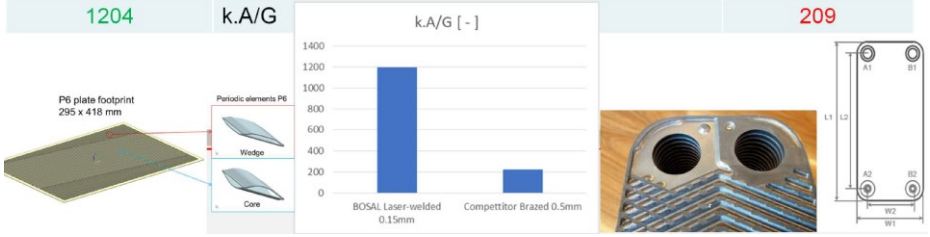

Figure 13. Comparison between laser-welded and vacuum-brazed solution.

There is a sizing calculator available on www.ECI.BOSAL.com based on this modeling with five non-dimensional parameters, k.A/G, gamma, z, NTU and effectiveness. Because these parameters are non-dimensional, this model can thus be used for any gas composition going from air, exhaust, H_2O, CO_2, CO, hydrogen or any other combination.

Generalization of theory towards catalytic active Hot-BoP components

We considered until now the temperature and entropy as the driving forces in the processes in the Hot-BoP component. Parallel to these processes and fundamentals, a similar logic or reasoning can be applied on the chemical conversions and their thermodynamic equilibria.

The catalysis material is used to accelerate the kinetics of the reaction to achieve the Thermodynamic Equilibrium of the redox reactions. Also here, as Shannon posed, nature will strive to make the amount of disorder as large as possible. In this case the Gibbs Free Energy (GFE) is applied. In practice, for such reaction descriptions one looks for the minima of the GFE which is based on maximizing the amount of disorder defined as

$$-\Delta g = T.\Delta s - \Delta h$$

The minus sign makes maximizing the Shannon Entropy similar as minimizing the Gibbs Free Energy. Also here, an ordered energy quantum management is required to get optimal usage of the energy flow. Creating the favourable conditions, such as the temperature and pressure windows, the energy quanta will disappear as thermal quanta and will appear as converted fuel, containing higher combustion value. So the reasoning is similar as we applied with the heat exchangers, only the scale to put the quanta on, differ. It is more an enthalpy scale as a temperature scale.

To realize this, BOSAL developed catalytic coated heat exchangers, one side coated for reductive, endothermal reactions to transform fuels, the other side with oxidative coatings to achieve optimal composition of exhaust gasses or facilitation of start-up processes.

Heat exchangers with integrated mixer are available which are designed in such a way that the mixture is within 3 milliseconds in the vicinity of the heat exchanging surface, to achieve a controlled temperature of the metal.

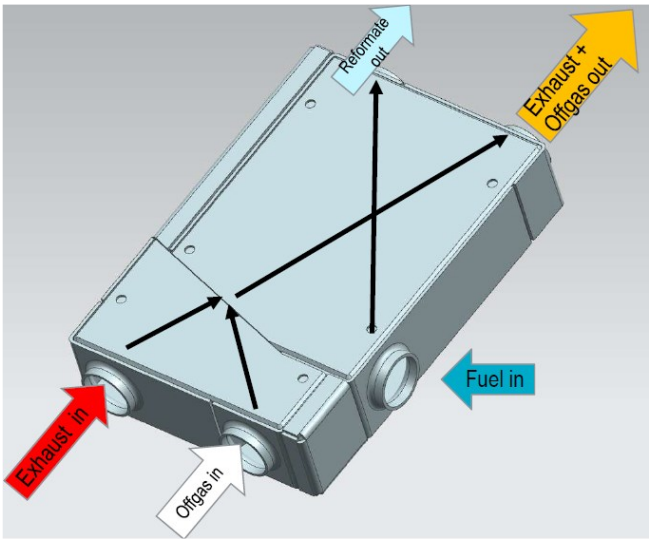

Figure 14 Picture of integrated mixer

Conclusion

Until now the description of the quality of counter-flow heat exchangers was mainly based on effectiveness and First Law of Thermodynamics. Effectiveness showed out to be a confusing quality parameter. Involving the Second Law of Thermodynamics and especially the Shannon 1948 entropy reveals a deeper look into the heat exchanger and its description. The definition of the “Shannon Isentropic heat exchanger” in combination with a quality factor k.A/G gives an unambiguous way to characterize a real counter-flow heat exchanger. A test method and curve fitting technique in a multi-dimensional space with 5 non-dimensional parameters offers an accurate method to quantify the involved parameters, which can be used by any gas composition. Such components can be applied in SOFC, SOEC and r-SOC for stationary and mobile applications.

References

1. C. E. Shannon, *A Mathematical Theory of Communication*, The Bell Technical Journal (1948).
2. W. M. Kays and A. L. London, *Compact Heat Exchangers*, Mc Graw-Hill (1964).
3. VDI *Heat Atlas, Second Edition*, VDI-Verlag (2010).

Keywords: EFCF2020, SOx
Session A16: System design & performance & BoP

https://doi.org/10.5281/zenodo.4556973

B0305

Manufacturing ScCeSZ/GDC Electrolyte Composite Layers for IT-SOFC by Reverse Aqueous Tape Casting

Abigail Snowdon, Zeyu Jiang, Robert Steinberger-Wilckens
Centre for Fuel Cell and Hydrogen Research
School of Chemical Engineering, University of Birmingham, B15 2TT Edgbaston/UK
Contact authors: www.EFCF.com/ContactRequest

Abstract

Recent advances in solid oxide cell (SOC) technology have been focusing on the materials so they to increase the power capability at reduced operating temperatures, from now typically around 800ºC to below 700ºC. In light of this, this work investigates the potential of a NiO/10Sc1CeSZ anode, and 10Sc1CeSZ electrolyte, with an La0.6Sr0.4Co0.2Fe0.8 Oxide (LSCF) cathode and Gd0.2Ce0.8 Oxide (GDC) barrier layer. It has previously been difficult to manufacture these cells via tape casting because the GDC barrier layer delaminates from the electrolyte layer upon high temperature sintering. This is due to thermal expansion coefficient (TEC) mismatch. Here, the capability of using reverse aqueous tape casting to manufacture anode supported cells (ASC) using a multi-layer technique is proven. GDC barrier layer, new electrolyte/barrier layer, electrolyte layer, anode functional layer (AFL) and anode substrate (AS) are tape cast effectively. The composite layer allows for a gradual transition from electrolyte to barrier layer eliminating the harsh step-change of TEC and, therefore, delamination upon sintering. Multiple cells were tested between 650 and 800ºC in a hydrogen/nitrogen mixture on the anode and air on the cathode side to yield a maximum power density of 0.4 W/cm^2.

https://doi.org/10.5281/zenodo.4557413

Introduction

In order for solid oxide fuel cells (SOFC) to become fully commercial, it is important to reduce the production costs and increase the lifetime. Research over the last decade has focused on reducing the degradation of the materials [1], optimising microstructure [2,3], dealing with fuel flexibility [4,5], and reducing the operating temperature from over 800ºC to below 700ºC in order to minimise thermally activated degradation effects and thermal stresses [6–8]. At high temperatures, the formation of $SrZrO_3$ insulating layers between the electrolyte and the cathode hinders the movement of oxygen ions across the electrolyte. The addition of a GDC barrier layer can stop Sr migration [9]. However, there are difficulties in manufacturing this barrier layer by the tape casting technique [10], due to the mismatch of thermal expansion coefficients, which leads to the GDC layer delaminating from the electrolyte upon high temperature sintering. In 2017, Menranjani et al. [11] discussed the impossibility of creating a bi-layer electrolyte by depositing a YSZ layer onto GDC due to the shrinkage mismatch. Furthermore, preliminary studies on the residual stresses of YSZ and GDC by Atkinson et al. [12] identified how the significant TEC of GDC weakened the electrolyte upon cooling down from the sintering temperature.

Screen-printing and physical vapour deposition (PVD) have been used in an attempt to combat this issue, however, they require additives that can reduce cell performance, are more costly, or are more time consuming in comparison to tape casting [13]. In 2013, Song et al. [14] found that the addition of a sintering aid to a screen printed GDC layer produced a dense barrier layer at higher sintering temperatures, but yielded a reduced electrochemical performance (0.385 Wcm^{-2}) compared to a cell fabricated without any sintering aid (0.86 Wcm^{-2}). In 2018, a research group demonstrated the ability of introducing a composite layer between a YSZ electrolyte and a GDC barrier layer through the magnetron sputtering technique. They manufactured graded deposits of GDC and YSZ to obtain cells that yielded 0.94 Wcm^{-2}, compared to their screen printed cells, 1.2 Wcm^{-2}, however, the degradation rate for these magnetron sputtered cells was very high (18%/1000 h) due to poor adhesion of the sputtered layer [9].

1. Scientific Approach

In this work, aqueous tape casting has been chosen as the method of fabrication because of its cost-effective and well-established method of producing homogeneous green tapes, suitable for industrial production without harmful solvents. The reverse tape casting approach established by Menzler et al. [15] was used in this work and adapted to include a tape cast barrier layer. The GDC layer was cast first, followed by the composite layer, the electrolyte layer, and the anode functional layer (AFL), each layer being oven-dried in between casting at 70ºC for 15 minutes. This was followed by casting the anode support (AS) and a final drying at 30ºC for 24 hours to produce a homogeneous green tape. To densify the half cells, they were co-sintered at 1000ºC and then fully sintered at 1400ºC. LSCF cathode ink was painted on the GDC side of the half cell and sintered at 975ºC. Fig. 1 illustrates the tape casting and cathode printing steps in sequence.

https://doi.org/10.5281/zenodo.4557413

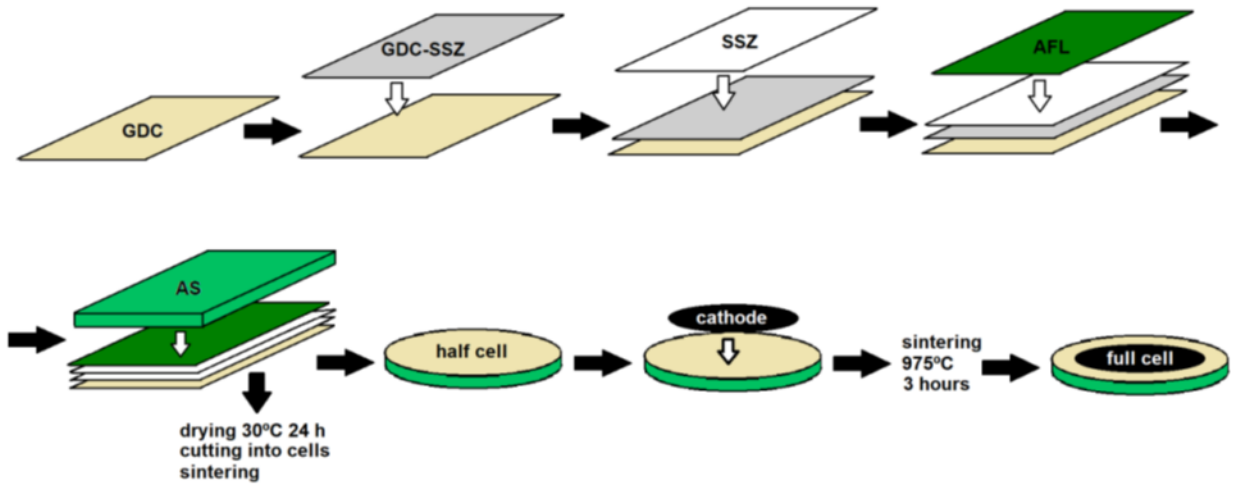

Fig. 1. Order of casting layers in five-layer anode-supported SOC manufacturing. Scheme adopted from [16].

2. Experimental Details

To produce a thin green tape, a Compact Tape Casting Film Coater with dryer and vacuum bed (MTI Corporation, USA) was used. The speed and gap height of the doctor blade was variable to allow for different thickness of green tapes. The cells fabricated and tested in this work were based on NiO/ScCeSZ material sets and the formulation based upon previous work by Arifin et al. [17]. Table 1 lists the materials used in in the tape casting procedure with their physical properties.

Table 1. Materials used in the anode supported composite cells.

Material	Function	d_{50} Particle Size (µm)	Supplier
NiO	Anode Layers (AFL and AS)	1- 2	Hart Materials, UK
10Sc1CeSZ	Electrolyte	0.8- 1	DKKK, Japan
10GDC	Barrier layer	0.6-1.4	Fuel Cell Materials, U.S.
LSCF	Cathode	0.9	Praxair, U.S.

For the anode substrate, the slurry consisted of 10ScCeSZ pre-calcined at 900ºC for 5 hours, with as-received NiO powder in a weight ratio of 65:35 (NiO:10ScCeSZ). Solvent (water), dispersant (Dispex, BASF), cermet powders and pore former (tapioca starch) were mixed together using spherical and cylindrical ZrO_2 beads, and homogenised at 120 rpm for 24 hours. The anode functional layer consisted of a 65:35 mixture of as-received NiO and as-received ScCeSZ powder, mixed together with the same solvent, and homogenised at 120 rpm for 24 hours. Binders, plasticisers I and II and antifoam were

added to each slurry and the mixture rolled for a further 12 h at 70 rpm. To eliminate any air bubbles, both slurries were filtered and de-gassed for 24 h, followed by a phase of 50 rpm slow-roll for 2 h to ensure a homogeneous mixture.

Table 2. Composition of anode layers.

Materials	Function	Composition (wt%)	
		AFL	AS
NiO	Electronic phase	35.8	35.8
ScCeSZ	Ionic phase	19.3	19.3
Tapioca starch	Pore former	-	1.5
BASF Dispex Ultra 4404®	Dispersant	1.0	1.0
Water	Solvent	35.4	29.9
Antifoam 204	Antifoam	0.2	0.2
PVA	Binder	4.1	5.4
PEG 200	Plasticiser I	2.7	3.45
Glycerol	Plasticiser II	1.4	3.45

The compositions for the electrolyte, barrier and composite layers are presented in Table 3. First, the solvent, dispersant, binder, anti-foam, and plasticiser were mixed together at 120 rpm for 24 hours. More binder, de-foamer, and the corresponding layer material powder were added and mixed for at least 4 hours at 120 rpm. The slurries were filtered and degassed for 1 hour to eliminate any gas bubbles.

Table 3. Composition of electrolyte, barrier and composite layers.

Materials	Function	Composition (wt%)		
		Barrier layer	Composite layer	Electrolyte
Water	Solvent	28	28	28
WB4101	Binder	19.3	19.3	19.3
DS001	Dispersant	2.0	2.0	2.0
DF002	Antifoam	0.4	0.4	0.4
PL005	Plasticiser	0.5	0.5	0.5
ScCeSZ	Ionic phase	-	24.9	49.8
GDC	Barrier layer	49.8	24.9	-

The GDC slurry was tape cast onto a thin polyester carrier film first, followed by the composite layer, then the electrolyte layer, and the AFL (Fig. 1). After tape casting, each single layer was dried in an oven at 70ºC. Finally, the AS was tape cast on top of the AFL and the green tape dried in an oven at 30ºC overnight. Cells were cut from the dried green tape using a hydraulic press and a circular die of diameter 40 mm. Cells were sintered at

1400ºC for four hours with an organic burnout stage at 550ºC, resulting in dense button half-cells with a diameter of 30 mm.

2.1 Cathode Ink Preparation

To prepare the cathode ink, LSCF (supplier Praxair) and GDC (supplier Fuel Cell Materials) were combined in a 50:50 wt% ratio. An ink vehicle (Fuel Cell Materials) was added to the powder to make an ink with a solid loading of 22.8 wt%. LSCF ink was made by mixing LSCF powder with the ink vehicle to receive a solid loading of 25.18 wt%. Both inks were homogenised using a triple roll mill (EXAKT).

2.2 Characterisation

The morphology of the cells was characterised by scanning electron microscopy (SEM) using a Hitachi table-top microscope TM3030Plus. Both cross-section and surface morphology micrographs were taken to examine the microstructure. Image analysis was used to determine the thickness of each layer and the particle size. Energy dispersive x-ray (EDX) images were taken at 15 kV and BSE mode to identify the elemental distribution throughout the cell. Particle size analysis after sintering was determined using ImageJ software. The density and porosity of the half cells were analysed by an AccuPyc II 1340 (Micromeritics) gas pycnometer using helium as the displacement medium. Three purges, followed by three readings for each sample were used to get average density and porosity values. AC impedance measurements were carried out with a Solartron 1470 E and 1455 FRA, sweeping from 0.01 Hz to 10 kHz at 0.7 V, 0.5V and at -0.001 A (near OCV) with an amplitude of 20 mV.

Table 4. Details of the differences in layers using the multi-layer manufacturing technique.

Name	GDC (µm)	Composite (µm)	Electrolyte (µm)	Total (µm)
Cell 333	7.0	7.0	7.5	21.5

Table 4 illustrates the tape casting process of each layer and the relative layer thickness. The label denotes the gap height of the doctor blade used when tape casting, for example, Cell 333 used a gap height of 3 µm for each layer. The AFL and AS layer thickness were approximately 30 µm and 500 µm, respectively.

The composite cells of Ni-ScCeSZ were fabricated into full cells with LSCF cathodes painted onto the GDC barrier layer, resulting in an active area of 2 cm^2, and sintered at 975ºC. The cells were placed in the testing rig, and heated at 5ºC/min to 800ºC, upon reaching which they were reduced overnight in hydrogen. Two cells underwent initial characterisation at 800ºC, with a 3:1 H_2:N_2 flow to the fuel electrode and air to the oxygen electrode.

3. Results

Fig. 2 presents the SEM micrograph of a cell after sintering at 1400ºC for 4 hours. The dense electrolyte and the gradual transition to the barrier layer can be clearly seen, with no cracks or delamination from the GDC barrier layer present after sintering, confirming the ability of this multi-layer method to produce robust cells.

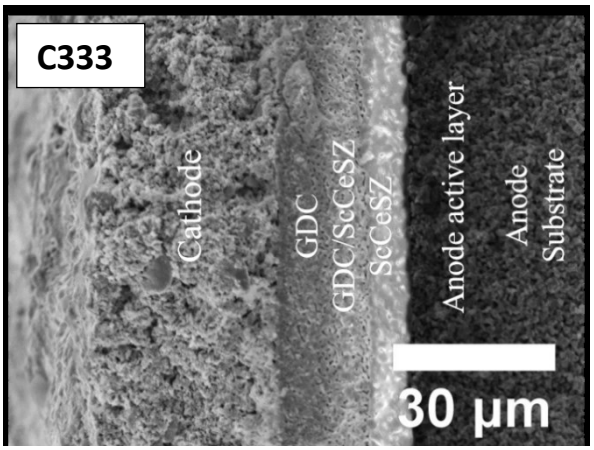

Fig. 2. SEM micrograph of the composite layer cross-section of Cell 333, after sintering for 4 hours at 1400ºC.

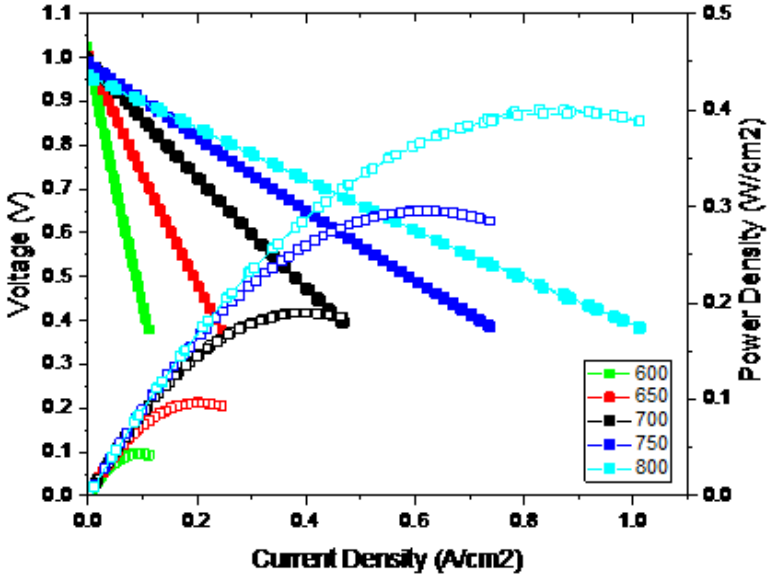

Fig. 3. Performance of Cell 333: Ni-ScCeSZ composite cell prepared by five-layer tape casting tested between 600 and 800ºC.

To investigate their potential as SOCs, the manufactured Ni-ScCeSZ cells were tested between 650 and 800ºC. Fig. 3. shows a polarisation curve of a Cell333 performance, which can be compared to Ni-ScCeSZ cells previously manufactured in our laboratory, with power densities of 0.39 Wcm^{-2} at 750ºC and Ni-YSZ cells with a power density of 0.53 Wcm^{-2} at 800ºC [17].

The area specific resistance (ASR) for the Ni-ScCeSZ cell tested at 700ºC was 1.29 Ωcm^2, and the ASR for Ni-ScCeSZ tested at 800ºC was 0.57 Ωcm^2. The results confirm that ScCeSZ cells tape cast in this novel five-layer technique are perfectly suitable for IT-SOFC applications.

Electrochemical impedance spectroscopy results in Table 5 reveal the resistivity of the whole cell and breaks this further down into electrochemical reactions (high frequency

contributions) and electrode reactions (low frequency contributions). The equivalent circuit used for fitting EIS data to calculate resistances was Rs-R1Q1-R2Q2, where Rs was the ohmic resistance and RQ was a parallel circuit consisting of a resistor and constant phase element, similar to models used by other researchers [18,19]. The impedance results revealed the lowest polarisation resistance for the Ni-ScCeSZ cell at 800ºC (0.16 Ωcm^2).

The ASR and internal resistance values are slightly higher than state of the art cells, however, this work aimed to prove that the method of adding another layer to the cell via tape casting, is a legitimate approach in cell manufacturing to minimise cost and maximise output. Further work will ensue to optimise this process to reduce resistances and increase cell performance.

Table 5. Cell resistances close to OCV for Ni-ScCeSZ composite cells at 700ºC and 800ºC.

T (ºC)	R_s (Ωcm^2)	$Q_1(Fcm^{-1})$	n	R_1 (Ωcm^2)	$Q_2(Fcm^{-1})$	n	R_2 (Ωcm^2)	R_p (Ωcm^2)
NiSSZ 700	0.69	0.012	0.59	0.58	0.47	0.99	0.093	0.67
NiSSZ 800	0.42	0.0042	0.91	0.081	0.97	0.66	0.078	0.16

3.3 Conclusions

The addition of an ScCeSZ-GDC composite layer in the tape casting fabrication of Ni-ScCeSZ SOCs has been proven. It has been possible to manufacture these layers, which successfully adhere to the electrolyte and GDC barrier layer for LSCF cathode cells, without delamination of the GDC barrier layer upon sintering.
After the functionality of the layer was established, these cells were electrochemically tested in a hydrogen/nitrogen mix to yield power densities of 0.40 Wcm^{-2} at 800 ºC. This can be compared with cells previously manufactured: Ni-ScCeSZ resulting in 0.39 Wcm^{-2} at 750ºC and Ni-YSZ cells with a power density of 0.53 Wcm^{-2} at 800ºC.

https://doi.org/10.5281/zenodo.4557413

References

[1] C. Graves, S.D. Ebbesen, S.H. Jensen, S.B. Simonsen, M.B. Mogensen, Eliminating degradation in solid oxide electrochemical cells by reversible operation, Nat. Mater. 14 (2014) 239–244. doi:10.1038/nmat4165.

[2] Z. Jiao, N. Takagi, N. Shikazono, N. Kasagi, Study on local morphological changes of nickel in solid oxide fuel cell anode using porous Ni pellet electrode, J. Power Sources. 196 (2011) 1019–1029. doi:10.1016/j.jpowsour.2010.08.047.

[3] V.Y. Podhurs'ka, Structural Changes in ScCeSZ-NiO Ceramics In a High-Temperature Hydrogen Environment, Mater. Sci. 46 (2010) 129–131. doi:10.1007/s11003-010-9307-z.

[4] K.S. Blinn, H. Abernathy, X. Li, M. Liu, L.A. Bottomley, M. Liu, Raman Spectroscopic Monitoring of Carbon Deposition on Hydrocarbon-Fed Solid Oxide Fuel Cell Anodes, Energy Environ. Sci. (2012) 7913–7917. doi:10.1039/C2EE21499G.

[5] S. Mcintosh, R.J. Gorte, Direct Hydrocarbon Solid Oxide Fuel Cells, Chem. Rev. 104 (2004) 4845–4846. doi:10.1021/cr020725g.

[6] V.A. Sadykov, N. V Mezentseva, R. V Bunina, G.M. Alikina, A.I. Lukashevich, V.I. Zaikovskii, O.F. Bobrenok, J. Irvine, O.D. Vasylyev, A.L. Smirnova, Design of Anode Materials for IT SOFC: Effect of Complex Oxide Promoters and Pt Group Metals on Activity and Stability in Methane Steam Reforming of Ni/YSZ (ScSZ) Cermets, J. Fuel Cell Sci. Technol. 7 (2010) 6–11. doi:10.1115/1.3117255.

[7] T. Ishihara, T. Shibayama, M. Honda, H. Nishiguchi, Y. Takita, Intermediate Temperature Solid Oxide Fuel Cells Using LaGaO3 Electrolyte, J. Electrochem. Soc. 147 (2000) 1332–1337. doi:S0013-4651(99)09-056-4.

[8] D.J.L. Brett, A. Atkinson, N.P. Brandon, S.J. Skinner, Intermediate temperature solid oxide fuel cells, Chem. Soc. Rev. 37 (2008) 1568–1578. doi:10.1039/b612060c.

[9] P. Coddet, M.-L. Amany, J. Vulliet, A. Caillard, A.-L. Thomann, YSZ/GDC bilayer and gradient barrier layers deposited by reactive magnetron sputtering for solid oxide cells, Surf. Coatings Technol. 357 (2019) 103–113. doi:10.1016/J.SURFCOAT.2018.09.085.

[10] N.M. Mcdonald, The Manufacturing and Testing of Anode Supported Ni10Sc1CeSZ SOFCs For Intermediate Temperature Operation, 2017.

[11] A.S. Mehranjani, D.J. Cumming, D.C. Sinclair, R.H. Rothman, Low-temperature co-sintering for fabrication of zirconia/ceria bi-layer electrolyte via tape casting using a Fe2O3 sintering aid, J. Eur. Ceram. Soc. 37 (2017) 3981–3993. doi:10.1016/J.JEURCERAMSOC.2017.05.018.

[12] A. Atkinson, A. Selçuk, Residual stress and fracture of laminated ceramic membranes, Acta Mater. 47 (1999) 867–874. doi:10.1016/S1359-6454(98)00412-1.

[13] N.H. Menzler, F. Tietz, S. Uhlenbruck, H. Peter Buchkremer, D. Stöver, Materials and manufacturing technologies for solid oxide fuel cells, J. Mater. Sci. 45 (2010) 3109–3135. doi:10.1007/s10853-010-4279-9.

[14] J.-H. Song, M.G. Jung, H.W. Park, H.-T. Lim, The Effect of Fabrication Conditions for GDC Buffer Layer on Electrochemical Performance of Solid Oxide Fuel Cells, Nano-Micro Lett. 5 (2013) 151–158. doi:10.5101/nml.v5i3.p151-158.

[15] N.H. Menzler, W. Schafbauer, R. Mücke, R. Kauert, O. Büchler, Advanced Manufacturing Technology for Solid Oxide Fuel Cells, in: N.P. Bansal, P. Singh, S. Widjaja, D. Singh (Eds.), Adv. Solid Oxide Fuel Cells VII, John Wiley & Sons Ltd (2011) 147–160. doi:10.1002/9781118095249.ch14.

[16] L. Blum, L.G.J. De Haart, J. Malzbender, N.H. Menzler, J. Remmel, R. Steinberger-Wilckens, Recent results in Jülich solid oxide fuel cell technology development, J. Power Sources. 241 (2013) 477–485. doi:10.1016/j.jpowsour.2013.04.110.

[17] N. Arifin, T. Button, R. Steinberger-Wilckens, Carbon-Tolerant Ni/ScCeSZ Via Aqueous Tape Casting for IT-SOFCs, in: ECS Trans., Electrochemical Society Inc (2017) 1417–1426.

[18] Y.-S. Yoo, M. Choi, J.-H. Hwang, H.-N. Im, B. Singh, S.-J. Song, La2NiO 4 as oxygen electrode in reversible solid oxide cells, Ceram. Int. 41 (2015) 6448–6454. doi:10.1016/j.ceramint.2015.01.083.

[19] E.-C. Shin, P.-A. Ahn, H.-H. Seo, D.T. Nguyen, S.-D. Kim, S.-K. Woo, J.H. Yu, J.-S. Lee, Pinning-down polarization losses and electrode kinetics in cermet-supported LSM solid oxide cells in reversible operation, Solid State Ionics. 277 (2015) 1–10. doi:10.1016/J.SSI.2015.04.009.

Keywords: EFCF2020, SOx
Session B03: Manufacturing Processes

B0313

Large cell, short-term stability testing of Au-Mo-modified Ni/GDC for solid oxide co-electrolysis

Nelson Thambiraj (1), Ivar Warnhus (1), Crina Ilea (1), Arild Vik (1), Charalampos Neofytidis (2), Evangelia Ioannidou(2), Fotios Zaravelis (2), Dimitris K. Niakolas (2), Vaibhav Vibhu (3), Izaak C. Vinke (3)

(1) Prototech AS, Fantoftvegen 38, 5072 Bergen/Norway

(2) Foundation for Research and Technology, Institute of Chemical Engineering Sciences, FORTH/ICE-HT, GR-26504 Patras/Greece

(3) Institute of Energy and Climate Research, IEK-9: Fundamental Electrochemistry, Forschungszentrum Jülich GmbH, 52425 Jülich/Germany

Contact authors: www.EFCF.com/ContactRequest

Abstract

Production of H_2 by electrochemical conversion of H_2O, through electrolysis can be achieved without expensive catalysts using Solid Oxide Electrolysis cells (SOECs). SOEC shows great dynamics to become commercially competitive against other electrolysis technologies (AEL, PEMEL), which are better established but more expensive and less efficient. On the other hand, SOECs are less mature and have issues regarding performance and durability that are currently important issues that need to be addressed. Indicatively, the latest State-of-the-Art (SoA) cells with NiO/YSZ and LSM as cathode and anode electrodes, respectively, show that the performance decreases for the H_2O electrolysis reaction, whereas for the H_2O/ CO_2 co-electrolysis process, the situation is even worse and the technology level is much behind than the commercialization thresholds.

In this respect, SElySOs project focuses on understanding the degradation and lifetime fundamentals on both SOFC electrodes. New electrode materials are developed, and the degradation mechanisms are investigated during the project. Overall, the target is to improve the stability, minimize the degradation and achieve better performance during H_2O electrolysis and CO_2 electrolysis. This paper presents short-term stability testing of large ESCs comprising Au-Mo-modified NiO/GDC compared with unmodified Ni-GDC as fuel electrode and LSCF as air electrode, under steam electrolysis operating conditions. The cells are tested in short stack configuration with metallic interconnects and sealing. The two stacks are operated with 0.5 A/ cm^2 at 835^{o}C. The results show a positive effect of the Au-Mo modified cell stack on the degradation rates during the stability tests. The observed degradation rate for the 3Au-3Mo-modified fuel electrode stack was 300 mV/kh as compared to 700 mV/kh with the non-modified Ni/GDC stack.

https://doi.org/10.5281/zenodo.4518874

Introduction

Green hydrogen is a strong candidate for a sustainable fuel. While many energy sources can be used to produce hydrogen, water electrolysis is one of the possible ways to transform renewable and other non-fossil sources of energy into hydrogen. High temperature electrolysis of steam (HTE) consumes lesser electrical energy than electrolysis at low temperature due to its thermodynamic and electrochemical kinetic conditions. Reversely operated Solid Oxide Fuel Cell (SOFC) performs as a Solid Oxide Electrolysis Cell (SOEC) by which HTE is achievable. Extensive SOFC research has demonstrated that low electrode over voltages can be achieved even for higher current densities. [1-3].

Degradation is identified as one of the important issues of SOEC. Literature studies report that lowest long-term degradation of SOEC under practical operation as 1.7%/1000h during 3600h at 1 A/cm² [4]. This accounts for twice the degradation of similar cells under fuel cell operation. In order to reduce the degradation, polarization and degradation mechanisms must be clearly identified. This will help to optimize the cell architecture by modifying or replacing one or both the electrodes with alternative materials.

The prime objective of SElySOs is to develop more efficient electrodes and understand the processes that causes degradation on both SOEC electrodes, by combining experiments with theoretical modelling over an extended range of operating conditions. Moreover, the technical goal of the project is to identify the key design parameters and acquire the necessary knowledge to guide the development of new SOECs that are less prone to degradation with improved performance and stability.

The paper is aiming at presenting the comparative electrochemical performance of H_2O electrolysis process in SOEC stack using the Ni/GDC electrodes modified by small amount of gold and molybdenum [5].

1. Experiments

1.1 Cell preparation

75mm x 75mm, 90µm 3YSZ electrolytes from Kerafol were first screen printed with a $Ce_{0.8}Gd_{0.2}O_{2-\delta}$ (GDC) layer (65mm x 65mm, thickness ~ 3-4 µm) on the oxygen electrode side and sintered at 1350°C for 1h under air. Then, the fuel electrode was deposited by means of the screen printing method, se reference for details [5]. After the screen printing of the fuel electrode, the cells were calcined at 1150ºC/2 h. The preparation of the ternary 3wt.% Au – 3wt.% Mo-NiO/GDC powder was made with the Deposition – Co Precipitation (D.CP.) method, as reported in a previous study [5]. After that, a layer of $La_{0.58}Sr_{0.4}Co_{0.2}Fe_{0.8}O_{3-\delta}$ (LSCF) as oxygen electrode (63mm x 63mm, thickness ~ 30µm) was screen printed on the GDC//3YSZ and sintered at 1080 °C for 3 h under air. Finally, additional layers for current collection and electrical contact, Nickel on the fuel side and LSM on the oxygen side were also added by screen printed. The active area of the cells was 42.25 cm².

https://doi.org/10.5281/zenodo.4518874

1.2 Experimental Set-up

The stack design used in the project was developed with special emphasis on electrolysis operation. Interconnects were formed by stamping 0.3mm AISI 441 Co-Ce pre-coated ferritic stainless steel purchased from Sandvik, Norway. The corrugated channels in the interconnect were formed with parallel flow directions (Co-flow). Nickel mesh of thickness 0.25 mm was used in the fuel side to improve the current collection and adjust the thickness.

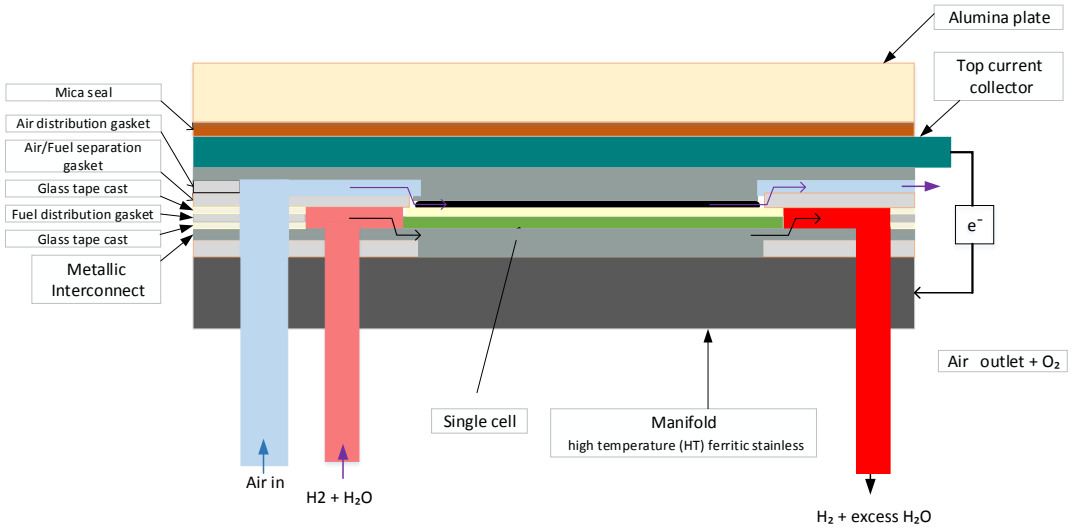

Figure 1: Cross sectional details of SElySOs short stack test setup with single cell.

The cross-section details of the SElySOs stack design is shown in Figure 1. It has tubes for inlet and outlet of fuel as well as inlet for air sweep. The sequence of a single cell short stack building is shown in the Figure 2. Glass tape (Keraglas from Kerafol) was used to prevent gas leakage in the stack and towards the manifold.

The voltage measurements were performed using platinum wires connected to the interconnects, thus, the resistance measured in the current-voltage (I-V) curves consists of repeatable unit which in SOFC mode includes the following elements: electrolyte resistance, fuel electrode resistance, dilution of fuel with produced H_2O, gas diffusion resistance, air electrode resistance and horizontal current collection through the interconnect. The different elements in the resistance cannot be separated in DC experiments, thus several experiments were required to optimize the performance.

The stacks were heated as per the sealing glass firing schedule. After completing the firing schedule, the stack with the modified electrodes was reduced at 845°C and the stack with the non-modified electrodes was reduced at 835°C. After reduction, the stack temperature was reduced to 835°C. The reason is the glass sealing tape that is designed to operate below 840°C.

https://doi.org/10.5281/zenodo.4518874

Figure 2: Sequence of a single cell stack assembly.

2. Results

2.1 Stack with Au-Mo-Ni/GDC fuel electrode

The stack with modified electrodes was operated at 830°C for 430 hours.

The initial I-V curve was recorded during fuel cell mode with fuel flow consisting of 90:10% of H_2 and N_2. Later the stack was operated with 50:50% of H_2 and H_2O. The I-V curves are recorded during fuel cell mode and electrolysis mode. The ASR values are shown in the Figure 6.

The long-term stack degradation is shown in Figure 4. The initial stack degradation measured for 250 hours was 300 mV/kh at a fuel utilisation of 37%. Later the stack was operated at higher fuel utilisation of 56% and experimented to operate without CO_2 supply first and later without the N_2 dilution of the fuel.

https://doi.org/10.5281/zenodo.4518874

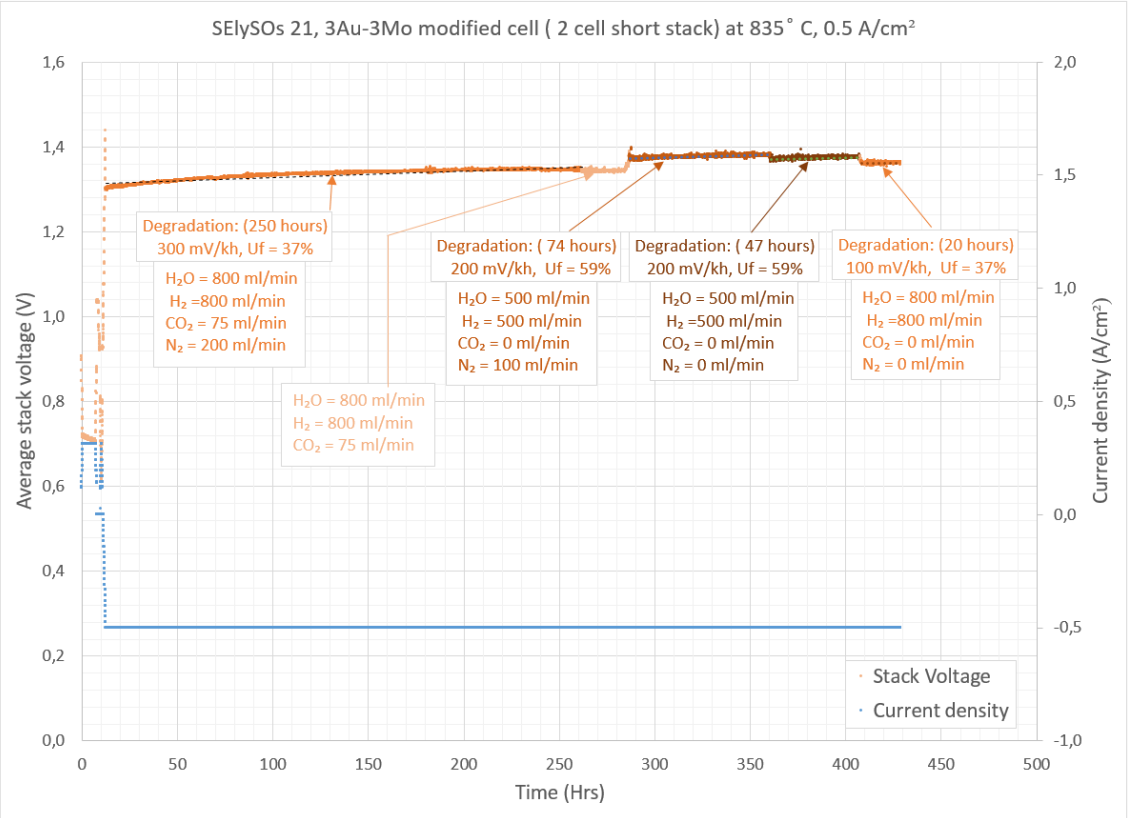

Figure 4: The stack degradation at various fuel utilization under constant current density.

Mass spectroscopy (MS) was used for analysis the exhaust from the stack. During steady state electrolysis operation, a hydrogen concentration of the dried gas of of 99% was reached, see Figure 5.

Figure 5: Variation of product composition obtained from Mass spectroscopy

https://doi.org/10.5281/zenodo.4518874

2.1 Stack with non-modified Ni/GDC electrode

The 2 cells short stack with non-modified cells (NiO/GDC) is still under operation. The stack has been operated for 200 hours till now, mainly under water electrolysis. The I-V curve in Figure 6 shows the comparison between the modified stack and non-modified stack. We can see that the unmodified stack has a slightly higher resistance when compared to modified stack both during fuel cell mode and also during H_2O electrolysis mode.

Figure 7 shows the operational history of the unmodified stack. Operated initially for about 20 hrs. in fuel cell mode at a current density of 0,3 A/cm^2 and after that the stack is operated in H_2O electrolysis mode. The observed stack degradation was 700mV/kh.

Discussion

Figure 8 shows the degradation comparative data between the stack built using cells with Au-Mo-Ni/GDC electrode and non-modified NiO/GDC electrode. We can observe that the initial degradation for the modified stack, refer Figure 4, is 300 mV/kh whereas at the similar stage for the unmodified stack the degradation is higher i.e., 700 mV/kh. This degradation can origin for numerous of different processes, however, this is a clear indication that the degradation of the Ni/GDC electrode can be reduced through Au-Mo-modification [5].

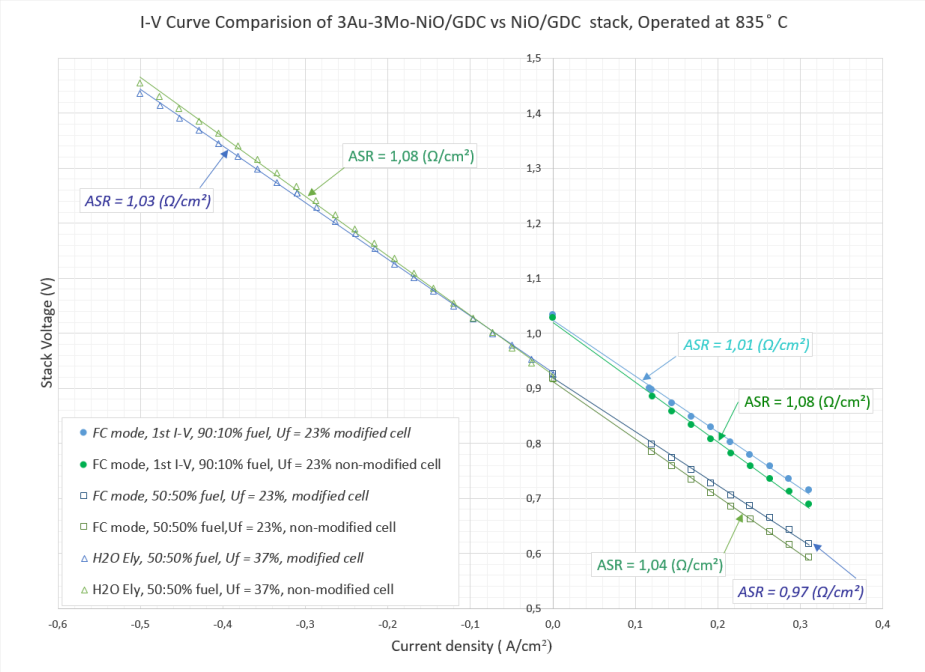

Figure 6: The variation of I-V curve with and without modified fuel electrode stack.

https://doi.org/10.5281/zenodo.4518874

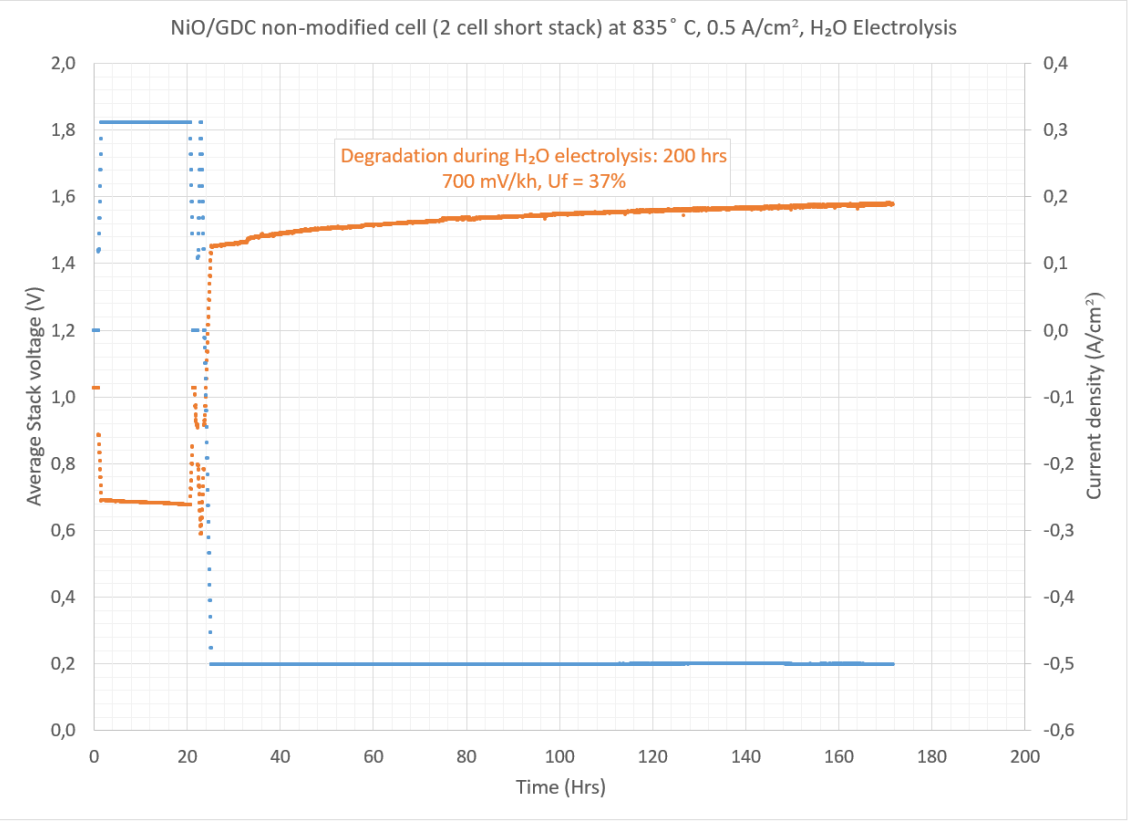

Figure 7: Degradation curve of non-modified electrode stack.

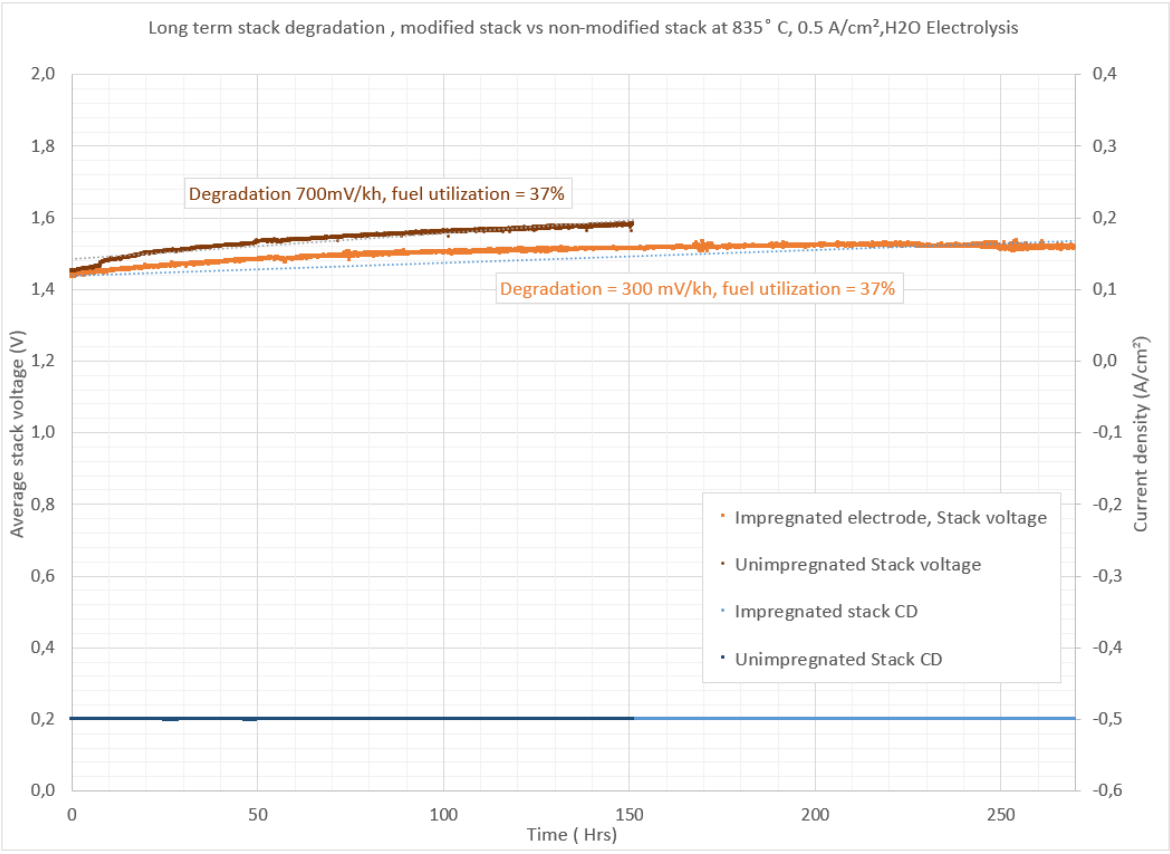

Figure 8: The degradation curves of modified and non-modified Ni/GDC electrode stacks.

https://doi.org/10.5281/zenodo.4518874

Acknowledgments

The research leading to these results has received funding from Fuel Cells and Hydrogen 2 Joint Undertaking under the project SElySOs with Grant Agreement No: 671481. This Joint Undertaking receives support from the European Union's Horizon 2020 Research and Innovation Programme with partners from Greece, Germany, Czech Republic, France, and Norway.

References

[1] Do¨nitz W, Dietrich G, Erdle E, Streicher R. Electrochemical high temperature technology for hydrogen production or direct electricity generation. Int J Hydrogen Energy 1988; 13(5):283–7.

[2] Erdle E, Do¨nitz W, Schamm R, Koch A. Reversibility and polarization behaviour of high temperature solid oxide electrochemical cells. Int J Hydrogen Energy 1992;17(10): 817–9.

[3] Herring JS, O'brien JE, Stoots CM, Hawkes GL, Hartvigsen JJ, Shahnam M. Progress in high-temperature electrolysis for hydrogen production using planar SOFC technology. Int J Hydrogen Energy 2007;32:440–50

[4] Annabelle Brisse, Josef Schefold, "High Temperature Electrolysis of EIFER, Main Achievements at Cell and Stack Level." Energy Procedia, Volume 29, 2012, pp. 55-63.

[5] Neofytidis, C.; Ioannidou, E.; Sygellou, L.; Kollia, M.; Niakolas, D.K. Affecting the H_2O electrolysis process in SOECs through modification of NiO/GDC; experimental case of Au-Mo-Ni synergy. *Journal of Catalysis* **2019**, *373*, 260-275

Keywords: EFCF 2020, SOx
Session B03: Manufacturing Processes

https://doi.org/10.5281/zenodo.4518874

B0317

Co- and Ni- free oxygen electrode performance improvement by electrode/electrolyte interface tuning

Claire Ferchaud, Frans van Berkel, Loek Berkveld, Mark Sillessen, Jakobert Veldhuis, Erik Schuring
TNO
Postbus 15 1755 ZG Petten/The Netherlands

Contact authors: www.EFCF.com/ContactRequest

Abstract

One of the present challenges for Solid Oxide Cells (SOC) developers is to produce durable and high performance cell units for high temperature electrolysis applications, utilizing cost efficient raw materials with low recycling costs to reach a large scale industrialization. Nickel and cobalt, which are state-of-the-art compounds in the manufacturing of SOC electrodes, bring critical concerns regarding the need of high conditioning and recycling costs related to their carcinogenic properties. In addition, cobalt is recognized since 2017 as Critical Raw Materials (CRM) for the EU community, due to the high economical risk associated to its supply within Europe (55% of the world's cobalt being sourced from Central Africa). Use of Co- and Ni- free electrode materials would provide a significant reduction of use of CRM in European SOC manufacturing, and offers SOC cell and stack manufacturers the benefit of a more environmental-friendly and lower cost manufacturing process and the potential of using recycled materials from previous manufacturing.

To this end, TNO has undertaken to develop a novel Co- and Ni-free oxygen electrode design based on the (La,Ca,Sr)FeO_3 perovskite class of materials. However the removal of nickel and cobalt in the oxygen electrode tends to increase the overpotential of the electrode. Taking into account this last drawback, TNO aims to optimize the performance of this new Co- and Ni-free compounds by microstructural improvement in terms of particle size, porosity and surface roughness. In addition, a novel electrode architecture is proposed by creating a patterned electrode/electrolyte interface, thus enhancing the triple phase boundary density between electrolyte and oxygen electrode. This novel concept is envisaged to improve the electrode performance and to prevent electrode delamination during SOC operations. A higher triple phase boundary density contributes to lower the local partial oxygen pressure between electrolyte and oxygen electrode, known as critical degradation phenomena of the oxygen electrode at high current density under electrolysis conditions.

The latest development of the novel Co- and Ni- free oxygen electrode design developed at TNO, within the FCHJU NewSOC project will be presented during the conference.

hhttps://doi.org/10.5281/zenodo.4792269

1. Introduction

The realization of a cost competitive integration of Solid Oxide Electrolyzer (SOE) in industrial scale applications demands a decrease in stack cost [1]. The reduction in stack cost can be realized by bringing down manufacturing process costs and decreasing the use of both high cost raw materials and/or critical raw material (CRM). Nickel and cobalt, state-of-the-art compounds in the Solid Oxide Cell (SOC) manufacturing, require high conditioning and recycling costs related to their carcinogenic properties. In addition, cobalt is considered as CRM by the EU community since 2017 [2], due to the high economical risk associated to its supply within Europe (55% of the world's cobalt being sourced from Central Africa). Though the amount of cobalt required within the SOE technology is limited (approximately <0.04 w% in stack), it is especially the huge demand for cobalt in other applications, like batteries for electrical vehicles [3], that makes the supply of cobalt critical. The research presented in this paper aims at reducing the use of cobalt and nickel in the SOC manufacturing, by exploring low cost Co- and Ni-free oxygen electrode materials, aiming towards competitive performance and lifetime for SOE applications.

A-site substituted perovskite-type lanthanum ferrites (La,Ca,Sr)FeO_3 have been reported frequently to be of interest as oxygen electrode for Solid Oxide Cells [4-26]. The main reported benefits of this class of material are a better match of coefficients of thermal expansion with zirconia-based electrolyte [4, 10, 19, 22, 24, 26] and relatively low reactivity with zirconia [6,8,12,16,19,21]. The claimed low reactivity of (La,Sr)FeO_3 (LSF) and (La,Ca)FeO_3 (LCF) materials with the zirconia electrolyte potentially enables the direct deposition on the electrolyte without the need for a ceria barrier layer [8,21]. This is in contrast with the state-of-the-art Co- and Ni-containing materials, where a ceria barrier layer is required in order to prevent chemical interaction between oxygen electrode and zirconia electrolyte.

This paper presents the first step in the development towards high performance and robust lanthanum ferrite based oxygen electrodes. The comparison in reactivity and electrochemical performance between lanthanum ferrites deposited directly on the zirconia electrolyte or in combination with a ceria barrier layer forms the subject of this study.

2. Scientific Approach

The performance of three compositions of lanthanum ferrite oxygen electrodes have been examined with respect to electrode microstructure, chemical compatibility with the electrolyte and electrochemical performance. Table 1 shows the materials being used in this study. LSCF is being used as reference Co-containing oxygen electrode material. CGO20 was selected as porous interfacial layer for this study. TZ3Y, commonly used as high strength electrolyte material in electrolyte supported cells, is the electrolyte material of choice.

Table 1. Compositions of the different cell components

Oxygen electrode	$(La_{0.6}Sr_{0.4})_{0.99}Co_{0.2}Fe_{0.8}O_{3-\delta}$ (LSCF) $La_{0.8}Sr_{0.2}FeO_{3-\delta}$ (LSF82) $La_{0.8}Ca_{0.2}FeO_{3-\delta}$ (LCF82) $La_{0.6}Sr_{0.4}FeO_{3-\delta}$ (LSF64)
Barrier layer	$Ce_{0.8}Gd_{0.2}O_{2-\delta}$ (CGO20)
Electrolyte	97%mol ZrO_2-3%mol Y_2O_3 (TZ3Y)

hhttps://doi.org/10.5281/zenodo.4792269

Symmetrical cells have been selected as cell configuration in order to get information on the electrochemical performance at zero current by means of electrochemical impedance spectroscopy (EIS). The ohmic resistance indicates the degree of electrode coverage on the electrolyte surface, the presence of spreading resistance and/or presence of poor conducting interface reaction products. The polarization resistance gives a good indication of the electrocatalytic activity of the different electrode compositions. The microstructure and presence of chemical interaction between the layers will be examined by SEM and EDX analysis of the fracture surface of the symmetrical cells.

3. Experiments

3.1 Preparation of the symmetrical cell

Commercial powders were used for the preparation of the symmetrical cells. The yttria-doped zirconia at 3%mol (TZ3Y) was provided from Tosoh. The gadolinium doped ceria $Ce_{0.8}Gd_{0.2}O_{2-\delta}$ (CGO20) and the air electrode materials $(La_{0.6}Sr_{0.4})_{0.99}Co_{0.2}Fe_{0.8}O_{3-\delta}$ (LSCF), $La_{0.6}Sr_{0.4}FeO_{3-\delta}$ (LSF64), $La_{0.8}Sr_{0.2}FeO_{3-\delta}$ (LSF82) and $La_{0.8}Ca_{0.2}FeO_{3-\delta}$ (LCF82) were supplied from Cerpotech. The oxygen electrode materials were manufactured with similar particle size distribution with a D_{50} = 0.9-1.2 μm. TZ3Y electrolyte supports, with 90 ± 1 μm thickness of diameter of 20.09 ± 0.03 mm, were produced by tape casting process of organic based slurries prepared with the commercial TZ3Y powder from Tosoh, and sintered at 1400°C for 1h. Subsequently, CGO20 and air electrode materials pastes were prepared on organic based recipe for deposit by screen-printing process. One layer of CGO20 was applied on both side of the electrolyte supports, with a diameter of 19.5 mm, and sintered to the temperature of 1300°C for 1h. Oxygen electrodes (LSCF, LSF82, LCF82 and LSF64) were subsequently produced two printed layers and sintered at 1100°C for 1h. Table 2 summarizes the different configurations of symmetrical cells prepared.

Table 2. Symmetrical cells configurations

Air electrode	TZ3Y electrolyte without barrier layer	TZ3Y electrolyte with porous CGO20 barrier layer
LSCF	A1	A2
LSF82	B1	B2
LCF82	C1	C2
LSF64	D1	D2

3.2 Materials morphology and composition characterization

Microstructural and elementary characterization of the symmetrical cells were performed by scanning electron microscopy (SEM), back-scattering electrons microscopy (BSE) and energy-dispersive X-ray spectroscopy (EDX) with a Hitachi SU70 equipment with Oxford Aztec 3.1 hard and software for EDX analysis. The microstructural characterization by SEM and BSE of the oxygen electrode surfaces and cross section of the symmetrical cells were conducted with 5kV. Compositional analysis made by EDX were performed at 15kV. Prior to EDX analysis the samples were coated with a 6nm thin Pt-Pd conductive layer for optimized EDX analysis. The analyses results are corrected for this layer.Thickness and porosity measurements were performed by image analysis with the ImageJ 1.52a software [27].

3.3 Electrochemical characterization

The electrochemical characterization of the symmetrical cells was performed by impedance (EIS) measurements with a ProboStat (Norecs) equipment, by conventional four-point DC technique. Gold grids of 100 mesh with thickness of 0.4 mm and a diameter of 20mm were

used. EIS measurements were conducted with an Ivium Vertex potentiostat, at open-circuit voltage (OCV) within a frequency range from 1MHz to 0.1Hz and an amplitude of 10mV, between 900 and 550°C. Measurement were performed under air conditions with a flow of 100ml/min. EIS spectra fitting was performed with the ZView software with two time constant equivalent circuit for high frequencies and low frequencies as shown in figure 1.

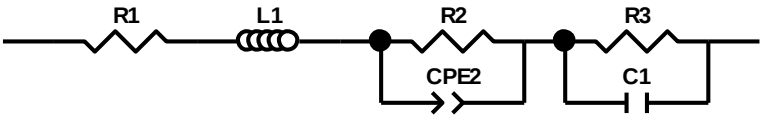

Figure 1: Equivalent circuit used for EIS spectra fitting

4. Results

4.1 Microstructure characterization and reactivity

An overview of the microstructural and compositional characterization of the symmetrical cells manufactured without (TZ3Y-air electrode) and with a ceria barrier layer (TZ3Y-CGO20-air electrode) are respectively presented in Table 1 and Table 2. In addition, Table 3 presents the layer thicknesses of the electrolyte, porous ceria layer and oxygen electrode obtained from the SEM imaging of the symmetrical cells prepared with barrier layer.

Table 1: Microstructural and compositional characterization of interface electrolyte-oxygen electrode for the symmetrical cells manufactured without ceria barrier layer (TZ3Y-air electrode)

Sample	Cross section imaging	Elementary analysis
A1	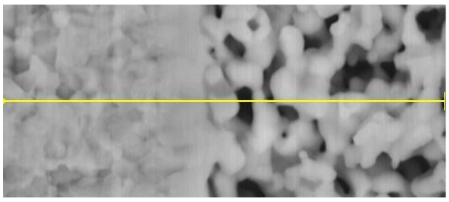	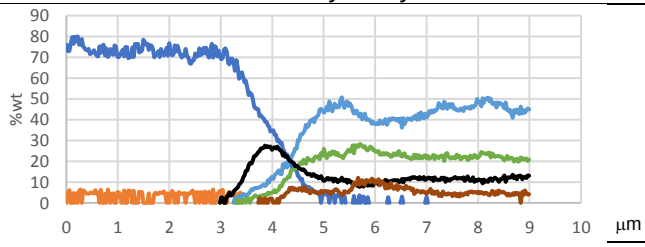
B1	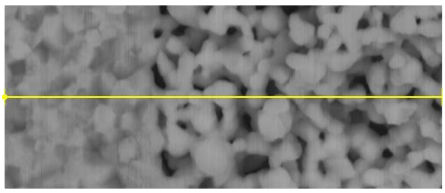	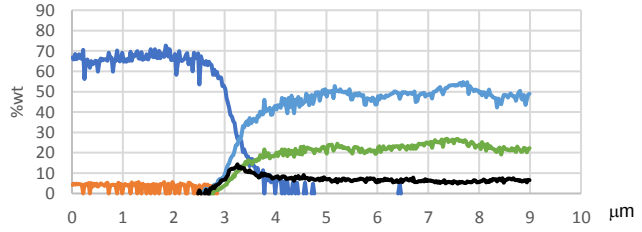
C1	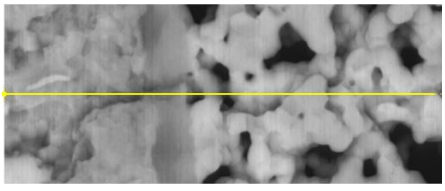	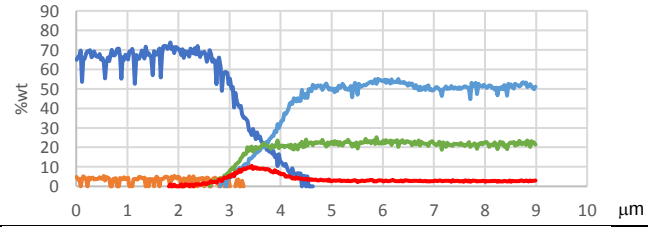
D1	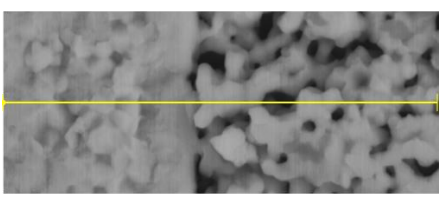	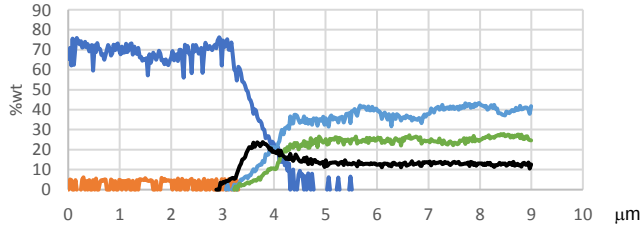

hhttps://doi.org/10.5281/zenodo.4792269

Table 2: Microstructural and compositional characterization of interface electrolyte-oxygen electrode for the symmetrical cells manufactured with a ceria barrier layer (TZ3Y-CGO20-air electrode)

Sample	Cross section imaging	Elementary analysis
A2	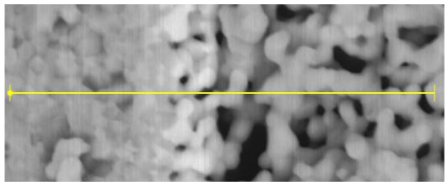	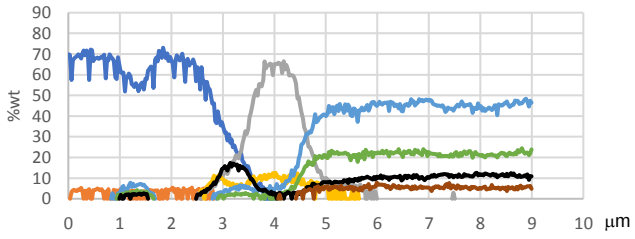
B2	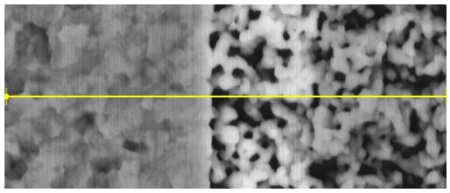	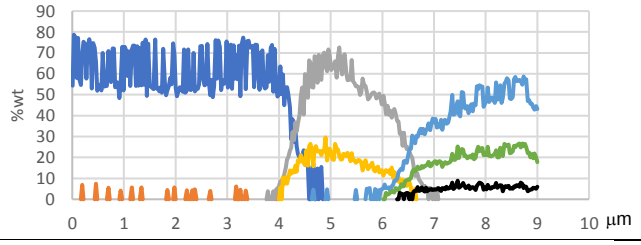
C2	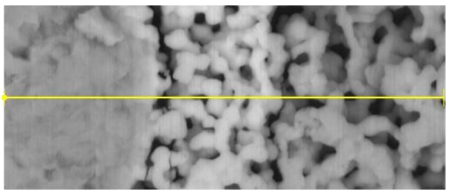	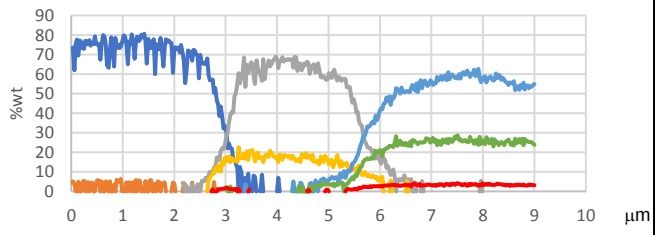
D2	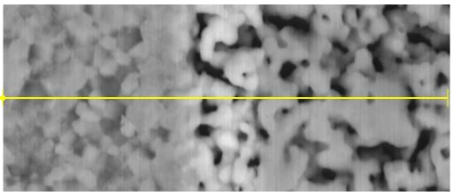	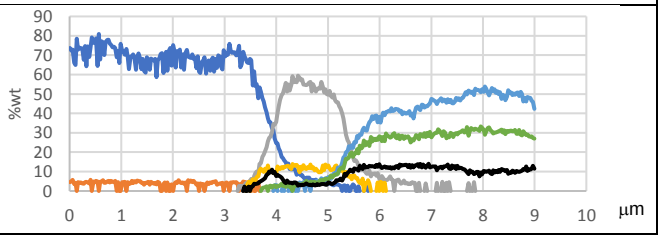

Table 3: Electrolyte, barrier layer and oxygen electrode layer thicknesses measured from SEM imaging analysis for the symmetrical cells manufactured with CGO20 barrier layer

Sample	TZ3Y electrolyte	CGO20 barrier layer	Air oxygen electrode
LSCF (A2)	89.0 ± 0.3 µm	1.37 ± 0.1 µm	19.3 ± 0.2 µm
LSF82 (B2)	88.5 ± 0.3 µm	2.30 ± 0.07 µm	21.3 ± 0.1 µm
LCF82 (C2)	90.5 ± 0.3 µm	2.63 ± 0.05 µm	10.4 ± 0.1 µm
LSF64 (D2)	89.7 ± 0.3 µm	1.64 ± 0.08 µm	8.5 ± 0.2 µm

Microstructural characterization

The microstructural characterization of the symmetrical cells prepared without ceria layer (Table 1) shows an overall good adhesion of the oxygen electrode at the surface of the electrolyte. For the symmetrical cells prepared with ceria layer (Table 2), similar observations can be made for the LSF64 and LSCF compositions, while weaker adhesion is found at CGO20 layer-electrolyte interface for LSF82 and LCF82. For all samples, the ceria barrier layer presents a porous microstructure, but layer thickness variations are observed between the samples (Table 3). A thinner ceria barrier layer (1.4-1.6 µm) is observed for the LSF64 and LSCF compositions compared the ones observed for LSF82 and LFC82 (2.3-2.6 µm). The different oxygen electrodes (Table 3) show variations in layer thickness between 8 and

20 μm. In addition, slight difference of grains coalescence and porosity can be remarked in Table 1 and Table 2, between the different oxygen electrode compositions. The symmetrical cells being manufactured with the same paste manufacturing protocol, screen-printing process (2 layers deposition) and sintering process (1100°C/1h for oxygen), an effect of the initial oxygen electrode material composition on the microstructure is certainly assumed. In later work, optimization of the screen-printing process (adjustment of layer deposition number) and sintering temperature program are required to achieve optimized electrode microstructure (porosity, grains coalescence, layer thickness) for each electrode composition.

Compositional characterization

The compositional characterization of the electrode-electrolyte interface of the symmetrical cells manufactured without ceria barrier layer (Table 1), shows formation of interdiffusion products for every sample. For the Sr-containing electrodes (LSCF, LSF82 and LSF64), a Sr migration is observed at the interface with a doubling of Sr weight percentage compared to the air electrode composition, and Zr diffusion is found over 1-3 μm within the electrode as previously seen in the study of Simner *et. al* [6]. For LSCF and LSF82, this observation is in agreement with the literature where the reactivity between LSCF and YSZ is known above a temperature of 1000°C [13], and above 950°C between YSZ and LSF82 [s]. The formation of $SrZrO_3$ and $La_2Zr_2O_7$ for each composition are assumed to occur respectively at the interface and within the oxygen electrode as seen in literature [5,11], but further compositional investigation are currently conducted as other interdiffusion products (e.g. $Sr_2Fe_2O_5$) are also mentioned in literature [6]. For LCF82, no Zr incorporation is observed in the electrode layer as previously observed by Anderson *et al.* [6], but unlike claimed in literature with use of 8YSZ, Ca and Fe migration takes place at the TZ3Y-LCF82 interface with 3 to 4 times higher concentration of Ca for a sintering temperature of 1100°C. Additional compositional characterization of the interdiffusion product is currently under investigation.

For the TZ3Y-CG20-air electrode symmetrical cell samples (Table 2), the presence of the CGO20 barrier layer although not dense, reduces and in the case of LSF82 completely prevents the formation of interdiffusion products after sintering. For LSCF and LSF64, a Sr/Zr reactivity is still visible spread from the electrolyte interface-CGO20 and within the barrier layer. But, the barrier layer seems preventing Zr migration in the electrode. No Zr migration can be observed for LSCF and lower Zr %wt in the LSF64 electrode. In the case of LCF82, the presence of Ca is still observable at electrolyte-CGO20 interface, but Fe migration seems prevented at the electrolyte interface.

The outcome of the microstructural and compositional characterization performed in this work can be summarized as followed:

- Both LSF and LCF oxygen electrode compositions applied directly on top of zirconia shows electrode good adhesion properties, but a significant amount of interface reaction products takes place at the sintering temperature of 1100°C.
- In presence of the current quality porous CGO20 layer, only LSF82 shows no detectable interface reaction products after sintering at 1100°C.
- Weaker CGO-electrolyte interface while thicker CGO 20 layer takes place for LSF82 and LCF82 having no or low reactivity compared to LSF64 and LSCF. An improvement of CGO-electrolyte interface adhesion will be therefore required in future work.

4.2 Electrochemical characterization

The EIS measurements conducted in this work give insight on the impact of the use of a ceria barrier layer with A-site substituted perovskite-type lanthanum ferrites $(La,Ca,Sr)FeO_3$ and assess the electrochemical performance of each Co-free oxygen electrode materials at different operating temperatures in comparison with the state-of-the-art SOC oxygen electrode material LSCF.

Impact of presence of ceria barrier layer

Figure 2 illustrates an example of the difference of electrochemical performance of A-site substituted perovskite-type lanthanum ferrites (La,Ca,Sr)FeO_3 with or without use of a 20GCO barrier layer and Table 4 gives the overview of the ohmic and polarization resistances obtained at OCV and 700°C for each oxygen electrode with and without ceria layer.

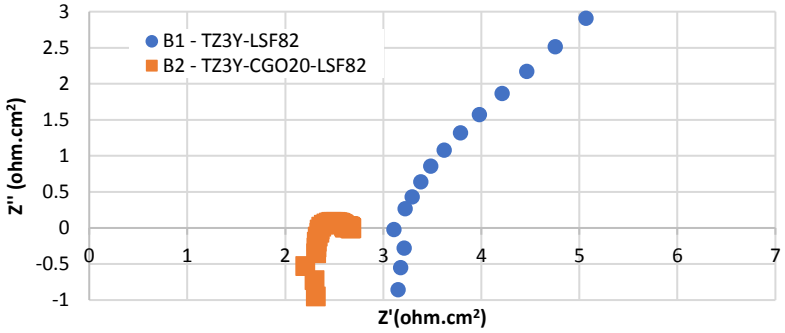

Figure 2: -Nyquist-plot at OCV at 700°C for the symmetrical cells manufactured with LSF82 without and with CGO20 barrier layer (respectively sample B1 and B2)

Table 4: Ohmic and polarization resistance in ohm.cm^2 at 700°C and OCV for LSF82, LCF82, LSF64 and LSCF with and without ceria layer

Air Electrode composition	Without 20GCO-layer *(sample series X1)*		With 20GCO-layer *(sample series X2)*	
	R_{ohm}	R_{pol}	R_{ohm}	R_{pol}
LSCF	2.18	1521.7	1.78	0.78
LSF82	2.81	126.1	2.35	0.31
LCF82	2.37	2001.4	2.34	0.73
LSF64	2.29	247.8	2.62	0.31

The presence of the 20GCO barrier layer results in a significant reduction of the polarization resistance for all A-site doped lanthanum ferrites, as observed for LSCF. Apart from LSF64 composition, the ohmic resistance for the samples with the 20GCO layer has slightly reduced resistance values, indicating that the ceria barrier layer diminishes reactions taking place at the electrode-electrolyte interface.

Electrochemical performance of lanthanum ferrite samples with GCO-barrier layer

Figure 3a and Figure 3b respectively present the ohmic and polarization resistance values as function of operating temperature (550-900°C), for the lanthanum ferrite oxygen electrodes manufactured on symmetrical cells with a CGO20 barrier layer.

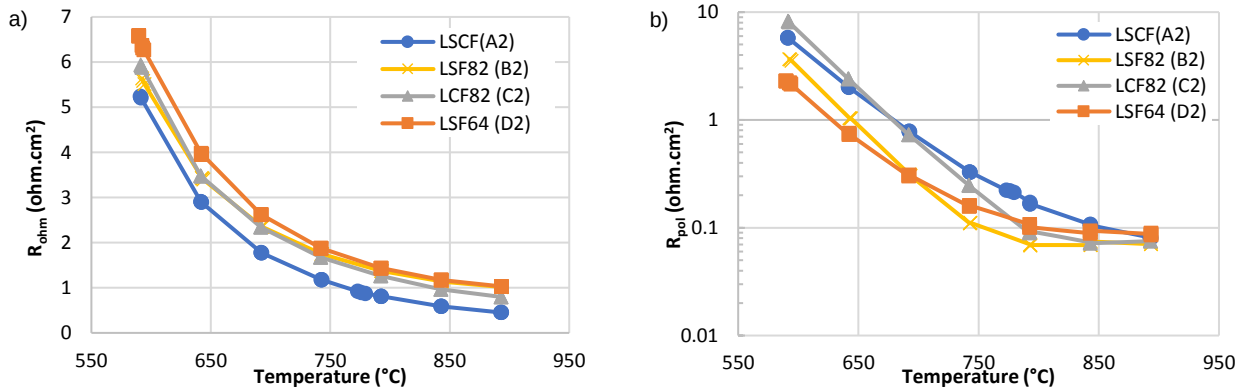

Figure 3: a) Ohmic and b) polarization resistance values as function of temperature for the lanthanum ferrite oxygen electrodes in presence of CGO20 barrier layer

For the ohmic contribution (Figure 3a), the following observations can be made:

- LCF and LSF oxygen electrode compositions have an overall higher ohmic resistance compared to LSCF over the all temperature range studied (550-900°C)
- The highest ohmic resistance is observed for LSF64 composition
- Similar T-dependence behavior of the ohmic resistance is observed between as LSF64, LCF82 and LSCF, while LSF82 presents a different T-dependency with lower increase of the ohmic resistance as function of temperature.

For the polarization contribution (Figure 3a), the following observations can be made:

- The LSF compositions have lower polarization resistance than LSCF over the all temperature range studied (550-900°C)
- LCF has lower polarization resistance than LSCF at high temperature (700-900°C)
- At low T-range the 82 compositions have similar T-dependency, the 64 compositions have also similar T-dependency but at different slope

As general outcome of the electrochemical characterization conducted on the lanthanum ferrite oxygen electrodes manufactured on symmetrical cells, LCF and LSF compositions have slightly higher ohmic resistance than LSCF. In presence of a CGO20 barrier layer, the polarization resistance is significantly improved for every oxygen electrode composition. LSF compositions show lower polarization resistances compared to LSCF on all operating temperature of SOC cells (550-900°C), while LCF82 only presents acceptable performance compared to LSCF for operating temperature above 700°C.

4.3 Discussion

In absence of ceria barrier layer, interface reaction products (Zr/Sr for LSF compositions and Ca/Fe/Zr for LCF82) very likely result in the observed slight increase in ohmic resistance and significant increase in polarization resistance. The reactivity observation is not completely in line with literature [6,8,12,16,19,21], showing relatively low reactivity for lanthanum ferrite materials and zirconia at the sintering temperature of 1100°C. A possible explanation is the sensitivity of reactivity to sintering temperature and exact starting composition or morphology of the starting powders.

The general outcome of the present work is that lanthanum ferrite samples perform better in presence of a ceria layer, confirming the outcome of some researches in literature [6]. In addition of promoting significantly the ionic conductivity at the electrolyte-oxygen electrode interface evidenced by a significant reduction of the polarization resistance, the ceria layer also promotes lower or no reactivity at the electrolyte-electrode interface (Table 2). Apparently the ceria layer, despite its observed porosity, has the potential to diminish the reactivity between the oxygen electrode and the zirconia electrolyte compounds. A correlation between observed ohmic resistance and reactivity is not clearly established. A similar temperature dependence behavior of the ohmic resistance is observed for LSF64, LCF82 and LSCF (Figure 3a), for which interdiffusion products are observed at the electrolyte-CGO interface (Table 2), while LSF82 showing no reactivity have a different T-dependency with lower increase of the ohmic resistance as function of temperature. However, LSCF showing the highest level of Sr/Zr reactivity at the ceria-zirconia interface still has the lowest ohmic resistance. The difference in ohmic resistance observed is probably also related to the differences in electronic conducting behavior for the different electrode compositions (Table 5) and rather low layer thickness values for several of the different electrodes (Table 3). A clear correlation between observed polarization resistance and reactivity cannot be given. It is remarkable that the LSF82 without observed reactivity performs at the low polarization

resistance comparable to LSF64, which has reaction products at the interface. LSCF with high Sr-segregation show higher polarization resistance in line with expectation.

Table 5: Electronic conductivity ($\sigma_{el.}$) values of the selected (La,Ca,Sr)FeO_3 and LSCF

Material	Composition	$\sigma_{el.}$ (S/cm)		ref
LSCF	$La_{0.6}Sr_{0.4}Co_{0.2}Fe_{0.8}O_{3-\delta}$	325 87	(600°C) (800°C)	[28] [4]
LSF82	$La_{0.8}Sr_{0.2}FeO_{3-\delta}$	57 80	(800°C) (460°C)	[12]
LSF64	$La_{0.6}Sr_{0.4}FeO_{3-\delta}$	283 128	(800°C) (800°C)	[13] [4]
LCF82	$La_{0.8}Ca_{0.2}FeO_{3-\delta}$	110	(700°C)	[22]

4. Conclusions

In the present work, the performance of three compositions of lanthanum ferrite oxygen electrodes (LSF82, LCF82 and LSF64) has been examined in the development towards high performance and robust Co-free oxygen electrodes for SOFC and electrolyzers applications. Electrode microstructure, chemical compatibility with the electrolyte and electrochemical performance were characterized on symmetrical cells without and with a porous ceria layer and compared with the performance of LSCF, currently used as state-of-the-art oxygen electrode material in the Solid Oxide Cell manufacturing. The comparison in reactivity and electrochemical performance between lanthanum ferrites deposited directly on the zirconia electrolyte or in combination with a ceria barrier layer permitted to give the following conclusions:

a/ A ceria barrier layer is needed for lanthanum ferrite materials, especially when the oxygen electrode is manufactured at sintering temperature of 1100°C, to reduce interdiffusion products formation and improve the ionic conductivity at the electrolyte-electrode interface.

b/ Using LSF82 does not require a fully dense ceria barrier layer in order to prevent reactivity at sintering temperature of 1100°C. It makes LSF82 a promising material to replace LSCF as high performance and robust Co-free oxygen electrodes.

In future work, further improvement of lanthanum ferrites electrodes is required with respect to ohmic resistance by varying electrode thickness, sintering temperature. In addition, polarization resistance can be further reduced by enhanced triple phase boundary density by microstructure engineering and using a patterned interface. Single cell implementation of the lanthanum ferrites will contribute to validate their performance under SOFC and electrolyzer conditions.

References

[1] O. Schmidt, A. Gambhir, I. Staffell, A. Hawkes, J. Nelson, S. Few, Future cost and performance of water electrolysis: An expert elicitation study International Journal of Hydrogen Energy 42 (2017) p.30470-30492

[2] Blengini, G.A., Blagoeva, D., Dewulf, J., Torres de Matos, C., Nita, V., Vidal-Legaz, B., Latunussa, C.E.L., Kayam, Y., Talens Peirò, L., Baranzelli, C., Manfredi, S., Mancini, L., Nuss, P., Marmier, A., Alves-Dias, P., Pavel, C., Tzimas, E., Mathieux, F., Pennington, D. and Ciupagea, C. Assessment of the Methodology for Establishing the EU List of Critical Raw Materials, Publications Office of the European Union, Luxemburg, 2017, 978-92-79-69611-4, doi:10.2760/130462, JRC106997

[3] Cobalt Institute website: https://www.cobaltinstitute.org/cobalt-uses.html

[4] H. Ullmann, N. Trofimenko, F. Tietz, D. Stover, A. Ahmad-Khanlou, Correlation between thermal expansion and oxide ion transport in mixed conducting perovskite-type oxides for SOFC cathodes, Solid State Ionics 138 (2000) p.79–90

[5] S.P. Simner, J.P Shelton, M.D. Anderson, J.W. Stevenson, Interaction between La(Sr)FeO_3 SOFC cathode and YSZ electrolyte, Solid State Ionic 161 (2003) p.11-18

[6] M.D. Anderson, J.W. Stevenson, S. P. Simner, Reactivity of lanthanide ferrite SOFC cathodes with YSZ electrolyte, Journal of Power Sources 129 (2004) 188–192
[7] W. Preis, E. Buchner, W.Sitte, Oxygen exchange kinetrics of $La_{0.4}Fe_{0.6}FeO_{3-\delta}$ by simultaneous application of conductivity relaxation and carrier gas coulometry, Solid State Ionics 175 (2004) p. 393-397
[8] W. Wang, Y. Huang, S. Jung, J.M. Vohs, R.J. Gorte, A comparison of LSM, LSF and LSCF for solid oxide electrolyzer anodes, Journal of the Electrochemical Society 153 [11] (2006) p. A2066-A2070
[9] N. Sata, K. Ikeda, F. Iguchi, H. Yugami, Synthesis of $La_{0.6}Fe_{0.4}FeO_{3-\delta}$ / $La_{0.6}Co_{0.4}FeO_{3-\delta}$ mixed ion conducting superlattices by PLD, Solid State Ionics 178 [29–30] (2007) p.1563-1567
[10] P. Plonczak, M. Gazda, B. Kusz, P. Jasinski, Fabrication of solid oxide fuel cell supported on specially performed ferrite-based perovskite cathode, Journal of Power Sources 181 (2008) p.1-7
[11] H. Yokokawa, N. Sakai, T. Horita, K. Yamaji, M.E. Brtio, H. Kishimoto, Thermodynamic and kinetic considerations on degradations in solid oxide fuel cell cathodes, Journal of Alloys and compounds 452 (2008) p.41-47
[12] U.F. Vogt, J. Sfeir, J. Richter, C. Soltmann, P. Holtappels, B-site substituted lanthanum strontium ferrites as electrode materials for electrochemical applications, Pure Appl. Chem. 80 [11] (2008), p.2543–2552
[13] M. Mosleh, M. Sogaard, P.V. Hendriksen, Kinetics and mechanisms of oxygen surface exchange on $La_{0.6}Fe_{0.4}FeO_{3-\delta}$ thin films, Journal of the Electrochemical Society 156 [4] (2009) p.B441-B457
[14] M.S. Hassan, K.B. Shim, O.B. Yang, Electrocatalytic behavior of calcium doped $LaFeO_3$ as cathode material for solid oxide fuel cell, Journal of Nanoscience and Nanotechnology 11 [2] (2011) p.1429-33
[15] M. Kuhn, S. Hashimoto K. Sato, K. Yashiro, J. Mizusaki, Oxygen non-stoichiometry, thermo-chemical stability and lattice expansion of $La_{0.6}Fe_{0.4}FeO_{3-\delta}$, Solid State Ionics 195 [1] (2011) p. 7-15
[16] S.V. Chavan, R.N. Singh, Preparation, properties and reactivity of lanthanum strontium ferrite as an intermediate temperature SOFC cathode, J Matter Sci 48 (2013) p.6597-6604
[17] P.M. Price E. Rabenberg, D. Thomsen S.T. Misture D. P. Butt, Phase Transformations in Calcium-Substituted Lanthanum Ferrite, Journal of the American Ceramic Society 97 [7] (2014), p.2241-2248
[18] P. M. Price, D. P., Butt, Stability and decomposition of Ca-substituted Lanthanum ferrite in reducing atmospheres, J. Am. Ceram. Soc. 98 [9] (2015) p. 2881-2886
[19] S. Kogler, A. Nenning, G. M. Rupp, A.K. Opitz, J. Fleig, Comparion of Electrochemical properties of $La_{0.6}Fe_{0.4}FeO_{3-\delta}$ thin film electrodes: oxidizing vs. reducing conditions, Journal of the Electrochemical Society 162 [3] (2015) p. F317-F326
[20] C. Berger, E. Bucher, W. Sitte, Solid State Ion., 299 (2017) p. 46-54
[21] C. Ni, M., Cassidy, J.T.S Irvine, Image analysis of the porous yttria-stabilized zirconia (YSZ) structure for a lanthanum ferrite-impregnated solid oxide fuel cell (SOFC) electrode, Journal of the European Ceramic Society 38 (2018) p.5463-5470
[22] C. Berger, E. Bucher, A. Windischbacher, A. D. Boese, W. Sitte, Strontium-free rare earth perovskite ferrites with fast oxygen exchange kinetics: Experiment and theory, Journal of Solid State Chemistry 259 (2018) p.57-66
[23] E. Buchner, C. Berger, M. Perz, A. Egger, N. Schold, C. Gspan, W. Sitte, Oxygen exchange kinetics of SOFC and SOE air electrodes affected by long term changes of surface composition, Proceedings 13th European SOFC & SOE Forum (2018) B1404
[24] C. Berger, E. Bucher, C. Gspan, W. Sitte, Crystal structure oxygen non-stoichiometry, and mass and charge transport properties of the Sr-free SOFC/SOEC air electrode material $La_{0.75}Ca_{0.25}FeO_{3-\delta}$, Journal of Solid State Chemistry 273 (2019) p.92–100
[25] J. Song, D. Ning, H.J.M. Bouwmeester, Influence of alkaline-earth metal substitution on structure, electrical conductivity and oxygen transport properties of perovskite-type oxides $La_{0.6}A_{0.4}FeO_{3-\delta}$ (A = Ca, Sr and Ba), Phys. Chem. Chem. Phys. 2020, 22 [21] (2020) p.11984-11995
[26] K. Kammer, Hansen, Evaluation of LSF based SOFC cathodes using cone-shaped electrodes and EIS, Solid State Ionics 344 (2020) 115096
[27] W. Rasband, ImageJ 1.52a, National Institutes of Health, USA, 23 April 2018, Java 1.8,0_112 (64-bit), website: https://imagej.nih.gov/ij/notes.html
[28] S. Ping Jiang, Development of lanthanum strontium cobalt ferrite perovskite electrodes of solid oxide fuel cells – A review, International Journal of hydrogen energy 44 (2019) p.7448-7493
[29] C. Rossignol, G. Constantin, P. Briois, A. Billard, E. Djurado, L. Dessemond, Interfaces and Durability for Different LSCF/CGO/YSZ Systems for IT-SOFC, Proceedings 227th ECS Meeting 1615 (2015)

Acknowledgement

This project has received funding from the Fuel Cells and Hydrogen 2 Joint Undertaking under grant agreement N. 874577. This Joint Undertaking receives support from the European Union's Horizon 2020 research and innovation program, Hydrogen Europe and Hydrogen Europe research.

Keywords: EFCF2020, SOx
Session B03: Manufacturing Processes

hhttps://doi.org/10.5281/zenodo.4792269

B0501

Strontium Titanate based SOFC anodes with nano scaled electrocatalysts

Peter Holtappels (1), Nasima Arshad (2), Daniel Bøgh Drasbæk (1), Nazan Muzaffar(1,2), Bhaskar Reddy Sudireddy (1), Marie Lund Traulsen(1)
(1) Technical University of Denmark, Department of Energy Conversion and Storage 2800 Kgs Lyngby/Denmark
(2) Department of Chemistry, Allama Iqbal Open University, 44000 Islamabad/Pakistan

Contact authors: www.EFCF.com/ContactRequest

Abstract

Ceramic SOFC anodes with nano scaled electrocatalyst particles are of current interest for low temperature application of SOCs and to increase robustness in terms of redox stability and coking tolerance. Strontium titanates are a materials class that is compatible with the state-of the art electrolyte yttria stabilized zirconia and possesses sufficient electronic conductivity under reducing conditions that make them attractive for SOC fuel electrodes. However, their electrocatalytic activity is rather poor and nano scaled electrocatalyst particles are infiltrated into the porous strontium titanate to achieve technically relevant performance. Various electroactive materials have been explored by infiltration into Strontium titanates. Ni, Co and Fe with and without ceria-gadolinia (CGO) have been infiltrated as metal particles into two different Strontium titanates, A-site deficient La-Sr-C-titanate (LSCT) modified with different elements (Cr, Mn, Zn) on the B-site and Niobium modified Strontium-titanate (STN). Zn substitution showed a positive effect on the pure LST electrodes and electrode area specific resistances down to 0.2 $\Omega \cdot cm^2$ have been achieved for LST-Zn electrodes infiltrated with Ni-CGO. The influence of backbone vs. electrocatalyst on the electrode performance will be presented in this contribution.

https://doi.org/10.5281/zenodo.4557454

Introduction

Ceramic SOFC anodes with nano scaled electrocatalyst particles are of current interest for low temperature application of SOCs, and as regards increase in robustness in terms of redox stability and coking tolerance.

Strontium titanates are a materials class that is compatible with the state-of the art electrolyte yttria stabilized zirconia and that possesses sufficient electronic conductivity under reducing conditions, which make them attractive for SOC fuel electrodes (1-5). However, their electrocatalytic activity is rather poor and nano scaled electrocatalyst particles are usually infiltrated into the porous strontium titanate to achieve technically relevant performance. Mostly Ni with or without ceria is infiltrated as electroctalysts, and promising results have been obtained for A and B-site modified strontium titanates including Nb-doped strontium titanate (STN), and La-Ca modified strontium titanate (LSCT) (4-6). However, even if redox stability could be achieved, problems with coking and sulphur poisoning are still a problem and associated with the use of Ni as electrocatalyst (7). Studies comparing different electrocatalysts on STN have been performed as regards their activity and tolerance to coking and exposure to high humidity contents (7-9).The results show clearly that the nature of the electrocatalyst, as well as the presence of CGO positively affects the electrode performance.

To better understand the role of the backbone material as electrocatalyst support on the fuel electrode performance, the variation of the strontium titanate backbone in relation to various electrocatalytically active infiltrates is on focus in the present study.

1. Scientific Approach

The approach is to investigate the electrochemical performance of different backbones and electrocatalysts as regards their electrochemical performance at OCV conditions. Ni, Co and Fe with and without ceria-gadolinia (CGO) have been infiltrated as metal particles into two different strontium titanates, niobium modified strontium-titanate (STN) and Ca modified A-site deficient La-Sr-titanate (LSCT) modified with different elements (Cr, Mn, Zn) on the B-site (LSCTC, LSCTM, LSCTZ, respectively). These elements have compatible ionic radii to Ti-ions, but due to different valence states can affect differently the defect chemistry and electronic properties of the host material.

2. Experiments

The synthesis of $La_{0.2}Sr_{0.25}Ca_{0.45}TiO_3$ (LSCTA) as well as B- site doping on the LSCTA with Zn, Mn and Cr (1%, 5%) was done by the Pechini method using nitrate salts as precursors (10). Stoichiometric amounts of the metals nitrates (Aldrich) were dissolved in an aqueous solution. The solution of ethylene glycol and citric acid (both Sigma-Aldrich) was added with a final molar ratio of metal ions to citric acid to ethylene glycol as 1:4:16. The solution was then heated on hot plate at 80-100 °C, to form the gel and subsequently heated at 300 °C for combustion. The resulting powder was dried and calcined in air for 5 hours at 1200 °C. The phase formation was identified by XRD (Bruker) using Cu-Kα radiation in the range of 20° – 80°.
The doped analogues of LSCTA are denoted LSCTZ1 ($La_{0.2}Sr_{0.25}Ca_{0.45}Ti_{0.99}Zn_{0.01}O_3$) and LSCTZ5 ($La_{0.2}Sr_{0.25}Ca_{0.45}Ti_{0.95}Zn_{0.05}O_3$), LSCTM1 ($La_{0.2}Sr_{0.25}Ca_{0.45}Ti_{0.99}Mn_{0.01}O_3$) and

https://doi.org/10.5281/zenodo.4557454

LSCTM5 ($La_{0.2}Sr_{0.25}Ca_{0.45}Ti_{0.95}Mn_{0.05}O_3$), LSCTC1 ($La_{0.2}Sr_{0.25}Ca_{0.45}Ti_{0.99}Cr_{0.01}O_3$) and LSCTC5 ($La_{0.2}Sr_{0.25}Ca_{0.45}Ti_{0.95}Cr_{0.05}O_3$).

B-site Nb substituted strontium titanate, $Sr_{0.94}Ti_{0.9}Nb_{0.1}O_3$, (STN94), was prepared from $SrCO_3$, TiO_2 and Nb_2O_5 (all materials >99.9 purity, Sigma-Aldrich, Germany) by solid-state reaction method.

For fabrication of the symmetrical cells, STN94 ink was spray deposited onto a pre-sintered 240 ±10 µm thick Sc_2O_3, Y_2O_3 co-stabilized ZrO_2 (Sc-YSZ) electrolyte. After deposition, the electrodes were sintered at 1200 °C for 8h in air, resulting in electrode thicknesses between 20 and 40 µm. A detailed description of the fabrication procedure of the symmetrical cells can be found in (11). After sintering, the cells were laser cut into smaller pieces of 0.6 cm × 0.6 cm.
The infiltration solutions were prepared by dissolving the respective metal nitrates in water along with a surfactant. Metal concentration in the solution was kept to 1M. Prior to infiltration, the symmetrical cells were weighted, and the infiltration was then performed by dropping the nitrate solution onto both porous electrode layers with subsequent heating to 350°C for 30 minutes. This infiltration procedure was repeated three times in total, with the last heat-treatment step at 350°C prolonged to two hours. The thus obtained catalyst loadings are around 0.6 -1 w% (8).

The microstructure of the cells was investigated from a fractured cross-section, without any pretreatment of the samples, using scanning electron microscopy (SEM) (ZEISS Merlin, Carl Zeiss, Germany).

Prior to the electrochemical characterization, the infiltrated cells were hand-painted with a Pt-paste current collection layer. Following this, the cells were mounted in an experimental setup allowing for simultaneous testing of four symmetrical cells per test. A detailed description of the setup can be found elsewhere (12). Cells were investigated by electrochemical impedance spectroscopy at OCV in hydrogen containing 3-4% or 50% water. A Gamry Reference 600 potentiostat was used and impedance spectra were recorded between 0.01Hz-1MHz with 10 points/decade applying a 50 mV amplitude.
Analysis of the impedance data was performed using the Python-based software RAVDAV developed at DTU Energy (13). The series resistances (Rs,) observed in the impedance data were not corrected for ohmic contributions arising from the Pt leads in the experimental setup, as the lead resistance based on previous experiments is estimated to be less than 5% of the measured ohmic resistance (Rs).

3. Results

Figure 1 shows the X-ray diffractograms for LSCT with and without modification by Cr, Mn and Zn. The main phase is the expected perovskite, however small impurity amounts LaO_2, TiO_2 have been observed, varying slightly with composition. The shift to higher 2θ angles for all additions (e.g. visible in the peak at 30° 2θ) suggests a slight reduction of the lattice parameter. The reduction, however, is higher for 1% than for 5% of Cr, almost similar for 1% or 5% Mn, while for Zn additions the lattice gets more reduced with increasing the Zn content from 1% to 5%.

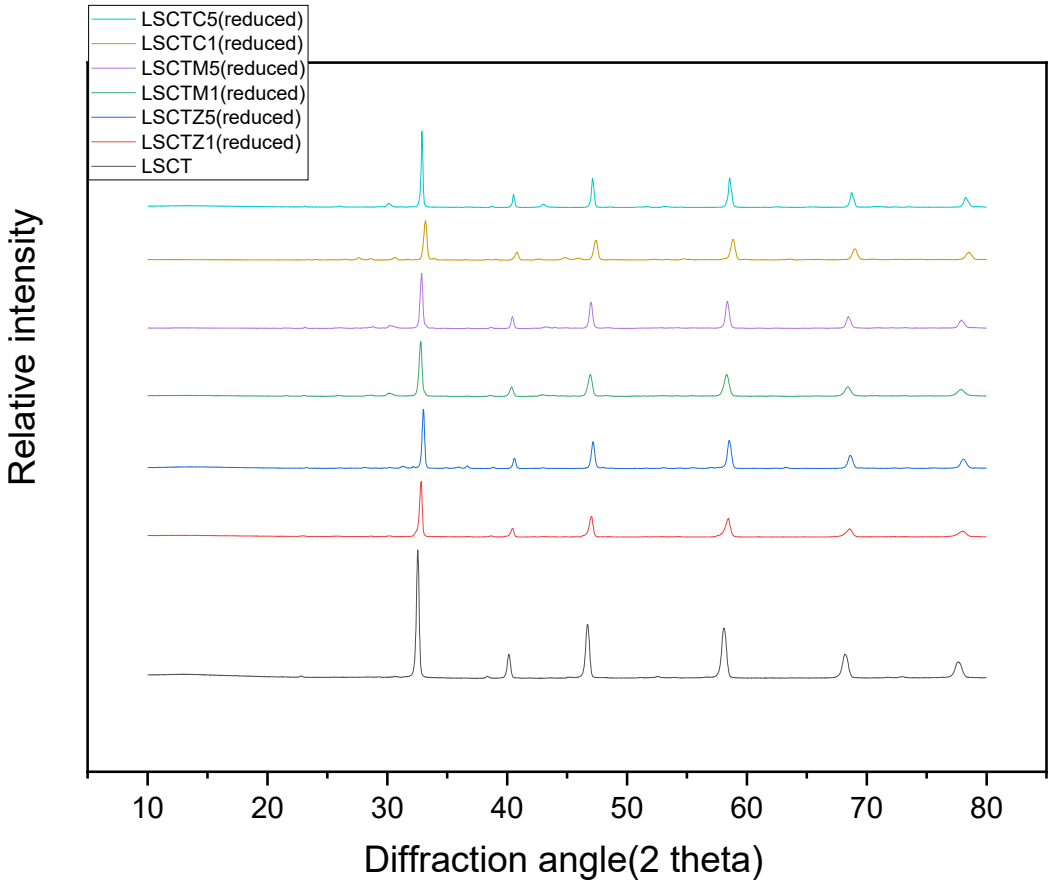

Figure 1 X-ray diffractogramms for LSCT, LSCTM, LSCTC and LSCTZ.

The porous electrode structure is shown in Figure 2 for LSCT with 1% and 5% Zn and shows a well adhering electrode/ electrolyte interface. The electrode microstructures are similar with pore and particle sizes of around 1 micron, which are slightly higher than the pore and particle sizes in STN94 electrodes (8).
Similar adhering electrode structures are obtained for Mn modified LSCT, while crack formation into the electrolyte was observed for Cr modified LSCT. This indicates differences in the sintering behavior of the various modified LSCT, which needs to be further investigated.

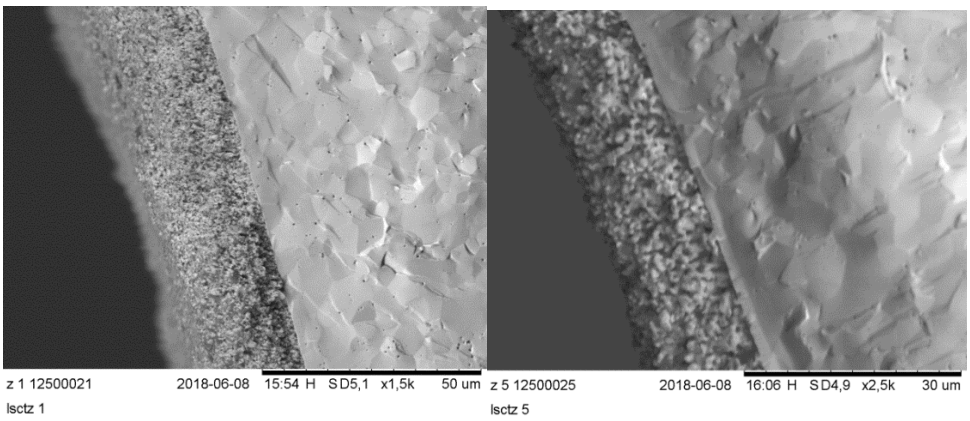

Figure 2 Electrolyte / electrode fracture cross section for LSCTZ1 (left) and LSCT5 (right) electrodes

https://doi.org/10.5281/zenodo.4557454

The dispersion of the infiltrated electrocatalyst into the LSCTZ5 porous electrode backbone can be estimated from Figure 3. The electrocatalysts are evenly distributed and particle sizes are below 100 nm for Ni particles, while slightly larger particles are indicated for Co and Fe. These infiltrate structure are comparable to similar elements infiltrated into STN94 electrodes (8).

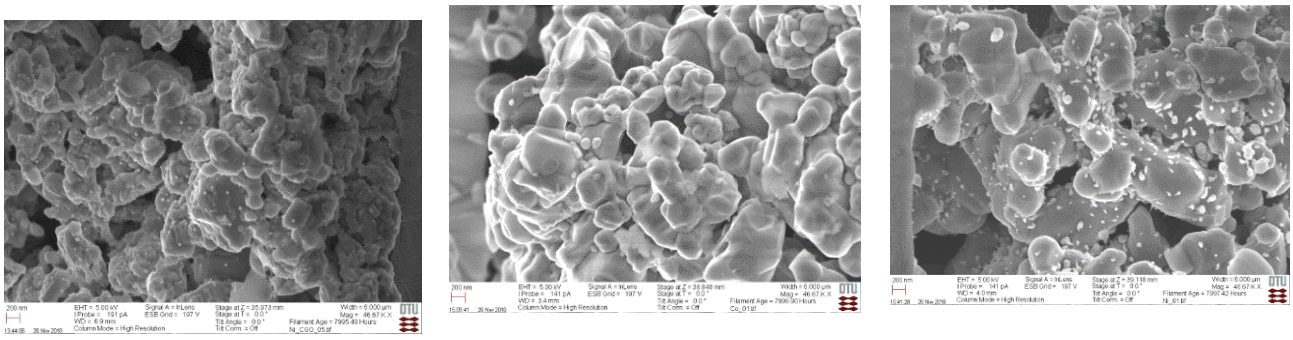

(a) (**b**) (**c**)

Figure 3 Cross-sectional micrographs of infiltrated symmetrical cells of LSCTZ5 after testing: (a) Ni-CGO infiltrated LSCTZ5, (b) Co-infiltrated LSCTZ5, (c) Fe-infiltrated LSCTZ5. (extracted from (14))

The impedance spectra for the non-infiltrated modified LSCTZ, LSCTC and LSCTM electrodes obtained at open circuit voltage and in hydrogen humidified with 4% water, are presented in Figure 4 for two sintering temperatures 1200 °C and 1250 °C. The higher sintering temperature leads to generally lower faradaic electrode resistances. However, the non symmetrical shape, different for the various modifications, point to different backbone activities. The faradaic electrode resistances for LSCTZ5 are with 25 to 30 Ωcm^2 slightly lower than those presented for STN94. However, a further activation by electrocatalyst addition is clearly needed to reach technically relevant performance.

The temperature dependence of the faradaic electrode resistance is provided in Table 4. Differences between the impedance spectra in Figure 4 and in the activation energies for the modified LSCT electrodes, indicate that the pure ceramic electrode performance is sensitive to composition, fabrication, and testing conditions.

https://doi.org/10.5281/zenodo.4557454

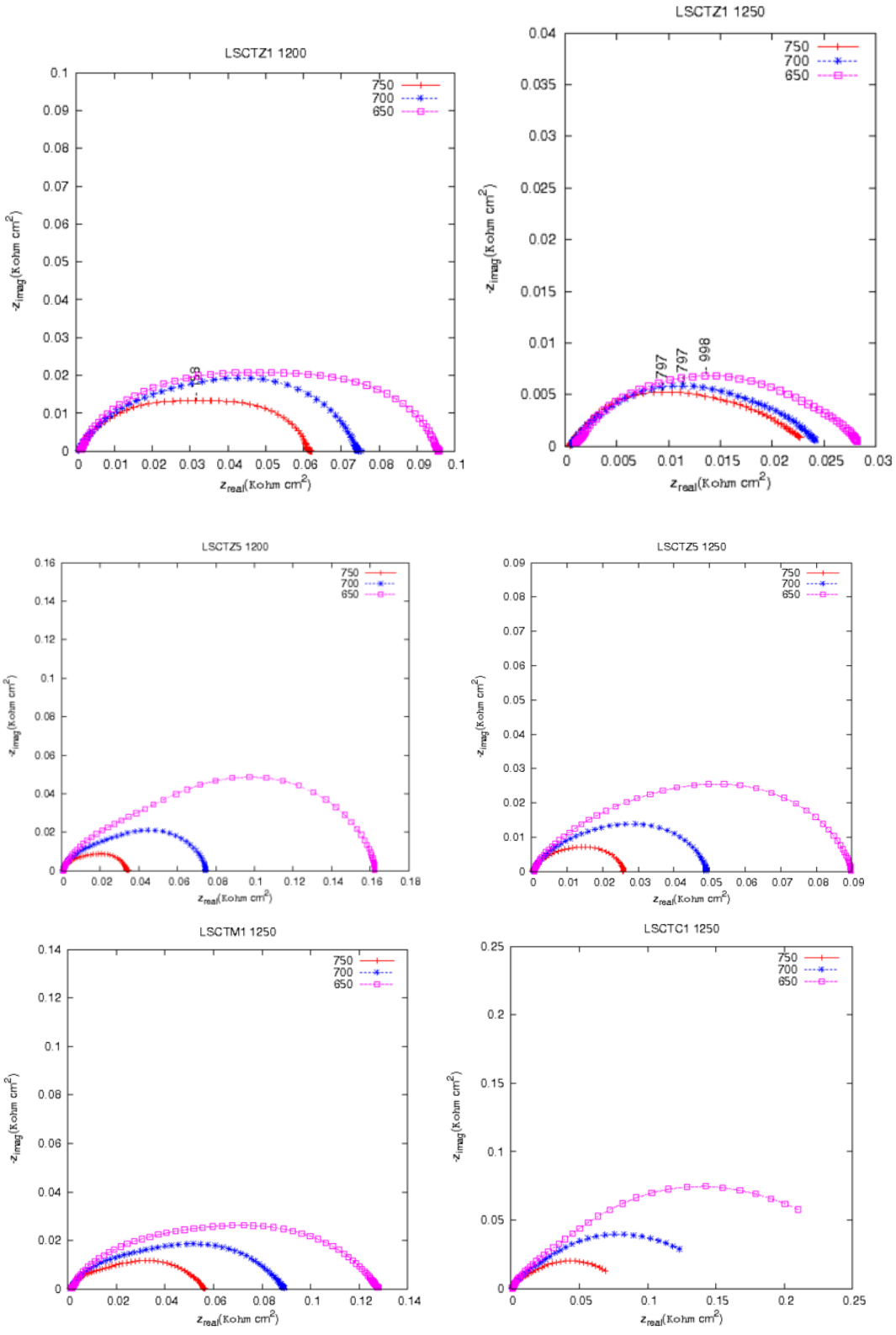

Figure 4 non-infiltrated LSCT electrodes in hydrogen humidified with 4% H_2O for Zn, Mn and Cr modified LSCT sintered at 1200 °C and 1250 °C.

https://doi.org/10.5281/zenodo.4557454

Table 4 Activation energy of the faradaic electrode resistance for the modified LSCT electrodes at OCV.

Samples	Ea (4% H_2O/ H_2)	
	($kJmol^{-1}$)	(eV)
LSCTZ1(1200)	33.42±1.196	0.346±1.196
LSCTZ1(1250)	14.21±0.504	0.147±0.504
LSCTZ5(1200)	124.37±0.527	1.29±0.527
LSCTZ5(1250)	98.43±0.489	1.02±0.489
LSCTM1(1200)	131.69±0.48	1.36±0.48
LSCTM1(1250)	33.58±0.35	0.34±0.35
LSCTC1(1200)	113.9±1.09	1.18±1.09
LSCTC1(1250)	97.52±0.54	1.01±0.54

The faradaic electrode resistances for Ni-CGO, Fe and Co infiltrated LSCTZ5 electrodes is provided in Figure 5 for two different water contents. Increasing the water content lowers the faradaic electrode resistance in case of Co, while it is significantly increased for Fe. As expected, co-infiltrated Ni-CGO shows the lowest faradaic electrode resistance with and decreases similar to Co with increasing water content. This behavior is similar to results on Ni, Co and Fe infiltrated STN94 electrodes (Figure 6). The low faradaic electrode resistance of Ni-CGO infiltrated LSCTZ5 of 0.2 Ωcm^2 at 650°C makes this electrode interesting for low temperature solid oxide fuel cells (14).

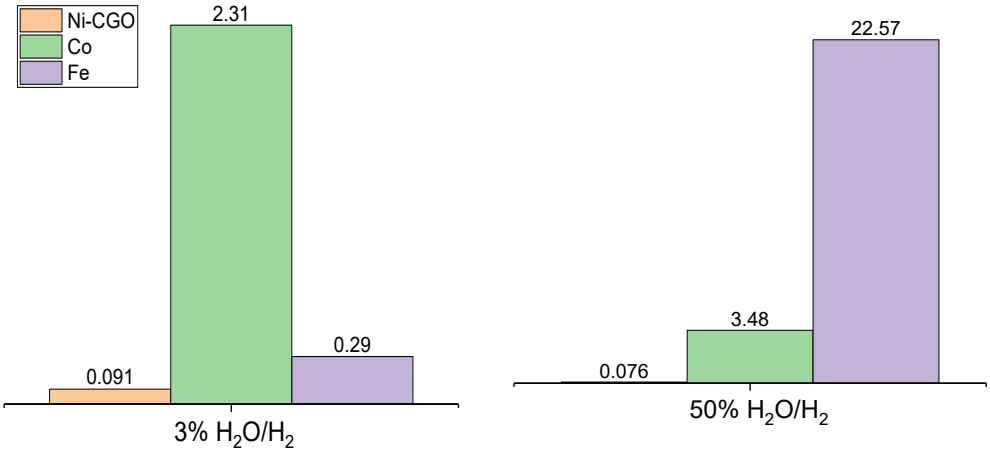

Figure 5 Faradaic electrode resistance for symmetrical LSCT electrodes infiltrated with Co, Fe and Ni-CGO at 750°C in hydrogen humidified with 3-4% water (left) and 50% water (right).

Figure 5 shows the influence of several metallic element infiltration into a STN94 electrode. While infiltration of Mo and W might be interesting in terms of sulphur tolerance,

a poor performance is observed at high water contents. Cu has been discussed as an anode material for direct hydrocarbon conversion, however the electrochemical performance is still inferior to Ni and Co infiltrated cells.

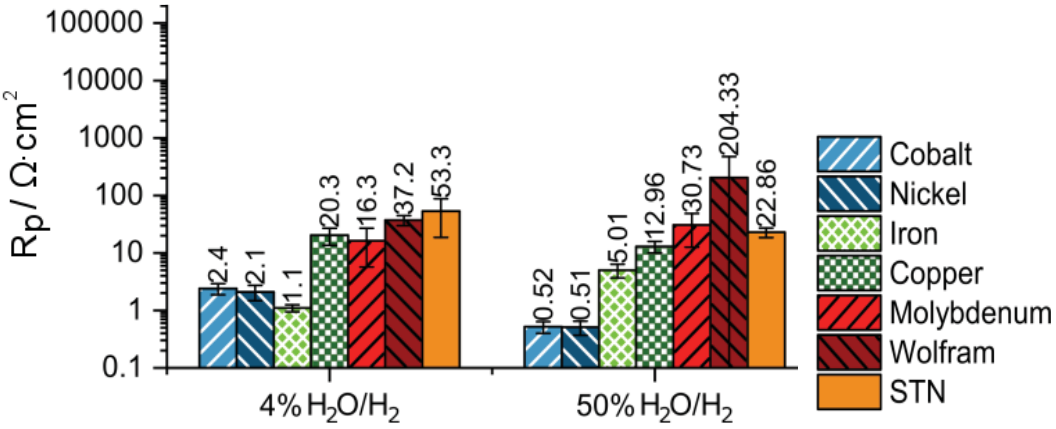

Figure 6 Initial faradaic resistances of metal infiltrated STN94 electrodes at 750°C in humidified hydrogen at OCV

The temperature dependence of the electrode reaction is given in Table 2 for the various infiltrated strontium titanate electrodes. A common trend is that increasing the water content and thus the oxygen partial pressure increases the apparent activation energies of the hydrogen water reaction. For metal only infiltrated electrodes, lower activation energies are observed in all cases for STN94 compared to LSCTZ5, indicating that both, the electrocatalyst and the backbone material are participating in the electrode reaction. Thus, tailoring both, infiltrate and backbone composition, can be utilized to optimize further the electrochemical performance for SOFC anodes.

Table 2 Activation energies of LSCTZ5 and STN94 backbone and infiltrated anodes.

Samples	**Activation energy(eV)***	
	(3-4% H_2O/ H_2)	(50% H_2O/ H_2)
LSCTZ5	**1.02**	**-**
STN94	1.06	1.27
LSCTZ5/Ni-CGO	**0.87**	**1.15**
STN94/Ni-CGO	0.68	1.01
LSCTZ5/Co	**1.20**	**1.59**
STN94/Co	0.96	1.48
LSCTZ5/Fe	**0.85**	**1.54**
STN94/Fe	1.52	1.89

*apparent activation energy, as likely not related to a single process

Acknowledgment

The authors would like to acknowledge the colleagues at DTU Energy for technical assistance and fruitful discussions. Furthermore, the authors would like to acknowledge the financial support from the project “BALANCE” (European Union’s Horizon 2020 research and innovation program under grant agreement number 731224). N. Muzaffar is thankful to the Higher Education Commission, Pakistan for providing the **IRSIP** scholarship.

References

[1] A. M. Hussain, J.V.T. Høgh, W. Zhang, N. Bonanos, Efficient ceramic anodes infiltrated with binary and ternary electrocatalysts for SOFCs operating at low temperatures, Journal of Power Sources. 2012, 216.

[2] T. Ramos, C. Bernuy-Lopez, B. R. Sudireddy, J. J. Bentzen, W. Zhang, P. S. Jørgensen, L. T. Kuhn, Performance-Microstructure Relations in Ni/CGO Infiltrated Nb-doped SrTiO3 SOFC Anodes. ECS Transactions. 2012, 45 (1).

[3] P. Blennow, K. K. Hansen, L. R. Wallenberg, M. Mogensen. Electrochemical characterization and redox behavior of Nb-doped SrTIO3, Solid State Ionics. 2009, 180.

[4] M. C. Verbraeken, B. Iwanschitz, A. Mai, J.T.S. Irvine, Evaluation of Ca Doped La0.2Sr0.7TiO3 as an Alternative Material for Use in SOFC Anodes, J. Electrochem. Soc., 2012, 159(11).

[5] Q. Ma, F. Tietz, A. Leonide, E. Ivers-Tiffée, Electrochemical performances of solid oxide fuel cells based on Y-substituted SrTiO3 ceramic anode materials, J. Power Sources. 2011, 196.

[6] T. Ramos, S. Veltzé, B. R. Sudireddy, P. S. Jørgensen, L. Theil Kuhn, P. Holtappels. Effect of Ru/CGO versus Ni/CGO Co-Infiltration on the Performance and Stability of STN-Based SOFCs, Fuel Cells 14. 2014, 6.

[7] D. B. Drasbæk, M. L. Traulsen, R. A.Walker, P. Holtappels, Testing Novel Nickel and Cobalt Infiltrated STN Anodes for Carbon Tolerance using In Situ Raman Spectroscopy and Electrochemical Impedance Spectroscopy, FUEL CELLS 19, 2019, No. 4, 484–493

[8] D.B. Drasbæk, M.L. Traulsen, B.R. Sudireddy, P.Holtappels, Understanding the Electrocatalytic Activity of Transition Metal Nanoparticles for Solid Oxide Cell Fuel Electrodes, Electrochimica Acta 327 (2019) 135004

[9] D.B. Drasbæk, M.L. Traulsen, B.R. Sudireddy, P. Holtappels, Combining Transition Metals – An approach towards High-performing Coking Tolerant Solid Oxide Fuel Cell Anodes, ECS Transactions, 91 (1) (2019) 1953-1961.

[10] C.D. Savaniu, D.N. Miller, J.T.S Irvine, Scale up and anode development for La-Doped SrTiO3 anode-supported SOFCs, J. Am. Ceram. Soc. 2013, 96, 1718–1723.

[11] T. Ramos, C. Bernuy-Lopez, B. R. Sudireddy, J. J. Bentzen, W. Zhang, P. S. Jørgensen, L. T. Kuhn, Performance-Microstructure Relations in Ni/CGO Infiltrated Nb-doped $SrTiO_3$ SOFC Anodes, ECS Transactions. 2012, 45 (1)

[12] T. Ramos, K. Thyden, M. Mogensen, Electrochemical characterization of Ni/(Sc) YSZ electrodes, ECS Transaction 28 (2010) https://doi.org/10.1149/1.3495837

[13] Chris Graves, RAVDAV Data Analysis Software, DTU, 2015, version 0.9.8

[14] N. Muzaffar, N. Arshad, D.B. Drasbæ, B.R. Sudireddy, P. Holtappels, Fabrication and Electrochemical Performance of Zn-Doped $La_{0.2}Sr_{0.25}Ca_{0.45}TiO_3$, Infiltrated with Nickel-CGO, Iron, and Cobalt as an Alternative Anode Material for Solid Oxide Fuel Cells, Catalysts 2019, 9, 269

Keywords: EFCF2020, SOx
Session B05: Fuel electrodes

https://doi.org/10.5281/zenodo.4557454

B0606

Exploitation of the surface chemistry of $La_{0.6}Sr_{0.4}CoO_{3-\delta}$ thin-film solid-oxide electrodes for the improvement of solid/gas interfaces

Ozden Celikbilek (1), Andrea Cavallaro (1), Gwilherme Kerherve (1), Ainara Aguadero (1), John A. Kilner (1,2), Stephen J. Skinner (1)
(1) Department of Materials, Imperial College London
Prince Consort Road, SW7 2BP London/United Kingdom
(2) International Institute for Carbon-Neutral Energy Research (I2CNER), Kyushu University, 744 Motooka, Nishi-ku, 819-0395 Fukuoka/Japan

Contact authors: www.EFCF.com/ContactRequest

Abstract

Advances in materials design in solid-state energy devices have opened up unprecedented opportunities for development in recent years. This work focuses on understanding, controlling and optimising the mechanism of oxygen reduction reactions (ORR) in complex transition metal oxides, in particular $La_{0.6}Sr_{0.4}CoO_{3-\delta}$ (LSC) thin films grown at different substrate temperatures by Pulsed Laser Deposition (PLD). We investigated the surface to bulk elemental distribution of the films with low-energy ion scattering spectroscopy and aimed to correlate it with the electrochemical activity and stability of the films.[1] Although the initial ORR activity of the film grown at high substrate temperature was better than the one grown at low substrate temperature, interestingly, it showed 2-times higher degradation rate in the long-term electrochemical tests. The better stability of the film grown at low substrate temperature is attributed to the segregation of Sr into protruding particles. In this way, Co content reached stoichiometry in the remaining surface. This study emphasizes the influence of processing temperature and post thermal treatments on the electrochemical activity and stability of the PLD films.

[1] Celikbilek, O., Cavallaro, A., Kerherve, G., Fearn, S., Chaix-Pluchery, O., Aguadero, A., Kilner, J. A., Skinner, S. J. 2020, “Surface Restructuring of Thin-Film Electrodes Based on Thermal History and Its Significance for the Catalytic Activity and Stability at the Gas/Solid and Solid/Solid Interfaces,” ACS Appl. Mater. Interfaces, 12, pp. 34388−34401.

https://doi.org/10.5281/zenodo.4557487

1. Introduction

Thin-film deposition techniques, such as pulsed laser deposition (PLD), grabbed significant attention over the last decade thanks to the easy tunability of conductivity and ion exchange/diffusion kinetics. The substrate choice, substrate temperature and background gas pressure during deposition become decisive on the microstructure, crystallinity and the stress/strain in a film. However, high-temperature operational requirements of ceramic solid oxide cells (SOC) may also affect the points mentioned above and thus be taken into consideration.

The (LaSr)$CoO_{3-\delta}$ based thin films were extensively studied in the literature as model electrodes due to their high electrochemical activity for oxygen reduction reactions (ORR). Few reports studied $La_{0.6}Sr_{0.4}CoO_{3-\delta}$ (LSC64) composition on single crystal (100)-oriented yttria-stabilised zirconia (YSZ) substrates with varying substrate temperatures and pressures during PLD deposition.[2-6] From these reports, a similar trend in terms of film crystallinity and microstructure can be deduced. In particular, a study by Cai *et al.* compared the ORR activity and the stability of LSC64 films deposited by the PLD at 450 and 650 °C substrate temperatures.[5] Both films exhibited oriented columnar microstructures on the single-crystal YSZ support. The authors showed that the film deposited at 450 °C were catalytically more active and stable than the one deposited at 650 °C. The enhancement with low temperature deposition was attributed to several combined effects; nano-porosity originating likely due to partly crystalline nature of the films, more uniform and nearly stoichiometric cations in the as-prepared states, less Sr segregation and phase separation upon annealing. Few others reported much higher performance LSC electrodes by post-annealing the films deposited at low temperatures (< 100 °C) and high oxygen pressures (> 0.1 mbar).[7-8] These films typically had large porous channels separating highly disordered nano-scale grain clusters.

All these previous reports indicate the importance of thermal history and processing of the SOC electrode films on the catalytic activity and stability. However, these studies lack a systematic and comparative analysis of the surface chemistry at the nanometer scale and below. Here, we studied two LSC64 films by PLD with different processing temperatures and thermal history. Detailed information can be found in reference [1]. Electrochemical activity and long-term stability were monitored by impedance spectroscopy and the surface elemental distributions by low-energy ion scattering spectroscopy. A correlation between thermal history, catalytic activity/stability and cationic distribution was evidenced.

2. Experiments

For thin film deposition, PLD targets were prepared from a commercial $La_{0.6}Sr_{0.4}CoO_{3-\delta}$ (LSC64) powder supplied by Praxair (99.9% purity). The films were deposited using a Neocera pulsed laser deposition system (COMPex 205 F, Coherent) with a 248 nm KrF excimer laser with 25 ns pulse duration. The laser repetition rate was 10 Hz and the target to substrate distance was set to 5 cm. The partial pressure of oxygen gas was 0.043 mbar. The substrate temperature was set as 100 °C and 750 °C. After the deposition, the oxygen partial pressure in the chamber was increased to 800 mbar to oxidize the films *in situ*. Consequently, the temperature was reduced at a 20 °C min^{-1} rate to room temperature before removal of the substrate. Single-side polished Si (001) substrates were used for structural and microstructural characterizations. For electrochemical characterization, polycrystalline pellets of 10% Gd doped ceria (GDC) (Praxair, 99.9%) were used as substrates. The film thicknesses were around 200 nm. The films deposited at 750 °C are referred to as high-temperature-grown, or simply as HT-grown, and those deposited at 100

°C followed by annealing at 600 °C for 4 h in ambient air post-deposition as post-annealed low-temperature-grown or simply as post-annealed LT-grown films.

The microstructure of the films was studied by scanning electron microscopy (SEM) using a Zeiss Auriga Cross microscope operating at an accelerating voltage of 5 kV and ~7 mm working distance. The surface morphology of the films was examined using an Asylum MFP-3D atomic force microscopy (AFM) instrument. AFM data were analyzed using the open-source software Gwyddion 2.53. The micrographs were taken on 1.0 x 1.0 μm^2 scan area using 512 x 512 px.

The electrochemical characterization of the films was performed using a Solartron 1260 frequency response analyzer, and in the frequency range of 13 MHz - 0.1 Hz at an amplitude of 20 mV. The samples were measured at the open-circuit potential. The samples were contacted with Pt grids (Goodfellow, 1500 wire/inches) and then sandwiched between Al_2O_3 blocks with gas channels, which were pressed to ensure maximum contact points. The impedance diagrams were fitted with electrical equivalent circuits using the ZView 2 software.

The outermost atomic surface and sub-surface chemical compositions were measured with a Qtac100 low-energy ion scattering spectroscopy (LEIS) instrument (ION-TOF GmbH, Münster, Germany) operated with normal incidence Ne^+ (5 keV) as primary beam sources coupled with a secondary ion beam sputtering source of 1 keV Ar^+ incident at 45° to normal. The primary beam scanning area was set as 1000 x 1000 μm^2 and the rastered area with the secondary ion beam was 1500 x 1500 μm^2.

3. Results

The surface topography of the LSC64 films was investigated by SEM and AFM. Figure 1a and b show the SEM top-views of the post-annealed LT-grown and HT-grown films deposited on oriented Si (001) substrates by PLD. The post-annealed film appeared to have homogeneously distributed protruding particles over the entire surface, whereas the HT-grown film was flat and smooth. Cracking can be observed in the HT-grown film, which is a result of differences in thermal expansion coefficients (TEC) between the films and the substrates. The cracking in the LT-grown film was avoided during deposition by setting slow heating and cooling rates (2 and 3 °C min^{-1}) during post-annealing.

Figure 1c and d show the surface topography of the films analyzed by AFM. The grain sizes were estimated to be ~ 30 ± 10 nm for the post-annealed LT-grown, whereas those of the HT-grown film showed ~ 60 ± 10 nm. The root mean square (rms) roughness of the films was calculated to be 3.24 ± 0.1 nm for the post-annealed film and 2.09 ± 0.1 nm for the HT-grown film. A horizontal line was drawn both in Figure 1c and d to measure the height of the protruding particles. Particularly, many particles reaching up to ~30 nm from the surface was observed for the post-annealed film (Figure 1c). Although the HT-grown film had a lower roughness compared to the post-annealed LT-grown film, the light-coloured particle under the horizontal line in Figure 1d was found to be ~20 nm high from the rest of the surface.

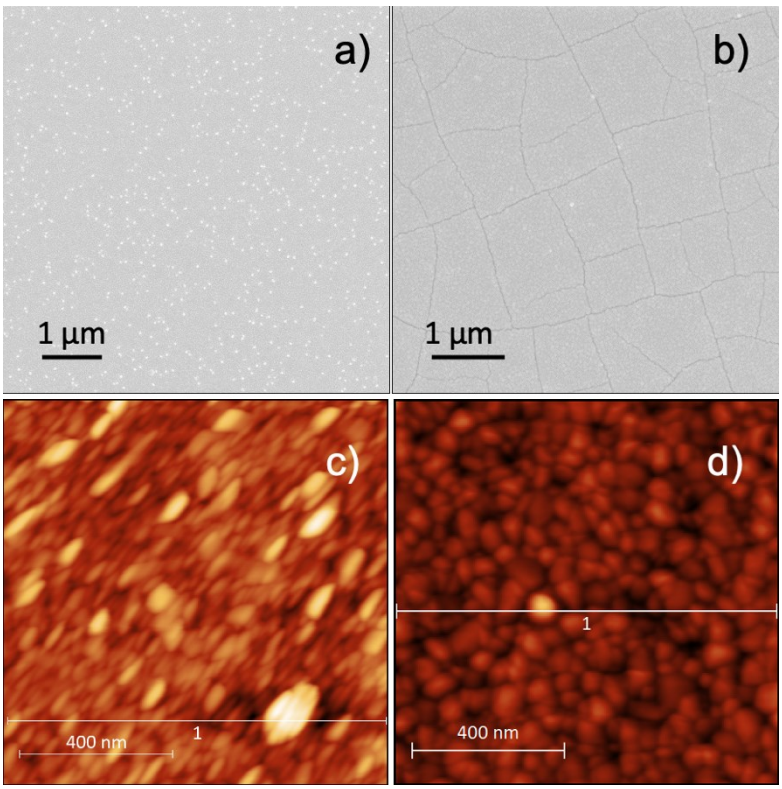

Figure 1 Top-view SEM micrographs (a, b) and AFM images (c, d) of LSC64 films deposited by the PLD on Si substrates: a) and c) showing post-annealed LT-grown film, b) and d) showing HT-grown film.[1] (https://pubs.acs.org/doi/10.1021/acsami.0c08308) Reprinted with the permission of the American Chemical Society. Further permissions related to the material excerpted should be directed to the ACS.

The ORR activity and the stability of the films were assessed by electrochemical impedance spectroscopy on symmetrical cells using GDC electrolytes. Figure 2 shows the Nyquist plots of LT-grown and HT-grown films measured at 500 °C, showing the 1st stable impedance plots (Figure 2a and c) and the 100th (Figure 2b and d). The LT-grown film post-annealed in situ. It took a few hours to get a stable Nyquist plot for the LT-grown film, since crystallization took place during the measurements. At least two resistive contributions are visible in the impedance plots. The corresponding equivalent circuit diagram is shown in Figure 2e. The resistance at the high-frequency arc (10^4-10^1 Hz) was attributed to the interfacial charge transfer resistance (denoted as R_i) and the low-frequency arc (10^1-10^{-1} Hz) to the surface resistance of the electrodes (denoted as R_s). L represents the inductance of the wires, R_{series} is the series resistance of the electrolyte, and both R_i and R_s are connected in parallel to a constant phase element (CPE). It can be observed that the post-annealed LT-grown film showed higher R_i values compared with the HT-grown one (Figure 2a and b). Although the R_s value of the HT-grown film was smaller than the LT-grown film in the initial measurement, it degraded faster. Figure 2f demonstrates the degradation rate between the 1st and 100th measurement at a constant temperature of 500 °C. It can be seen that the R_s value of the HT-grown film degraded ~2 times faster than the LT-grown film (~2.40%/h vs 1.12%/h).

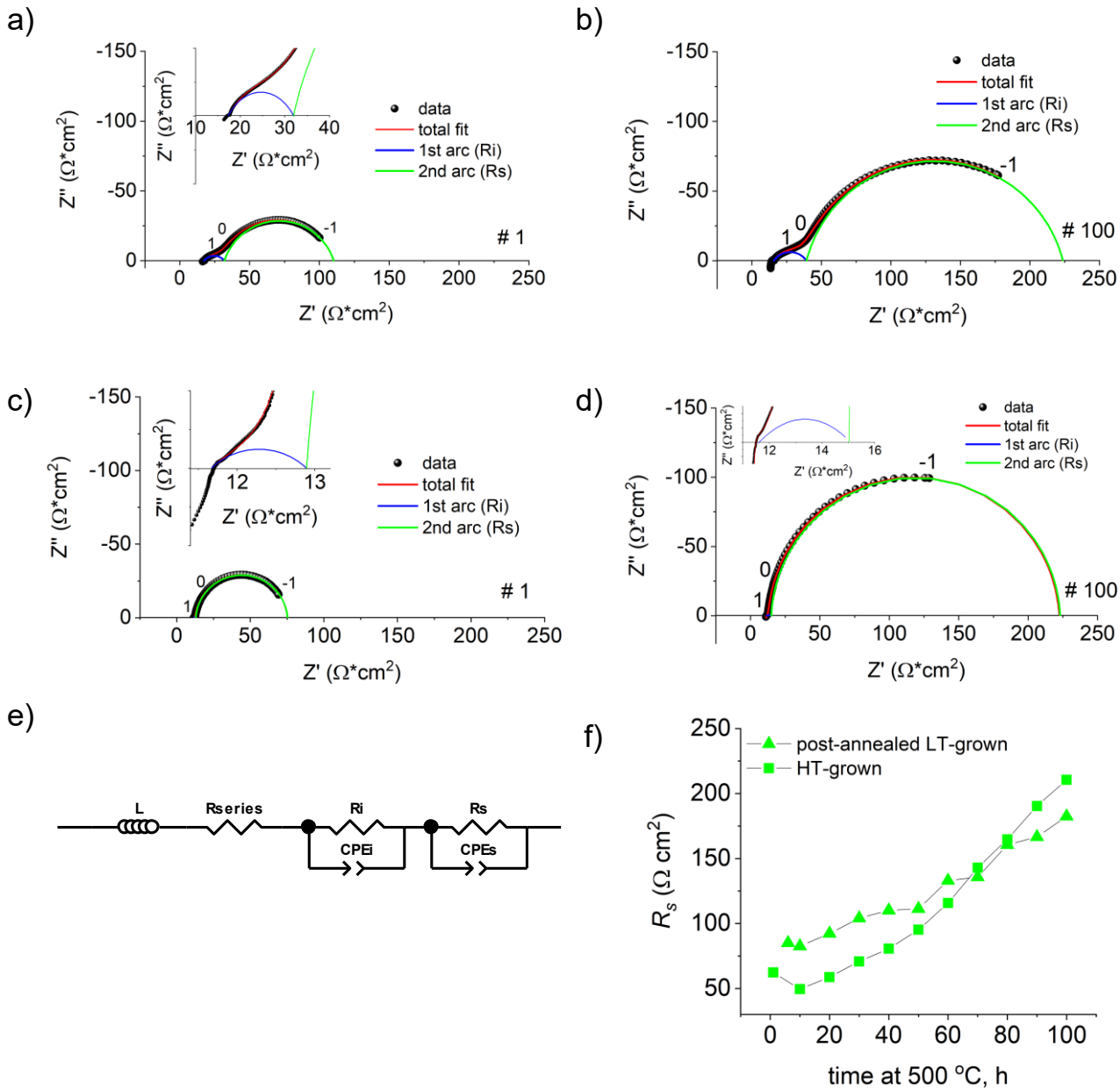

Figure 2. Nyquist plots of the 1st and the 100th measurements of (a,b) post-annealed LT-grown and (c,d) HT-grown films measured at 500 °C in OCV in ambient air. A dwell time of 1 h was set between the measurements. Equivalent circuit element is shown in e). The evolution of R_s as a function of time at a stable 500 °C is shown in f). [1] (https://pubs.acs.org/doi/10.1021/acsami.0c08308) Reprinted with the permission of the American Chemical Society. Further permissions related to the material excerpted should be directed to the ACS.

Next, LEIS analysis was used to survey the distribution of cation composition from the outermost surface layer to a few tens of nanometers below the surface. Figure 3 shows the LEIS depth profiling of the films. The data provide qualitative information and compare the cationic compositional evolution between the two films. The x-scale in the depth profiles refers to sputtering Ar^+ ion dose, in which, the small values indicate outermost to sub-surface composition, whereas, increased values refer to the sub-surface to bulk composition. The analysis depth at Ar^+ ion sputter density of $85x10^{15}$ atoms/cm^2 corresponds to approximately 18 nm depth. Horizontal lines with the same colour of each element were added as a guide to the eye, and they indicate the approximate bulk composition, deduced from the steady data points at high Ar^+ ion dose.

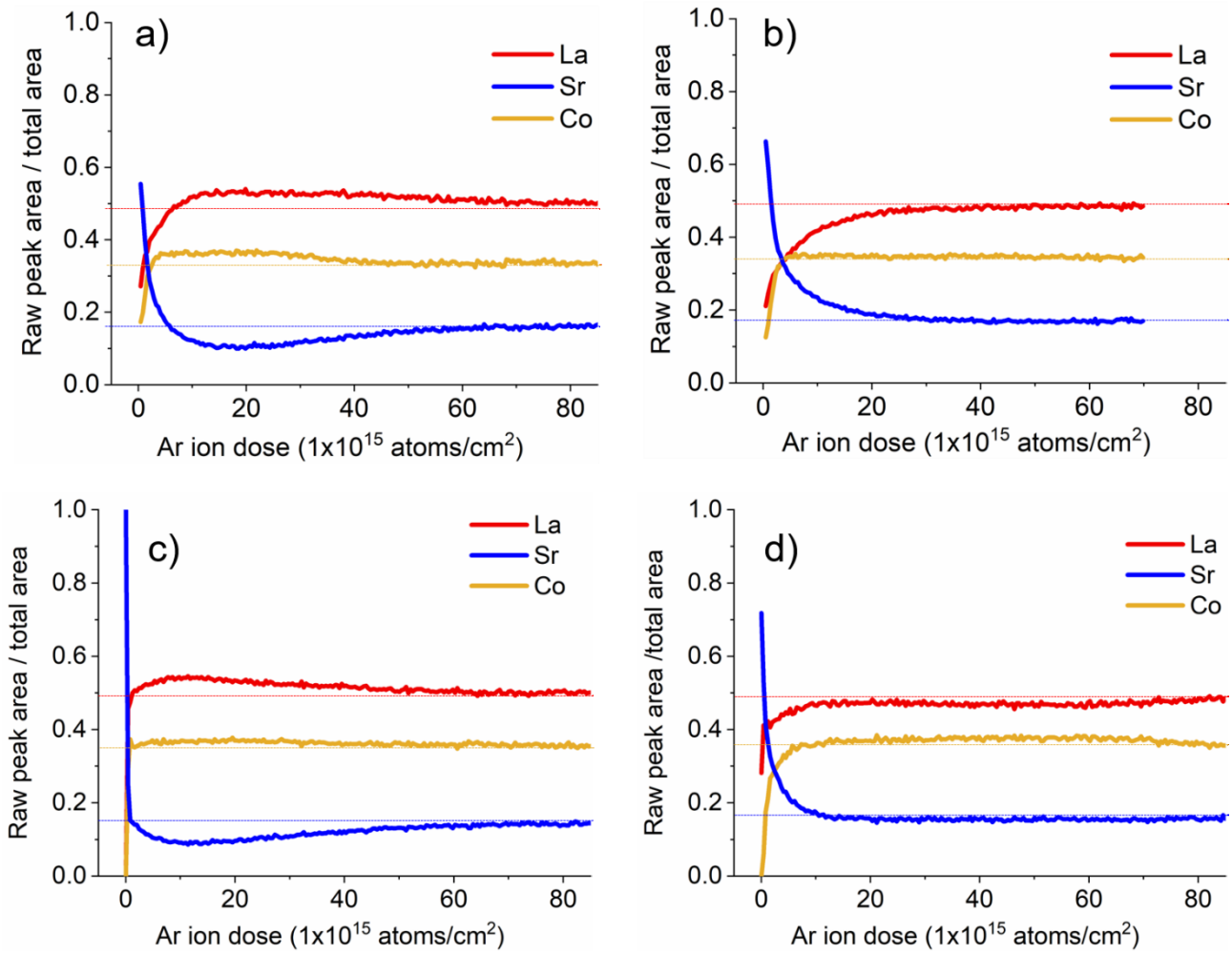

Figure 3 LEIS depth profiling of as-obtained films of a) post-annealed LT-grown, and b) HT-grown films; after long term stability tests at 500 °C for 100 h of c) post-annealed LT-grown and d) HT-grown films.[1] (https://pubs.acs.org/doi/10.1021/acsami.0c08308) Reprinted with the permission of the American Chemical Society. Further permissions related to the material excerpted should be directed to the ACS.

The enrichment of Sr in the outermost surface layer in the as-obtained films has been proven for both films in this study (Figure 3a and b), as has been previously observed with other Sr-containing perovskites.[9-11] At the same depth, La and Co were depleted at the surface and a few atomic layers below. A marked difference between the films was observed in the sub-surface, approximately between 1 nm and 10 nm below the surface. Notably, a region with highly depleted Sr and increased La concentration appeared in the post-annealed LT-grown film, whereas an enriched Sr layer was observed for the HT-grown film which continued up to ~ 6 nm below the surface.

Figure 3c and d investigate the chemical distribution of the same films after long-term annealing at 500 °C in ambient air for 100 h. It can be observed that the outermost surface layer of the post-annealed LT-grown film entirely consisted of Sr-based species (Figure 3c). However, Co concentration substantially increased immediately below this layer and reached its bulk stoichiometry. The HT-grown film showed a mixed La- and Sr-based termination (Figure 3d). Below the outermost surface layer, Sr remained in excess for a few nanometers, while Co remained deficient.

4. Conclusions

This study focuses on the influence of thermal history on the catalytic activity and stability of $La_{0.6}Sr_{0.4}CoO_{3-\delta}$ (LSC64) thin films. The films were grown by Pulsed Laser Deposition (PLD) at different substrate temperatures. The microstructure, surface topography and elemental distribution of the films were investigated and compared with the electrochemical response. In terms of ORR activity, the initial response was in favour of HT-grown film. However, long-term tests appeared to influence the catalytical stability significantly. The post-annealed LT-grown film showed two-times smaller grain size than the HT-grown film, with a rough surface comprising ~30 nm thick protruding particles. LEIS analysis indicated that Sr segregation enhanced near the surface, leaving a deficient Sr layer at the subsurface. Sr segregation is believed to proceed through clustering into the protruding particles as observed in SEM and AFM. Therefore, this type of segregation enabled the remaining surface to reveal catalytically important Co cations. On the other hand, the flat and smooth surface of the HT-grown film led to a more homogeneously distributed and thicker Sr-rich surface region near the surface compared with the post-annealed LT-grown film. Thus, thermally induced surface restructuring is believed to be the reason for the differences in the catalytic activity and long-term stability of the films.

References

[1] Celikbilek, O., Cavallaro, A., Kerherve, G., Fearn, S., Chaix-Pluchery, O., Aguadero, A., Kilner, J. A., Skinner, S. J. 2020, “Surface Restructuring of Thin-Film Electrodes Based on Thermal History and Its Significance for the Catalytic Activity and Stability at the Gas/Solid and Solid/Solid Interfaces,” ACS Appl. Mater. Interfaces, 12, pp. 34388−34401.

[2] Januschewsky, J., Ahrens, M., Opitz, A., Kubel, F., Fleig, J. 2009, “Optimized La0.6Sr0.4CoO3-δ Thin-Film Electrodes with Extremely Fast Oxygen-Reduction Kinetics,” Adv. Funct. Mater., 19, pp. 3151–315.

[3] Rupp, G. M., Tellez, H., Druce, J., Limbeck, A., Ishihara, T., Kilner, J., Fleig, J. 2015, “Surface Chemistry of La0.6Sr0.4CoO3-δ Thin Films and Its Impact on the Oxygen Surface Exchange Resistance,” J. Mater. Chem. A, 3, pp. 22759–22769.

[4] Kubicek, M., Rupp, G. M., Huber, S., Penn, A., Opitz, A. K., Bernardi, J., Stöger-Pollach, M., Hutter, H., Fleig, J. 2014, “Cation Diffusion in La0.6Sr0.4CoO3−δ below 800 °C and Its Relevance for Sr Segregation,” Phys. Chem. Chem. Phys., 16 (6), pp. 2715–2726.

[5] Cai, Z., Kubicek, M., Fleig, J., Yildiz, B. 2012, “Chemical Heterogeneities on La0.6Sr0.4CoO3−δ Thin Films—Correlations to Cathode Surface Activity and Stability,” Chem. Mater., 24 (6), pp. 1116–1127.

[6] Kubicek, M., Limbeck, A., Fromling, T., Hutter, H., Fleig, J. 2011, “Relationship between Cation Segregation and the Electrochemical Oxygen Reduction Kinetics of La0.6Sr0.4CoO3−δ Thin Film Electrodes,” J. Electrochem. Soc., 158 (6), pp. B727–B734.

[7] Garbayo, I., Esposito, V., Sanna, S., Morata, A., Pla, D., Fonseca, L., Sabaté, N., Tarancón, A. 2014, “Porous La0.6Sr0.4CoO3-δ Thin Film Cathodes for Large Area Micro Solid Oxide Fuel Cell Power Generators,” J. Power Sources, 248, pp. 1042–1049.

[8] Hwang, J., Lee, H., Yoon, K. J., Lee, H.-W., Kim, B.-K., Lee, J.-H., Son, J.-W. 2012, “Study on the Electrode Reaction Mechanism of Pulsed-Laser Deposited Thin-Film La1-XSrxCoO3-δ (x = 0.2. 0.4) Cathodes,” J. Electrochem. Soc., 159 (10), pp. F639–F643.

[9] Druce, J., Téllez, H., Burriel, M., Sharp, M. D., Fawcett, L. J., Cook, S. N., McPhail, D. S., Ishihara, T., Brongersma, H. H., Kilner, J. A., 2014 “Surface Termination and Subsurface Restructuring of Perovskite-Based Solid Oxide Electrode Materials,” Energy Environ. Sci., 7 (11), pp. 3593–3599.

[10] Celikbilek, O., Thieu, C.-A., Agnese, F., Calì, E., Lenser, C., Menzler, N. H., Son, J.-W., Skinner, S. J., Djurado, E., 2019 “Enhanced Catalytic Activity of Nanostructured, A- Site Deficient (La0.7Sr0.3)0.95(Co0.2Fe0.8)O3-δ for SOFC Cathodes,” J. Mater. Chem. A, 7, pp. 25102–25111.

[11] van den Bosch, C. A. M., Cavallaro, A., Moreno, R., Cibin, G., Kerherve, G., Caicedo, J. M., Lippert, T. K., Doebeli, M., Santiso, J., Skinner, S. J., Aguadero, A. 2019, “Revealing Strain Effects on the Chemical Composition of Perovskite Oxide Thin Films Surface, Bulk, and Interfaces,” Adv. Mater. Interfaces, 1901440, pp. 1–10.

Keywords: EFCF2020, SOx
Session B06: Advanced characterization I

https://doi.org/10.5281/zenodo.4557487

B0609

SOFC In-Field Test of a Tool for Advanced Monitoring, Diagnostics and Lifetime Prognostics

J.P. Ouweltjes (1), M. Gallo (2), P. Polverino (2), F. Galiano (3), S.N. Pofahl (4), P. Boškoski (5), G. Nusev (5), P. Caliandro (6), A. Leonardi (7)
(1) SOLIDpower S.A.
26 Av. des Sports, CH-1400 Yverdon-les-Bains/Switzerland
(2) Department of Industrial Engineering, Universita Degli Studi di Salerno
Via Giovanni Paolo II 132, 84084 Fisciano/Italy
(3) Bitron S.p.A.
Str. del Portone, 95, 10095 Grugliasco/Italy
(4) Research and Technology Development, Fuel Cell, AVL List
Hans-List-Platz 1, 8020 Graz/Austria
(5) Department of Systems and Control, Institut Jozef Stefan
Jamova cesta 39, 1000 Ljubljana/Slovenia
(6) Group of Energy Materials, Ecole Polytechnique Fédérale de Lausanne
Rue de l'industrie 17 , CH-1951 Sion/Switzerland
(7) SOLIDpower S.p.A.
Via Trento, 115/117, 38017 Mezzolombardo/Italy

Contact authors: www.EFCF.com/ContactRequest

Abstract

Accurate state-of-health (SoH) monitoring is considered a key element in avoiding faulty operation of fuel cell stacks. Such faulty operation could relate to problems in the balance-of-plant, having a global effect on the stack performance, or to problems in the stack itself, where the effect could initially be very local. This research topic was addressed in the European project INSIGHT, with the final aim to demonstrate advanced SoH monitoring in a real environment by implementing newly developed hardware equipped with novel perturbation routines and data fitting routines in a µ-CHP system from SOLIDpower. The results of the test that followed, including validation of the routines and hardware as well as simulation of different kinds of faulty operation, are reported here.

https://doi.org/10.5281/zenodo.4557524

1. Introduction

Solid Oxide Fuel Cells (SOFCs) are attractive technology in the field of combined heat and power generation due to their high power-to-heat ratio. In order to compete with other CHP technologies, SOFCs must be durable, with high, predictable performance and low maintenance costs. Thus, knowing the conditions of the system, with accurate health analysis, life prediction, fault analysis, fault prediction and fault mitigation, are essential. This has led to interest in analyzing process signals that contain information about the system's state of health (SoH), existing or imminent faults by means of fault detection and isolation (FDI) and prediction of the remaining useful life (RUL).

An important aspect in FDI is the comparison of the system performance with one that could be expected under non-faulty conditions. This can be assessed in several ways. Firstly, the actual performance can be compared with the one that is calculated by modeling under non-faulty conditions. Preferably, dynamic, quantitative models based on first principles are used. A popular classifier that uses such model data is the so-called fault signature matrix (FSM) that results from fault-tree analysis (FTA) [1-2]. Secondly, classifiers based on data-driven approaches have been reported, including wavelet transform [3-5], hybrid principal component analysis [6], support vector machine (SVM) [7], random forests (RFs) [8], neural networks [9-14], supervised self-organizing maps [15], and deep-learning networks [16]. Knowledge-based expert systems combined with a Bayesian network as a reasoner have been reported as well [17]. Thirdly, approaches that combine a quantitative model with a support vector machine or random forests data-driven classifier have been reported, which appear to be more effective than purely model-driven methods or data-driven methods, in particular where it concerns weak or complex interdependencies between faults and resulting symptoms, which are nonlinear by nature [18-19, 8]. Similarly encouraging results have been reported by combining a dynamic model with a multi-layer SVM classifier that preferably is linked with Fault Inference Tree Analysis (FITA) [20].

Available literature on SOFC-oriented remaining useful life (RUL) prediction is still relatively scarce. Some authors report about using the stack voltage as RUL indicator [7, 21-22]. Thus, the predictions are only valid when the operating conditions don't change over time. In a publication from Dolenc et al., the area specific resistance of the stack as signal for RUL prediction, supported by a nonlinear stack model, is therefore considered to be more useful than just the stack voltage [23].

In this paper, Electrochemical Impedance Spectroscopy (EIS), including both sine wave and pseudo-random binary signal (PRBS) excitation and Total Harmonic Distortion Analysis (THDA) have been deployed for fault detection on an EnGen-2500 system from SOLIDpower, housing two SOFC stacks with a total nominal power output of 2.5 kWe. Both EIS and THDA rely on imposing an AC perturbation on the DC load that is applied during fuel cell operation. With regard to EIS, results from a parametric study on SOLIDpower short-stacks have been reported by Ouweltjes et al. [24], revealing the following contributions in the impedance spectra:

- Peak below 1 Hz: Typically small peak that appeared when pure oxygen at the air electrode side was replaced with air, and thus suggested to be related to oxygen adsorption/desorption process;
- Peak around 4 Hz: Typically large peak related to gas conversion;
- Peak around 30 Hz: Typically small peak related to both cathode and anode, most likely gas diffusion through the anode substrate and cathode bulk diffusion;
- Peak around 1 kHz: Typically large peak that vastly diminished with current increase, related to the anode charge transfer reaction.

https://doi.org/10.5281/zenodo.4557524

Similar investigations were carried out by Caliandro et al. [25]; by comparing the Distribution of Relaxation Times (DRT) results with outcomes from dynamic numerical model calculations that include gas and solid phase transport coupled with charge transfer and chemical reactions it was possible to assign 6 peaks where, deviating from the parametric study by Ouweltjes et al. [24], the peak below 1 Hz was also found to be dependent on fuel mass transport, while an additional peak revealed above 5 kHz, with unknown origin. Finally, a peak was found in the DRT graphs between 100 and 500 Hz that was related to the fuel composition but also was thermally activated. Therefore, there is a suspicion that this peak is partially caused by incomplete deconvolution of the charge transfer peak appearing at higher frequency [25].
THDA relies on imposing one or several perturbation signals in order to detect nonlinearities that indicate faulty operation, which appear as harmonics when the frequency distribution of the signal is analysed. While first demonstrated on PEM fuel cells [26] and then further improved and commercialized by AVL List, it has recently also been applied to SOFC stacks by Malafronte et al. to detect limits for fuel utilization [27]. Other nonlinearities besides fuel starvation could in principle be detected as well; in a publication from Thomas et al. [28] it was shown that the technique could distinguish oxidant related nonlinearities, detectable at frequencies below 100 Hz, and fuel related nonlinerarities, appearing below 15 Hz. So by imposing two perturbation frequencies at the same time, both nonlinearities could be accurately identified.

In the next sections, a description of the tests performed on the commercial SOFC system from SOLIDpower is given. This includes the manufacture and usage of a so-called Monitoring, Diagnostic and Lifetime Tool (MDLT), equipped with algorithms to drive the power converter housed in the fuel cell system, and algorithms to perform advanced signal processing and lifetime prediction. This work was carried out in the European project INSIGHT.

2. Experimental

2.1 Description of the fuel cell system

The system that was used for the tests is schematically depicted in Figure 1. It is centered around a two-stack fuel cell arrangement for anode-supported cells operated around 750 °C delivering 2.5 kWe in total, controlled by a DC/DC power converter. The oxidant is preheated ambient air. The fuel is natural gas that is partially converted to syngas by means of an external steam reforming catalyst. Remaining fuel at the fuel cell outlet is burnt in an afterburner.

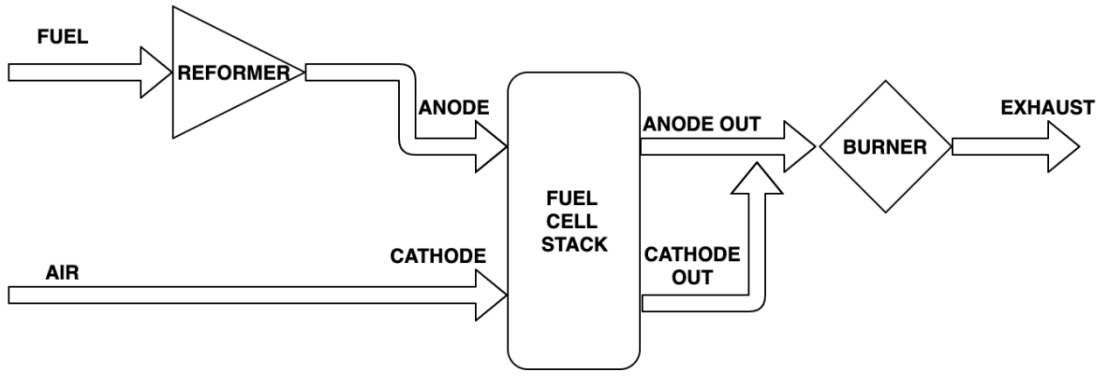

Figure 1. Flow scheme of the commercial SOFC system from SOLIDpower, called EnGen-2500.

Based on an inventory made by the project consortium in an early phase of the project, taking into account the operational experience of the project partners as well as field experience with the system, the following faults were identified as those that would be the most detrimental for the system:

- Anode reoxidation due to fuel starvation
- Carbon deposition in the reformer and/or stack due to steam shortage
- Gas leakage due to the failure of sealants in the stack

The diagnositic routines developed in the project were concentrating on the above 3 faults, with the assumption that other, less prominent faults and combined faults could be added after completion of the project by following the same rationale. Developed routines were validated by means of tests on short stacks representative of the SOLIDpower full stacks at EPFL and CEA, on full stacks at VTT and CEA, and on full stacks housed in a commercial system at SOLIDpower [29]. The experimental results shown below report about this last test.

2.2 Description of the developed diagnostic routines

The developed probing algorithms are dealing with imposing a sinusoidal perturbation or a pseudo-random binary signal (PRBS), both aiming at scanning the stack reponse between 10 kHz and 0.1 Hz, and single frequency sinusoidal perturbation used for THDA. While impedance spectra constructed from sinusoidal perturbation rely on calculating the phase shift in the imposed signal by the probed system, PRBS perturbs the system with a broadband signal, where the impedance is computed not at a single frequency but at a continuum of frequencies of interest by means of a continuous wavelet transform. Compared with sinusoidal perturbation, PRBS allows for significantly shortening the probing time, which is attractive for on-line fault detection [30].

Based on the considered faults and the available impedance spectroscopy and THDA algorithms, the fault signature matrix (FSM) was constructed, considering relevant features extracted from both spectrum deconvolution by means of DRT and Equivalent Circuit Modelling (ECM) approaches. The constructed FSM states that fuel starvation will appear as an increased gas conversion peak appearing in the low frequency part in impedance spectra, while it would slightly shift towards lower frequency. In addition, a drop in stack voltage, increased voltage fluctuations, and changes in pressure drops and temperatures in the system are anticipated. A shortage in steam most likely first reveals in the reformer where, once carbon starts to deposit, changes in reformer temperature and pressure drop will occur. As long as the reformer is not fully blocked while carbon deposition takes place, the amount of fuel that leaves the reformer will be less than normal, while it will be more enriched with hydrogen due to the dehydrogenation reaction. Much like fuel starvation, steam shortage will cause an increase of the gas conversion impedance while it shifts to lower frequency. Sealant failure will likely be most detrimental when it happens prior to the stack (e.g. in the fuel manifold) or within the stack close to the inlet. Considering the fact that only the stack voltage is probed, it will likely be difficult to detect sealant failures that affect only one repeat element in an early phase. For more severe sealant leakages, the effects will be similar to those observed for fuel starvation.

2.3 Description of the developed hardware

In order to diagnose the SOFC system from SOLIDpower, the company Bitron developed the Monitoring, Diagnostics and Lifetime Tool (MDLT). Where possible, the MDLT is based on widely available hardware components. It includes a custom-made analog front-end

board for sampling the SOFC current and voltage, a BeagleBone Black for running the selected configuration, accepting user inputs, acquisition commanding and for data storage, and a Raspberry Pi for running diagnostic algorithms and for showing outputs, an ethernet switch to realise communication between the 3 boards and the graphical user interface, and a power supply unit. The usage of a double board (i.e. the BeagleBone Black and the Raspberry Pi) allows for increasing the rapidity of the data aquisition and treatment.

https://doi.org/10.5281/zenodo.4557524

An impression of how the MDLT was mounted on the system is shown in Figure 2.

Figure 2. MDLT mounted on the EnGen-2500 system from SOLIDpower: top: MDLT; bottom left: location of the MDLT at the back of the SOFC EnGen-2500 system; bottom right: front side of the Engen 2500 installed in its testing location

3. Results

3.1 Test evolution

The system was tested over a time period of almost 7000 hours, see Figure 3. Advanced diagnosis was carried out only on one of the two stacks housed in the system. During the first two months (phase A), basic functionality tests with the MDLT took place, using algorithms that were developed during the European project HEALTHCODE, dealing with diagnosing PEMFC systems, and thus not yet optimized for SOFC operation. This helped to check proper communication between the MDLT and the DC/DC converter, and remote operaton of the MDLT. During the following 6 months (phase B), validation with the SOFC algorithms took place, allowing the project partners to test and, if necessary, improve their algorithms. This test period was interrupted by a periodic regular maintenance at the SOLIDpower facilities after 2800 h of operation. After 5200 h of operation one of the stacks -not the one that was probed- deteriorated. This also affected the operation point of the probed stack. It was then decided to replace the faulty stack in order to complete the tests in a controlled way. After 6100 h of operation, issues occurred with the MDLT device that were solved by replacing the MDLT device with a bug-free copy.

As the time that remained in the project was limited, the FDI routine was only validated for fuel starvation. But in principle it would have been fit for detecting the other considered faults as well, as well as predicting the remaining useful life (RUL). During the experiments, the fuel utilization was kept modest, considering the normal operating conditions of the system, but that guaranteed sufficient stability over the test period to validate the algorithms. This validation took place both at 1030 W stack power output and 570 W stack power output (note that this is the power ouput of the probed stack), where the fuel utilization was systematically varied between 60 and 72%, and where a boundary for faulty operation was artificially set at 70%.

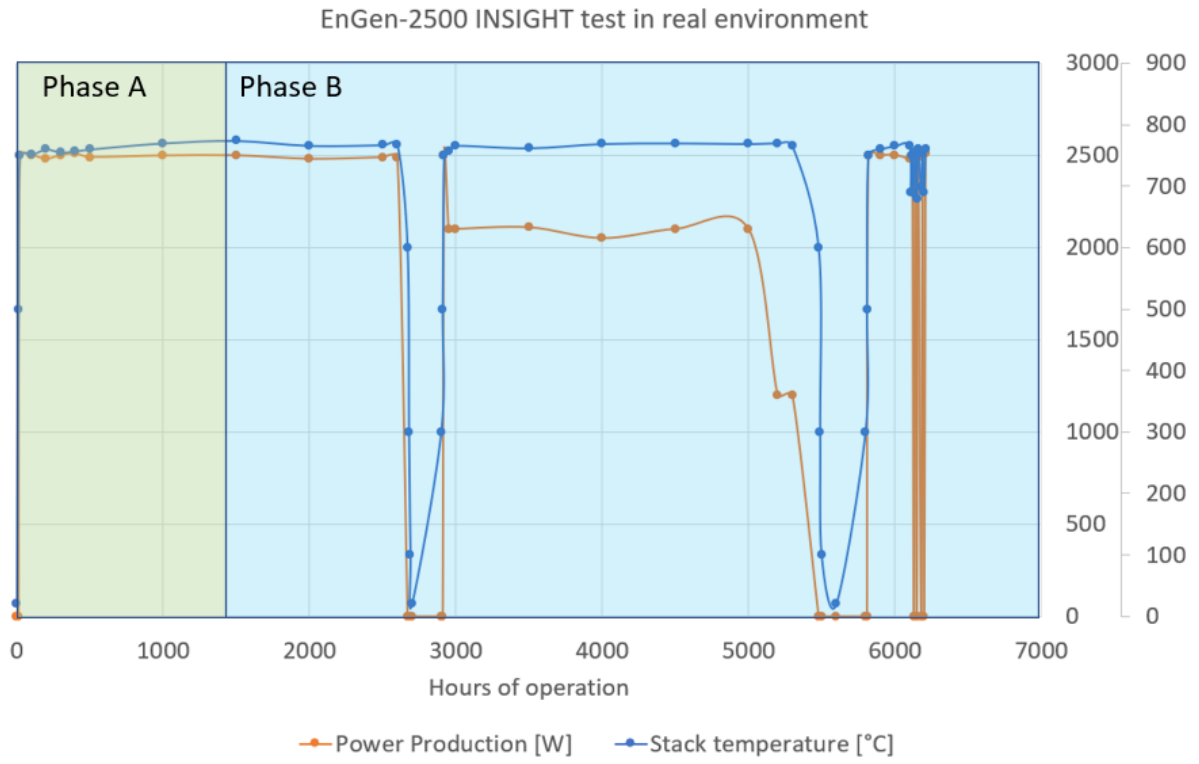

Figure 3. Evolution of the total stack power and stack temperature during the test.

3.2 THDA results

The experiments with respect to total harmonic distortion were designed to test the impact of the perturbation frequencies (between 0.1 and 1.0 Hz) and perturbation amplitudes (between 1 and 5 A) at different fuel utilizations. In addition, measurements were carried out at steady state to understand the stability of the voltage signal without perturbation.
The results from the steady-state measurements, depicted in Figure 4, a strong periodic component of approximately 0.1 Hz can be observed, where an additional distortion in the voltage perturbation is present. This is typically not seen for stacks operated in dedicated test benches. This fluctuations are therefore thought to be related to the system control, which will complicate analyses that rely on signal perturbation.

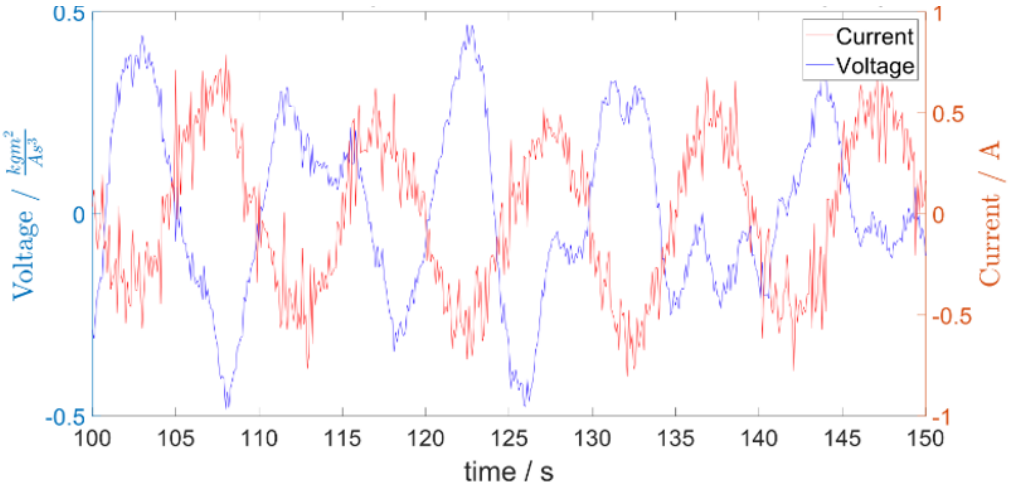

Figure 4. Voltage and current fluctuations in steady state at 61% fuel utilization

Figure 5 highlights some important findings from the THD analysis. From the graph on the left it can be observed that, apart from measurements that took place at 61% fuel utilization, the nonlinearity of the signal increases with increasing fuel utilization, while the detectability of the nonlinearity increases with perturbation amplitude. While this could be related to a better signal-to-noise ratio, it should also be realised that higher AC amplitude drives the system more towards the nonlinear region. And from the graph on the right side it can be seen that for the perturbation amplitude of 5 A, the best discrimination is obtained at the lowest perturbation frequencies.

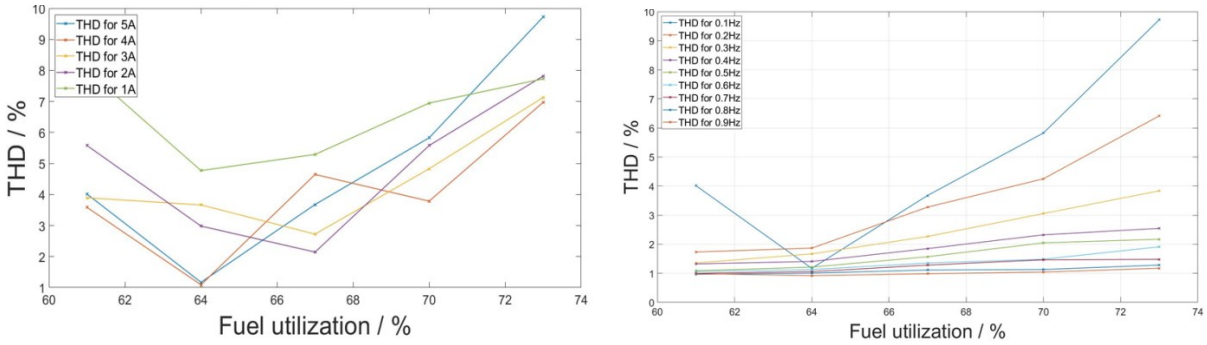

Figure 5. THD signal as a function of perturbation amplitude and fuel utilization at a perturbation frequency of 0.1 Hz (left side), and THD signal as a function of perturbation frequency and fuel utilization at a perturbation amplitude of 5 A (right side), all at a stack power output of 1030 W at 19.7 A DC current.

3.3 Impedance spectrocopy results

As explained previously, impedance spectra were obtained both by sinusoidal perturbation and PRBS, using 1.5 A perturbation in both cases. Examples of the quality of the obtained spectra are shown in Figure 6, from which it can be seen that the spectra basically contain two features, i.e. one with a maximum around 6 kHz (left arc in the plots) that is likely related to the anode charge transfer reaction, and one with a maximum around 0.2 Hz (right arc in the plots) that is likely related to gas conversion. At low frequency, the spectra are noisy and hard to interpret,which is further highlighted by the voltage response in the time domain while the spectra were recorded.

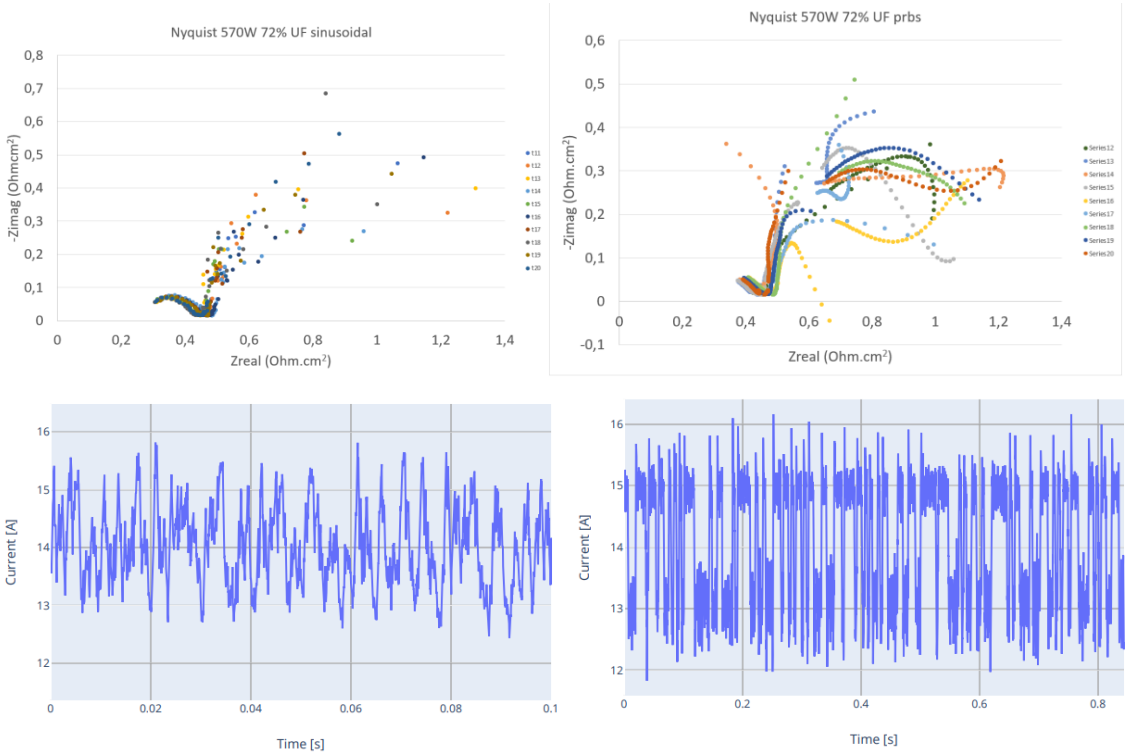

Figure 6. Impedance spectra (top) and assoiated voltage response in the time domain (bottom) obtained by sinusoidal perturbation (left) and by PRBS perturbation (right).

In order to better visualise the impact of the test conditions on the stack impedance, the spectra that belonged to the same series have been averaged in Figure 7. Obviously better quality spectra are obtained now, where it can be seen that increased fuel utilization causes a considerable increase of the low frequency feature. A shift towards lower frequency was not observed for the considered dataset. In addition, a slight increase in Ohmic resistance can be seen in the plots at 1030 W, but this is not the case at 570 W.

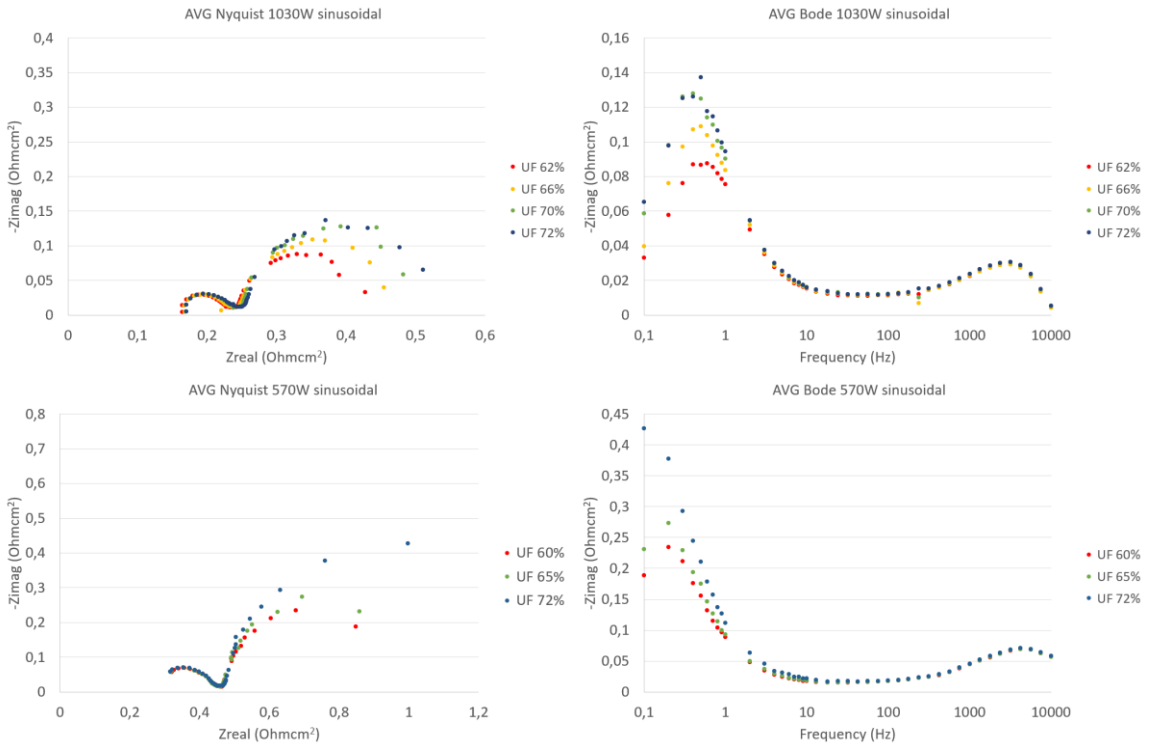

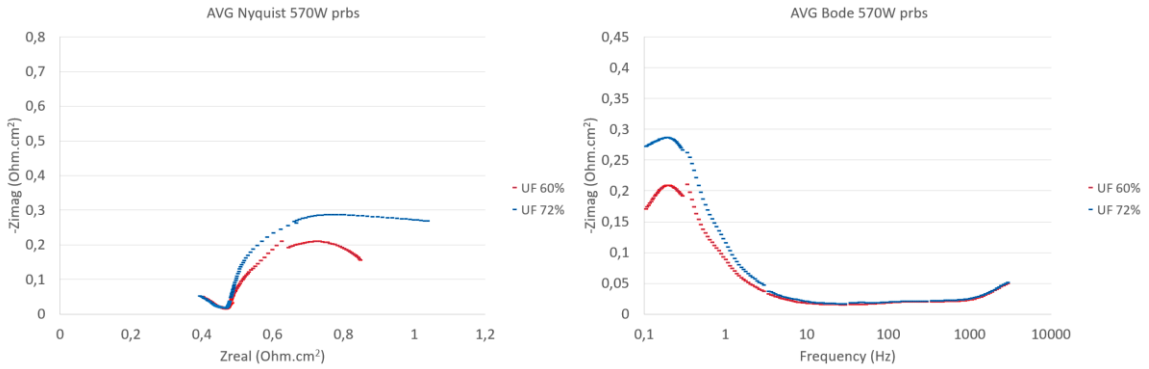

Figure 7. Averaged Nyquist plots (left) and Bode plots (right) obtained at 1030 W (top) and 570 W (middle) for sinusoidal perturbation, and at 570 W (bottom) for PRBS perturbation.

In Figure 8, the DRT graphs are shown for the sinusoidal impedance spectra displayed in Figure 7, obtained after Tikhonov regularization with inductance correction within the regularization problem [25], a method that worked well for datasets obtained on short stacks in an earlier phase of the project (results not reported here). Generally good reproducibility can be observed for frequencies above 1 kHz. At lower frequencies, the results are less clear. This implies that the method requires further improvement, for which additional good quality datasets under well defined conditions that are obtained in the system under investigation are needed.

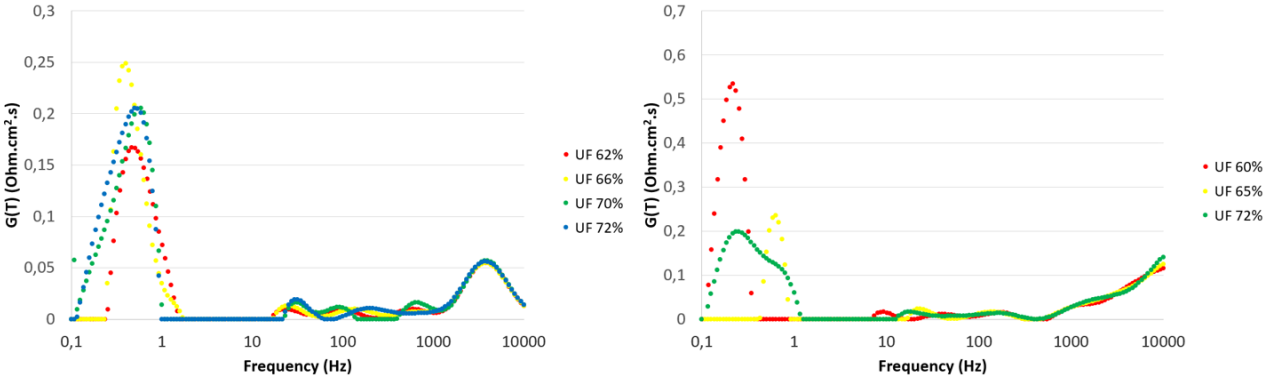

Figure 8. Sinusoidal impedance spectra deconvoluted by DRT at 1030 W (left) and 570 W (right)

3.4 Fault detection and isolation results

The FDI algorithm includes a design part that is constructed prior to the online measurements, and an application part that compares the actual status with the design part. Important steps in the offline part were parameter extractions from representative tests done under controlled conditions (experimental data obtained by EPFL, DTU and CEA, results not reported here) by means of a proprietary ECM deconvolution algorithm [31], the subsequent determination of threshold levels of these parameters, and the final construction of the fault signature matrix (FSM). For the online monitoring, the same algorithm for parameter extraction is used, the values of which are compared with the FSM, and ultimately leading to fault isolation and state of health assessment.

As an example, Figure 9 shows the extracted low frequency resistances for the sinusoidal impedance measurements performed at 1030W power. It can be seen that the FDI algorithm detects fuel starvation when the fuel utilization exceeds 70%, with 71% accuracy at 70% fuel utilization, and 91% at 72% fuel utilization. Similar scores were obtained at 570 W power and 72% fuel utilization.

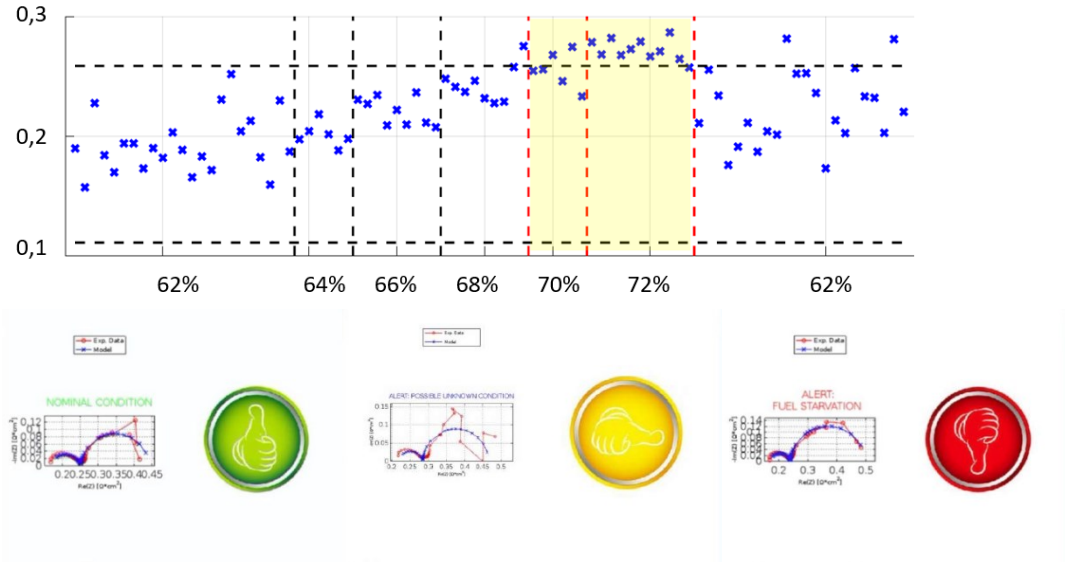

Figure 9. Gas conversion impedance (Ohm.cm2) at 1030 W extracted by means of the ECM routine (top) as a function of fuel utilization that ranged between 62 and 72%, and subsequent output examples of the FDI algorithm shown on the GUI (Graphical User Interface), which is the actual output of the board running real time with the stack, distinguishing normal operation (green), faulty operation (red) and unclear faulty operation (yellow) while driving the system towards fuel starvation.

4. Conclusions

Important steps towards SoH monitoring of a commercial SOFC system by means of total harmonics distortion and impedance spectroscopy have been made. The results show that the developed hardware and diagnostic routines for stack perturbation and fault detection accurately detect fuel starvation. An important finding was that the analysed process signals contained noise that is likely caused by the system control. The noise can be suppressed by increasing the perturbation, which was demonstrated for THDA, or by signal averaging, which was demonstrated for impedance spectroscopy by means of sinusoidal perturbation and PRBS perturbation. In addition, it was shown that the developed routine to deconvolute impedance spectra by DRT, which was previously succesfully validated for short stacks, requires further improvement to be used in the commercial system.

It was further shown that the FDI algorithm detects fuel starvation on the system when the fuel utilization exceeds 70%, with 71% accuracy at 70% fuel utilization, and 91% at 72% fuel utilization.

It is expected that the findings provide a good basis for further maturing the SoH monitoring approach for other faults, where deeper implementation in the control and fault mitigation strategy can be considered.

https://doi.org/10.5281/zenodo.4557524

Acknowledgement

The research leading to these results has received funding from the Fuel Cells and Hydrogen 2 Joint Undertaking under the European Union's Horizon 2020 research and innovation programme under grant agreement No 735918 (INSIGHT project, http://www.Insight-project.eu).

References

[1] Steiner Y., Hissel D., Moçotéguy P., Candusso D., Marra D., Pianese C, Sorrentino M., Fuel Cells, 2012, 12(2), 302-309
[2] Polverino P., Sorrentino M., Pianese C., Appl. En. 2017, 204, 1198-1214
[3] Peng Z.K., Chu F.L., Mech. Syst. And Sign. Proc. 2004, 18, 199-221
[4] Wang K., thesis, Université de Franche-Comté, 2012
[5] Pahon E., Steiner Y., Jemei S., Hissel D., Péra M.C., Wang K., Moçotéguy P., Int. J. Hydr. En. 2016, 41, 13678-13687
[6] Murshed A.M., Huang B., Nandamumar K., Asia-Pac. J. Chem. Eng., 2011, 6(2), 204-219
[7] Wu X., Ye Q., J. Power Sour. 2016, 321, 47–56
[8] Costamagna P., Di Giorgi A., Gotelli A., Magistri L., Moser G., Sciaccaluga E., Trucco A., Sensors 2016, 16, 1336
[9] Arriagada J., Olousson P., Selimovic A., J. Power Sour. 2002, 112, 54-60
[10] Wu X.J., Zhu X.J., Cao G.Y., Tu H.Y., J. Power Sour. 2007, 167, 145-150
[11] Milewski J., Świrski K., Int. J. Hydr. En. 2009, 34, 5546-5553
[12] Sorrentino M., Marra D., Pianese C., Guida M., Postiglione F., Wang K., Pohjoranta A., En. Proc. 2014, 45, 298-307
[13] Pohjoranta A., Sorrentino M., Pianese C., Amatruda F., Hottinen T., En. Proc. 2015, 81, 173-181
[14] Wu X.L., Xu Y.W., Xue T., Zhao D.Q., Jiang J., Deng Z., Fu X. Li X., Appl. En. 2019, 248, 126-140
[15] Wu X.J., Liu H., J. El. En. Conv. Stor. 2015, 12(3)
[16] Zang Z., Li S.H., Xiao Y., Yang Y., Appl. En. 2019, 233-234, 930-942
[17] Wang K., Péra M.C., Hissel D., Yousfi Steiner N., Pohjoranta A., Pofahl S., IFAC Proc. Vol. 2012, 45(21), 675-680
[18] Pellaco L., Costamagna P., Greco A., Moser G., De Giorgi A., Magistri L., Trucco A., El. Lett. 2014 , 50(11), 824–826.
[19] Moser G., Costamagna P., Di Giorgi A., Greco A., Magistri L., Pellaco L., Trucco A., Math. Probl. Eng. 2015, 2015, 1-12
[20] Li S., Cao H., Yang Y., J. Power Sour., 2018, 378, 646–659
[21] Zaccaria V., Tucker D., Traverso A., J. Power Sour. 2016, 311, 175-181
[22] Marra D., Sorrentino M., Pianese C., Iwanschitz B., J. Power Sour. 2013, 241, 120-129
[23] Dolenc B., Boškoski P., Stepančič M., Pohjoranta A., Juričić Đ., En. Conv. Man. 2017, 148, 993-1002
[24] Ouweltjes J.P., Caliandro P., Diethelm S., Wuillemin Z., Nakajo A., SOSLEM project deliverable 4.2, downloadable from the SOSLeM web site (www.soslem.eu)
[25] Caliandro P., Nakajo A., Diethelm S., Van Herle J., J. Power Sour. 2019, 436, 226838
[26] Ramschak E., Peinecke V., Prenninger P., Schaffer T., J. Power Sour. 2006, 157, 837
[27] Malafronte L., Morel B., Pohjoranta A., Fuel Cells 2018, 18(4), 476-489
[28] Thomas S., Lee S.C., Sahu A.K., Park S., Int. J. Hydr. En. 2014, 39, 4558-4565

[29] Mougin J., Morel B., Ploner A., Caliandro P., Van herle J., Boškoski P., Dolenc B., Gallo M., Polverino P., Pohjoranta A., Nieminen A., Pofahl S.N., Ouweltjes J.P., Diethelm S., Leonardi A., Galiano F., Tanzi C., ECS Transactions, 91 (1) 731-743 (2019)
[30] Debenjak A., Boškoski P., Musizza B., Petrovčič J., Juričić, J. Power Sour. 2014, 254, 112-118
[31] Petrone R., Pianese C., Polverino P., Sorrentino M., Int. Patent Number WO2016/071801

Keywords: EFCF2020, SOx
Session B06: Advanced characterization I

B1202

Improved mesoporous scaffolds for composite electrodes in solid oxide devices for direct hydrogen production

Simone Anelli (1), Federico Baiutti (1), Aitor Hornés (1), Lucile Bernadet (1), Marc Torrell (1), Albert Tarancón (1,2)
(1) Catalonia Institute for Energy Research (IREC), Department of Advanced Materials for Energy, 1 Jardins de les Dones de Negre, 08930 Barcelona/Spain
(2) ICREA: Catalan Institution for Research and Advanced Studies, Barcelona/Spain

Contact authors: www.EFCF.com/ContactRequest

Abstract

The utilization of nanocomposite electrodes has been proven as an effective approach to enhance the performances of Solid Oxide Cell (SOC) devices. Among different strategies, the employment of mesoporous materials synthetized by hard-template methods came to the fore because of their elevated degree of porosity and the high level of provided percolation. Moreover, their use mitigates the formation of high current-density paths. Nano casting method allows the fabrication of high ordered microstructures presenting good thermal distribution through the electrode. Gadolinium-doped ceria (CGO - $Ce_{1-x}Gd_xO_{2-x/2}$) is one of the state-of-the-art materials on SOC devices [1] due to its remarkable ionic conductivity and its high thermochemical stability. CGO is employed as a porous backbone and is typically infiltrated by perovskite catalysts such $La_{1-x}Sr_xCoO_{3-\delta}$ (LSC), $La_{1-x}Sr_xMnO_3$ (LSM) or $La_{1-x}Sr_xCo_{1-y}FeyO_{3-\delta}$ (LSCF) [2] for the fabrication of SOC oxygen electrodes. The large utilization of mesoporous CGO backbones have been limited so far by: i) thermal stability during the processing steps of the device and ii) silica contamination coming from the template, which could inhibit the ionic conductivity of the material and affect the final performances [3].
A two-fold route was developed for overcoming such drawbacks by ex-situ chemical removal of the residual SiO_2 and by decoration with cobalt oxide (sintering aid) and presented in a dedicated study [4]. The CGO mesoporous powders were used as backbone for the oxygen electrode fabrication in a complete SOC, which was electrochemically tested in SOFC and SOEC configuration, showing high performances (1.35 W cm^{-2} at 0.7 V and an injected current of 1.30 A cm^{-2} at 1.3 V, respectively, at T = 750 °C) overcomes state-of-the-art benchmark cells with similar configuration and sparks the interest towards novel strategies based on ceramic nanocomposites for SOC application [4].
In this contribution is reported the electrochemical characterization by impedance spectroscopy after a durability test made on this device for 1000 h at 750 °C applying a current density of 0.5 A cm^{-2}. Such test showed a degradation rate of ≈125 mV kh^{-1}.

https://doi.org/10.5281/zenodo.4557607

Introduction

In the recent years the increasing demand for sustainable energy sources and for new and more efficient conversion strategies, focused the attention on solid oxide cells (SOCs) [5]. SOCs can work as fuel cells to produce energy from hydrogen or other biofuels (e.g. Methane) or as electrolyser cells, to produce hydrogen from the separation of water or syngas trough the co-electrolysis process of water and carbon dioxide [6,7]. In particular, the production of syngas is of great importance for the generation of chemicals or liquid fuels via Fischer-Tropsch synthesis [8]. SOC are characterized by high efficiencies, which grant high energy conversion percentage (70-80%), due to the relatively high operating temperature (600-900 °C) [9,10].

The typical materials used for manufacturing such devices are nickel oxide and yttria-stabilized zirconia (NiO-YSZ) for the fuel electrode, which is often the thicker layer and is generally the part of the cell that should also provide mechanical stability. The dense electrolyte is usually made of YSZ, which should guarantee a good ionic conductivity and the gas tightness of the system [2]. The oxygen electrode is generally composed by perovskite materials because they can provide an excellent electronic conductivity, as happens for $La_{1-x}Sr_xMnO_3$ (LSM), and even a mixed ionic-electronic conductivity (MIEC) as in the case of $La_{1-x}Sr_xCoO_{3-\delta}$ (LSC), or $La_{1-x}Sr_xCo_{1-y}Fe_yO_{3-\delta}$ (LSCF) [2]. However, the ionic conductivity of these materials is not sufficient to guarantee high performances, therefore they are often coupled with other types of ceramics like gadolinium-doped ceria (CGO - $Ce_{1-x}Gd_xO_{2-x/2}$), which is known to be an excellent ionic conductor [11]. Together they can form highly efficient composite electrodes and increase the triple phase boundary (TPB), which is formed between ionic and electronic conductor species when they are contact with the gas [1,12].

Among different characteristics, the electrode should guarantee a certain degree of porosity (to allow the penetration of the gas to the active part), mechanical stability and, as already mentioned, both ionic and electronic conductivity [13].

A beneficial approach for maximizes the performances of such electrodes is the infiltration of nanostructured architectures, which can provide a good thermal distribution on the area of the electrode and a high surface area. In previous reports of our group were produced ceria-based mesoporous materials (pore size 2-50 nm) with measured BET areas > 100 g cm^{-2} [14]. Such mesoporous materials are synthetized via hard templating method by the utilization of a commercial silica template (KIT-6), which is usually removed through the washing by an alkaline solution [14]. Unfortunately, a considerable silica contamination remains localized at the grain boundaries of the mesoporous powders causing some limitation to the ionic conductivity of the material [3]. Moreover, such mesoporous materials cannot be fired at high temperature because their high reactivity. Such reactivity generates also a certain evolution of the nanostructure with the temperature, reaching the extreme case of the collapse of the backbone structure for temperature above 1000 °C [15].

For such reasons, a dedicated study was conducted, focused on the solution of these two specific issues [4]. The approach involved an additional cleaning step by hydrofluoric acid, known for its ability to easily dissolved silica, and to the utilization of Co oxide as sintering aid, to decrease the firing temperature of the mesoporous CGO [16,17]. The performances showed were high, with a peak power density ≈1.35 W cm^{-2} at 0.7 V in fuel cell configuration and an injected current of ≈1.30 A cm^{-2} at 1.3 V in co electrolysis mode at T = 750 °C [4]. A durability test of overall 1000 h was conducted in co electrolysis showing a drop in performances around 125 mV kh^{-1} [4]. In this contribution is reported the electrochemical characterization made on the cell by impedance spectroscopy before and after the durability test. Such results, together with a microstructural characterization of the cell after operation, are here discussed to explain the reasons of the degradation.

https://doi.org/10.5281/zenodo.4557607

1. Scientific Approach

Mesoporous $Ce_{0.8}Gd_{0.2}O_{1.9}$ was synthetized by hard template method using a commercial silica template named KIT-6. Nitrate precursor in stoichiometric proportion ($Ce(NO_3)_3$ $6H_2O$ and $Gd(NO_3)_3$ $6H_2O$) were dissolved in ethanol together with the KIT-6, dried and then calcinated at 600 °C for 5 h. Subsequently, the silica was removed by washing firstly with a solution 2M of NaOH and secondly with water. A detailed description of the method could be find elsewhere [18].
The mesoporous powder was etched also with hydrofluoric acid (2.5 %v/v) to remove the residual SiO_2 contamination coming for the template and decorated with Co Oxide (1 %mol) as sintering aids, to lower the firing temperature of the scaffold. The procedure is exposed in detail in a dedicate work of the group [4].
A complete SOC with a thick fuel electrode (300 μm) of NiO-YSZ and a dense electrolyte of YSZ (7 μm) both made by tape casting (SOLIDpower, SPA). On top of the half-cell was deposited a CGO barrier layer by PLD to separate the YSZ form the Sr-rich species present in the oxygen electrode (≈1 µm, sintered at 1200 °C) and a rugosity layer of commercial CGO powder by airbrush (sintered at 1250 °C). Subsequently the CGO mesoporous scaffold was airbrushed on top of the rugosity layer (thickness ≈10-15 μm) and sintered at 850 °C. The backbone was infiltrated by LSCF precursor solution and calcinated afterward at 800 °C. Eventually a final layer of commercial LSCF was airbrushed (≈20-25 μm) on top of the CGO scaffold and sintered at 850 °C [4].
A Durability of 1000 h was conducted in COSOEC configuration (65% H_2O, 25% CO_2 and 10% H_2, gas composition at the fuel electrode) applying 0.5 A cm^{-2} at 750 °C, highlighting a voltage increase of 125 mV kh^{-1} [4].
In this contribution firstly, a microstructural characterization of the mesoporous powders synthetized for fabricating the function layer is reported. Secondly, the electrochemical characterization of the cell by impedance spectroscopy, before and after the durability test is presented and discussed. Eventually SEM cross section micrographs of different part of the cell are presented to rationalize the results obtained from the fitting of the impedance spectra.

2. Experiments

The microstructural analysis was conducted using a Carl ZEISS Auriga scanning electron microscope (SEM) with an energy dispersive X-ray spectroscopy (EDX) detector, by X-ray diffraction (XRD) measurements (2θ range 20° to 90°) on a Bruker-D8 Advance instrument at room temperature using Cu-Kα radiation and by Expert-Pro Diffractometer (Cu-Kα1 and Cu-Kα2 radiation) in the 2θ range 0.2° and 5°. The SOC was tested inside a ProboStat™ (NorECS AS) station, using a tubular furnace to reach the operating temperature (750 °C) and Ceramabond™ (Aremco) as sealant, to ensure the gas separation between the two electrodes. An M9700 electronic load from Maynuo Electronic Co was used to test the electrochemical properties of the cell, under co-electrolysis (gas composition 65% H_2O, 25% CO_2 and 10% H_2), while a Novocontrol spectrometer from NOVOCONTROL Technologies GmbH & Co. KG was utilized for the EIS characterization.

3. Results

Fig. 1 shows two SEM images at different magnification (Fig. 1a and Fig. 1b) where is presented the repetitive structure of the mesoporous. One can notice the presence of some elongated particles together with the synthesized CGO powders, which are probably due to the incomplete removal of the silica.

https://doi.org/10.5281/zenodo.4557607

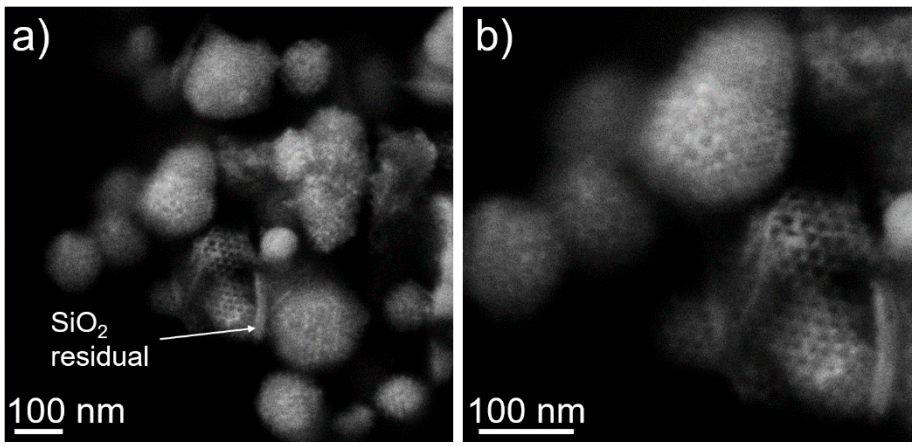

Fig. 1: a) Micrograph of the mesoporous CGO after the cleaning by NaOH. b) High magnification picture of the same zone.

Fig. 2 shows the results of the characterization on the mesoporous powders etched by HF and decorated by Co oxide. The synthetized powders analyzed by XRD (Fig 2a) show the typical peaks of the CGO, while after the etching by HF some new peaks appear on the pattern. Such peaks have been recognized as Gd and Ce-rich fluorite phases due to a partial etching of the hydrofluoric acid to the mesoporous powders [4]. However, the small angle XRD analysis of Fig. 2b demonstrates that the repetitive structure of the mesoporous CGO it is not affected by the etching. In the aforementioned work of the group focused on the optimization of such structures, the amount of SiO_2 after and before the etching is measured by Inductively coupled plasma mass spectrometry (ICP-MS), with the silica content which passes form 0.9 %wt. to 0.2 %wt. respectively [4].

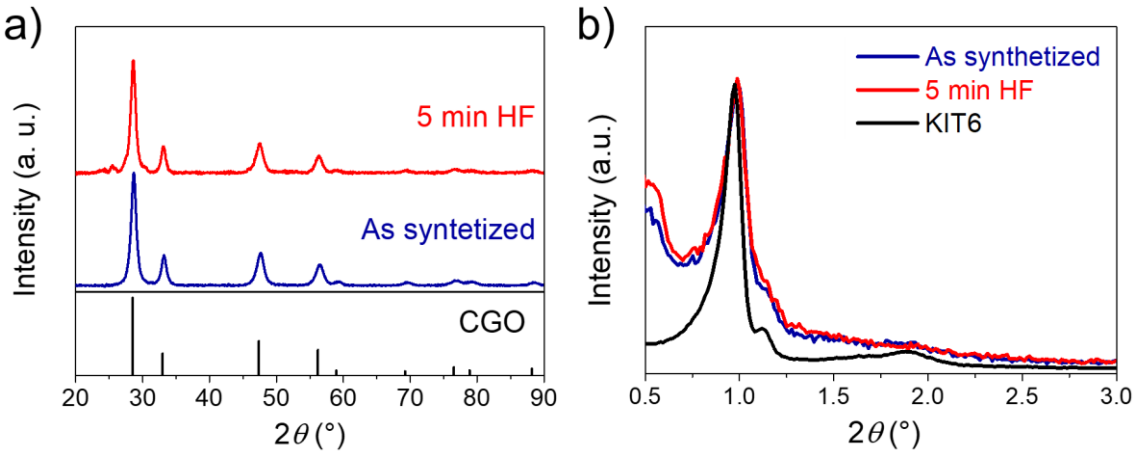

Fig. 2: a) XRD on the mesoporous powders before and after the etching by HF and b) small angle XRD of the two powders compared with the pattern from the KIT-6 template.

The cell produced with the nanostructured functional layer, was tested on co-electrolysis mode for 1000 h with an applied current 0.5 A cm^{-2}, showing an increment of voltage of 125 mV kh^{-1} [4]. EIS spectroscopy measurement at the OCV were conducted after (Fig. 3a) and before (Fig. 3b) the durability test. An equivalent circuit (inset figures 3a and 3b), made by and inductance (L), a serial resistance (Rs) and two ZARC elements ($R_{p1}Q_1$ and $R_{p2}Q_2$) was utilized for the fitting of the impedance spectra.

https://doi.org/10.5281/zenodo.4557607

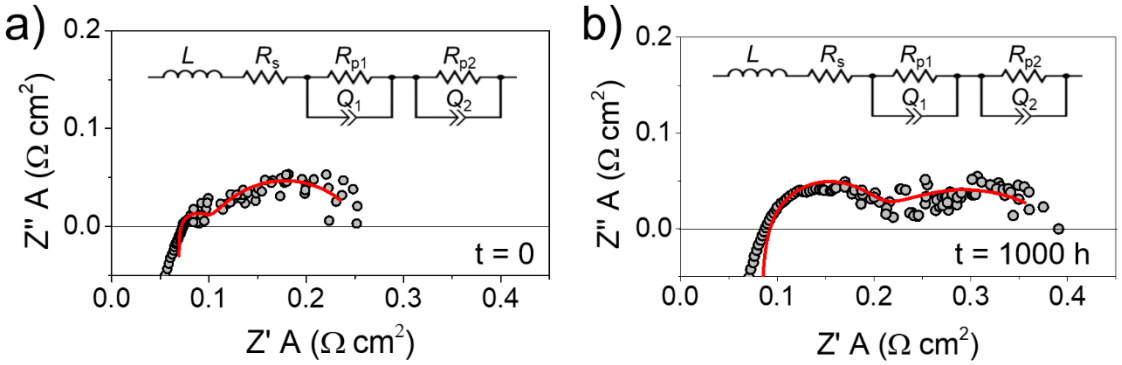

Fig. 3: EIS measurements were conducted at OCV b) at the starting point and c) after 1000 h of durability test. The fitting was made using an equivalent circuit with 2 ZARC elements.

The results of the fitting, which are reported on table 1, highlight two different contribution one at ≈1000 Hz ($R_{p1}Q_1$) and a second one at ≈1 Hz ($R_{p2}Q_2$). The first element presents a capacitance value which passes from 5.9 10^{-3} F cm^2 to 5.3 10^{-4} F cm^2. The characteristic frequencies and the capacitance values are typical for charge transfer phenomena happening at the composite electrodes [19,20]. On the other hand, the second ZARC element presents a capacitance which remains in both cases around 10^{-1} F cm-2 and considering the characteristic frequency (≈1 Hz) could be assign to gas diffusion phenomena or gas conversion, processes usually dominated by the fuel electrode which is the thicker layer [19–21].

Table 1: Results of the fitting on the impedance measurements of Fig. 3a and 3b.

	t = 0	t = 1000 h
L (H)	1.1 10^{-7}	1.7 10^{-7}
R_s (Ω cm2)	6.8 10^{-2}	8.1 10^{-2}
R_{p1} (Ω cm2)	3.1 10^{-2}	1.1 10^{-1}
C_{p1} (F cm-2)	5.9 10^{-3}	5.3 10^{-4}
f_1 (Hz)	8.9 10^{2}	2.6 10^{3}
R_{p2} (Ω cm2)	1.6 10^{-1}	2.0 10^{-1}
C_{p2} (F cm-2)	5.3 10^{-1}	1.6 10^{-1}
f_2 (Hz)	1.9	4.9
ASR_{pol} (Ω cm2)	0.19	0.32
ASR_{tot} (Ω cm2)	0.26	0.40

The results reported on table 1 clarify that the high frequency element is the one which shows the more consistent evolution during the degradation, with a resistance which passes form 3.1 10^{-2} Ω cm^2 to 1.1 10^{-1} Ω cm^2. This could be explained by both an evolution of the mesoporous structure after many hours of operation, due to an increase of the reactivity of the CGO due to the removal of the SiO_2 particles or by a degradation at the fuel electrode level, which could be caused by a progressive deactivation of the metallic Ni present in the cermet. These deactivation phenomena are extensively studied in literature and are mainly caused by coarsening of the metallic Ni particles or by its evaporation from the electrode [22,23].

Fig. 4 shows the cell microstructure after the degradation. On Fig. 4a the oxygen electrode is presented, while Fig. 4b shows the electrolyte with the CGO barrier layer.

Fig. 4c shows a micrograph obtained using a SEM in-lens detector and acquired at low voltage acceleration (≈1 kV) in which the bright zones represent the percolating metallic Ni, while the dark ones are the ensemble of YSZ and all the non-percolating Ni particles [24,25]. Fig. 4d presents a high magnification image of the barrier layer where some nanosized voids can be observed [26].

Probably the nanosized voids formation on the barrier layer do not have a strong impact on the performance of the cell. Their presence should be affecting mostly the ohmic contribution, which passes form 6.8 10^{-2} Ω cm2 to 8.2 10^{-2} Ω cm2 from the starting point to the end of the durability test.
The significant growth of the high frequency arc should be correlated by a microstructural evolution of the electrodes. Even if an evolution of the oxygen electrode could not be excluded, the fuel electrode presents poor electronic percolation near the electrolyte after the durability test (Fig.c). Therefore, the main cause of degradation could be attributed to a certain deactivation of the cermet close to the interface with the dense YSZ layer.

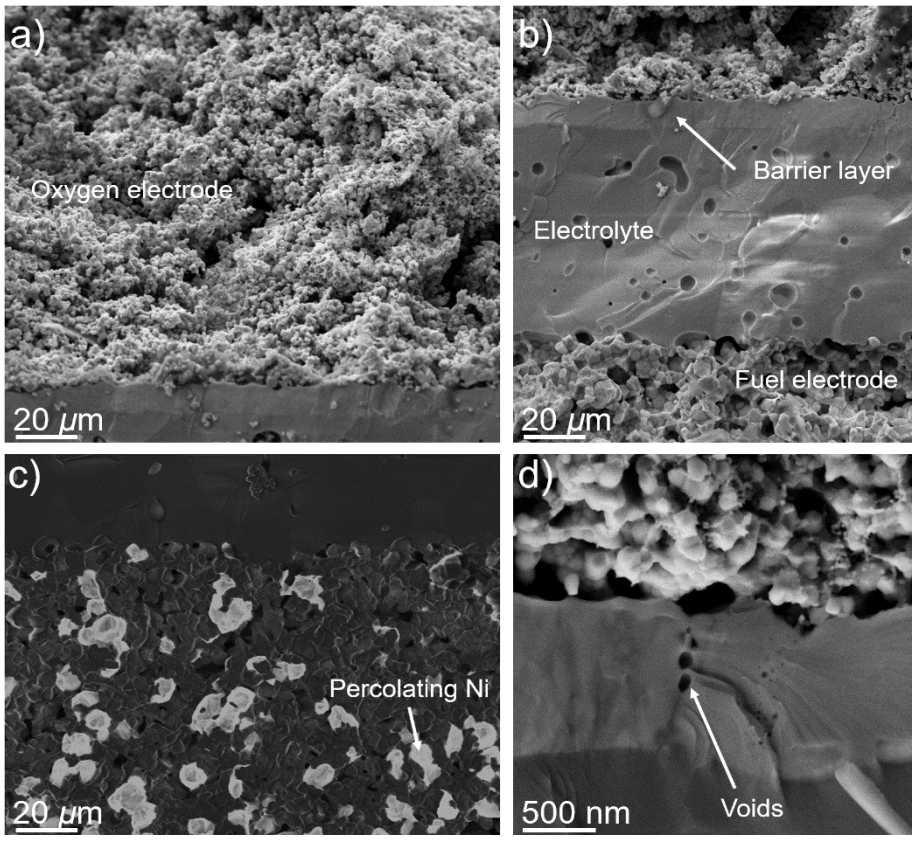

Fig. 4: the figure shows a) the oxygen electrode made of mesoporous CGO infiltrated by LSCF solution, b) the electrolyte and barrier layer of the measured cell. An in-les picture c) taken at low acceleration voltage of the fuel electrode and d) a high magnification picture of defects of the barrier layer.

Conclusion

A solid oxide cell device with a nanostructured CGO oxygen electrode infiltrated by LSCF was tested in co-electrolysis (65% H_2O, 25% CO_2 and 10% H_2) for 1000 h applying a current of 0.5 A cm^2. The cell presented a degradation around 125 mV kh^{-1} and impedance spectroscopy measurements were made after and before the durability test.
Two different arcs were individuated by EIS characterization at 1000 Hz and at 1 Hz attributed to charge transfer processes which could happen at both electrodes and to gas diffusion or conversion at the fuel electrode, respectively. The former seems to be the responsible of the degradation of the cells, passing from 3.1 10^{-2} Ω cm^2 to 1.1 10^{-1} Ω cm^2.
The microstructural characterization highlights the presence of nanosized voids at the barrier layer, which should not be related with the evolution of the high frequency arc, and of a certain lack of electronic percolation in the vicinity of the interface fuel electrode/electrolyte. Such depletion of percolating metalling Ni is strongly affecting the degradation process.

https://doi.org/10.5281/zenodo.4557607

Acknowledgements

The authors want to acknowledge the financial support of the “Generalitat de Catalunya” (2017 SGR 1421, NANOEN) and the IREC fellowship grant. Part of the research has received founding form the ECo project (ref. 699892) and the 3D-MADE project (ENE2016-74889-C4- 1-R).

References

[1] M. Mogensen, S. Primdahl, M.J. Jørgensen, C. Bagger, Composite electrodes in solid oxide fuel cells and similar solid state devices, J. Electroceramics. 5 (2000) 141–152. doi:10.1023/A:1009910202330.

[2] N. Mahato, A. Banerjee, A. Gupta, S. Omar, K. Balani, Progress in material selection for solid oxide fuel cell technology: A review, Prog. Mater. Sci. 72 (2015) 141–337. doi:10.1016/j.pmatsci.2015.01.001.

[3] L. Ge, Q. Ni, G. Cai, T. Sang, L. Guo, Improving SiO2 impurity tolerance of Ce0.8Sm0.2O1.9: Synergy of CaO and ZnO in scavenging grain-boundary resistive phases, J. Power Sources. 324 (2016) 582–588. doi:10.1016/j.jpowsour.2016.05.135.

[4] S. Anelli, F. Baiutti, A. Hornés, L. Bernadet, M. Torrell, A. Tarancón, Improved mesostructured oxygen electrodes for highly performing solid oxide cells for co-electrolysis of steam and carbon dioxide, J. Mater. Chem. A. 3 (2019) 10031–10037. doi:10.1039/C9TA07373F.

[5] X.G. Zhu, S.P. Long, D.R. Ort, Advanced technology paths to global climate stability: Energy for a greenhouse planet, Annu Rev Plant Biol. 61 (2010) 235–261. doi:10.1146/annurev-arplant-042809-112206.

[6] Z. Zhan, W. Kobsiriphat, J.R. Wilson, M. Pillai, I. Kim, S.A. Barnett, Syngas production by coelectrolysis of CO 2/H 2O: The basis for a renewable energy cycle, Energy and Fuels. 23 (2009) 3089–3096. doi:10.1021/ef900111f.

[7] Z. Ud Din, Z.A. Zainal, Biomass integrated gasification-SOFC systems: Technology overview, Renew. Sustain. Energy Rev. 53 (2016) 1356–1376. doi:10.1016/j.rser.2015.09.013.

[8] W.L.L. Becker, R.J.J. Braun, M. Penev, M. Melaina, Production of Fischer–Tropsch liquid fuels from high temperature solid oxide co-electrolysis units, Energy. 47 (2012) 99–115. doi:10.1016/j.energy.2012.08.047.

[9] M.A. Laguna-Bercero, Recent advances in high temperature electrolysis using solid oxide fuel cells: A review, J. Power Sources. 203 (2012) 4–16. doi:10.1016/j.jpowsour.2011.12.019.

[10] Y. Zheng, J. Wang, B. Yu, W. Zhang, J. Chen, J. Qiao, J. Zhang, A review of high temperature co-electrolysis of H2O and CO2 to produce sustainable fuels using solid oxide electrolysis cells (SOECs): advanced materials and technology, Chem. Soc. Rev. 46 (2017) 1427–1463. doi:10.1039/C6CS00403B.

[11] S. Wang, T. Kobayashi, M. Dokiya, T. Hashimoto, Electrical and Ionic Conductivity of Gd-Doped Ceria, J. Electrochem. Soc. 147 (2000) 3606. doi:10.1149/1.1393946.

[12] J. Nielsen, T. Jacobsen, M. Wandel, Impedance of porous IT-SOFC LSCF:CGO composite cathodes, Electrochim. Acta. 56 (2011) 7963–7974. doi:10.1016/j.electacta.2011.05.042.

[13] P.A. Connor, X. Yue, C.D. Savaniu, R. Price, G. Triantafyllou, M. Cassidy, G. Kerherve, D.J. Payne, R.C. Maher, L.F. Cohen, R.I. Tomov, B.A. Glowacki, R.V. Kumar, J.T.S. Irvine, Tailoring SOFC Electrode Microstructures for Improved Performance, Adv. Energy Mater. 8 (2018) 1–20. doi:10.1002/aenm.201800120.

[14] E. Hernández, F. Baiutti, A. Morata, M. Torrell, A. Tarancón, Infiltrated mesoporous oxygen electrodes for high temperature co-electrolysis of H 2 O and CO 2 in solid

oxide electrolysis cells, J. Mater. Chem. A. 6 (2018) 9699–9707. doi:10.1039/C8TA01045E.
[15] L. Almar, T. Andreu, A. Morata, M. Torrell, L. Yedra, S. Estradé, F. Peiró, A. Tarancón, High-surface-area ordered mesoporous oxides for continuous operation in high temperature energy applications, J. Mater. Chem. A. 2 (2014) 3134–3141. doi:10.1039/c3ta13951d.
[16] J. Bae, Properties of La0.6Sr0.4Co0.2Fe0.8O3-d (LSCF) double layer cathodes on gadolinium-doped cerium oxide (CGO) electrolytes I. Role of SiO2, Solid State Ionics. 106 (1998) 247–253. doi:10.1016/S0167-2738(97)00428-1.
[17] D. Pérez-Coll, P. Núñez, J.C.C. Abrantes, D.P. Fagg, V. V. Kharton, J.R. Frade, Effects of firing conditions and addition of Co on bulk and grain boundary properties of CGO, Solid State Ionics. 176 (2005) 2799–2805. doi:10.1016/j.ssi.2005.06.023.
[18] M. Torrell, L. Almar, A. Morata, A. Tarancón, Synthesis of mesoporous nanocomposites for their application in solid oxide electrolysers cells: microstructural and electrochemical characterization, Faraday Discuss. 182 (2015) 423–435. doi:10.1039/c5fd00035a.
[19] E. Perry Murray, M.J. Sever, S.A. Barnett, Electrochemical performance of (La, Sr)(Co, Fe)O3–(Ce, Gd)O3 composite cathodes, Solid State Ionics. 148 (2002) 27–34. doi:10.1016/S0167-2738(02)00102-9.
[20] H. Fan, M. Keane, N. Li, D. Tang, P. Singh, M. Han, Electrochemical stability of La0.6Sr0.4Co0.2Fe0.8O3−δ-infiltrated YSZ oxygen electrode for reversible solid oxide fuel cells, Int. J. Hydrogen Energy. 39 (2014) 14071–14078. doi:10.1016/j.ijhydene.2014.05.149.
[21] P. Caliandro, A. Nakajo, S. Diethelm, J. Van herle, Model-assisted identification of solid oxide cell elementary processes by electrochemical impedance spectroscopy measurements, J. Power Sources. 436 (2019) 226838. doi:10.1016/j.jpowsour.2019.226838.
[22] P. Tanasini, M. Cannarozzo, P. Costamagna, A. Faes, J. Van Herle, A. Hessler-Wyser, C. Comninellis, Experimental and theoretical investigation of degradation mechanisms by particle coarsening in sofc electrodes, Fuel Cells. 9 (2009) 740–752. doi:10.1002/fuce.200800192.
[23] M. Hubert, J. Laurencin, P. Cloetens, B. Morel, D. Montinaro, F. Lefebvre-Joud, Impact of Nickel agglomeration on Solid Oxide Cell operated in fuel cell and electrolysis modes, J. Power Sources. 397 (2018) 240–251. doi:10.1016/j.jpowsour.2018.06.097.
[24] K. Thydén, Y.L. Liu, J.B. Bilde-Sørensen, Microstructural characterization of SOFC Ni-YSZ anode composites by low-voltage scanning electron microscopy, Solid State Ionics. 178 (2008) 1984–1989. doi:10.1016/j.ssi.2007.12.075.
[25] M.H. Pihlatie, A. Kaiser, M. Mogensen, M. Chen, Electrical conductivity of Ni-YSZ composites: Degradation due to Ni particle growth, Solid State Ionics. 189 (2011) 82–90. doi:10.1016/j.ssi.2011.02.001.
[26] F. Tietz, D. Sebold, A. Brisse, J. Schefold, Degradation phenomena in a solid oxide electrolysis cell after 9000 h of operation, J. Power Sources. 223 (2013) 129–135. doi:10.1016/j.jpowsour.2012.09.061.

Keywords: EFCF2020, SOx
Session B12: Oxygen electrodes I

B1210

Combined effects of A-site non-stoichiometry, crystal structure, and microstructure for the enhanced catalytic activity of (LaSr)(CoFe)$O_{3-\delta}$ cathodes for IT-SOFCs

Ozden Celikbilek (1,2), Cam-Anh Thieu (3,4), Fabio Agnese (5), Eleonora Cali (2), Christian Lenser (6), Norbert H. Menzler (6), Ji-Won Son (3,4), Stephen J. Skinner (2), Elisabeth Djurado (1)

(1) Univ. Grenoble Alpes, Univ. Savoie Mont Blanc, CNRS, Grenoble INP, LEPMI, 38000, Grenoble/France

(2) Department of Materials, Imperial College London
Prince Consort Road, SW7 2BP, London/United Kingdom

(3) Center for Energy Materials Research, Korea Institute of Science and Technology (KIST), Hawolgok-dong, Seongbuk-gu, 02792 Seoul/Korea

(4) Division of Nano & Information Technology, KIST School, Korea University of Science and Technology (UST), Hawolgok-dong, Seongbuk-gu, 02792 Seoul/Korea

(5) Univ. Grenoble Alpes, INAC-SyMMES, F-38054 Grenoble Cedex 9/France

(6) Forschungszentrum Jülich GmbH, Institute of Energy and Climate Research: Materials Synthesis and Processing (IEK-1), 52425 Jülich/Germany

Contact authors: www.EFCF.com/ContactRequest

Abstract

The high oxygen reduction reaction (ORR) activity of the A-site deficient $(La_{0.7}Sr_{0.3})_{0.95}(Co_{0.2}Fe_{0.8})O_{3-\delta}$ (LSCF) film makes it an excellent cathode material for intermediate temperature solid oxide fuel cell (IT-SOFC) applications. The cathode was deposited by the electrostatic spray deposition (ESD) technique which provided microstructural details at the nanometre length scale (~100 nm).[1] The area-specific resistance values as low as 0.037 and 0.1 Ω cm^2 were measured in a symmetrical cell and power density of 0.87 and 0.50 W cm^{-2} at 0.7 V in a Ni/YSZ anode-supported cell at 650 and 600 °C, respectively were obtained. The A-site deficiency resulted in the precipitation of a B-site spinel phase composed of $CoFeO_x$ (CFO), while the perovskite structure of LSCF was modified to closely related two-phase perovskite structures. Detailed microstructural analyses showed that well-dispersed, nanoscale (~10-20 nm) CFO phase decorated the LSCF surfaces. Such substantial increase in the ORR kinetics was attributed to the catalytically active and nanostructured CFO precipitates and the very high active surface area of the ESD film.

[1] O. Celikbilek, C.-A. Thieu, F. Agnese, E. Cali, C. Lenser, N. H. Menzler, J.-W. Son, S. J. Skinner and E. Djurado, *J. Mater. Chem. A*, 2019, **7**, 25102–25111.

https://doi.org/10.5281/zenodo.4557625

1. Introduction

The low-temperature operation provides great benefits for the deployment of solid oxide cells (SOCs) in the mobile/transport applications.[2,3] However, the reaction kinetics of existing materials become sluggish at low temperatures. Microstructure and materials design were shown effective to improve the electrodes' performance up to an order of magnitude.[4]

In terms of materials design, combinations of slight A- or B-site excess/deficiency have been explored in the ABO_3-type family of perovskites. Particularly, it was shown that A-site deficiency created additional oxygen vacancies to improve the ionic conductivity and the stability of a phase.[5] In terms of composition, $(LaSr)(CoFe)O_{3-\delta}$ (LSCF) is among the most studied ABO_3-type perovskites and still attracts a lot of interest. However, a very narrow stability regime was shown for these types of materials.[6] Slight deviations from A-site to B-site ratio result in the formation of a Ruddlesden-Popper type layered perovskite in the case of A-site excess and a spinel oxide in the case of B-site excess. It is, however, unclear how the catalytic activity is affected by the secondary phase formations as a result of the changes in the stoichiometry.

In this work, $(La_{0.7}Sr_{0.3})_{0.95}(Co_{0.2}Fe_{0.8})O_{3-\delta}$ (referred to as A-site deficient LSCF) composition was investigated by structural, microstructural, and electrochemical characterization techniques. The films were deposited by the electrostatic spray deposition (ESD) technique which provided microstructural features at the nanometre length scale.[7] Scanning electron microscopy (SEM), powder X-ray diffraction (XRD), scanning transmission electron microscopy (STEM) coupled with energy-dispersive X-ray spectroscopy (EDX), and electrochemical impedance spectroscopy (EIS) were employed to study the catalytic effect of A-site deficiency on the electrode performance.

2. Experiments

The cathode layer included a double layer architecture consisting of LSCF layer deposited by the ESD and topped by a screen-printed current collecting layer (CCL). ESD films were deposited using a vertical setup starting from precursor salt solutions. Appropriate amounts of $La(NO_3)_3.6H_2O$ (Prolabo, 99.99%), $SrCl_2.6H_2O$ (Strem Chemicals, 99%), $Co(NO_3)_2.6H_2O$ (Sigma-Aldrich, 99.999%) and $Fe(NO_3)_2.9H_2O$ (Sigma-Aldrich, 99.99%) salts were dissolved in absolute ethanol (99.9%; Prolabo) and butyl carbitol (99+%; Acros Organics) with a 1:2 volume ratio and a total salt concentration of 0.02 mol L^{-1}. The solution was sprayed onto the substrate. ESD deposition parameters comprise a substrate temperature of 300 °C, a nozzle to substrate distance of 15 mm, the voltage of ~5-6 kV, and a flow rate of 1.5 mL h^{-1}. Crystallization of the films and sintering were achieved at 900 °C for 2 h at a 2 °C min^{-1} heating rate and a 3 °C min^{-1} cooling rate. The targeted stoichiometry of the LSCF was $La_{0.6}Sr_{0.4}Co_{0.2}Fe_{0.8}O_{3-\delta}$ (LSCF 6428). However, analysis by inductively coupled plasma-optical emission spectrometry (ICP-OES) (iCAP 6500 Thermo Scientific, USA) showed the average stoichiometry of the film to be $(La_{0.71}Sr_{0.29})_{0.95}Co_{0.17}Fe_{0.83}O_{3-\delta}$. In the text, it was simplified to $(La_{0.7}Sr_{0.3})_{0.95}Co_{0.2}Fe_{0.8}O_{3-\delta}$ and will be referred to as A-site deficient LSCF.

Scanning electron microscopy (SEM) was used to study the microstructure of the films, using a field emission gun (ZEISS Ultra 55) operating at an accelerating voltage of 3 kV and an average of 7 mm working distance. The HR-TEM analysis was carried out on a

JEOL 2100F microscope equipped with an Oxford Instruments EDX detector. EDX was performed in STEM mode with an annular dark field detector.

Impedance spectroscopy was used to evaluate the electrochemical response. Symmetrical cell measurements in open-circuit voltage (OCV) mode were carried out in ambient air with between 450 and 650 °C. An Autolab frequency response analyzer operating between 10 kHz and 0.05 Hz was used. The amplitude of the measuring signal was adjusted to 20 mV. The data were fitted with electrical equivalent circuits using the EC-Lab® software (V10.44).

Single-cell tests were performed on anode-supported cells prepared at Forschungszentrum Jülich, Germany. The cells were based on tape-cast NiO-YSZ supports of ~300 µm thickness, and screen-printed NiO-YSZ anodes were obtained from CeramTec GmbH (Marktredwitz, Germany). The 1.5 µm thin YSZ electrolyte was prepared by the sequential deposition of YSZ nano-dispersion and polymeric sol, followed by co-sintering of the half-cell at 1400 °C.[8] Subsequently, a ~ 0.5 µm thin $Gd_{0.2}Ce_{0.8}O_{1.9}$ diffusion barrier layer was deposited via Magnetron Sputtering. The LSCF cathode prepared via ESD had 10 x 10 mm² dimension. A-site deficient $La_{0.58}Sr_{0.4}Co_{0.2}Fe_{0.8}O_{3-\delta}$ ink (FZ-Jülich, Germany) was screen printed on the LSCF films deposited by the ESD to serve as CCL and sintered at 850 °C for 2 h in air. Measurements were performed in the temperature range of 450-650 °C, using an Iviumstat test apparatus in a frequency range between 1 MHz and 0.1 Hz. Air on the cathode side and humidified H_2 on the anode side with a fuel composition of 97 vol. % H_2 and 3 vol. % H_2O at a flow rate of 200 standard cm^3 min^{-1} (sccm) was used. A modified interconnect rib design with gold mesh with openings of 250 µm by 250 µm was used for the cell test. Current vs voltage data were recorded between 650 °C and 450 °C at each 50 °C in descending order. A Solartron impedance analyser with an electrochemical interface (SI 1260) and an Iviumstat electrochemical analyser (Iviumstat, Ivium Technologies) was used to obtain these EIS and I-V-P curves. The AC amplitude of the impedance measurements was set to 50 mV.

3. Results

ESD is a unique technique to obtain micrometre-thick films with nanometric features. SEM micrographs in Figure 1 demonstrate the micro- and nanostructure of ~10 µm-thick cathode films made up of large columnar-like blocks separated by ~1-2 µm wide interconnected gas diffusion channels. The grain and porosity sizes within the columnar blocks show a scale of ~100 nm. The cross-sectional view (Figure 1d) provides an overview of the nanometre length scale features of the LSCF ESD films compared with screen printed CCL of the same material. In a previous work, the porosity, specific surface area and tortuosity values of LSCF ESD films were calculated as 22 ± 7 %, 19 ± 6 μm^{-1}, and 1.50 ± 0.2, respectively.[7]

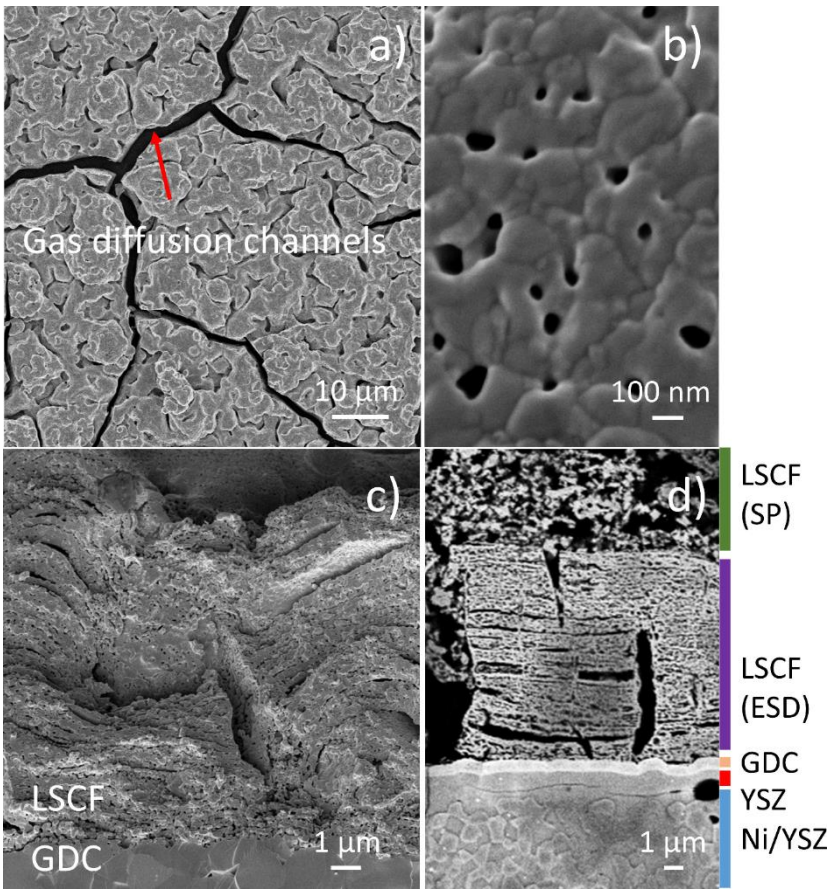

Figure 1. a-b) Plan view SEM micrographs of LSCF film sintered at 900 °C for 2 h in air, Cross-sectional SEM micrograph of c) LSCF film on GDC electrolyte and d) As-deposited LSCF film on anode-supported bi-layer electrolyte cell. The colored bars next to d) show each layer in the cell. Reproduced from Ref. [1] with permission from The Royal Society of Chemistry.

Figure 2a shows the XRD pattern and the structural refinement of the ESD cathode layer on the GDC electrolyte. Notably, three phases can be observed; the LSCF phase (ICDD: 04-020-8368) with $R\bar{3}c$ space group (No. 167), the GDC phase (ICDD: 04-012-3418) with $Fm\bar{3}m$ space group (No. 225), and a third phase corresponding well to a spinel crystal structure ($Fd\bar{3}m$) with a unit cell parameter of 8.3204(7) Å. The amount of this phase with respect to the LSCF was found to be ~6 wt. %. As can be seen in the inset of Figure 2a, the refinement of the LSCF with one rhombohedral phase did not yield a good fitting. Instead, two rhombohedral phases with slightly different *a, b* and *c* parameters gave an improved fit (Figure 2b). Similar behaviour was observed in previous reports on A-site non-stoichiometric LSCF.[9] The first phase was fitted with *a, b* = 5.48(8) Å and *c* = 13.50(2) Å and the second phase was fitted with *a, b* = 5.47(9) Å and *c* = 13.56(4) Å.

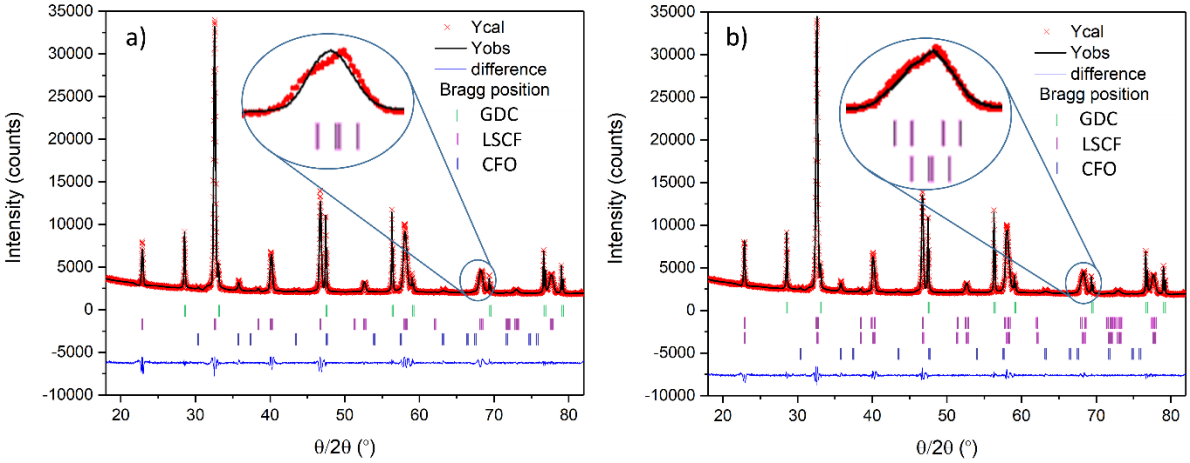

Figure 2. XRD lattice parameter refinement of an LSCF film deposited on GDC electrolyte sintered at 900 °C for 2 h in air. a) one rhombohedral phase and b) two rhombohedral phases. Reproduced from Ref. [1] with permission from The Royal Society of Chemistry.

Next, STEM-EDX was used to investigate the elemental composition of the minority third phase. The STEM-EDX maps in Figure 3 demonstrate the presence of only La, Sr, Co, Fe, and O elements with some particles containing solely Co and Fe and O. These particles are smaller than a typical LSCF grain, with an average grain size of ~20 nm.

Elemental point analysis at three different locations shows that the particle containing Co and Fe elements had a Co: Fe ratio of approximately 1.0. In the literature, common cobalt ferrite spinel structures were reported as $CoFe_2O_4$ (ICDD: 04-006-4147) and Co_2FeO_4 (ICDD: 04-016-3952). In the rest of the text, $CoFeO_x$ will be referred to as CFO. Point analyses from the other two locations gave La: Sr ratio of ~3.7. It is important to note that, this value is higher than the value obtain from ICP-OES analysis (~2.4). The discrepancy can be due to the amount of investigated particles. While ICP-OES provides average information from the ensemble of all particles, EDX gives point analysis on a few selected particles. Nevertheless, both techniques gave A: B site ratio as ~0.95:1.00. As mentioned above, the targeted stoichiometry for the cathode film was LSCF 6428. The origins of the A-site deficiency is not known at the moment, but it might be related to the precursor purity and/or solubility limits of the metal-nitrates as well as the non-equilibrium state of the ESD technique.

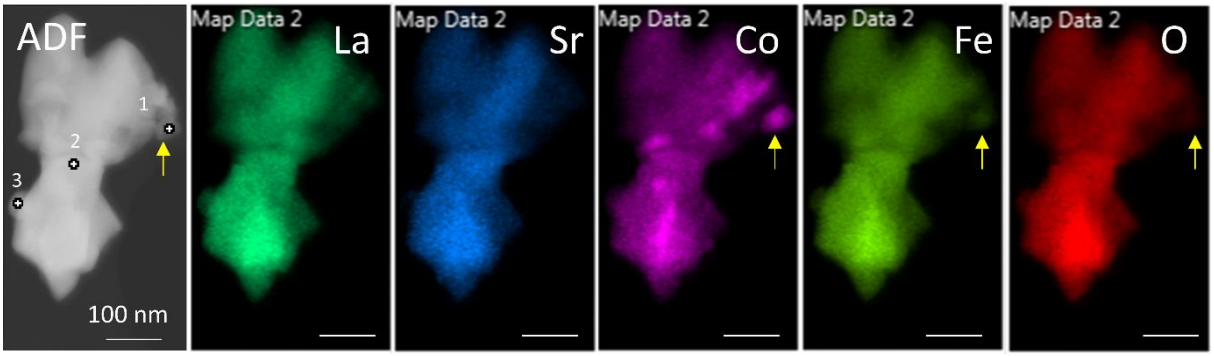

Figure 3. STEM ADF-EDX elemental maps of the particles removed from the film. The intensity of the maps represents the net EDX counts after corrections for background and peak overlap. Reproduced from Ref. [1] with permission from The Royal Society of Chemistry.

Figure 4 shows the Arrhenius plot of area-specific polarization resistance (ASR) of various LSCF films on GDC electrolytes measured between 450-650 °C in air and under OCV. The plot shows ASR values of as low as 0.037 and 0.1 Ω cm^2 at 650 and 600 °C, respectively for LSCF (ESD). Moreover, it shows an activation energy (E_a) value of ~1.5 eV.

To separate the catalytic activity of CFO nanoparticles from the structural changes due to A-site non-stoichiometry, new experiments were designed. Stoichiometric LSCF 6428 (Sigma-Aldrich, 10-14 m^2 g^{-1}) were measured as bare samples. Then, a CFO solution was infiltrated into the LSCF backbone. The infiltration method was selected as it can mimic the amount and the particle sizes of CFO, as obtained in ESD films. The infiltrated films were measured on-heating and then on-cooling. The Arrhenius plots show a substantial decrease in both the ASR and the E_a values on heating, suggesting that the increased catalytic activity is in fact due to CFO nanoparticles. It can be seen that during cooling, both values increased. Notably, the E_a value increased from ~1.0 (on heating) to ~1.5 eV (on cooling) and became similar to LSCF (ESD) films. This is attributed to the agglomeration of CFO nanoparticles, similar to those reported for Co_3O_4 at elevated temperatures.[10]

These experiments suggest that CFO nanoparticles indeed improve the catalytic activity when decorated on LSCF films. We would like to point out the importance of micro- and nanostructure optimisation of cathode layers. Architectural engineering of ESD films topped with CCL can decrease the ASR values up to an order of magnitude.

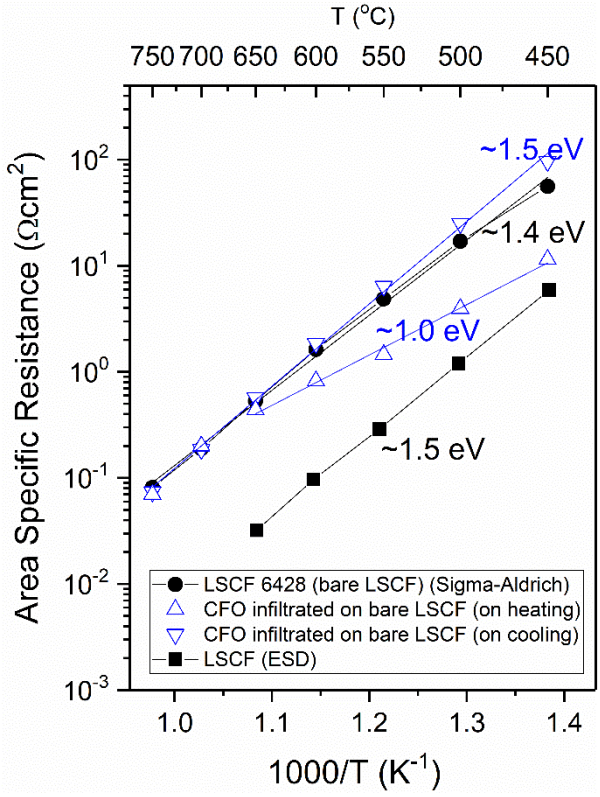

Figure 4 Arrhenius plot of ASR of total polarization losses of symmetrical LSCF 6428 bare (commercial powder), CFO infiltrated LSCF 6428, and LSCF (ESD). Reproduced from Ref. [1] with permission from The Royal Society of Chemistry.

Figure 5 shows the current-voltage-power (I – V – P) curves and the corresponding Nyquist plots measured at 0.75 V. The current density at a cell voltage of 0.7 V was 1.2

and 0.7 A cm^{-2} at 650 and 600 °C, respectively. The peak power density at 600 °C in this work is among the highest values for LSCF-based cathodes.[11,12] Unlike this work, the electrodes in references [11,12] contain an LSCF/GDC layer either as a barrier layer or as a current-conducting layer. On the other hand, similar to our columnar-like LSCF cathode microstructure, Hsu *et al.* also used the ESD technique to deposit an LSCF cathode on Ni-SDC based anode-supported cells.[13] They reported a 0.9 W cm^{-2} peak power density at 600 °C with a significantly lower current density at 0.7 V in comparison to this work.

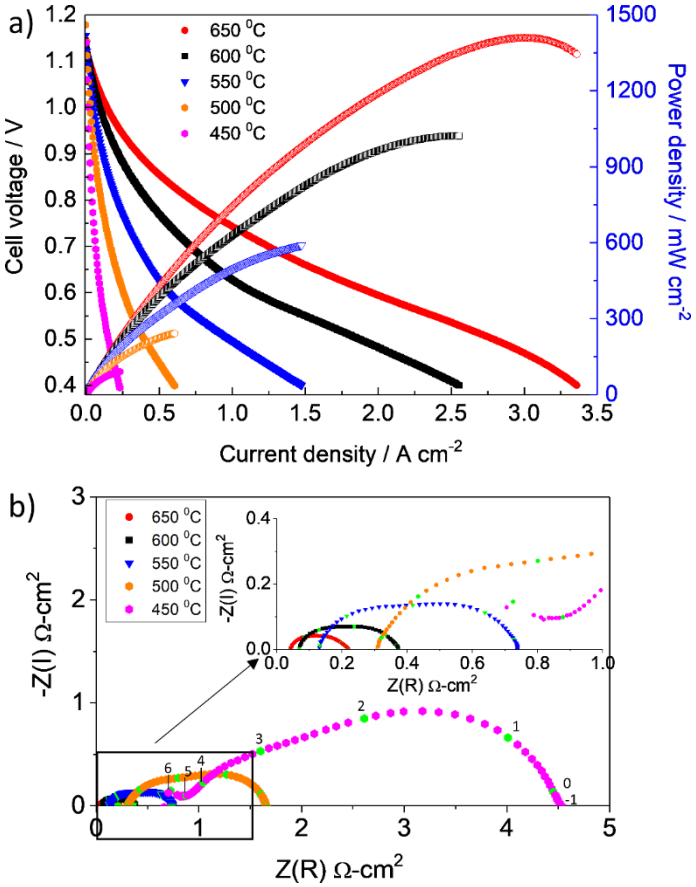

Figure 5. **I-V-P curves and corresponding Nyquist impedance plots of LSCF/GDC/YSZ/Ni-YSZ cells measured at 0.75 V with 3 % humidified hydrogen in the anode side.** The green points are frequency values on a logarithmic scale. Reproduced from Ref. [1] with permission from The Royal Society of Chemistry.

4. Conclusions

A-site deficient $(La_{0.7}Sr_{0.3})_{0.95}Co_{0.2}Fe_{0.8}O_{3-\delta}$ (LSCF) films prepared by the ESD technique were investigated as air electrodes for high-performance SOCs. A-site deficiency caused the precipitation of B-site elements and also led to the separation of single-phase rhombohedral LSCF into two closely related rhombohedral phases. The precipitated nanoparticles of B-site elements ~$CoFeO_x$ (CFO) had an average particle size of ~20 nm and they homogeneously decorated the LSCF surfaces. The films gave very low ASR values of 0.037, 0.100 Ω cm^2 on symmetrical cells, and power densities of 1.2 and 0.7 A cm^{-2} at 0.7 V on a Ni/YSZ anode-supported cell at 650 and 600 °C, respectively. The catalytic effect of CFO nanoparticles was investigated on an additional set of controlled experiments. CFO solution was infiltrated on the stoichiometric LSCF phase to separate the A-site non-stoichiometry effects from the catalytic activity of CFO nanoparticles. A decrease in both the activation energy and ASR values was observed. These findings

demonstrate that high performance is partly due to the nanostructured B-site precipitates decorating the LSCF surfaces and partly to the unique microstructural details in the ESD films.

References

[1] Celikbilek, O.; Thieu, C.-A.; Agnese, F.; Calì, E.; Lenser, C.; Menzler, N. H.; Son, J.-W.; Skinner, S. J.; Djurado, E., 2019 “Enhanced catalytic activity of nanostructured, A-site deficient (La0.7Sr0.3)0.95(Co0.2Fe0.8)O3-δ for SOFC cathodes” J Mater Chem A, **7**, pp 25102–11.

[2] Hussain, A. M.; Wachsman, E. D., 2019 “Liquids-to-Power Using Low-Temperature Solid Oxide Fuel Cells” Energy Technol., **7** (1), pp. 20–32.

[3] Udosmilp, D.;Rechberger, J.; Neubauer, R.; Bischof, C.; Thaler, F.; Schafbauer, W.; Menzler, N.H.; de Haart, L.G.J.; Nenning, A.; Opitz, A.K.; Guillon, O.; Bram, M., 2020 ”Metal-supported solid oxide fuel cells with excetionally high power density for range extender systems” Cell Reports Phys. Sci. **1,** pp. 100072

[4] Ma, W.; Kim, J. J.; Tsvetkov, N.; Daio, T.; Kuru, Y.; Cai, Z.; Chen, Y.; Sasaki, K.; Tuller, H. L.; Yildiz, B., 2015 “Vertically Aligned Nanocomposite La0.8Sr0.2CoO3 /(La0.5Sr0.5)2CoO4 Cathodes – Electronic Structure, Surface Chemistry and Oxygen Reduction Kinetics” J. Mater. Chem. A, **3** (1), pp. 207–219.

[5] Mineshige, A.; Izutsu, J.; Nakamura, M.; Nigaki, K.; Abe, J.; Kobune, M.; Fujii, S.; Yazawa, T., 2005 “ntroduction of A-Site Deficiency into La0.6Sr0.4Co0.2Fe0.8O3–δ and Its Effect on Structure and Conductivity” Solid State Ionics, **176** (11–12), pp. 1145–1149.

[6] Morin, F.; Trudel, G.; Denos, Y., 1997 “The Phase Stability of La0.5Sr0.5CoO3-δ” Solid State Ionics, **96** (97), pp.129–139.

[7] Celikbilek, O.; Jauffrès, D.; Siebert, E.; Dessemond, L.; Burriel, M.; Martin, C. L.; Djurado, E., 2016 “Rational Design of Hierarchically Nanostructured Electrodes for Solid Oxide Fuel Cells” J Power Sources, **333**, pp. 72–82.

[8] Menzler, N. H.; Malzbender, J.; Schoderböck, P.; Kauert, R.; Buchkremer, H. P., 2014 “Sequential Tape Casting of Anode-Supported Solid Oxide Fuel Cell” Fuel Cells, **14** (1), pp. 96–106.

[9] Hansen, K. K.; Vels Hansen, K., 2007 “A-Site Deficient (La0.6Sr0.4)1-SFe0.8Co0.2O3-δ Perovskites as SOFC Cathodes” Solid State Ionics, **178** (23–24), pp. 1379–1384.

[10] Ren, Y.; Cheng, Y.; Gorte, R. J.; Huang, K., 2017 “Toward Stabilizing Co3O4 Nanoparticles as an Oxygen Reduction Reaction Catalyst for Intermediate-Temperature SOFCs” J. Electrochem. Soc., **164** (10), pp. F3001–F3007.

[11] Oh, E. O.; Whang, C. M.; Lee, Y. R.; Park, S. Y.; Prasad, D. H.; Yoon, K. J.; Son, J. W.; Lee, J. H.; Lee, H. W., 2012 “Extremely Thin Bilayer Electrolyte for Solid Oxide Fuel Cells (SOFCs) Fabricated by Chemical Solution Deposition (CSD)” Adv. Mater., **24** (25), pp. 3373–3377.

[12] Jang, I.; Kim, S.; Kim, C.; Yoon, H.; Song, T., 2018 “Enhancement of Oxygen Reduction Reaction through Coating a Nano-Web-Structured La0.6Sr0.4Co0.2Fe0.8O3-δ Thin-Film as a Cathode/Electrolyte Interfacial Layer for Lowering the Operating Temperature of Solid Oxide Fuel Cells” J. Power Sources, **392**, pp. 123–128.

[13] Hsu, C.-S. S.; Hwang, B.-H. H.; Xie, Y.; Zhang, X, 2008 “Enhancement of Solid Oxide Fuel Cell Performance by La0.6Sr0.4Co0.2Fe0.8O3−δ Double-Layer Cathode” J. Electrochem Soc., **155** (12), pp. B1240–B1243.

Keywords: EFCF2020, SOx
Session B12: Oxygen electrodes I

https://doi.org/10.5281/zenodo.4557625

B1301

Conditioning optimization in Sandvik Sanergy® HT 441 after the forming process

Pablo Collantes-Jiménez, Carlos Bernuy-López, Ulf Bexell, Jörgen Westlinder
Surface Research, Strategic Research, AB Sandvik Materials Technology
81181 Sandviken/Sweden

Contact authors: www.EFCF.com/ContactRequest

Abstract

Stainless steel-based interconnects for Solid Oxide Fuel Cells (SOFC) are essential parts in obtaining competitive devices. Pre-coated stainless steels can be produced in a roll-to-roll process and large volumes, which reduce the cost of interconnect fabrication. The cost-effective AISI 441 ferritic stainless steel grade can be used with a Ce/Co nanocoating in order to form a protective spinel oxide layer. This material is manufactured by Sandvik Materials Technology under the name Sandvik Sanergy® HT 441. Mechanical stresses during fabrication of an interconnect causes microcracks in the coating exposing the substrate material which can impact the oxidation behaviour negatively. Despite this, the metal coating experiences a volume expansion when the oxide scale is formed. This enables to cover the areas where there is no coating present and protecting them in what is called the 'self-healing' effect.
The aim of the present study is to provide insights about how several pre-oxidation treatments influence the self-healing properties of the cracks generated in the coating in as-formed state. This includes the analysis of microstructural and chemical changes in order to obtain the best recipe for pre-oxidation. Thus, different series of temperature (isochronous and isothermal from 600 to 850 °C) and several pre-treatments times (1 h to 24 h) were tested. The same area was carefully marked (figure 1) and followed by means of SEM surface characterization and chemical analysis in order to follow the same crack distribution area. The results from this work indicate that an adequate self-healing of the material can be achieved within short times using isothermal pre-treatments at temperatures over 750 °C.

https://doi.org/10.5281/zenodo.4557639

Introduction

Materials based on ferritic stainless steels and high chromium alloys are cost-effective materials for SOFC interconnects [1-4]. The TEC matches closely the one of the electrodes and electrolytes with the benefit of higher toughness and strength. In addition, the implementation of protective coatings is an effective solution in order to mitigate the chromium vaporization issue in this technology and also avoid high corrosion resistance [1]. Surface layers of Reactive Element Oxides (REOs), rare earth perovskites and composite spinel oxides have shown good properties to reduce oxide growth kinetics, increase oxide scale conductivity and improve oxide scale-to-metal adhesion [2]. The combination of composite layers of REOs (Ce, La, Y) and composite spinels of the Mn-Co system effectively reduce the high-temperature oxidation rate [3] while still retaining high conductivity and reducing chromium evaporation [4].
Coatings such as Ce/Co can be deposited in metallic state with techniques such as Physical Vapor Deposition (PVD) [6] in a continuous roll-to-roll process [5]. The metallic pre-coating withstands the forming operations without spalling [5]. After forming, the pre-coating is oxidized at high temperatures and reacts with the Mn diffusing from the steel, generating the desired final $(Co,Mn)_3O_4$ spinel coating [7, 8] over a seed layer of Cerium oxide. It has been observed that the forming operations can crack the surface of the pre-coating exposing the substrate materials, eliminating the protection against Cr-evaporation.
Nevertheless, previous studies have shown that the micrometer size cracks can be self-healed at high temperatures due to the instant volume expansion of the coating as it oxidizes [9]. In order to make SOFC cost-effective and commercially attractive, longer service lives of the materials are needed to decrease the cost per kWh. An important cost lowering factor is process optimization and devise new operating conditions (temperatures and times) that can help to obtain durable materials in scalable production ways.
The purpose of this work is to obtain knowledge about the self-healing properties of the interconnect. Coatings like Ce/Co produce a protective layer that effectively stops chromia evaporation by different mechanisms. With increased temperatures, some elements in the steel substrate can be diffused outwards and form different oxides when combined with the elements in the coating. These oxides experience a volume expansion that is able to cover the exposed areas in the material where there is no coating present, protecting them in what is called the 'self-healing' effect. Although previous studies (5, 9, 10) have shown that this mechanism is effective in pre-treatments at high temperature (>800°C), investigations about the effect of self-healing properties at medium to low temperatures are limited and, therefore, a systematic study varying temperature and time is performed and evaluated by SEM techniques.

1. Experiments

1.1 Materials and Sample preparation

The material for analysis was a ferritic stainless steel Sandvik Sanergy® HT 441, which incorporates a coating of Ce/Co with thickness below 1 µm. [11]. It was deposited in metallic state using a Physical Vapor Deposition (PVD) roll-to-roll processin Sandvik Material Technology AB. Prior to this study, Sandvik Sanergy® 441 HT samples were obtained in the form of 20 cm^2 sheets by 0.3 mm in thickness and they were submitted to the modified Erichsen test. An initial circumference of 5 cm in diameter was marked on top of the surface, and the sheet was punched until a 12% biaxial deformation (Figure 1)

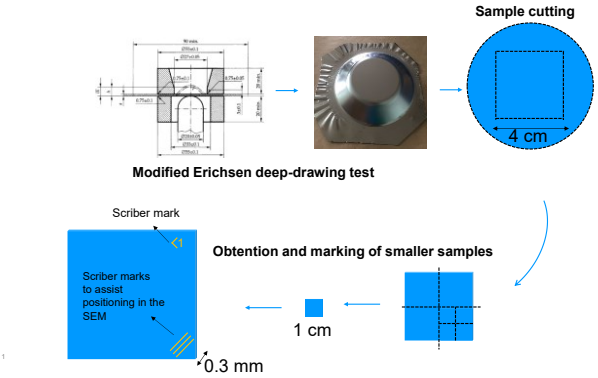

Figure 1. Sample obtention and marking prior exposure and SEM characterization

1.2 Pre-oxidation exposure

Information was needed for a vast array of the possible conditionings depending on time and temperature presented in Table 1. The treatments were grouped in two experimental sets to simulate different manufacturing conditions, isothermal and isochronous. Three series of isothermal pre-oxidation treatments and another three isochronous were designed. A sample was assigned to each of the series. To be able to study the properties in the same area, the experiments had to be performed alternating analysis and treatment.

Table 1: Pre-oxidation treatment matrix

T/t	AS FORMED	1h	5h	24h
600	A0	A1	A3	A5
750	D0	D1	D3	D5
850	F0	F1	F3	F5

For every treatment, the heating and cooling ramps were set to 5 °C/min. A Type K thermocouple connected to a Data Logger TC-08 was installed next to the sample to performed on-line temperature measurements.

1.3. Analytical methods

The analysis process and the exposures were conducted in alternate stages synchronously. Scanning Electron Microscopy (SEM) was used for both imaging and chemical analysis with Energy Dispersive x-ray Spectroscopy (EDS). A Zeiss EVO 50 VP scanning electron microscope has been used in this research. The samples were fixed in a disk holder which was set perpendicular to the beam. The accelerating voltage was set to 20 keV and the probe current was adjusted between 160 and 900 pA. The working distance was set to 10 or 11 mm and kept constant within the series.

2. Results

2.1 Cracks Development Analysis Through SEM Imaging

The morphological evolution of the oxides on the coating and the substrate (open cracks) was evaluated before and after the treatments by top-down SEM. The image acquisition was performed in a small area next to the scriber mark for reference.

2.1.1. Isothermal treatments

Figure 2 presents an overview of all isothermal treatments. A considerable spread in the crack size can be observed at 600 °C. After 1 h, signs of oxidation were already visible which effectively close the small cracks (< 1 µm). However, it remained unsuccessful for achieving complete self-healing. Spallation could be seen in some of the coating oxide scales. After 5 h and even 24 h of exposure, none appreciable differences were observed. The features observed in the center of the images were identified as impurities coming from the cutting process.

The magnitude of the average crack width in the 750 °C series was slightly greater than in the 600 °C one. After 1 h, the sample surface exhibited submicron crack closure as a result of the volume expansion. The medium size cracks of 1 to 2 µm were also reduced to a great extent. Spallation was not observed on the coating. After 5 hours of treatment a similar crack size and healing characteristics on the coating was observed. However, a substantial difference in the morphology of the sample was observed after 24 h. The precipitates on the coating kept growing in size and began to cover the surface homogeneously. At the same time, the growth of precipitates of the same structure on the substrate surface was observed.

The same crack size distribution already seen for the other samples is observed for the 850 °C series. A similar development as the 750 °C series was observed but with a quicker development thanks to the increased treatment temperature. After 1 h the volume expansion of the oxidized coating covered the sub-micron cracks, with extended effect after 5 h. An advanced state of self-healing effect is observed after 24 hours. The surface is completely covered with coarse precipitates (up to 2 µm) and there is almost no distinction between the coating and the exposed areas anymore.

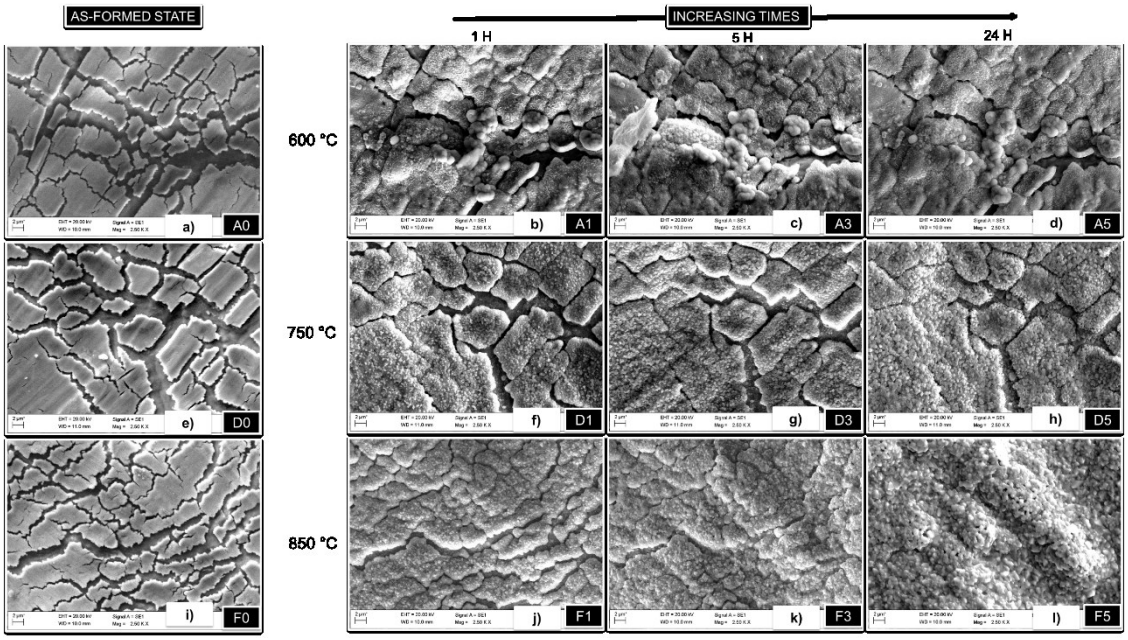

Figure 2: Overview of the top-down SEM images of the crack tracking analysis for all isothermal treatments.

2.1.2. Isochronous treatments

Figure 3 presents an overview of all isochronous treatments. After 1 h of the isochronous series, comparable features to all the samples can be observed. The largest (> 2 µm) cracks present in the as-formed state are not healed completely even at high temperatures. A very small effect in the healing was appreciated by volume expansion.

Increasing the length of the isochronous treatment to 5 h did not result in substantial differences in the morphology. Small micrometric cracks heal as an effect of the immediate volume expansion in the same way as observed before. However, some signs of spallation in the coating edges at the bottom left side which remained through all further steps. Despite the closure of minor size cracks, the largest ones (> 2 µm) remained unhealed even at high temperatures.

The development of the morphology and phases was the most distinct for the 24 h series. However, only the samples exposed at higher temperatures, i.e. 850 °C shows a full self-healing of the cracks. At 650 °C and 750 °C only smaller cracks were healed although the effect is considerably larger than for lower isochronous treatments.

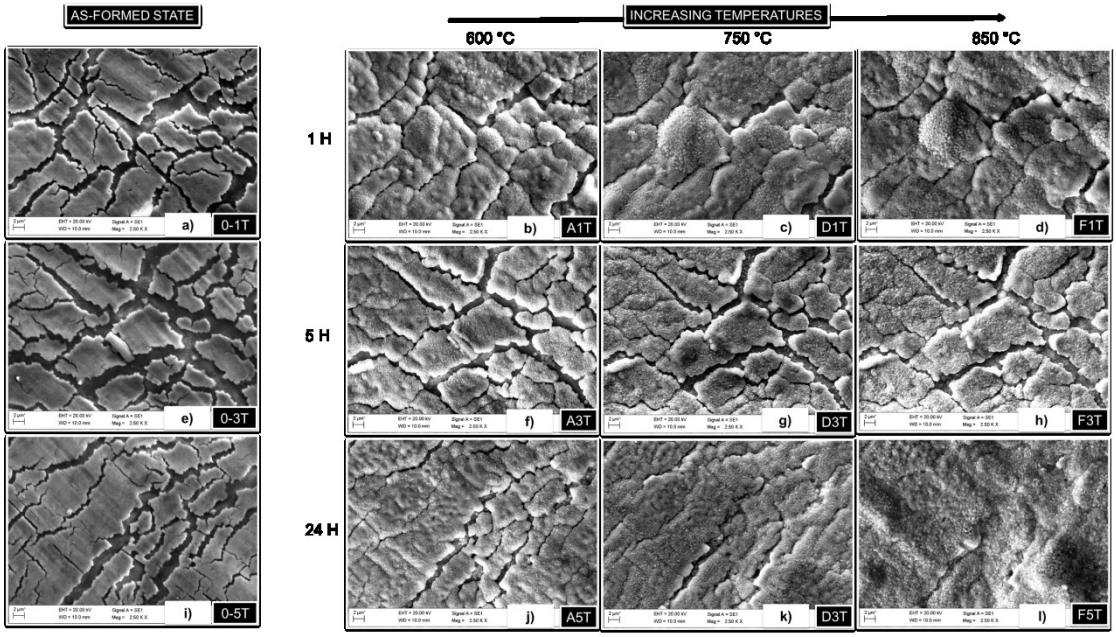

Figure 3: Overview of the top-down SEM images of the crack tracking analysis for all isochronous treatments

2.2 Oxide Growth Through EDS analysis

Previous data showed the effectiveness of the isothermal treatments as an effective solution for increasing the self-healing and therefore, deeper EDS analysis for the series at 750 and 850 °C were performed.

2.2.1. Isothermal series at 750 °C.

Figure 4 I presents the obtained spectra on the selected area of the crack. The most representative elements in the formation of protective coatings of ferritic steel interconnects are represented in the table of the figure. Their composition is given in atomic per cent to give information about the oxide stoichiometry. The analysis areas through the different exposures are marked in red in the images. Data collected from

Figure 4 I a in the as-formed state shows that only iron and chromium were detected. This shows a very similar proportion to the average composition of the steel. Co was detected from the first-hour treatment in the area of analysis of Figure 4 I b. At longer treatment times, the selected spot in Figure 4 I c indicates that the composition of the newly formed oxides was rich in Mn and Co.

The corresponding analysis of the coating is seen in Figure 4 II. The obtained data from Figure 4 II a revealed the presence of Cr and Fe in the coating in the as-formed state composition. The atomic content of Fe, Co, Cr and O remained stable in the analysis from the areas in Figure 4 II b to d. It should be noted that in Figure 4 II c, the analysis area selected was of the opposite side of the crack.

I) II)

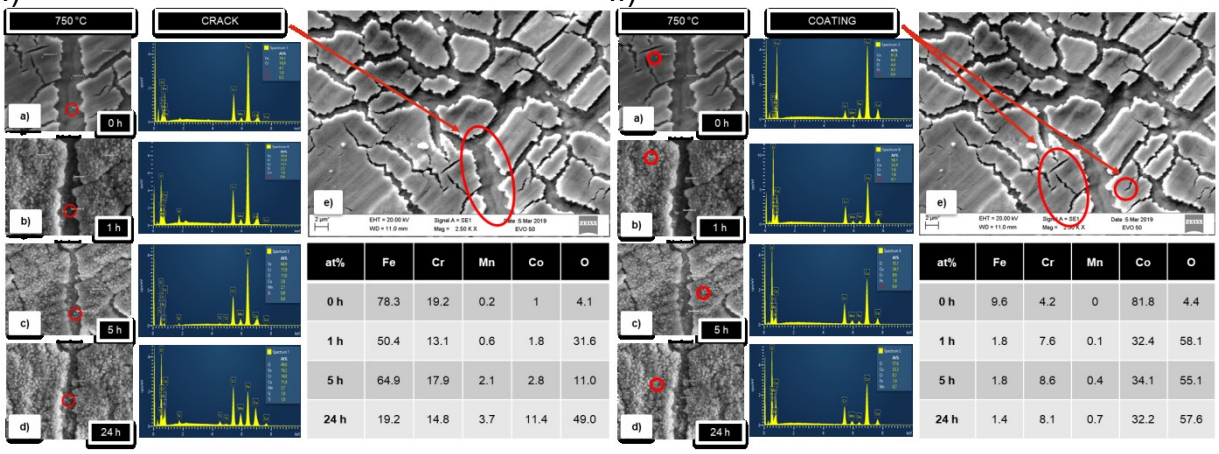

at%	Fe	Cr	Mn	Co	O
0 h	78.3	19.2	0.2	1	4.1
1 h	50.4	13.1	0.6	1.8	31.6
5 h	64.9	17.9	2.1	2.8	11.0
24 h	19.2	14.8	3.7	11.4	49.0

at%	Fe	Cr	Mn	Co	O
0 h	9.6	4.2	0	81.8	4.4
1 h	1.8	7.6	0.1	32.4	58.1
5 h	1.8	8.6	0.4	34.1	55.1
24 h	1.4	8.1	0.7	32.2	57.6

Figure 4: Oxide growth on the crack I) and on the coating II) surface by EDS analysis in the 750 °C isothermal series at a) as formed, b) 1 h, c) 5 h and d) 24 h. The measurement area can be seen in e) and the atomic composition in the table directly below.

2.2.2. Isothermal series at 850 °C.

The as-formed F0 sample from these series was not analysed since the composition of crack and coating was determined in D0 from the previous series. Both samples were belonging to the same piece of material in the untreated state.
Figure 5 I presents the EDS analysis through different stages of isothermal treatments at 850 °C in the crack area. The red ellipse in Figure 5 I d delimits where the EDS was obtained. The embedded table in Figure 5 I shows that all representative elements are visible in the analysis from the first stage in the treatments. Furthermore, it depicts a steady increase of Cr, Mn and Co content through the treatments in Figure 5 I.
The analysis of the coating is presented in Figure 5 II. As can be seen in the table the trends are comparable to what was seen in Figure 5 II. Between Figure 5 II a and b, there is not a large difference in Cr content, but it is double in Figure 5 II c. The increase is even more pronounced in the Mn content. Co content is steadily decreased during the treatments. Mn is found in the coating in Figure 5 II d in the same proportion as in the crack in Figure 5 I.

https://doi.org/10.5281/zenodo.4557639

I) II)

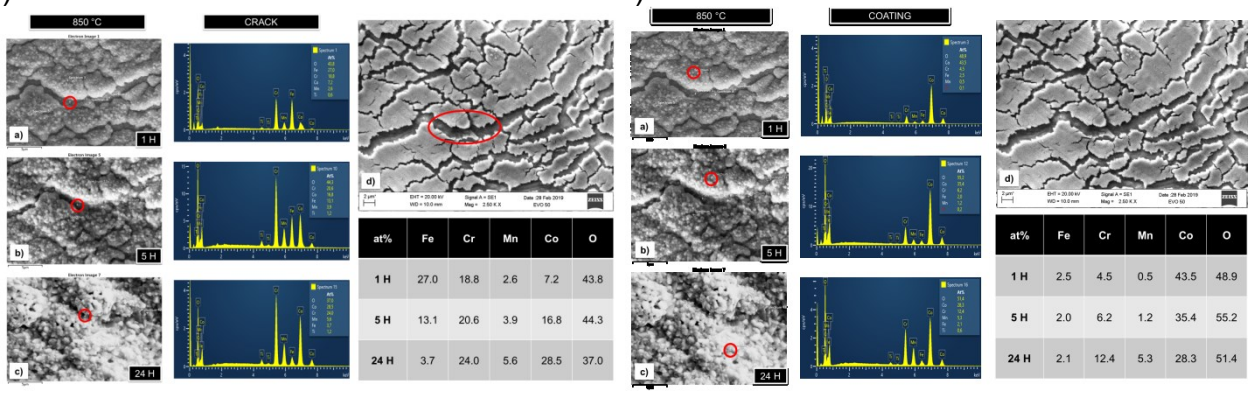

at%	Fe	Cr	Mn	Co	O
1 H	27.0	18.8	2.6	7.2	43.8
5 H	13.1	20.6	3.9	16.8	44.3
24 H	3.7	24.0	5.6	28.5	37.0

at%	Fe	Cr	Mn	Co	O
1 H	2.5	4.5	0.5	43.5	48.9
5 H	2.0	6.2	1.2	35.4	55.2
24 H	2.1	12.4	5.3	28.3	51.4

Figure 5: Oxide growth on the crack I) and the coating II) surface by EDS analysis in the 850 °C isothermal series at a) 1 h, b) 5 h and c) 24 h. The measurement area can be seen in d) and the atomic composition in the table directly below.

3. Discussions

3.1. Influence of pre-oxidation treatment design on the self-healing properties

The ability to develop a protective and homogeneous oxide layer that protects the substrate against chromia evaporation is the greatest factor in self-healing properties [5, 2, 7, 12]. Having a general view over the isothermal treatments in Figure 2 it is possible to observe some trends. It is appreciable that an instant volume expansion of the coating covered effectively the smaller submicrometric cracks regardless of the treatment temperature. Besides, the morphology of the precipitates on the coating is appreciably changed during the series. On the other hand, Figure 2 b to d showed a big effect of spallation in low-temperature series that was not so pronounced in higher temperatures. Ultimately, higher temperature treatments were considerably regarded to be more effective in achieving self-healing properties and to display higher levels of homogenization within shorter periods of time.

Previous studies from Froitzheim et al. [7] have reported that the process of oxidation of a metallic cobalt coating of similar thickness is produced within the first 30 seconds of the exposure. In that time, most of the cobalt coating is stratified in a double layer of Co_3O_4 oxide formed at the surface while CoO is found in the inner part. Froitzheim et al. also observed that after an hour of treatment at 800 °C, the oxidation to Co_3O_4 is completed, and the volume increases. Bridging the gap with the present study, the volume expansion in the coating observed after the first hours of treatment is most probably related to that transformation.

The deformation process in the as-formed state does not seem to affect the adhesion properties of the scales. However, Figure 2 b and f show that the edges of some scales are spalled-off in the first hour of treatments at 600°C and 750 °C respectively. Scale spallation has been discussed in some studies as the result of the formation of a subscale silica layer in high Si content steels. Silicon concentrates in Laves phases within the steel, which are thermodynamically stable at low temperature [13]. At high temperatures, an oversaturation of Si in Laves phases can lead to the formation of a silica layer in the metal-oxide interface and create stresses [13]. However, this theory opposes the observed spallation at lower temperatures. On the other hand, it has also been proved that metal-oxide adhesion is favored by the presence of REs such as Ce [14]. The mechanisms of how Ce helps to reduce spallation have been researched elsewhere [15, 16]. It has been suggested that Ce limits ion diffusion in the Cr_2O_3 boundaries, reducing the effect of impurities and other defects. This could explain why spallation seems to be more

significant in the biggest exposed areas where Ce is not present, in combination with the substrate deformation effect.
The morphological evolution described for isothermal treatments applies as well for the isochronous treatments, regarding the volume expansion and the morphology of the oxides on the coating at different temperatures. However, it is known that thermal cycles in discontinuous treatments affect oxidation behavior [12]. In a sequence of isothermal treatments, the influence in short times is less significant as the treatments have the same contribution in the overall result. However, in isochronous treatments, the different diffusion temperatures can generate successive microstructural changes. Figure 3 f to h demonstrates that short treatment times of one hour did not allow a sufficient diffusion to create a homogeneous layer of oxides even at high temperatures. The longest 24-hour treatments at the other end only showed substantial healing at 850 °C (Figure 3 l). An explanation for this could be attributed to the difficulted element diffusion through the inner oxide layers formed at lower temperatures. The progression of the morphology in the 5-hour temperature series (Figure 3 f to h) also seems to agree with this idea, as the improvement of the self-healing properties seems to be very minimal despite the longer treatment times than the 1-hour series.

3.2. Chemical Development of the Self-Healing properties

From the image analysis, it was observed that the samples undergoing isothermal exposures at 750 and 850 °C showed a steady development of self-healing properties. In the isothermal 750 °C series, the as-formed composition is very similar to the specified composition for the steel grade (Figure 6 a). Increased exposure times allow for Mn diffusion to the top layer which generates a $(Cr,Mn)_3O_4$ spinel. Fe could also be present in the spinel, but its source is indiscernible from the contribution of the substrate to the total amount. The enrichment of Co, Cr and Mn in the crack surface (Figure 6 b) is in agreement with the observed results from other authors [6, 16]. The low amount of Mn detected in the analysis after 5 hours indicates that not enough time was given for diffusion. On the other hand, the increase of Co content at 24 hours (Figure 6 c) can be explained by the surface diffusion of the coating which was previously observed in Figure 24 I d) and observed from different sources [13, 16]. However, the crystallite formation in the crack surface would have resulted from the combination of Co with the Mn upward diffusion [16, 17].

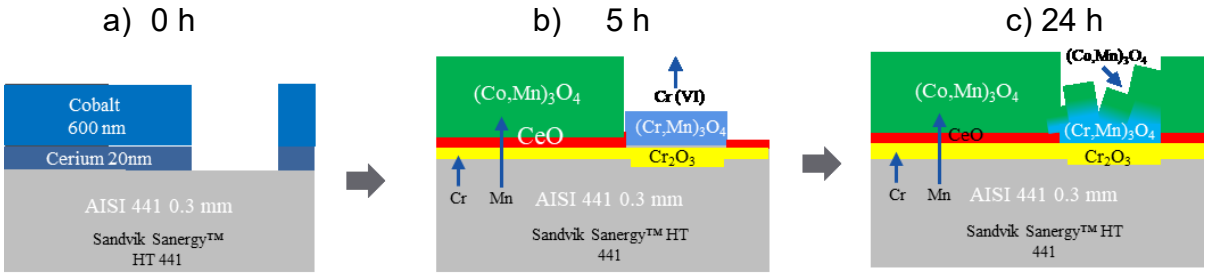

Figure 6. Evolution of the chemical composition over time (0 h, 5 h, 24 h) for samples exposed at 750 °C

The increased temperature in the 850 °C series resulted in a faster obtention of the self-healing. The growth of this scale is much faster in high temperatures as the rate-limiting step for oxide growth is solid state diffusion, observed in the paralinear mass gain behavior by several authors [10, 16]. The increase in homogenization towards the end of the treatments which was observed by image analysis was confirmed by the chemical analysis. In the first hour, the crack was covered in $(Co,Mn)_3O_4$ and the Co was incorporated in substitutional solution (Figure 7). The Cr content in the crack increased

linearly as the chromia scale was formed, with a 10% increase from what was observed at 750 °C . Co content increased to more than twice the amount seen at 750 °C at 24 h due to surface diffusion, and higher Mn content was also observed. Both Co and Mn reached similar values in the analysis of the coating and the crack, which suggests that the formation of a $(Co,Mn)_3O_4$ continuous layer was complete.

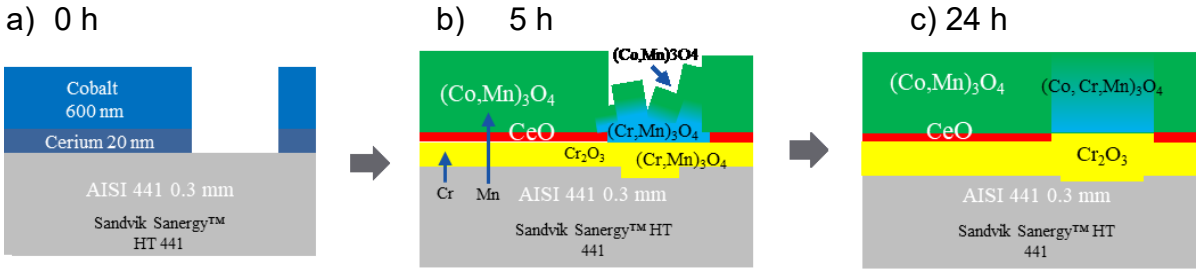

Figure 7. Evolution of the chemical composition over time (0 h, 5 h, 24 h) for samples exposed at 850 °C

4. Conclusions

The aim of the present study was to provide insight about how several pre-oxidation treatments influence the self-healing properties of the cracks generated in the material during the forming process.

It was observed that pre-oxidation temperature had a big impact on most morphological transformations of the coating and the substrate within the treatment times studied. Below 750 °C, the material would not develop significant signs of healing aside from the initial volume expansion. Moreover, the development of the self-healing properties of the oxide layer by alternative choices of isothermal or isochronous treatment design were observed. In particular, it was found that discontinuous isothermal treatments yielded a consistent evolution and homogenisation of the spinel oxides through the treatments compared to the isochronous series. This contrast was attributed to internal microstructural changes over the different temperatures.

Using EDS point analysis in exposed and coated areas, an advanced stage of self-healing was found in the 850 °C series after 24 hours. The formation of a cobalt spinel coating $(Co,Mn)_3O_4$ over the Cr_2O_3 layer is observed. The 750 °C series also showed promising results, as the decreased temperature translated in a reduction of the Cr content, possibly indicating that a thinner chromia layer was formed. Nevertheless, Co oxides and Mn were found over coating and cracks allegedly reducing the rate of Cr evaporation.

Further work must be performed to find the relevance of the healing properties found in the general performance of the material. The experimental conditions in a box furnace are not able to reproduce some accelerate corrosion mechanisms in the operating conditions found in dual atmosphere [8] such as breakaway corrosion, which may differ significantly from the expected protective behavior of the oxide layer. Furthermore, the growth of the chromia scale and its effect on the conductivity would also needs to be investigated.

References

[1] N. Shaigan, W. Qu, D. G. Ivey, W. Chen, “A review of recent progress in coatings, surface modifications and alloy developments for solid oxide fuel cell ferritic stainless steel interconnects,” Journal of Power Sources, vol. 195, no. 6, pp. 1529-1542, 2010.

[2] J. C.W. Mah, A. Muchtar, M. R. Somalu, M. J. Ghazali, “Metallic interconnects for solid oxide fuel cell: A review on protective coatings and deposition techniques” International Journal of Hydrogen Energy, vol. 42, no. 14, pp. 9219-9229, 2017.

[3] S. Fontana, R. Amendol, S. Chevalier, P. Piccardo, G. Caboche, M. Viviani, R. Molins, M. Sennour, "Metallic interconnects for SOFC: Characterisation of corrosion resistance and conductivity evaluation at operating temperature of differently coated alloys," Journal of Power Sources, vol. 171, no. 2, pp. 652-662, 2007.
[4] Z. Yang, G.-G. Xia, X.-H. Li and J. W.Stevenson, "$(Mn,Co)_3O_4$ spinel coatings on ferritic stainless steels for SOFC interconnect applications," International Journal of Hydrogen Energy, vol. 32, no. 16, pp. 3648-3654, 2007.
[5] M. W. Lundberg, J. Westlinder, H. Holmberg, Robert Berger, "Self Healing Precoated AISI 441 for Solid Oxide Fuel Cell Interconnects," SMT R&D Surface Technology AB Sandvik Material Technology, 2018.
[6] E. Alvarez, A. Meier, K. Scott Weil, Zhenguo Yang, "Oxidation Kinetics of Manganese Cobaltite Spinel Protection Layers on Sanergy HT for Solid Oxide Fuel Cell Interconnect Applications," International Journal of Applied Ceramic Technology , vol. 8, no. 1, pp. 33-41, 2011.
[7] J. Froitzheim, S. Canovic, M. Nikuma, R.Sachitanand, L.G. Johansson, J.E. Svensson, "Long term study of Cr evaporation and high temperature corrosion behaviour of Co coated ferritic steel for solid oxide interconnects," Journal of Power Sources , vol. 220, pp. 217-227, 2012.
[8] S. Fontana, S. Chevalier, G. Caboche. C. a. G. C. S. Fontana, "Metallic Interconnects for Solid Oxide Fuel Cell:Performance of Reactive Element Oxide Coating During 10, 20 and 30 Months Exposure," Oxidation of Metals,, vol. 78, no. 5-6, pp. 307-328, 2012.
[9] U. Bexell, M. Olsson and M. W. Lundberg, "High Temperature Oxidation of Plastically Deformed Ferritic Interconnect Steel," in 12th International Symposium on Solid Oxide Fuel Cells (SOFC), Montreal, 2011.
[10] H. Falk Windisch, M. Sattari, J. E. Svensson and J. Froitzheim, "Chromium vaporization from mechanically deformed pre-coated interconnects in SOFC," Journal of Power Sources, vol. 297, pp. 217-223, 2015.
[11] J. G. Grolig, "Coated Ferritic Stainless Steels as Interconnects in SOFC," PhD thesis. Chalmers University, Göteborg, Sweden 2015.
[12] J. G. Grolig, J. Froitzheim and J. E. Svensson, "Coated Stainless Steel 441 as Interconnect Material for Solid Oxide Fuel Cells: Oxidation Performance and Chromium Evaporation," Journal of Power Sources, vol. 248, no. doi:10.1016/j.jpowsour.2013.08.089, pp. 1007-1013, 2014.
[13] P. D. Jablonski, C. J.Cowen and J. S.Sears, "Exploration of alloy 441 chemistry for solid oxide fuel cell interconnect application," Journal of Power Sources, vol. 195, no. 3, pp. 813-820, 2010.
[14] J. S. P.Y.Hou, "The effect of reactive element additions on the selective oxidation, growth and adhesion of chromia scales," Materials Science and Engineering: A, vol. 202, no. 1-2, pp. 1-10, 1995.
[15] S. Chevalier, "What did we learn on the reactive element effect in chromia scale since Pfeil's patent?," Materials and Corrosion, vol. 65, no. 2, pp. 109-115, 2014.
[16] P. Guo, Y. Lai, Y. Shao, Y. Zhang, H. Sun and Y. Wang, "Oxidation Characteristics and Electrical Properties of Doped Mn-Co Spinel Reaction Layer for Solid Oxide Fuel Cell Metal Interconnects," Coatings, vol. 42, no. 8, 2017.
[17] P. Kofstad, High Temperature Corrosion, London: Elsevier Applied Science, 1988.

Keywords: EFCF2020, SOx
Session B13: Cells, stacks, and interconnects

B1308

New concepts for solid oxide cells manufacturing: The use of 3D printing technologies

Arianna Pesce (1)*, Maritta Lira Dos Santos (1), Natalia Kostretsova (1), Aitor Hornes (1), Alex Morata (1), Marc Torrell (1), Albert Tarancon (1,2)
(1) IREC, Catalonia Institute for Energy Research
Jardins de les Dones de Negre 1, 2º, Sant Adrià del Besós, Barcelona, 08930, Spain
(2) ICREA, Passeig Lluís Companys 23, 08010, Barcelona

Contact authors: www.EFCF.com/ContactRequest

Abstract

Manufacturing processes and final shapes of solid oxide cells (SOC) are, nowadays, constrained by ceramic fabrication technologies capable of shaping used materials with reasonable time and costs (tape casting and screen printing). The use of additive manufacturing technologies and its free-forming design for SOC manufacturing overcomes the commented limitations. Performance, durability and reliability are shown to be improved due to the enhancement of the active area and the addition of new geometrical features on SOC. For this purpose, electrolyte supported cells based on structured electrolytes were produced by stereo-lithography (SLA) 3D printing of 8YSZ. This pieces have demonstrated to present an improvement of the performance directly proportional to the increase on the active area induced by their structuration. A further implementation of this technology is the hybridization of SLA with a robocasting system as a multimaterial hybrid printer system to produce a one-step printed monolithic SOFC stack. This approach reduces the manufacturing steps and the waste material while avoiding the manual steps and multiple sintering steps of the conventional process. Complete SOFC fully printed by SLA+Robocasting hybrid printing are here presented. Challenges and results of the processing and co-sintering are discussed.

https://doi.org/10.5281/zenodo.4561823

Introduction

The interest of renewable energies have been increased as the alternative to overcome the depletion of fossil fuels and the reduction of greenhouse gases emissions in a new energy scenario. This alternative energy sources presents their main drawback in the discontinuity of energy production. To overcome this problem different solutions based on energy storage have been proposed such as batteries that are leading the recent research. However, fuel cells are also widely developed and play an important role as one of the most perspective approaches due to the capability to directly convert chemical energy stored in the hydrogen bonds into electrical power with a high efficiency under continuous operation.

Implementation of fuel cells based devices into the energetic grid provides an opportunity to save excess of renewable energy in hydrogen form and restoring this electricity during high demanding hours due to the reversibility of the devices. [1] In contrast to other types of fuel cells, SOFCs present the higher efficiency and the possibility of working not only with hydrogen, but with a wider range of fuels. [2-3]

Due to the ceramic nature of the materials that form the electrolyte, the devices based on SOC technology are mostly constraint into two shapes: tubular and flat devices, [4] derived from manufacturing technologies like tape casting, screen printing, extrusion and infiltration. Other techniques are precluded because of to the material's stiffness which makes them hard to machine with high cost and tool consumption. Those aspects precluded are limiting the design of the electrolyte and consequently the improvements related to a potential structuration of the surface. Some efforts to increase the performance of these devices through an increase of their surface area were made by *Cebollero et al.* [5-6] through micro-laser machining of the surface. In this sense, a possible solution was proposed by *Ruiz-Morales et al.* [7] suggesting the use of additive manufacturing for energy applications. In particular, they explored works in the field of SOFCs and batteries. At the time of the publication, the studies on 3D printing of SOFCs were focused on the inkjet and aerosol jet printing of electrolyte and cathode layers. According to previous works [8-18] the use of 3D printing technologies was limited to the deposition of a functional layer on top of a support layer, usually the anode or the electrolyte. Additive manufacturing techniques offer the possibility of realize free-design shapes, exploring solution forbidden by other production techniques. To achieve the maximum output of the device, simulation of different electrolyte geometries with different aspect ratio have been performed in the last years and the 3D printing has been proposed to obtain these untraditional structures. [19-20] Due to the intrinsic features of additive manufacturing techniques some studies have been devoted to increase the output of the device increasing the area of the electrolyte, which plays the role of supporting layer, and consequentially increasing the surface of the entire device. [21-24]

1. Scientific Approach

The work here presented is dedicated to prove the advantage and capability of the use of 3D printing technologies to the SOCs manufacturing and how the performance of these devices may be implemented thanks to the freedom of design achievable by these technologies.

The significant advantage of the additive manufacturing is the high automation of the process, compared with others techniques. A study from *Weimar et al.* shows how the production of a commercial stacks requires more than a hundred steps [25], the *Cell3Ditor European project,* [26-27] proposed the use of 3D printing to manufacture a stack in a single production and a single sintering step. In this frame, a stereo-lithography system has been equipped with a robocasting one, with four nozzles to enable the production of

pieces made of five different materials at the same time. Preliminary results on this implementation in a fuel cell are here presented.

2. Experiments

Electrolytes are printed out from a commercial slurry of 8mol%YSZ (3DMix, France), which is made of ceramic particles and organic compounds (monomer and photo initiator), which appear as a high viscosity paste [28]. The slurry is fed into a commercial ceramic 3D printer (3DCERAM, France)[29-30], a piston supply the necessary amount of the paste onto the building surface after which a double doctor blade system spreads the paste over the printing platform to get a thin and homogenous layer of 25 µm. A diode UV laser focused at the building surface reproduces the pattern designed by CAD (Computer assisted Design) software. Under UV exposure, the polymerization process takes place and the paste is solidified according to the desired shape. After each stage, the platform moves down and the process is repeated; since the curing depth of the laser is higher than the thickness of the layer deposited by tape casting, each slice is attached to the previous, generating a three dimensional structure (Figure 1).

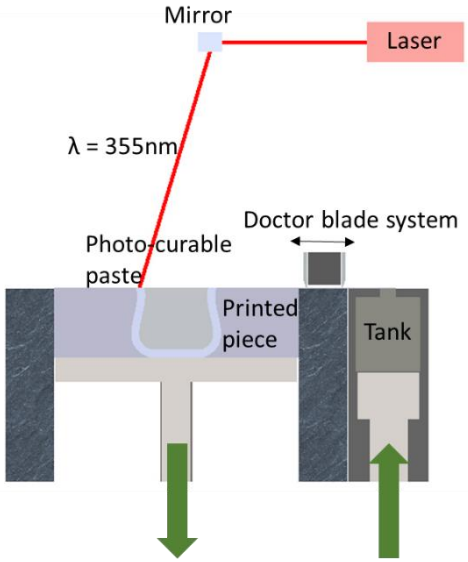

Figure 1: Scheme of stereo-lithography system.

Pursuing the improve of the performance changing the area with structuration of the electrolyte, a wave profile (Figure 2.b) extruded in a direction was produced with the technique described here, allowing an increase of active area of 57% compared with a flat design of the same external dimensions, used as comparison as typical geometry of traditional manufacturing as tape casting and screen printing (Figure 2.a).
At the end of the printing process, it is necessary to collect the uncured paste to be re-used in further printing, before fire the parts at high temperature in order to remove the organic compounds and sintering the ceramic part, to get the final mechanical properties of the pieces.
In order to reduce the ohmic losses of the final produced cells [31] electrolytes are printed as membranes (thickness of 300 µm), a thick ring (3mm) is added to the structure to increase its mechanical integrity and help with its handling [21,23], moreover, the design of this ring has been adapted for installation and sealing inside the testing station. The electrolytes have been sintered at 1300ºC for 3 hours to ensure fully densification.

The freedom of design, producing a wave profile, changing the external dimensions and improving the structural structures to improve the assembly of the pieces, are features proving the advantage of additive manufacturing technologies, these same solutions would be forbidden by traditional manufacturing or obtained at high cost, time and consumption of the tools.

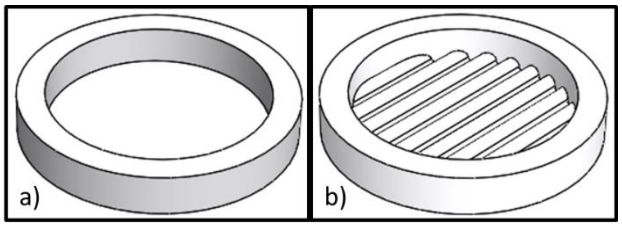

Figure 2: CAD designs used in this work, a) flat design, b) corrugated design, as well called wave..

Commercial inks are used for the electrodes: NiO-YSZ (Fuelcellmaterials, USA) as fuel electrode and LSM-YSZ (Fuelcellmaterials, USA) as oxygen electrode, attachment optimization is not reported here and can be found previous publications of the same authors. [23]

Fully printed cells were manufactured with the same printer hybridized with a robocasting system. This consists on a robotic arm, equipped with four syringes, valves and needles integrated to allow the printing of five materials at the same time. In this work SLA system was used to produce the electrolyte, which gives the mechanical support of the electrodes produced by robocasting. State-of-the-art materials for electrolyte supported cells were used, 8YSZ for the electrolyte, LSM-YSZ for the air electrode and NiO-YSZ for the fuel one. After the removal of the organic compounds, through a debinding process, the cells were co-sintered at 1250ºC for two hours.

All the cells based on the printed electrolytes have been tested in co-electrolysis and fuel cell mode. The electrochemical characterizations are performed in a commercial ProboStatTM (NorECs AS, Norway), the sample holder of which is placed inside a high temperature tubular furnace, tests were run at 850º-900ºC. Gold meshes and inks were employed as current collector for both electrodes. Ceramabond™ (Aremco, USA) sealant paste was applied to ensure gas tightness between the anodic and the cathodic chambers. The electrochemical performance is evaluated through I-V curves performed by a multimeter (Parstat 2273, PAR, USA), voltage is measured at each current step up to a maximum potential of 0,6V in fuel cell mode and 1,4V in co-electrolysis mode to limit degradation. The polarization curves are extrapolated up to 0,4V to show the maximum power output. Electrochemical Impedance Spectroscopy (EIS) is carried out using a potentiostat/galvanostat frequency response analyzer (Parstat 2273, PAR, USA) in the frequency range of 100 kHz down to 100 mHz and an amplitude of 50 mV under OCV and operative conditions, at 0,7V for SOFC mode and 1,3V for co-SOEC mode, conditions in which the resistive behavior is linear. During fuel cell mode measurements, the anodic side was fed with 22,2ml/min·cm^2 of hydrogen, and the cathodic one with synthetic air at 55ml/min·cm^2. In co-electrolysis mode the fuel electrode was fed with a mixture of 11,6 mg/min·cm^2 of water, 5,52 ml/min·cm^2 of carbon dioxide and 2,22 ml/min·cm^2 of hydrogen while the oxygen electrode was supplied with 45 ml/min·cm^2 of synthetic air. The fully printed cells have been tested only in SOFC mode, the same preparation and test conditions have been applied.

Microstructural characterization is performed using an AURIGA Scanning Electron Microscope (SEM) from ZEISS (Germany), equipped with a Schottky gun and an Energy Dispersive X-Ray Analyser (SEM-EDX) to measure the composition of the samples.

3. Results

Cells based on electrolytes produced by stereo-lithography

Stereo-lithography has been proved to be a suitable way to manufacture gas-tight electrolytes, showing properties comparable with the ones produced by traditional manufacturing. The final electrolytes show low and not-interconnected porosity, as it can be seen in Figure 3, where small pores are present, but the total density is over 97% of the theoretical value. The suitable density has been proved further on by electrochemical characterization, showing proper OCV values, above 1.05V. Gas tightness is critical issue, since pinholes and other defects could affect the performance of the cell

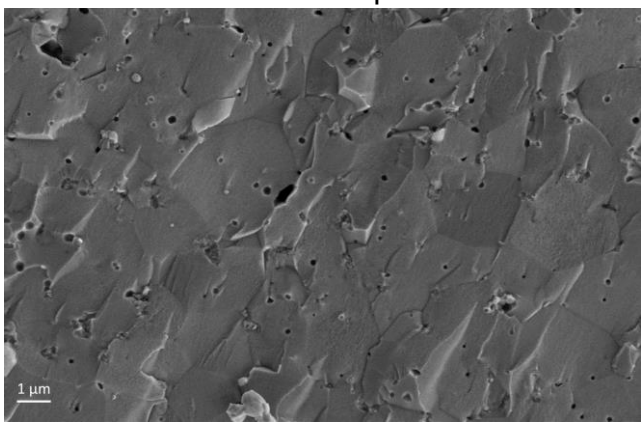

Figure 3: SEM micrography of the printed electrolyte after sintering at 1350ºC.

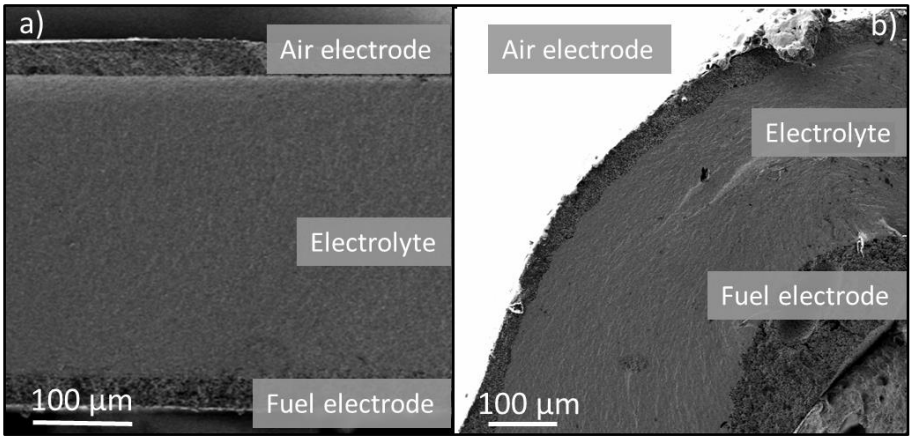

Figure 2: Post-mortem analysis of the tested cells, a) planar cell, b) wave cell. The active layers are reported.

Figure 4 presents the overall structure of the electrolytes produced as it has been previously described, showing proper thickness of the electrodes and confirming the reproduction of the CAD designs. It is possible to observe a proper porosity of the electrodes, allowing the diffusion of gases, and their good adhesion to the electrolyte.

As first step of the electrochemical characterization, the Open Circuit Voltage is measured and recorded over time during the *in situ* reduction of the fuel electrode, the values obtained are used to follow the reduction process and to confirm the gas-tightness of the cell and the sealing. Figure 5 shows the behavior of the voltage over time, the steps observed are related with the increase of the hydrogen against the argon in the fuel

electrode chamber, the final value of the OCV, before the measurement was stabilized at 1.14 V, confirming the gas-tightness of the electrolyte and of the applied sealing.

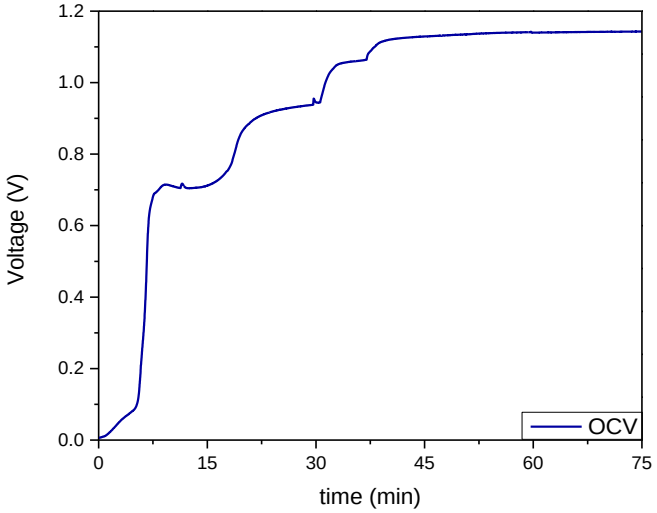

Figure 3: OCV over time at 850ºC during the reduction until before the measurement

The I-V polarization curves performed on fuel cell mode shown an important improvement due to the corrugation of the electrolyte (Figure 6.a). The maximum output power is improved from 287 mW/cm^2 to 455 mW/cm^2, corresponding the increase on the active area. Looking into detail of the Nyquist plots obtained by Electrochemical Impedance Spectroscopy (Figure 6.b), it is highlighted how the decreasing of the resistance is present, but not limited, to the serial resistance, which collects all the ohmic contributions, cables, electrolytes, etc., and to the polarisation resistance. In particular, the decrease ascribed to the reduce in the serial resistance, decreasing from 0.38 Ω·cm^2 to 0.32 Ω·cm^2, contribute for the 13% to the overall decrease in ASR, from 1.14 Ω·cm^2 to 0.68 Ω·cm^2, while the bigger contribution, ca. 87% is ascribed to the polarization resistance, which decrease from 0.75 Ω·cm^2 to 0.36 Ω·cm^2.

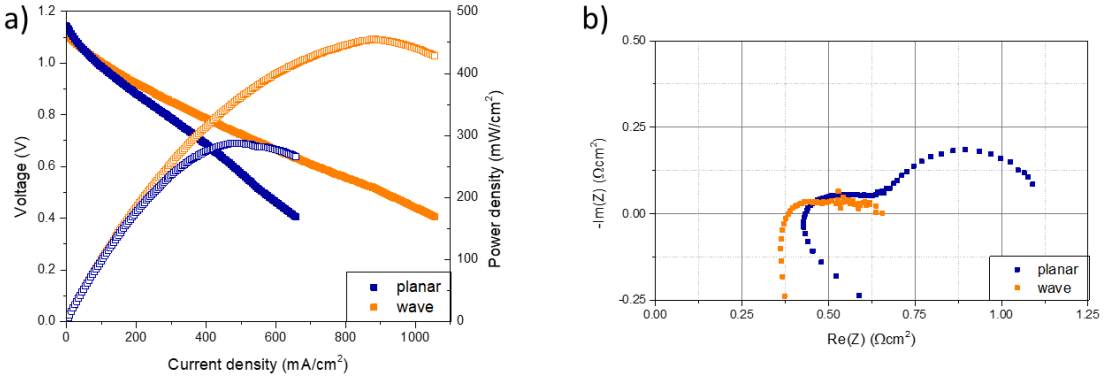

Figure 6: Electrochemical characterization of the cells based on printed electrolytes, carried out in SOFC mode at 900ºC. a) IV curves of planar and wave cells, b) Nyquist plot of the EIS at 0.7 V.

The cells have been tested in co-SOEC mode, to prove their suitability to be used to reduce CO_2. The improvement correlated with the area is maintained, but less relevant than the observed in SOFC mode, in this case the performance is evaluated comparing the injected current at 1.3V. The injected current is 432 mA/cm^2 for the planar, while for the corrugated one, the value increase up to 567 mA/cm^2, corresponding to an increase of 31%, lower than the improve of 57% of the area. This difference can be ascribed to water feeding or diffusion issues. The same problem was detected in the recording of the EIS, the instability of the measurement does not allow a good resolution of the arcs. In this case, only the serial resistance has been considered, showing a decrease of 0.128 Ω·cm^2,

which cannot be the only contribution to the increase in the performance, corresponding only to a 25% reduction in resistance.

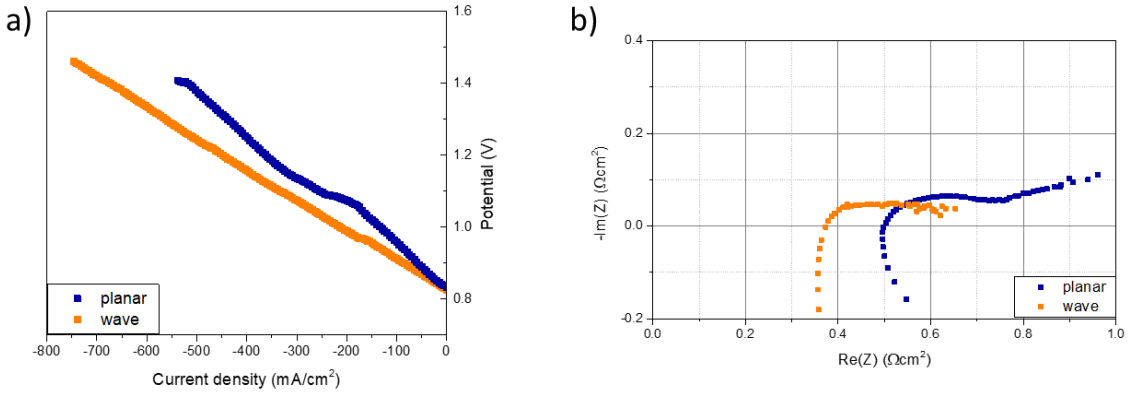

Figure 7: Electrochemical characterization of the cells based on printed electrolytes, carried out in co-SOEC mode at 900ºC. a) IV curves of planar and wave cells, b) Nyquist plot of the EIS at OCV.

Hybrid cell

Another approach based on the 3D printing of SOC devices is to hybrid printing (SLA+Robocasting) of complete cells. Here the preliminary results are presented for the single step manufacturing, in which all the components were produce by additive manufacturing techniques, robocasting for the electrodes and stereo-lithography for the electrolyte, which plays the role of support layer. The printed cell was co-sintering at 1250ºC, after the removal of the organics by a debinding thermal treatment.

Series of Figure 8 shows the microstructure of the different components of the cells after the co-sintering, respectively, the air electrode, the electrolyte and the fuel electrode. The LSM-YSZ electrode shows a non-optimized densification, open to further development, it is important to notice that although the lower sintering temperature compared with the samples presented before (Figure 3), the electrolyte appears dense, with small and not connected porosity. The NiO-YSZ electrode presents higher porosity compared to the LSM-YSZ, due to the higher sintering temperature of this material.

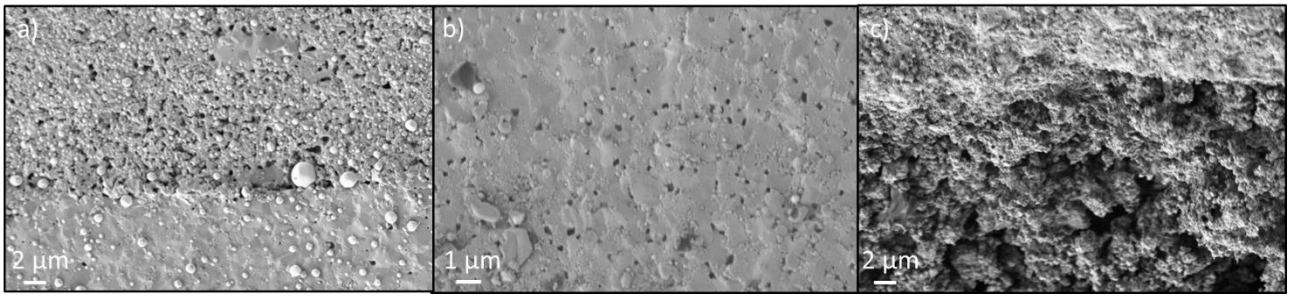

Figure 8: SEM analysis of the post-mortem: a) air electrode, b) electrolyte, c) fuel electrode of the fully printed cell, co-sintered at 1250ºC for 2 hours.

Figure 9 reports the electrochemical characterization in fuel mode, the OCV is lower than the value obtained on the cells reported before, this behaviour is ascribed to pinholes and cracks in the electrolyte generated by the thermal stress during the sintering.

The maximum output power at 900ºC is 80 mW/cm^2, this result is very promising, since the resistance is in accordance with the thickness of the cell. Higher output power is expected optimizing the porosity of the electrodes and improving the initial OCV of the cell.

https://doi.org/10.5281/zenodo.4561823

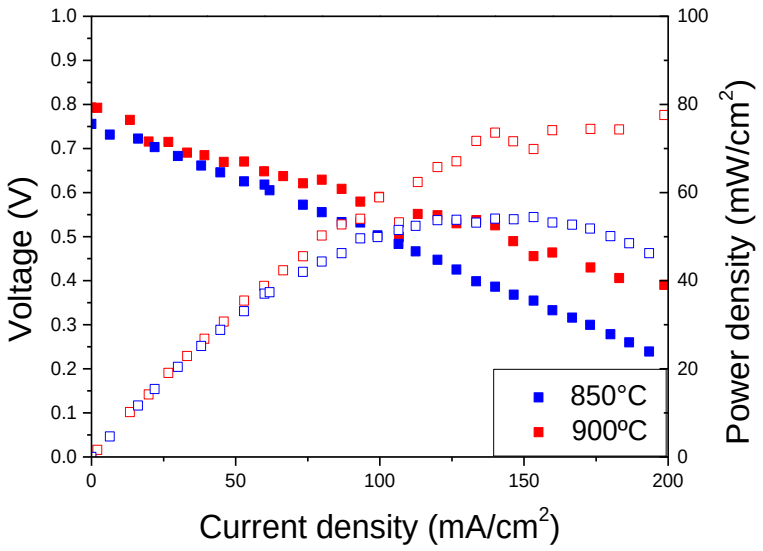

Figure 9: Potentiostatic curves of the fully printed and co-sintered cell at 850ºC and 900ºC.

4. Conclusion

In this work we explored the capability of the 3D printing in the Solid Oxide Cells scenario, stereo-lithography has been applied to improve the performance of the devices accordingly to the increase of the area. The performance improves of 58% in SOFC mode and of 31% upfront an increase of the area of the 57%.
Preliminary results on a fully printed and co-sintered cell are here reported, although the performance are lower compared with the cells based on the printed electrolytes, a promising possibility in the production of fuel cell has been proved.

Acknowledgement

The authors want to acknowledge the Nanoionics and Solid State Energy Devices Group (reference number: 2017 SGR 1421) for the support during the tests and the received on the frame of the RETOS call for the 3D-Progress (PID2019-107106RB-C31). and the Cell3Ditor project (project reference: 700266).

References

[1] K. Chen, S. S. Liu, N. Ai, M. Koyama, and S. P. Jiang, “Why solid oxide cells can be reversibly operated in solid oxide electrolysis cell and fuel cell modes?,” Phys. Chem. Chem. Phys., vol. 17, no. 46, pp. 31308–31315, 2015.

[2] E. D. Wachsman and K. T. Lee, “Lowering the temperature of solid oxide fuel cells,” Science, vol. 334, pp. 935–939, 2011.

[3] A. B. Stambouli and E. Traversa, “Solid oxide fuel cells (SOFCs): A review of an environmentally clean and efficient source of energy,” Renew. Sustain. Energy Rev., vol. 6, no. 5, pp. 433–455, 2002.

[4] K. C. Wincewicz and J. S. Cooper, “Taxonomies of SOFC material and manufacturing alternatives,” J. Power Sources, vol. 140, no. 2, pp. 280–296, 2005.

[5] J. A. Cebollero, R. Lahoz, and A. Larrea, “Tailoring the electrode-electrolyte interface of Solid Oxide Fuel Cells (SOFC) by laser micro-patterning to improve their electrochemical performance,” J. Power Sources, vol. 360, pp. 336–344, 2017.

[6] A. Larrea et al., “Characterization of laser-processed thin ceramic membranes for electrolyte-supported solid oxide fuel cells,” Int. J. Hydrogen Energy, vol. 42, no. 19, pp. 13939–13948, 2017.

[7] J. C. Ruiz-Morales et al., “Three dimensional printing of components and functional devices for energy and environmental applications,” Energy Environ. Sci., vol. 10, no. 4, pp. 846–859, Apr. 2017.

[8] A. M. Sukeshini et al., “Aerosol Jet Printing and Microstructure of SOFC Electrolyte and Cathode Layers,” vol. 35, no. 1, pp. 2151–2160, 2011.

[9] A. M. Sukeshini, R. Cummins, T. L. Reitz, and R. M. Miller, “Inkjet Printing of Anode Supported SOFC: Comparison of Slurry Pasted Cathode and Printed Cathode,” Electrochem. Solid-State Lett., vol. 12, no. 12, p. B176, Dec. 2009.

[10] C. Gadea, Q. Hanniet, A. Lesch, D. Marani, S. H. Jensen, and V. Esposito, “Aqueous metal-organic solutions for YSZ thin film inkjet deposition,” J. Mater. Chem. C, vol. 5, no. 24, pp. 6021–6029, 2017.

[11] M. A. Sukeshini, R. Cummins, T. L. Reitz, and R. M. Miller, “Ink-jet printing: A versatile method for multilayer solid oxide fuel cells fabrication,” J. Am. Ceram. Soc., vol. 92, no. 12, pp. 2913–2919, 2009.

[12] R. I. Tomov et al., “Direct ceramic inkjet printing of yttria-stabilized zirconia electrolyte layers for anode-supported solid oxide fuel cells,” J. Power Sources, vol. 195, no. 21, pp. 7160–7167, 2010.

[13] C. Li, H. Shi, R. Ran, C. Su, and Z. Shao, “Thermal inkjet printing of thin-film electrolytes and buffering layers for solid oxide fuel cells with improved performance,” Int. J. Hydrogen Energy, vol. 38, no. 22, pp. 9310–9319, 2013.

[14] C. Li, H. Chen, H. Shi, M. O. Tade, and Z. Shao, “Green fabrication of composite cathode with attractive performance for solid oxide fuel cells through facile inkjet printing,” J. Power Sources, vol. 273, pp. 465–471, 2015.

[15] G. D. Han et al., “Fabrication of lanthanum strontium cobalt ferrite (LSCF) cathodes for high performance solid oxide fuel cells using a low price commercial inkjet printer,” J. Power Sources, vol. 306, pp. 503–509, 2016.

[16] N. Yashiro, T. Usui, and K. Kikuta, “Application of a thin intermediate cathode layer prepared by inkjet printing for SOFCs,” J. Eur. Ceram. Soc., vol. 30, no. 10, pp. 2093–2098, Aug. 2010.

[17] H. Shimada, F. Ohba, X. Li, A. Hagiwara, and M. Ihara, “Electrochemical Behaviors of Nickel/Yttria-Stabilized Zirconia Anodes with Distribution Controlled Yttrium-Doped Barium Zirconate by Ink-jet Technique,” J. Electrochem. Soc., vol. 159, no. 7, pp. F360–F367, 2012.

[18] V. Esposito et al., “Fabrication of thin yttria-stabilized-zirconia dense electrolyte layers by inkjet printing for high performing solid oxide fuel cells,” J. Power Sources, vol. 273, pp. 89–95, 2015.
[19] C.-C. Chueh, A. Bertei, and C. Nicolella, “Design guidelines for the manufacturing of the electrode-electrolyte interface of solid oxide fuel cells,” J. Power Sources, vol. 437, no. July, p. 226888, Oct. 2019.
[20] A. Bertei, F. Tariq, V. Yufit, E. Ruiz-Trejo, and N. P. Brandon, “Guidelines for the rational design and engineering of 3D manufactured solid oxide fuel cell composite electrodes,” J. Electrochem. Soc., vol. 164, no. 2, pp. F89–F98, 2017.
[21] S. Masciandaro, M. Torrell, P. Leone, and A. Tarancón, “Three-dimensional printed yttria-stabilized zirconia self-supported electrolytes for solid oxide fuel cell applications,” J. Eur. Ceram. Soc., vol. 39, no. 1, pp. 9–16, 2019.
[22] L. Wei et al., “A novel fabrication of yttria-stabilized-zirconia dense electrolyte for solid oxide fuel cells by 3D printing technique,” Int. J. Hydrogen Energy, vol. 44, no. 12, pp. 6182–6191, 2019.
[23] A. Pesce, A. Hornés, M. Núñez, A. Morata, M. Torrell, and A. Tarancón, “3D printing the next generation of enhanced solid oxide fuel and electrolysis cells,” J. Mater. Chem. A, 2020.
[24] B. Xing, C. Cao, W. Zhao, M. Shen, C. Wang, and Z. Zhao, “Dense 8 mol% yttria-stabilized zirconia electrolyte by DLP stereolithography,” J. Eur. Ceram. Soc., vol. 40, no. 4, pp. 1418–1423, 2020.
[25] M. R. Weimar, D. W. Gotthold, L. A. Chick, and G. A. Whyatt, “Cost Study for Manufacturing of Solid Oxide Fuel Cell Power Systems,” 2013.
[26] Cell3Ditor, “Cell3Ditor,” http://www.cell3ditor.eu/, 2016. .
[27] “Cell3Ditor project on 3D printing tech for SOFC stacks,” Fuel Cells Bull., vol. 2016, no. 10, p. 12, 2016.
[28] C. Hinczewski, S. Corbel, and T. Chartier, “Stereolithography for the fabrication of ceramic 3D parts,” Rapid Prototyp. J., vol. 4, no. 3, pp. 104–111, 1998.
[29] F. Doreau, C. Chaput, and T. Chartier, “Stereolithography for manufacturing ceramic parts,” Adv. Eng. Mater., vol. 2, no. 8, pp. 493–496, 2000.
[30] C. Chaput, T. Chartier, and F. Doreau, “Method and composition for making ceramic parts by stereolithography and use in dentistry,” WO 03/066326 A2, 2003.
[31] E. Ivers-Tiffée, A. Weber, and D. Herbstritt, “Materials and technologies for SOFC-components,” J. Eur. Ceram. Soc., vol. 21, no. 10–11, pp. 1805–1811, 2001.

Keywords: EFCF2020, SOx
Session B13: Cells, stacks, and interconnects

B1409

Extension of catalyst lifetime for application of diesel-fueled pre-reforming in a commercial SOFC system

Tobias Schiekel, Elmar Pohl
OWI Science for Fuels gGmbH
Kaiserstraße 100, DE-52134 Herzogenrath

Contact authors: www.EFCF.com/ContactRequest

Abstract

While pre-reforming of natural gas with nickel catalysts is an industrially established process, pre-reforming of higher hydrocarbons like diesel is more challenging, as the nickel catalysts used in the process show rapid catalyst deactivation. The reasons for this are sulfur poisoning, coke deposition and sintering [1]. Coke formation can be minimized by keeping a certain steam-to-carbon ratio and by running the process at a temperature which is high enough to prevent polymeric gum formation and below temperatures where whisker carbon can be formed. Christensen et al. [2] present suitable values for these parameters, but heat integration and recirculation of mass flows in a SOFC system make temperature control in the adiabatic pre-reformer significantly more complex than in a laboratory reactor. As sulfur poisoning cannot be prevented effectively when commercial diesel is used for process gas generation, a selective adsorber is placed upstream of the pre-reformer to remove sulfur components. Currently running experiments shall validate the assumed catalyst lifetime enhancement when using fully desulfurized diesel.
Non-ideal conditions can lead to an early catalyst failure going along with a slip of higher hydrocarbons through the reactor. As this can cause severe damage at the anode downstream of the reformer, the operator of the system must always know the condition of the catalyst. Therefore, a method for online measurement of the catalyst condition is required. Previous experiments have shown that the temperature profile, which arises in the adiabatic pre-reformer due to endothermic reforming reaction and exothermic methanation and water-gas-shift reaction, is suited for this purpose. One aim of the experiments is to find a method that allows extrapolation of catalyst lifetime at an early stage of deactivation.
So far more than 3000 hours of continuous pre-reforming with complete conversion of higher hydrocarbons have been achieved [3]. The objective of diesel pretreatment and adjustment of reforming parameters is pushing the catalyst lifetime to more than 8000 hours so that the SOFC system can be operated one year without catalyst change.

https://doi.org/10.5281/zenodo.4561846

Introduction

Unlike PEM based fuel cell systems, stationary SOFC systems are typically fueled with natural gas, as the internal reforming of methane at the anode can be used for cooling the fuel cell stack. Furthermore, in contrast to hydrogen there is an existing pipeline network for natural gas. However, for certain mobile applications like shipping or heavy-duty traffic liquid fuels like diesel profit from their significantly higher volumetric energy density as well as easy storage and transportability. Compared to compressed hydrogen at 700 bar the volumetric calorific value of diesel is more than four times higher and compared to liquefied natural gas it is about twice as high [4]. Therefore, SOFC systems using diesel fuel are a promising way for ship owners to reduce pollutant emissions arising from on-board electricity generation. Additionally, the high electric efficiency of up to 60 % leads to a reduction of greenhouse gas emissions of up to 25 % compared to electricity generation with gas turbines or diesel fueled internal combustion engines.
To be used in the fuel cell, diesel as well as natural gas must be converted into a hydrogen rich gas mixture by steam reforming. Natural gas mainly consists of methane, carbon dioxide and small amounts of higher hydrocarbons like ethane and propane, whereas diesel is a mixture of many different compounds like alkanes and aromatics ranging from 9 to 22 carbon atoms per molecule. Therefore, the reforming of diesel tends to form carbonaceous deposits on the catalyst narrowing the values for parameters such as temperature and steam-to-carbon ratio to a small operating window. Another reason for rapid catalyst deactivation is sulfur poisoning, since even small amounts of sulfur which can be found in ultra-low sulfur diesel strongly adsorb on the active sites of nickel catalysts and block them for further reactions [5].
The objective of this work is to prove that catalyst deactivation during diesel pre-reforming can be reduced to an acceptable degree for a commercial application when using fully desulfurized diesel and applying suitable operating parameters.

1. Scientific Approach

Adiabatic pre-reforming of light feedstocks like natural gas or naphtha is an established process used in the chemical industry to convert all higher hydrocarbons in the feed stream and thereby preventing soot formation in the reformer. Unlike steam reforming which is carried out at temperatures above 800 °C, a pre-reformer is typically operated in the range of 400 – 500 °C. This causes a shift in the chemical equilibrium resulting in an incomplete conversion of methane. The remaining share of methane, which is about 10 – 15 % of the dry gas volume, is beneficial for heat integration of an SOFC system. The reason for this is the fact that the endothermic reforming reaction of methane takes places at the anodic part of the fuel cell using excess heat produced during fuel cell operation.
Feasibility of pre-reforming heavier feedstock like diesel has been proven by many authors [5,6]. The endothermic reforming reaction is irreversible for all hydrocarbons except methane. Therefore, the reactions in the process can be summarized as irreversible reforming (1) accompanied by reversible methanation (3) and water-gas-shift (2).

$$C_xH_y + x\ H_2O \rightarrow x\ CO + (x + y/2)\ H_2 \text{ (reforming) (1)}$$
$$CO + H_2O \leftrightarrow CO_2 + H_2 \text{ (water-gas-shift) (2)}$$
$$CO + 3\ H_2 \leftrightarrow CH_4 + H_2O \text{ (methanation) (3)}$$

Christensen et al. [2] provide a detailed understanding of catalyst degradation mechanisms as there are mainly coke formation and sulfur poisoning. They describe seven different types of carbonaceous deposits formed during pre-reforming of higher

hydrocarbons mainly depending on steam-to-carbon ratio and temperature level. Due to the heterogenous character of diesel fuel coke formation cannot be completely prevented, yet it can be sufficiently reduced for a long-term process when applying suitable process parameters. The other dominating degradation mechanism when reforming diesel fuel is sulfur poisoning. Sulfur strongly adsorbs on the active sites of nickel catalysts and blocks them for further reactions. Even small concentrations of less than 10 ppm sulfur which can be present in European road diesel according to DIN EN 590 cause rapid catalyst failure. Even though these mechanisms are thoroughly investigated and understood [2], diesel pre-reforming has not been developed to a technology readiness level that would make it suitable for commercial applications. Besides the complex desulfurization of diesel to values below 1 ppm sulfur, reasons for this might be the generally higher costs of diesel compared to natural gas as well as the lack of an application that would profit from using liquid fuels. However, as regulations for pollutant and greenhouse-gas emissions in shipping are becoming stricter, mobile diesel fueled SOFC systems seem to be a promising technology that depends on a stable reforming process.

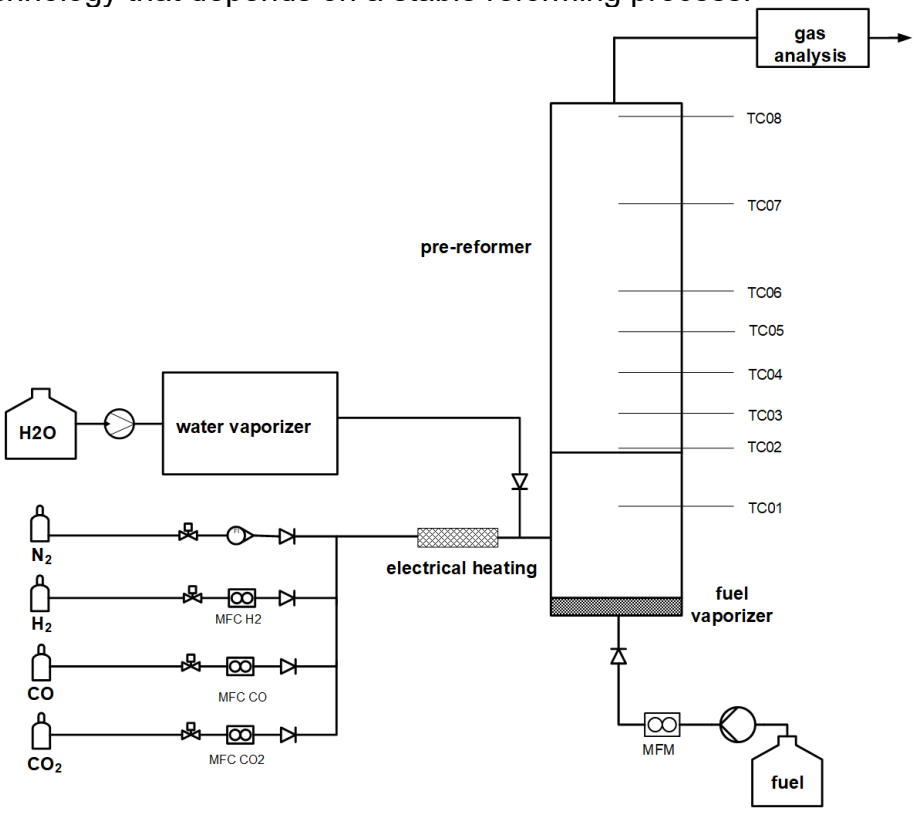

Figure 1: Experimental setup with gas supply via mass flow controller controllers (MFC) and temperature measurement along the reactor length with thermocouples (TC)

2. Experiments

Experiments for the determination of catalyst lifetime depending on operating parameters and sulfur content were carried out in a tubular reactor with an active volume of about one liter. Given the small size of the reactor an adiabatic operation was not feasible. Therefore, heat losses were partly compensated with an external electrical heating. As the reformer is intended as a part of the SOFC system, a recirculation of anode off-gas was simulated by dosing hydrogen, carbon dioxide and carbon monoxide into the reactor. The respective volume flows for each component were calculated with a system model. Diesel was evaporated on a heated mesh and mixed with water vapor and recirculated gases before

entering the reformer. The experiments were executed at atmospheric pressure. The inlet temperature of the reformer was derived from a system model as well and set between 500 and 600 °C. Temperatures in the reformer are only influenced by external heat losses and the energy needed for the endothermic reforming reaction. Hence, the temperature profile in the reactor provides valuable information about the status of the reaction and the ageing of the catalyst. To visualize the temperature profile in the reformer, eight thermocouples where placed along the flow direction. At the same positions small tubes for gas removal were placed to analyze the gas composition alongside the reactor. Concentrations of carbon dioxide, carbon monoxide and methane were measured with a nondispersive infrared sensor. Hydrogen concentrations were determined via thermal conductivity. At the reformer outlet the product gas was completely condensed and analyzed for traces of higher hydrocarbons. Catalyst failure was defined as the operation time at which significant amounts of higher hydrocarbons could be measured at the reformer outlet. This can be seen in an increase of total organic carbon from about 5 ppm to several hundred ppm and in a thin oil phase on the condensate of the product gas.
In several short-term pre-tests the commercial nickel-based catalyst AR-401 by Haldor Topsoe showed the best performance when reforming ultra-low sulfur diesel and was therefore chosen for the long-term experiments. The range of possible values for steam-to-carbon ratio to prevent soot formation was determined via equilibrium calculations and verified by previous experiments. The focus of the investigations for catalyst lifetime enhancement was therefore put on the influence of small amounts of sulfur. In the first experiment a US-diesel according to ASTM D 975 with 15 ppm sulfur was used for continuous pre-reforming till catalyst failure. In the second run those results were compared to a desulfurized diesel with less than 1 ppm sulfur.

3. Results

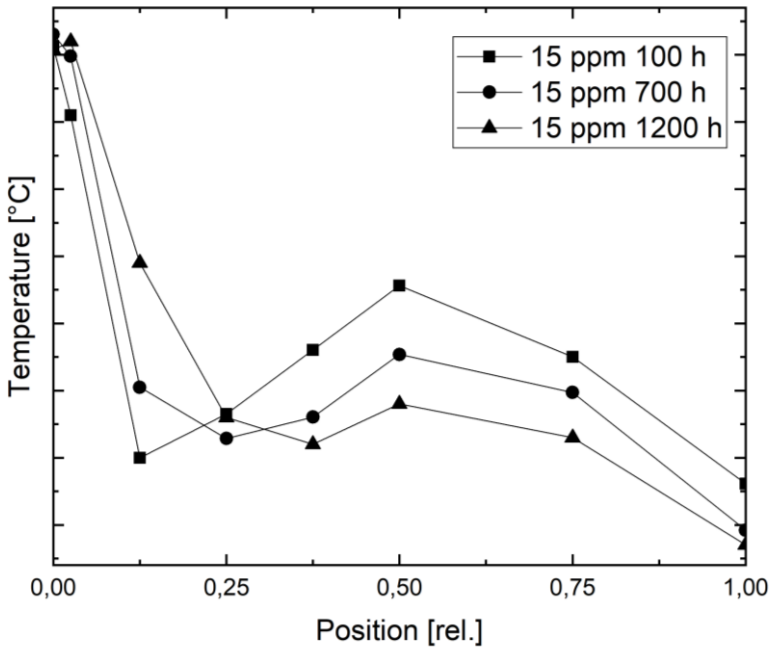

Figure 2: Change of temperature profile over reactor length during pre-reforming of diesel fuel with 15 ppm sulfur in the first 1200 hours of continuous reforming

https://doi.org/10.5281/zenodo.4561846

Figure 2 shows a typical temperature profile that occurs during diesel pre-reforming. Starting from the temperature in the mixing chamber there is a strong initial temperature drop when entering the catalyst caused by the endothermic reforming reaction. After passing a temperature minimum the exothermic methanation leads to a rise of the reactor temperature to a second maximum. As the overall reaction is endothermic the temperature at the reformer outlet is significantly lower than the inlet temperature.
In the first experiment (Figure 2) diesel with 15 ppm sulfur is used for the reforming process. After 100 hours of reforming the temperature profile in the reactor is characterized by a steep temperature drop till about 1/8 of the reactor length followed by a linear rise till half of the reactor length indicating a high catalyst activity. Yet, when compared to the profile that arises when using diesel with less than 1 ppm sulfur (Figure 3), a major difference can be seen when focusing on the first thermocouple just behind the reactor inlet. While the temperature drops about 50 K between mixing chamber and first thermocouple after 100 hours of reforming with < 1 ppm diesel it sinks only about 10 K after reforming with 15 ppm diesel for the same time. This shows that catalyst activity at the reformer entrance is significantly lowered after only a short time of reforming with 15 ppm diesel. Even after 700 and 1200 hours of process operation only minor changes in the temperature profile of the < 1 ppm experiment can be measured indicating a very slow catalyst degradation. The initial drop between mixing chamber and first thermocouple is still 35 K after 1200 hours of operation. In contrast, the temperature profile of the 15 ppm sulfur experiment changes drastically after 700 and 1200 operation hours.
Between mixing chamber and first thermocouple no temperature-drop and consequently no reaction can be seen after 700 hours of reforming. The temperature minimum moves downstream the reactor to 1/4 of the reactor length after 700 hours and to 3/8 after 1200 hours going along with a general flattening of the profile. Catalyst failure with slip of higher hydrocarbons occurred after 2700 hours in the experiment with 15 ppm sulfur. The experiment with less than 1 ppm sulfur was still running at the time of this publication. As the temperature profile only showed minor changes in the first 1200 hours, methods for extrapolation of catalyst lifetime which are based on the shift of the profile couldn`t be applied.

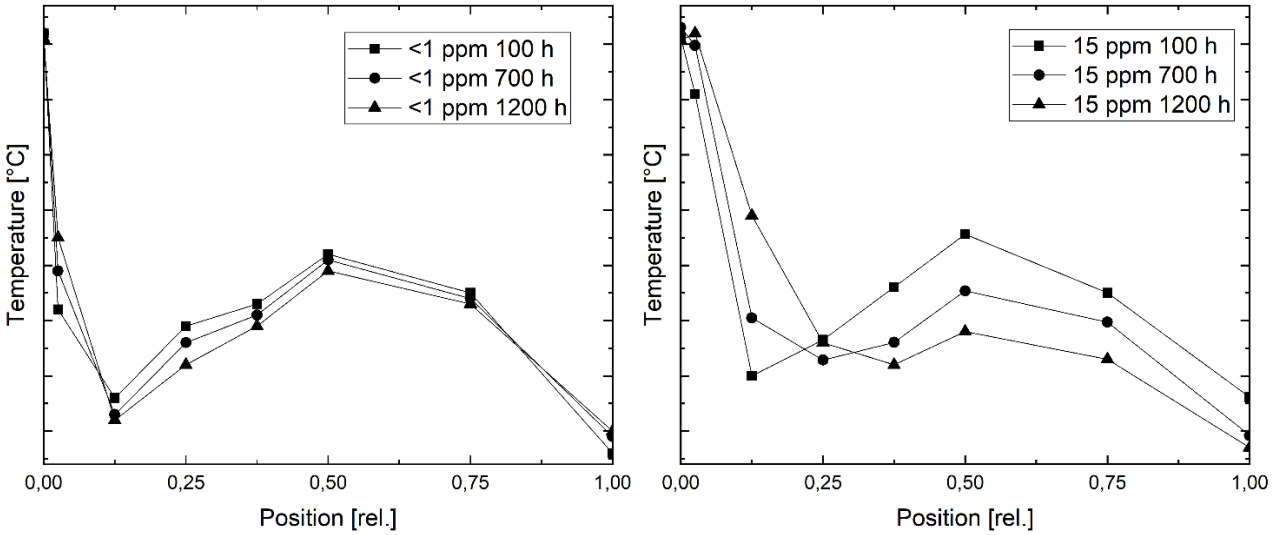

Figure 3: Comparison of changes in temperature profiles over reactor length during pre-reforming of diesel fuel with < 1 ppm sulfur (left side) and 15 ppm sulfur (right side) in the first 1200 hours of continuous reforming

https://doi.org/10.5281/zenodo.4561846

Another possibility to determine catalyst activity is by measuring methane concentrations along the reactor length. As no methane is present in the recirculated gas, all methane is produced by methanation. Figure 4 shows methane concentrations for the first 1000 hours of the 15 ppm sulfur experiment. Concentrations rise till they reach chemical equilibrium and only change slightly from that point as the temperature changes over reactor length cause minor changes in the position of the equilibrium concentrations. After 24 hours of operation methane concentrations reach chemical equilibrium at 1/4 of the reactor length. After 1000 hours the increase is significantly slower due to catalyst degradation and reaches the equilibrium at half of the reactor length. At the end of the reactor all gas concentrations reached chemical equilibrium even after slip of higher hydrocarbons. When comparing these profiles to the experiment with less than 1 ppm sulfur present in the fuel (Figure 5), it becomes evident, that a strong catalyst degradation already takes place in the first 24 hours of the 15 ppm experiment. While equilibrium in the 15 ppm experiment is reached after 1/4 of the reactor length after 24 hours, methane concentrations reach the equilibrium after 1/8 of the reactor length in the <1 ppm experiment. Although catalyst degradation is clearly visible in this experiment, the equilibrium concentration after 1000 hours is still reached at 1/4 of the reactor length.

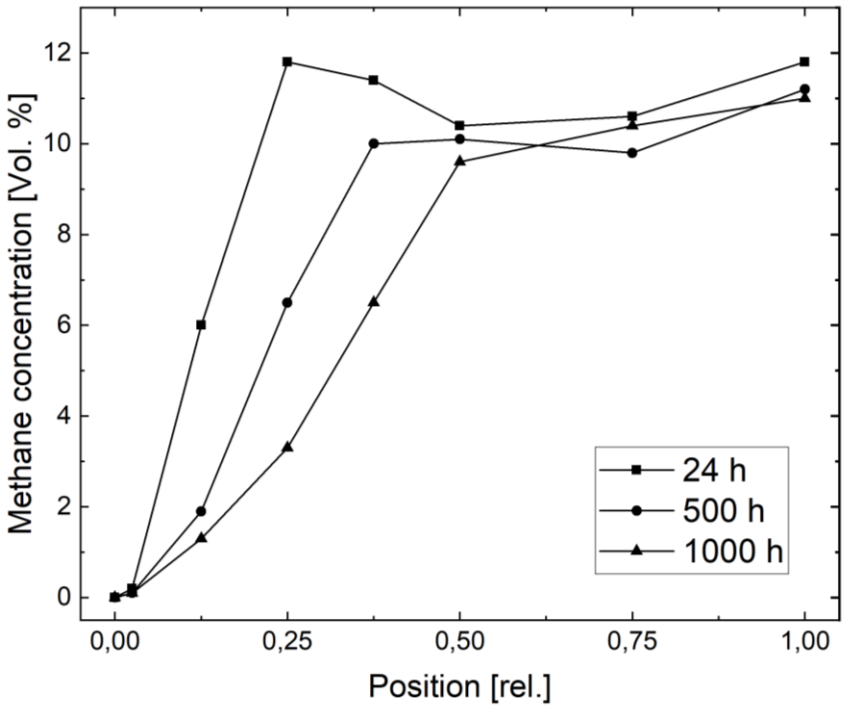

Figure 4: Change of methane concentrations over reactor length during 1000 hours of pre-reforming with 15 ppm sulfur diesel

Therefore, it can be concluded that catalyst activity after 1000 hours of reforming with diesel with less than 1 ppm sulfur is similar to the activity after only 24 hours when reforming with 15 ppm sulfur diesel.

https://doi.org/10.5281/zenodo.4561846

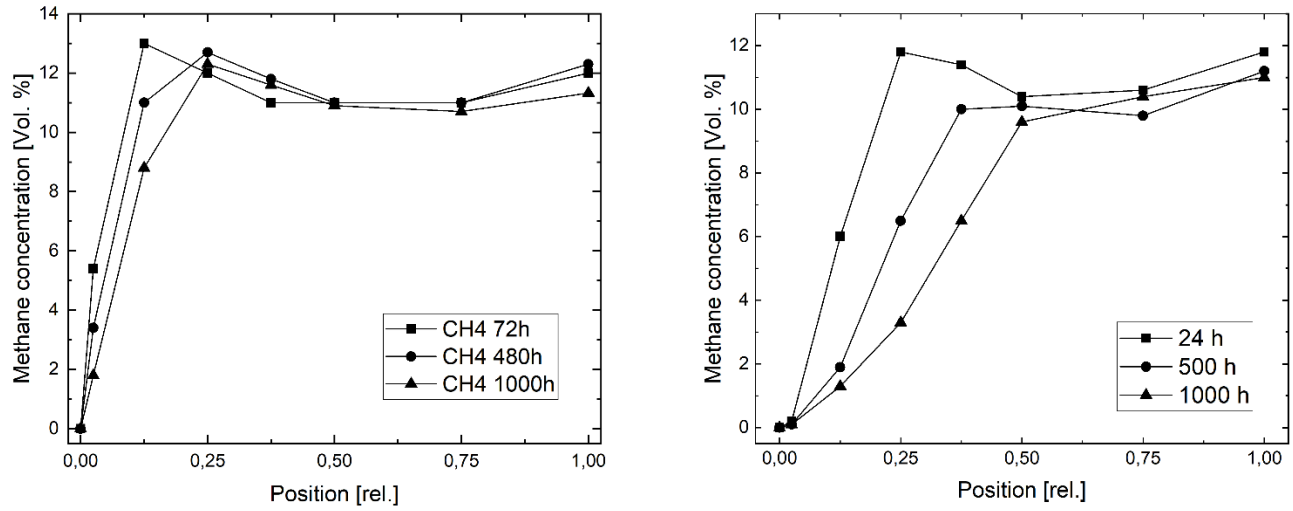

Figure 5: Comparison of changes of methane concentrations over reactor length during 1000 hours of pre-reforming with < 1 ppm (left side) and 15 ppm sulfur (right side) diesel

4. Conclusion

The experiments showed that even small amounts of sulfur have an enormous influence on catalyst degradation. While the catalyst degraded very quickly with 15 ppm sulfur in the fuel, almost no loss in catalyst activity could be seen with less than 1 ppm sulfur. As expected, the change of the temperature profile in the reactor is an easy and reliable possibility to evaluate catalyst activity. Due to the low catalyst degradation when using diesel with less than 1 ppm sulfur, methods for extrapolating catalyst lifetime could not be applied, as they are based on the movement of characteristic points in the temperature profile along the reactor.
Measuring methane concentrations along the reactor length also provides valuable information about the progress of catalyst degradation, yet it does not seem to be an option for commercial systems. The gas composition at the reformer outlet however, is not suited to evaluate catalyst degradation, as it still reaches chemical equilibrium when higher hydrocarbons slip through the reactor. Although the experiment with less than 1 ppm sulfur wasn`t finished at the time of publication, the low catalyst degradation in the first 1200 hours of operation indicates that a catalyst lifetime of 8000 hours, which was defined as sufficient for the intended commercial application, can be reached.

Acknowledgement

The presented work is conducted within the project “MultiSchIBz“. Coordinated by: Nationale Organisation Wasserstoff- und Brennstoffzellentechnologie Promoted by: Bundesministerium für Verkehr und digitale Infrastruktur (BMVI) im Rahmen des Nationalen Innovationsprogramms Wasserstoff- und Brennstoffzellentechnologie (NIP)
Special thanks to Ali Padidar, Salim Oualitsen, Karol Biercewicz and Nils Eden from the project team at OWI for realizing the experimental setup.

References

[1] J. Cross, G. Jones, M. A. Kent, An introduction to pre-reforming catalysis, 2016
[2] Thomas S. Christensen, Jens Rostrup-Nielsen, Catalyst deactivation in adiabatic prereforming: experimental methods and models for prediction of performance, 1996.
[3] Nils Kleinohl, J. B. Hansen, P. Nehter, H. Modarresi, A. Bauschulte, J. vom Schloß, K. Lucka, Pre-reforming of hydrocarbons as fuel processing technology for fuel cells, in European Fuel Cell Forum, Lucerne, (2013), B0503.
[4] Lenz, Barbara, et al., Shell LNG-Studie: Verflüssigtes Erdgas-Neue Energie für Schiff und Lkw? Fakten, Trends und Perspektiven, 2019.
[5] Nils Kleinohl, J. B. Hansen, P. Nehter, H. Modarresi, A. Bauschulte, J. vom Schloß, K. Lucka, SOFC fed with European standard road diesel by an adiabatic pre-reforming fuel processor, in European Fuel Cell Forum, Lucerne, (2014), B1510.
[6] Jurriaan Boon, Eric van Dijk, Adiabatic Diesel Pre-reforming Literature Survey, 2008.

Keywords: EFCF2020, SOx
Session B14: Oxygen electrodes II

https://doi.org/10.5281/zenodo.4561846

B1503

Post-mortem analysis from barrier layer's large-area cells made by PLD aged for 14,000 h in SOFC mode

L. Bernadet (1), M. Torrell (1), D. Montinaro (2), A. Morata (1), A. Tarancón (1,3)
(1) IREC, Catalonia Institute for Energy Research, Dept of Advanced Materials for Energy Applications
Jardins de les Dones de Negre 1, 08930, Sant Adrià del Besós/Barcelona
(2) SOLIDPower SpA
Viale Trento 117, 38017 Mezzolombardo/Italy
(3) ICREA
Passeig Lluís Companys 23, 08010 Barcelona/Spain

Contact authors: www.EFCF.com/ContactRequest

Abstract

Gadolinium-doped ceria (CGO) barrier layer placed between yttrium-stabilized zirconia (YSZ) electrolyte and strontium-based electrode aims to avoid the formation of insulating phase $SrZrO_3$ during solid oxide fuel cell operation. However, this phase was observed in as-fabricated state-of-the-art cells, which evidences cation inter-diffusion during the sintering process [1]. The use of vacuum techniques such as sputtering and Large Area Pulsed Laser Deposition (LA-PLD) allows the implementation of dense layers at lower temperature compared with traditional deposition techniques (i. e. screen printing). CGO barrier layer deposition and annealing parameters were optimized in a previous work from the group and led to an increase of 70% in power density at 750ºC and 0.7 V compared to a state-of-the-art button cell. Remarkable results were also obtained when the PLD barrier layer was up-scaled to large area cells of 80 cm^2 and tested in short-stack configuration for long-term operation [2].
This short-stack, that includes state-of-the-art cells as well as the large-area PLD ones, was aged for a total of 14,000 h at 750ºC for the first 8,000 h and 700ºC until the end of the experiment. Cells with PLD barrier layer showed enhanced initial performances with a low degradation rate.
This work presents a post-mortem characterization of the barrier layers and interfaces in both types of cells. Scanning-electronic microscope, Electron Probe Micro Analysis with Wavelength Dispersive X-Ray (EPMA-WDX) and micro-Raman spectroscopy were used to observe any microstructural changes as well as any changes in composition due to cation inter-diffusion.

[1] Morales et al., Journal of Power Sources 344 (2017) 141-151.
[2] Morales et al. ACS Applied Energy Materials 1 (2018) 1955-1964.

https://doi.org/10.5281/zenodo.4561854

Introduction

Many SOFCs are now using the mixed ionic−electronic conductor $La_{1-x}Sr_xCo_{1-y}Fe_yO_3$ (LSCF) as material for the cathode in order to get higher performance and to avoid typical problems of delamination when using $La_{1-x}Sr_xMoO_3$ (LSM) [1]. However, insulating phases such as strontium zirconate ($SrZrO_3$) and lanthanum zirconate ($La_2Zr_2O_7$) are formed when LSCF is in contact with state-of-the-art (SoA) yttria-stabilized zirconia (YSZ) electrolyte [2]. Secondary phases with low conductivity like Co_3O_4, $Co_2Fe_2O_4$, or $La_{0.6}Sr_{0.4-x}FeO_3$ can also be favoured at regions where Sr diffused and got expelled from the LSCF structure [3,4]. To avoid the diffusion of Sr and Zr from the cathode and the electrolyte, respectively, and so the formation of insulating phases, a barrier layer made of CeO_2 doped with Gd, Sm or Y is placed between the two layers [5]. SoA barrier layers are usually made by screen-printing and densified at high sintering temperatures (≥ 1,200 ºC), which consequently activates inter-diffusion processes between ceria and YSZ and leads to the formation of solid solutions, dopant migration and even Kirkendall voids [6,7].

Alternative deposition techniques to avoid reaching such high temperatures are vacuum deposition methods able to fabricate dense and thin layers between room temperature and 1,000 ºC [8-12]. Especially, pulsed laser deposition (PLD) has been used to produce thin and dense CGO barrier layers (0.6-2 µm) but did not prevent the formation of $SrZrO_3$ at the YSZ/CGO interface despite the fabrication at low temperature [13,14,4]. It appears that there are fast diffusion pathways along the columnar grain boundaries due to the epitaxial growth of the barrier layer. Barrier layer annealing was conducted to reduce the number of grain boundaries but did not fully blocked the $SrZrO_3$ formation at the CGO/LSFC interface under polarization at high operation temperatures (900-1,000 ºC) [4].

Optimization of the sintering temperature of a CGO barrier layer deposited at low temperature (600 ºC) by PLD had been studied in a previous work of this group [15]. Sr and Zr inter-diffusion was limited applying a sintering temperature of 1,150 ºC. This low sintering temperature also allowed minimizing the loss of Gd dopant from the CGO. Moreover, button cells with PLD barrier layer presented performances above 70 % compared to SoA cells made with screen-printed barrier layer. Those excellent results led to the fabrication of large-area cells of ~80 cm^2 with PLD CGO barrier layer and their electrochemical characterization in a stack together with SoA cells, tested in realistic conditions for long-term operation. After 6,500 h of real operation, the large-area cells with PLD barrier layer still presented higher performance and a degradation profile similar to the SoA large-area cells.

In this work, we made a post-operation analysis of the PLD barrier layer from the aforementioned large-area cells after extending the long-term test up to 14,000 h of operation. The effect of the long-term operation on the PLD barrier layer efficacy to limit the cation inter-diffusion at the LSCF/CGO/YSZ interfaces had been investigated by combining different analytical techniques such as Secondary Electron Microscopy, Electron Probe Micro Analysis with Wavelength Dispersive X-Ray (EPMA-WDX) and micro-Raman spectroscopy.

Experiments

Three anode-supported large-area cells were fabricated with standard techniques except for the barrier layer. Ni-YSZ cermet of 250 µm and YSZ electrolyte were manufactured by aqueous tape-casting and co-sintered above 1,400 ºC. A dense CGO barrier layer of 2 µm

was deposited on top of the dense electrolyte by PLD technique at 600 ºC, using a PVD5000 system (PVD Products). An annealing process was then realized at 1,150 ºC. This temperature was optimized in a previous work in order to avoid the migration of Zr through the layer as well as limit the loss of Gd dopant and limit the diffusion of Sr during the cathode sintering step [15]. Finally, the LSFC-CGO composite cathode was deposited on top of the barrier layer by screen-printing and sintered, defining an active area of 80 cm^2.
Those large-area cells were electrochemically tested for 14,000 h in a stack made with 33 repeating units grouped in 11 clusters of cells with identical design and composition. Ferritic stainless steel cassette coated by ceramic protected coating to prevent Cr evaporation were used as interconnectors. A glass ceramic seal ensured the gas tightness between the anode and cathode chambers. Durability test was carried out by reproducing realistic operating conditions, which consisted in feeding the stack with natural gas partially steam reformed at a current density of 0.4 $A \cdot cm^{-2}$, corresponding to 80 % of fuel utilization. Air was sent at the cathode. The operating temperature was set to 750 ºC for 10,000 h (corresponding to 8,000 h of real operation) and then lowered to 700 ºC until the end of the test. The operating temperature was self-sustained by the exothermic reactions occurring in the stack while the testing bench was not equipped with resistances to maintain a constant temperature. More details can be found in previous works [16-18].

Post-mortem analysis of the large-area cells and especially of the PLD barrier layer was performed by a complementary characterization of the cell cross-section by Scanning Electron Microscopy (SEM), Electron Probe Micro Analysis with Wavelength Dispersive X-Ray (EPMA-WDX) and Confocal Laser Raman Spectroscopy. Cross-section microstructure was examined by a Zeiss Auriga SEM. Elemental analysis was performed with a JEOL JXA-8230 Scanning Electron Microscope (SEM) equipped with an EPMA-WDX instead of an Energy Dispersive X-Ray analyzer due to an overlap of the emission lines for the Lα-series in the characteristic X-ray spectra of Sr and Zr. The spatial distributions of Ce, Gd, Zr, Y and Sr elements were determined by EPMA-WDX line scans over YSZ/CGO/LSCF-CGO interfaces in order to evaluate their chemical reaction behavior. The spatial resolution of this equipment was equal to 0.5 µm. Raman spectra were recorded on the LSCF/CGO/YSZ cross section using a high resolution, confocal Spectrometer HR800 (LabRAM Series, Horiba Jobin Yvon). An excitation line of 532 nm and a 100× objective were employed. The laser spot size was equal to 0.5 µm. Spectra were recorded each 0.5 µm along a line across the area YSZ/CGO/LSCF-CGO.

Results

Figure 1 presents the average voltage evolution with time of the cluster composed by three large-area cells with the PLD barrier layer, included in a stack operated with natural gas partially steam reformed at 0.4 $A \cdot cm^{-2}$ and 80 % of fuel utilization. An initial voltage drop is observed during the first 500 h that is usually ascribed to particle coarsening and microstructure stabilization. The evolution of the voltage is then quite stable despite the thermal cycles operated for maintenance and/or improved thermal insulation (corresponding to the missing points). Before decreasing the temperature, after 10,200 h at 750 ºC, the average degradation rate for the three large-area cells was equal to 0.47 $\%\cdot kh^{-1}$ from the beginning and 0.24 $\%\cdot kh^{-1}$ when removing the initial stabilization phase. Once the temperature was decreased to 700 ºC, no more degradation was observed. It is worth mentioning that the clusters of SoA cells followed similar degradation profile even if they had lower performance (around 4 %) all over the test.

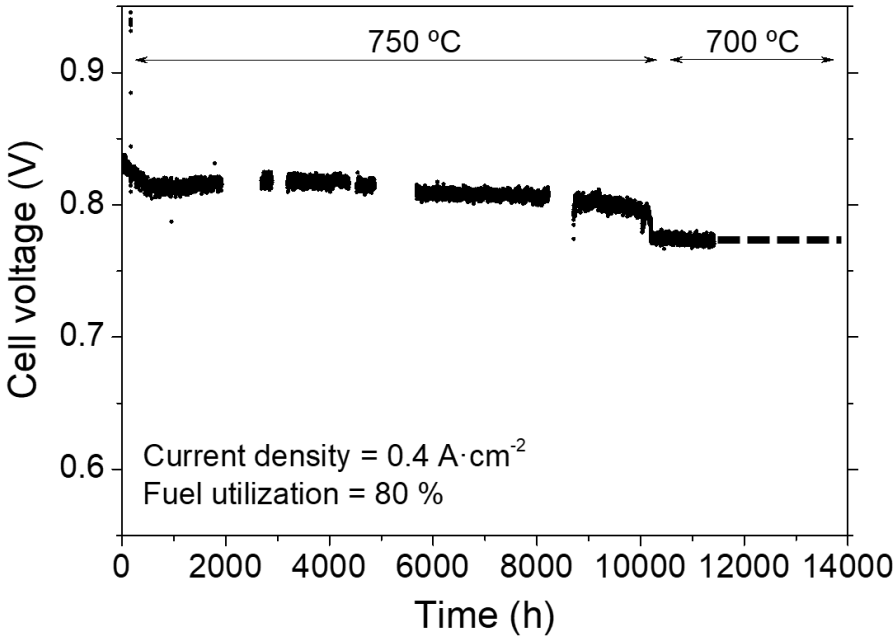

Figure 1. Average degradation curve of a three cells cluster, made with PLD CGO barrier layers, aged in a stack fuelled with natural gas partially steam reformed at the anode and air at the cathode.

Figure 2 shows the microstructure of the different layers of the large-area cells. One can see that after 14,000 h of operation, no obvious microstructural changes can be observed. There is still a good attachment of the cathode and the anode onto the barrier layer and the electrolyte respectively (**Figure 2a-c**). The dense barrier layer deposited by PLD is also perfectly attached to the electrolyte (**Figure 2a,b,d**). Moreover, the electrolyte does not present any visible cracks. However, it seems that some porous of the electrolyte, usually considered as closed porosity, look bigger than before operation and are connected between each other. Bigger porosity is also observed at the interlayer anode/electrolyte that could result from a migration of the Ni as well as the Zr (**Figure 2a,c**). Finally, **Figure 2d** shows the presence of tiny porosity in some localized parts of the CGO barrier layer.

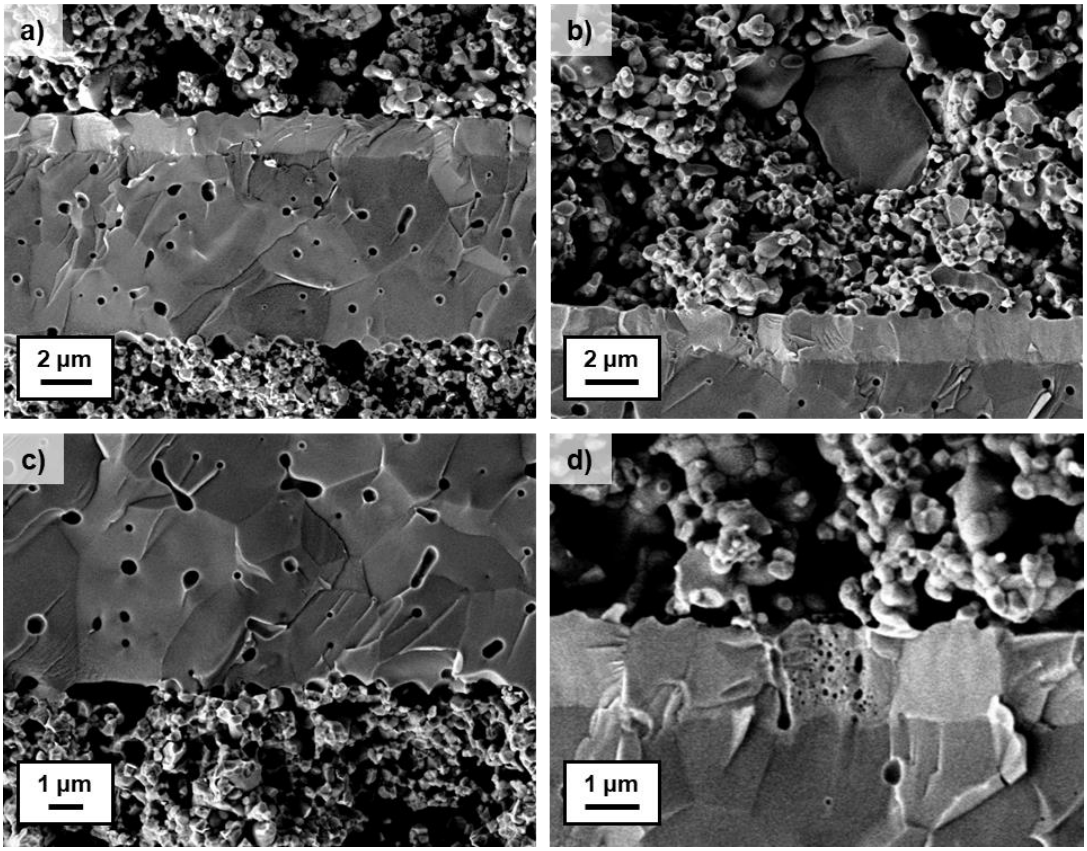

Figure 2. Cross-section SEM of the large-area cell with PLD CGO barrier layer aged for 14,000 h centered on a) the electrolyte, b) the interlayer electrolyte/PLD barrier layer/cathode, c) the interlayer anode/electrolyte and d) the PLD barrier layer.

Figure 3 presents the spatial distribution of the elements around the YSZ/CGO/LSCF-CGO area obtained by EPMA-WDX in order to verify if the PLD barrier layer played its role by blocking the inter-diffusion of Sr and Zr. The elements with high concentration (Ce, Zr) were plotted on one graph while the ones with lower concentration (Gd, Y and Sr) were gathered in a second one. The grey scale of the picture is also reported to identify better the transition between the different layers. The brightest part corresponds to the barrier layer while the darkest part can be attributed to a pore inside the cathode. First of all, the profile of Ce and Zr at the interlayer electrolyte/barrier layer shows an inter-diffusion of those species over 1 µm. The same profile is observed for the Y and Gd. This inter-diffusion was already observed on non-aged cells and ascribed to high temperature sintering steps of the cell manufacturing [15]. Then, a low and constant amount of Gd is detected along the electrolyte. A complementary study would be necessary to determine if it is a proper loss of dopant from the barrier layer and what would be the impact on its behavior. Moreover, a tiny bump is detected in the signal of Sr inside the PLD barrier layer close to the interface YSZ/CGO. As Zr is also detected at the same place, a small quantity of $SrZrO_3$ might have been formed there. A small amount of Zr was also detected close to the barrier layer/cathode interface, which can indicate the presence of the insulating phase $SrZrO_3$.

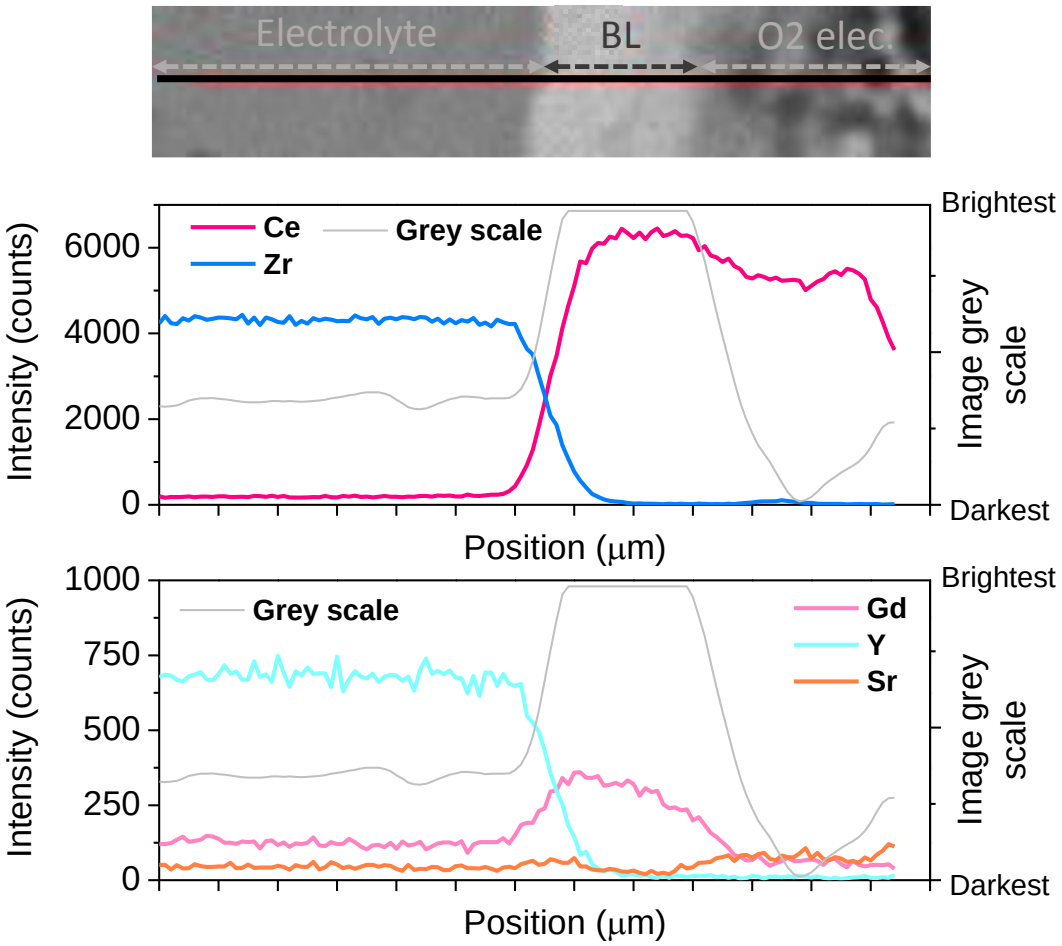

Figure 3. WDX line scan at the interlayer YSZ/CGO/LSCF-CGO.

Raman analysis around the PLD barrier layer is presented **Figure 4** to assess the possible loss of dopant and the formation of insulating secondary phases. The most intense peak detected at ~460 cm^{-1} inside the cathode can be assigned to the main peak of cubic CGO [19]. This peak shifts to ~465 cm^{-1} when reaching the barrier layer and the first microns of the electrolyte. This value can correspond to pure CeO_2, which would evidence a loss of Gd as dopant of the CGO compound [6,20]. Regarding the results obtained by WDX, a complete loss of Gd does not seem to have happened, however the detection of Gd inside the electrolyte is consistent with the results obtained by Raman. Moreover, a peak at ~555 cm^{-1} is detected together with a small peak at ~695 cm^{-1} inside the barrier layer and the electrolyte. The nature of the corresponding phase is not clear. It can be assigned to the insulating phase $SrZrO_3$ that presents characteristic peaks at those values but some other intense peaks at 160 and 413 cm^{-1} are missing. Further investigation is necessary to clearly evidence the formation of $SrZrO_3$ during the operation of those cells made with a dense barrier layer deposited by PLD.

https://doi.org/10.5281/zenodo.4561854

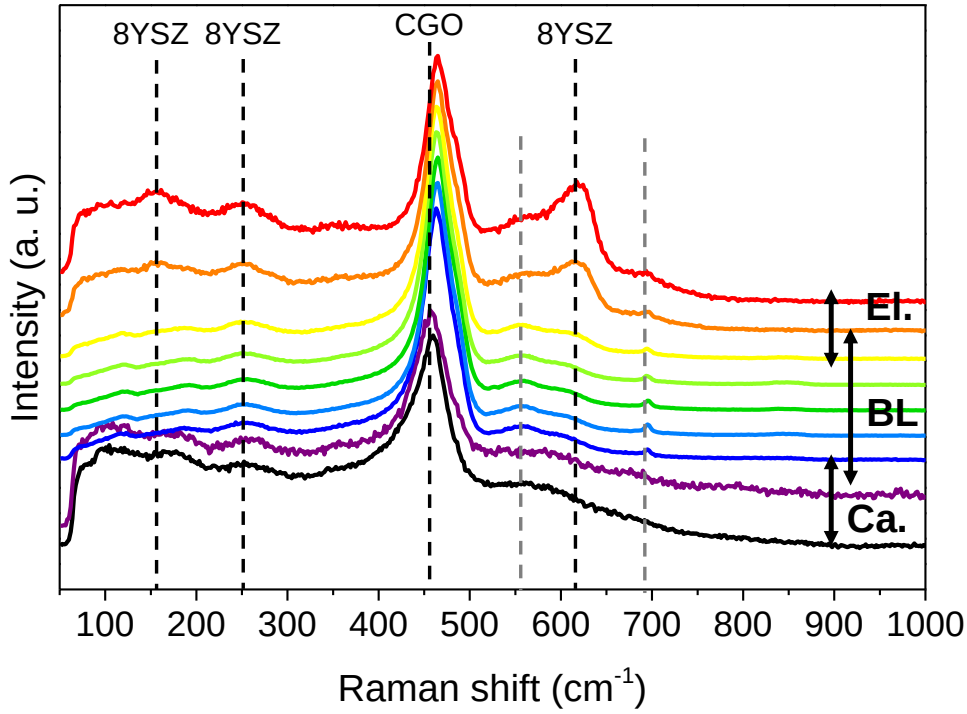

Figure 4. Raman microprobe spectra measured on a cell cross-section, every 0.5 µm at the interlayer YSZ/CGO/LSCF-CGO.

Conclusions

In the present study, large-area cells with a CGO barrier layer deposited by PLD at low temperature and operated in a stack with realistic operating conditions were aged for 14,000 h in SOFC mode and then microstructurally characterized. Low degradation rates were observed all along the degradation profile, despite the decrease of the voltage due to a typical stabilization phase for the first 500 h and various thermal cycles due to maintenance and thermal optimization of the test bench. Post-mortem analysis, made by SEM, EPMA-WDX and Raman, were focused around the interlayer YSZ/CGO/LSCF-CGO. Main microstructure changes could not be evidenced by SEM. The barrier layer was perfectly attached to the electrolyte but small porosity was observed within localized spots of the layer. WDX results showed a small quantity of Sr at the electrolyte/barrier layer interface as well as some traces of Zr inside the oxygen electrode. Moreover, Gd was detected inside the electrolyte, which would correspond to a loss of dopant from the CGO layer. This result is aligned with the observation made by Raman spectroscopy where the main peak of CGO was shifted to higher wavelengths inside the barrier layer and first microns of the electrolyte, corresponding to a loss of dopant of the ceria. Regarding the inter-diffusion of Sr and Zr, two peaks appeared inside the YSZ and CGO that might be characteristic of the $SrZrO_3$. However, part of the main peaks related to $SrZrO_3$ are missing, which makes necessary complementary analysis to confirm the formation of the insulating phases and the loss of Gd during the long-term operation.

https://doi.org/10.5281/zenodo.4561854

Bibliography

[1] Mahato N, Banerjee A, Gupta A, Omar S, Balani K. Progress in material selection for solid oxide fuel cell technology: A review. Prog Mater Sci 2015;72:141–337.
[2] Kostogloudis, G. Ch.; Tsiniarakis, G.; Ftikos, Ch. Chemical reactivity of perovskite oxide SOFC cathodes and yttria stabilized zirconia. Solid State Ionics 2000, 135, 529−535.
[3] Laurencin, J.; Hubert, M.; Ferreira Sanchez, D.; Pylypko, S.; Morales, M.; Morata, A.; Morel, B.; Montinaro, D.; Lefebvre-Joud, F.; Siebert, E. Degradation Mechanism of $La_{0.6}Sr_{0.4}Co_{0.2}Fe_{0.8}O_{3-\delta}/Gd_{0.1}Ce_{0.9}O_{2-\delta}$ Composite Electrode Operated Under Solid Oxide Electrolysis and Fuel Cell Conditions. Electrochim. Acta, 2017, 241, 459-476.
[4] Wang, F.; Brito, M. E.; Yamaji, K.; Cho, D. H.; Nishi, M.; Kishimoto, H.; Horita, T.; Yokokawa, H. Effect of Polarization on Sr and Zr diffusion Behavior in LSCF/GDC/YSZ System. Solid State Ionics 2014, 262, 454-459.
[5] Eguchi, K.; Setoguchi, T.; Inoue, T.; Arai, H. Electrical properties of Ceria-Based Oxides and their Application to Solid Oxide Fuel Cells. Solid State Ionics 1992, 52, 165-172.
[6] Morales, M.; Miguel-Pérez, V.; Tarancón, A.; Slodczyk, A.; Torrell, M.; Ballesteros, B.; Ouweltjes, J. P.; Bassat, J. M.; Montinaro, D.; Morata, A. Multi-scale analysis of the Diffusion Barrier Layer of Gadolinia-Doped Ceria in a Solid Oxide Fuel Cell Operated in a Stack for 3000 h. J. Power Sources 2017, 344, 141-151.
[7] Martínez-Amesti, A.; Larrañaga, A.; Rodríguez-Martínez, L. M.; Nó, M. L.; Pizarro, J. L.; Laresgoiti, A.; Arriortua, M. I. Chemical Compatibility Between YSZ and SDC Sintered at Different Atmospheres for SOFC Applications. J. Power Sources 2009, 192, 151-157.
[8] Chrisey, D.; Hubler, G. Pulsed Laser Deposition of Thin Films. John Wiley & Sons, Inc., 1994.
[9] Smith, D. L. Thin-Film Deposition: Principles & Practice, McGraw-Hill Professional, 1995, ISBN 0–07-058502-4.
[10] Hong, Y. S.; Kim, S. H.; Kim, W. J.; Yoon, H.; Curr, H. Fabrication and Characterization GDC Electrolyte Thin films By E-Beam Technique for IT-SOFC. Appl. Phys. 2011, 11, S163-S168.
[11] Jordan, N.; Assenmacher, W.; Uhlenbruck, S.; Haanappel, V. A. C.; Buchkremer, H. P.; Stöver, D.; Mader W. $Ce_{0.8}Gd_{0.2}O_{2-\delta}$ Protecting Layers Manufactured by Physical Vapor Deposition for IT-SOFC. Solid State Ionics 2008, 179, 919–923.
[12] Schuegraf, K. K. Handbook of Thin Film Deposition Processes and Techniques (Materials and Processing Technology), William Andrew, 2002.
[13] Knibbe, R.; Hjelm, J.; Menon, M.; Pryds, N.; Søgaard, M.; Wang, H. J.; Neufeld, K. Cathode-Electrolyte Interfaces with CGO Barrier Layers in SOFC. J. Am. Ceram. Soc. 2010, 93(9), 2877-2883.
[14] Nurk, G.; Vestli, M.; Möller, P.; Jaaniso, R.; Kodu, M.; Mändar, H.; Romann, T.; Kanarbik, R.; Lusta, E. Mobility of Sr in Gadolinia Doped Ceria Barrier Layers Prepared Using Spray Pyrolysis, Pulsed Laser Deposition and Magnetron Sputtering Methods. J. Electrochem. Soc. 2016, 163, F88-F96.
[15] Morales M, Pesce A, Slodczyk A, Torrell M, Piccardo P, Montinaro D, et al. Enhanced Performance of Gadolinia-Doped Ceria Diffusion Barrier Layers Fabricated by Pulsed Laser Deposition for Large-Area Solid Oxide Fuel Cells. ACS Appl Energy Mater 2018;1:1955–64.
[16] Alyousef, Y.; Alenazey, F.; Montinaro, D.; Modena, S.; Bertoldi, M.; Diethelm, S.; Wuillemin, Z. High Performing SOFC stacks for SOFC and SOEC Applications. EFC 2013 - Proceedings of the 5th European Fuel Cell Piero Lunghi Conference 2013, 361-362.

[17] Alenazey, F.; Alyousef, Y.; Brancaccio, E.; Montinaro, D. Parameters Affecting CO_2 Production in a Planar Anode Supported SOFC Based System. Int. J. Hydrogen Energy 2015, 40(1), 642–651.
[18] Alenazey, F.; Alyousef, Y.; Almisned, O.; Almutairi, G.; Ghouse, M.; Montinaro, D.; Ghigliazza, F. Production of Synthesis Gas (H_2 and CO) by High-Temperature Co-Electrolysis of H_2O and CO_2. Int. J. Hydrogen Energy 2015, 40(32), 10274–10280.
[19] McBride, J. R.; Hass, K. C.; Poindexter, B. D.; Weber, W. H. Raman and X-Ray Studies of $Ce_{1-x}RE_xO_{2-y}$, where RE = La, Pr, Nd, Eu, Gd, and Tb. J. Appl. Phys. 1994, 76 (4), 2435−3244.
[20] Tompsett, G. A.; Sammes, N. M.; Yamamoto, O. Ceria-Yttria-Stabilized Zirconia Composite Ceramic Systems for Applications as Low-Temperature Electrolytes. J. Am. Ceram. Soc. 1997, 80, 3181-3186.

Keywords: EFCF2020, SOx
Session B15: Lifetime: Cells, components and interfaces

https://doi.org/10.5281/zenodo.4561854

B1511

Effect of Strontium Segregation on Electrochemical Impedance Spectra for $La_{0.6}Sr_{0.4}Co_{0.2}Fe_{0.8}O_{3-\delta}$ Cathodes

Hirofumi Sumi (1), Hongqian Wang (2), Scott A. Barnett (2)
(1) National Institute of Advanced Industrial Science and Technology (AIST)
2266-98, Anagahora, Shimo-shidami, Moriyama-ku, 463-8560 Nagoya/Japan
(2) Northwestern University
2220, Campus Drive, Evanston, 60208 Illinois/USA
Contact authors: www.EFCF.com/ContactRequest

Abstract

Microtubular solid oxide fuel cells (SOFCs) with $La_{0.6}Sr_{0.4}Co_{0.2}Fe_{0.8}O_{3-\delta}$ (LSCF) cathodes were aged in ambient air at temperatures ranging from 700 to 1000 °C for up to 700 h. The amount of segregated Sr, present both on LSCF surfaces and in Sr-rich particles, increased with increasing aging temperature. Distribution of relaxation times (DRT) analysis of electrochemical impedance spectroscopy (EIS) measurements indicated an increase in the cathode resistance with increasing aging temperature up to 900 °C. Analysis of microstructural data, which were collected with focused ion beam-scanning electron microscopy (FIB-SEM) 3D tomography, and the EIS data using the Alder-Lane-Steele (ALS) model indicates that the Sr surface segregation increases cathode resistance via a decreased oxygen surface exchange coefficient.

https://doi.org/10.5281/zenodo.4561880

Introduction

$La_{0.6}Sr_{0.4}Co_{0.2}Fe_{0.8}O_{3-\delta}$ (LSCF) is widely used as a cathode material for solid oxide fuel cells (SOFCs). However, LSCF can be susceptible to degradation by mechanisms including reactions with yttria-stabilized zirconia (YSZ) electrolytes [1], Cr poisoning from steel stack components [2-4], microstructural coarsening [5,6] and Sr surface segregation [7]. Coarsening and sintering of porous electrodes are expected at sufficiently high temperatures, long times, and small particle sizes. However, it is difficult to predict whether a given electrode will be susceptible to coarsening/sintering because of the strong dependence of coarsening rate on initial feature size. For example, coarsening of initially ~ 50-nm-diameter infiltrated LSCF to > 100 nm after aging for ~ 1000 h at ≥ 700 °C has been shown to measurably increase polarization resistance [5,6]. On the other hand, no coarsening was observed for LSCF with larger feature sizes of ~300 nm particle size aged for ~ 1000 h at up to 800 °C [7] or for LSCF with 550 nm feature size aged for 1000 h at 600 – 900 °C [8]. In the latter study, an increase in polarization resistance was observed after aging at 600 and 750 °C, despite no change in microstructure [8]; this may have been due to Sr segregation, which was not tested in that study.

Here, we present results on LSCF cathodes on microtubular SOFCs with aging at 700 – 1000 °C for up to 700 h. The cells utilize $Ce_{0.9}Gd_{0.1}O_{1.95}$ (GDC) electrolytes, so there is no issue with LSCF/YSZ reactions. Silver paste and wire were used as current collectors in order to avoid Cr poisoning and thereby focus on the effects of coarsening/sintering and Sr segregation with focused ion beam-scanning electron microscopy (FIB-SEM) 3D tomography. Electrochemical Impedance Spectroscopy (EIS) data taken before and after aging under various conditions is analyzed using distribution of relaxation times (DRT) methods to isolate the cathode polarization resistance.

1. Experiments

Anode microtubes were composed of 60 wt.% NiO (Sumitomo Metal Mining)-40 wt.% GDC (Anan Kasei). The anode microtubes were extruded with pore former (acrylic resin with 5 μm in grain size; Sekisui Plastic) and binder (Cellulose; Yuken Kogyo) powders. The GDC electrolyte was formed by dip-coating using a slurry with a binder (polyvinyl butyral; Sekisui Chemical), a dispersant (tallow propylene diamine; Kao) and a plasticizer (dioctyl adipate; Wako Pure Chemical Industries) in ethanol and toluene solvents. The GDC thin-film electrolyte (5 μm in thickness) and NiO anode microtube (200 μm) were co-sintered in air for 3 h at 1450 °C. Then, the LSCF (Kusaka Rare Metal) thin-film cathode (20 μm) was coated and sintered in air for 1 h at 1050 °C. The outside diameter of microtube was 1.8 mm, and the cathode length was 10 mm after sintering. The microtubular cells were aged at 700, 800, 900 and 1000 °C in a tube furnace exposed to ambient air. Two aging times, 300 and 700 h, were used at each temperature. An as-prepared cell was used as a reference “control” sample, for comparison with the aged cells.

In preparation for 3D tomography, the pores within the LSCF cathodes were infiltrated with a low-viscosity epoxy prior to the observation. The serial sectioning and imaging were carried out using a FEI Helios system with 2 kV electron beam energy and backscattered electron (BSE) detector. The image resolution was 15 × 15 nm and the spacing between images was 30 nm. The imaged area was located close to the cathode/electrolyte interface and the milling direction was perpendicular to the tube axis. For Sr surface segregation measurements, the cell fragments were separately stirred in ultrapure H_2O for 10 min after cutting with a diamond saw. Subsequently, the samples were transferred into a 12 $mol \cdot L^{-1}$ HCl solution and stirred until the cathodes were completely dissolved. The tubes with ultrapure H_2O solution were then centrifuged and

only the upper part of the solution was used, in order to eliminate any loose particles. The ultrapure H_2O and the concentrated HCl solutions were mixed with the appropriate amounts of H_2O/HCl/HNO_3 to yield 0.36 mol·L^{-1} HCl/0.72 mol·L^{-1} HNO_3 solutions for inductivity coupled plasma-optical emission spectrometer (ICP-OES) analysis.

EIS measurement was performed with a potentiostat/galvanostat and an impedance analyzer (Bio-Logic Science Instruments VSP) at open circuit voltage (OCV) in the frequency range from 1 MHz to 0.1 Hz with 20 steps per logarithmic decade. The operating temperature was 550 °C. A mixture of H_2 : H_2O : N_2 = 20 : 3 : 77 was supplied as fuel at a flow rate of 100 mL/min to the anode side, and a mixture of O_2 : N_2 = 21 : 79 was supplied as oxidant at 100 mL/min to the cathode side. DRT analysis was done as described in Refs. [9-12]. The software package FTIKREG [13] was used to solve an ill-posed inverse problem in DRT analysis by Tikhonov regularization.

2. Results and Discussion

Figure 1 presents 2D FIB-SEM cross-sectional images from the control and aged LSCF electrodes. Only the 700 h aged samples are shown here, since the 300 h aged samples have similar structure. The lighter contrast particles are identified as LSCF, whereas the darker contrast indicates pore. It can be clearly seen that the LSCF particles of the sample aged at 1000 °C for 700 h have significantly larger size relative to the others, indicating substantial coarsening of LSCF at this temperature. Regions with intermediate grey contrast, indicated by white arrows, are apparent in the 800C-700h and 900C-700h images, suggesting that another phase is present. These are not seen in the 700C-700h image. EDS element mapping, conducted on the area indicated in Fig. 1 (d) and shown in Fig. 1 (f), shows that the third phase contains primarily Sr.

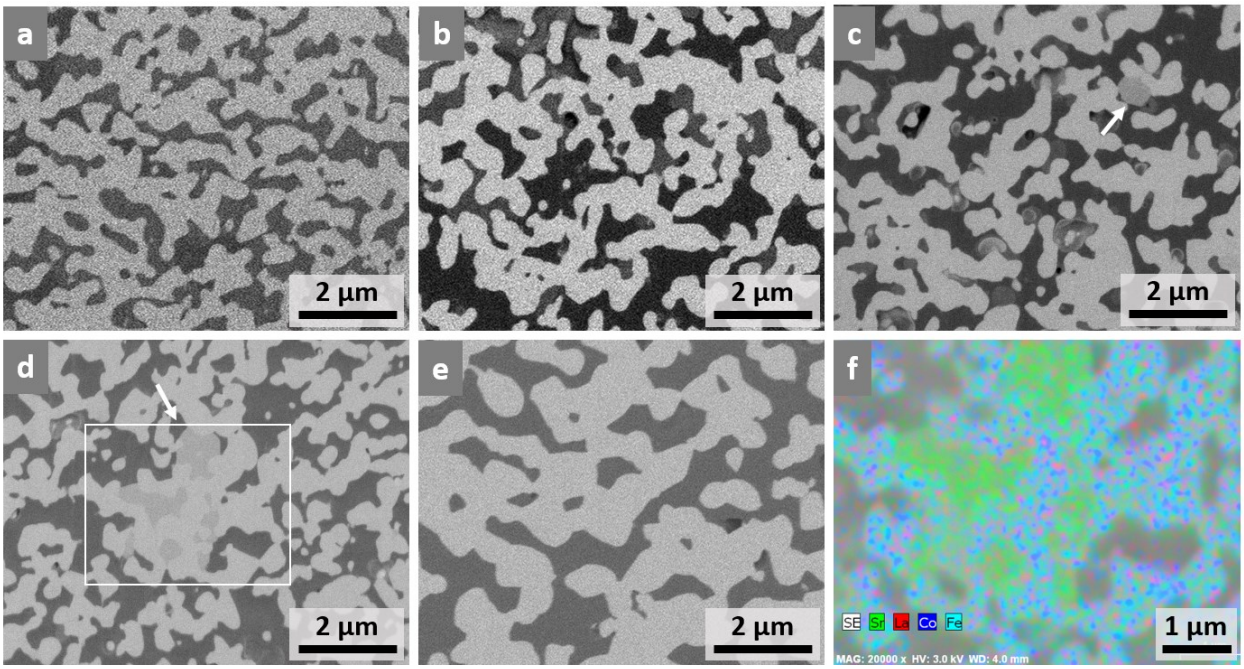

Fig. 1 SEM images of the (a) control, (b) 700C-700h, (c) 800C-700h, (d) 900C-700h and (e) 1000C-700h aged LSCF electrodes. (f) EDS element mapping of the boxed area shown in (d).

The macrohomogeneous microstructural parameters obtained from the 3D image data are summarized and plotted in Fig. 2. The porosity varied between 36 and 43% for all cathodes; while this variation is slightly greater than the 5% accuracy, it is difficult to establish any meaningful trend. Tortuosity values followed the trend expected, i.e., decreasing with increasing phase volume fraction. Thus, tortuosity was lower, ~ 1.1, for LSCF (~ 60 % volume fraction) compared to ~ 1.2 for the pore phase (~ 40 % volume fraction). The LSCF specific surface area decreased by > 30 % for 1000C-300h and 1000C-700h samples, respectively, indicating LSCF coarsening likely occurred under these aging conditions. Although there appears to also be smaller decreases in specific surface area with increasing aging temperature below 1000 °C, at least for the 700 h case, it is difficult to be sure of this trend given experimental errors. LSCF particles grew measurably only after aging at the highest temperature, 1000 °C, and further increased in size with increasing aging time from 300 to 700 h. The 900C-700h sample did not show change in average particle size relative to the control sample, but had slightly increased volume fraction at ~ 1150 nm. Again, these large particles are likely due to treating Sr-rich phase as LSCF particles during segmentation. Based on the above results, it can be concluded that the LSCF did not coarsen significantly at ≤ 900 °C, consistent with the surface area results in Fig. 2.

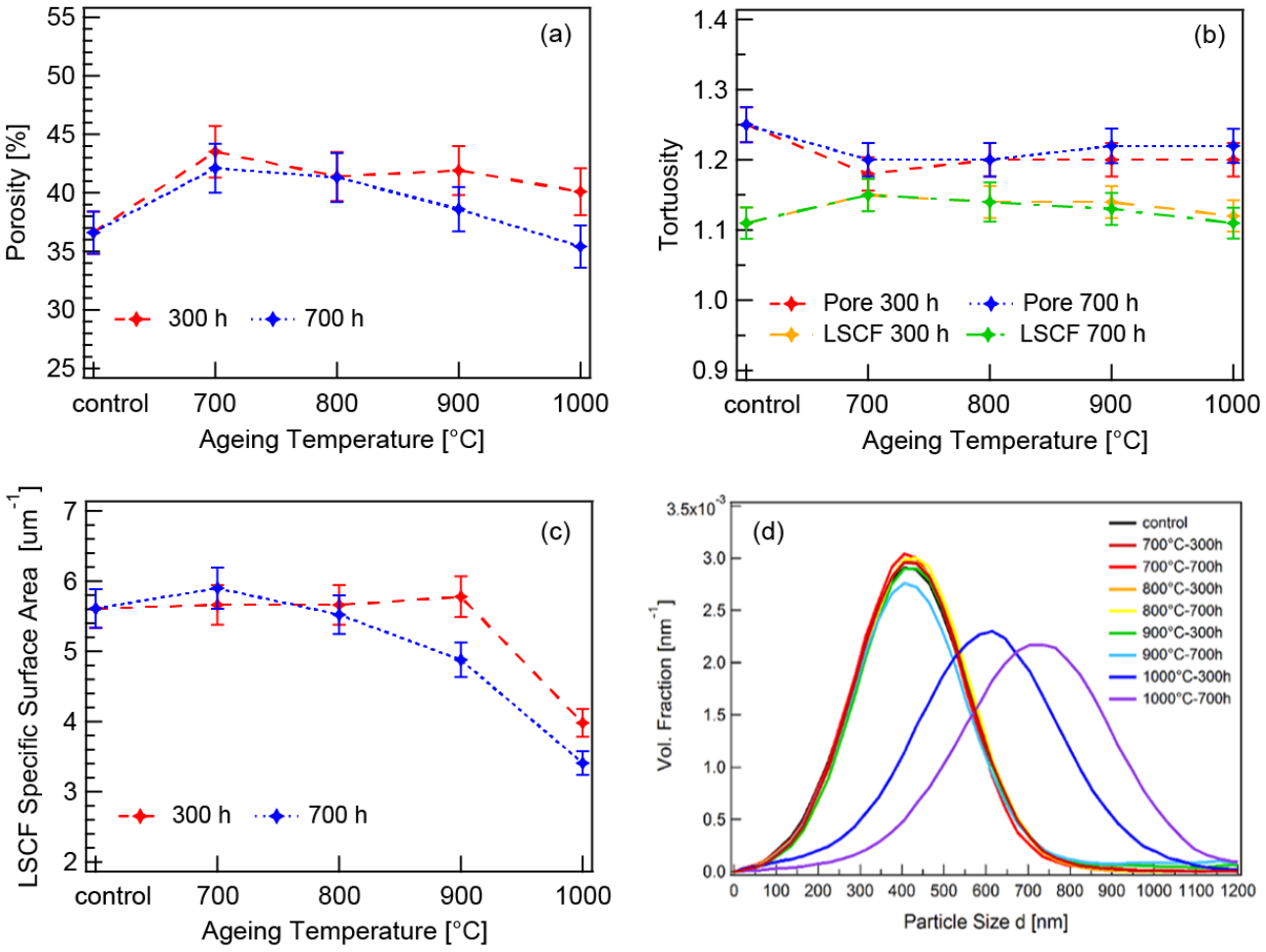

Fig. 2 (a) Porosity, (b) pore and LSCF phase tortuosity, (c) LSCF specific surface area, versus temperature for cells aged for 300 and 700h, and (d) LSCF particle size distributions determined from measured 3D structural data.

Figure 3 (a) shows the amount of Sr dissolved in ultrapure water for the control and aged cells, detected by ICP-OES, normalized to the measured electrode volume. Previous results show that only Sr-rich surface layers or phases are water-soluble, while the bulk LSCF is insoluble in water [7], so the detected Sr amount can be used as a measure of the total amount of surface segregated Sr and the Sr-rich phase. The amount of Sr increased with increasing aging time and temperature up to 900 °C, from 0.28 ± 0.03 × 10^5 nmol/cm^3 for the control sample to 1.28 ± 0.17 × 10^5 nmol/cm^3 for the 900C-700h sample. However, increasing the aging temperature from 900 to 1000 °C resulted in much smaller surface Sr amount, 0.45 ± 0.02 × 10^5 nmol/cm^3 for the 300 h sample and 0.52 ± 0.02 × 10^5 nmol/cm^3 for the 700 h sample. It is plausible that this high aging temperature suppresses the Sr surface segregation, an explanation that is consistent with the low surface Sr amount observed for the control sample, which was fired at 1050 °C. It is estimated that most of the Sr detected was segregated on LSCF surfaces, versus in Sr-rich particles. Using this and assuming that the segregated phase is a dense homogeneous SrO coverage with a (100) orientation, the nominal SrO monolayer (ML) coverage increases from ~ 0.8 ML for the control sample up to ~ 3.5 ML for 900C-700h sample, but decreases to ~ 1.9 ML for 1000C-700h sample (Fig. 3 (b)).

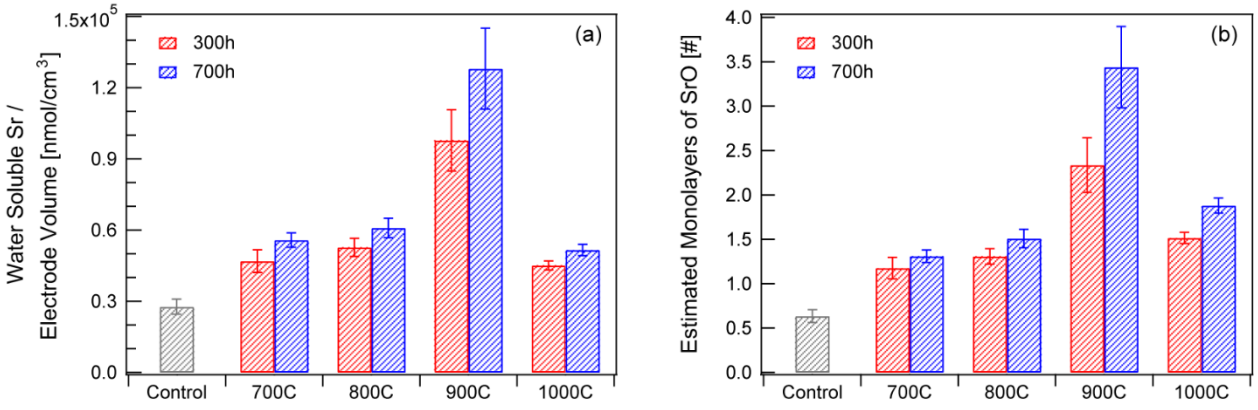

Fig. 3 (a) The amount of Sr dissolved in ultrapure water for the control and aged cells normalized to the measured electrode volume. (b) The corresponding nominal number of SrO monolayers estimated assuming dense homogeneous SrO coverage with a (100) orientation. The error bars were calculated from standard deviation of 3 measurements.

Figure 4 (a) shows the impedance spectra for the control and aged microtubular cells measured between the anode and cathode under OCV at 550 °C. The ohmic loss for the aged samples was slightly larger than that for the control sample. There was a substantial increase in the polarization resistance after aging that increased with increasing aging temperature. DRT analysis was applied to this impedance data to separate each response – the results are shown in Fig. 4 (b). Three large peaks were detected at 0.1 – 100 Hz by the DRT analysis for all samples. The small DRT peak around 1 kHz (P_1^a) was ascribed to the fuel oxidation process on the anode for microtubular cells [11]. On the other hand, we confirmed by another experiment that the DRT peak around 7 Hz (P_1^d) increased with decreasing hydrogen concentration in the anode [11]. This peak is ascribed to gas diffusion process for anode-supported cells. After aging, the DRT peak around 1 Hz (P_2^d) appeared. This peak is also related to gas diffusion with consideration of frequency. Thus, the increase in impedance at ~ 1 Hz is presumably caused by a change in the anode morphology during aging.

The peak around 100 Hz (P_2^c) was ascribed to the oxygen reduction reaction on the LSCF electrode [12]. In this study, we focus on the chemical resistance R_{chem} and time constant t_{chem} of P_2^c. Prior studies in the literature have shown that the impedance of porous mixed-conducting cathodes with fast electronic transport, such as LSCF, is co-

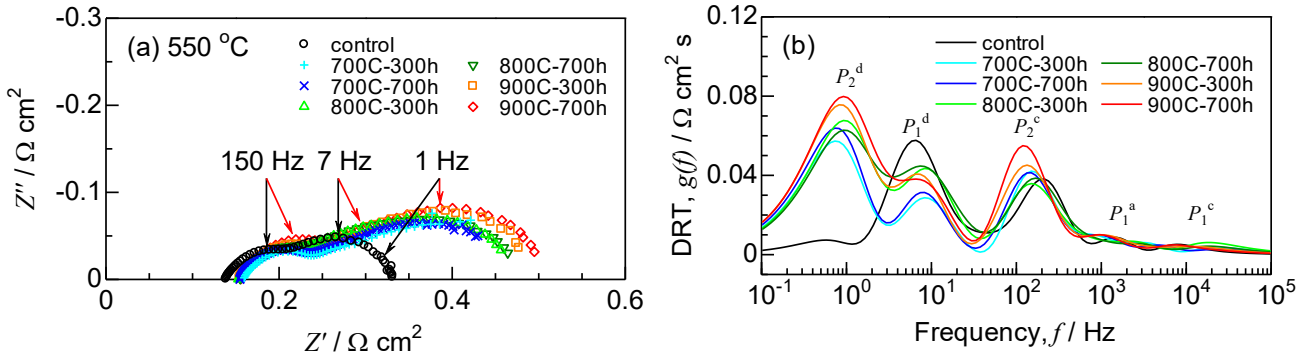

Fig. 4 (a) Impedance and (b) DRT spectra for the control and aged microtubular cells measured between the anode and cathode under OCV at 550 °C.

limited by the oxygen surface exchange and solid-state oxygen ion diffusion processes, and can be expressed as described in [14]:

$$Z_G = \frac{R_{chem}}{\sqrt{1 + j\omega t_{chem}}} \quad (1)$$

where j is the imaginary unit. Figure 5 shows the R_{chem} and t_{chem} of P_2^c derived by fitting as a Gerischer impedance Z_G. Both R_{chem} and t_{chem} increased after aging. The values of R_{chem} for the samples aged at 900 °C were larger than those at 700 and 800 °C, while the values of t_{chem} was independent on the aging temperature from 700 to 900 °C.

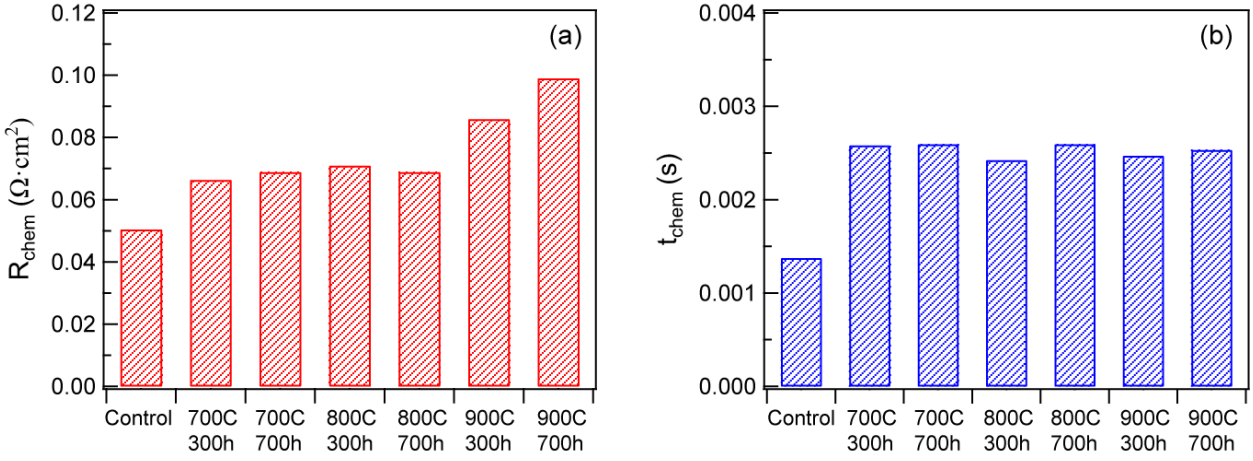

Fig. 5 (a) Chemical resistance R_{chem} and (b) time constant t_{chem} of P_2^c for the control and aged microtubular cells.

Based on the electrochemical and microstructural data, Adler-Lane-Steele (ALS) model was applied to examine the effect of aging on the oxygen reduction reaction [15]. The values of R_{chem} and t_{chem} are related to the microstructural, thermodynamic and kinetic properties of the electrode:

$$R_{\text{chem}} = \frac{RT}{4F^2}\left(\frac{\tau A_0^{\,2}}{4a(1-\varepsilon)k_{\text{chem}}D_{\text{chem}}c^2\chi}\right)^{1/2}(p_{O_2})^{-1/4} \quad (2)$$

$$t_{\text{chem}} = \frac{(1-\varepsilon)\chi}{4a\,k_{\text{chem}}}(p_{O_2})^{-1/2} \quad (3)$$

where porosity ε, LSCF tortuosity τ, and specific surface area a are given in Fig. 2. The oxygen lattice site concentration c, oxygen vacancy fraction χ, and thermodynamic enhancement factor A_0 for this LSCF composition at operating temperature of 550 °C are found in the literature to be 0.083 mol/cm^3, 0.0037, and 1.11, respectively [16-18]. With the values of these parameters known, and R_{chem} and t_{chem} values obtained from the DRT analysis, the oxygen surface exchange coefficient k_{chem} and oxygen diffusion coefficient D_{chem} were obtained, and are shown in Fig. 6. While k_{chem} and D_{chem} are chemical coefficients, prior measurements of LSCF at 550 °C were done by isotope exchange depth profiling (IEDP) coupled with secondary ion mass spectrometry (SIMS), which yields the tracer coefficients k^* = 5.51 × 10^{-8} – 1.40 × 10^{-7} cm/s and D^* = 3.47 × 10^{-11} – 4.58 × 10^{-11} cm^2/s [19,20]. Conversion of these to chemical coefficients using the expressions $k_{\text{chem}} = (A_0 / \chi)\, k^*$ and $D_{\text{chem}} = (A_0 / \chi)\, D^*$ [18] yields k_{chem} = 1.65 × 10^{-5} – 4.19 × 10^{-5} cm/s and D_{chem} = 1.05 × 10^{-8} – 1.38 × 10^{-8} cm^2/s. The present k_{chem} values are in good agreement. The present D_{chem} values are 5 – 10 times lower, possibly due to differences between the dense LSCF samples used in IEDP/SIMS and the present porous LSCF electrodes. The k_{chem} values after aging are substantially lower than for the control sample, indicating that the Sr surface segregation inhibited the oxygen surface exchange. However, there is no clear trend in k_{chem} between 700, 800 and 900 °C aging temperatures. Although increase in Sr surface segregation with temperature and time has been observed by ICP-OES measurement, it cannot be directly associated with the change in k_{chem}, as the measurement cannot distinguish between a uniform coverage of the LSCF surface and Sr-rich 3D islands. The isolated 3D islands, which were observed for samples aged at 800 and 900 °C, are expected to have little impact on k_{chem}. On the other hand, we believe that the variations in D_{chem} between the control sample and those aged at 700-800 °C results from the combined error of the 3D tomography data, the EIS measurement, and the DRT analysis. That is, Sr surface segregation has relatively small impact on the oxygen diffusion process below 900 °C. However, D_{chem} decreases with aging time for samples aged at 900 °C. This might be due to a change in the LSCF composition resulting from Sr surface segregation, giving a slightly increased La/Sr ratio. Comparison with Fig. 5 shows that the R_{chem} increase after aging at 700 – 800 °C was mainly due to the decrease in k_{chem}, whereas the further increase at 900 °C was due to the decrease in D_{chem}.

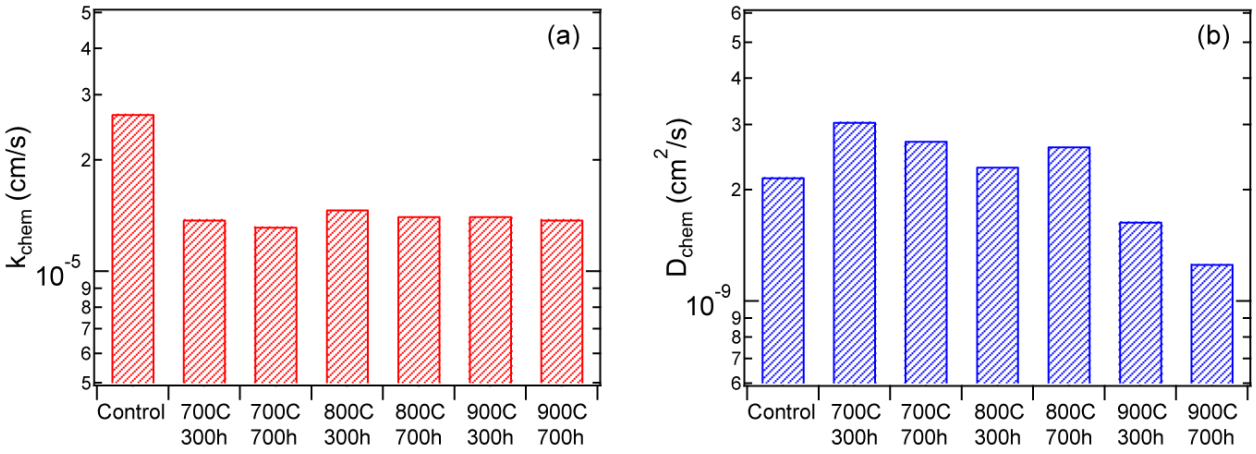

Fig. 6 (a) Surface exchange k_{chem} and (b) oxygen diffusion coefficients D_{chem} for the control and aged microtubular cells.

4. Conclusion

Microtubular SOFCs with LSCF cathodes were aged at elevated temperatures ranging from 700 to 1000 °C, for 300 and 700 h. 3D tomographic measurements done by FIB-SEM serial sectioning indicated that the LSCF surface area did not decrease significantly until aging temperatures were increased above 900 °C. Sr surface segregation, measured by a chemical etching technique, increased with increasing aging temperature up to 900 °C, but decreased with further increase in temperature to 1000 °C. The segregated Sr was present mainly as a thin layer covering LSCF surfaces, with a smaller amount present as Sr-rich particles. EIS measurements with DRT analysis revealed a response associated with co-limiting oxygen surface exchange and oxygen diffusion processes in the LSCF cathode. The chemical resistance and time constant associated with this response increased after aging. The EIS data, analyzed using the ALS model together with measured microstructural data, indicate that aging under any condition decreases the oxygen surface exchange coefficient by a factor of ~ 2, whereas the oxygen diffusion coefficient decreased only for 900 °C aging. Thus, Sr surface segregation appears to be the primary mechanism causing degradation of LSCF electrodes.

Acknowledgement

The work was supported in part by Minister of Economy, Trade and Industry, under the Japan–U.S. Cooperation Project for Research and Standardization of Clean Energy Technologies. The authors at Northwestern gratefully acknowledge financial support from the National Science Foundation under grant Number DMR-1506925. The FIB-SEM tomography data was collected at the Electron Probe Instrumentation Center (EPIC) at the NUANCE Center-Northwestern University, which has received support from the MRSEC program (NSF DMR-1121262) at the Materials Research Center; the International Institute for Nanotechnology (IIN); and the State of Illinois, through the IIN. Special thanks to Dr. Jürgen Fleig and Dr. Ghislain M. Rupp for development of the chemical etching method for measuring Sr surface segregation.

References

[1] Z. Gao, L. V. Mogni, E. C. Miller, J. G. Railsback, S. A. Barnett, Energy Environ. Sci., **9**, 1602-1644 (2016).
[2] K. Huang, P. Y. Hou, J. B. Goodenough, Solid State Ionics, **129**, 237-250 (2000).
[3] K. Hilpert, D. Das, M. Miller, D. H. Peck, R. Weiss, J. Electrochem. Soc., **143**, 3642-3647 (1996).
[4] S. P. Simner, M. D. Anderson, G. G. Xia, Z. Yang, L. R. Pederson, J. W. Stevenson, J. Electrochem. Soc., **152**, A740-A745 (2005).
[5] A. V. Call, J. G. Railsback, H. Wang, S. A. Barnett, Phys. Chem. Chem. Phys., **18**, 13216-13222 (2016).
[6] M. Shah, P. W. Voorhees, S. A. Barnett, Solid State Ionics, **187**, 64-67 (2011).
[7] H. Wang, K. J. Yakal-Kremski, T. Yeh, G. M. Rupp, A. Limbeck, J. Fleig, S. A. Barnett, J. Electrochem. Soc., **163**, F581-F585 (2016).
[8] C. Endler-Schuck, J. Joos, C. Niedrig, A. Weber, E. Ivers-Tiffee, Solid State Ionics, **269**, 67-79 (2015).
[9] H. Schichlein, A. C. Muller, M. Voigts, A. Krugel, E. Ivers-Tiffee, J. Appl. Electrochem., **32**, 875-882 (2002).
[10] A. Leonide, V. Sonn, A. Weber, E. Ivers-Tiffee, J. Electrochem. Soc., **155**, B36-B41 (2008).
[11] H. Sumi, T. Yamaguchi, K. Hamamoto, T. Suzuki, Y. Fujishiro, T. Matsui, K. Eguchi, Electrochim. Acta, **67**, 159-165 (2012).
[12] H. Sumi, T. Yamaguchi, K. Hamamoto, T. Suzuki, Y. Fujishiro, J. Power Sources, **220**, 74-78 (2012).
[13] J. Weese, Comput. Phys. Commun., **69**, 99-111 (1992).
[14] S. B. Adler, Chem. Rev., **104**, 4791-4843 (2004).
[15] S. B. Adler, J. A. Lane, B. C. H. Steele, J. Electrochem. Soc., **143**, 3554-3564 (1996).
[16] Y. Fukuda, S.-i. Hashimoto, K. Sato, K. Yashiro, J. Mizusaki, ECS Trans., **25**, 2375 (2009).
[17] M. Kuhn, Y. Fukuda, S. Hashimoto, K. Sato, K. Yashiro, J. Mizusaki, ECS Trans., **35**, 1881-1890 (2011).
[18] K. Yakal-Kremski, L. V. Mogni, A. Montenegro-Hernandez, A. Caneiro, S. A. Barnett, J. Electrochem. Soc., **161**, F1366-F1374 (2014).
[19] A. Esquirol, J. Kilner, N. Brandon, Solid State Ionics, **175**, 63-67 (2004).
[20] B. C. H. Steele, J. M. Bae, Solid State Ionics, **106**, 255-261 (1998).

Keywords: EFCF2020, SOx
Session B15: Lifetime: Cells, components and interfaces

https://doi.org/10.5281/zenodo.4561880

B1602

Ink-jet printing of Cu-Co-Mn Oxide spinel as protective coating on solid oxide fuel cell interconnects

Samaneh Daviran (1), Manuel Bianco (1), Victor Costa Bassetto (2), Wanderson Oliveira Da Silva (2), Hubert Girault (2), Jan Van Herle (1)
(1) Group of Energy Materials (GEM)
(2) Laboratory of Physical and Analytical Electrochemistry (LEPA)
École Polytechnique Fédérale de Lausanne (EPFL), CH-1951, Sion/Switzerland
Contact authors: www.EFCF.com/ContactRequest

Abstract

In the present study, ink-jet printing was used to deposit layers of Cu-Co-Mn-oxide. The advantage of the technique lies in the flexibility of the coating design, low fabrication cost and the very low amount of wasted material.

Cu-doped $MnCo_2O_4$ spinel nanoparticles were produced in house via the Pechini method. The material was characterized with X-Ray Diffraction (XRD), Scanning Electron Microscopy (SEM), Particle Size Analysis (PSA) and Thermogravimetric Analysis (TGA). The present study focuses on the preparation of a stable, well-dispersed and agglomerate-free particle dispersions that will be subsequently tuned as ink. Ink composition and printing parameters were optimized to obtain high-resolution printing. To assess these properties, stability, viscosity and the surface tension were measured for the ink and droplet interpolation, jetting frequency for the printing process. The printable ink was deposited on an interconnect steel substrate and then cured at 600°C.

https://doi.org/10.5281/zenodo.4561900

Introduction

The degradation of ferritic stainless steel (FSSs) interconnects is one of the main issues in Solid Oxide Fuel Cells (SOFCs). The chromium oxide thermally grown on the steel surface causes ohmic losses and its vapors poison the cathode perovskites.

In order to prevent cathode poisoning, protective coatings are an established solution, with spinel oxides being the most employed materials. Regarding the coating deposition technique there is a choice of methods, with those leading to good performance like PVD being counterbalanced by the deposition cost. Interest in rapid prototyping has increased dramatically in recent years, where Ink-Jet Printing (IJP) in particular is studied for the deposition of thin films. IJP is attracting interests due to its high resolution, low-cost, simplicity, contactless process, feasibility to use for a wide range of materials/substrates, possibility to use for large scales, and low material waste.

Depending on the printing mechanism, an ink-jet printer can be operated in two different modes: continuous ink-jet (CIJ) and drop-on-demand (DOD) printing. The DOD mode is a process in which droplets are jetted only when desired. Thermal and piezoelectric actuations are the two main actuation mechanisms of a DOD inkjet printer [1]. In the piezoelectric process, a voltage pulse is applied to the piezoelectric elements placed on the ink reservoir walls, which creates a mechanical pressure. The pressure squeezes the functional ink through the nozzle generating a droplet [1].

The objective of this study is to use drop-on-demand ink-jet printing to deposit a thin film of Cu-doped $MnCo_2O_4$ spinel on ferritic stainless steel K41 (the SOFC interconnect substrate) as protective coating. The powders were synthesized using the Pechini method [2] and then characterized. The ink formulation and printing process will be subsequently explained in detail. The operating printing parameters were studied: substrate/printhead temperature, drop spacing, jetting waveform, applied voltages to the nozzles, substrate/printhead distance, and number of nozzles to achieve a qualified printing layer.

Material and Experiments

Powder synthesis

The Pechini method was used to synthesize $Mn_{1.4}Co_{1.4}Cu_{0.2}O_4$ nanoparticles. Considering the desired stoichiometry, proper amounts of $Mn(NO_3)_2.4H_2O$, $Co(NO_3)_2.6H_2O$, and $Cu(NO_3)_2.3H_2O$ (all from Sigma Aldrich) were dissolved in a mixture of distilled water and ethylene glycol which was then stirred to a homogenous solution. Citric acid was added during stirring and heating up to 70°C. The solution was finally stirred at 150°C for one hour. In this stage a viscous gel is obtained. The gel was dried at 250°C for 2 hours, and the dried gel calcined at different temperatures (500°C, 550°C, 600°C and 800°C).

Ink preparation

A successful ink-jet printing process is linked to the proper adjustment of (i) the physicochemical properties of the ink (mainly viscosity, surface tension, and solubility/dispersibility of the material to be printed), (ii) printing parameters (e.g., piezoelectric actuation), (iii) ink–substrate interaction (wetting behavior), and (iv) post-processing (to convert the ink after drying into a solid functional material) [3].

https://doi.org/10.5281/zenodo.4561900

A suitable solvent for the ink should meet requirements for the printing. In terms of surface tension, too low surface tension leads to spontaneous ink dripping from the nozzles, while too high values make jetting impossible [4]. The dynamic viscosity affects the shape, size and velocity of the ejected droplets and is a crucial physical parameter of the ink [5]. The printability of an ink can be checked using the inverse of Ohnesorge number (Z) [6], defined as $Z = 1/Oh = \sqrt{\gamma\rho\alpha}/\eta$ where γ, η, ρ, and α are the surface tension, viscosity, density of the ink, and characteristic length (here the nozzle diameter with α =21.5 µm), respectively.

Rapid drying of the solvent is another issue which may also cause blocking of the nozzles [1] or produce a non-uniform layer due to the change in substrate/ink interaction. This phenomenon may be suppressed by using cosolvents that dry relatively slowly [1]. Based on the mentioned points, a mixture of 1,2 propanediol (95%, Sigma Aldrich), isopropanol and water were found to meet the criteria as solvent. Amounts of 4 mg spinel nanoparticles were added to 2 mL solvent and then dispersed with ultrasound for 120 minutes at 60% amplitude with on/off circle of 5s. The prepared ink was then characterized. The viscosity was measured by SV-1 A series viscometer (A&D, Japan) to a value of 5.96 mPas at 25 °C. The surface tension was measured using Drop Shape Analyzer DA30 S (Krüss, Germany), equal to 31.22 $\pm$1 mN·m^{-1}. Then, the Z parameter was obtained as 4.09, which is within the acceptable range of 1<Z<10 [6].

The other bottleneck of ink-jet printing is to avoid nozzle blocking due to particle agglomeration. The size of the particles in an inkjet ink should be at least two orders of magnitude smaller than the diameter of the nozzle orifice in the printhead to prevent clogging and nozzle blockage [7] Roll milling was used to control particle size in order to avoid nozzle clogging during printing.

The stability of the ink is referred to as non-agglomerated and non-sedimented ink. Here, the agglomeration of the ink was checked by Dynamic Light Scattering (DLS), (model: ZetaSizer Nano ZS, Malvern, UK), in which the particle size was measured after certain elapsed times. The DLS measurement of the ink showed the same distribution at different standing times up to 30 hours, which indicates no detectable agglomeration of the particles. Although the 30 hours of stability was proper for printing, while polyvinyl pyrrolidone (PVP; MW 10′000, Sigma-Aldrich) additive was used to improve ink stability for long-term usage.

Printing

In piezoelectric drop on-demand (DOD) inkjet printing, a pulsed voltage is applied to the piezoelectric actuator which causes piezoelectric crystal deformation; the generated stress results in droplet formation. Hence, the applied waveform is effective on the droplet shape. Drop spacing is an important factor during printing which is defined as the distance between the center of two adjacent droplets on the substrate and can greatly affect film surface coverage [7]. If drop spacing is either too large or too small then it can cause a non-uniform and low resolution layer. Inkjet printing was performed using a Dimatix DMP-2850 inkjet printer equipped with disposable cartridges containing 16 nozzles with 10 pL nominal droplet volume, 254 µm spacing and 21.5 µm in diameter.

The suitable drop spacing for the prepared ink to print on stainless steel K41 was optimized as 35 µm. A single nozzle was used for printing to get higher resolution. The printhead was adjusted on a distance of 1mm from the substrate. The operating temperature was also optimized. Both printhead and substrate/stage were heated to 40°C and 60°C respectively. Then the sample was thermally cured at 600°C for 1 hour.

Results and discussion

$Mn_{1.4}Co_{1.4}Cu_{0.2}O_4$ nanoparticles were synthesized using the Pechini method. Structural characterization was checked on a D8 Advance Bruker X-ray diffractometer (XRD) with Cu-Kα radiation source.

Fig.1 displays XRD patterns of Cu-doped $MnCo_2O_4$ spinel powders at different calcination temperatures: 500, 550, 600, 800°C. The XRD pattern of the non-calcined powder is showing that the crystalline phase is not formed yet. It seems that the cubic spinel phase is formed after calcination at 500°C. It is obvious that there is a phase transition between 500°C and 550°C. The reference lines of the cubic and tetragonal $MnCo_2O_4$ spinel in Fig.1 confirm the phase transition from cubic to tetragonal crystalline phase. The cubic spinel can be identified by nine peaks which can be respectively assigned to the diffraction lines produced by the (111), (220), (311), (222), (400), (331), (422), (511) and (440) planes of $MnCo_2O_4$.

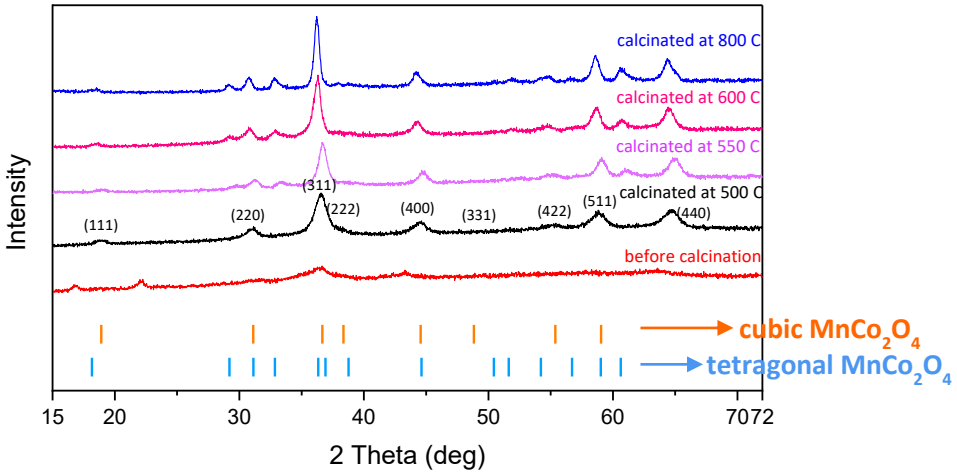

Fig.1. XRD patterns of synthesized $Mn_{1.4}Co_{1.4}Cu_{0.2}O_4$ nanoparticles at different calcination temperature

Comparing tetragonal spinel patterns, it is found that by increasing calcination temperature the dominant peak at around 36° is getting sharper which means the crystalline quality is improving. This can be also confirmed by SEM images (Fig.2) in which the crystalline facets can be easily distinguished for the powder calcined at 800°C. Later, it is shown that the particle size measured by DLS is in agreement with SEM images.

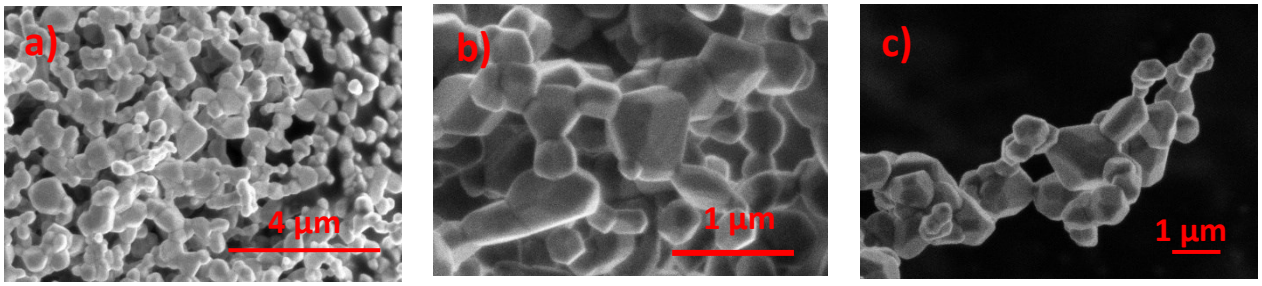

Fig.2. SEM images of the synthesized $Mn_{1.4}Co_{1.4}Cu_{0.2}O_4$ nanoparticles via the Pechini method (and calcined at 800° C)

Thermogravimetric analysis (TGA) was performed on around 8 mg of spinel powder using alumina crucibles (Fig.3). The mass change was recorded between room temperature and 900°C in flowing air (20 mL/min) at 10°C/min heating and cooling rates. Measurement was performed for the samples calcined at different temperatures. It is observed that the weight change is largest for the sample which was calcined at 400°C followed by the one calcined

at 500°C. Considering these two powders, the weight loss in the first 200°C come from water evaporation and at higher temperatures can be the result of impurity removal and the cubic/tetragonal phase transformation. The powders calcined at 600°C and 800°C show more stable trends, since the higher calcination temperature already removed the impurities. It can be concluded that the spinel powders calcined at 600°C and 800°C are stable at high temperature. Hence, the Cu-doped $MnCo_2O_4$ synthesized powder was selected to use in ink-jet printing.

As described in the previous section, particle size is one of the key parameters in ink-jet printing. Particle size can be controlled within the last two steps of the Pechini synthesis

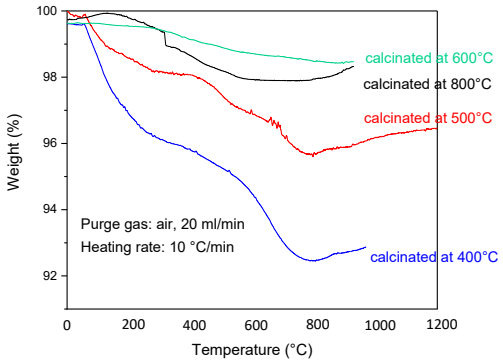

Fig.3. Thermogravimetric analysis of Cu-doped $MnCo_2O_4$ powder and the weight change as a function of temperature

process: milling and the calcination temperature/ramp (the schematic of the method is displayed in Fig.4a). Figs.4b & 4c show the particle size distribution before and after milling. DLS measurement (Fig.4b) showed that as-synthesized particles' size (non-milled particles) were on average in the range of 340 nm. Although this was still acceptable for printing, particles were milled further to control the size and obtain a homogeneous powder in order to improve the ink quality and to avoid agglomeration and nozzle clogging. Fig.4c displays nanoparticle size distribution after using roll milling, in the range of 200nm. Milling was performed before calcination; otherwise, if it is performed after crystalline formation, it may destroy powder crystallinity. Fig.4d shows an image of the formulated ink, and in Fig.4e the surface tension measurement of the ink is observed.

https://doi.org/10.5281/zenodo.4561900

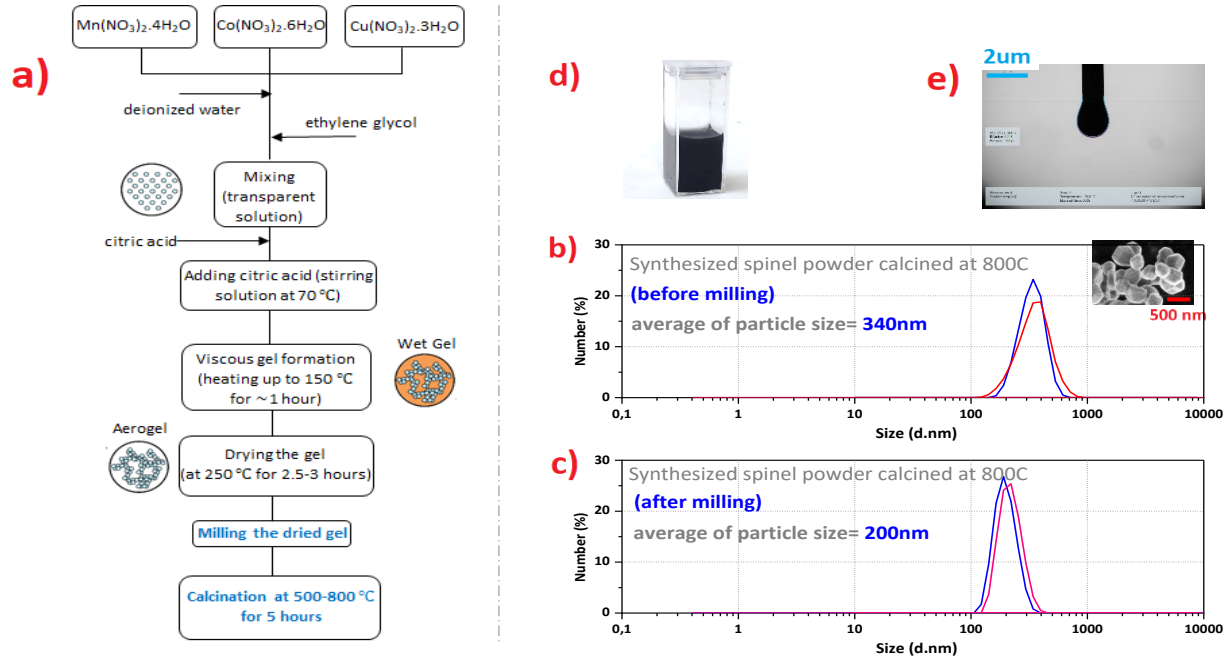

Fig.4. a) Schematic of Pechini process used to synthesize Cu-doped $MnCo_2O_4$ spinel powders, b) particle size distribution of the non-milled synthesized powder calcined at 800°C, c) particle size distribution of the synthesized powder after milling and then calcined at 800°C, d) an image of formulated ink, e) surface tension measurement of the ink using pendant drop method

The formulated ink containing milled synthesized particles (calcined at 800°C) was used for DOD ink-jet printing, with the schematic displayed in Fig.5a. On the jetting waveform, we can control the shape of the pulse to the nozzle to eject the droplets. Fig.5b shows the applied waveform which creates the pulsed voltage on the piezoelectric and then the piezoelectric deformation results in drop formation. Thus, it makes sense that the drop shape is highly dependent on the jetting waveform, ink surface tension and viscosity. If jetting waveform is not appropriate or if the properties of the ink are not meeting criteria, then the single droplet may not form. In this case, the droplets may eject with satellites or tails, which decrease the printing resolution and will deposit a non-uniform layer. In Fig.5e different drop formations are shown as the result of different nozzle voltage. From right to left (in Fig.5e) voltages of 14-26V were applied to the nozzles at the same time. The formed droplets show that the higher the voltage applied, the faster the drop formation. The tail effect is dominant at higher voltages. A satellite droplet is also observed applying 16V to the nozzle. So here the nozzle with 14V applied voltage is the only case which formed a single droplet. In Fig.5c & 5d, the drop formation from the nozzles with 14V and 22V applied voltages are compared in detail. The drop formation is shown with elapsed time intervals, in which the tail effect and the single droplet can be found for the nozzles with 14V and 22V respectively. On the other hand, it should also be considered that too low voltage can be insufficient to eject the droplet and clog the nozzles. The results were obtained in the state of substrate and printhead heating up to 60°C and 40°C, respectively. It should be noted that temperature also affects the drop shapes (because viscosity is temperature-dependent), and a small change in temperature may form different droplets at the same mentioned applied voltage.

https://doi.org/10.5281/zenodo.4561900

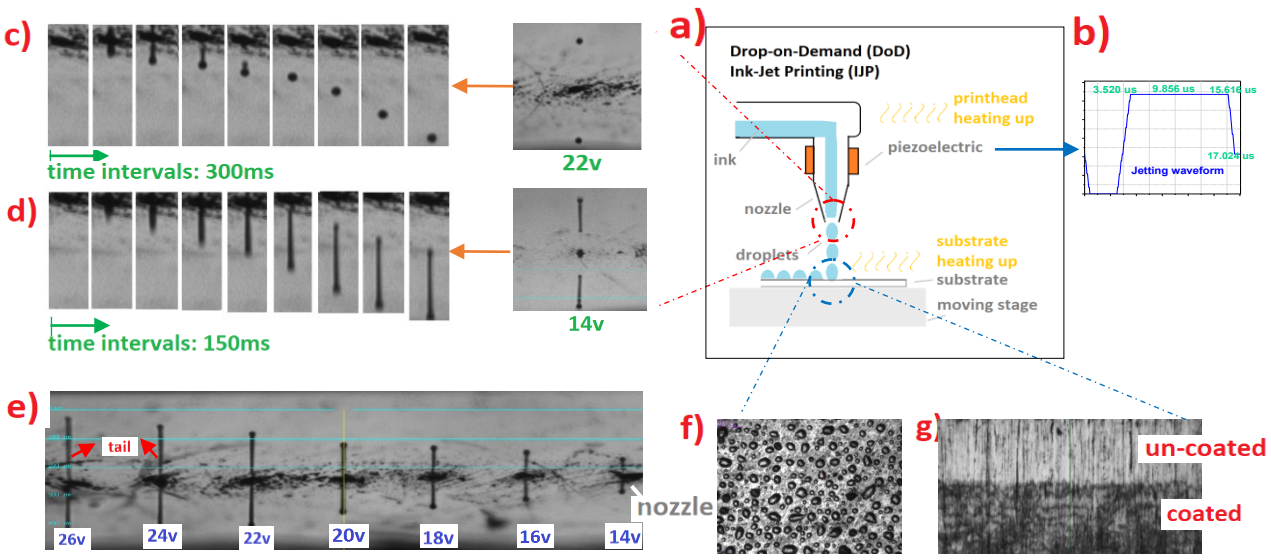

Fig.5. a) Schematic of DoD ink-jet printing with piezoelectric actuator, b) pulsed jet applied to the nozzle, c) drop ejection from a nozzle with applied 22V in different time intervals, d) drop ejection from a nozzle with applied 14V in different time intervals, e) satellite and tail effects of droplets using different jet frequencies, f) non-ideal drop spacing (large spacing), g) printed layer of $Mn_{1.4}Co_{1.4}Cu_{0.2}O_4$ spinel powders on stainless steel K41

Drop spacing is also one of the key parameters to print a uniform layer, as explained above. It highly depends on the ink-substrate interaction and ink properties itself. So, the drop spacing should be optimized for any specific ink. Here, 35µm was found to be the optimum spacing. The short drop spacing causes drop overlaps and the large spacing results in a non-uniform printing (Fig.5f shows a case of a large drop spacing). Finally, based on the mentioned operating parameters, the formulated ink was printed.
on the substrate and then thermally cured at 600°C for one hour. Fig.5g shows a printed sample , and film characterization will be performed next.

Conclusion

$Mn_{1.4}Co_{1.4}Cu_{0.2}O_4$ spinel nanoparticles were synthesized using the Pechini method and characterized. The purpose is to coat a spinel layer on SOFC interconnects (stainless steel K41) as protective layer in terms of chromium mitigation using the ink-jet printing method. A printable ink was formulated in which the synthesized powders were dispersed. First printing was performed using the formulated ink. The following points are drawn as conclusion:

- Calcination temperature for the synthesized powder was optimized. Based on the results, the sample calcined at 800°C showed more qualified crystallinity.
- Different solvents were studied and a mixture of 1,2 propanediol, isopropanol and water including Cu-doped $MnCo_2O_4$ with 200nm average size was considered as ink for printing.
- Polyvinyl pyrrolidone (PVP) additive was used to improve ink stability for long-term usage and to obtain a well-dispersed and agglomerated-free ink.
- The Z parameter (printability factor) was obtained as 4.09, which is within the acceptable range.

https://doi.org/10.5281/zenodo.4561900

- The operating printing parameters were optimized: substrate/printhead temperature, drop spacing, jetting waveform, applied voltages to the nozzles, substrate/printhead distance, and number of nozzles for printing.

Acknowledgment

This project has received funding from the European Union's Horizon 2020 research and innovation program under grant agreement no. 874577 for the NewSOC project.

References

[1] Johan E. ten Elshof and Yang Wang, Advances in Ink-Jet Printing of MnO2-Nanosheet Based Pseudocapacitors, Small Methods 3, 1800318, 2018.

[2] Dimesso L., Pechini Processes: An Alternate Approach of the Sol–Gel Method, Preparation, Properties, and Applications, Handbook of Sol-Gel Science and Technology, Springer International Publishing Switzerland 2016.

[3] Lesch A., Print-Light-Synthesis of Platinum Nanostructured Indium-Tin-Oxide Electrodes for Energy Research, Adv. Mater. Technol. 3, 1700201, 2018.

[4] P. Calvert, Inkjet Printing for Materials and Devices, Chem. Mater. 13, 3299, 2001.

[5] N. Reis, C. Ainsley, B. Derby, Viscosity and Acoustic Behavior of Ceramic Suspensions Optimized for Phase-Change Ink-Jet Printing, J. Am. Ceram. Soc. 2005, 88, 802.

[6] B. Derby, Annu. Inkjet Printing of Functional and Structural Materials: Fluid Property Requirements, Feature Stability, and Resolution Rev. Mater. Res. 40, 395, 2010.

[7] O.N. Aoife Morrin, Eimer O'Malley, Nigel Kent, Simon E. Moulton, M.R.S. Gordon, G. Wallace, Anthony J. Killard, The Fabrication and Characterization of Inkjet Printed Polyaniline Nanoparticle Films, Electrochim. Acta 53, 5092–5099, 2008.

Keywords: EFCF2020, SOx
Session B16: Lifetime: Interconnects and contact layers

B1607

Application of composite coatings as protection/contacting layers for metallic *high-chromium-content* SOFC interconnect material

Viktar Sauchuk (1), Nikolai Trofimenko (1), Stefan Megel (1), Stefan Rothe (1), Jochen Schilm (1), Martin Andritschky (2), Michael Hiller (3), Claudia Goebel (4), Jan Froitzheim (4), Mihails Kusnezoff (1)
(1) Fraunhofer IKTS
Winterbergstraße 28, 01277 Dresden/Germany
(2) Minho University, Center of Physics, Braga/Portugal
(3) High Tech Coatings GmbH – a Miba Group company, Vorchdorf/Austria
(4) Chalmers University of Technology, Göteborg/Sweden

Contact authors: www.EFCF.com/ContactRequest

Abstract

Oxidation of the surface of metallic chromium oxide forming metallic interconnect (MIC) can cause up to one third of the total SOFC stack degradation during the long-time operation at elevated (750 - 850 °C) temperatures. The application of protective coatings is the most effective method not only for reduction of the growth of oxide scales but also for prevention of evaporation of Cr-containing species from MIC and of the poisoning of the air electrode. Two approaches to form the protective layers on the surface of CFY interconnect material with high chromium content (~ 94 %) have been tested. The CuNiMn-spinel (CNM) coatings were deposited using the wet powder spraying (WPS) of the slurries. As an alternative approach physical vapour deposition (PVD) method was used to apply thin metallic films on the surface of MIC and to form the protection layer by in-situ oxidation under the stack relevant conditions. The experiments were carried out at first using the model samples of different geometries to evaluate the properies and efficiency of the coatings. Composite pastes with addition of perovskite powders were also tested, because the CNM layers densify at SOFC operating conditions and shrinkage during long-term operation can cause the decrease of the contact area between the components and accelerate the degradation of the stack performance. The experiments have shown that the perovskite additive can efficiently reduce the shrinkage compared to the pure CNM material and match it well to the shrikage of other stack components. Moreover, the perovskite additive do not deteriorate the electrical properties of the composite since the perovskites have electrical conductivity comparable to CNM. The PVD coatings were tested in combination with CNM containing contacting layers applied by screen printing to reduce the chromium release rate. The experiments have shown a good compatibility and mechanical stability between the contacting layer and PVD protective coating during operation and thermal cycling. The materials and composites have been characterized by scanning electron microscopy (SEM/EDX), optical dilatometry and electrical conductivity measurements. Finally, the most promising material combinations obtained for model samples were transferred to SOFC stacks MK35x and evaluated under real operation condition.

https://doi.org/10.5281/zenodo.4561995

Introduction

Degradation of the stack performance during the long-term operation is the main challenge in the development and application of the solid oxide fuel cells. The oxidation of the interconnect material accompanied by the growth of the oxide scale (i) and the Cr-evaporation (ii) from the metallic interconnect are considered to be the main factors influencing the degradation of the stack operating at high temperatures (above 800 °C). The growth of the oxide scale takes place at the interconnect surface even in the reducing ambience of the anode gas [1] since the small quantities of oxygen or moisture (H_2O, OH^-) can be enough to form the oxide scale on the MIC surface. There are different approaches to create the reliable protective layers on the surface of interconnects to prevent or reduce their oxidation. The perovskite layers applied by atmospheric (APS) or high-velocity oxygen fuel (HVOF) spraying are used for a long time [2, 3] as the relative reliable protective coatings at the cathode side of SOFC interconnects. The perovskite layers applied by these methods are dense and stable. However they have often the layered structure with various micro-cracks typically generated during the spraying process [4], facilitating the penetration of oxygen to the metallic surface of interconnect. Apart from, the dense perovskite layer hinder the interlayer diffusion of elements, what can result in formation of high ohmic overlays (like Cr_2O_3, SiO_2) accelerating dramatically the stack performance degradation. The spinel materials are good alternatives to the perovskite protective coatings [5]. First of all, they can be densified at the SOFC stack operating temperatures allowing relatively easy interdiffusion of the elements (Cr, Mn, Co, Ni: depending on interconnect and spinel compositions) from interconnect, which is important for metal interconnect materials with high chromium contents (like CFY). Such a feature of spinel materials leads to the doping of the spinel protective layer or even to formation of the solid solution having good electric conductivity at the stack operating temperatures. Due to their good sinterability and reactivity the spinel protective layers can be suitable for application by relatively low-price deposition methods: wet powder spraying (WPS), screen printing, roll-coating. One of the promising ways to form the protective layers on interconnect surface is the vacuum deposition (PVD, CVD) of thin metallic films with well defined stoichiometry followed by their in-situ oxidation during the stack sealing and initialization.
A chromium-based alloy CFY containing 5 % iron by weight as well as the traces of yttrium was used as metallic interconnect (MIC) material. Physical properties of the CFY alloy make it ideal for use in high-temperature fuel cells, however a very high content of chromium sets down the special requirements to the properties and to the quality of protective layers. Two types of coatings were tested in our experiments: CuNiMn-spinel (CNM) pastes were deposited using the wet powder spraying (WPS) and physical vapour deposition (PVD) method was used to sequentially apply thin metallic films on the MIC surface and to form the protective layer by in-situ oxidation under the stack relevant conditions.

1. Experimental

A modified spray gun TR 80 LCD of the company REKA was used to apply the CNM spinel slurries (pastes) by the wet powder spraying (WPS). An advantage of this gun is the possibility to vary the temperature of the sprayed medium (from room temperature up to 100 °C and even higher), which allows the flexibility in setting the slurry viscosity and, correspondingly, effective control of the uniformity of the layers deposited on interconnects with structured surface. Physical vapour deposition (PVD) method was used as a second deposition technique to apply the thin metallic films on the surface of MIC. The coatings

were deposited by unbalanced magnetron sputtering from three pure metallic targets Co, Mn and a rare earth (RE) metal. The samples were mounted on a substrate holder, introduced into a vacuum system, pumped to a base pressure < $2 \cdot 10^{-5}$ mbar and subjected to a plasma treatment to remove some native oxide scales and to activate their surface, enhancing the adhesion of the metallic coating. The metallic coating was deposited adjusting the power to the Co and Mn targets to achieve a Co:Mn ratio of 50:50. The overall coating thickness of as-deposited metals was approximately 4 µm. The formation of protective layer was carryed out by in-situ heat treatment of the sample or interconnect under the stack relevant conditions to achieve a uniform transformation of the metallic layer into a metallic oxide (RE-CoMn-Oxide). To evaluate the properies and efficiency of the coatings, the coating materials were testet initially using the model samples of high chromium material CFY. The chromium evaporation tests were carried out at the Chalmers University using the denuder technique described in [6]. The structured symmetrically joined samples with area of 20×20 mm^2 cut from the interconnects were prepared for the time dependent measuremnts of electrical resistance. The contact ribs in symmetric samples were applied in all the cases by the screen printig of the CNM-pastes. The resistance measurements (ASR) were carried out withing two thermal cycles in the stagnant air ambience at the stack relevant temperatures. The samples were cut and polished for the cross-section analysis using SEM imaging and EDX analysis.

2. Results and discussions

Influence of protective coatings on Cr-evaporation from the CFY interconnect material

The efficiency of different types of protective coatings for the CFY MIC material was firstly tested in chromium evaporation experiments at temperature 850 °C under humidified (3 % H_2O) air gas flow. The possibility of the time resolved measurements with the denuder technique gives information about the rate of chromium evaporation from the material as a function of time. Figure 1 shows the Cr vaporization versus exposure time for the uncoated, the PVD RE-CoMn-coated, and the CNM paste-coated CFY interconnect material.

The uncoated CFY material does evaporate significantly more chromium compared to the coated samples: the Cr vaporization rates for both the RE-CoMn PVD- and CNM WPS-coated coupons were more than one order of magnitude lower than the rate for the uncoated material. The difference between the RE-CoMn PVD- and CNM WPS-coated samples was not so pronounced as in the case of uncoated material (only 10 – 15 % difference). However, it should be noted that the thickness of the PVD layer was about three times smaller after formation of oxide scale in comparison with the CNM ones.

https://doi.org/10.5281/zenodo.4561995

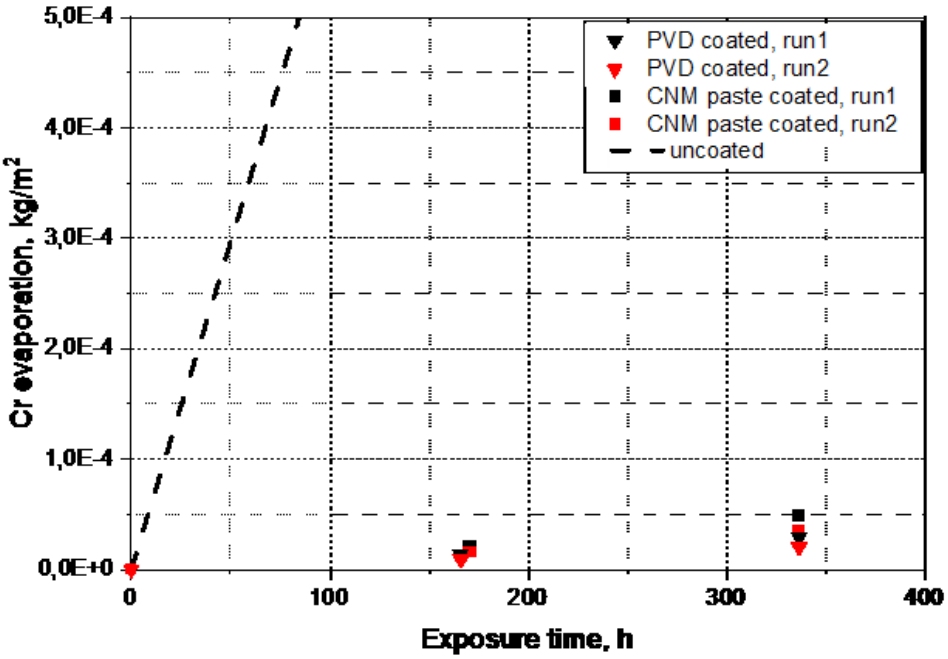

Fig. 1. Cr-evaporation as a function of exposure time for PVD-coated (triangles), CNM paste-coated (squares) and uncoated (dashed line) CFY samples in air containing 3% H_2O with a flow rate of 6000 sml/min (two runs for each type of samples).

Electrical Resistance

The influence of different protective coatings on performance of the CFY MIC material was also tested using the time dependent measurements of resistance of symmetrically joined samples within two thermal cycles at the SOFC stack relevant operating conditions via 4-probe method. The the area specific resistance (ASR) values can be then evaluated from resistance using the simple equations:

$$R = \frac{U}{I};\ ASR_{sample} = R \cdot A,$$

and, taking into account the symmetrical cell assembly: $ASR = \frac{R \cdot A}{2}$,

R – resistance, *U* – voltage; *I* – current; *A* – contact area.

The diagram of the change of resistance of the CFY samples with the RE-CoMn PVD and CNM WPS coatings within two thermal cycles is presented in Figure 2.

https://doi.org/10.5281/zenodo.4561995

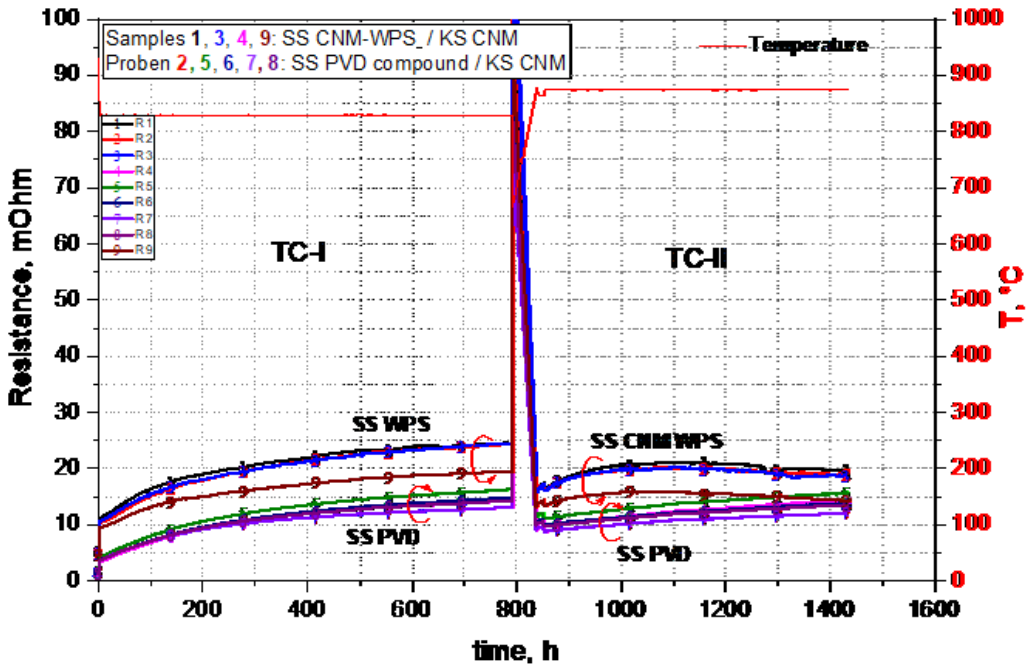

Fig. 2. Time dependent development of resistance of symmetric model samples coated with RE-based PVD- and CNM spinel WPS-layers (SS) within two thermal cycles and contacted with CNM paste (KS). TC-I: T ~840 °C; TC-II: T ~875 °C.

Both types of coatings have shown the similar behaviors during the first thermal cycle of measurements: (i) an increased parabolic gain of resistance at initial phase of the experiment (150 – 200 h) followed by (ii) slow nearly linear further increase of resistance. The parabolic behavior of the resistance dependence is typical for the metallic interconnect materials and is determined by oxidation processes at the MIC surface. At the beginning of the process, the coatings are not dense enough and cannot prevent the penetration of oxygen to the surface of interconnect. Oxidation of the MIC is accompanied in both cases by the intensive initial formation of the oxide scale at the metal surface due to reaction of chromium with penetrating oxygen. Apart from, the oxidation of deposited metallic films takes place in the samples prepared by the PVD techniques contributing to acceleration of the oxide scale formation. In the samples prepared by WPS from the CNM spinel paste the formation of the dense protection layer takes place gradually due to the sintering of the powder particles of CNM material. After formation of the densified protective layers, the growth of the oxide scale at the MIC surface goes more slowly (stage ii). The samples with the PVD coating have the lower starting resistance due to the smaller total thickness of the layer as compared to CNM WPS layer even after complete oxidation of deposited metallic components. The surprising behavior of the samples with the CNM spinel coating was observed during the second thermal cycle of the resistance measurements. This cycle was carried out at temperature of 875 °C that is about 25 – 30 °C higher than the standard stack operation temperature and was aimed to simulate conditions of accelerated stack degradation. The parabolic-like course of the resistance dependence at the beginning of the second cycle was similar to one in the first cycle. However the negative value of resistance change was observed in these samples after nearly 200 h of measurements. Such a behavior of the samples we can attribute to high reactivity of the spinel materials at increased temperatures. At the beginning of the second thermal cycle, the change of composition of the adjacent to interconnect protection layer on the basis of CNM spinel takes place due to enhanced diffusion of chromium atoms to interconnect surface and owing to increase of the thickness of the chromium oxide scale.

https://doi.org/10.5281/zenodo.4561995

Chromium oxide have much higher resistivity than the pure CNM material [5, 7]. Therefore the resistance of the CNM-coated samples increases at the beginning of the second cycle. After saturation of the surface layer with chromium oxide, the further oxidation of MIC is hindered. The high temperature process is further governed by diffusion of chromium into the CNM coating resulting in the mutual doping or even in formation of solid solution on basis chromium containing species and CNM, which have the higher electrical conductivity as compared to pristine compounds [5]. Additionally, the sintering CNM is accelerated due to increased temperature. This leads to reduction of the total layer thickness, to improvement of the contact area and to negative tendency of the resistance dependency during the second thermal cycle.

The dramatic influence of amount of chromium oxide on conductivity of the CNM coatings was proved by measurements of resistance of the CNM samples with different content of admixed chromium oxide powder. Three powder compositions with ratios CNM:Cr_2O_3 as high as 90:10, 75:25 and 50:50 (mol. %) were prepared by thorough mixing of corresponding powders and compared with pure CNM material. The standard screen printing pastes were manufactured from these compositions, printed as the rectangular samples onto 8YSZ substrates and sintered at temperature 1100 °C for 50 hours. The temperature dependence of resistance of the samples was measured via 4-probe method in temperature range between room temperature and 950 °C. Figure 3 shows the temperature dependence of resistance of the samples with different content of chromium oxide.

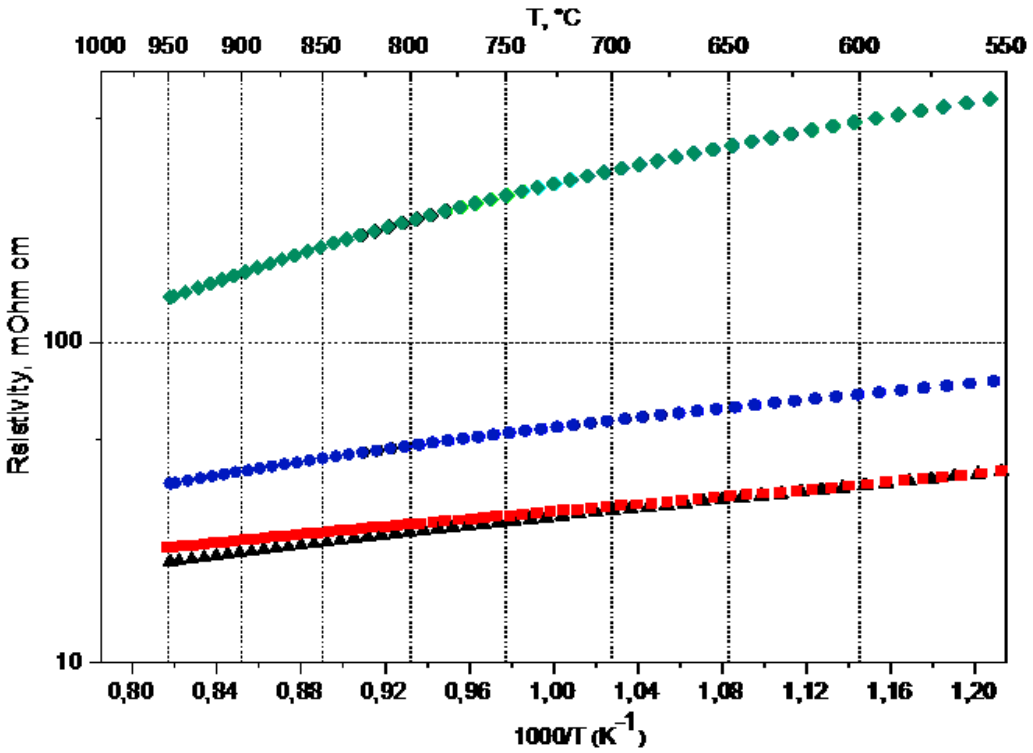

Fig. 3. Temperature dependence of resistance of sintered paste samples containing different ratios of CNM spinel compound and Cr_2O_3 (■ - pure CNM material; ▲ - CNM:Cr_2O_3=90:10; ● - CNM:Cr_2O_3=75:25; ◆ - CNM:Cr_2O_3=50:50).

It can be seen that the presence of small amounts of chromium oxide in the spinel layer do note deteriorate sufficiently the electrical conductivity of the material, which can be attributed to formation of the doped CNM spinel or of solid solution with chromium oxide. However the resistance of the composition increases remarkable with the increase of the Cr_2O_3 content in the samples. The resistance of the sample containing 50 % of high

resistive chromium oxide is one order of magnitude higher compared to the resistance of material with low content of Cr_2O_3.

Microstructure of coatings

Microstructure of the coatings was analyzed after two cycles of measurements (total time about 1600 h) at the stack relevant conditions. The SEM images of polished cross-sections of the samples are presented in the Figure 4.

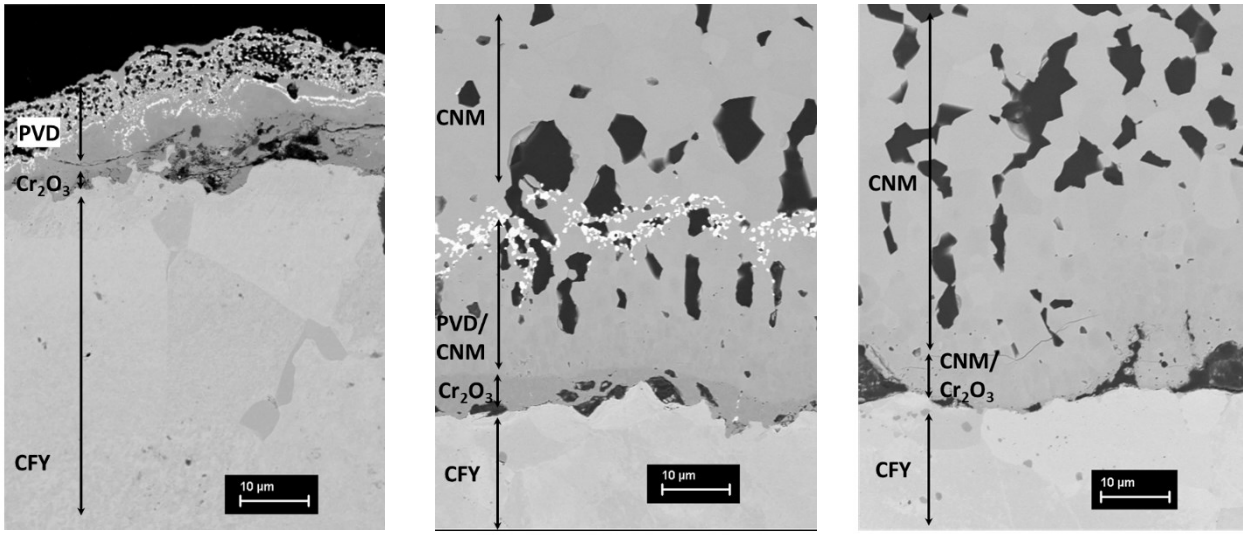

a b c

Fig. 4. SEM images of polished cross-sections of the layers formed from PVD-deposited RE-CoMn thin films (a), PVD-deposited films in contact with CNM paste (b), and WPS-deposited CNM paste (c).

The oxidation process of thin metallic RE-CoMn thin films deposited by PVD is accompanied by the exchange of Co and Mn between the layers at 850°C and should, ideally, result in formation of the uniform interlayer at the surface of the metallic interconnect. In fact, it can be seen, that the RE-CoMn PVD deposit forms the multicomponent structure. Moreover, this structure is dense only at the interface to MIC whereas the surface of the newly formed layer is pretty porous (Fig. 4a). Apart from, the oxidized RE-metal forms an additional interlayer which is very thin and is not continuous.
On the other hand, the formation of the dense protective layer from the CNM spinel particles applied by WPS technique takes place during high temperature treatment of the deposited paste/slurry (Fig. 4c). Due to good sinterability of the CuNiMn spinel compound at temperatures below 900 °C, the formed layer possess only the closed porosity, is uniform and has a good adhesion to interconnect surface. It can be seen from the SEM images of cross-sections in Figure 4, that the layer formed from the PVD deposited metal films in combination with CNM contact paste (Fig. 4b) has the dense uniform microstructure at the interface to interconnect. The RE-based interlayer probably provides an additional barrier against the chromium diffusion into the coating hindering its diffusion to CNM and evaporation of chromium volatile components at operating temperatures of the SOFC stack. The efficiency of such approach is illustrated by the chromium distribution analysis presented in Figure 5. Chromium concentration was lower in the structure formed from the PVD + CNM combination as compared to solely CNM WPS layer at equal distances to interconnect surface. The sharp drop of Cr concentration is remarkable between the points 2 and 3 in the layer combination RE-CoMn PVD + CNM as compared to slow decrease one in the samples with only CNM-WPS layer, confirming the higher efficiency of PVD + CNM-paste combination.

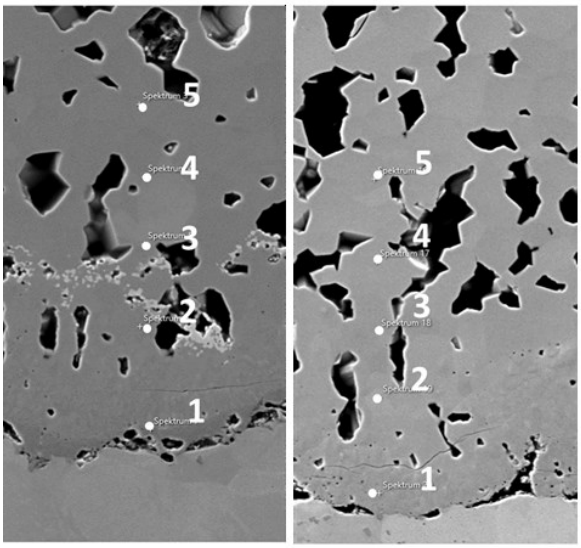

a b

	Chromium concentration, at. %	
Position	PVD+CNM	CNM
1	32,12	22,21
2	7,84	8,72
3	4	7,14
4	4,65	4,89
5	2,84	4,08

c

Fig. 5. Cross-sections of layers formed from PVD deposited RE-CoMn films + CNM paste (a) and only from WPS CNM paste (b), and chromium distribution in these layers (c).

The similar microstructure resulting from this material combination was also observed in the real SOFC stack post-test analysis of cross-sections of the interconnects after operation for 3000 h (Fig. 6).

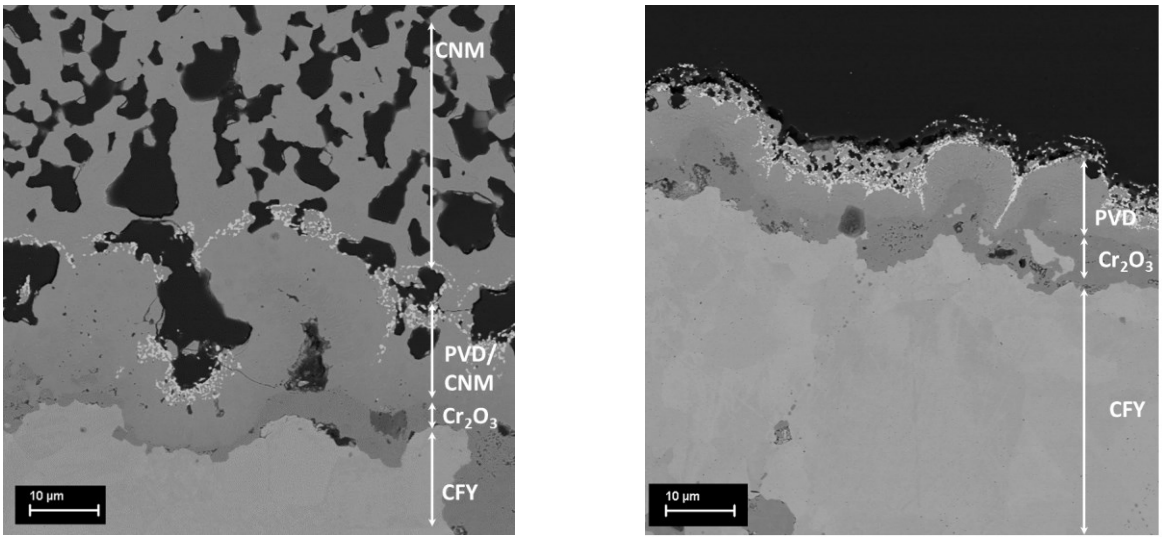

a b

Fig. 6. SEM images of polished cross-sections of interconnect samples with RE-CoMn-PVD coating cut from the real stack after operation for 3000 h at different positions: a) PVD-deposited films in contact with CNM rib; b) air flow channel with PVD coating only.

The porosity of the composite layer in the stack (Fig. 6a) is higher than in the model samples (Fig. 4b) because of almost twice longer holding time at high temperature (3000 h and 1600 h correspondingly) and therefore longer sintering time of the CNM material.

https://doi.org/10.5281/zenodo.4561995

Influence of perovskite addition on high temperature behavior of CNM spinel material

Due to the good reactivity of its constituents, the spinel materials, based on combinations of Mn, Co, Fe, Ni, Cu components, show an enhanced sinterability at operation temperatures of SOFC stacks, facilitating the possibility of formation of reliable contacting between different components of the stack. At the same time, the sufficient shrinkage of the material can occur during a long operation times of the SOFC stack at elevated temperatures. This causes in turn the reduction of the contact area between the stack components up to full contact loss due to mechanical disruption, especially during the thermal cycling because of difference of the thermomechanical properties of the stack components: interconnect, protective/contact layer, sealing glass, electrolyte. In this case, the formation of the composite layers consisting of mixtures between the spinel and perovskite materials can be used as an effective countermeasure. Figure 7 demonstrates the temperature dependence of the shrinkage of the material composed from mixture of CuNiMn-spinel and LSM-based perovskite (50:50 by weight) in comparison to the samples made from the pure CNM-spinel. The holding of the samples at temperature of 950 °C (~100 °C higher than the stack operating temperature) was applied to simulate the accelerated degradation conditions.

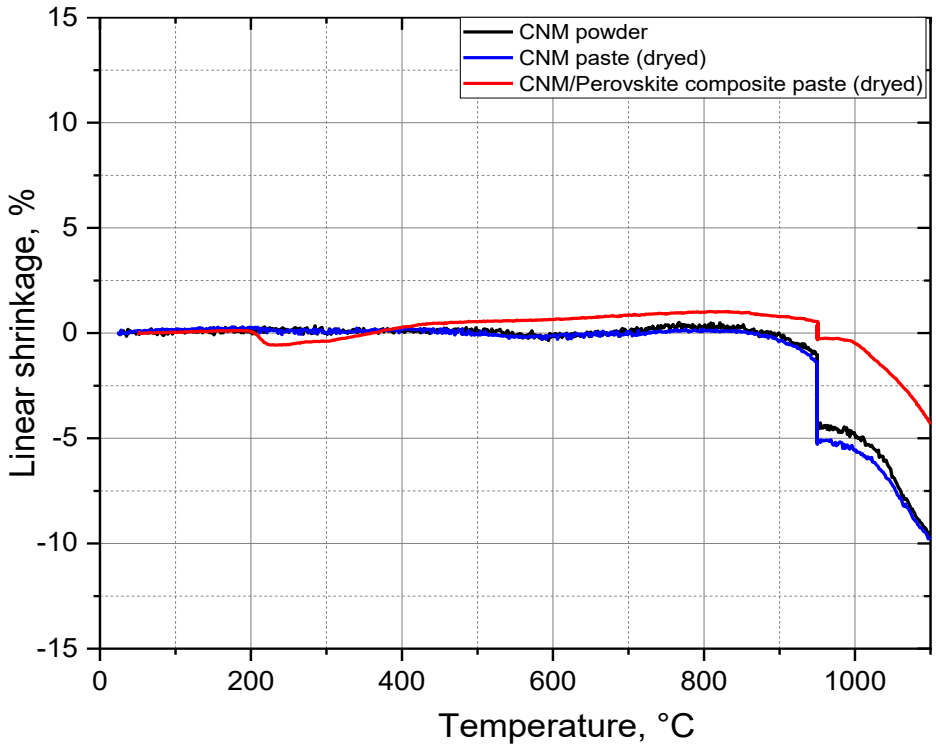

Fig. 7. Comparison of linear shrinkage of pure CNM spinel material and of composite CNM + LSM based perovskite.

Perovskites have the higher sintering temperature (> 1100 °C) [8] and cannot be dense sintered at SOFC stack operating temperatures (~850 to 950 °C). The CNM material acts in this case as the sintering aid for the mixed composition CNM + LSM based perovskite providing the good joining of particles in the composite layer and for almost no change of electrical properties as compared to the pure CNM material (Fig. 8). At the same time the perovskite particles form the backbone matrix preventing excessive sintering and the shrinkage of the combination protection/contacting layer.

https://doi.org/10.5281/zenodo.4561995

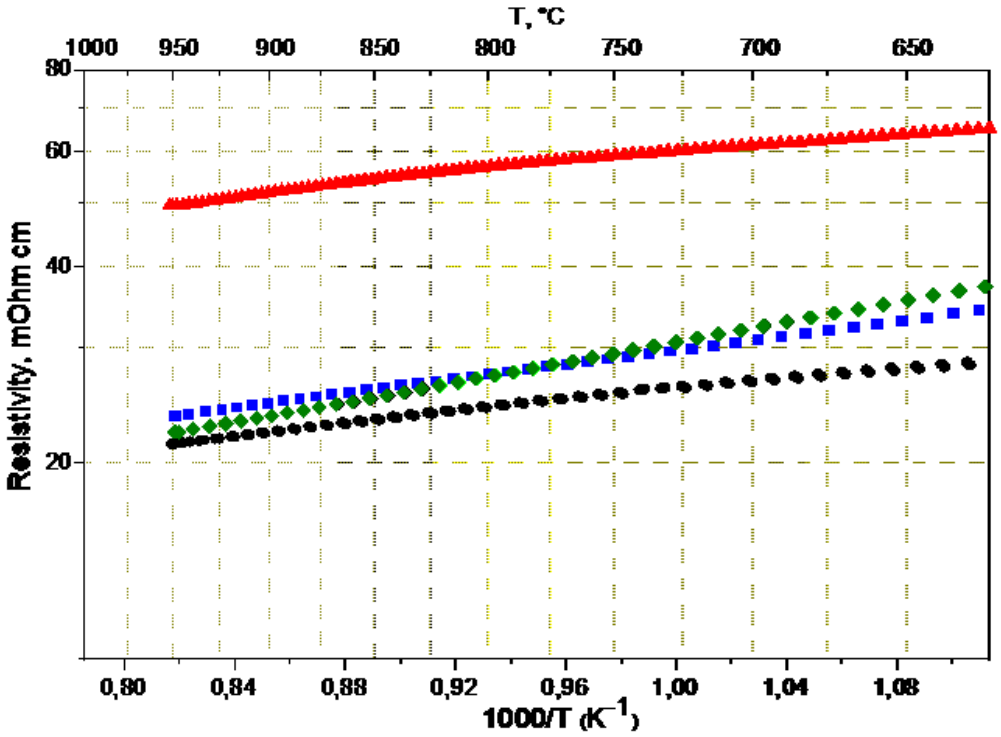

Fig. 8. Resistivity of sintered at 950 °C composite CNM:LSM = 75:25 (mol.%) (◆) in comparison with resistivity of samples sintered from pure CNM (■), LSM (▲), and perovskite cathode (●) sintered at 1350 °C.

Conclusions

Effective chromium retention coatings could be prepared on the surface of the *high-chromium-content* CFY interconnect material by different techniques: the CuNiMn-spinel coatings were deposited using the wet powder spraying (WPS) method; thin metal Co, Mn, and RE (RE-CoMn) films were applied by physical vapour deposition (PVD) followed by in-situ oxidation at SOFC stack operation conditins. Both types of coatings have shown comparable efficiency to reduce the release of chromium volatile components from CFY interconnect material. The Cr vaporization rates for both the RE-CoMn PVD- and CNM paste-coated material were more than one order of magnitude lower than the Cr vaporization rate of the uncoated material. The combination of both techniques results in formation of the coating/contacting composite layer with enhanced chromium retention and improved electrical properties. The composite layers formed on the basis of perovskite and CNM spinel powder mixtures can be used to improve the long-term thermomechanical and electrical performance of the coating and contacting layers. Testing of these materials combinations is now in progress in the SOFC stacks.

Acknowledgments

The authors are kindly grateful to Federal Ministry for Economic Affairs and Energy (BMWi) for funding of these researches (support code 03ET6120A).

References

[1] Mihails Kusnezoff, Viktar Sauchuk, Christoph Folgner, Alexander Michaelis, Influence of metal coatings on the morphology and the structure of interconnect surface in anode gas ambience. Proceedings of the 41st International Conference on Advanced Ceramic and Composites. Ceramic Engineering and Science Proceedings, 2017, 38(3), pp.17–34

[2] Chun-Liang Chang, Chang-sing Hwang, Chun-Huang Tsai, Sheng-Fu Yang, Wei-Ja Shong, Te-Jung Darong Huang, Ming-Hsiu Wu, Development of Plasma Sprayed Protective LSM Coating in Iner, Advances in Solid Oxide Fuel Cells and Electronic Ceramics II: Ceramic Engineering and Science Proceedings, 2019, 37(3), XXXVII, pp. 19–30

[3] Jan Gustav Grolig, Gino Longo, Andreas Ma., Chromium Oxidation and Evaporation on Interconnects from a Stack and CHP- Systems Perspective, ECS Transactions, 2019, 91 (1), pp. 2181–2188

[4] Daniel Tejero-Martin, Milad Rezvani Rad, Andre McDonald, Tanvir Hussain, Beyond Traditional Coatings: Review on Thermal-Sprayed Functional and Smart Coatings, J. Therm Spray Tech., 2019, 28, pp. 598–644

[5] Viktar Sauchuk, Mihails Kusnezoff, Nikolai Trofimenko, Stefan Megel, Hans-Peter Baldus, Andreas Reinert, Development of effective protective materials for SOFC metallic interconnects. Proceedings of the 8th EFCF, Lucerne, Switzerland, July 2008, A0902

[6] J. *Froitzheim*, H. *Ravash*, E. Larsson, L. G. Johansson, J. E. *Svensson,* Investigation of Chromium Volatilization from FeCr Interconnects by a Denuder Technique, J. Electrochem. Soc., 157, (*2010*), pp. B1295–B1300

[7] D. de Cogan, G. A. Lonegran, Electrical conduction in Fe_2O_3 and Cr_2O_3, Solid State Communications, 15 (1984), 1517 - 1519

[8] Zongping Shao, Mozes O. Tadé, Intermediate-temperature Solid Oxide Fuel Cells, Chapter 5: Interconnect Materials for IT-SOFC, pp. 178 – 183 (2016)

Keywords: EFCF2020, SOx
Session B16: Lifetime: Interconnects and contact layers